

# **EXPERIMENTAL SEISMIC STUDY OF PRESSURIZED FIRE SPRINKLER PIPING SUBSYSTEMS**

by

Yuan Tian

November 9<sup>th</sup>, 2012

A dissertation submitted to the  
Faculty of the Graduate School of  
the University at Buffalo, State University of New York  
in partial fulfillment of the requirements for the  
degree of

Doctor of Philosophy

Department of Civil, Structural, and Environmental Engineering

UMI Number: 3554510

All rights reserved

INFORMATION TO ALL USERS

The quality of this reproduction is dependent upon the quality of the copy submitted.

In the unlikely event that the author did not send a complete manuscript and there are missing pages, these will be noted. Also, if material had to be removed, a note will indicate the deletion.



UMI 3554510

Published by ProQuest LLC (2013). Copyright in the Dissertation held by the Author.

Microform Edition © ProQuest LLC.

All rights reserved. This work is protected against unauthorized copying under Title 17, United States Code



ProQuest LLC.  
789 East Eisenhower Parkway  
P.O. Box 1346  
Ann Arbor, MI 48106 - 1346

Copyright by  
Yuan Tian  
2012

## ACKNOWLEDGEMENTS

For someone like me who is in his twenties, five years is quite a long period of time. The journey of obtaining a Ph.D. degree is like digging a tunnel accompanied by so much unknown, frustration and excitement. When I look back on the time I have spent in the Department of Civil, Structural and Environmental Engineering (CSEE) at University at Buffalo (UB), I feel that I have been extremely fortunate and blessed to be able to have an advisor like Dr. André Filiatrault. It does not take me long to feel his kindness to people, his attitude of diligence towards work, and the passion for life, all of which have had a great influence on me ever since I worked with him. From the bottom of my heart, I would like to express my sincere gratitude to Prof. André Filiatrault for his guidance, mentoring, leadership, and warmth throughout the period of my doctoral studies. Without his support, encouragement and patience during the difficult time I would never have been able to finish this journey.

I am also extremely grateful for the invaluable instruction and advice for the research work that I have received from Prof. Gilberto Mosqueda, who has been acting as my co-advisor and giving me countless precious assistance and suggestions throughout the period of my doctoral studies. My appreciation also goes to my committee member, Prof. Andrei M. Reinhorn, for reviewing this dissertation and providing me with his valuable comments.

Since this dissertation is primarily based on tremendous amount of experimental work, I would like to extend my gratitude to the technical staff of the Structural Engineering and Earthquake Simulation Laboratory (SEESL): Duane Kozlowski, Robert Stainiszewski, Chris Budden, Jeffrey

Cizdziel, Lou Moretta, Scot Weinreber, Chris Zwierlein, Goran Josipovic, Gerald Meyers, Mark Pitman and Myrto Anagnostopoulou. I would also like to thank Karol Przelazloski, Shawn Evilsizor and Jessica Fuchs for their strenuous efforts in the execution of experimental work and data processing.

The funding for this research work is provided by National Science Foundation under Grant No. CMMI-0721399 to the George E. Brown, Jr., Network for Earthquake Engineering Simulation Research (NEES Research). I am grateful for this support and the opportunity to get involved in such an exciting research program.

Last but not least, I would like to express my deepest gratitude to my parents, Shaoping Liao and Wen Tian, for their limitless love, faith, and support. Without them I would not have succeeded in making it to the end.

*Dedicated to my parents, Shaoping Liao & Wen Tian,*

*And my best friends, Xi Chen, Yuemin Liang, Zhiyuan Yu, & Wei Xie*

## TABLE OF CONTENTS

<b>ACKNOWLEDGEMENTS .....</b>	<b>iii</b>
<b>TABLE OF CONTENTS .....</b>	<b>vi</b>
<b>LIST OF TABLES .....</b>	<b>xii</b>
<b>LIST OF FIGURES .....</b>	<b>xiv</b>
<b>ABSTRACT.....</b>	<b>xxiii</b>
<b>Chapter 1 INTRODUCTION .....</b>	<b>1</b>
1.1 Project Background.....	1
1.2 Pressurized Automatic Fire Sprinkler System .....	2
1.3 Vertical Hangers and Seismic Bracing Systems .....	3
1.4 Code Provisions for Seismic Design of Fire Sprinkler Systems.....	6
1.5 Performance of Fire Sprinkler Subsystems during Previous Earthquakes .....	18
1.6 Aftermath of Fire Sprinkler System Failures during Earthquakes.....	26
1.6.1 Property loss .....	26
1.6.2 Loss of function .....	28
1.6.3 Fire hazard .....	28
1.6.4 Threat to life safety.....	29
1.7 Research Objectives.....	29
1.8 Organization of the Dissertation .....	31

<b>Chapter 2 LITERATURE REVIEW .....</b>	<b>32</b>
2.1 Study on Seismic-brace Components .....	32
2.2 Study on Joint Connections .....	34
2.2.1 Study by Antaki and Guzy (1998) .....	34
2.2.2 Study by Wittenberghe et al. (2010).....	35
2.3 Study on Piping Systems .....	37
2.3.1 Study by Dillingham and Goel (2002) .....	37
2.3.2 Study by Goodwin et al. (2007).....	39
2.3.3 Study by Hoehler et al. (2009).....	41
2.3.4 Study by Martínez (2007).....	42
2.4 Discussions .....	45
<b>Chapter 3 EXPERIMENTAL ASSESSMENT OF PRESSURIZED FIRE SUPPRESSION</b>	
<b>SPRINKLER PIPING TEE JOINTS.....</b>	<b>47</b>
3.1 Introduction.....	47
3.2 Selection of Materials and Joint Types.....	48
3.3 Description of Experimental Set-up and Test Specimens.....	50
3.3.1 Experimental set-up.....	50
3.3.2 Construction of test specimens .....	52
3.4 Test Program.....	55
3.5 Testing Protocol .....	57
3.6 Instrumentation .....	58
3.7 Definition of Damage State .....	61



3.8 Specimens Damage Observations.....	62
3.8.1 Damage observations on black iron pipe with threaded connections.....	63
3.8.2 Damage observations on CPVC pipe with cement joints.....	65
3.8.3 Damage observations on steel pipe with groove-fit connections .....	67
3.9 Experimental Results .....	73
3.9.1 Test results .....	73
3.9.2 Comparison of cyclic response of specimens with four joint types .....	76
3.9.3 Analysis of test data.....	77
3.9.4 Seismic fragility assessment of pressurized fire suppression sprinkler piping .....	79
3.10 Summary.....	84
<b>Chapter 4 EXPERIMENTAL ASSESSMENT OF FULL-SCALE PRESSURIZED FIRE SUPPRESSION SPRINKLER PIPING SUBSYSTEM .....</b>	<b>88</b>
4.1 Introduction.....	88
4.2 The University at Buffalo Nonstructural Component Simulator (UB-NCS).....	89
4.3 Testing Protocol .....	91
4.4 Selection of Materials and Joint Types .....	95
4.5 Description of Experimental Set-up and Test Specimens.....	97
4.5.1 Materials used in testing.....	97
4.5.2 Typical specimen geometry .....	107
4.5.3 Construction of test specimens .....	110
4.6 Test Program.....	112
4.7 Instrumentation .....	115

4.7.1 Acceleration.....	115
4.7.2 Rotation .....	118
4.7.3 Force .....	119
4.7.4 Displacement .....	122
4.8 Specimens Performance Observations.....	126
4.8.1 Specimen 1 .....	126
4.8.2 Specimen 2 .....	131
4.8.3 Specimen 3 .....	135
4.9 Experimental Results .....	139
4.9.1 Dynamic characteristics of test specimens .....	140
4.9.2 Comparison of dynamic response of test specimens .....	141
4.10 Summary .....	159
<b>Chapter 5 PARAMETERIZATION AND NUMERICAL MODELING OF FIRE</b>	
<b>SUPPRESSION SPRINKLER PIPING SYSTEMS .....</b>	<b>161</b>
5.1 Introduction.....	161
5.2 Development of Analytical Models for Piping Tee Joints.....	162
5.2.1 Evaluation of experimental hysteretic behavior of piping tee joints .....	162
5.2.2 Multi-linear Pivot model .....	164
5.2.3 Pinching4 Material model .....	172
5.2.4 Hysteretic Material model .....	176
5.3 Numerical Modeling of Fire Sprinkler Piping Systems.....	181

5.3.1 Implementation and validation of piping tee joint model in SAP2000 .....	181
5.3.2 Validation of piping tee joint model in OpenSees.....	193
5.4 Summary and Discussions .....	197
5.4.1 Summary.....	197
5.4.2 Discussions .....	197
<b>Chapter 6 INCREMENTAL DYNAMIC ANALYSES OF FIRE SPRINKLER PIPING SYSTEMS.....</b>	<b>199</b>
6.1 Introduction.....	199
6.2 Process of Incremental Dynamic Analyses (IDA).....	200
6.3 MCEER WC70 Building Model.....	202
6.3.1 Prototype of building model.....	202
6.3.2 Building model configurations .....	207
6.4 Earthquake Ground Motions.....	210
6.5 Seismic Fragility Analyses for Inelastic Building Models .....	214
6.5.1 Definition of failure (collapse of building model).....	214
6.5.2 Fragility analyses .....	215
6.6 Incremental Dynamic Analyses for Fire Sprinkler Piping Systems .....	220
6.7 IDA Results and Discussions.....	225
6.8 Summary.....	233
<b>Chapter 7 SUMMARY, CONCLUSIONS AND RECOMMENDATIONS FOR FUTURE RESEARCH .....</b>	<b>235</b>
7.1 Summary.....	235

7.2 Conclusions.....	237
7.2.1 Conclusions from the experimental studies.....	237
7.2.2 Conclusions from the numerical study.....	239
7.3 Recommendations for Future Work.....	240
<b>REFERENCES.....</b>	<b>242</b>
<b>APPENDIX A: RESULTS OF QUASI-STATIC TESTS .....</b>	<b>247</b>
<b>APPENDIX B: RESULTS OF DYNAMIC TESTS.....</b>	<b>296</b>
<b>APPENDIX C: OPTIMIZED PARAMETERS FOR NUMERICAL MODELS .....</b>	<b>346</b>

## LIST OF TABLES

Table 1-1 Piping weights for determining horizontal load .....	12
Table 1-2 Seismic coefficient table.....	13
Table 3-1 Experimental test program .....	56
Table 3-2 Summary of observed physical damage in tee joint specimens .....	72
Table 3-3 Measured moment and rotation capacities at first leakage for all tee joint specimens .....	74
Table 3-4 Summary of average axial slip for specimens made of black iron and CPVC.....	79
Table 3-5 Summary of first leakage fragility curve parameters .....	81
Table 3-6 Summary of first leakage fragility curve parameters specimens made of black iron and CPVC in terms of average axial slip .....	84
Table 4-1 Peak demand of dynamic testing protocol.....	94
Table 4-2 Details of test specimens .....	97
Table 4-3 Summary of support systems.....	110
Table 4-4 Testing program.....	113
Table 4-5 Peak accelerations and maximum inter-story drifts for all testing intensities.....	114
Table 4-6 instrumentation .....	124
Table 4-7 Observed damage in Specimen 1 .....	131
Table 4-8 Observed damage in Specimen 2 .....	135
Table 4-9 Observed damage in Specimen 3 .....	139
Table 4-10 Natural periods of fully braced fire sprinkler piping systems .....	141
Table 4-11 Summary of peak accelerations (BIT: Black Iron Threaded, CPVC: Thermoplastic, DF: Dyna-Flow Schedule 7).....	144

Table 4-12 Summary of peak rotations (BIT: Black Iron Threaded, CPVC: Thermoplastic, DF: Dyna-Flow Schedule 7) .....	150
Table 4-13 Summary of peak axial forces (BIT: Black Iron Threaded, CPVC: Thermoplastic, DF: Dyna-Flow Schedule 7) .....	155
Table 5-1 Descriptions of parameters for Multi-linear Pivot model.....	165
Table 5-2 Descriptions of parameters for Pinching4 Material model (from OpenSeesWiki, 2012).....	174
Table 5-3 Descriptions of parameters for Hysteretic Material model (from OpenSeesWiki, 2012).....	178
Table 5-4 Rayleigh damping for numerical models .....	185
Table 5-5 Comparison of natural periods obtained from dynamic tests and numerical model .....	185
Table 5-6 Comparison of experimental result and numerical prediction for joint leakage .....	192
Table 6-1 Member properties of the building model .....	205
Table 6-2 Floor seismic weights .....	206
Table 6-3 Modal properties of building model .....	206
Table 6-4 Characteristics of reduced and unscaled ground motion ensemble.....	213
Table 6-5 Comparison of geometric mean, median and arithmetic mean of spectral accelerations .....	214
Table 6-6 Median Sa for collapse of three building models.....	219
Table 6-7 Combinations of fire protection system configurations and building models.....	222
Table 6-8 Summary of median PFA and dispersion for first leakage of the fire sprinkler piping systems for all combinations considered.....	226

## LIST OF FIGURES

Figure 1-1 Description of typical fire sprinkler system (from Regency Fire Protection Inc. 2012) .....	3
Figure 1-2 Typical bracing system (from Malhotra et al. 2003).....	4
Figure 1-3 Typical bracing systems and vertical supports (from Erico Inc. 2009) .....	4
Figure 1-4 Typical Vertical Hanger (after Erico Inc. 2009) .....	5
Figure 1-5 Typical Sway Bracing Systems (from Erico Inc. 2009) .....	6
Figure 1-6 Rupture of sprinkler pipe at the elbow joint (from FEMA E-74, 1994) .....	20
Figure 1-7 Water leakage caused by pipe damage at joint (from Degenkolb Engineers, 1994) ..	21
Figure 1-8 Failure of lateral bracing system (from Mason Industries, 1994).....	21
Figure 1-9 Brace sheared off at the Santiago Airport (from E. Miranda, 2011).....	25
Figure 1-10 Fracture of tee joint threaded connection at the Santiago Airport (from E. Miranda, 2011).....	25
Figure 1-11 Water damage from broken sprinkler heads at Concepcion Airport (from E. Miranda, 2011).....	26
Figure 1-12 Typical investment of building construction (from Miranda, 2003).....	27
Figure 2-1 Components of a seismic brace (from Malhotra et al. 2003) .....	33
Figure 2-2 Schematical view of the four-point bending fatigue setup (from Wittenberghe et al. 2011).....	36
Figure 2-3 Timber building model (from Dillingham and Goel, 2002) .....	37
Figure 2-4 Layout of fire sprinkler system (from Dillingham and Goel, 2002) .....	38
Figure 2-5 Experimental setup: (a) schematic of the setup; and (b) final setup (from Goodwin et al. 2007) .....	40

Figure 2-6 (a) Seven-story building on the shake table and (b) Nonstructural system on the first floor (from Hoehler et al. 2009) .....	42
Figure 2-7 Victaulic test setup at Lehigh University's ATLSS laboratory (from Martínez, 2007).....	43
Figure 2-8 Displacement time histories that served as input to the hydraulic actuators (from Martínez, 2007).....	44
Figure 2-9 Finite element model of the Victaulic test setup in ABAQUS (from Martínez, 2007).....	45
Figure 3-1 Pipe materials and joint types selected for testing .....	49
Figure 3-2 Experimental set-up .....	51
Figure 3-3 Three-dimensional rendering of test set-up.....	51
Figure 3-4 Specimen made of cast iron pipe with threaded connections .....	52
Figure 3-5 Specimen constructed with CPVC pipe with cement joints.....	53
Figure 3-6 Typical Victaulic piping coupling.....	54
Figure 3-7 Specimen made of steel pipe with groove-fit connections.....	55
Figure 3-8 Loading Protocol for Cyclic Tests .....	57
Figure 3-9 Load cells used to measure shear force at both ends of specimens .....	58
Figure 3-10 Linear potentiometers attached to a tee joint .....	59
Figure 3-11 Illustration of calculation of rotation.....	60
Figure 3-12 Non-contact coordinate measurement system.....	61
Figure 3-13 Typical damage of cast iron pipe with threaded connections .....	63
Figure 3-14 Failed specimens made of cast iron pipe with threaded connections.....	65
Figure 3-15 Typical damage of CPVC pipe with cement joints.....	66



Figure 3-16 large inelastic rotation at the end of pipes.....	67
Figure 3-17 Typical damage of schedule 40 steel pipe with groove-fit connections .....	68
Figure 3-18 Typical damage of schedule 10 steel pipe with groove-fit connections .....	70
Figure 3-19 Rotational capacities at first leakage for all tee joint specimens; .....	75
Figure 3-20 Moment capacities at first leakage for all tee joint specimens; .....	75
Figure 3-21 Moment-rotation cyclic response for tee joint specimens with 2-in. diameter; the red dot indicates occurrence of first leakage (damage state DS <sub>1</sub> ) .....	77
Figure 3-22 Variations of variation of average axial joint slip with pipe diameter .....	78
Figure 3-23 First leakage fragility curves for fire suppression sprinkler piping joints; .....	82
Figure 3-24 First-leakage fragility curves for black iron pipe with threaded connections and CPVC pipe with cement joints in terms of average axial slip.....	84
Figure 4-1 Nonstructural Component Simulator at University of Buffalo (from SEESL, 2010). ..	89
Figure 4-2 General view of NCS testing frame .....	90
Figure 4-3 Testing protocol for dynamic test program.....	92
Figure 4-4 Floor response spectra.....	95
Figure 4-5 Dyna-Flow high-strength light wall sprinkler pipes (from Allied Tube Inc., 2011)...	96
Figure 4-6 General view of outriggers welded on the UB-NCS machine .....	98
Figure 4-7 Location of steel braces for outriggers.....	99
Figure 4-8 Plane view of outriggers and steel braces .....	100
Figure 4-9 Steel tube simulating floor slab.....	101
Figure 4-10 Fire-resistant mineral wool (from Roxul Inc., 2012) .....	101
Figure 4-11 SAMMY screw (from Dickson Supply Co., 2011).....	102
Figure 4-12 SAMMY screw for steel (from Diamond Tool and Fasteners, Inc., 2012) .....	103

Figure 4-13 Locations of ceiling boxes .....	104
Figure 4-14 Rigid ceiling box supported by steel angles.....	104
Figure 4-15 Flexible ceiling box supported by splay wires .....	105
Figure 4-16 Gypsum drywall .....	106
Figure 4-17 Acoustic tile .....	106
Figure 4-18 Three-dimensional rendering of the sprinkler piping test specimen .....	107
Figure 4-19 Layout of second level .....	108
Figure 4-20 Layout of first level and riser .....	109
Figure 4-21 Components of support systems.....	111
Figure 4-22 Locations of accelerometers (Note: AP indicates accelerometers for pipes).....	116
Figure 4-23 Accelerometers instrumentation for sprinkler heads.....	117
Figure 4-24 Accelerometer attached to the tee joint connected to sprinkler head.....	117
Figure 4-25 Linear potentiometers instrumentation for piping tee joints (PM indicates potentiometers).....	118
Figure 4-26 Linear potentiometers attached to the tee joints.....	119
Figure 4-27 Miniature universal load cell.....	120
Figure 4-28 Miniature universal load cell installed in the middle of the vertical hanger .....	120
Figure 4-29 Location of miniature load cells for vertical hangers (LCR indicates load cells for vertical hanger rods).....	121
Figure 4-30 Location of the miniature load cells for wire restraints (LCW indicates load cells for wire restraints).....	122
Figure 4-31 Location of linear string potentiometers (SP indicates string potentiometer).....	123
Figure 4-32 Overview of Specimen 1 .....	126

Figure 4-33 Failure of vertical hanger .....	128
Figure 4-34 Buckling of vertical hanger (Configuration 1-6, 100% MCE level).....	129
Figure 4-35 Damage of ceiling boxes.....	129
Figure 4-36 Failure of quick response pendant sprinkler head (Configuration 1-6, 100% MCE level).....	130
Figure 4-37 Overview of Specimen 2.....	132
Figure 4-38 Rupture of vertical hanger (Configuration 2-3, 100% MCE level) .....	133
Figure 4-39 Fracture of the CPVC branch line (Configuration 2-4, 100% MCE level).....	133
Figure 4-40 Damage of ceiling tiles (Configuration 2-4, 100% MCE level) .....	134
Figure 4-41 Overview of Specimen 3.....	136
Figure 4-42 Failures of vertical hangers .....	137
Figure 4-43 Damage of ceiling box .....	138
Figure 4-44 Mode shapes of fire sprinkler piping system .....	140
Figure 4-45 Locations and directions of accelerometers (Note: AP indicates accelerometers for pipes) .....	142
Figure 4-46 Comparison of peak acceleration response at AP-2 for three specimens across materials .....	145
Figure 4-47 Comparison of peak acceleration response at AP-8 for three specimens across materials (BIT: Black Iron Threaded, CPVC: Thermoplastic, DF: Dyna-Flow Schedule 7).....	146
Figure 4-48 Comparison of peak acceleration for three specimens across configurations.....	147
Figure 4-49 Locations of measurement for rotation .....	149

Figure 4-50 Comparison of peak rotations for three specimens at R29-30 across configurations .....	151
Figure 4-51 Comparison of peak rotation response at R29-30 for three specimens across materials (BIT: Black Iron Threaded, CPVC: Thermoplastic, DF: Dyna-Flow Schedule 7) .....	152
Figure 4-52 Locations of miniature load cells on vertical hanger rods .....	153
Figure 4-53 Comparison of peak axial forces for three specimens at LCR-15 across configurations .....	156
Figure 4-54 Comparison of peak axial forces for three specimens at LCR-5 across materials .....	157
Figure 4-55 Comparison of peak axial forces for three specimens at LCR-16 across materials .....	158
Figure 5-1 Moment-rotation cyclic response of 4-inch black iron pipes with threaded joints ...	163
Figure 5-2 Moment-rotation cyclic response of 2-inch CPVC pipes with cement joints .....	163
Figure 5-3 Moment-rotation cyclic response of 4-inch Schedule-10 steel pipes with groove-fit connections .....	164
Figure 5-4 Multi-linear Pivot model (from CSI, 2012) .....	166
Figure 5-5 Procedure of optimization of parameter set for numerical models .....	168
Figure 5-6 Comparisons of numerical and experimental results for 4-inch steel pipe with grooved-fit connections .....	169
Figure 5-7 Comparisons of numerical and experimental results for 2-inch black iron pipe with threaded joints .....	170

Figure 5-8 Comparisons of numerical and experimental results for 3/4-inch CPVC pipe with cement joints .....	171
Figure 5-9 Pinching4 Material model (from OpenSeesWiki, 2012).....	173
Figure 5-10 Comparisons of experimental data and numerical model .....	176
Figure 5-11 Hysteretic Material model (from OpenSeesWiki, 2012) .....	177
Figure 5-12 Comparisons of experimental data and numerical model for 2-inch black iron pipe with threaded joints .....	179
Figure 5-13 Comparisons of experimental data and numerical model for 2-inch CPVC pipe with cement joints .....	180
Figure 5-14 Illustration of simulation for tee joint in SAP2000 .....	183
Figure 5-15 Numerical model of fire sprinkler piping system in SAP2000 .....	184
Figure 5-16 Locations of responses for numerical model validation .....	186
Figure 5-17 Comparison of experimental results and numerical predictions (fully braced Specimen 1) .....	187
Figure 5-18 Comparison of hysteresis loops obtained from experiment and numerical model for tee joint R29-30 (fully braced Specimen 1) .....	188
Figure 5-19 Comparison of experimental results and numerical predictions (unbraced Specimen 1) .....	189
Figure 5-20 Comparison of experimental results and numerical predictions (fully braced Specimen 2) .....	190
Figure 5-21 Comparison of experimental results and numerical predictions (unbraced Specimen 2) .....	191

Figure 5-22 Comparison of the maximum joint rotation predicted by numerical model with probability of leakage predicted by the fragility curve for the 2-inch CPVC pipe with cement joints .....	192
Figure 5-23 Numerical model of fire sprinkler piping system in OpenSees .....	195
Figure 5-24 Locations of responses for numerical model validation .....	195
Figure 5-25 Comparison of experimental results and numerical predictions (fully braced Specimen 1) .....	196
Figure 6-1 Process of IDA on fire sprinkler piping systems .....	200
Figure 6-2 Plan view of WC70 .....	203
Figure 6-3 Elevation view of WC70 (N-S frame, Line B) .....	203
Figure 6-4 2-D model of WC70 with section numbers .....	205
Figure 6-5 Elastic modes of vibration of the building .....	207
Figure 6-6 Flexural strength degradation model (Filiatrault et al., 2001) .....	208
Figure 6-7 Static pushover curves .....	209
Figure 6-8 Time histories of ten Far-Field earthquake ground motions (GM indicates ground motion record) .....	211
Figure 6-9 Acceleration response spectra of scaled ground motions (GM indicates ground motion record) .....	214
Figure 6-10 Fragility analyses for building models (Sa indicates spectral acceleration, and PFA indicates peak floor acceleration) .....	216
Figure 6-11 IDA curves for elastic building .....	217
Figure 6-12 Collapse fragility curve for elastic building model .....	217
Figure 6-13 IDA curves for inelastic building without degradation .....	218

Figure 6-14 Collapse fragility curve for inelastic building model without degradation.....	218
Figure 6-15 IDA curves for inelastic building with degradation .....	219
Figure 6-16 Collapse fragility curve for inelastic building model with degradation.....	219
Figure 6-17 Comparison of collapse fragility curves for building models.....	220
Figure 6-18 Layout of first level of test specimen .....	221
Figure 6-19 Three-dimensional rendering of layout .....	221
Figure 6-20 Illustration of IDA curves for fire sprinkler piping system.....	223
Figure 6-21 First-leakage fragility curves of fire sprinkler piping system (Combination #1)....	224
Figure 6-22 Comparison of fragility curves for fully braced fire sprinkler piping systems made of black iron piping with threaded connections .....	229
Figure 6-23 Comparison of frequency content .....	230
Figure 6-24 Comparison of first leakage fragility curves for fire sprinkler piping systems in terms of piping materials and bracing systems (BIT indicates black iron piping with threaded connections for branch lines, and CPVC indicates CPVC piping with cement joints for branch lines) .....	232
Figure 6-25 Procedures of conducting fragility analyses for fire sprinkler piping systems .....	234

## ABSTRACT

A fire extinguishing sprinkler piping subsystem not only accounts for a significant portion of typical investment in building construction, but also represents one of the key components that ensures the functionality and safety of a building. However, recent earthquake events have demonstrated the vulnerability and sometimes poor performance of fire extinguishing sprinkler piping subsystems, which can cause a wide range of damage resulting in substantial property loss, loss of building functionality, as well as posing a significant hazard in potential fire spread and loss of life. Limited research has been conducted on sprinkler piping subsystem under seismic loading and information obtained from previous studies is not sufficient to fully describe their dynamic response and failure mechanisms. In order to better understand the seismic behavior of fire suppression systems and their interaction with other structural members and nonstructural subsystems, experimental and numerical studies were conducted as part of George E. Brown, Jr., Network for Earthquake Engineering Simulation - Nonstructural Grand Challenge Project (NEES - NGC).

Two test series were carried out in the Structural Engineering and Earthquake Simulation Laboratory (SEESL) at the State University of New York in Buffalo. In the first series, a total of 48 tee joint components for sprinkler piping systems with nominal diameters from 3/4" to 6" and made of various materials and joint types (black iron with threaded joints, chlorinated polyvinyl chloride (CPVC) with cement joints, and steel with groove-fit connections) were tested under reverse cyclic loading to determine their rotational capacities at which leakage and/or fracture occurred. The failure mechanisms observed in the piping joints were identified and the ATC-58 framework was applied to develop a seismic fragility database for pressurized fire suppression



sprinkler joints. The fragility curves used joint rotation as the demand parameter. Structural analysis models of sprinkler piping systems would be required to generate fragility curves in terms of more global demand parameters, such as floor accelerations.

Subsequently, two-story, full-scale (11 ft. × 29 ft.) fire extinguishing sprinkler piping subsystems were tested on the University at Buffalo Nonstructural Component Simulator (UB-NCS). A total of three specimens with different materials and joint arrangements were tested with various level of bracing systems under dynamic loading. All three fully braced specimens performed well under a Maximum Considered Earthquake (MCE) level of loading, validating current code-based requirements for bracing system design. However, the unbraced systems, which are typically installed in low to moderate seismic regions or could exist in older construction, did not perform as well as the fully braced systems. Damage to sprinkler heads, failures of vertical hangers, as well as a branch line fracture, were observed during the tests.

A number of hysteresis models were introduced to simulate the nonlinear moment-rotation behavior of tee joint components made of various materials and joint types. The proposed hysteresis models were capable of capturing the strength degradation, change of stiffness during unloading, as well as energy dissipation. As a result, nonlinear rotational springs using the calibrated analytical models were used to model full-scale fire sprinkler piping subsystems. To validate the numerical model, simulations based on the UB-NCS seismic tests were conducted. Nonlinear response-history dynamic analyses were performed to predict the seismic test results.

Results obtained from the numerical simulations showed close agreement with the experimental results in terms of displacement, acceleration, and moment – rotation relation at piping joints.

Finally, a hypothetical acute care facility equipped with full-scale fire sprinkler systems was selected as an example of the use of the numerical model to develop seismic fragility curves for sprinkler piping systems with floor accelerations as the demand parameter. For this purpose, Incremental Dynamic Analyses (IDA) were conducted, and fragility curves associated with various performance objectives in terms of pipe leakage were developed. This study focused only on the failure of joints and did not consider other failure mechanisms of sprinkler piping systems, including impact with ceilings and other surrounding structural and nonstructural components.

# Chapter 1

## INTRODUCTION

### 1.1 Project Background

Nonstructural components do not contribute to the structural load-bearing system, but are subjected to the same dynamic environment of the building structure during a seismic event (Whittaker and Soong, 2003). According to FEMA E-74 (FEMA, 2011), nonstructural components can be divided into three broad categories:

- **Architectural Components** such as partitions, ceilings, storefronts, glazing, cladding, veneers, chimney, fences, and architectural ornamentation.
- **Mechanical, Electrical, and Plumbing (MEP) Components** such as pumps, chillers, fans, air handling units, motor control centers, distribution panels, transformers, and distribution systems including piping, ductwork and conduit.
- **Furniture, Fixtures, and Equipment (FF&E), and Contents** such as shelving and book cases, industrial storage racks, retail merchandise, books, medical records, computers and desktop equipment, wall and ceiling mounted TVs and monitors, file cabinets, kitchen, machine shop or other specialty equipment, industrial chemicals or hazardous materials, museum artifacts, and collectibles. ”

Traditionally, the understanding and quantity of research studies on the behavior and mechanisms of nonstructural components under earthquake loading is considerably less than that of building structures that house them. Until recently, tremendous efforts have been made by

numerous researchers and practicing engineers to shed light on the importance of nonstructural components and the urgent necessity of improving their performance. These efforts are motivated by the fact that repeated earthquake events have shown that failure of nonstructural components not only causes large economic losses, but also in some instances pose hazards to human life.

This research was conducted as part of the *Simulation of the Seismic Performance of Nonstructural Systems* NEES Grand Challenge Project funded by The George E. Brown, Jr., Network for Earthquake Engineering Simulation (NEES) research program of the National Science Foundation (NSF). The project goals are to better understand, predict and improve the seismic performance of the ceiling-piping-partition (CPP) system, an important class of nonstructural components. Although these three subsystems are designed and installed independently, they are physically connected and thus the CPP is considered as a system from a mechanics standpoint. As part of the first phase of this project, experimental and numerical studies on pressurized automatic fire sprinkler systems have been conducted and the results are presented and discussed in this dissertation.

## **1.2 Pressurized Automatic Fire Sprinkler System**

A fire sprinkler system is an integrated active pressurized fire protection system designed in the United States following fire protection engineering standards NFPA 13 (NFPA, 2010). Typically, the basic components of a fire sprinkler system include water supply line, alarm valve, sprinkler head and system piping (*Figure 1-1*). While the water supply line provides adequate water

pressure and is usually buried underground, the portion of the fire sprinkler piping system above ground is a network of specially sized or hydraulically designed water distribution piping systems installed in a structure, onto which fire sprinkler heads are connected in a systematic pattern (NFPA, 2010).

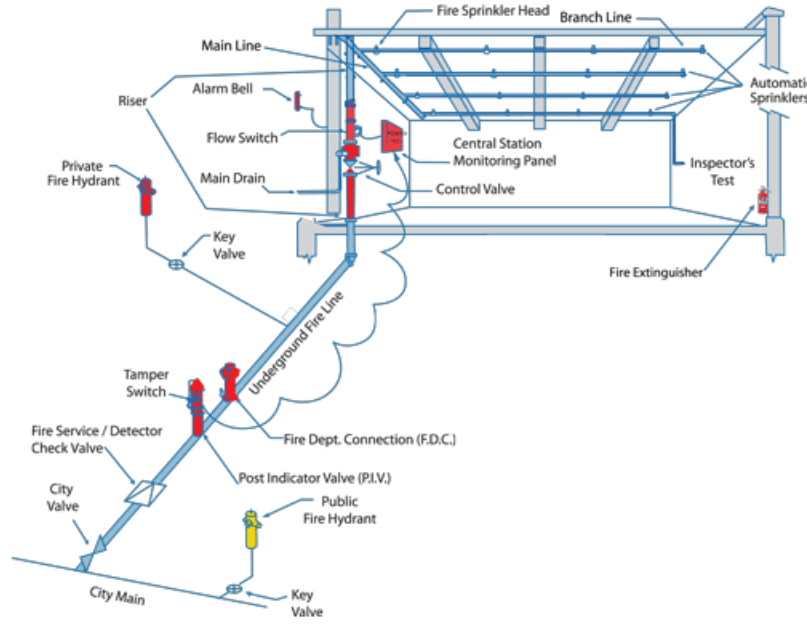
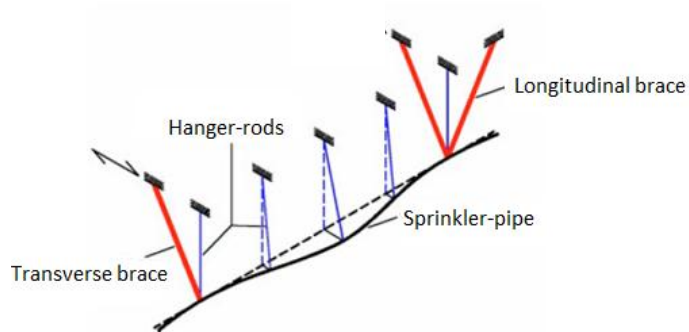


Figure 1-1 Description of typical fire sprinkler system (from Regency Fire Protection Inc. 2012)

### 1.3 Vertical Hangers and Seismic Bracing Systems

The gravity loads, consisting of the weight of pipes and their contents, are supported by ordinary vertical supports (SMACNA, 1991). However, extra bracing systems are required in seismically-prone areas in order to resist horizontal and vertical forces caused by earthquake motions (Figure 1-2). To account for the directionality of seismic forces, it is customary to brace the piping system longitudinally (parallel to the piping) and transversely (perpendicular to the piping). The

following sections briefly describe the typical vertical hangers and seismic bracing systems used in fire sprinkler systems (*Figure 1-3*).



*Figure 1-2 Typical bracing system (from Malhotra et al. 2003)*



*(a) Transverse Brace*

*(b) Longitudinal Brace (Left)*

*(c) Vertical Hanger (Right)*

*Figure 1-3 Typical bracing systems and vertical supports (from Erico Inc. 2009)*

## Vertical Hangers

Vertical hangers are designed to transfer the gravity load from the sprinkler piping to the supporting structure. Generally, hangers may consist of a single component, such as a U-hook, or up to three components: ceiling plate as the building-attached component, clevis hanger as the pipe attachment component, and all thread rod connecting the building attachment component with the pipe attachment component, as illustrated in *Figure 1-4*. Unless proved adequate by fire tests, hangers and their components should be ferrous (NFPA, 2010).

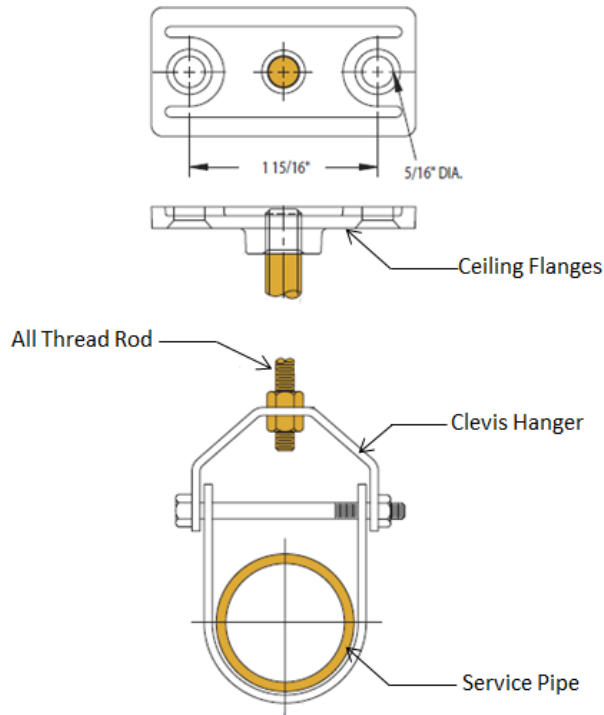


Figure 1-4 Typical Vertical Hanger (after Erico Inc. 2009)

## Sway Bracing Systems

Sway braces, including transverse (perpendicular to the piping) and longitudinal (parallel to the piping) bracing, are provided to restrain excessive movement of system piping (*Figure 1-5*). Since pipe shifting due to building motion usually leads to fracture of fittings and pullout failures of hangers, sway bracing systems are required to protect fire sprinkler systems against excessive deflections and deformations.

Sway bracing is typically installed at an angle between 30 and 90 degrees from vertical. When a strut made of pipe is used (a “brace pipe”, not to be confused with the water supply pipes), it is

designed to resist both compression and tension loads, and special attention needs to be paid to the schedule and the length of the brace in order to prevent buckling.

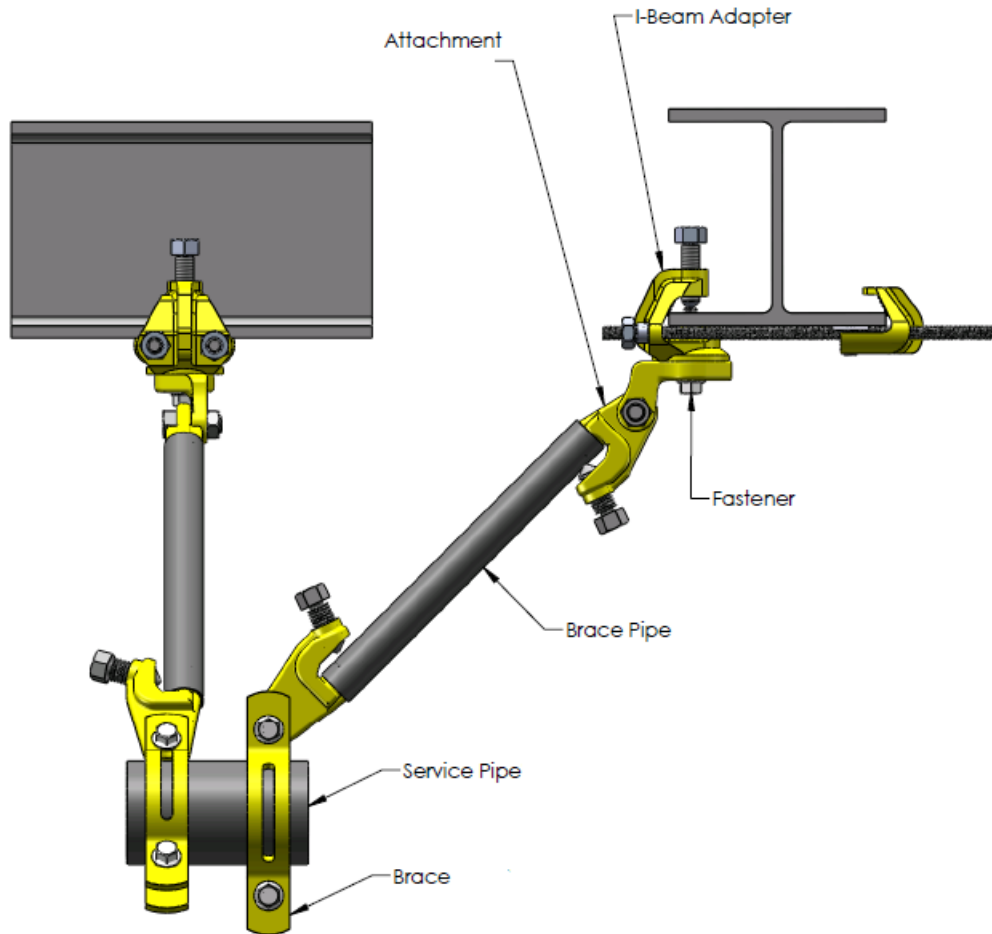


Figure 1-5 Typical Sway Bracing Systems (from Erico Inc. 2009)

#### 1.4 Code Provisions for Seismic Design of Fire Sprinkler Systems

As one of the most important nonstructural components in a building structure, fire sprinkler subsystems are required to follow code provisions for installation based on design lateral forces if the building structure is located in seismically active area. The most widely employed seismic design requirements for nonstructural components in the United States. have historically been



described in the Uniform Building Code (UBC) (Bachman, 1998). Since the year 2000, the UBC has been replaced by the International Building Code (IBC), whose seismic provisions were mainly converted from the 1997 National Earthquake Hazard Reduction Program (NEHRP) Recommended Provision for Seismic Regulations for New Buildings.

As a minimum building standard, UBC was adopted by the State of California in 1991, and meanwhile the NFPA 13 (NFPA, 1989) (hereafter “NFPA 13” refers to the 2010 edition) published by National Fire Protection Association was adopted as standard for fire sprinkler system design (Dillingham and Goel, 2002). Previously, the California Office of Statewide Health Planning and Development (OSHPD) had approved the guidelines published by the Sheet Metal and Air Conditioning Contractors National Association (SMACNA) to provide technical guidance for the design of seismic restraints of mechanical and piping systems. Currently, NFPA 13 (NFPA, 2010) serves as the national standard for the installation of fire sprinkler piping system.

Stevenson (1998) pointed out that “design by rule” and “design by analysis” were the two main procedures for the actual seismic design of piping systems. By controlling the spacing between various types of supports, the “design by rule” method implicitly attempts to assure the seismic stresses and deformations in the piping and supports remain within permitted limits. This procedure is extracted from numerous observations and evaluations of behavior of piping during earthquakes in the past years. In the “design by analysis” method, stresses induced from seismic load and other applicable loads are combined together to determine the stress resultants in the pipe and loads on the supports, and code allowable values are compared to carry out the design.

The “design by analysis” procedures can be performed as described by the applicable standards summarized as follows:

### 1997 UBC

The UBC (ICBO, 1997) calculates the total design lateral seismic force for nonstructural components with the following formula:

$$F_p = \frac{a_p C_a I_p}{R_p} \left(1 + 3 \frac{h_x}{h_r}\right) W_p \quad (1.1)$$

with

$$0.7 C_a I_p W_p \leq F_p \leq 4.0 C_a I_p W_p \quad (1.2)$$

where:

$F_p$  = total design lateral seismic force on the component

$a_p$  = in-structure Component Amplification Factor, varies from 1.0 to 2.5 (1997 UBC Table 16-O)

$C_a$  = Seismic Coefficient (1997 UBC Table 16-O)

$I_p$  = component importance factor, varies from 1.0 to 1.5 (1997 UBC Table 16-K)

$R_p$  = Component Response Modification Factor, varies from 1.0 to 4.0 (1997 UBC Table 16-O)

$h_x$  = element or component attachment elevation with respect to grade

$h_r$  = structure roof elevation with respect to grade

$W_p$  = weight of the component

## ASCE 7-10

Both the 2009 IBC and the NFPA 13 refer to ASCE 7-10 (ASCE, 2010) for seismic design provisions of nonstructural components, which define the total design lateral seismic force for nonstructural components with the following equation:

$$F_{ph} = \frac{0.4a_p S_{DS} W_p}{\left( \frac{R_p}{I_p} \right)} \left( 1 + 2 \frac{z}{h} \right) \quad (1.3)$$

with

$$0.3S_{DS} I_p W_p \leq F_{ph} \leq 1.6S_{DS} I_p W_p$$

where:

$F_{ph}$  = seismic design force on the component

$a_p$  = Component Amplification Factor varies from 1.0 to 2.5 ( $a_p = 2.5$  for piping systems)

$S_{DS}$  = design spectral response acceleration for short periods

$I_p$  = component importance factor, varies from 1.0 to 1.5 ( $I_p = 1.5$  for sprinkler systems)

$R_p$  = Component Response Modification Factor ( $R_p = 12.0$  for piping systems with ASME welded, and  $R_p = 4.5$  for piping systems with threaded joints)

$z$  = height above the base in structure of point of attachment of component

$h$  = average roof height of structure above the base

$W_p$  = operating weight of the component

The Sheet Metal and Air Conditioning Contractors National Association (SMACNA, 1991) have adopted the “design by rule” procedures, which served as the only available guidelines

nationwide for years. The general requirements for bracing of pipes in SMACNA are summarized as follows:

- 1) Lateral sway bracing is required for all pipes with  $2\frac{1}{2}$  in. in nominal diameter and larger;
- 2) Transverse bracing is required at a maximum spacing of 40 ft.;
- 3) Longitudinal bracing is required at maximum spacing of 80 ft.;
- 4) Transverse bracing for one pipe section shall be allowed to act as longitudinal bracing for a pipe section of the same size connected perpendicular to it if the bracing is installed within 24 in. of the elbow or tee;
- 5) It is required to provide flexibility in joints where pipes pass through building seismic joints or expansion joints or where rigidly supported pipes connect to equipment with vibration isolators;
- 6) Vertical risers shall be laterally braced with a riser clamp at each floor.

Both “design by rule” and “design by analysis” procedures are included in NFPA 13-10. For the “design by analysis” method, Equation (1.3) used in ASCE 7-10 for determining seismic lateral forces for nonstructural components is included in NFPA 13 (NFPA, 2010). This approach can be replaced by a simplified equation as follow:

$$F_{ph} = C_p W_p \quad (1.4)$$

where  $W_p$  is the subsystem weight, and can be calculated with the help of *Table I-1*. For lateral braces:  $W_p$  is taken as the operational weight of main and branch piping in the zone of influence; for longitudinal braces:  $W_p$  is the operational weight of the main piping only in the zone of influence. In the zone of influence method, both branch lines and mains are considered to

contribute to seismic loads on lateral braces, but only main lines are considered to contribute to the loads in longitudinal braces because these forces are not uniformly transferred during earthquake motion.  $C_p$  is the seismic coefficient using 0.5 as the default value or can be selected from *Table 1-2* based on the short period response parameter  $S_s$ , which is the seismic acceleration representing a two percent probability of being exceeded in 50 years and can be obtained from maps developed by the United States Geological Survey (USGS) in the World Wide Web (<http://geohazards.usgs.gov/designmaps/us/application.php#>).

Table 1-1 Piping weights for determining horizontal load

Nominal Dimensions		Weight of Water-Filled Pipe	
in.	mm	lb/ft	kg/m
<b>Schedule 40 Pipe</b>			
1	25	2.05	3.05
1¼	32	2.93	4.36
1½	40	3.61	5.37
2	50	5.13	7.63
2½	65	7.89	11.74
3	80	10.82	16.10
3½	90	13.48	20.06
4	100	16.40	24.41
5	125	23.47	34.93
6	150	31.69	47.16
8*	200	47.70	70.99
<b>Schedule 10 Pipe</b>			
1	25	1.81	2.69
1¼	32	2.52	3.75
1½	40	3.04	4.52
2	50	4.22	6.28
2½	65	5.89	8.77
3	80	7.94	11.82
3½	90	9.78	14.55
4	100	11.78	17.53
5	125	17.30	25.75
6	150	23.03	34.27
8*	200	40.08	59.65

\* Schedule 30

Table 1-2 Seismic coefficient table

$S_s$	$C_p$
0.33 or less	0.35
0.40	0.38
0.50	0.40
0.60	0.42
0.70	0.42
0.75	0.42
0.80	0.44
0.90	0.48
0.95	0.50
1.00	0.51
1.10	0.54
1.20	0.57
1.25	0.58
1.30	0.61
1.40	0.65
1.50	0.70
1.60	0.75
1.70	0.79
1.75	0.82
1.80	0.84
1.90	0.89
2.00	0.93
2.10	0.98
2.20	1.03
2.30	1.07
2.40	1.12
2.50	1.17
2.60	1.21
2.70	1.26
2.80	1.31
2.90	1.35
3.00	1.40

The seismic load determined by Equation (1.3) or (1.4) is combined with other applicable loads (e.g. gravity) to derive the stress resultants in the pipe and loads on the supports. The combined stresses are multiplied by 0.7 and compared to the allowable resistance of the pipe components and supports to determine the size of pipes, hangers and sway braces.

The “design by rule” procedures in the NFPA13 (NFPA, 2010) consist of six distinct requirements regarding: (1) flexible couplings, (2) separation, (3) clearance, (4) sway bracing, (5) restraint for branch line, and (6) hanger and fastener. Each of them is described in detail as follows:

#### 1) Flexible couplings requirements

Flexible couplings shall be installed as follows:

- Within 24 in. (610 mm) of the top and bottom of all risers, unless the following provisions are met:
  - In risers less than 3 ft. (0.9 m) in length, flexible couplings are permitted to be omitted;
  - In risers 3 ft. to 7 ft. (0.9 m to 2.1 m) in length, one flexible coupling is adequate.
- Within 12 in. (305 mm) above and within 24 in. (610 mm) below the floor in multistory buildings. When the flexible coupling below the floor is above the tie-in main to the main supplying that floor, a flexible coupling shall be provided on the vertical portion of the tie-in piping.
- On both sides of concrete or masonry walls within 1 ft. (0.3 m) of the wall surface, unless clearance is provided in accordance with Section 9.3.4.



- Within 24 in. (610 mm) of building expansion joints.
- Within 24 in. (610 mm) of the top and bottom of drops to hose lines, rack sprinklers, and mezzanines, regardless of pipe size.
- Within 24 in. (610 mm) of the top of drops exceeding 15 ft. (4.6 m) in length to portions of systems supplying more than one sprinkler, regardless of pipe size.
- Above and below any intermediate points of support for a riser or other vertical pipe.

## 2) Separation requirements

- A specific type of assembly is required to be used with building separation.
  - Installation of a primary main is required on one side of the building and a secondary main on the opposite side.
  - Mains are connected with a series of branch lines that run perpendicular to each main.
  - Presence of several 90-degree elbows (ells) added to each branch line must be included in the hydraulic calculations, and their presence most likely will increase the branch-line size at least one size, making the system even more expensive.
  - More compact proprietary assemblies are available (e.g. Metraloop).

## 3) Clearance requirements

- General Requirements
  - Clearance shall be provided for piping that penetrates concrete and/or masonry floor/ceiling and wall assemblies.
  - A specific nominal annular space is required to be provided around the pipe penetrating the assembly.

- Specific requirements
  - One-inch annular space is required around 1-3 ½ in. pipe.
  - Two-inch space is required around pipes that are 4 in. and larger.
  - In lieu of large clearances, the standard allows for a flexible coupling to be installed on either side of the assembly within 12 in. of the face of the penetration (see above).

#### 4) Sway bracing requirements

- General requirements
  - Sway braces shall be designed for both tension and compression unless approved tension-only components are used.
  - The slenderness ratio of a brace member,  $l/r$ , shall not exceed 300.
- Requirements for lateral sway bracing
  - Lateral sway bracing shall be provided for main and branch line pipes with 2 in. nominal diameter and larger.
  - Spacing of lateral sway bracing shall not exceed a maximum interval of 40 ft. (12.2 m).
  - Lateral sway bracing shall be provided within 20 ft. of each end of a main run.
  - Lateral sway bracing is required on the first piece of pipe 6 ft. from the end of a main line.
- Requirements for longitudinal sway bracing
  - Longitudinal sway bracing shall be provided for all main line pipes.
  - Spacing of longitudinal sway bracing shall not exceed a maximum interval of 80 ft. (24.4 m).

- Longitudinal sway bracing shall be located within 40 ft. of each end of a main run.
- Transverse bracing for one pipe section shall be allowed to act as longitudinal bracing for a pipe section of the same size connected perpendicular to it if the bracing is installed within 24 in. of the elbow or tee.
- Requirements for 4-way Bracing
  - 4-way Bracing is used to restrict the movement of pipes installed in a vertical position (e.g. riser).
  - 4-way Bracing must be located within 24 in. of the top of the riser.

#### 5) Restraint of branch line requirements

- Restraint is considered a lesser degree of resisting loads than bracing and shall be provided by use of one of the following:
  - A listed sway brace assembly.
  - A wraparound U-hook satisfying the requirements of 9.3.5.3.9.
  - No. 12, 440 lb. (200 kg) wire installed at least 45 degrees from the vertical plane and anchored on both sides of the pipe.
  - Other approved means.
  - A hanger not less than 45 degrees from vertical installed within 6 in. (152mm) of the vertical hanger arranged for restraint against upward movement, provided it is utilized such that  $l/r$  does not exceed 400, where the rod shall extend to the pipe or have a surge clip installed.

- Wire used for restraint shall be located within 2 ft. (610 mm) of a hanger. The hanger closest to a wire restraint shall be of a type that resists upward movement of a branch line.
- The end sprinkler on a line shall be restrained against excessive vertical and lateral movement.

#### 6) Hanger and fasteners requirements

- Where seismic protection is provided, C-type clamps (including beam and large flange clamps) used to attach hangers to the building structure shall be equipped with a restraining strap unless the provisions of 9.3.7.1.1 are satisfied.
- The restraining strap shall wrap around the beam flange not less than 1 in. (25.4 mm).
- A lock nut on a C-type clamp shall not be used as a method of restraint.
- A lip on a “C” or “Z” purlin shall not be used as a method of restraint.
- Where purlins or beams do not provide a secure lip to a restraining strap, the strap shall be through-bolted or secured by a self-tapping screw.
- In areas where the horizontal force factor exceeds  $0.50 W_p$ , powder-driven studs shall be permitted to attach hangers to the building structure where they are specifically listed for use in areas subject to earthquake.

### 1.5 Performance of Fire Sprinkler Subsystems during Previous Earthquakes

#### 1964 Alaska Earthquake

A report prepared by the National Research Council (NRC, 1973) described the damage to both building structures and various nonstructural systems. The region struck by the magnitude 9.2 Alaska earthquake had a total population of about 140,000 people. Although the quantity of

structures and facilities affected by the earthquake was relatively small, a number of failures of fire sprinkler systems were recorded.

A sprinkler head in the gymnasium of the Central Junior High School was installed improperly right under the cross bracing of the roof, which struck the sprinkler head and activated it when the building started to vibrate during the earthquake. Besides the multipurpose room in the same school, torn ceiling tiles were also reported at the Providence Hospital. As the ceiling system was not as well braced as the fire sprinkler system, shaking caused differential movement between the two suspension systems, during which many surface-mounted sprinkler heads cut through the tiles in the acoustic-tile ceiling system. Some cuts in the tiles were more than 1-foot long.

### **1994 Northridge Earthquake**

A post-earthquake damage assessment entitled “The Northridge Earthquake: A Report to the Hospital Building Safety Board on the Performance of Hospitals” was prepared and published by Office of Statewide Health Planning and Development (OSHPD) (1995). A total of 472 facilities were reviewed and observations have shown that nonstructural systems and components that were installed with proper bracing systems according to the code generally performed well, with the exception of water piping and fire sprinkler systems. Leakage and water damage resulting from fire protection systems (*Figure 1-6, Figure 1-7, and Figure 1-8*) forced the temporary evacuation of a number of buildings. Based on the surveys conducted respectively by Ayres et al. (1996) and Fleming (1998), damage data and information of fire sprinkler systems in 13 hospitals was collected and described. For example, in the 8-story Professional Tower of Cedars-Sinai Medical Center, sprinkler heads on a 1-inch branch line, which went across the seismic

separation, was activated due to pounding with other building components. The same failure occurred from Floors 4 through 8 as a result of insufficient flexibility provided by the installed 90-degree offsets on each side of the seismic separation. For Holy Cross Medical Center, short drops (6-10 inches long) to sprinkler heads encountered failures at screwed tee when pipe or heads struck the hard (rated) ceiling, and replacements of 1,200 sprinkler heads and 401 two-piece escutcheons were reported by sprinkler repair contractors. Besides, sprinklers damaged by impact against ceiling systems, vertical supports pulled out, and failures of branch lines of small size were also reported from other hospitals.

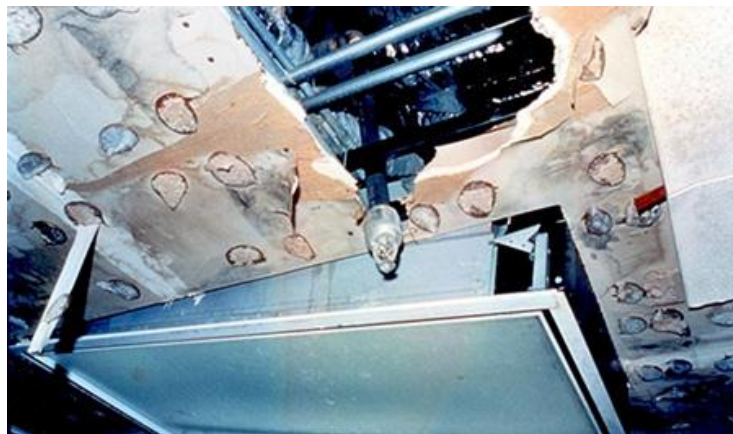


*Figure 1-6 Rupture of sprinkler pipe at the elbow joint (from FEMA E-74, 1994)*



*Figure 1-7 Water leakage caused by pipe damage at joint (from Degenkolb Engineers, 1994)*



*Figure 1-8 Failure of lateral bracing system (from Mason Industries, 1994)*

## **2001 Nisqually Earthquake**

This was one of the two largest earthquakes that struck Washington area in the last 50 years. The 2001 Nisqually Earthquake (M6.8) occurred 32 miles below the earth's surface and ultimately resulted in \$4 billion financial loss, as well as one death and over 400 injuries. This was much less severe compared to the 1994 Northridge Earthquake (M6.7), which had a very similar magnitude but resulted in 72 deaths and economic damage of more than \$12 billion. This difference could be attributed to the great depth of fault rupture for the 2001 earthquake and the attenuation of the seismic waves before reaching the ground surface. (EQE, 2001) Because of the moderate ground motions, modern buildings generally behaved well during the earthquake. However, a reconnaissance report prepared by Filiatrault *et al.* (2001) concluded that the performance of nonstructural components was not as favorable as the observed structural performance, and a large portion of the reported loss was related to the failure of nonstructural components.

It was also reported (EQE, (2001) that failed fire sprinklers were among the major types of nonstructural damage in the North Satellite Building, and as a result, the Sea Tac International Airport, located about 25 miles from the epicenter, was only reopened for partial service after the earthquake.

Based on statistics compiled by FM Global Inc. (2001), 35 sprinkler impairments among 450 FM Global-insured sites were reported as a result of the earthquake. Partial collapse of ceiling systems, roofs, brick walls or pallet racks resulted in sprinkler systems impairments in at least four locations. Besides, broken small-diameter piping and leakage at grooved pipe coupling



joints on larger pipes occurred in a number of locations. Furthermore, damage of the automatic fire-protection system due to breaks of lead-ins or underground mains was observed at six locations.

### **2006 Hawaii Earthquake**

A report published by EERI (Chock, 2006) summarized observations of damage to fire sprinkler systems during the magnitude 6.7 Hawaii earthquake that occurred on October 15, 2006. With only a few exceptions, most buildings constructed in recent years performed well. Although schools and healthcare facilities sustained little structural damage, they were not fully operational for weeks following the earthquake as a result of substantial damage to the nonstructural systems.

In the Mauna Kea Resort, the main ballroom suffered considerable water damage from the broken sprinkler lines. Besides nonstructural failures such as fallen ceilings and light fixtures, damage to fire sprinkler systems was also found to be one of the primary causes that led to the evacuation for the Kona Community Hospital. For Hale Ho'ola Hamakua healthcare facility, a number of sprinkler heads were broken due to interaction with the suspended ceiling system, which resulted in not only significant flooding in the building but also impaired other nonstructural components such as the exterior cladding, soffits and the interior ceiling and wall systems. Consequently, 49 patients needed to be evacuated and housed in tents.

## 2010 Chile Earthquake

The Chilean code enforced at the time of the earthquake shared many similarities with the United States seismic provisions for nonstructural systems. Moreover, measures used to provide support and bracing systems to nonstructural components in Chile were also highly comparable to practice in the United States. The February 27, 2010 Chile Earthquake, magnitude 8.8, provided earthquake engineers from the United States as well as other parts of the world a unique and valuable opportunity to look into the dynamic behavior and performance of nonstructural components in a large-magnitude seismic event.

What's more, the 2010 Chile Earthquake is another example where functionality of critical facilities was impaired by the failure of sprinkler piping systems. In the central south region of the country, four hospitals were rendered inoperable, and 12 hospitals lost almost 75% of their functionalities due to failures of nonstructural components, including fire sprinkler piping (Ju, 2011).

Fire sprinkler piping system damage was one of the major reasons that led to the shut-down of airport terminal at Santiago. Several braces were sheared off as shown in *Figure 1-9*. Fractures of tee joint threaded connections were also reported at the Santiago Airport (*Figure 1-10*).

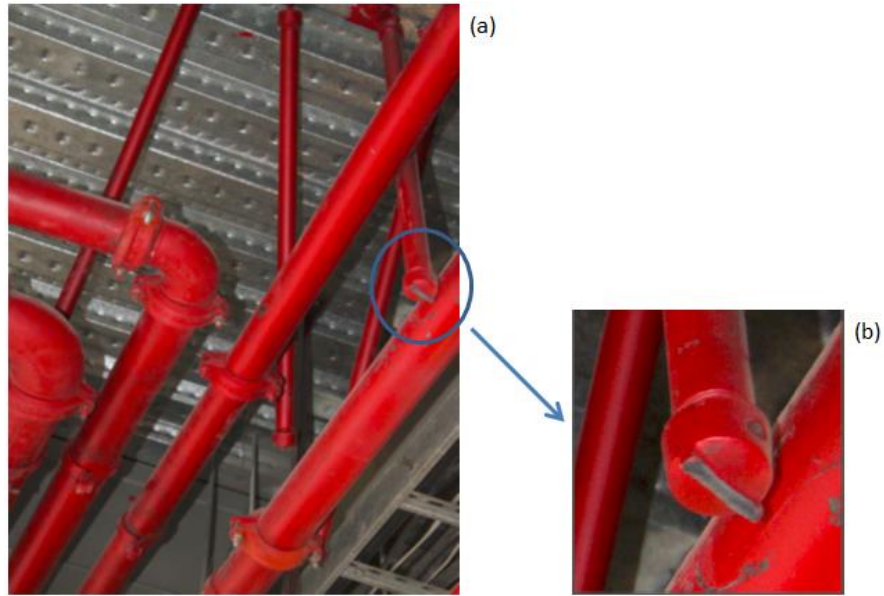


Figure 1-9 Brace sheared off at the Santiago Airport (from E. Miranda, 2011)

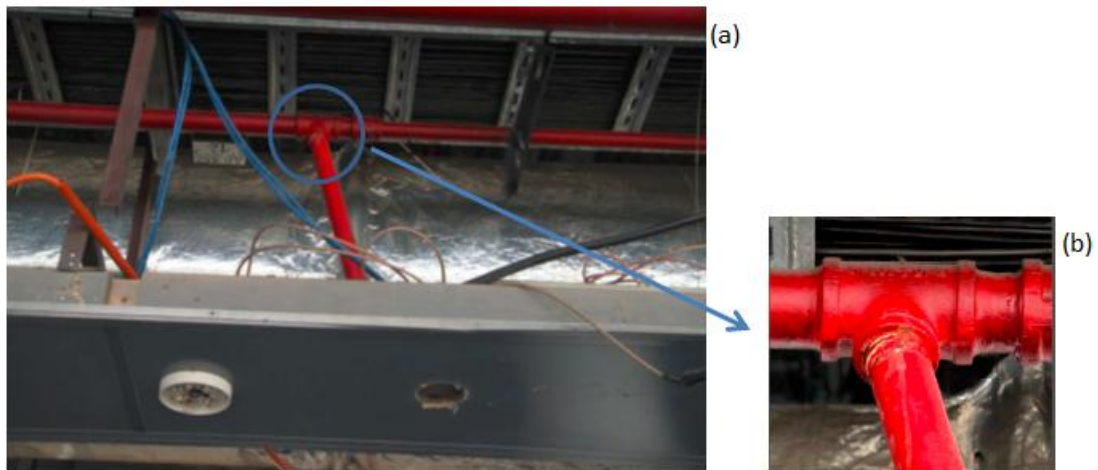
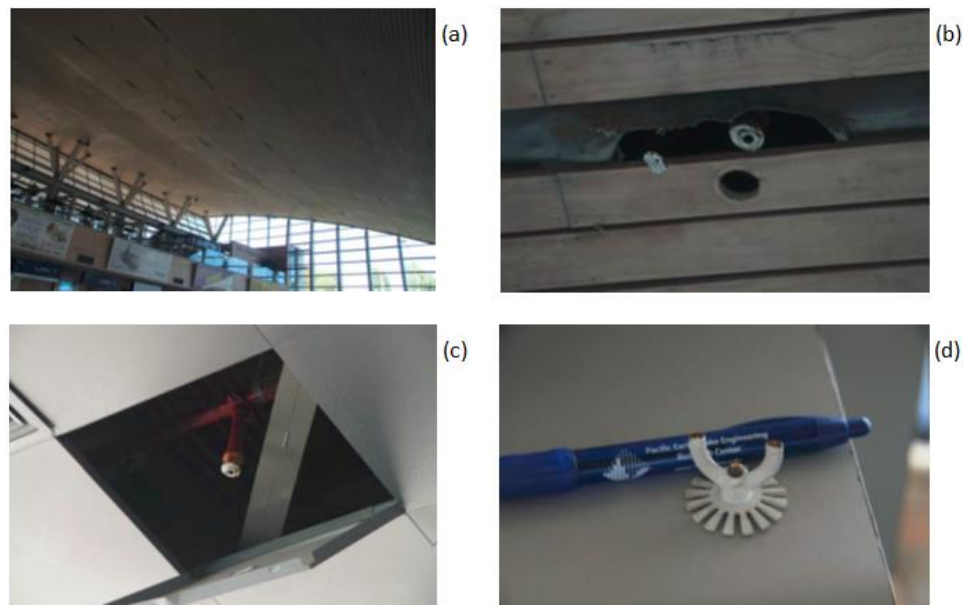


Figure 1-10 Fracture of tee joint threaded connection at the Santiago Airport (from E. Miranda, 2011)

Damage of sprinkler heads was commonly observed at the Concepcion Airport as shown in Figure 1-11. Sprinkler heads were sheared off due to differential displacement with the ceiling

system. For other cases, sprinkler heads were moved upwards and pushed through the wood ceiling because of the significant vertical accelerations effect.



*Figure 1-11 Water damage from broken sprinkler heads at Concepcion Airport (from E. Miranda, 2011)*

## **1.6 Aftermath of Fire Sprinkler System Failures during Earthquakes**

Property loss, loss of building function, fire hazard, and threat to life safety are the four major consequences caused by failures of fire protection system during earthquakes. Although they are discussed separately in this section, in reality they are closely related and cannot be isolated from each other.

### **1.6.1 Property loss**

*Figure 1-12* summarizes the statistics assembled by Miranda (2003) that demonstrates that nonstructural components and building contents account for a far larger portion of the overall

building value compared to structural systems. Moreover, nonstructural systems represent 75% of the economic losses of buildings in the United States exposed to earthquake and account for 78% in estimated future earthquake losses of the nation based on a study conducted by FEMA (2000). For example, direct economic loss of non-residential buildings during the 1994 Northridge earthquake was approximately \$6.3 billion, which was dominated by damage of nonstructural components and building contents, and only about \$1.1 billion was due to structural damage (Kircher, 2003).

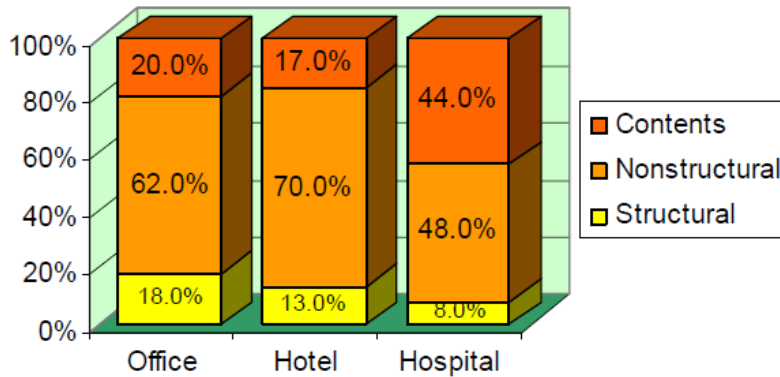


Figure 1-12 Typical investment of building construction (from Miranda, 2003)

Fire sprinkler systems, in particular, have been identified as some of the most seismically vulnerable nonstructural systems and the top rank claim for property loss by many insurance companies. The economic loss not only comes from repair and replacement of local damaged components, such as braces, piping and joints; even greater cost results from water damage from leakage in broken joints or sprinkler heads, causing damage to expensive electrical equipment and other building contents.

### **1.6.2 Loss of function**

Critical infrastructures like hospitals, power stations and airports have to remain operational after earthquakes, as these facilities provide key support to first responders. For example, the functionality of airports is crucial for transporting rescue teams and relief supplies, not to mention the importance of hospitals for emergency services. However, it has been witnessed repeatedly that these kind of essential facilities have been put out of service after earthquakes due to failure of nonstructural components. For instance, 10 out of 12 sprinkler-equipped hospitals assessed by Ayres *et al.* (1996) after the 1994 Northridge earthquake suffered severe water damage and loss of function. Moreover, the international airport terminal in Santiago was forced to shut down due to water damage from fire sprinkler system failures and damage from other nonstructural components after the 2010 Chile earthquake (Miranda *et al.*, 2010).

Secondly, business interruption due to loss of building function also plays an important role in contributing to substantial economic loss. During the 2010 Chile earthquake, LAN airline, the largest airline company in Chile, reported loss of approximately \$25 million due to the closure of international airports in Santiago and Concepcion, which handle more than two thirds of the air traffic in Chile (EERI, 2010).

### **1.6.3 Fire hazard**

Fire is one of the most common ensuing hazards after earthquakes and one of the major factors that can produce serious injuries, heavy casualties, and substantial loss of property. Fire protection systems are designed to be able to control and suppress fire by discharging water over the area after sprinkler heads are activated by heat from fire. However, this essential function of

fire sprinkler systems will be compromised by its own damage and failures when these systems are subjected to seismic loading. Damage of sprinkler heads, fracture of distribution lines, and collapse of main lines were frequently reported during previous earthquakes.

#### **1.6.4 Threat to life safety**

Violent dynamic loading due to earthquakes commonly results in an extensive variety of nonstructural damage such as broken glass, collapse of architectural partition walls, falling of suspended ceilings and light fixtures, which are all potential hazards. During the 1994 Northridge earthquake, at least five deaths and over seven thousand injuries were related to nonstructural component failures (McKevitt *et al.*, 1995).

For fire sprinkler systems, damage to sprinkler heads and distribution lines are often identified as the main reasons for unintentional water discharge and interruption of water transportation, which consequently leads to insufficient working pressure for the systems. As the fire protection system loses its function, fire spread resistance of buildings is significantly reduced and poses great potential threat to loss of life.

#### **1.7 Research Objectives**

Poor seismic performance of fire sprinkler systems have been highlighted from past earthquake events, and damage at joint connections was identified as one of the most commonly observed failures. As a result, this dissertation presents results of experimental and numerical studies on pressurized fire sprinkler piping systems to better clarify the behavior of tee joint connections and fire sprinkler systems under seismic loading.

The objectives of the experimental studies were:

- 1) To better characterize the mechanical response and identify the failure mechanism of pressurized sprinkler piping tee joints made of various materials (threaded black iron, groove-fit steel, and cement thermoplastic CPVC) and nominal diameters (3/4 in. to 6 in.) under reverse cyclic loading;
- 2) To determine the bending moment and joint rotation capacities at which leakage and/or fracture occur, and with all the data collected during the experimental investigation, to develop a seismic fragility database for pressurized fire suppression sprinkler piping joints;
- 3) To compare the seismic performance and dynamic characteristics of full-scale fire sprinkler systems made of different materials and joint arrangements at the system level under various input intensities;
- 4) To enhance the understanding of interaction between suspended ceiling systems and fire sprinkler systems ; and
- 5) To examine the effect of story differential movement on vertical risers.

The objectives of the numerical studies were:

- 1) To develop and validate an appropriate numerical framework based on a number of hysteresis models to predict the moment-rotation hysteretic behavior of various types of tee joint connections under reverse cyclic loading;
- 2) To incorporate the numerical framework into various models created with the SAP2000 and OpenSees software to predict the dynamic response of the full-scale sprinkler-piping sub-assembly tested on the University at Buffalo Nonstructural Component Simulator (UB-NCS); and



- 3) To conduct Incremental Dynamic Analyses (IDA) of a prototype building incorporating fire sprinkler piping systems to demonstrate the procedure for generating seismic fragilities of sprinkler piping systems in terms of floor accelerations.

## **1.8 Organization of the Dissertation**

A literature review of previous experimental studies on fire sprinkler systems is outlined in Chapter 2. Chapter 3 presents the results of cyclic testing conducted on 48 sprinkler piping joints of various materials and joint types. Chapter 4 summarizes the test procedures and test results obtained from the dynamic tests conducted on a two-story full-scale pressurized fire sprinkler piping systems installed on the Nonstructural Component Simulator (NCS). Chapter 5 describes the proposal, implementation, and validation of various numerical models in the quasi-static analysis of piping joints and dynamic analysis of full-scale fire sprinkler subsystem. Incremental Dynamic Analyses (IDA) conducted on a fire sprinkler system installed in a hypothetical hospital building located in Southern California are summarized in Chapter 6 along with the development of seismic fragility curves for sprinkler piping systems in terms of floor acceleration.. A summary and conclusions drawn from this research study are presented in Chapter 7. References quoted in the dissertation are listed in Chapter 8. Finally, appendices present the instrumentation details and summary of the various test results obtained from the experimental studies.

## Chapter 2

### LITERATURE REVIEW

Despite the repeated occurrence of failures during previous earthquakes, few research studies have been conducted on the seismic behavior of fire sprinkler piping systems. In this section, research related to this subject that is available in the public literature is briefly reviewed.

#### 2.1 Study on Seismic-brace Components

##### Study by Malhotra et al. (2003)

Malhotra et al. (2003) examined sprinkler seismic brace components by proposing a uniform-amplitude deformation-controlled loading history model that would cause damage equivalent to the non-uniform deformation history to the sprinkler-pipe seismic-brace components. A statistical analysis was conducted to determine how many cycles of a certain seismic load that a sprinkler-pipe seismic-brace component must resist during earthquake shaking. Uncertainties were addressed by selecting 32 strong-motion records from 18 buildings of various structural types shaken by the 1994 Northridge earthquake. The 90-percentile value of number of cycles that the brace components must resist was 11 for the Northridge earthquake, and this number was adjusted to 15 for the design earthquake in regions of high seismicity.

Furthermore, 144 tests (66 monotonic and 78 cyclic tests) were carried out in this study to evaluate the mechanical behavior of brace components. As the brace-pipe and the fastener were generally much stiffer than the pipe-attached and the building-attached components, it was reasonable to assume that most of the deformation would take place in the pipe-attached and

building-attached components (*Figure 2-1*). As a result, this test program was conducted for two types of pipe-attached components from one manufacturer and two types of building-attached components from two different manufacturers. Specimens were tested in a servo-hydraulic machine, which was capable of applying a 4-inch displacement in monotonic tension and compression, and 0.5-inch cyclic displacement at 5 Hz. The main objective of this test program was to gain insight into the scatter of test results, effect of load-rate and load-angle, as well as degradation in strength and stiffness, and the energy dissipation of brace components.

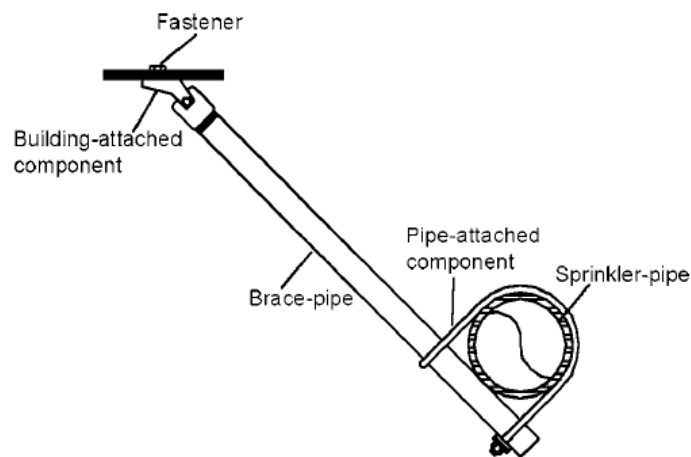


*Figure 2-1 Components of a seismic brace (from Malhotra et al. 2003)*

A number of conclusions were reached through this experimental research:

- 1) In terms of the scatter in test results, the coefficient of variation (CoV) of load in the 15<sup>th</sup> cycle ranged from 2 percent for some tests to 47 percent for other tests;
- 2) Friction-based components, deriving their strength from friction between the brace-pipe and the sprinkler-pipe, exhibited lower strength at higher frequencies, while non-friction-based components showed greater strength at higher frequencies;

- 3) Building-attached components were very flexible in the 90 degree orientation compared to the 30 and 60 degree orientations;
- 4) Under cyclic conditions, brace components exhibited significant degradation in strength if the applied deformation was over one-third the ultimate deformation measured under monotonic conditions;
- 5) Monotonic and cyclic loadings resulted in considerably different failure modes for the brace components.

Malhotra et al. (2003) lastly proposed a test protocol to determine the load that a seismic-brace component was capable of resisting for 15 cycles without breaking (structural failure) or generating excessive deformation (functional failure). This protocol included a series of monotonic tension, monotonic compression, and cyclic tests. The monotonic tension and monotonic compression tests must be conducted first to obtain information for the cyclic tests, and the load rating was determined from the results of the cyclic tests.

## **2.2 Study on Joint Connections**

### **2.2.1 Study by Antaki and Guzy (1998)**

Antaki and Guzy (1998) conducted four-point bending tests on 16 simply supported pipe specimens pressurized at 150 psi. The test specimens included 2-inch and 4-inch schedule 40 carbon steel pipes with groove-fit couplings (12 specimens) and with threaded joints (4 specimens) at mid-span. Experimental load-deflection curves were obtained up to the first leakage point of each pipe specimen. It was found that the 4-inch groove-fit coupling system was

much stiffer than the 2-inch counterpart. The joint rotations at first leakage were significantly larger for the 2-inch groove-fit coupling than those of the 4-inch groove-fit coupling. Failure of the 4-inch groove-fit coupling was characterized by partial fracture of the flange coupling. Three of the four threaded joint specimens failed through rupture at the first exposed thread, while the fourth threaded joint specimen failed by stripping of the engaged threads (Antaki and Guzy, 1998). The findings of this study were verified in this dissertation through the experimental program on sprinkler piping joints described in Chapter 3.

Dynamic shake table tests on 16 pressurized (150 psi) pipes, 16-feet long and incorporating groove-fit couplings (12 specimens) and threaded joints (4 specimens) at their ends were also conducted by Antaki and Guzy (1998). A flange at the end of each pipe specimen was bolted vertically onto a shake table and was connected to the tested joint. All 16 pipe specimens acting as vertical cantilevers were tested simultaneously under horizontal sinusoidal input motions at increasing amplitudes. Leakage of the groove-fit coupling systems was observed at 70% of their static moment capacity. Flexural failures similar to that observed in the static tests were also observed in the dynamic tests. First leakage of the threaded joints, however, was observed at only 25% to 50% of their static moment capacity.

### **2.2.2 Study by Wittenberghe et al. (2010)**

Wittenberghe et al. (2010) performed a fatigue test on a threaded pipe connection to evaluate the crack propagation with the use of an optical dynamic 3D displacement measuring technique. The four-point bending test setup is schematically illustrated in *Figure 2-2*.

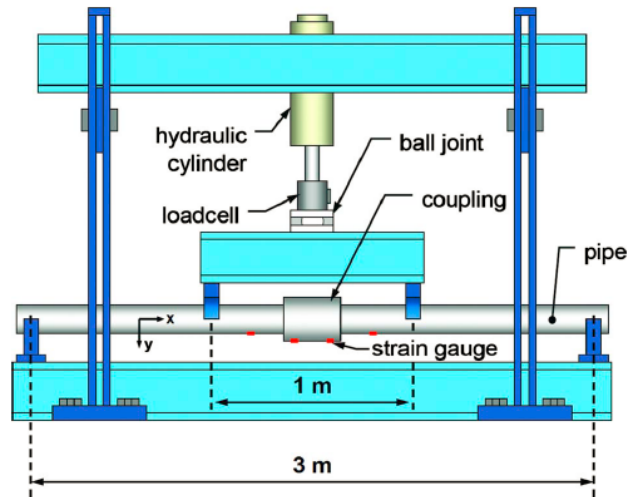


Figure 2-2 Schematical view of the four-point bending fatigue setup (from Wittenberghe et al. 2011)

The test specimen consisted of two steel pipe segments with an outside diameter of 4.5 inches, connected by a threaded coupling in the middle. Twenty-one reflective optical markers and two linear variable differential transformers (LVDT) were attached to the specimen to measure the pipe deflection and the crack opening, respectively. Both measurements were in very good correspondence with simplified finite element simulations. It was found that the threads of the threaded pipe couplings acted as stress raiser that could initiate fatigue cracks. These cracks tended to initiate in the contact interface at the thread roots away from the outer surface of the pipes, which made it hard to define a clear distinction between crack initiation and propagation. It was found that the use of an optical dynamic 3D displacement analysis technique was able to provide reasonably accurate results to monitor the crack propagation in a threaded pipe assembly.

## 2.3 Study on Piping Systems

### 2.3.1 Study by Dillingham and Goel (2002)

To investigate the dynamic properties of fire sprinkler systems constructed with different materials, a series of shake table tests were carried out by Dillingham and Goel (2002). A small version of a one-story timber building structure (*Figure 2-3*) equipped with a simple sprinkler design was built and attached to a 3 feet by 3 feet shake table (*Figure 2-4*). Three fire protection systems were installed with 1-inch CPVC (fire rated) plastic pipes, while a fourth one used schedule 40 carbon steel pipes.



*Figure 2-3 Timber building model (from Dillingham and Goel, 2002)*

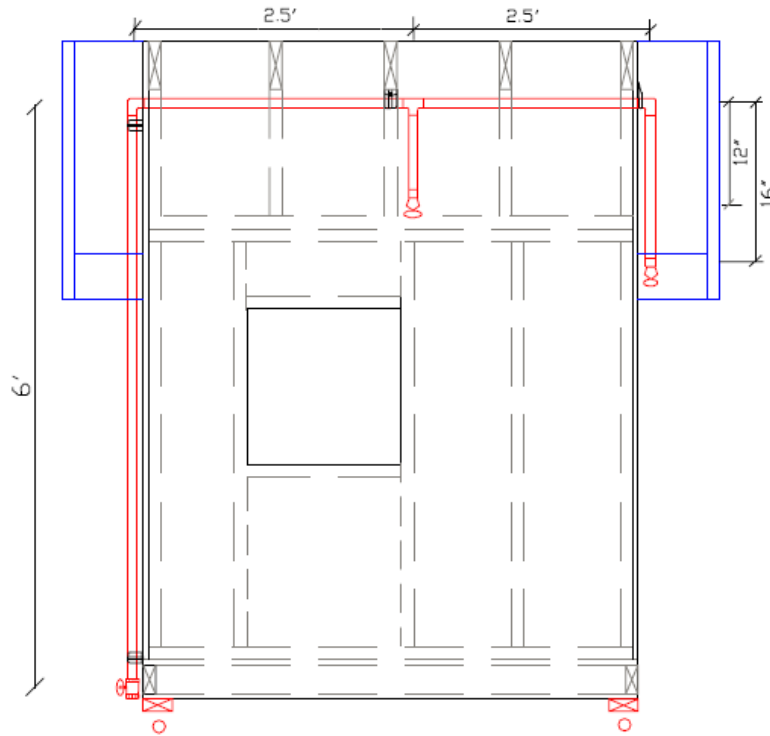


Figure 2-4 Layout of fire sprinkler system (from Dillingham and Goel, 2002)

The fire protection systems were filled with water to indicate any potential leakage and system failure. Analytical models were constructed with the SAP2000 software to verify the observed fundamental frequencies. Each specimen was mounted to the shake table and then first tested in the longitudinal direction before being rotated 90 degree and tested again in the transverse direction. A sine sweep with an increasing frequency at a constant acceleration was used as the loading protocol. Time histories of accelerations at various locations based on particular points of interest were recorded during each test. All four tested fire sprinkler systems that were installed in accordance code requirements performed well without any failures. Large acceleration amplifications were observed in both the building structure and the fire sprinkler systems, and the 16-inch unsupported drop experienced the highest level of amplification, 35



times the base level acceleration, which was identified as a potential cause of failure at the threaded connection.

### **2.3.2 Study by Goodwin et al. (2007)**

Goodwin et al. (Goodwin *et al.*, 2007) conducted a series of shake table tests on two typical hospital piping subassemblies. (*Figure 2-5*) One specimen was made of forged steel pipe with welded connections, while the other one was constructed with cast iron pipe with threaded connections. Both of the welded and threaded hospital piping subassemblies were subjected to increasing level of input motions with and without seismic bracing systems.

The objectives of this research program were to understand the seismic behaviors and identify the failure modes and drift capacities of the typical welded and threaded hospital piping systems under braced and unbraced conditions. A variety of instrumentation was installed to measure the accelerations and displacements on the pipes, as well as axial forces transmitted through the vertical hanger rods.

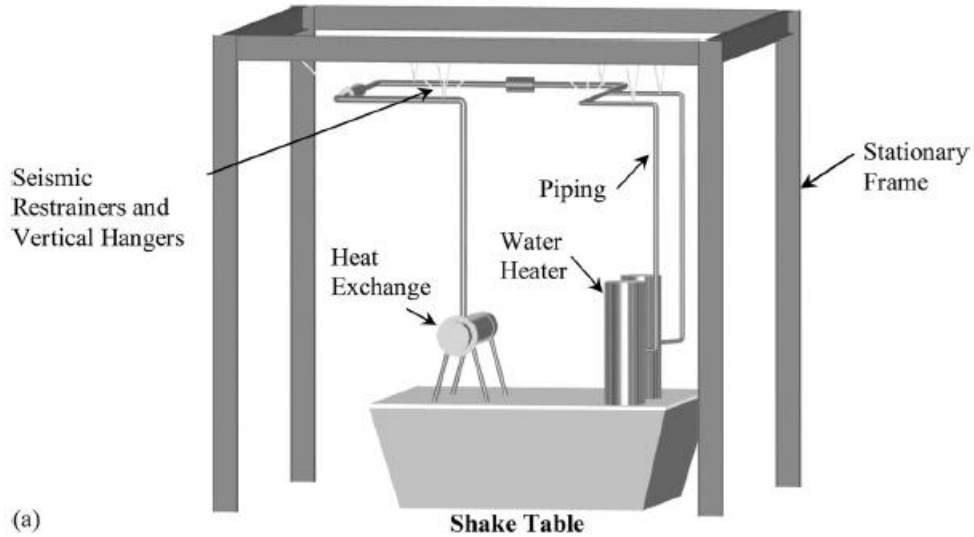


Figure 2-5 Experimental setup: (a) schematic of the setup; and (b) final setup (from Goodwin et al. 2007)

It was found in this testing program that the welded hospital subassemblies had a much better performance than the threaded subassemblies due to the superior ductility. The welded systems withstood up to 4.34% story drift without any damage, while the threaded systems showed either complete failure or severe leakage at the same level of story drift. The seismic bracing systems were effective in restraining excessive displacement response of both piping assemblies.

### 2.3.3 Study by Hoehler et al. (2009)

Hoehler et al. (2009) performed an extensive investigation into performance of suspended pipes and the forces applied on the post-installed anchors in a full-scale 7-story reinforced concrete test building subjected to a diverse range of earthquake ground motions. On the first, fourth and seventh floors of the building, a group of six cast iron pipes with an outside diameter of 6 inches was mounted to trapezes connected to the slabs. (*Figure 2-6 b*) The trapezes were made for square steel channel strut and suspended from the slab by using threaded rods. The hanger of gravity support was covered by a piece of strut to prevent buckling of threaded rods, and five seismic braces were installed to resist seismic forces. A total of 16 out of 39 anchors were instrumented with axial strain gauges so that time histories of axial forces in the anchorages of the pipe support systems could be derived after testing. Accelerometers were attached to both pipes and slabs to record time histories of accelerations at various locations.

Hoehler et al. (2009) concluded that maximum pipe accelerations increased with the ground motion intensity, while the amplification of the ground accelerations measured on the pipes decreased with an increase of ground motion intensity due to the development of nonlinear behavior in the building structure. It was also observed that the accelerations recorded on the pipes were slightly larger than those calculated by using the equation in ASCE 7-05 (2005) designated for nonstructural components (*Equation 1.3*). Hoehler et al. also found that the axial loads induced by the earthquake motions on the gravity support anchors were generally larger than those in the seismic brace anchors, and the maximum axial force in the anchors was approximately 30% of the mean ultimate tension capacity. Some of these findings were verified

in this dissertation through the experimental program on a two-story full-scale pressurized fire sprinkler piping systems described in Chapter 4.



Figure 2-6 (a) Seven-story building on the shake table and (b) Nonstructural system on the first floor (from Hoehler et al. 2009)

### 2.3.4 Study by Martínez (2007)

A series of full-scale earthquake tests and finite element analysis (FEA) of a water piping system were conducted by Martínez (2007) to study its dynamic behavior under seismic loading. A rigid truss simulating the roof of a building was suspended from a steel support frame. A full-scale

water piping system made of steel pipes with Victaulic grooved end couplings was supported from the rigid truss by hangers and braces. Both ends of the piping assembly were welded to a strong wall in the Advanced Technology for Large Structural Systems (ATLSS) laboratory at Lehigh University (*Figure 2-7*). Three tests with pipe diameters ranging from 4 in. to 16 in. were performed. All the specimens were filled with water and pressurized at 200 psi. The displacement time histories for the input motions (see *Figure 2-8*) were generated by the software SIMQKE (Gasparini and Vanmarke, 1976), following the International Code Council Evaluation Service's *Acceptance Criteria for Seismic Qualification by Shake-Table Testing of Nonstructural Components and Systems* (AC156, 2004).



*Figure 2-7 Victaulic test setup at Lehigh University's ATLSS laboratory (from Martínez, 2007)*

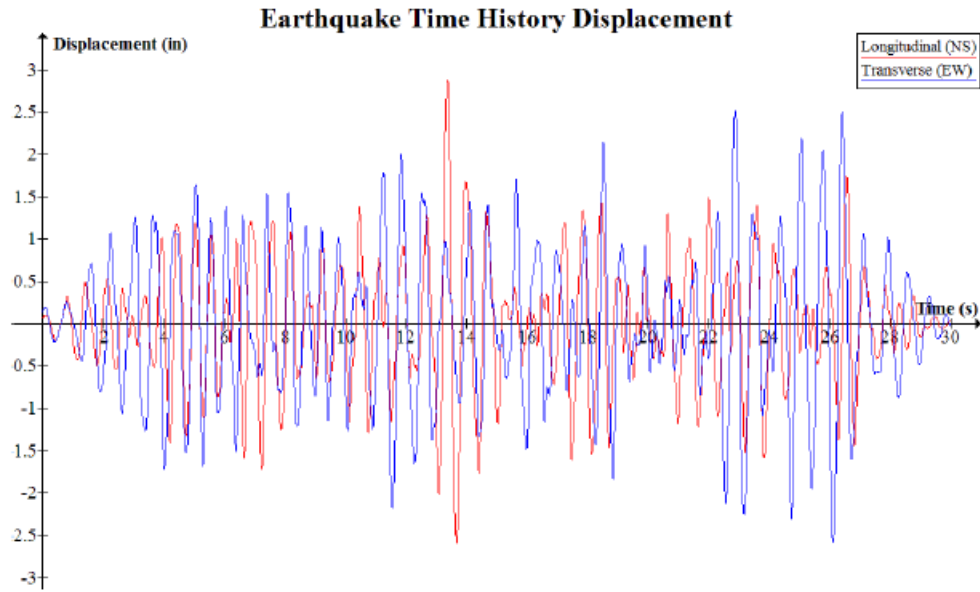


Figure 2-8 Displacement time histories that served as input to the hydraulic actuators (from Martínez, 2007)

Before the numerical modeling of the water piping assembly was done, a series of static tests were carried out in order to determine the rotational stiffness properties of the Victaulic couplings. Two finite element models (steel pipe with welded joints, and steel pipe with Victaulic couplings) were created and analyzed in the finite element software ABAQUS (SIMULIA, 2007), as shown in *Figure 2-9*. A finite element static analysis and a modal analysis were performed to verify the model and determine the natural frequencies of vibration of the test setup. Also, implicit linear dynamic tests with the same input motion defined in *Figure 2-8* were carried out.

All three test setups of water piping systems made of steel pipes with Victaulic coupled joints performed well during the seismic shake table tests and no leakage or damage was observed.

Flexible couplings improved the localized flexibility of the system, modifying the stiffness

properties and seismic response. It was found that finite element models of water piping systems constructed using ABAQUS were not consistently accurate in predicting the response of seismic shake table tests. Roughly 70% of the recorded the uniaxial accelerations on the pipes was predicted accurately by the finite element models.

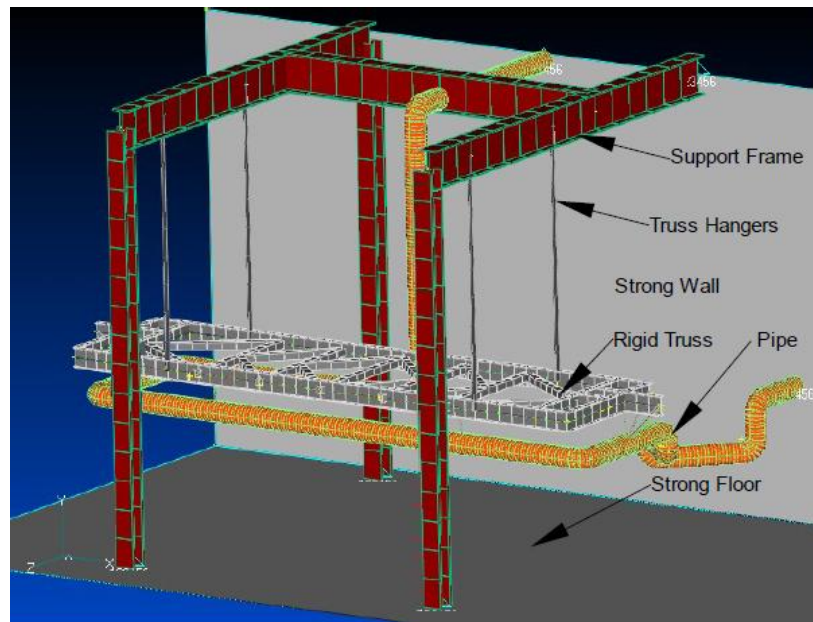


Figure 2-9 Finite element model of the Victaulic test setup in ABAQUS (from Martínez, 2007)

## 2.4 Discussions

Countless instances of damage and failure of fire protection systems subjected to seismic loading have demonstrated that one of the most vulnerable parts in the entire systems lies in the joint connections. Previous research and studies however seldom tried to characterize and gain an in depth understanding of the failure modes and mechanical behaviors of joint connections. Although the research carried out by Antaki and Guzy (1998) covered sprinkler pipes with both groove-fit couplings and threaded joints, there were also two major limitations: (1) the lack of full coverage of pipe sizes and pipe schedules; and (2) the omission of CPVC (fire-rated) plastic

pipes with cement joints, which nowadays regularly replace copper pipes with solder connections in residential and light commercial markets as a result of their low cost and ease of installation. (Dillingham and Goel, 2002)

Previous shake table dynamic tests conducted on piping subassemblies were either limited by the scale of the specimens or lacked some of the most typical layouts and designs observed in sprinkler piping systems, which differ from other piping subassemblies such as plumbing and ductwork. For instance, failures of the unsupported armovers and interaction between sprinkler heads with other structural and nonstructural components were frequently mentioned in the damage reports from previous seismic events; emphasis and information on this subject was missing from previous experimental studies.

This literature review has once again highlighted the necessity and importance of more research and studies in order to fill the gap in knowledge about the failure mechanisms and seismic performance of fire sprinkler piping systems. The main objective of this dissertation is to contribute to a better understanding of the seismic behavior of pressurized fire sprinkler piping systems through the experimental programs and analytical studies described in Chapters 3 to 6.



## Chapter 3

### EXPERIMENTAL ASSESSMENT OF PRESSURIZED FIRE SUPPRESSION

#### SPRINKLER PIPING TEE JOINTS

##### 3.1 Introduction

As the first series of experimental studies of the NEES-NGC Project performed in this dissertation, a testing program designed to evaluate the behavior of full-scale sprinkler piping tee joints was conducted in the Structural Engineering and Earthquake Simulation Laboratory (SEESL) at the University at Buffalo (UB). A total of 48 pressurized sprinkler piping tee joint specimens were tested under monotonic and reverse cyclic loading. These sprinkler tee joints were constructed with various materials (black iron with threaded joints, chlorinated polyvinyl chloride (CPVC) with cement joints, and steel with groove-fit connections), and with nominal pipe diameters ranging from  $\frac{3}{4}$  in. to 6 in..

The objectives of this experimental program were:

- 1) To observe and describe the failure mechanism of sprinkler piping tee joints;
- 2) To measure and determine the moment and rotational capacities of the tee joints when leakage and/or fracture occurred;
- 3) To construct a seismic fragility database for pressurized fire suppression sprinkler joints of various materials and joint types based on the ATC-58 framework;
- 4) To provide input for the design and execution of dynamic tests in the sub-system level presented in Chapter 4 of this dissertation ; and

- 5) To provide a large set of recorded data for the development, validation and calibration of numerical models simulating the hysteretic behaviors of sprinkler piping joints presented in Chapter 5 of this dissertation.

This chapter provides a detailed presentation of the test set-up, test plans and test procedures, as well as a summary of the main experimental observations and analyses of the test results.

### **3.2 Selection of Materials and Joint Types**

Materials considered for the sprinkler piping tee joint specimens included black iron with threaded joints, chlorinated polyvinyl chloride (CPVC) with cement joints, and steel with groove-fit connections (*Figure 3-1*). Black (cast) iron pipe with threaded joints is the most commonly used, especially in commercial buildings, since it can be used in both branch lines with small diameter pipes and in main lines with large diameter pipes. To reflect their range of applications, black iron pipes with nominal diameters ranging from  $\frac{3}{4}$  in. to 6 in. were included in the test matrix. CPVC piping has started to be installed since the 1950s and has gradually replaced copper pipes in residential and light commercial applications with the advantage of cost-effectiveness and ease of handling and installation. However, considerable concerns remain about the survival of CPVC piping when it is exposed to elevated temperatures during a fire. Furthermore, CPVC pipes are not listed for use in ordinary hazard or extra hazard areas (NFPA, 2010). CPVC pipe diameters of  $\frac{3}{4}$  in. 1 in. and 2 in. were considered for testing. Grooved end piping is a relatively new product that has started to gain tremendous popularity in seismic-prone areas because of the added localized flexibility it provides to sprinkler piping systems.



(a) Black iron pipes (from Forchase Inc., 2009)



(b) Black iron female tee (from Lowes, 2012)



(c) CPVC cement (from Family Handyman Inc., 2012)



(d) CPVC pipe and fittings (from GFPiping, 2012)



(e) Steel pipes with Groove-fit joints



(f) Groove-fit connections (from Victaulic Company, 2012)

Figure 3-1 Pipe materials and joint types selected for testing

Steel pipes with welded joints were also one of the popular-used materials and configurations in fire suppression sprinkler piping market and was initially included in the test program. However, welded pipes were taken out from the test matrix after preliminary testing on a few specimens showed that the stroke limitation of the loading actuator prevented reaching the point of any leakage or damage in the joints.

### 3.3 Description of Experimental Set-up and Test Specimens

#### 3.3.1 Experimental set-up

For each specimen, the sprinkler piping tee joint was connected to two in-line pipes of various lengths,  $L$ , to form a simply supported beam, as shown in *Figure 3-2*. The perpendicular branch of the tee-joint was connected to a pipe attached to a 20-kip linear hydraulic actuator with 6-inch stroke capacity to simulate a mid-span point load. This actuator was fixed to a rigid reaction frame bolted to the strong floor. Both ends of the test specimens were sealed with caps and held in place by steel collars, which served as pin-pin connections. The steel collar (as seen in *Figure 3-4* and *Figure 3-5*) was made by welding an approximately 1.5-inch-long steel tube onto a steel plate, which was attached to pedestals fixed to the strong floor. The inside diameter of the steel tube was slightly larger than the outside diameter of the pipe cap in order to allow small rotation at the end of the pipe. Two load cells were attached to the collars to measure the shear force at each side. The test specimens were also braced against buckling in the direction of loading. The specimens were pressurized to 40 psi to simulate average municipal water pressure. A three-dimensional rendering of the test set-up is shown in *Figure 3-3*.

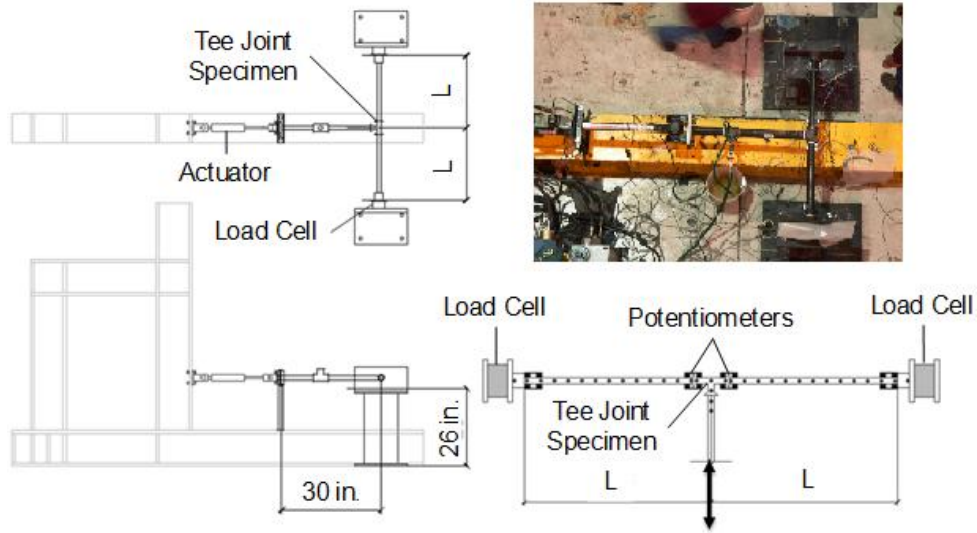


Figure 3-2 Experimental set-up

The length,  $L$ , of the pipes was varied in the test setup to control the amount of rotation and moment demands at the joints within the 6-inch stroke capacity of the actuator. As shown in *Table 3-1*, longer pipes were used for specimens with larger diameters.

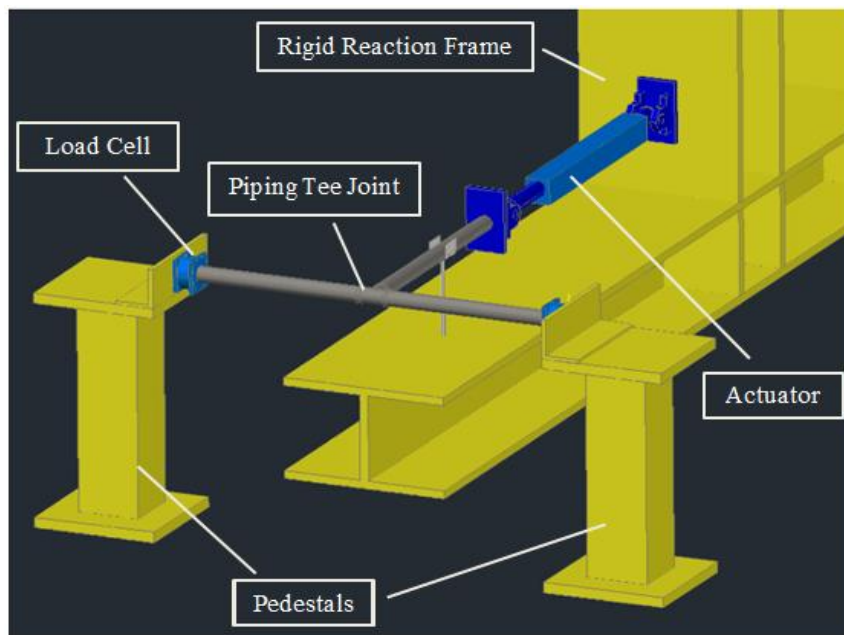


Figure 3-3 Three-dimensional rendering of test set-up

### 3.3.2 Construction of test specimens

#### Black iron pipe with threaded connections

Visual inspection of each pipe component was first performed to ensure that the pipe threads were clean and in good condition. Teflon tapes, which acted as a lubricant allowing more thread engagement and prevented formation of spiral leak paths by filling the gap between the crests and roots of mating threads, were applied to the male threads at the end of pipes (CIRCOR, 2012). Special attention was paid to ensure the proper application of Teflon tapes to prevent tapes coming unwound as the pipe fittings were tightened. Pipes were screwed into the tee joint by hand with the help of pipe wrench.

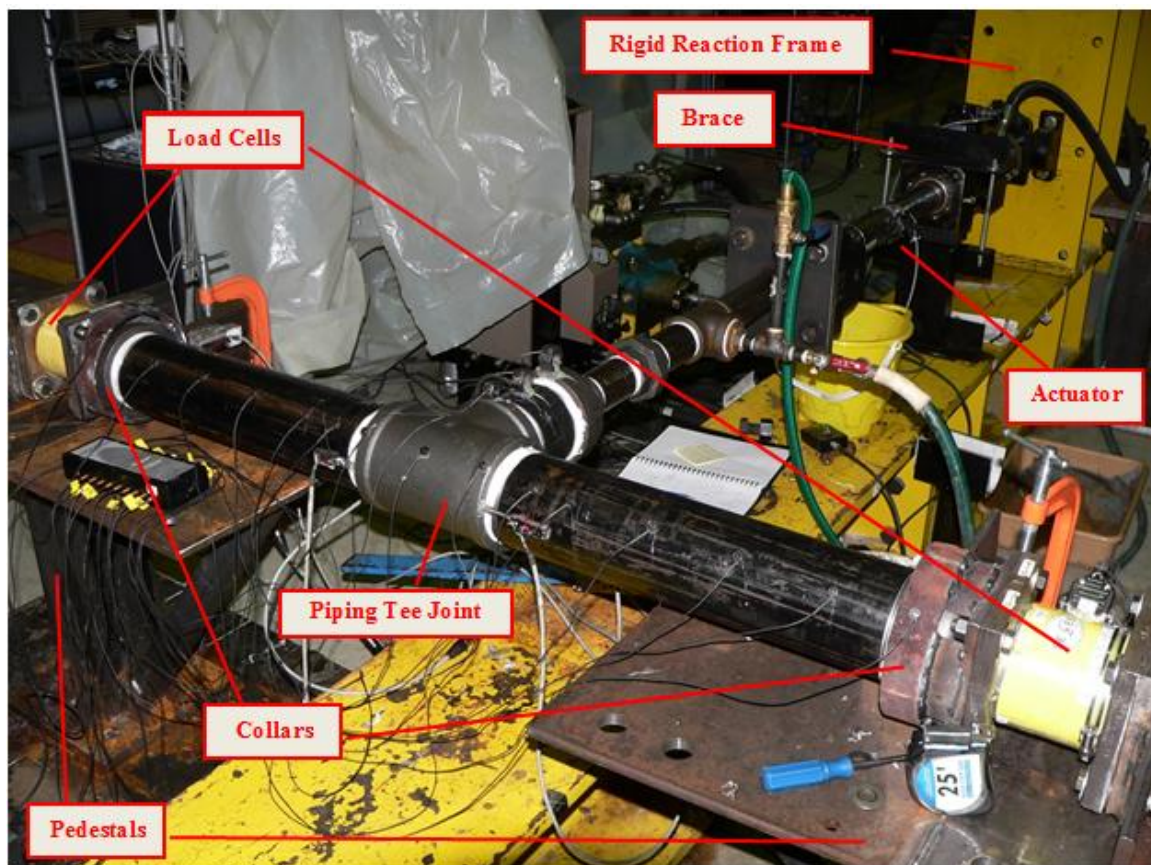


Figure 3-4 Specimen made of cast iron pipe with threaded connections

### Chlorinated polyvinyl chloride (CPVC) pipe with cement joints

Both outside ends of each CPVC pipe were sanded to remove any burrs before the application of approved CPVC solvent cement. The solvent was spread on the inside surface of the fittings and on the outside surface of the pipe ends. The CPVC cement was evenly applied to the end of the pipe at a depth equal to the depth of the fitting socket. The CPVC pipe was fully pushed into the fitting and slowly twisted another 1/8 to 1/4 turn when it touched the bottom edge of the fitting. The specimen was held for approximately 30 seconds to prevent the pipe from moving out from the tee joint. Excessive cement bead coming out from the juncture of the pipe and fitting was wiped off with a rag. (CORR, 2002). As the necessary curing time for the CPVC cement varies from one hour to twelve hours depending on the temperature, humidity and pipe size, after assembling, all specimens were put aside overnight (more than twelve hours) before testing to provide enough time for the CPVC cement to cure. Checking for leaks was conducted on each specimen before the tests.

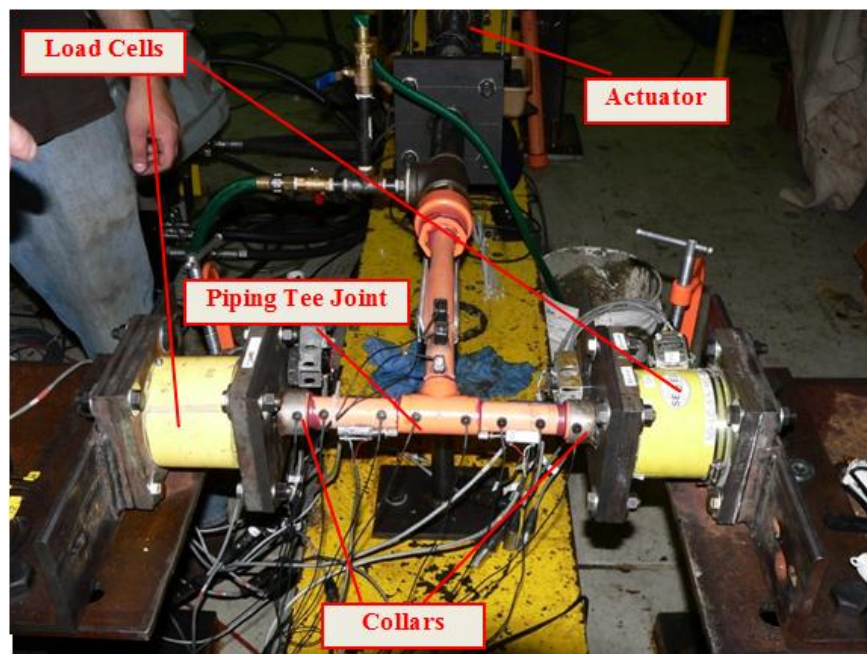
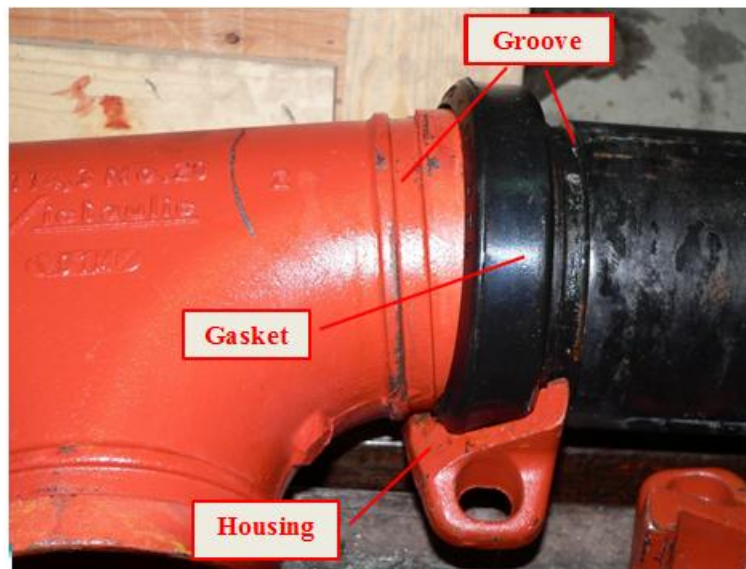


Figure 3-5 Specimen constructed with CPVC pipe with cement joints

## Steel pipe with groove-fit connections

Grooved end piping fittings manufactured by Victaulic were purchased and used for the construction of the steel pipe specimens with groove-fit connections. The Victaulic grooved coupling consists of the housing (coupling flange), the gasket, as well as bolts and nuts. A typical coupling is shown in *Figure 3-6*.



*Figure 3-6 Typical Victaulic piping coupling*

The exterior groove and ends of the pipe were inspected and kept from any dirt or grease before installation. A fine layer of approved silicon lubricant was applied to the edges and outer surface of the gasket. The gasket was then slid into the center of the grooved portions between the pipe and the fitting. The housing was placed over the gasket and the housing keys of the coupling flange were fully engaged into the grooves. Hexagonal nuts were tightened alternately between the bolts on each side of the coupling until the proper torque was reached according to the installation manual (Victaulic, 2008). The coupling flanges were positioned both parallel (*Figure*



3-17 a) and perpendicular (Figure 3-17 b) to the loading direction of the actuator in order to consider any possible effect of the load direction on the failure modes of the coupling flanges and on the force required to reach the same kind of damage. A specimen made of steel pipe with groove-fit connections ready for test is illustrated in Figure 3-7.

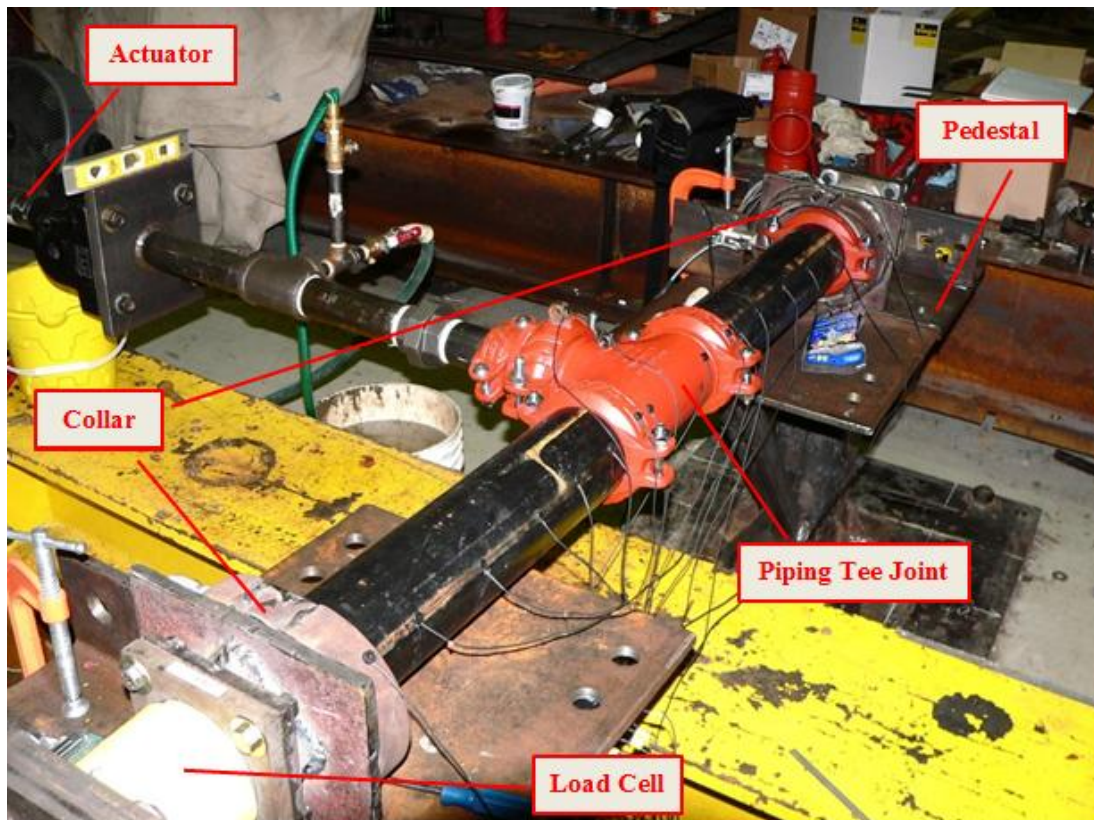


Figure 3-7 Specimen made of steel pipe with groove-fit connections

### 3.4 Test Program

The variables considered in the testing program included (1) pipe material, (2) joint configuration, (3) pipe schedule, and (4) pipe size. Table 3-1 lists the details of the sprinkler piping joint test program.

Table 3-1 Experimental test program

Material and Joint Type	Nominal Pipe Size (in)	Outside Pipe Diameter D <sub>o</sub> (in)	Pipe Wall Thickness (in)	Pipe Length L (in)	Number of Monotonic Tests	Number of Cyclic Tests
Black Iron with Threaded Connection	6	6.63	0.28	46	1	3
	4	4.50	0.24	20	1	3
	2	2.38	0.15	24	1	3
	1	1.32	0.13	24	1	3
	3/4	1.05	0.11	24	1	3
CPVC with Cement Joint	2	2.38	0.15	24	1	3
	1	1.32	0.13	5.5	1	3
	3/4	1.05	0.11	5.5	1	3
Schedule 40 Steel with Groove Fit Connection	4	4.50	0.24	20	1	3
	2	2.38	0.15	9.5	1	3
Schedule 10 Steel with Groove Fit Connection	4	4.50	0.13	20	1	3
	2	2.38	0.11	9.5	1	3
Total Number of Specimens						48

Table 3-1 outlines the 48 tee joint specimens considered for the testing program. Four different materials and joint types were considered: 1) black iron with threaded joints, 2) chlorinated polyvinyl chloride (CPVC) with cement joints, 3) schedule 40 steel with groove-fit connections and 4) schedule 10 steel with groove-fit connections. The nominal diameters (sizes) of the pipes varied as follows: 3/4 in. to 6 in. for the black iron threaded joints; 3/4 in. to 2 in. for the CPVC joints and 2 in. and 4 in. for both schedules of the steel groove-fit connections. The range of diameters tested for each type of joint is representative of their use in practice.

### 3.5 Testing Protocol

For each tee joint configuration, one monotonic and three cyclic tests were conducted. All tests were conducted at a low speed of 0.01 in./sec. For the monotonic tests, the displacement of the loading actuator (see *Figure 3-4*) was controlled according to a unidirectional ramp. For the cyclic tests, a sine sweep function with gradually increasing amplitude was adopted. The displacement of the loading actuator was controlled according to the displacement-history shown in *Figure 3-8*. This cyclic loading protocol was developed specifically for evaluating the seismic fragility of nonstructural components, and more details about this loading protocol can be found in Retamales *et al.* (2008; 2011). The maximum cyclic amplitude of  $\pm 3$  inch was limited by the 6-inch stroke of the actuator.

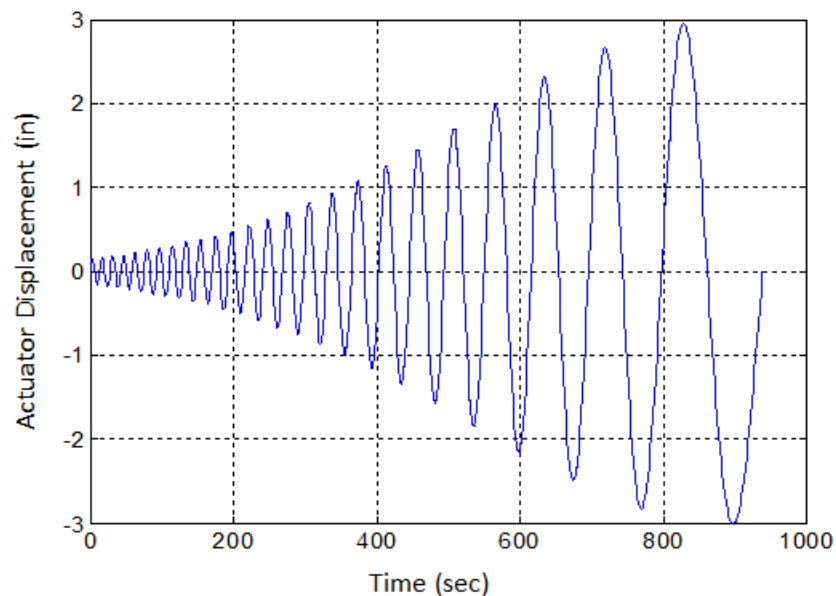


*Figure 3-8 Loading Protocol for Cyclic Tests*

### 3.6 Instrumentation

Extensive instrumentation was implemented to measure the displacement and force imposed on the specimens and the axial displacement along the pipe surface at the juncture of tee joint and the pipe. Shear load cells (*Figure 3-9*) were installed at both ends of the test specimens to measure the end reactions,  $R$ . The bending moment applied at each joint of the tee,  $M$ , could then be obtained from:

$$M = RL_j \quad (3.1)$$

where  $L_j$  is the distance from the pin end of the pipe to the center of each tee joint.

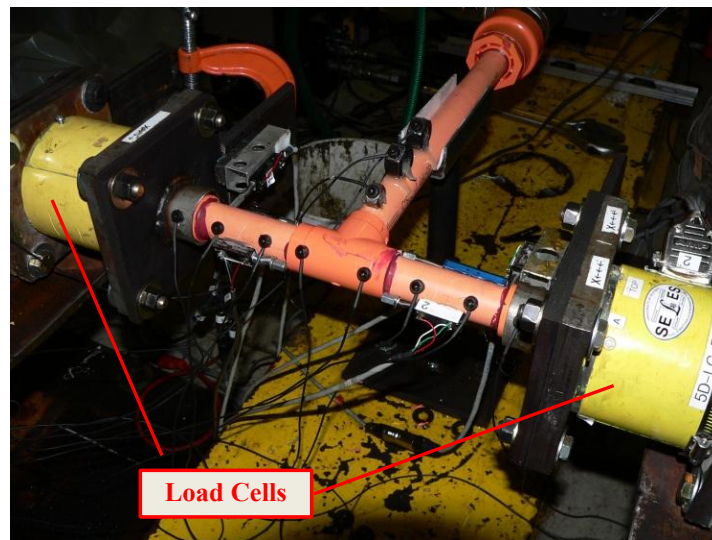


*Figure 3-9 Load cells used to measure shear force at both ends of specimens*

Linear potentiometers, as shown in *Figure 3-10*, were installed across each side of each joint of the tee (i.e. four potentiometers total). Each potentiometer was connected to a small magnet attached to the edge of the tee joint. The potentiometers were glued to the pipes in such a way that the axes were placed around the mid-point of the stroke in order to measure the axial

displacement,  $d$ , in both extension and compression on each side of the tee joint. The rotation of each joint of the tee,  $\theta$ , could then be obtained from:

$$\theta = \frac{2\bar{d}}{D_o + 2e} \quad (3.2)$$

where  $\bar{d}$  is the average axial displacement measured by the potentiometers on both sides of a joint;  $D_o$  is the outside diameter of the pipe; and  $e$  is the eccentricity between the centerline of the potentiometers and the outside surface of the joint (0.16 in.). A graphical illustration of the calculation of the rotation,  $\theta$ , for a CPVC joint specimen is shown in *Figure 3-11*. From Equations (3.1) and (3.2) the moment-rotation relationship can be obtained for each joint of the tee.



*Figure 3-10 Linear potentiometers attached to a tee joint*

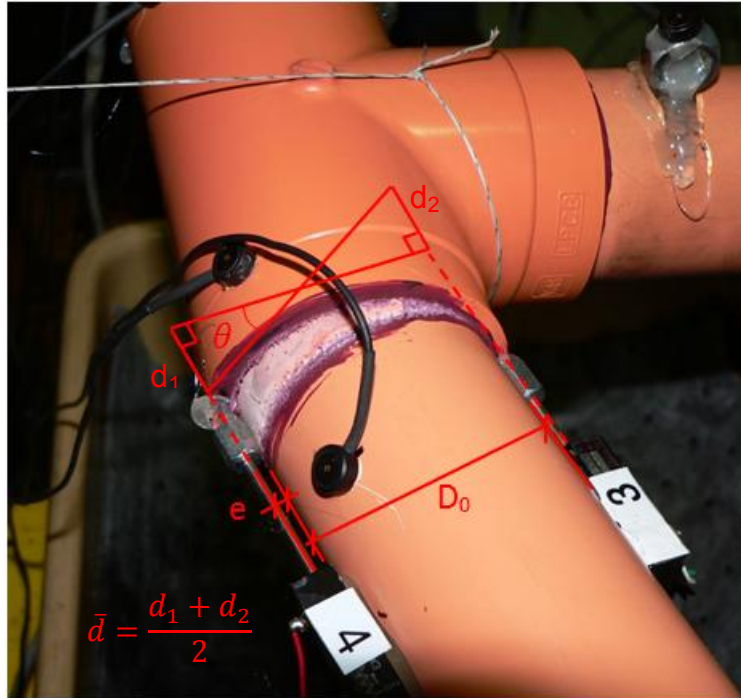
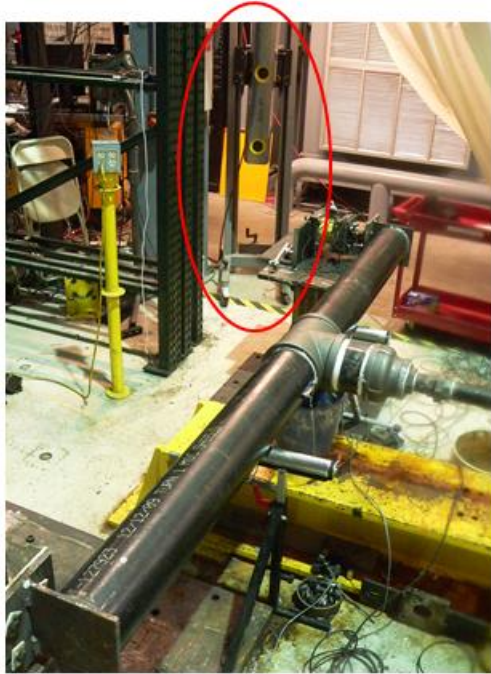


Figure 3-11 Illustration of calculation of rotation

An optical dynamic mobile coordinate measurement system (Nikon Metrology, 2012) was also used to measure the displacements at a number of locations along the piping specimens. Light Emitting Diodes (LEDs) were attached to each of the piping specimens to deliver real-time coordinate information along the pipe surface to a camera station. The camera station sat beside the test set-up (*Figure 3-12*) to prevent contact or water spray as leakage of specimens occurred. The number of LEDs was varied with the various configurations as the length of pipe changed. The rotations obtained by integrating this displacement field were compared with the local rotation measurements at the joints from Equation (3.2). Very good match was observed between the two sets of measurement systems. A detailed description of the instrumentation and channel information for each specimen is presented in Appendix A.



(a) Krypton camera station



(b) LEDs attached to the piping specimen

Figure 3-12 Non-contact coordinate measurement system

One extra channel was prepared for an electrical switch, which was activated manually and created a sharp current impulse during the data acquisition to help determine the occurrence of the first major leakage and/or fracture of each tee joint specimen.

### 3.7 Definition of Damage State

Two different Damage States (DS) were originally considered for the test program: 1) DS<sub>1</sub>: occurrence of first significant leakage and 2) DS<sub>2</sub>: physical fracture of the pipe/joint. For damage state DS<sub>1</sub>, first significant leakage was achieved when water sprayed from the joint without interruption when the joint closed. Therefore damage state DS<sub>1</sub> represents the threshold of water damage compromising the operation of a building. For damage state DS<sub>2</sub>, a joint was considered

fractured when the force in the actuator, after reaching the peak force, decreases to 80% of that peak value (FEMA, 2007). Damage state DS<sub>1</sub> was achieved during cyclic loading of all tee joint specimens. For pipe specimens incorporating CPVC with cement joints, black iron with threaded connections of small diameters (3/4 in. and 1 in.) and steel (schedule 40) with groove fit connections, both damage stages DS<sub>1</sub> and DS<sub>2</sub> occurred simultaneously as fracture of the joints was accompanied by the first significant water leakage. For larger diameter black iron pipes (2 in., 4 in. and 6 in.) with threaded joints, damage state DS<sub>2</sub> could only be observed for the monotonic tests where the actuator could be fully extended from zero to six inches. For the cyclic tests, the ±3 in. stroke limitation of the actuator prevented the damage state DS<sub>2</sub> to be reached. Based on the above, and considering that a joint would need full replacement after it has leaked significantly; only damage state DS<sub>1</sub> is reported herein.

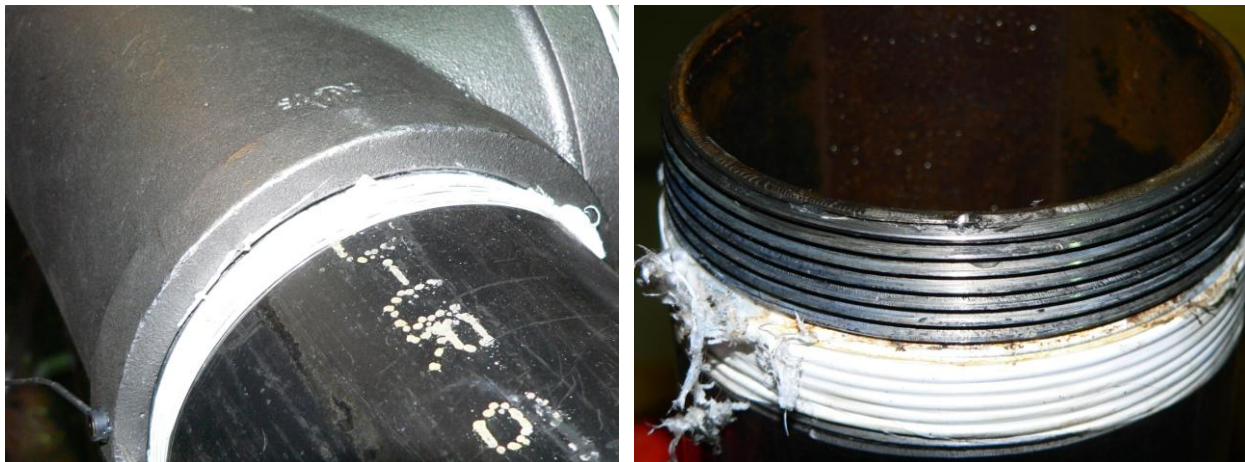
### **3.8 Specimens Damage Observations**

A detailed damage survey was performed after the completion of each test. The damage survey included visual observation of the exterior of the specimen, taking pictures, disassembly of the specimen to inspect possible damage inside the tee joint and pipe, and documenting a detailed assessment of damage for each specimen. It was found that the piping tee joint specimens constructed with various materials and joint configurations exhibited significant differences in physical damage and failure mechanism. However, the observed damage at first leakage was consistent for each pipe material and joint type tested. Details of the observed physical damage and failure mechanism for various configurations are described and compared in this section.



### 3.8.1 Damage observations on black iron pipe with threaded connections

A total of five nominal diameters ( $\frac{3}{4}$  in., 1 in., 2 in., 4 in. and 6 in.) were selected for the testing of cast iron pipe with threaded connections. Similar damage and failure mechanisms were observed for all five configurations up to the first leakage. First leakage of the black iron pipe with threaded joints occurred when the threads in the pipes slipped from the mating threads in the tee joint. This was accompanied by degradation of the thread sealant (Teflon tape) and in some cases significant damage in the threads themselves. Eroding of threads due to slippage also led to the formation of spiral leak paths. Complete fracture of the pipes occurred simultaneously with the first major leakage for pipes with small nominal diameters ( $\frac{3}{4}$  in. and 1 in.) Pipes with larger nominal diameters, on the other hand, did not reach the damage state DS<sub>2</sub> before the actuator reached its  $\pm 3$  in. stroke limit. The typical observed damage on black iron pipes with threaded joints is shown in *Figure 3-13*.



(a) Spiral leak path and gap between tee joint and pipe

(b) Degradation of Teflon tape

*Figure 3-13 Typical damage of cast iron pipe with threaded connections*



(c) Opening of threads in the pipe



(d) Eroding of threads due to slippage



(e) Fracture of pipe



(f) Sheared threads in the pipe

Figure 3-13 Typical damage of cast iron pipe with threaded connections (Cont'd)

For all specimens, significant inelastic rotations were concentrated at the ends of the pipes on both sides of the tee joint (as seen in *Figure 3-14*). The ends of the pipes on both sides of the tee joint are the weakest part of the assembly because the roots of the male threads in the pipes have the thinnest wall thickness and the smallest moment of inertia due to the threading process. As a result, the roots of the male threads in the pipes have the least rotational resistance capacities and consequently allow more inelastic deformation and become the first portion to yield and fail

compared to the crests of the threads in the pipes and threads in the tee joint. This was observed for all specimens with nominal diameters of  $\frac{3}{4}$  in. and 1 in., which experienced both DS<sub>1</sub> (first leakage) and DS<sub>2</sub> (fracture of the pipe). The opening or fracture of the threads was initiated from the roots of the male threads in the pipes.



(a) Large inelastic rotation occurred at the ends of the pipes on both sides of the tee joint



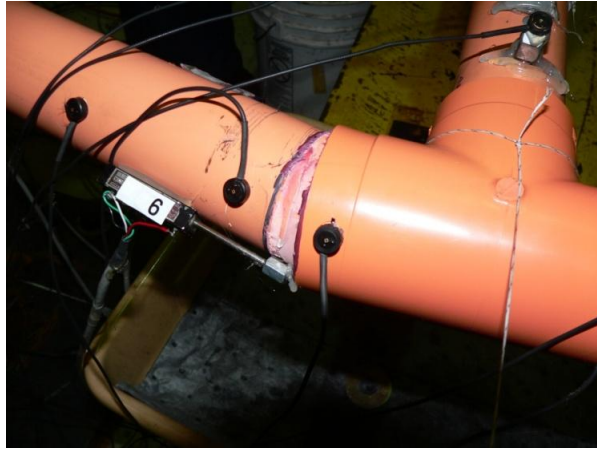
(b) Fracture of pipe occurred at the juncture of fitting and tee joint

Figure 3-14 Failed specimens made of cast iron pipe with threaded connections

### 3.8.2 Damage observations on CPVC pipe with cement joints

The behavior at first leakage of the CPVC pipes with cement joints was governed by slippage of the cement glue from the pipe surfaces (Figure 3-15). This caused the pipes to pull-out completely from the tee-joint. In most instances, the inner surface of the tee joints peeled off with the cement glue, indicating that the glue was stronger than the piping material. For

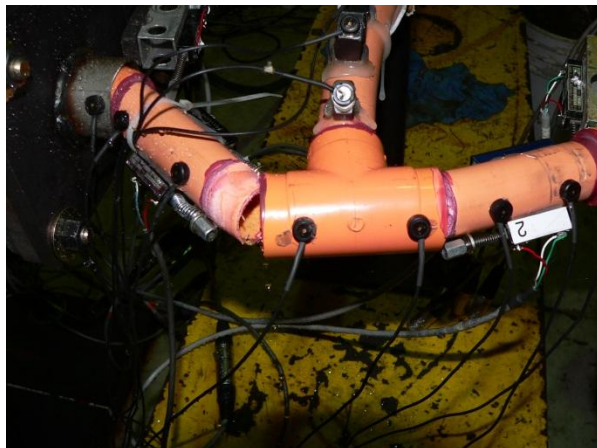
specimens with smaller diameters ( $\frac{3}{4}$  in. and 1 in.), complete fracture of the pipe at the end along the edge of the tee joint was observed in a few cases (*Figure 3-15 d*).



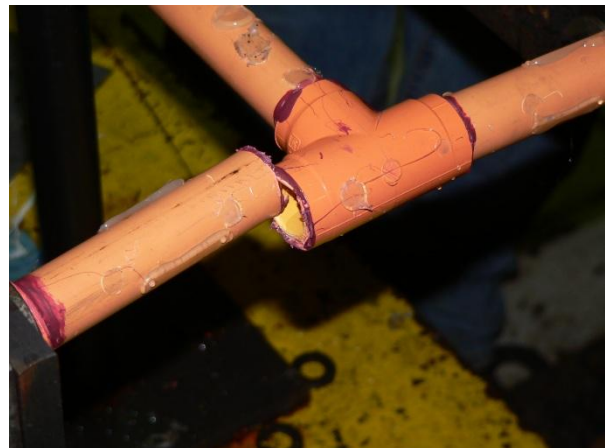
(a) Pipe pulled out from tee joint



(b) Inner surface of the tee joints peeled off with the cement glue



(c) Pipe pulled out from tee joint



(d) Fracture of pipe along the edge of tee joint

*Figure 3-15 Typical damage of CPVC pipe with cement joints*

Again for all specimens, significant inelastic rotations, as shown in *Figure 3-16*, were concentrated at the ends of the pipes on both sides of the tee-joint. Note that both damage states DS<sub>1</sub> (first leakage) and DS<sub>2</sub> (fracture of the pipe) occurred simultaneously for the CPVC pipes with cement joints.

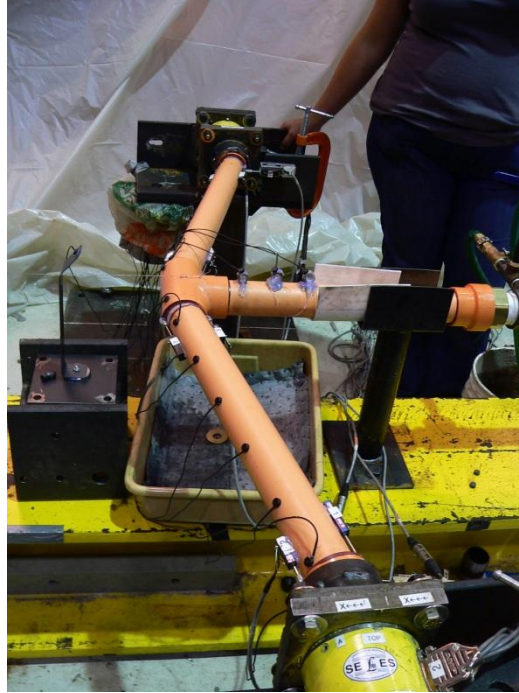


*Figure 3-16 large inelastic rotation at the end of pipes*

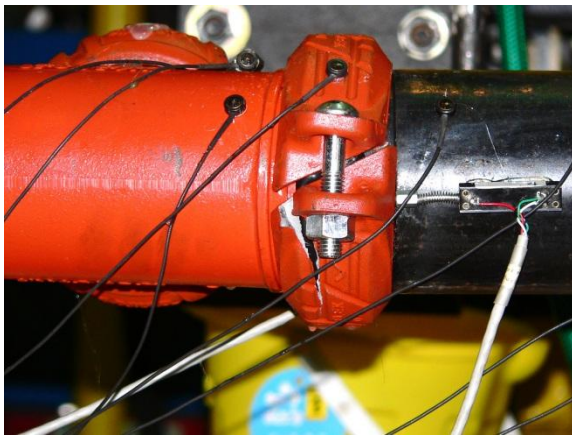
### **3.8.3 Damage observations on steel pipe with groove-fit connections**

The behavior of the steel pipes with groove-fit connections was diverse. For the schedule 40 steel pipes (0.24 in. wall thickness), the failure of specimens was dominated by damage in the coupling flanges. First leakage occurred when the coupling flanges connecting the tee joints and the pipes fractured. A number of failure mechanisms were observed during the test and summarized as follows:

- 1) Fracture was initiated either from the angle pad in contact with the other coupling flange (*Figure 3-17 a*), and housing keys that were designed to be engaged in the groove in the tee joint (*Figure 3-17 b and Figure 3-17 c*), or from the coupling holes for the bolts (*Figure 3-17 d*);

- 2) The edge of the groove in the tee joint sheared off due to the interaction with the coupling flanges (*Figure 3-17 e*);
- 3) The outer surfaces of the pipes around the edge of the groove showed significant wearing damage due to the interaction with the coupling flanges (*Figure 3-17 f*).

For these thicker wall pipes, both damage states DS<sub>1</sub> and DS<sub>2</sub> occurred simultaneously since the rubber gasket slipped after failure of the coupler.



(a) Fracture of coupling flange initiated from the angle pad



(b) Fracture of coupling flange initiated from the housing key

*Figure 3-17 Typical damage of schedule 40 steel pipe with groove-fit connections*



*(c) Fracture of coupling flange initiated from the housing key*



*(d) Fracture of coupling flange initiated from the coupling hole*



*(e) Edge of groove sheared off in the tee joint*



*(f) Wearing damage around the groove in the pipe*

*Figure 3-17 Typical damage of steel pipe with groove-fit connections (Cont'd)*

For the schedule 10 steel pipes (0.13 in. wall thickness), first leakage was controlled by inelastic deformations of the thinner pipe walls and occurred before fracture of the coupling flanges. The typical damage observed for the schedule 10 steel pipes are outlined as follows:

- 1) Fractures similar to those of schedule 40 steel pipes were observed in the coupling flanges  
(Figure 3-18 a);

- 2) In some instances, only damage state DS<sub>1</sub> was reached, and the coupling flanges remained intact after the test. However, the hexagonal nuts were pushed outwards and a gap was generated between the angled pads of the two coupling flanges (*Figure 3-18 b*);
- 3) Significant inelastic deformation was observed in the cross section between the end of the pipe and the groove (*Figure 3-18 c*);
- 4) The outer surfaces of the pipes around the edge of groove showed significant wearing damage due to interaction with the coupling flanges (*Figure 3-18 d*).



(a) Fracture of coupling flange initiated from the housing key



(b) Gap generated between angled pads



(c) Significant inelastic deformation in the pipe section







(d) Wearing damage around the groove in the pipe

*Figure 3-18 Typical damage of schedule 10 steel pipe with groove-fit connections*



For all steel pipes with groove-fit connections, significant inelastic rotations were concentrated at the ends of the pipes on both sides of the tee joint. It was also observed that coupling flanges that were positioned either parallel (*Figure 3-17 a*) or perpendicular (*Figure 3-17 b*) to the direction of loading had little effect on the failure modes of the specimens. The detailed damage documented for various specimens is presented in *Table 3-2*.

Table 3-2 Summary of observed physical damage in tee joint specimens

Material and Joint Type	Damage Description	Photographs
Black Iron with Threaded Joints	<p>Pipe threads slip from tee threads;</p> <p>Pipe threads erode due to slippage;</p> <p>Thread sealant (Teflon tape) degrades;</p> <p>Pipe end bends due to imposed rotation.</p>	
CPVC with Cement Joints	<p>Cement glue slips;</p> <p>Pipe pulls out from tee joint;</p> <p>Pipe peels off the inner surface of tee joint;</p> <p>Pipe fractures at the edge of tee;</p> <p>Pipe end bends due to imposed rotation.</p>	
Schedule 40 Steel with Groove-Fit Connections	<p>Fracture of coupling flanges connecting the tee joint and the pipe;</p> <p>Pipe end bends due to imposed rotation;</p> <p>Groove of pipe wears away.</p>	
Schedule 10 Steel with Groove-Fit Connections	<p>Groove of pipe wears away;</p> <p>Cross section of pipe yields and deforms;</p> <p>Pipe end bends due to imposed rotation.</p>	

### 3.9 Experimental Results

In this section, the rotation and moment capacities defined for damage state DS<sub>1</sub> are presented. The hysteretic behaviors for the 2-in. specimens made of four different materials and joint types are compared. Data analysis is conducted to gain an in-depth understanding of the failure mechanisms. Detailed experimental results and plots of both force-displacement and moment-rotation relationship for each specimen are presented in Appendix B.

#### 3.9.1 Test results

The moment and rotation capacities at first leakage (damage state DS<sub>1</sub>) were calculated for each specimen based on Equation (3.1) and (3.2). Summary of the moment and rotation capacities for all tee joint specimens tested is listed in *Table 3-3*. The same rotation and moment capacity results are shown graphically in *Figure 3-19* and *Figure 3-20*, respectively. No data are shown for the monotonic test on the 4-in. schedule 10 steel pipe with groove-fit connections as first leakage was not observed during this test due to the stroke limitation of the loading actuator. All joint types exhibit significant rotational capacities ranging from 0.005 rad. to 0.405 rad.

As shown in *Figure 3-20*, the monotonic rotational capacities at first leakage for both, black iron threaded and CPVC cement joints are significantly larger than their corresponding cyclic rotational capacities. This result indicates that these types of joints are susceptible to cumulative damage during small earthquakes, which could reduce their rotational capacities during larger events. On the other hand, monotonic and cyclic rotational capacities at first leakage are similar for steel pipes incorporating groove-fit connections, as shown in *Figure 3-19*.

Table 3-3 Measured moment and rotation capacities at first leakage for all tee joint specimens

Material and Joint Type	Nominal Pipe Size (in)	Monotonic Test				Cyclic Tests			
				Test No. 1		Test No. 2		Test No. 3	
		Rotation Capacity $\theta_{leak}$ (rad)	Moment Capacity (kip-in)	Rotation Capacity $\theta_{leak}$ (rad)	Moment Capacity (kip-in)	Rotation Capacity $\theta_{leak}$ (rad)	Moment Capacity (kip-in)	Rotation Capacity $\theta_{leak}$ (rad)	Moment Capacity (kip-in)
Black Iron with Threaded Joints	6	0.0227	275.15	0.0074	244.75	0.0069	304.25	0.0051	239.90
	4	0.0449	134.00	0.0130	124.48	0.0087	116.68	0.0093	132.30
	2	0.0804	20.30	0.0151	22.19	0.0134	24.64	0.0125	24.34
	1	0.1157	7.65	0.0302	5.43	0.0275	7.45	0.0366	6.14
	3/4	0.0671	2.23	0.0383	2.90	0.0334	3.23	0.0501	3.61
CPVC with Cement Joints	2	0.1483	8.15	0.0796	2.41	0.0995	2.32	0.0868	2.86
	1	0.2716	1.700	0.1527	1.62	0.1486	1.89	0.1435	1.49
	3/4	0.4053	0.80	0.1386	0.96	0.1543	0.88	0.1690	0.83
Schedule 40 Steel with Groove-Fit Connections	4	0.0386	109.59	0.0199	77.59	0.0218	83.89	0.0216	80.45
	2	0.0732	19.23	0.0657	22.21	0.0750	23.09	0.0921	22.38
Schedule 10 Steel with Groove-Fit Connections	4	---	---	0.0748	116.18	0.0735	112.46	0.0888	122.53
	2	0.0738	31.89	0.0546	26.11	0.0663	23.40	0.0569	21.31

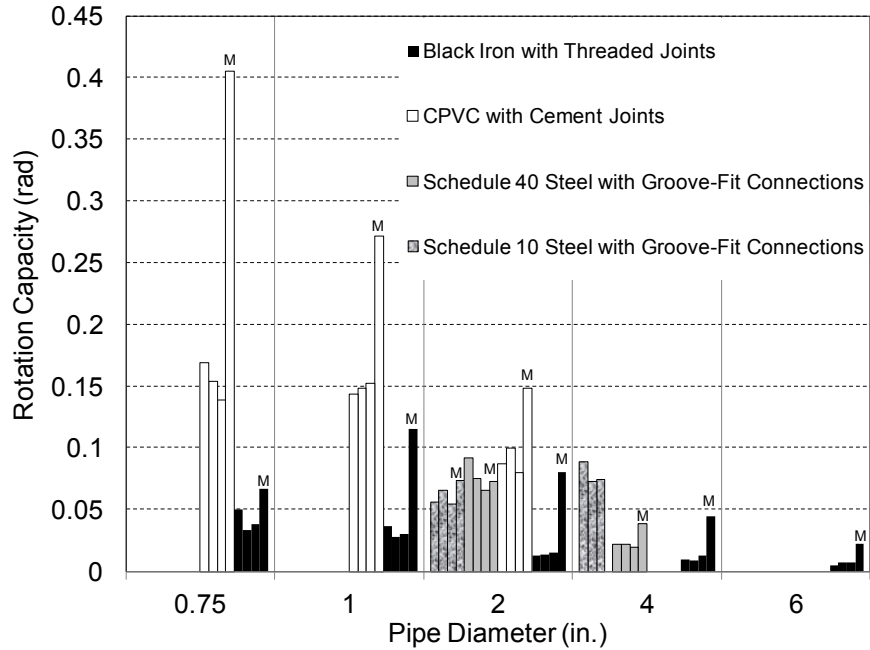


Figure 3-19 Rotational capacities at first leakage for all tee joint specimens; "M" indicates monotonic tests

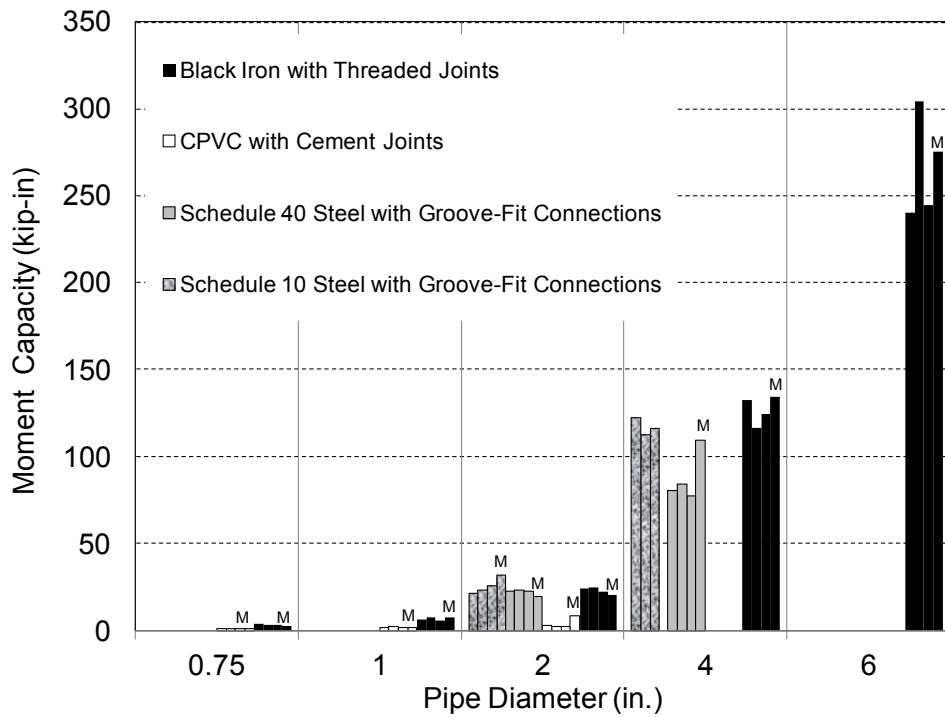
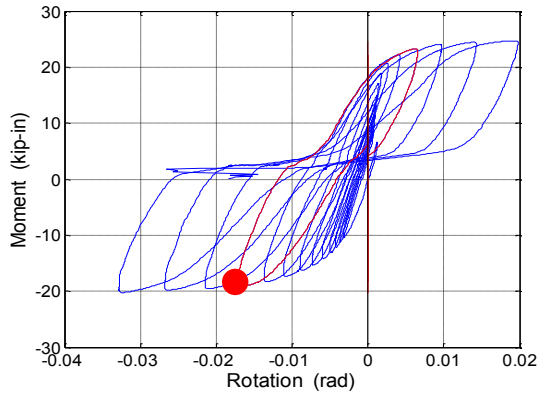


Figure 3-20 Moment capacities at first leakage for all tee joint specimens; "M" indicates monotonic tests

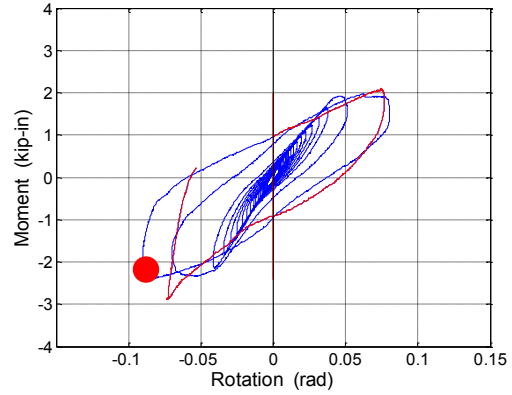
### 3.9.2 Comparison of cyclic response of specimens with four joint types

*Figure 3-21* compares the moment-rotation cyclic responses for the four types of joint specimens tested with a nominal size of 2 in. The occurrence of first leakage (damage state DS<sub>1</sub>) is indicated by a solid red dot on each plot, and the red loop indicates the cycle during which leakage occurs. After first leakage, the tests were continued up to the stroke limit of the loading actuator. Damage state DS<sub>2</sub> was reached for the test specimens made of CPVC pipe with cement joints and steel pipe (schedule 40) with groove-fit connections. The cyclic shapes and amplitudes are widely different for the various materials and joint types. The cyclic response of black iron pipes with threaded joints exhibits gradual strength and stiffness degradations with good energy dissipation. The CPVC pipes with cement joints had the largest rotational capacities at first leakage (near 0.10 radiant for the 2-in. specimen shown in *Figure 3-21*), but also had the smallest moment capacities (one tenth of the other joint types). The cyclic response of steel pipes with groove-fit connections, on the other hand, is characterized by triangularly pinched hysteresis loops with minimal energy dissipation. The steel pipe wall thickness (schedule 10 or schedule 40) had very little influence on the cyclic shape of groove-fit connections.

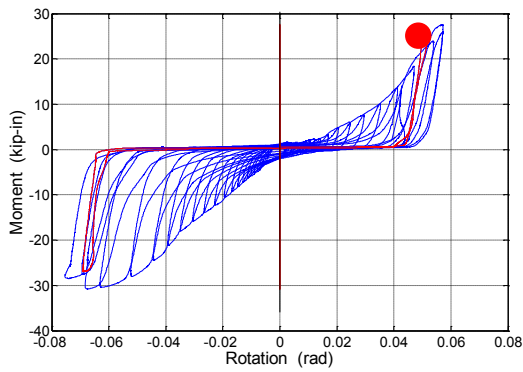
Comparing the rotational capacities at first leakage for pipes having a diameter of 2 in., for which all joint types were tested, the CPVC pipes with cement joints offer the largest rotational capacities, followed by the steel pipes with groove-fit connections and the black iron pipes with threaded joints. The same trend is also partially observed for the other diameter pipes.



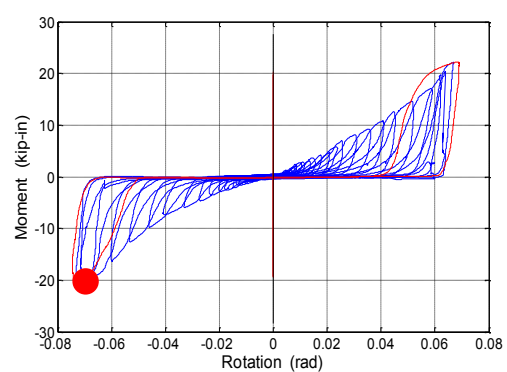
(a) Black iron with threaded joints



(b) CPVC with cement joint



(c) Schedule 10 steel with groove-fit connections



(d) Schedule 40 steel with groove-fit connections

Figure 3-21 Moment-rotation cyclic response for tee joint specimens with 2-in. diameter; the red dot indicates occurrence of first leakage (damage state DS<sub>1</sub>)

### 3.9.3 Analysis of test data

The rotational capacities at first leakage reduce with an increase of pipe diameter for black iron threaded and CPVC cement joints, as shown in *Figure 3-19*. This result can be explained by determining the average axial slip,  $\bar{s}$ , (analogous to strain in bending assuming plane sections remain plane) across a joint through:

$$\bar{s} = \frac{D_o}{2} \theta_{leak} \quad (3.3)$$

where  $\theta_{leak}$  is the rotational capacity at first leakage (see Table 3-3). Table 3-4 summarizes the average axial slip for all specimens made of black iron and CPVC. Figure 3-22 shows the variation of  $\bar{s}$  with pipe diameters for black iron threaded and CPVC cement joints. The results shown in the figure are only from cyclic tests. It can be seen that  $\bar{s}$  for a given joint type is essentially a constant for all pipe diameters and can be characterized by the median values shown in the figure. This result indicates that black iron pipes with threaded joints and CPVC pipes with cement joints behave essentially as flexural beams with first leakage occurring when a “critical extreme fiber strain” is reached. Knowing  $\bar{s}$  for a given joint type allows for the prediction of rotation at leakage for any pipe diameter through Equation (3.3).

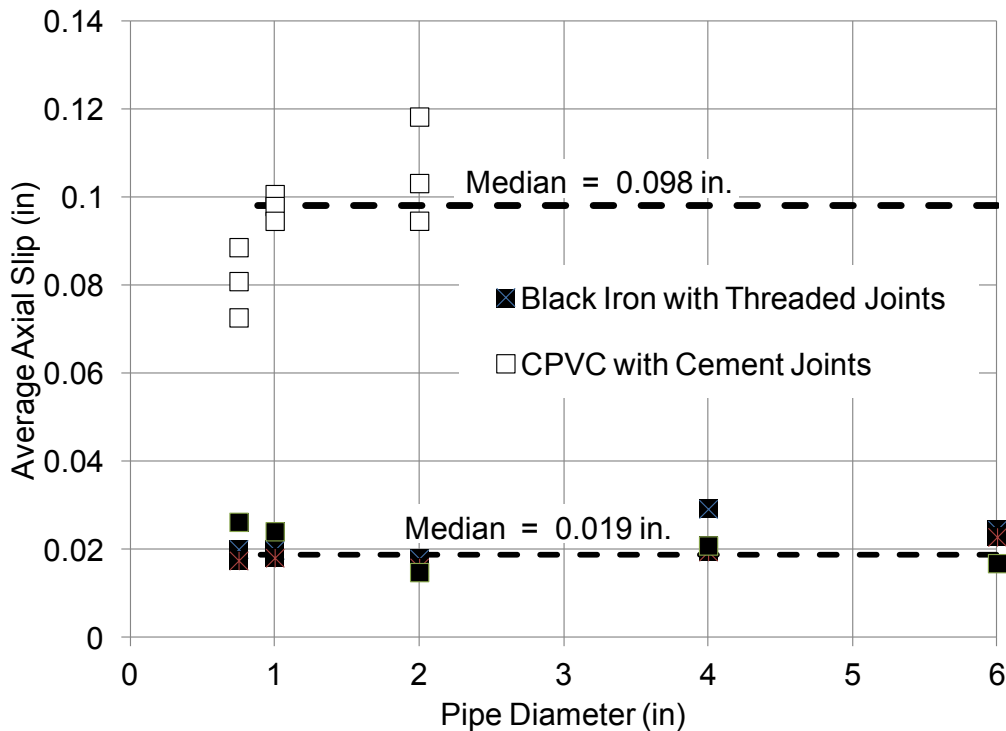


Figure 3-22 Variations of variation of average axial joint slip with pipe diameter



Table 3-4 Summary of average axial slip for specimens made of black iron and CPVC

Material and Joint Type	Nominal Pipe Size (in)	Cyclic Tests		
		Test No. 1 Average Axial Slip $\bar{s}$ (in.)	Test No. 2 Average Axial Slip $\bar{s}$ (in.)	Test No. 3 Average Axial Slip $\bar{s}$ (in.)
Black Iron with Threaded Joint	6	0.0245	0.0229	0.0169
	4	0.0293	0.0196	0.0209
	2	0.0180	0.0159	0.0149
	1	0.0199	0.0182	0.0242
	3/4	0.0201	0.0175	0.0263
CPVC with Cement Joint	2	0.0947	0.1184	0.1033
	1	0.1008	0.0981	0.0947
	3/4	0.0728	0.0810	0.0887

### 3.9.4 Seismic fragility assessment of pressurized fire suppression sprinkler piping

The experimental results from the cyclic tests described above were processed to populate a seismic fragility database for pressurized fire suppression sprinkler piping joints. The cyclic behavior of the piping joints was governed primarily by joint rotation, thus this is the only demand parameter considered. Only the first leakage damage state ( $DS_1$ ) was considered in the seismic fragility analysis. Inspired by the framework proposed by Porter *et al.* (2007), experimental first leakage fragility curves were defined for the four materials and joint types considered in the experimental program based on the measured rotational capacities listed in Table 3-3. Log-normal fragility curves were constructed for each piping material and joint type. For this purpose, the median rotational capacity at first leakage,  $\theta_m$ , and associated logarithmic standard deviation,  $\beta$ , were computed for each piping material, joint type and pipe size as follows:

$$\theta_m = e^{\frac{1}{N} \sum_{i=1}^N \ln \theta_i} \quad (3.4)$$

$$\beta = \sqrt{\frac{1}{N-1} \sum_{i=1}^N [\ln(\theta_i / \theta_m)]^2} \quad (3.5)$$

where  $\theta_i$  denotes the i-th measured first leakage rotational capacity (see *Table 3-3*) and  $N$  is the number of cyclic tests conducted for each material, joint type and pipe size ( $N = 3$  in this study). *Table 3-5* summarizes the first leakage median,  $\theta_m$ , and logarithmic standard deviation,  $\beta$ , obtained for each piping material, joint type and pipe size. *Figure 3-23* compares all the fragility curves derived from the experimental data. Note that in the framework proposed by Porter *et al.* (2007), a correction factor should be added to the  $\beta$  value given by Equation (3.5) to account for the fact that all specimens experienced the same loading history. This correction factor was not considered herein but could be easily added. The Lilliefors goodness-of-fit test at the 5% significance level (Lilliefors, 1967) was assessed. All data considered passed the Lilliefors test.

Table 3-5 Summary of first leakage fragility curve parameters

Material and Joint Type	Nominal Pipe Size (in)	Median First Leakage Rotational Capacity $\theta_m$ (rad.)	Logarithmic Standard Deviation of First Leakage Rotational Capacity $\beta$	Lilliefors Test Result
Black Iron with Threaded Joint	6	0.006	0.204	Pass
	4	0.010	0.216	Pass
	2	0.014	0.094	Pass
	1	0.031	0.146	Pass
	3/4	0.040	0.206	Pass
CPVC with Cement Joint	2	0.088	0.112	Pass
	1	0.148	0.031	Pass
	3/4	0.153	0.099	Pass
Schedule 40 Steel with Groove Fit Connections	4	0.021	0.049	Pass
	2	0.077	0.170	Pass
Schedule 10 Steel with Groove Fit Connections	4	0.079	0.105	Pass
	2	0.059	0.102	Pass

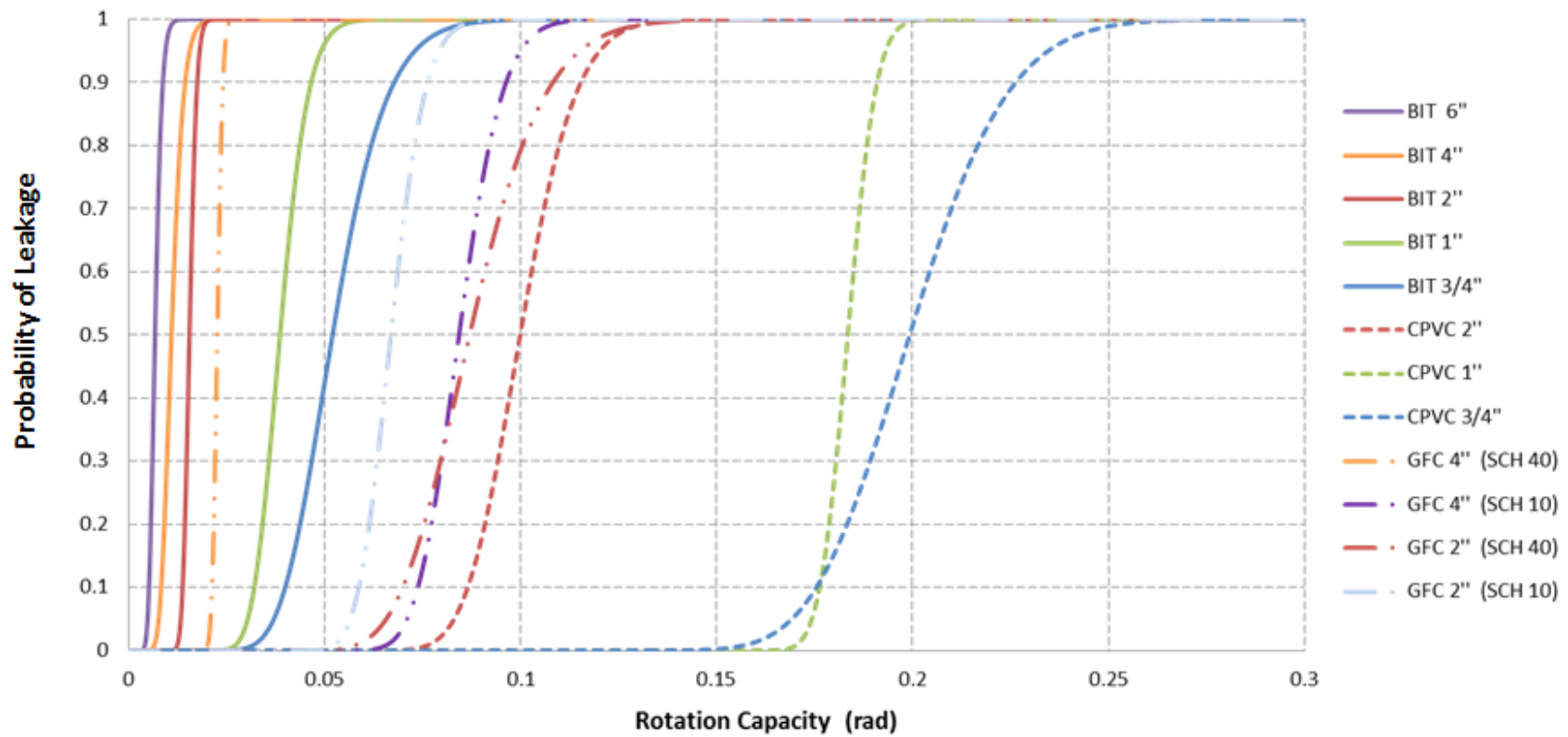


Figure 3-23 First leakage fragility curves for fire suppression sprinkler piping joints;

BIT: Black Iron Threaded, CPVC: Thermoplastic, S10-GFC: Schedule 10 Groove-Fit, S40-GFC: Schedule 40 Groove-Fit

For pipes made of black iron with threaded connections or CPVC with cement joints, it may be cumbersome to try to predict the first leakage by referring to the rotation measured at the joint according to the nominal pipe diameter. As defined before in Section 3.9.3, the average axial slip across a joint,  $\bar{s}$ , can replace the joint rotation, and can be used as a variable to indicate the first leakage for any pipe diameter. As a result, additional experimental first leakage Log-normal fragility curves were constructed for the black iron pipe with threaded connections and CPVC pipes with cement joints based on the average axial slip across a joint,  $\bar{s}$ , which is listed in *Table 3-4*. In this case, the average axial slip across a joint,  $\bar{s}$ , and associated logarithmic standard deviation,  $\beta$ , were computed for each piping material as follows:

$$\bar{s}_m = e^{\frac{1}{N} \sum_{i=1}^N \ln \bar{s}_i} \quad (3.4)$$

$$\beta = \sqrt{\frac{1}{N-1} \sum_{i=1}^N [\ln(\bar{s}_i / \bar{s}_m)]^2} \quad (3.5)$$

where  $\bar{s}_i$  denotes the  $i$ -th average axial slip across a joint (see *Table 3-4*) and  $N$  is the number of cyclic tests conducted for each material ( $N = 15$  for black iron pipe with threaded connections and  $N = 9$  for CPVC pipe with cement joints in this case). *Table 3-6* summarizes median average axial slip at the first leakage,  $\bar{s}_m$ , and logarithmic standard deviation,  $\beta$ , obtained for each piping material, and the fragility curves for both piping materials are presented in *Figure 3-24*.

Table 3-6 Summary of first leakage fragility curve parameters specimens made of black iron and CPVC in terms of average axial slip

Material and Joint Type	Median First Leakage Average Axial Slip $\bar{s}_m$ (in.)	Logarithmic Standard Deviation of First Leakage Rotational Capacity $\beta$	Lilliefors Test Result
Black Iron with Threaded Joint	0.019	0.193	Pass
CPVC with Cement Joint	0.098	0.141	Pass

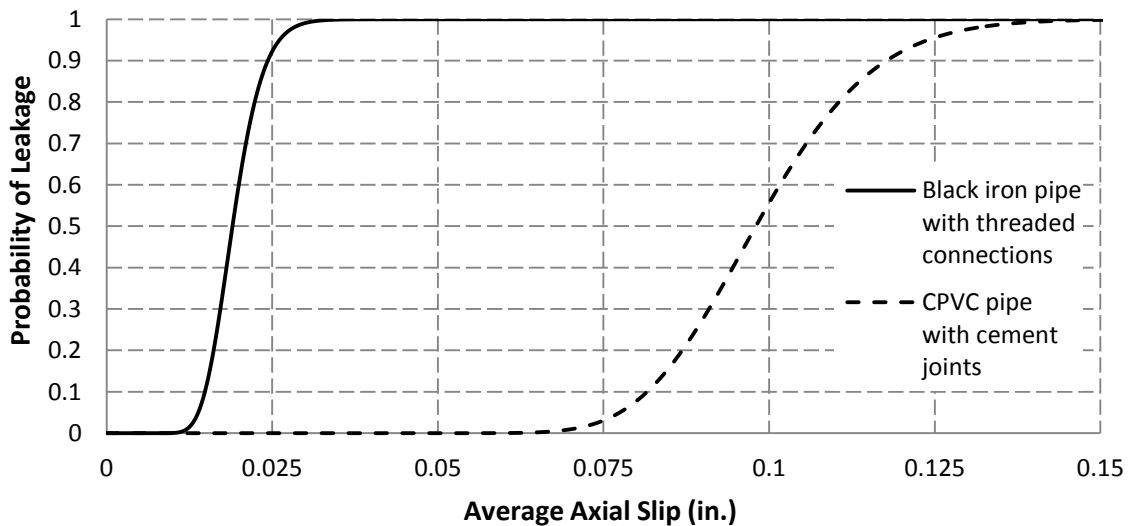


Figure 3-24 First-leakage fragility curves for black iron pipe with threaded connections and CPVC pipe with cement joints in terms of average axial slip

### 3.10 Summary

Monotonic and reverse cyclic testing were conducted on forty-eight pressurized fire suppression sprinkler piping tee joints as part of this dissertation. The main objective of the tests was to determine the rotational capacities of the piping joints at which leakage and/or

fracture occur. Four different materials and joint types were considered: 1) black iron with threaded joints, 2) thermoplastic (CPVC) with cement joints, 3) schedule 40 steel with groove-fit connections and 4) schedule 10 steel with groove-fit connections. The nominal diameters of the pipes varied as follows:  $\frac{3}{4}$  in. to 6 in. for the black iron threaded joints;  $\frac{3}{4}$  in. to 2 in. for the CPVC and 2 in. and 4 in. for both schedules of the steel groove fit connections. The ATC-58 framework was then applied to the test data to develop a first leakage seismic fragility database for pressurized fire suppression sprinkler joints in terms of joint rotations (engineering demand parameter).

The observations from this phase of experimental program can be summarized as follow:

- All joint types exhibited significant rotational capacities at first leakage ranging from 0.005 rad. to 0.405 rad.
- Among the four joint types tested, the CPVC pipes with cement joints had the largest rotational capacities at first leakage but also had the smallest moment capacities (one tenth of the other joint types). CPVC piping, especially if unbraced, may experience large joint rotation demands due to its lower strength and stiffness.
- The monotonic rotational capacities at first leakage for both, black iron threaded and CPVC cement joints were significantly larger than their corresponding cyclic rotational capacities. This result indicates that these types of joints are susceptible to cumulative damage during small earthquakes, which could reduce their rotational capacities during larger events. On the other hand, monotonic and cyclic rotational capacities at first leakage were similar for the steel pipes with groove-fit connections.

- The rotational capacities at first leakage decreased with an increase of pipe diameter for black iron pipes with threaded joints and CPVC pipes with cement joints. This result can be explained by the fact that the average axial slip across a joint at first leakage of a given type is essentially a constant for all pipe diameters. This result indicates that pipes with black iron threaded and CPVC cement joints behave essentially as flexural beams in which first leakage occurs when a “critical extreme fiber strain” is reached, allowing for the prediction of rotation at leakage for any pipe diameter.
- The observed behavior of steel pipes with grove-fit joints was different depending on their wall thickness. For the thicker schedule 40 steel pipes (0.24 in. wall thickness), first leakage coincided with failure of the coupling flanges causing the rotational capacities to reduce with an increase of pipe diameter (2 in. to 4 in. pipes). For the thinner schedule 10 steel pipes (0.13 in. wall thickness), significant inelastic deformations occurred in the pipe sections before failure of the couplings. For this group, the rotational capacities increased with pipe diameter.

The experimental first leakage fragility curves developed in this study use joint rotation as the demand parameter. Structural analysis models of sprinkler piping systems could be used in conjunction with the fragility curves developed in this study to generate first leakage fragility curves for fire pressurized suppression sprinkler systems in terms of more global demand parameters, such as floor accelerations. Such structural analysis models could simulate the cyclic response of pipe joints by equivalent nonlinear rotation springs that can be constructed from the test data present herein, along with a non-simulated damage state ( $DS_1$ ) associated with the



rotation causing first leakage of any of the pipe joints. An example of this system fragility analysis is presented in Chapter 6 of this dissertation.

## Chapter 4

# EXPERIMENTAL ASSESSMENT OF FULL-SCALE PRESSURIZED FIRE SUPPRESSION SPRINKLER PIPING SUBSYSTEM

### 4.1 Introduction

The second series of experimental studies of the NEES-NGC Project conducted as part of this dissertation was designed to evaluate the seismic performance of pressurized fire suppression sprinkler piping subsystem. The test specimen represented one of the largest three-dimensional fire protection systems tested, though the input excitation was only in one horizontal direction. The two-story, full-scale (11 ft. × 29 ft.) fire extinguishing sprinkler piping subsystems were constructed according to NFPA 13 (NFPA, 2010) and tested on the University at Buffalo Nonstructural Component Simulator (UB-NCS) at the Structural Engineering and Earthquake Simulation Laboratory (SEESL). A total of three specimens with different materials and joint arrangements for the branch lines were tested with various bracing systems. For each bracing system, the specimens were subjected to dynamic loading with increasing input intensities.

The major objectives of this testing program were:

- 1) To provide a realistic scenario to observe the dynamic characteristics and compare the seismic performance of full-scale fire sprinkler piping systems made of different materials and joint types at the subsystem level under various intensities of dynamic loading;
- 2) To enhance the understanding of interaction between suspended ceiling systems and fire sprinkler piping systems ;

- 3) To examine the effect of story differential movement on vertical riser;
- 4) To provide a wide set of recorded data for the development, validation and calibration of numerical models simulating the dynamic response of sprinkler piping subsystems presented in Chapter 5 of this dissertation; and
- 5) To establish correlations between the behaviors of sprinkler piping joints in the quasi-static experiments (described in Chapter 3) and the dynamic testing in terms of failure mechanism and performance.

#### 4.2 The University at Buffalo Nonstructural Component Simulator (UB-NCS)

The UB-NCS, shown in *Figure 4-1*, is a versatile two-level controllable platform that provides innovative and unique capability to evaluate the performance of full-scale nonstructural components and equipment located at the upper levels of multi-story buildings under realistic full-scale strong seismic floor motions.



*Figure 4-1 Nonstructural Component Simulator at University of Buffalo (from SEESL, 2010)*

The UB-NCS system consists of two square 12.5 feet platforms with an inter-story height of 12 feet at the bottom level and 14 feet at the upper level. The NCS testing frame is activated by four identical high performance dynamic actuators. Each actuator has a load capacity of 22 kips and a displacement stroke of 80 inches. For a full-scale nonstructural system up to 6.9 kips (3.1 metric tons), the NCS testing frame is capable of subjecting the specimen to peak horizontal accelerations of up to 3g, peak velocities of 100 in./s and displacements of  $\pm 40$  inches. These characteristics allow the NCS to replicate the seismic response observed at the upper levels of multi-story buildings during earthquakes. Furthermore, different input motions can be implemented at each level so that the UB-NCS allows for induced damage to both displacement sensitive and acceleration sensitive nonstructural components. In order to facilitate the constructions of the two-story full-scale sprinkler piping systems, the NCS testing frame was located in a trench inside the laboratory, as shown in *Figure 4-2*.



*Figure 4-2 General view of NCS testing frame*

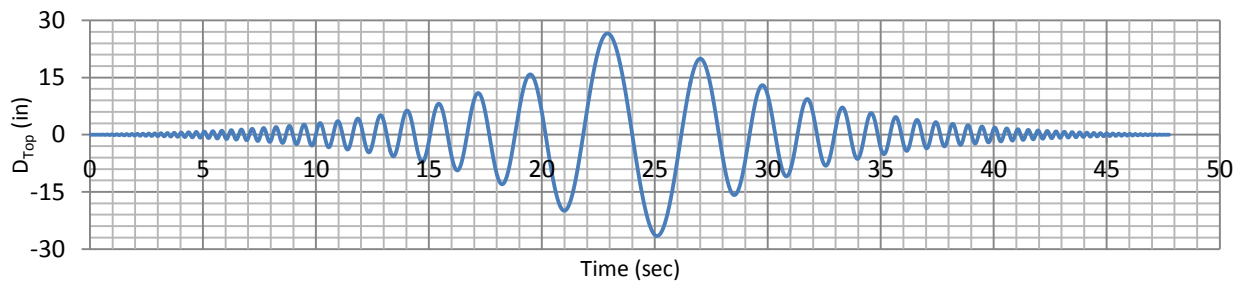
### 4.3 Testing Protocol

Shake table testing protocols used for experimental seismic qualification and fragility analysis of nonstructural components, such as AC 156 (ICC-ES, 2007), FEMA 461 (FEMA, 2007), and IEEE 693 (IEEE, 2006), focus on either displacement-sensitive or acceleration-sensitive nonstructural components, and are limited by the displacement capabilities of conventional shaking tables. Ceiling Piping and Partition (CPP) systems, may be sensitive to both accelerations and inter-story drifts when they are combined together or with other systems. In order to better assess the seismic performance of nonstructural components, equipment and building contents, an innovative testing protocol has been developed at UB by Retamales *et al.* (2008), taking full advantage of the UB-NCS capabilities.

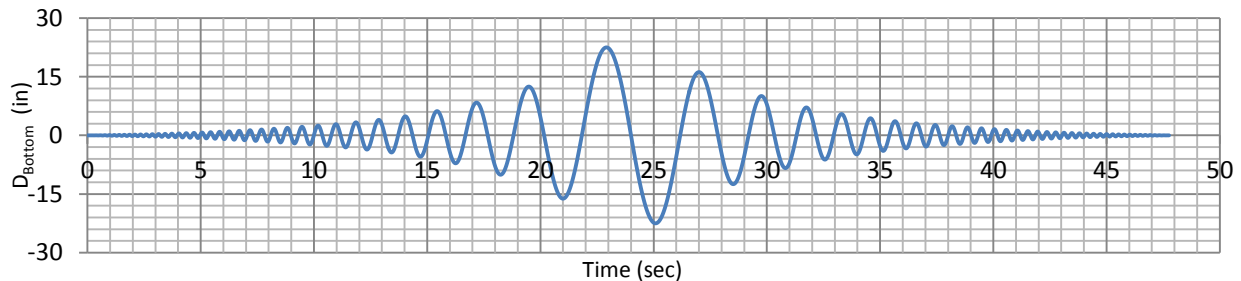
The testing protocol specially developed for the UB-NCS frame is composed of a pair of displacement histories for the bottom and the top levels of the NCS test frame that simultaneously match: (1) a target ground (or floor) acceleration response spectrum, and (2) a generalized inter-story drift spectrum. Furthermore, this testing protocol, independent of building or earthquake record, is capable of simultaneously subjecting specimens to expected absolute floor accelerations and inter-story drifts (Davies, 2010). The closed-form equations defining the dynamic fragility testing protocol are derived based on a series of input variables, including: (1) the local seismic hazard, in terms of the design spectral acceleration at short period,  $S_{ds}$ , and design spectral acceleration at 1-second period,  $S_{d1}$ , defined in ASCE 7 (ASCE, 2010), (2) the normalized building height above grade at which the nonstructural system is located,  $h/H$ , and (3) the target peak inter-story drift ratio,  $\Delta_{Max}$ . For this dynamic test program, a generic site with spectral accelerations  $S_{ds}=1g$  and  $S_{d1}=0.6g$ , and a maximum inter-story drift ratio,  $\Delta_{Max}=3\%$ , was

chosen for fragility assessment purposes. The normalized building height,  $h/H$ , is set to be equal to 1 as the fire sprinkler piping system is considered to be located at the roof building level. The time histories of input motions for the first and the second level of the UB-NCS platforms are exhibited in *Figure 4-3*.

In addition, the effective frequency limits for the testing protocol are set between 0.2 Hz to slightly higher than 5.0 Hz. As seen from *Figure 4-3*, both of the platform motions have a testing frequency transition starting at high frequencies-low displacements, shifting to low frequencies-high displacements, and coming back to high frequencies-low displacements again. *Figure 4-3* also shows the time history of maximum inter-story drift. The amplitude of the inter-story drift history is inversely proportional to that of the acceleration history.

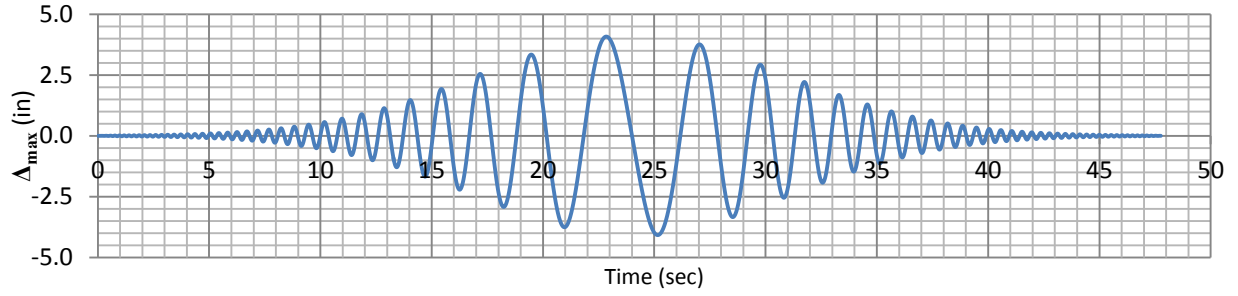


(a) Platform displacement history for the second level

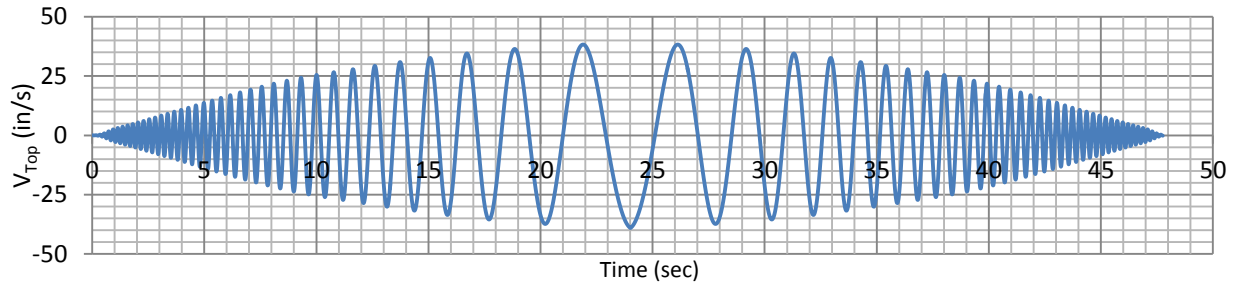


(b) Platform displacement history for the first level

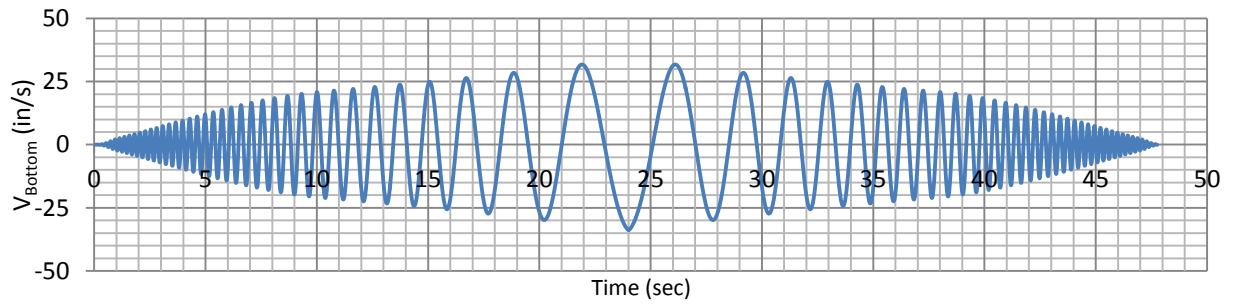
*Figure 4-3 Testing protocol for dynamic test program*



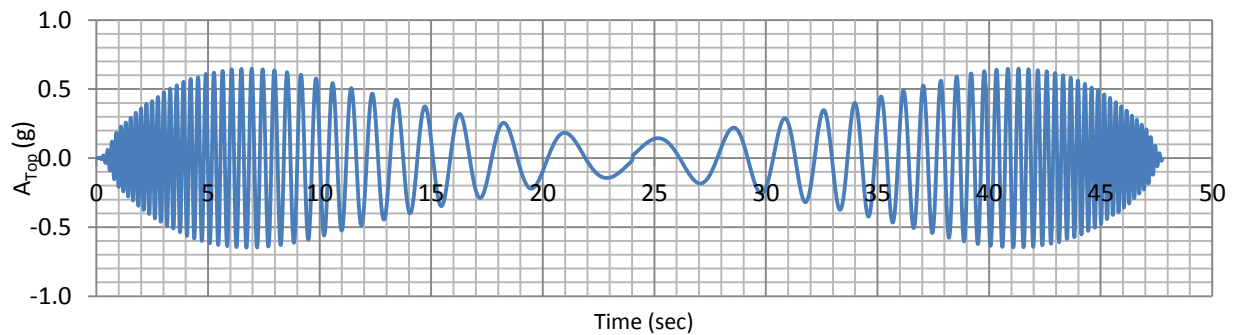
(c) Inter-story drift history



(d) Platform velocity history for the second level

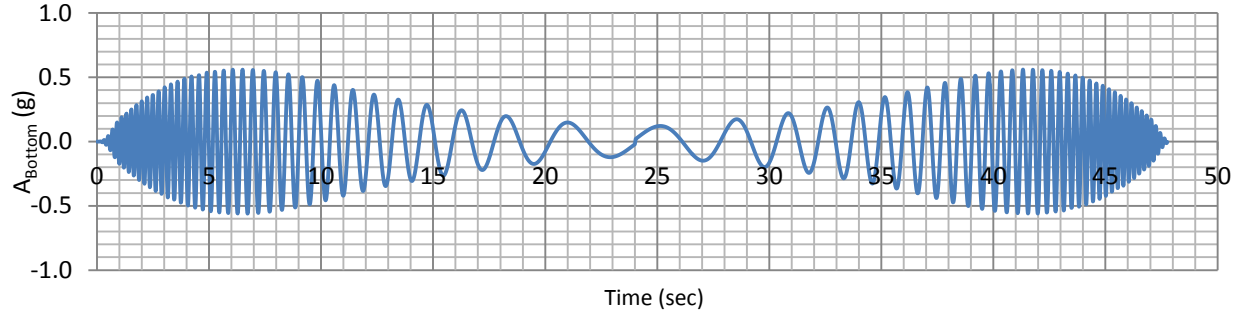


(e) Platform velocity history for the first level



(f) Platform acceleration history for the second level

Figure 4-3 Testing protocol for dynamic test program (Cont'd)



(g) Platform acceleration history for the first level

Figure 4-3 Testing protocol for dynamic test program (Cont'd)

Table 4-1 shows the peak demand of the input motions for the dynamic testing protocol.

Table 4-1 Peak demand of dynamic testing protocol

<b>Testing Protocol Envelopes</b>			
<u>Bottom level protocol</u>			
Xmax	22.5	in	Maximum bottom level platform displacement
Vmax	33.9	in/s	Maximum bottom level platform velocity
Amax	0.56	g	Maximum bottom level platform acceleration
<u>Top level protocol</u>			
Xmax	26.6	in	Maximum top level platform displacement
Vmax	39.0	in/s	Maximum top level platform velocity
Amax	0.65	g	Maximum top level platform acceleration
<u>Interstory drift protocol</u>			
$\Delta$ max	4.08	in	Maximum interstory drift

The Maximum Considered Earthquake (MCE) level response spectra for the top level protocol and the bottom level protocol are compared with the floor response spectrum defined by Equation 3.3-1 and Equation 3.3-2 in the FEMA 450 (FEMA, 2003) and the comparison is presented in Figure 4-4. It can be observed that the MCE level response spectra for both the top and bottom level protocol envelop the floor response spectra.



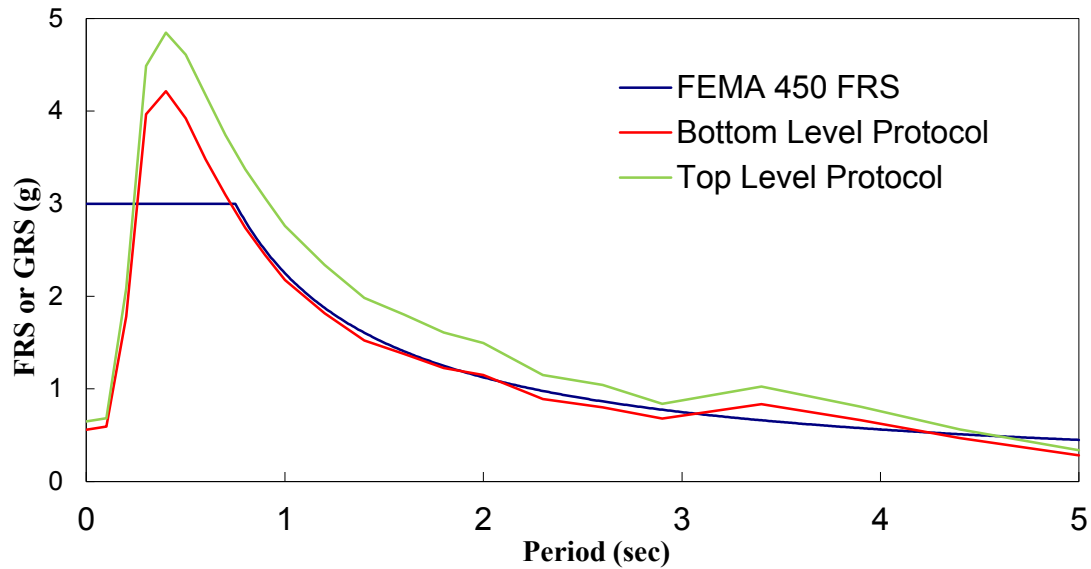


Figure 4-4 Floor response spectra

#### 4.4 Selection of Materials and Joint Types

In order to provide a good correlation between the quasi-static experiments and the dynamic testing program, piping materials and joint types adopted for the second series of experiments were mainly selected from those tested during the first series of quasi-static experiments presented in details in Chapter 3. The longitudinal main line and cross main line for all three specimens were constructed with 4-inch steel pipes (schedule 10) with groove-fit connections, while the branch lines ranged from black iron pipes (schedule 40) with threaded connections, CPVC pipes (schedule 40) with cement joints to steel pipes (schedule 7) with groove-fit connections.

As seen in *Figure 4-5*, the schedule 7 steel pipes, which are also called Dyna-Flow high-strength light wall sprinkler pipes, are currently considered by industry as the best alternative to the

schedule 10 sprinkler pipes. Besides the advantages of light weight and easiness for cutting and installation, Dyna-Flow pipes have an inside diameter (ID) up to 7% larger than the schedule 10 steel pipes. It allows for potential downsizing of the entire fire protection systems and related components, and results in possible cost savings. The schedule 7 steel pipes were not tested during the quasi-static testing program. Based on the input from The Practice Committee and the Advisory Board of the NEES Nonstructural Grand Challenge Project, the steel pipes (schedule 7) with groove-fit connections were included into the test matrix as a result of their popular use in the fire protection systems, particularly in the western United States.



*Figure 4-5 Dyna-Flow high-strength light wall sprinkler pipes (from Allied Tube Inc., 2011)*

The details of piping materials and joint arrangements utilized for each of the three test specimens are listed in *Table 4-2*.

Table 4-2 Details of test specimens

Specimen ID	Material and Joint Type	
	Main Line, Cross Main and Vertical Riser	Branch Lines
1		Schedule 40 black iron pipes with threaded connections
2	Schedule 10 steel pipe with groove-fit connections	Schedule 40 CPVC pipes with cement joints
3		Schedule 7 steel pipes with groove-fit connections

## 4.5 Description of Experimental Set-up and Test Specimens

### 4.5.1 Materials used in testing

#### Outriggers and Concrete slabs

Each platform of the UB-NCS test frame is 12.5 feet by 12.5 feet. In order to perform dynamic tests with the full-scale (11 ft. × 29 ft.) fire extinguishing sprinkler piping subsystems, two W8x18 steel beams were welded on the second level and another one W8x18 steel beam was attached to the first level of platforms as outriggers to provide extra space to support the vertical hangers and bracing systems (*Figure 4-6*). Furthermore, concrete slabs (*Figure 4-6*) were also provided at each level of the UB-NCS in order to provide support for the vertical hangers.

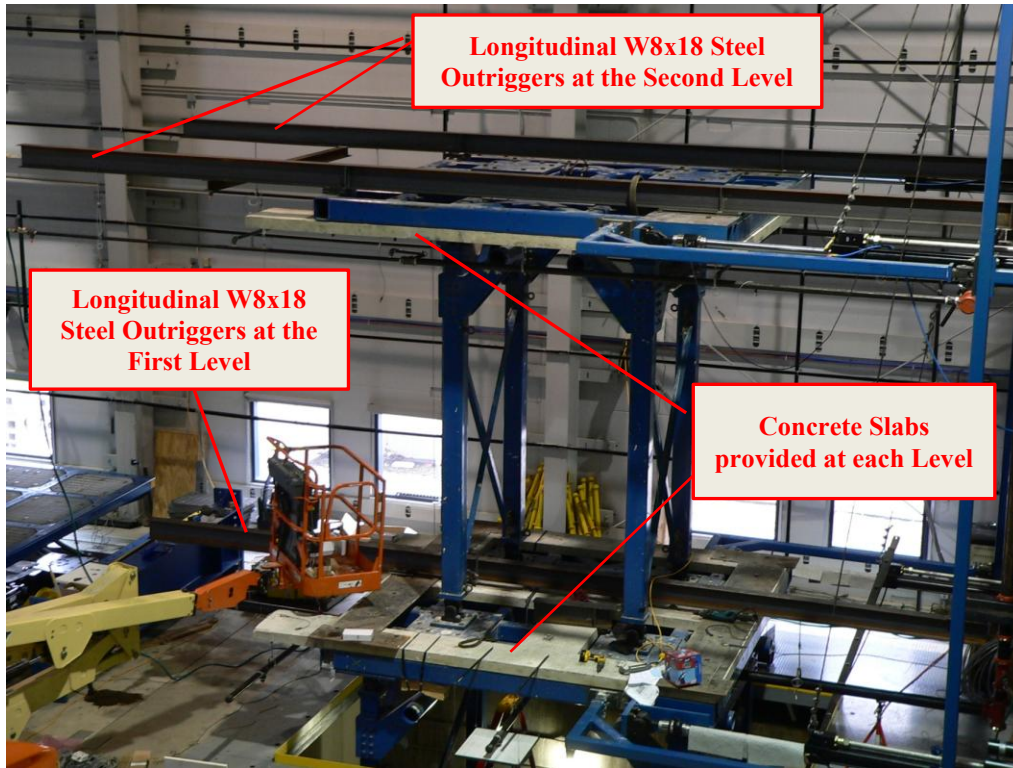


Figure 4-6 General view of outriggers welded on the UB-NCS machine

The operating frequency of the NCS system is between 0.2 Hz to 5.0 Hz. As shown in *Figure 4-7*, two W4x13 steel beams were welded transversely to the underneath of the two longitudinal w8x18 steel beams at the second level to act as transverse braces in order to prevent the two longitudinal W8x18 steel outriggers from resonating with the NCS system. Furthermore, the W4x13 steel beam on the west side of the UB-NCS platform provided support to the hangers and wire restraints of the transverse branch lines at the second level. The W4x13 steel beam on the east of the platform provided the necessary support and restraint for the vertical riser of the fire sprinkler piping systems. The plan views of the outriggers on each level of the UB-NCS platforms are shown in *Figure 4-8*.



*Figure 4-7 Location of steel braces for outriggers*

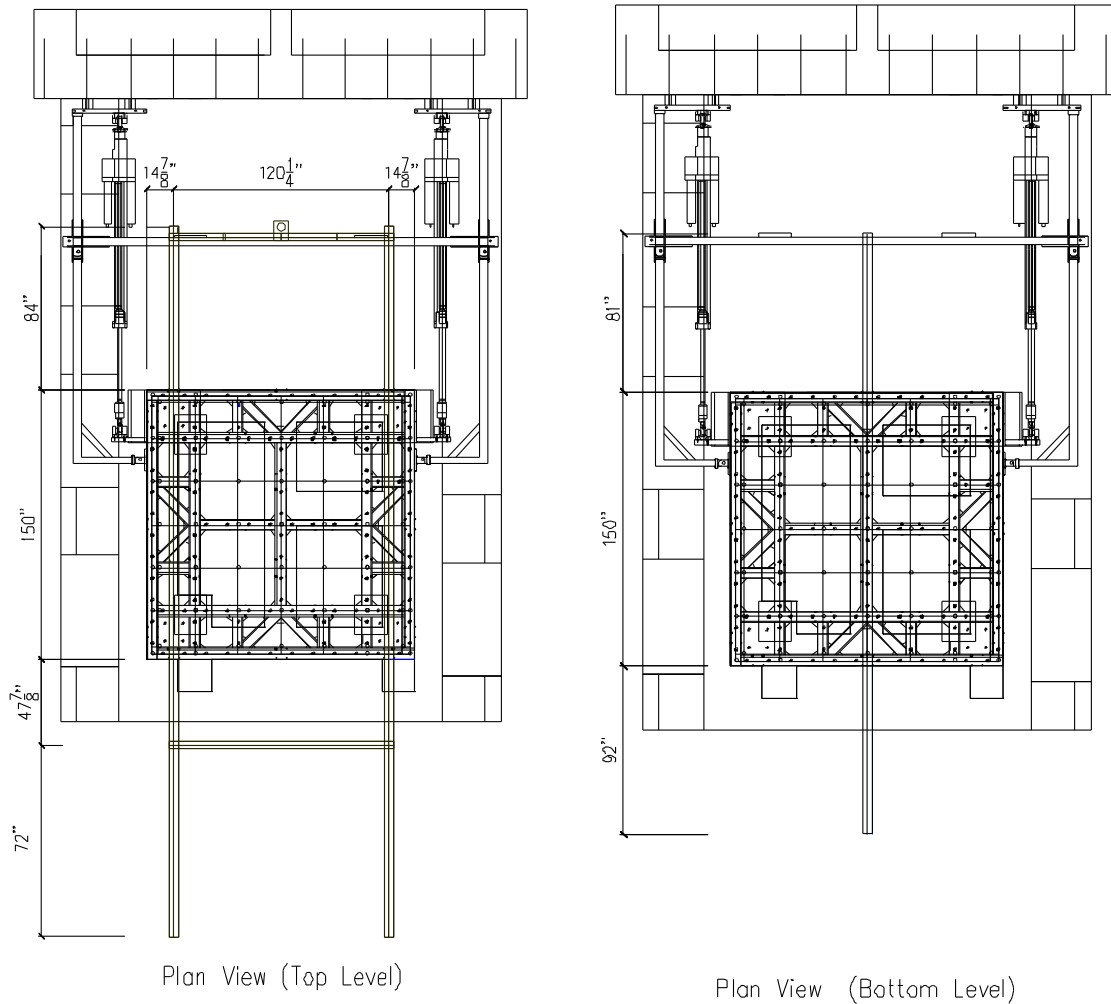
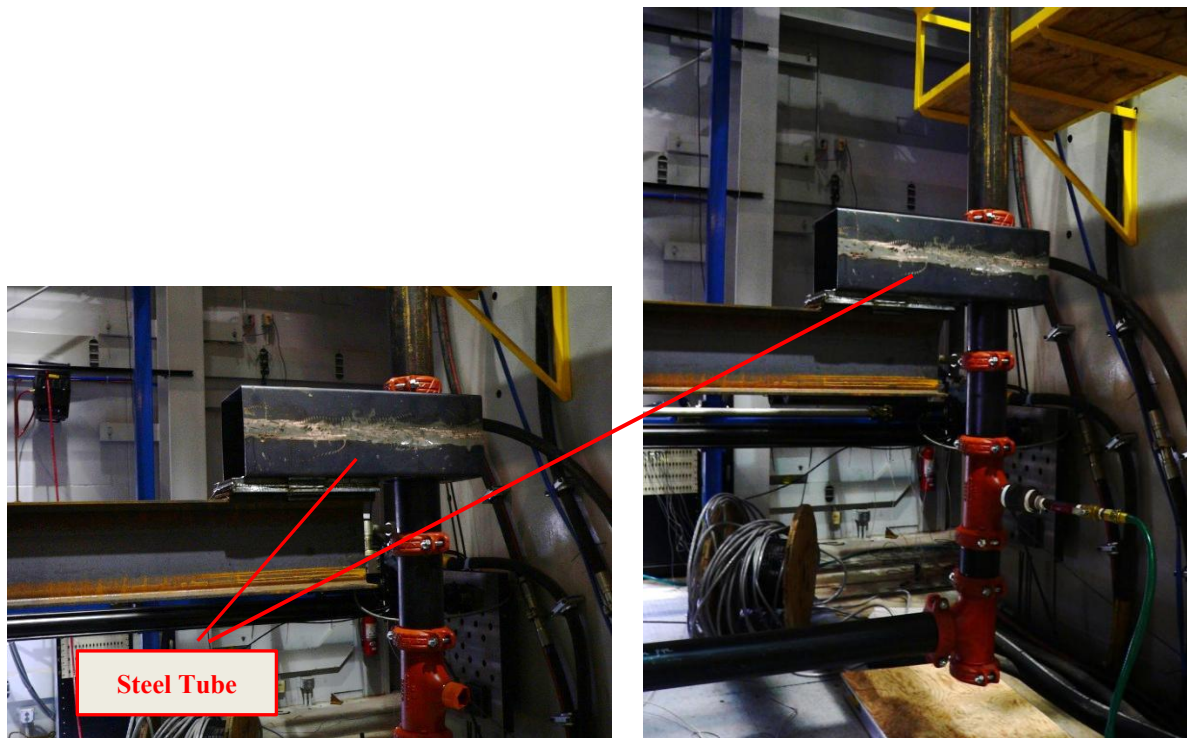


Figure 4-8 Plane view of outriggers and steel braces

### Floor slab penetration

As shown in *Figure 4-9*, a 3-foot-long HSS 8x8x3/16 steel tube was welded on the east end of the steel outrigger at the first level of the UB-NCS. A 4.5-inch diameter opening was cut within the steel tube with the use of an oxy-acetylene cutting rig to allow the vertical riser of the fire protection system to go through (*see Figure 4-13*), so as to simulate the vertical riser penetrating the floor slab in a real building, as well as the interaction between the vertical riser and the floor

slab when subjected to seismic loading. The gap between the vertical riser and the steel tube was filled with fire-resistant mineral wools (*Figure 4-10*), following the industry practice to create an insulated and fire-rated seal to prevent flame and smoke from penetrating into adjacent floors through the gap between the vertical risers and the floor slab.



*Figure 4-9 Steel tube simulating floor slab*



*Figure 4-10 Fire-resistant mineral wool (from Roxul Inc., 2012)*

## SAMMY screws

SAMMY screws for concrete and steel were used to anchor the various supporting elements of the sprinkler test subsystem. The CST 20 SAMMY crews for concrete (*Figure 4-11*) has an ultimate pullout strength of 2400 lbs. The installation requires a ¼ in. pre-drilled pilot hole with a depth of 2 in. into the concrete slab. After pre-drilling, the SAMMY screw is inserted into the nut driver placed into the electric drill set before inserting into the concrete. When the nut driver spins free on the screw, installation is completed.



*Figure 4-11 SAMMY screw (from Dickson Supply Co., 2011)*

In terms of SAMMY screws for steel (*Figure 4-12*), the installation method is almost the same, except that the insertion of the SAMMY screws doesn't require the pre-drilling. Special attention needs to be paid to the fact that the SAMMY screws for steel can only be installed into steel member with the thickness ranging from Gauge #22 (0.025 inch) to ½" inch.





*Figure 4-12 SAMMY screw for steel (from Diamond Tool and Fasteners, Inc., 2012)*

### **Ceiling boxes**

As shown in *Figure 4-13*, a total of six artificial ceiling boxes supporting a single tile were installed at various locations to assess the interaction between the suspended ceiling system and the fire sprinkler piping system during earthquake shaking. Since the dynamic properties of the entire suspended ceiling system are related to a number of factors and it is difficult to estimate and determine the stiffness of a representative suspended ceiling system for a given size, two extreme conditions were considered. Two types of ceiling boxes, the rigid frame and the flexible hanging frame, were incorporated in the experimental study. Each ceiling box was 2 feet by 2 feet, supported by two types of materials at the four corners. Steel angles (5/8'' x 5/8'' x 1/8'') were first selected to support the ceiling box and simulate rigid suspended ceiling subsystems (*Figure 4-14*). It should be noted that sprinkler piping does not run that close to the ceiling in practice and the short drop connecting the sprinkler heads to the pipes used in this series of dynamic testing may not be typical.

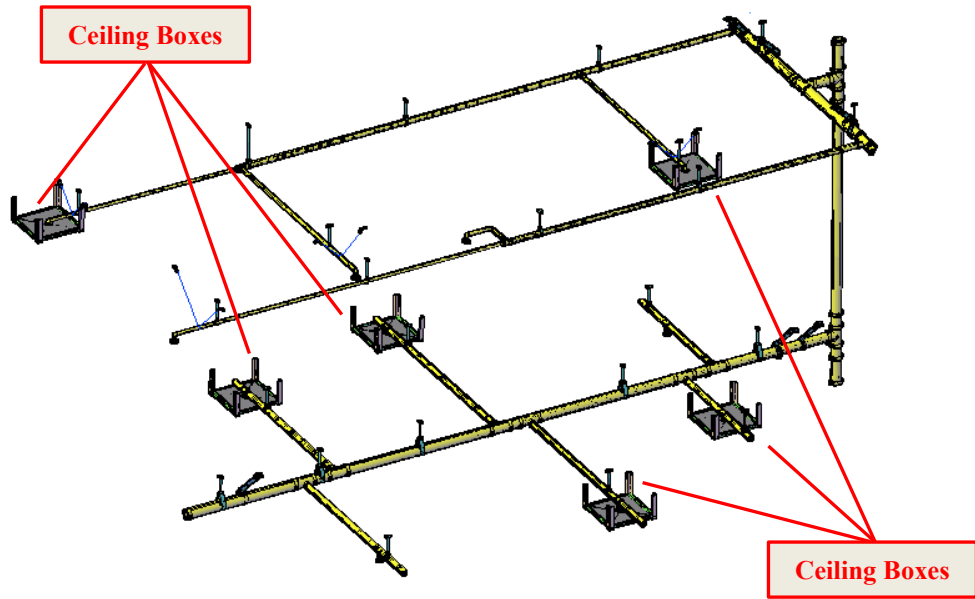
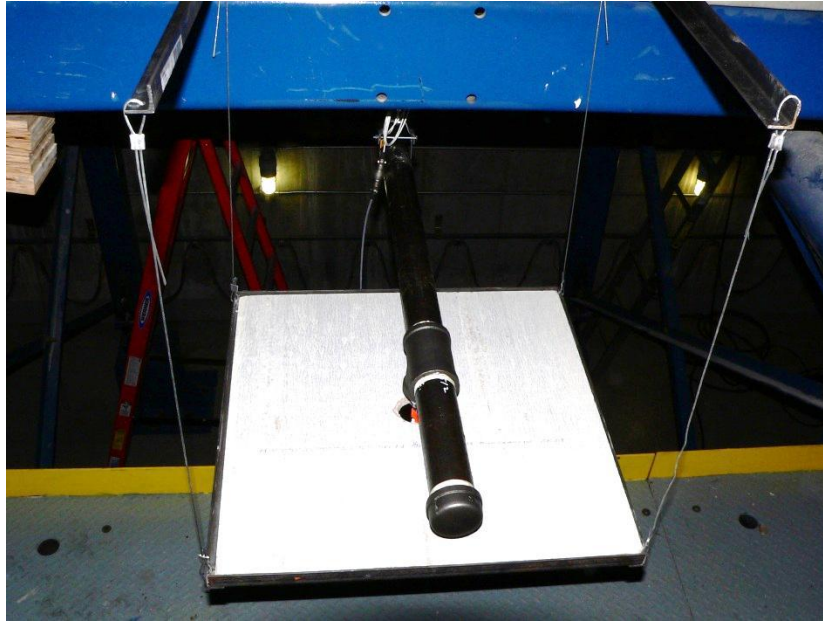


Figure 4-13 Locations of ceiling boxes



Figure 4-14 Rigid ceiling box supported by steel angles

As shown in the *Figure 4-15*, Gauge #12 splay wires were utilized as the second type of materials to support the ceiling box supports to simulate a flexible suspended ceiling subsystem, which behaves as a pendulum and swings freely.



*Figure 4-15 Flexible ceiling box supported by splay wires*

Gypsum drywalls (*Figure 4-16*) and acoustic tiles (*Figure 4-17*) were inserted in ceiling boxes. These two types of tiles are the two most popularly used for ceiling systems in the US. A 2-inch diameter opening was cut within the ceiling tile in order to accommodate the pendant sprinkler head. Conventional thru-ceiling fittings were placed around the sprinkler heads to fill the gap between the sprinkler head and the ceiling tile.



Figure 4-16 Gypsum drywall

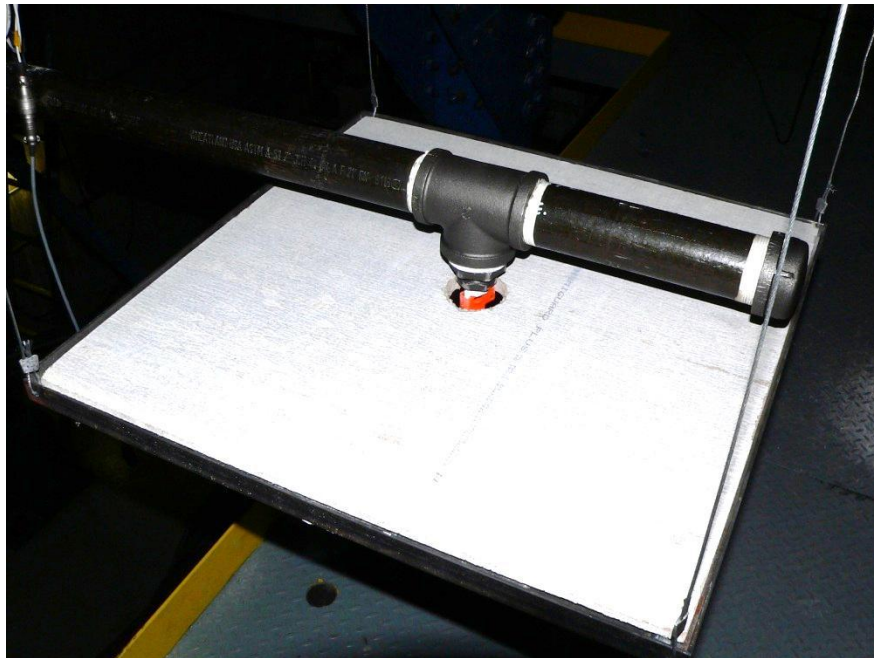


Figure 4-17 Acoustic tile

#### 4.5.2 Typical specimen geometry

Each specimen consisted of two floor levels of piping layout connected through a vertical riser. Each floor level was approximately 11 feet wide by 29 feet long. The top level was designed to evaluate the seismic behavior of the unsupported elbow armover, cross main line, as well as longitudinal and transverse branch lines. The bottom level was designed to assess the performance of a longitudinal main line and longer transverse branch lines subjected to earthquake shaking.

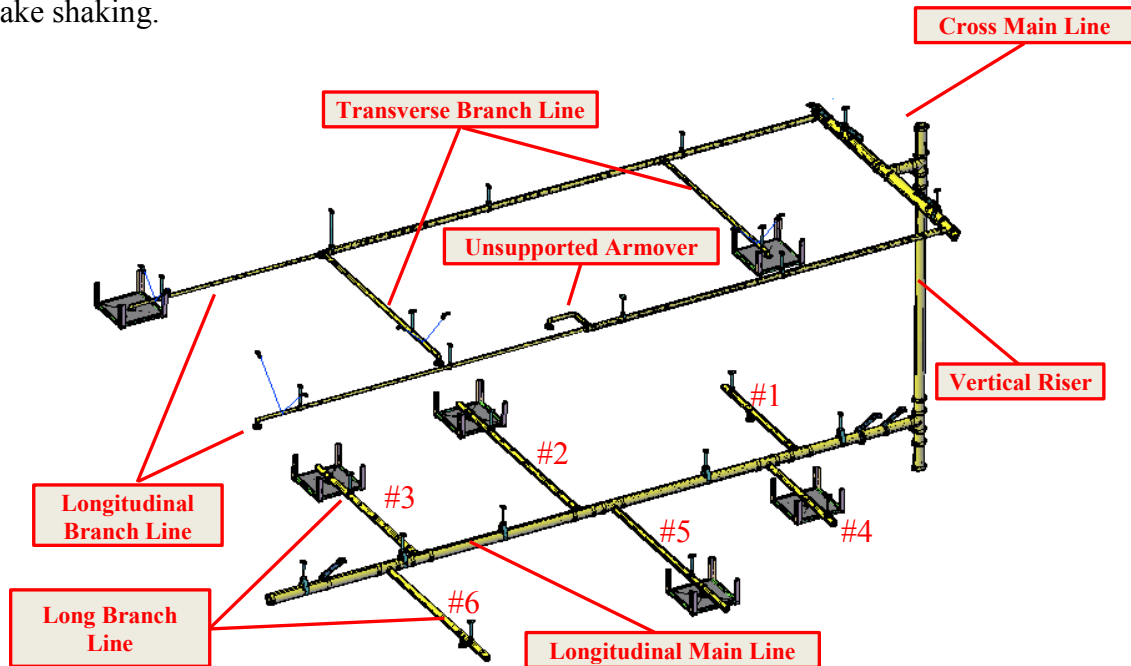
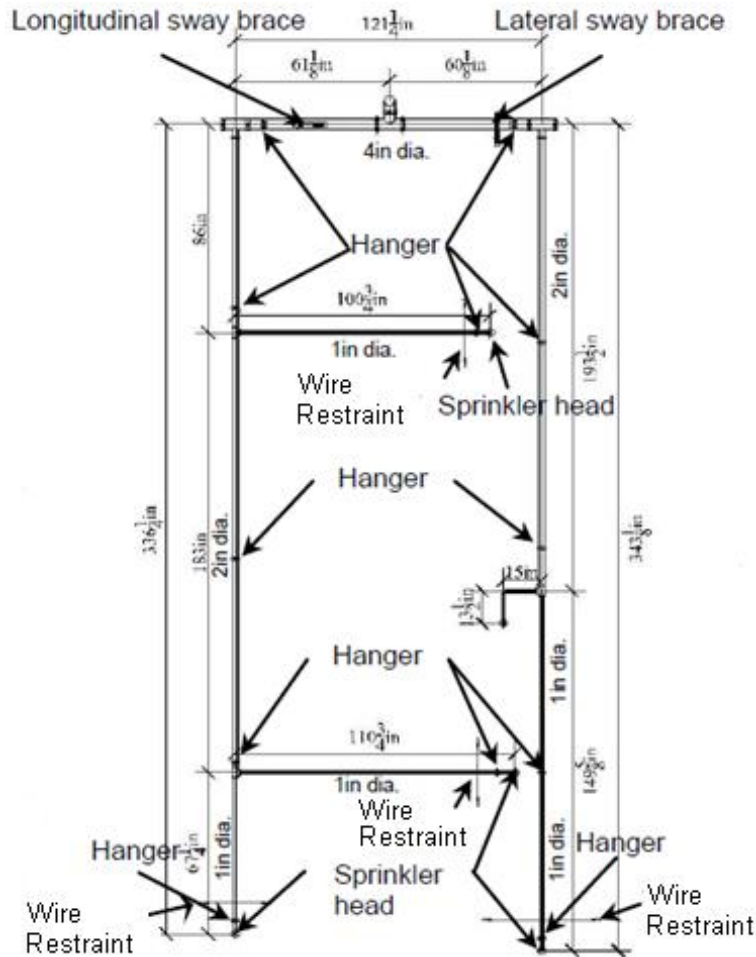


Figure 4-18 Three-dimensional rendering of the sprinkler piping test specimen

The second level was composed of a comprehensive layout that incorporated a variety of representative sprinkler piping components, including an 11-foot-long cross main line, two pieces of 29-foot-long longitudinal branch lines, two pieces of 9-foot-long transverse branch lines, and one unsupported elbow armover. The first level consisted of a 28-foot-long longitudinal main run, and the main line was connected to six branch lines that were

perpendicular to the direction of input motion. The layout of the second level, locations of vertical hangers and bracings, and diameter of the piping are shown in *Figure 4-19*.



*Figure 4-19 Layout of second level*

In order to take into account the fact that a typical branch line in a fire sprinkler piping system is usually over 30 feet long and the UB-NCS system is only able to impose uniaxial ground shaking for this phase of experimental study, extra mass blocks were attached to the end of each transverse branch line at the first level such that each transverse branch line had the same natural

frequency as that of a branch line that was over 30-feet long. The detailed layout of the first level and the riser is illustrated in *Figure 4-20(a)*.

The two levels of the specimen were connected together by a 15-foot-long vertical riser (*Figure 4-20 b*) and turned into a complete two-story full-scale fire sprinkler piping system. To detect leakage, all pipes were filled with water under an average municipal water pressure of 40 psi.

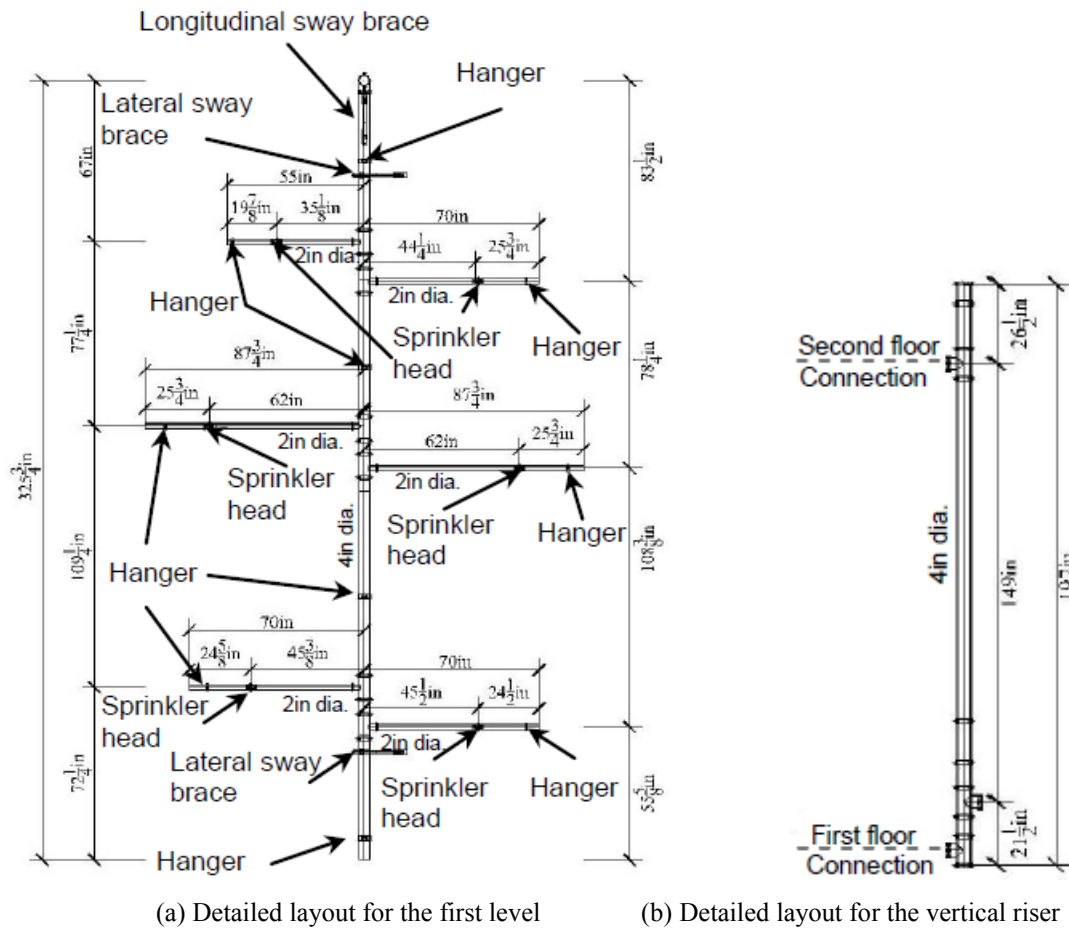


Figure 4-20 Layout of first level and riser

### 4.5.3 Construction of test specimens

Details of installation of piping joints were explained in the previous chapter. This section mainly describes the support systems for the tested specimens.

#### Support systems

A typical support for the fire sprinkler piping subsystems consists of four types of components as follow:

- Building-attached component;
- Fastener, which attaches the building-attached components to the building structure;
- Hanger assembly, which is connected to the sprinkler piping; and
- Connecting piece, which attaches the building attachment component to the pipe attachment components.

The typical supports used for this phase of the experimental study are presented in *Figure 4-23* and *Table 4-3*. All the components are selected and sized according to the NFPA-13 provisions presented in *Chapter 1*.

*Table 4-3 Summary of support systems*

<b>Support</b>	<b>Building-attached component</b>	<b>Fastener</b>	<b>Hanger assembly</b>	<b>Connecting piece</b>
Vertical hanger	SAMMY screws	SAMMY screws	Clevis hanger	3/8" All-threaded rod
Brace	Universal structural attachment	I beam adapter	Double U-bolt	1" schedule-40 steel pipe
Wire restraint	Steel angle	Gauge #12 splay wire	Gauge #12 splay wire	Gauge #12 splay wire





(a) SAMMY screw for concrete (from ARGCO, 2012)



(b) SAMMY screw for steel (from ARGCO, 2012)



(c) Standard clevis hanger (from Focus Tech., 2012)



(d) Universal structural attachment (from CADDY, 2012)



(e) I-beam adaptor (from CADDY, 2012)



(f) Standard universal sway brace (from CADDY, 2012)

Figure 4-21 Components of support systems

#### 4.6 Test Program

The general concept for the experimental testing program was to start with fully braced fire sprinkler piping systems according to the provisions defined in NFPA-13 (NFPA, 2010), then gradually reduce the level of bracing, and finish with fully unbraced fire protection systems. The fully unbraced system means that the fire extinguishing sprinkler piping subsystem is connected to the NCS testing frame without any sway braces or wire restraints and is supported only with vertical hangers. The fully unbraced systems are typically installed in low to moderate seismic regions or could be present in existing older buildings. The testing plan consists of six different configurations in terms of the level of bracing systems. For each configuration, the intensity of input motions for both platforms was increased from 25%, 50%, 66.7% (DBE level), to 100% (MCE level). The peak accelerations at each platform and the maximum inter-story drift associated with each of these testing intensities are listed in *Table 4-5*. If any damage is observed before the test program reaches the MCE level, necessary repairs were carried out before the next test.

This testing plan was repeated for all three specimens. However, the testing program for the second specimen was terminated early to prevent possible severe flooding and damage to electronic devices in the lab after a major water leakage occurred at the fourth phase (100% of MCE level).

The details of the fire sprinkler piping systems testing program are listed in *Table 4-4*.

Table 4-4 Testing program

Specimen	Configuration	Percentage of Testing Protocol	Date Test	Description of Bracing System
1	1-1	25%	06-03-11	Fully braced specimen (bracing systems installed according to NFPA 13)
		50%		
		67%		
		100%		
	1-2	25%	06-03-11	Lateral and longitudinal braces removed from cross main line at the second level
		50%		
		67%		
		100%		
	1-3	25%	06-06-11	Lateral and longitudinal braces removed from main line at the first level
		50%		
		67%		
		100%		
	1-4	25%	06-08-11	Wire restraints removed (fully unbraced two-story specimen)
		50%		
		67%		
		100%		
1-5	25%	06-13-11	Vertical riser disconnected, lateral and longitudinal braces reinstalled for main line at the first level	
	50%			
	67%			
	100%			
1-6	25%	06-15-11	Lateral and longitudinal braces removed from main line at the first level (fully unbraced specimen)	
	50%			
	67%			
	100%			
2	2-1	25%	06-24-11	Fully braced specimen (bracing systems installed according to NFPA 13)
		50%		
		67%		
		100%		
	2-2	25%	07-20-11	Lateral and longitudinal braces removed from cross main line at the second level
		50%		
		67%		
		100%		
	2-3	25%	07-20-11	Lateral and longitudinal braces removed from main line at the first level (fully unbraced single-story specimen)
		50%		
		67%		
		100%		
2-4	25%	07-21-11	Wire restraints removed (fully unbraced two-story specimen)	
	50%			
	67%			
	100%			

Table 4-4 Testing program (Cont'd)

Specimen	Configuration	Percentage of Testing Protocol	Date Test	Description of Bracing System
3	3-1	25%	08-30-11	Fully braced specimen (bracing systems installed according to NFPA 13)
		50%		
		67%		
		100%		
	3-2	25%	08-30-11	Lateral and longitudinal braces removed from cross main line at the second level
		50%		
		67%		
		100%		
	3-3	25%	08-31-11	Lateral and longitudinal braces removed from main line at the first level
		50%		
		67%		
		100%		
	3-4	25%	08-31-11	Wire restraints removed (fully unbraced two-story specimen)
		50%		
		67%		
		100%		
	3-5	25%	08-31-11	Vertical riser disconnected, lateral and longitudinal braces reinstalled for main line at the first level
		50%		
		67%		
		100%		
	3-6	25%	08-31-11	Lateral and longitudinal braces removed from main line at the first level (fully unbraced specimen)
		50%		
		67%		
		100%		

Table 4-5 Peak accelerations and maximum inter-story drifts for all testing intensities

Testing Intensity	Peak Accelerations (g)		Maximum inter-story drift $\Delta_{Max}$ (in.)
	Bottom Level	Top Level	
25%	0.14	0.16	1.02
50%	0.28	0.33	2.04
67%	0.38	0.44	2.73
100%	0.56	0.65	4.08

## 4.7 Instrumentation

A variety of instrumentation was installed to record the displacements, forces and absolute accelerations imposed on the specimens by the UB-NCS testing frames. The instrumentation included a total of 109 channels at various critical locations.

### 4.7.1 Acceleration

*Figure 4-22* shows the location of accelerometers used to record the acceleration histories along the cross main lines, longitudinal branch lines at the second level, longitudinal main line at the first level, as well as at the end of all the lateral branch lines at both levels. Since the direction of shaking imposed by the actuators was uniaxial, all the accelerometers were unidirectional in the direction of shaking, except that AP-2, AP-3 and AP-6 were designed to measure the acceleration perpendicular to the direction of shaking for the longitudinal pipes.

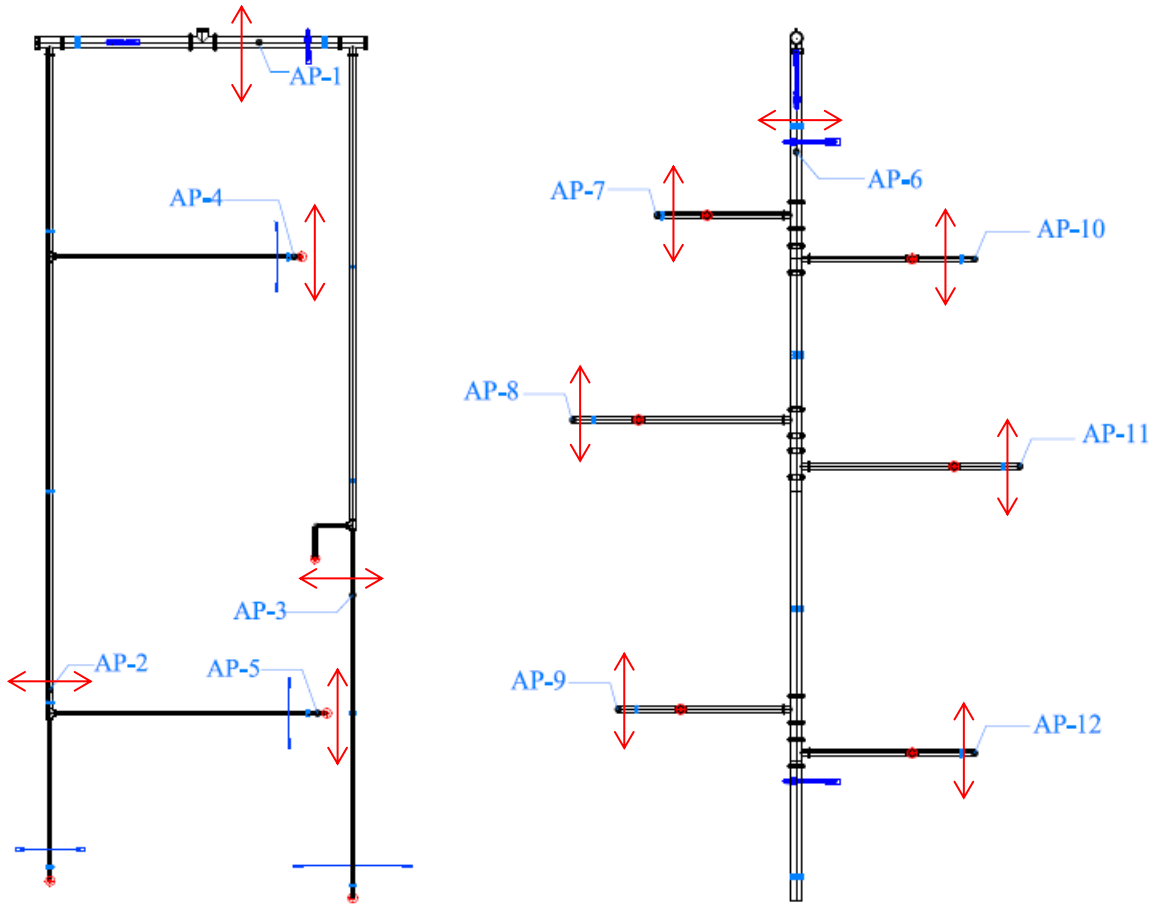


Figure 4-22 Locations of accelerometers (Note: AP indicates accelerometers for pipes)

Besides those shown in *Figure 4-22*, accelerometers were also attached on each sprinkler head (*Figure 4-23* and *Figure 4-24*) to measure the difference in acceleration levels between sprinkler heads with and without impact imposed by the ceiling boxes due to the differential movements. The directions of the accelerometers were again identical to the direction of shaking.

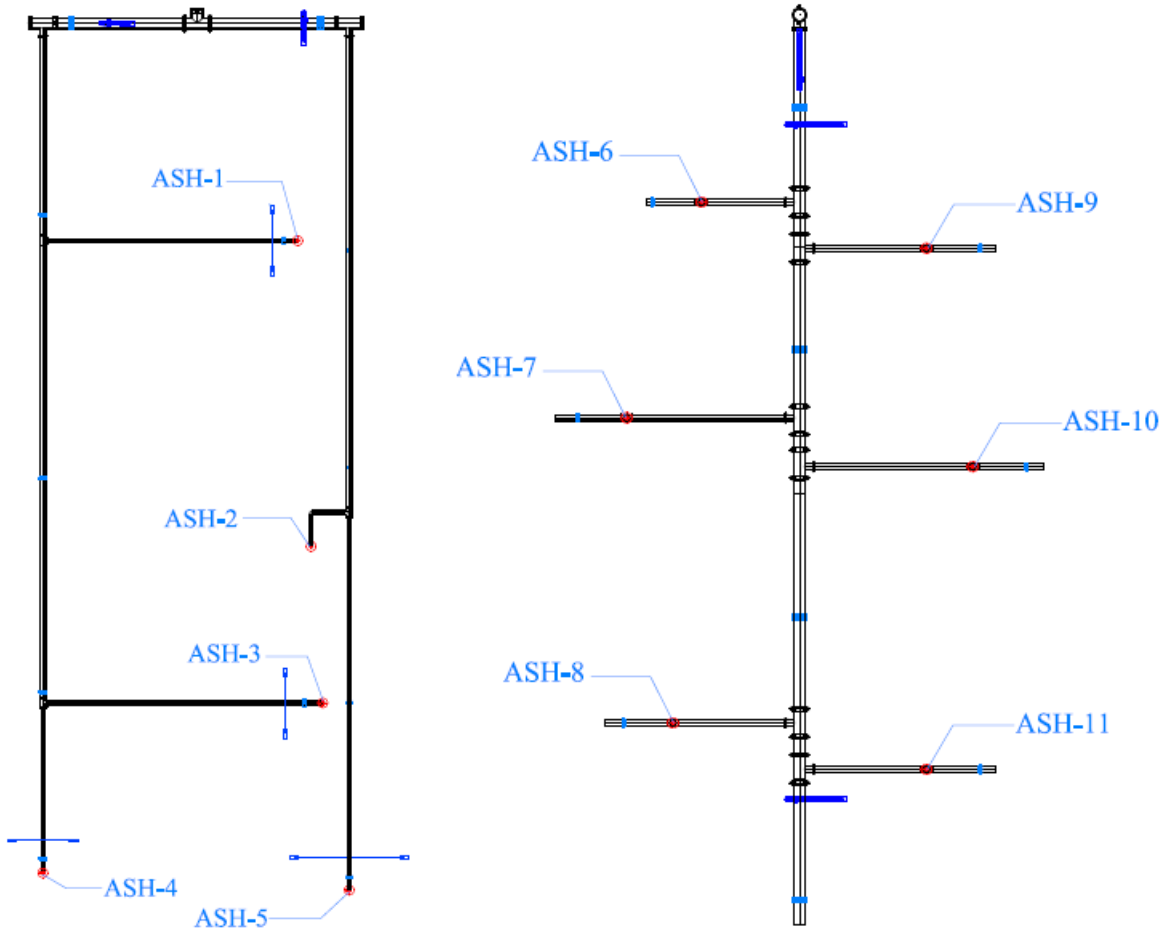


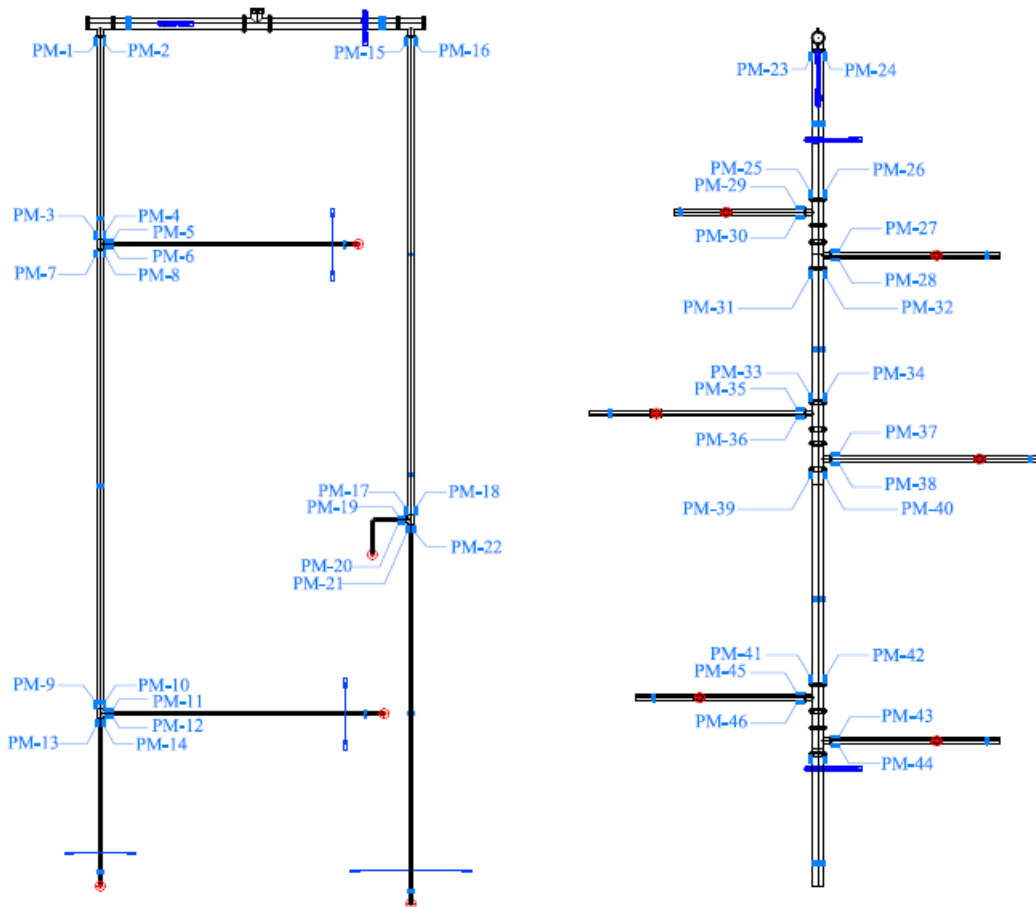
Figure 4-23 Accelerometers instrumentation for sprinkler heads  
 (Note: ASH indicates accelerometers for sprinkler heads)



Figure 4-24 Accelerometer attached to the tee joint connected to sprinkler head

## 4.7.2 Rotation

A total of 46 channels were assigned to linear potentiometers to measure the axial displacement along the pipe surface at the juncture of tee joint and the pipe. The rotation of each joint of the tee,  $\theta$ , could then be calculated from the displacement recorded by the linear potentiometers glued on each side of the piping tee joint. *Figure 4-25* shows the location of the 46 linear potentiometers. The installation of the potentiometers (*Figure 4-28*) was similar to the quasi-static tests presented in *Chapter 3*.



*Figure 4-25* Linear potentiometers instrumentation for piping tee joints (PM indicates potentiometers)



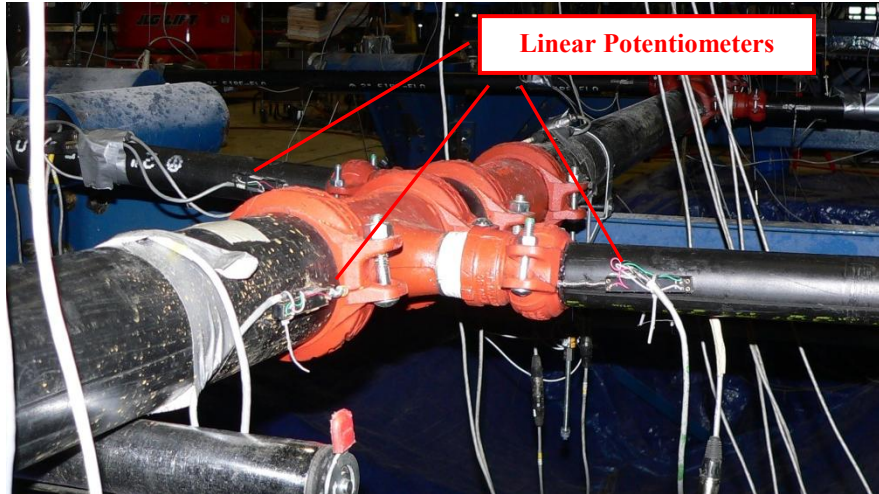


*Figure 4-26 Linear potentiometers attached to the tee joints*

#### **4.7.3 Force**

A miniature universal load cell provided by the Hilti Corporation (*Figure 4-27*) was inserted in line with each of the vertical hanger rods (*Figure 4-28*) and the wire restraints to measure the forces during the dynamic testing, including both the axial tension and compression force in the vertical hanger rod, and the tension force in the wire restraint. These load cells have a  $\pm 2000$  lb. capacity (Omegadyne Inc., 2012) and are manufactured by Omegadyne (model: LC202-2K).

*Figure 4-29* and *Figure 4-30* show the location of the miniature universal load cells for the vertical hangers and the wire restraints respectively.



Figure 4-27 Miniature universal load cell

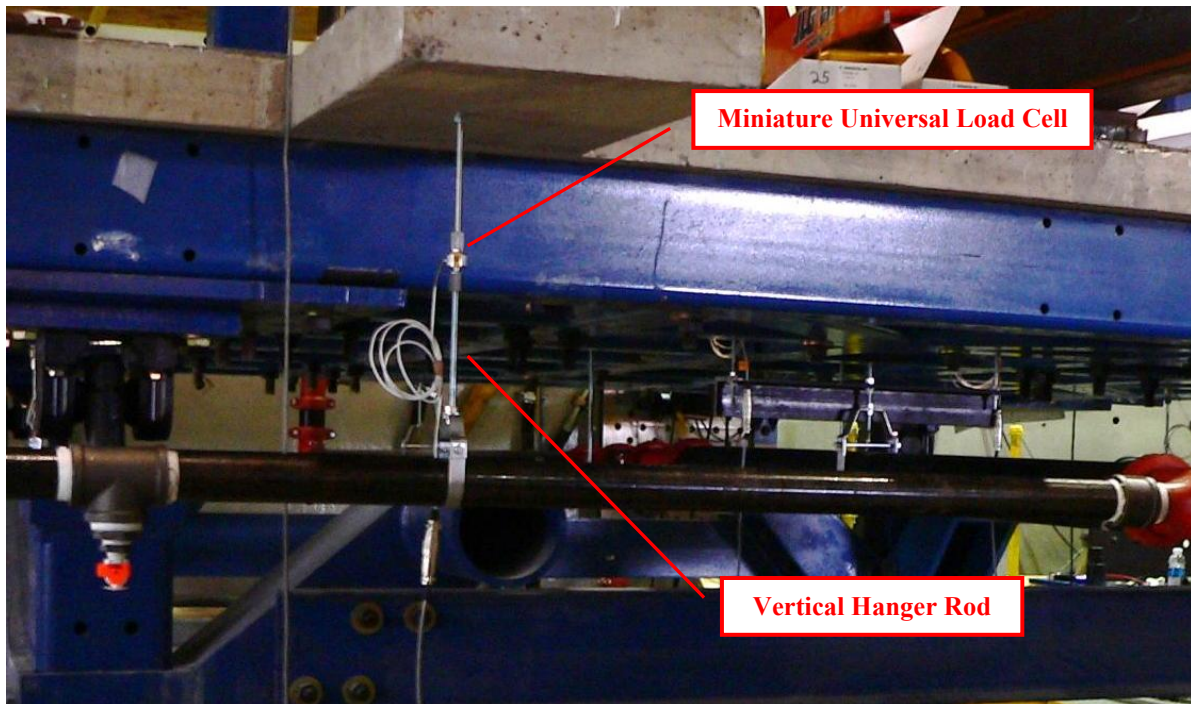


Figure 4-28 Miniature universal load cell installed in the middle of the vertical hanger

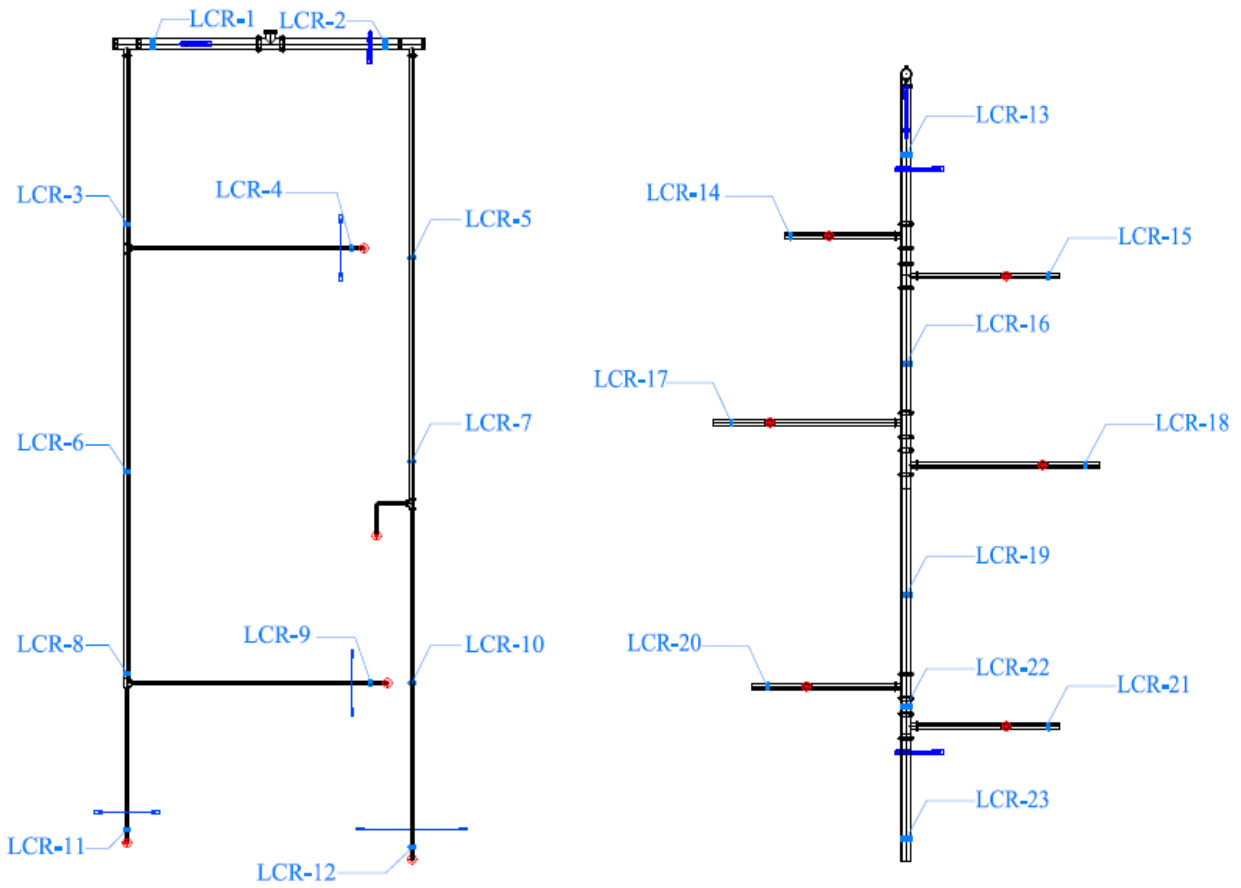


Figure 4-29 Location of miniature load cells for vertical hangers (LCR indicates load cells for vertical hanger rods)

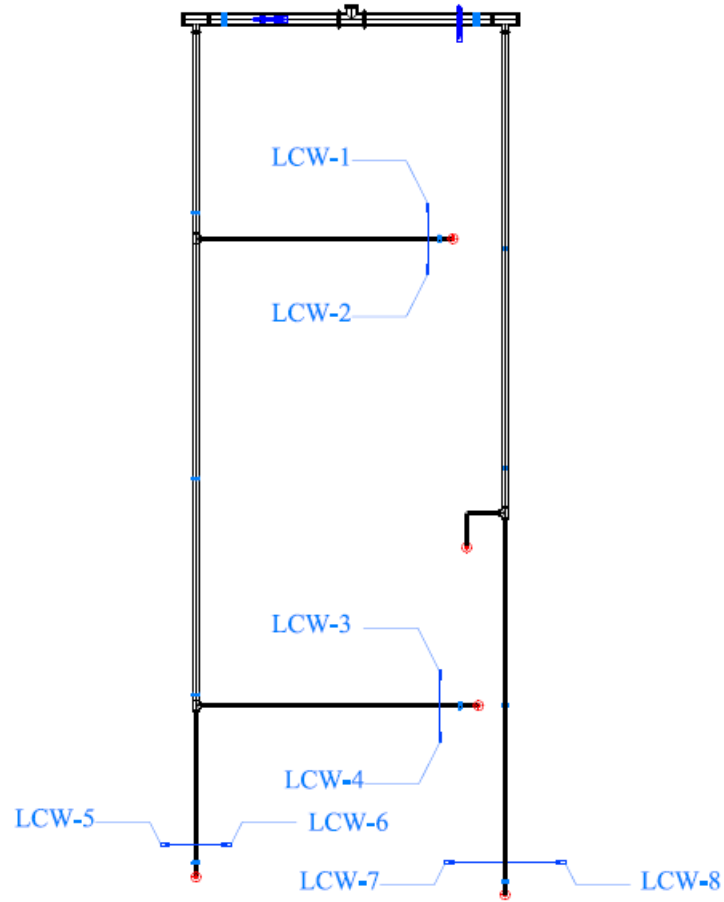


Figure 4-30 Location of the miniature load cells for wire restraints (LCW indicates load cells for wire restraints)

#### 4.7.4 Displacement

A total of nine linear string potentiometers were utilized to measure the displacement, relative to the reaction wall, on the cross main line at the second level and at the end of branch lines at both levels. *Figure 4-31* shows the location of the linear string potentiometers at each level of the tested specimens.

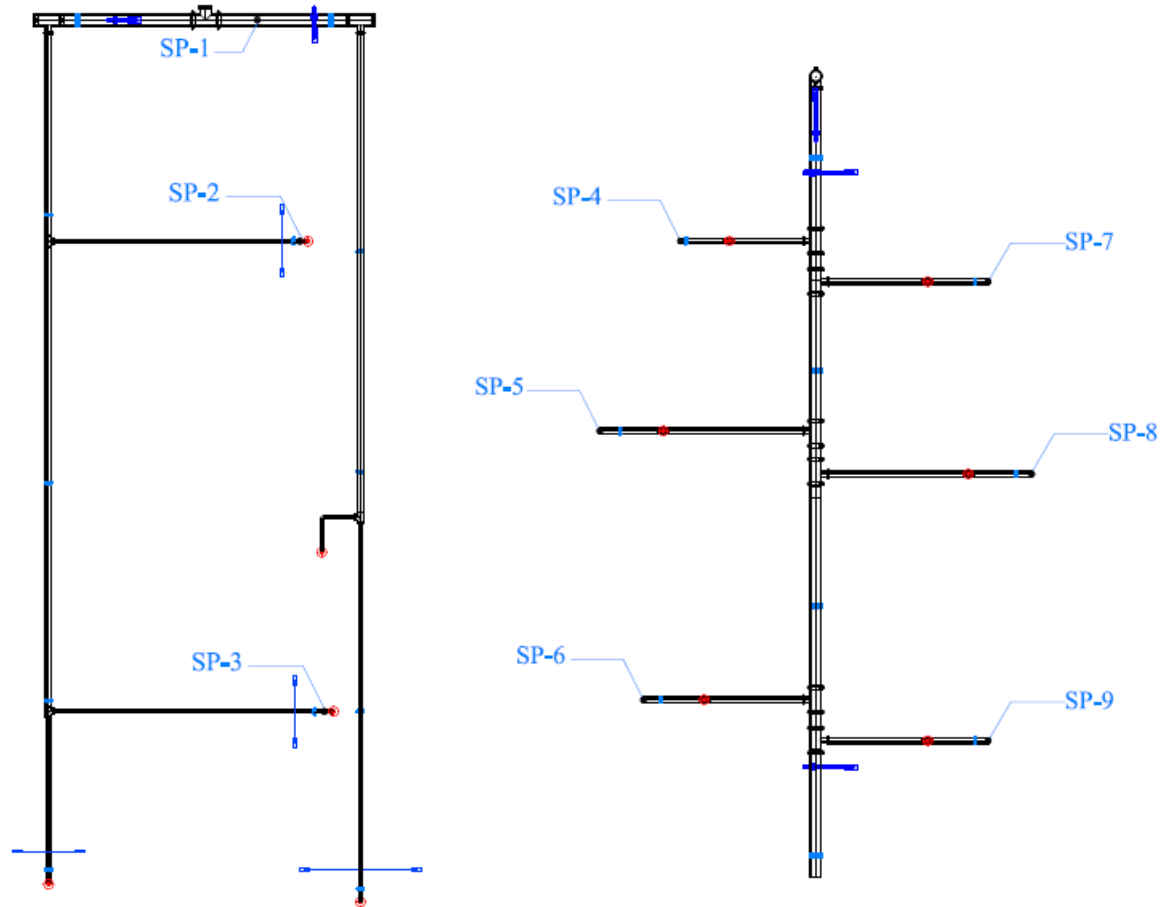


Figure 4-31 Location of linear string potentiometers (SP indicates string potentiometer)

A complete list of instrumentation is shown in Table 4-6.



Table 4-6 instrumentation (Cont'd)

GAUGE NAME	DEVICE	DESCRIPTIONS
PM 40	Potentiometer	Measure displacement of main line relative to tee joint on 1st level
PM 41	Potentiometer	Measure displacement of main line relative to tee joint on 1st level
PM 42	Potentiometer	Measure displacement of main line relative to tee joint on 1st level
PM 43	Potentiometer	Measure displacement of main line relative to tee joint on 1st level
PM 44	Potentiometer	Measure displacement of main line relative to tee joint on 1st level
PM 45	Potentiometer	Measure displacement of main line relative to tee joint on 1st level
PM 46	Potentiometer	Measure displacement of main line relative to tee joint on 1st level
LCR 1	Load Cell	Measure the force of vertical hanger on 2nd level
LCR 2	Load Cell	Measure the force of vertical hanger on 2nd level
LCR 3	Load Cell	Measure the force of vertical hanger on 2nd level
LCR 4	Load Cell	Measure the force of vertical hanger on 2nd level
LCR 5	Load Cell	Measure the force of vertical hanger on 2nd level
LCR 6	Load Cell	Measure the force of vertical hanger on 2nd level
LCR 7	Load Cell	Measure the force of vertical hanger on 2nd level
LCR 8	Load Cell	Measure the force of vertical hanger on 2nd level
LCR 9	Load Cell	Measure the force of vertical hanger on 2nd level
LCR 10	Load Cell	Measure the force of vertical hanger on 2nd level
LCR 11	Load Cell	Measure the force of vertical hanger on 2nd level
LCR 12	Load Cell	Measure the force of vertical hanger on 1st level
LCR 13	Load Cell	Measure the force of vertical hanger on 1st level
LCR 14	Load Cell	Measure the force of vertical hanger on 1st level
LCR 15	Load Cell	Measure the force of vertical hanger on 1st level
LCR 16	Load Cell	Measure the force of vertical hanger on 1st level
LCR 17	Load Cell	Measure the force of vertical hanger on 1st level
LCR 18	Load Cell	Measure the force of trapeze hanger on 1st level
LCR 19	Load Cell	Measure the force of trapeze hanger on 1st level
LCR 20	Load Cell	Measure the force of vertical hanger on 1st level
LCR 21	Load Cell	Measure the force of vertical hanger on 1st level
LCR 22	Load Cell	Measure the force of vertical hanger on 1st level
LCR 23	Load Cell	Measure the force of vertical hanger on 1st level
LCW 1	Load Cell	Measure the force of wire restraint on 2nd level
LCW 2	Load Cell	Measure the force of wire restraint on 2nd level
LCW 3	Load Cell	Measure the force of wire restraint on 2nd level
LCW 4	Load Cell	Measure the force of wire restraint on 2nd level
LCW 5	Load Cell	Measure the force of wire restraint on 2nd level
LCW 6	Load Cell	Measure the force of wire restraint on 2nd level
LCW 7	Load Cell	Measure the force of wire restraint on 2nd level
LCW 8	Load Cell	Measure the force of wire restraint on 2nd level
SP 1	String Pot	Measure the displacement of cross main on 2nd level in the EW direction
SP 2	String Pot	Measure the displacement of east transverse branch line on 2nd level in the EW direction
SP 3	String Pot	Measure the displacement of west transverse branch line on 2nd level in the EW direction
SP 4	String Pot	Measure the displacement of north rear branch line on 1st level in the EW direction
SP 5	String Pot	Measure the displacement of north middle branch line on 1st level in the EW direction
SP 6	String Pot	Measure the displacement of north front branch line on 1st level in the EW direction
SP 7	String Pot	Measure the displacement of south rear branch line on 1st level in the EW direction
SP 8	String Pot	Measure the displacement of south middle branch line on 1st level in the EW direction
SP 9	String Pot	Measure the displacement of south front branch line on 1st level in the EW direction

## 4.8 Specimens Performance Observations

All three fully braced specimens performed well with no damage observed under the Maximum Considered Earthquake (MCE) level of loading, validating the current code-based requirements for bracing system design. However, the unbraced systems, which are typically installed in low to moderate seismic regions, did not perform as well as the fully braced systems, when they were subjected to the level of shaking that corresponded to high seismic zones. Damage to sprinkler heads, failures of vertical hangers, as well as a branch line fracture were observed during the tests.

### 4.8.1 Specimen 1

The branch lines of the first specimen were made of black iron pipes (schedule 40) with threaded connections. An overview of the specimen ready for testing is presented in *Figure 4-32*.

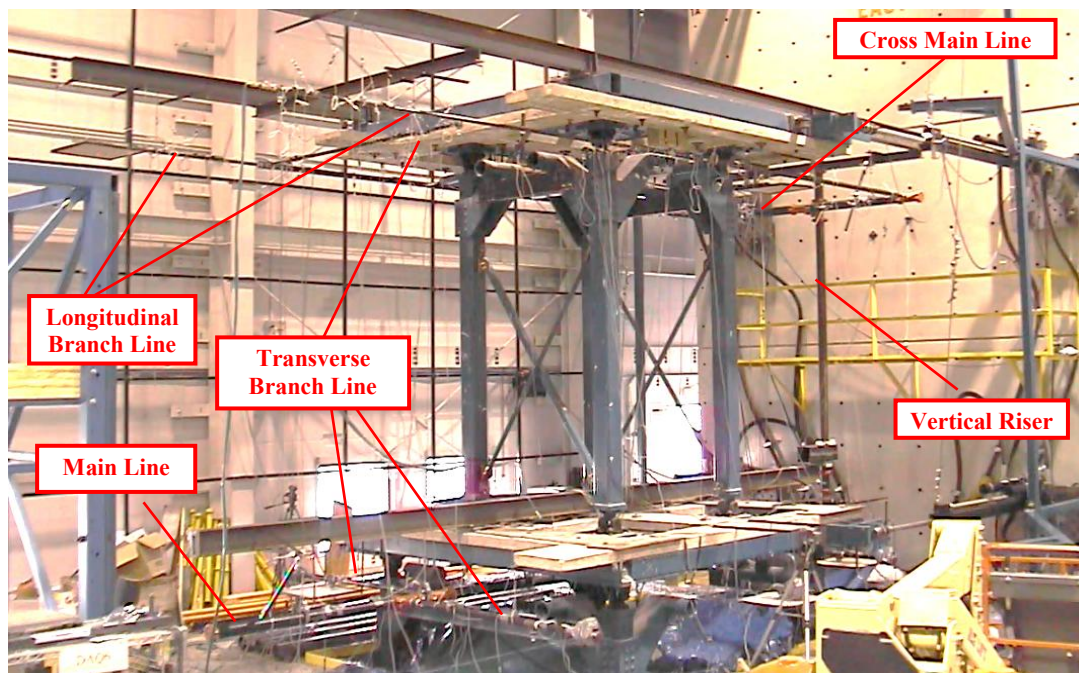


*Figure 4-32 Overview of Specimen 1*



The vertical hanger attached to the LCR-17 load cell (*Figure 4-29*) supporting the branch line on the first level pulled out from the concrete slab due to the failure of the building-attached component at 100% of MCE level. Although the data recorded by the miniature load cell indicated that the axial force was within half of the pullout strength limit of the SAMMY screw, it obviously showed that the failure mechanism of the SAMMY screw was dominated by the shear force in this case (*Figure 4-33*). In addition, as shown in *Figure 4-34*, the vertical hanger attached to the LCR-13 load cell (*Figure 4-29*) supporting the main line on the first level buckled when the first level of the fire sprinkler piping system was fully braced and separated from the vertical riser, indicating that there was substantial vertical displacement.

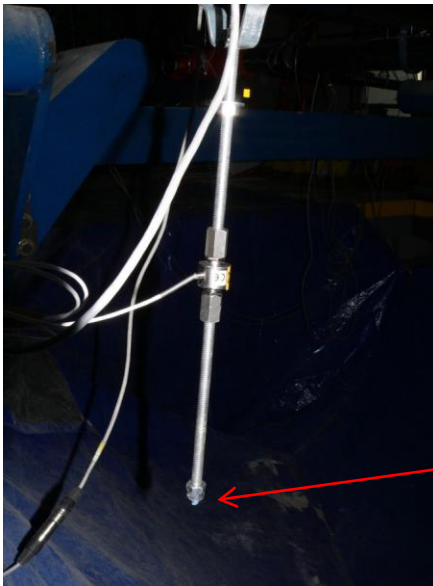
During dynamic testing, the rigid ceiling boxes moved in unison with the UB-NCS platforms due to the stiff steel angles attached to the concrete slab fixed to the platforms. The flexible ceiling boxes, on the other hand, were able to move freely since the wire restraints provided little lateral stiffness. However, both types of ceiling boxes experienced significant differential displacement compared to the specimen because the fire sprinkler protection system also moved relative to the UB-NCS testing frame. As a result, severe pounding occurred between the sprinkler heads and the ceiling tiles. As shown in *Figure 4-35*, large openings were cut through due to the pounding. Similar ceiling damage was observed repeatedly in past earthquakes. For example, extensive openings were cut through at a number of airports during the 2010 Chile Earthquake described in *Chapter 1*.



(a) SAMMY screw sheared off  
(Configuration 1-5, 100% MCE level)



(b) Remnant of SAMMY screw in the concrete slab  
(Configuration 1-5, 100% MCE level)



(c) Vertical hanger pulled out from concrete slab (Configuration 1-6, 100% MCE level)



Figure 4-33 Failure of vertical hanger

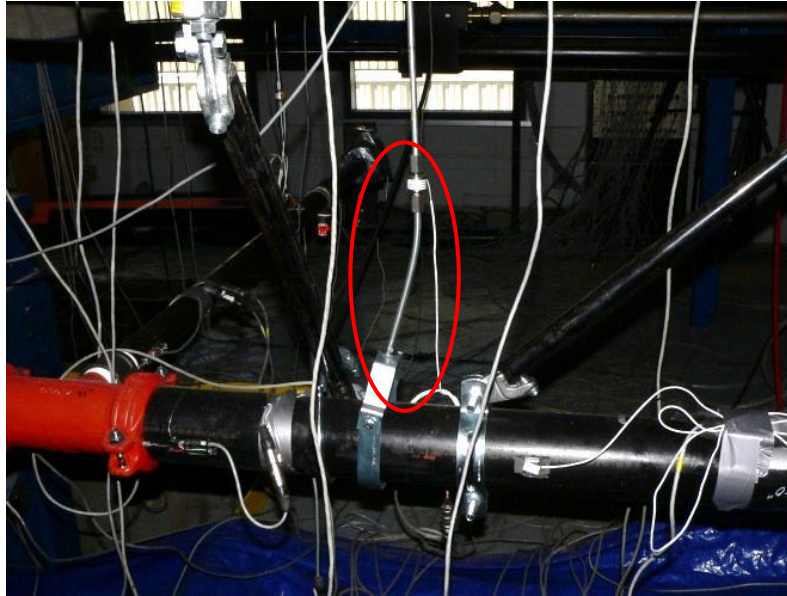


*Figure 4-34 Buckling of vertical hanger (Configuration 1-6, 100% MCE level)*



*(a) Damage of rigid ceiling box  
(Configuration 1-6, 100% MCE level)*



*(a) Damage of flexible ceiling box  
(Configuration 1-6, 100% MCE level)*

*Figure 4-35 Damage of ceiling boxes*

For the fully unbraced single-story system (Configuration #6), leakage was observed from the quick response pendant sprinkler head tagged with ASH-9 (*Figure 4-23*) in the branch line at the first level. The red glass bulb (*Figure 4-36*), acting as the plug which prevented water from

flowing out, was broken and activated water release as the sprinkler head collided with the sharp debris around the opening of the ceiling tile.



*Figure 4-36 Failure of quick response pendant sprinkler head (Configuration I-6, 100% MCE level)*

A list of damage observation for each test is presented in *Table 4-7*.

Table 4-7 Observed damage in Specimen 1

Specimen	Test Series	Percentage of Testing Protocol	Date Test	Description of Bracing System	Observed Damage
1	1-1	25%	06-03-11	Fully braced specimen (bracing systems installed according to NFPA 13)	No damage observed
		50%			No damage observed
		67%			No damage observed
		100%			No damage observed
	1-2	25%	06-03-11	Lateral and longitudinal braces removed from cross main line at the second level	No damage observed
		50%			No damage observed
		67%			No damage observed
		100%			No damage observed
	1-3	25%	06-06-11	Lateral and longitudinal braces removed from main line at the first level	No damage observed
		50%			No damage observed
		67%			No damage observed
		100%			No damage observed
	1-4	25%	06-08-11	Wire restraints removed (fully unbraced specimen)	No damage observed
		50%			No damage observed
		67%			No damage observed
		100%			No damage observed
	1-5	25%	06-13-11	Vertical riser disconnected, lateral and longitudinal braces reinstalled for main line at the first level	No damage observed
		50%			No damage observed
		67%			One branch line leaks
		100%			Vertical Hanger (LCR-17) was pulled out & Sprinkler Head (ASH-7) failed
1-6	25%	06-15-11	Lateral and longitudinal braces removed from main line at the first level (fully unbraced specimen)	No damage observed	
	50%			No damage observed	
	67%			No damage observed	
	100%			Vertical Hanger (LCR-13) was pulled out & Sprinkler Head (ASH-9) failed	

#### 4.8.2 Specimen 2

The branch lines of the second specimen were constructed with CPVC pipes (schedule 40) with cement joints. An overview of the second specimen is presented in *Figure 4-37*. As a result of the complete fracture of branch line #1 (*Figure 4-18*) at the first floor that occurred in the fourth

configuration, the testing program was terminated to prevent potential threat of severe flooding and damage to electronic devices in the lab after the major water leakage.



*Figure 4-37 Overview of Specimen 2*

Two major failures were observed during testing of the second specimen. The first one occurred to the third configuration when the two-story specimen was subjected to 100% of MCE level of testing protocol and supported only by vertical hangers and braced with wire restraints. As shown in *Figure 4-38*, the vertical hanger attached to the LCR-18 load cell (*Figure 4-29*) supporting the branch line #5 at the first level ruptured due to local necking at the connection to the SAMMY screw.

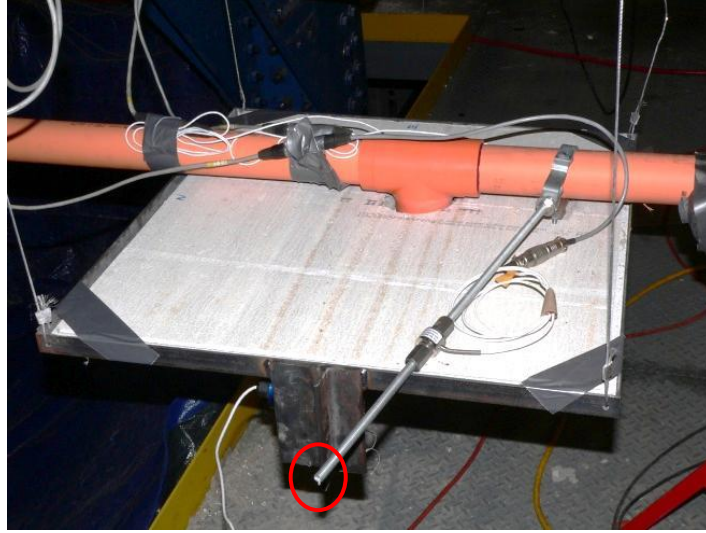


*Figure 4-38 Rupture of vertical hanger (Configuration 2-3, 100% MCE level)*

At the 100% MCE level of testing protocol, the fully unbraced specimen had a complete fracture at the tee joint of the branch line #1 at the first level, as shown in *Figure 4-39*. Unlike the failure mechanisms that were observed from the quasi-static tests on the piping tee joints described in Chapter 3, the complete fracture occurred at the root of the CPVC tee joint instead of at the end of pipes along the edge of the tee joints.

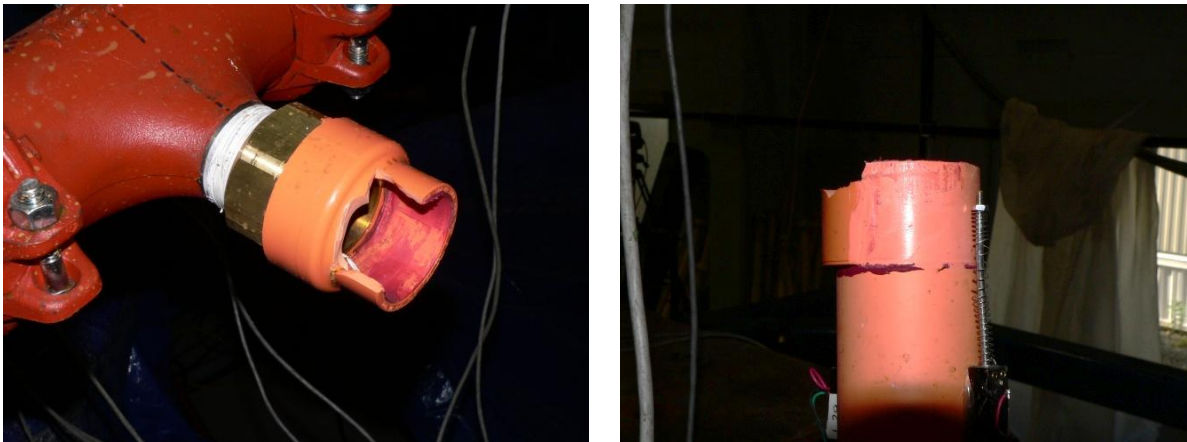


*Figure 4-39 Fracture of the CPVC branch line (Configuration 2-4, 100% MCE level)*

As shown in *Figure 4-40*, severe damage of ceiling tiles as a result of pounding with pendant sprinkler heads was again observed during the testing on the second specimen.

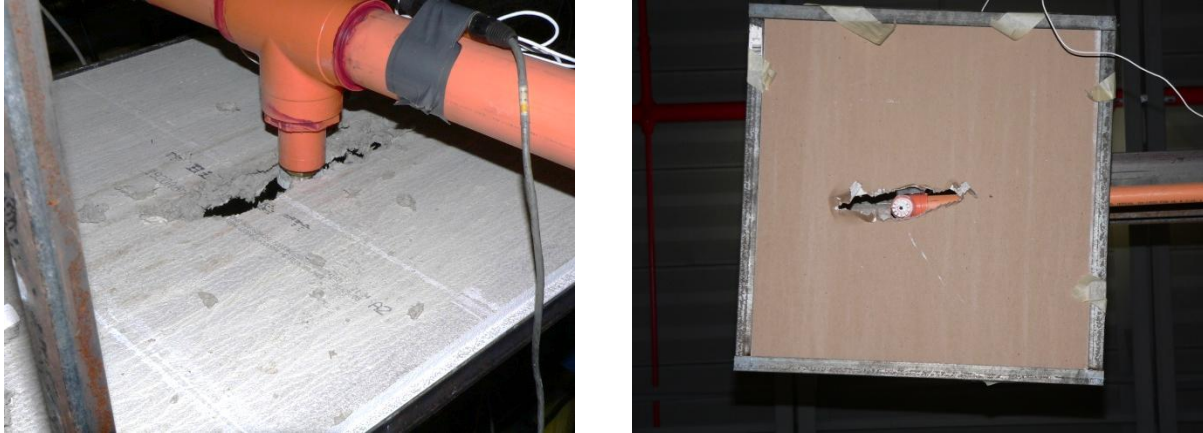


*Figure 4-40* Damage of ceiling tiles (Configuration 2-4, 100% MCE level)

For the second specimen, the observed damage for each configuration is listed in *Table 4-8*.



Table 4-8 Observed damage in Specimen 2

Specimen	Test Series	Percentage of Testing Protocol	Date Test	Description of Bracing System	Observed Damage
2	2-1	25%	06-24-11	Fully braced specimen (bracing systems installed according to NFPA 13)	No damage observed
		50%			No damage observed
		67%			No damage observed
		100%			No damage observed
	2-2	25%	07-20-11	Lateral and longitudinal braces removed from cross main line at the second level	No damage observed
		50%			No damage observed
		67%			No damage observed
		100%			No damage observed
	2-3	25%	07-20-11	Lateral and longitudinal braces removed from main line at the first level	No damage observed
		50%			No damage observed
		67%			No damage observed
		100%			Vertical Hanger (LCR-18) failed
	2-4	25%	07-21-11	Wire restraints removed (fully unbraced specimen)	No damage observed
		50%			No damage observed
		67%			No damage observed
		100%			Branch line #1 fractured completely

### 4.8.3 Specimen 3

The branch lines of the last specimen were made of steel pipes (schedule 7) with groove-fit connections. An overview of the third specimen is presented in *Figure 4-41*.

Similar to the first and second specimen, the failures observed during the testing of the third specimen, concentrated on the vertical hangers and the ceiling tiles. A number of photos of the failures are shown in *Figure 4-42*. The vertical hanger attached to the LCR-23 load cell supporting the 4-inch main line at the first level failed as the SAMMY screw for steel was sheared off. In addition, another SAMMY screw (LCR-7) attached to the concrete slab at the second level lost grip and was entirely pulled out from the concrete member. Again, pounding

with the pendant sprinkler heads during the dynamic tests led to significant damage to the ceiling tiles (*Figure 4-43*).



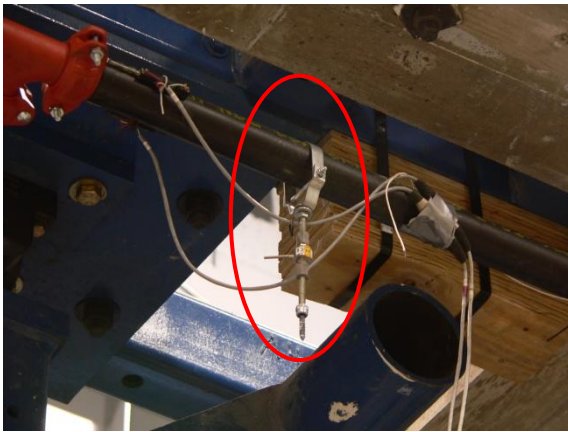
*Figure 4-41 Overview of Specimen 3*



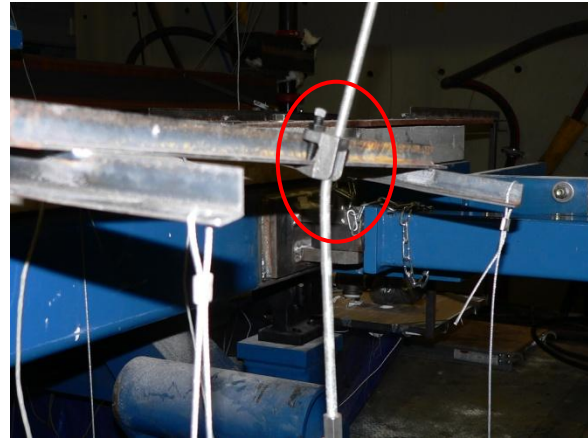
(a) Vertical hanger sheared off  
(Configuration 3-5, 100% MCE level)



(b) Excessive deformation of main line  
after failure of vertical hanger  
(Configuration 3-5, 100% MCE level)



(c) Vertical hanger pulled out from concrete  
slab (Configuration 3-2, 100% MCE level)



(d) Yielding of Vertical hanger  
(Configuration 3-5, 100% MCE level)

Figure 4-42 Failures of vertical hangers



*Figure 4-43 Damage of ceiling box*

The observed damage of each test for all configurations is shown in details in *Table 4-9*.

Table 4-9 Observed damage in Specimen 3

Specimen	Test Series	Percentage of Testing Protocol	Date Test	Description of Bracing System	Observed Damage
3	3-1	25%	08-30-11	Fully braced specimen (bracing systems installed according to NFPA 13)	No damage observed
		50%			No damage observed
		67%			No damage observed
		100%			No damage observed
	3-2	25%	08-30-11	Lateral and longitudinal braces removed from cross main line at the second level	No damage observed
		50%			No damage observed
		67%			No damage observed
		100%			Vertical hanger LCR-7 failed
	3-3	25%	08-31-11	Lateral and longitudinal braces removed from main line at the first level	No damage observed
		50%			No damage observed
		67%			No damage observed
		100%			No damage observed
	3-4	25%	08-31-11	Wire restraints removed (fully unbraced specimen)	No damage observed
		50%			No damage observed
		67%			No damage observed
		100%			Branch line #4 and #5 leaked at the connection with main run
	3-5	25%	08-31-11	Vertical riser disconnected, lateral and longitudinal braces reinstalled for main line at the first level	No damage observed
		50%			No damage observed
		67%			No damage observed
		100%			Vertical hangers LCR-18 and LCR-23 failed
3-6	25%	08-31-11	Lateral and longitudinal braces removed from main line at the first level (fully unbraced specimen)	No damage observed	
	50%			No damage observed	
	67%			No damage observed	
	100%			No damage observed	

#### 4.9 Experimental Results

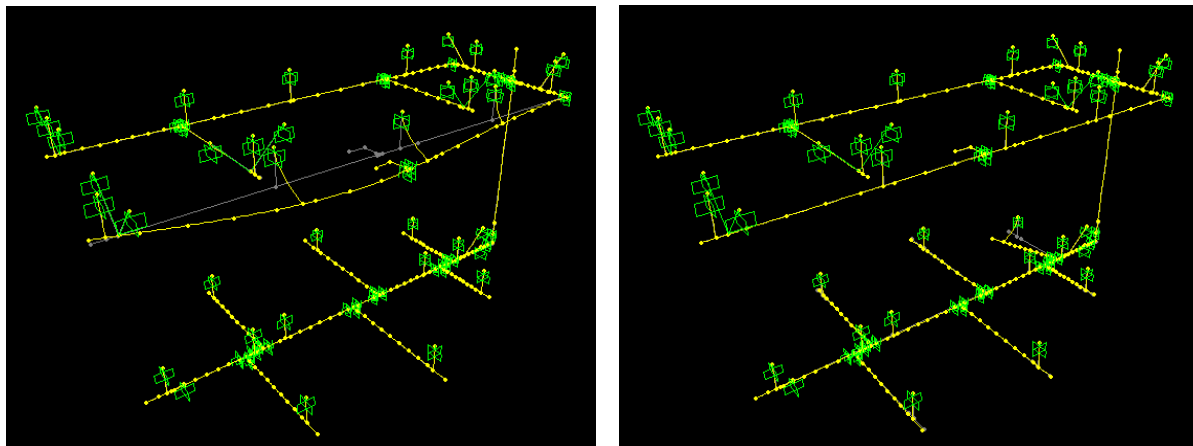
In this section, the dynamic characteristic of fire sprinkler piping systems, selected peak rotation and acceleration at various locations for all three specimens are presented and compared.

Furthermore, data analysis is carried out to gain an in-depth understanding of the seismic

performance and dynamic characteristics of full-scale fire sprinkler systems made of different materials and joint arrangements at the subsystem level under various input intensities. The detailed and complete experimental results for the dynamic tests are presented in Appendix C.

#### 4.9.1 Dynamic characteristics of test specimens

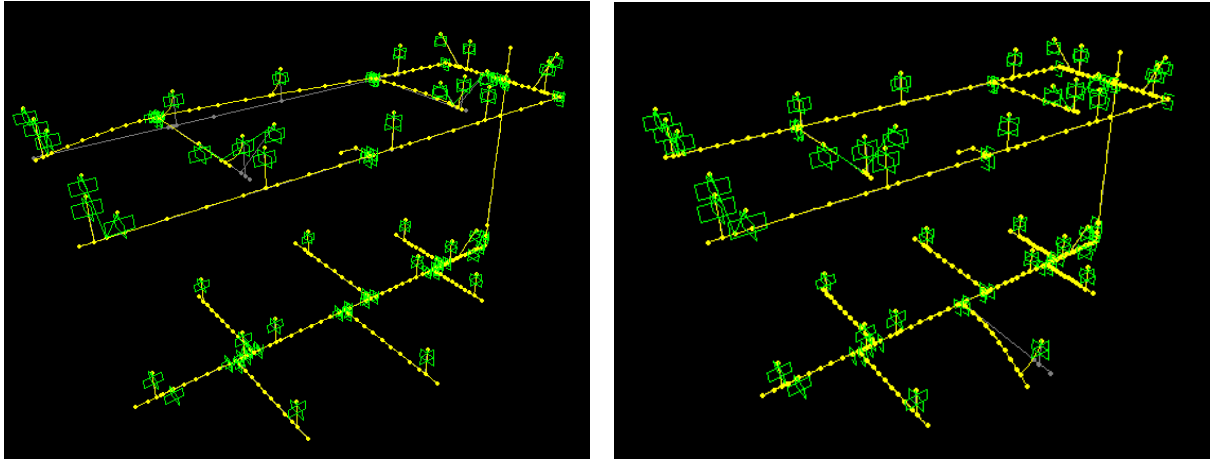
The natural periods and the mode shapes of fully braced fire sprinkler piping systems were determined and obtained by applying Transfer Functions (TFs) to the acceleration response of piping systems and the NCS platforms. The natural periods for each test specimens are listed in *Table 4-10*, and the mode shapes are presented in *Figure 4-44*.



(a) 1<sup>st</sup> mode

(b) 2<sup>nd</sup> mode

*Figure 4-44 Mode shapes of fire sprinkler piping system*



(c) 3<sup>rd</sup> mode

(d) 4<sup>th</sup> mode

Figure 4-44 Mode shapes of fire sprinkler piping system (Cont'd)

As shown in Figure 4-44, the first four mode shapes of fire protection systems are all local vibrations of branch lines.

Table 4-10 Natural periods of fully braced fire sprinkler piping systems

Mode No.	Test Specimen 1		Test Specimen 2		Test Specimen 3	
	Period (sec)	Frequency (Hz)	Period (sec)	Frequency (Hz)	Period (sec)	Frequency (Hz)
1	0.58	1.74	2.20	0.46	0.97	1.03
2	0.53	1.88	2.05	0.49	0.89	1.13
3	0.47	2.15	1.96	0.51	0.83	1.21
4	0.46	2.18	1.87	0.54	0.80	1.25

#### 4.9.2 Comparison of dynamic response of test specimens

##### Acceleration

Figure 4-45 shows the locations and directions of the accelerometers. The peak value for every test recorded by the accelerometers attached at the tip of each of the six branch lines located at

the first level is summarized in *Table 4-11*. No data are shown for the CPVC pipes with cement joints for Configuration #4 at 100% level, Configuration #5 and Configuration #6, as the testing program for the second specimen was terminated prematurely due to the severe water leakage.

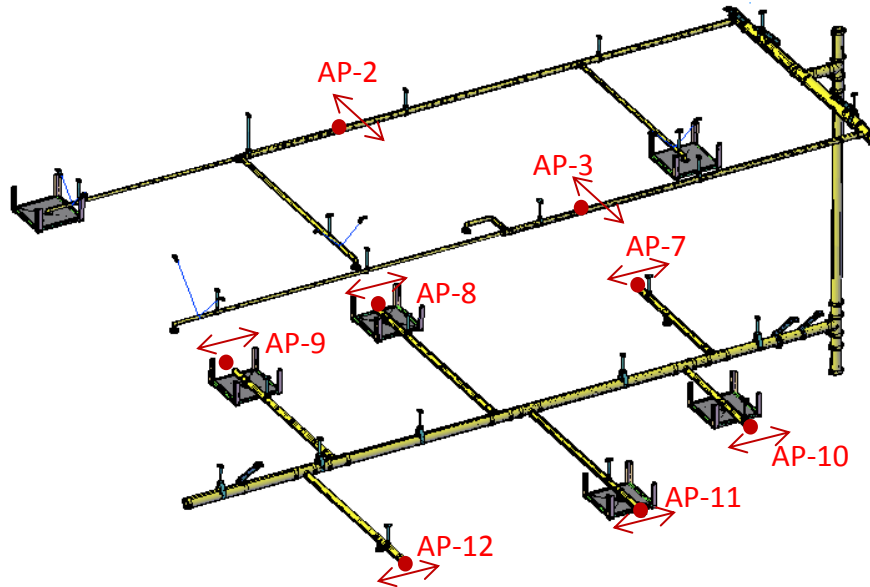


*Figure 4-45 Locations and directions of accelerometers (Note: AP indicates accelerometers for pipes)*

Comparing the peak accelerations observed for the specimens with three types of joint configurations, the results do not show consistent trends. This can be partially explained by the fact that four out of the six branch lines at the first level were equipped with ceiling boxes, which restrained their response to some degree. The remaining two free branch lines may not be sufficient to draw conclusions. For some particular locations such as AP-2 and AP-8, however, it can be seen that for all four configurations, the CPVC pipes with cement joints exhibited the largest acceleration response. Similarly, the test specimens made of Dyna-Flow pipes with groove-fit connections had the smallest acceleration responses at the tips of branch lines, as shown in *Figure 4-46* and *Figure 4-47*.



*Figure 4-48* compares the peak acceleration responses for the AP-2 and AP-7 locations for each of the three test specimens.

Table 4-11 Summary of peak accelerations (BIT: Black Iron Threaded, CPVC: Thermoplastic, DF: Dyna-Flow Schedule 7)

Configuration	Bracing System	Percentage of Loading Protocol	BIT AP-7	CPVC AP-7	DF AP-7	BIT AP-8	CPVC AP-8	DF AP-8	BIT AP-9	CPVC AP-9	DF AP-9	BIT AP-10	CPVC AP-10	DF AP-10	BIT AP-11	CPVC AP-11	DF AP-11	BIT AP-12	CPVC AP-12	DF AP-12
			(g)	(g)	(g)	(g)	(g)	(g)	(g)	(g)	(g)	(g)	(g)	(g)	(g)	(g)	(g)	(g)	(g)	(g)
Configuration #1	Fully braced specimen (bracing systems installed according to NFPA 13)	25%	0.590	0.989	0.606	0.528	0.669	0.375	0.682	0.778	0.444	0.137	0.751	0.440	0.552	1.201	0.347	0.554	0.954	0.387
		50%	1.407	1.830	2.087	1.158	2.041	0.904	1.029	1.542	1.507	0.152	1.373	0.908	1.225	2.519	0.826	0.882	1.852	1.400
		67%	2.678	2.467	3.146	1.927	3.031	1.094	1.487	2.129	2.454	1.678	1.469	1.194	1.329	3.216	1.005	1.142	2.115	1.792
		100%	3.690	3.451	5.398	2.952	4.841	1.772	2.665	3.048	3.824	3.100	1.797	2.032	3.223	5.032	3.392	2.501	2.764	3.219
Configuration #2	Lateral and longitudinal braces removed from cross main line at the second level	25%	0.657	1.339	0.326	0.651	0.837	0.307	0.435	0.638	0.610	0.650	0.890	0.465	0.508	2.237	0.564	0.508	0.970	0.318
		50%	1.187	2.582	1.912	1.126	2.358	0.643	0.917	1.966	1.477	1.028	1.246	1.005	1.240	3.477	1.253	0.773	1.673	1.354
		67%	2.217	3.218	3.135	1.446	3.762	0.833	1.384	2.263	2.204	1.548	1.396	1.368	1.670	3.558	2.893	1.047	2.020	1.947
		100%	2.594	4.156	4.752	2.960	6.442	1.353	2.692	3.632	4.917	2.852	1.835	2.447	3.129	3.848	4.354	1.912	2.454	2.989
Configuration #3	Lateral and longitudinal braces removed from main line at the first level	25%	0.712	1.138	0.312	0.663	0.735	0.284	0.562	0.828	0.483	0.587	0.828	0.373	0.508	1.997	0.488	0.575	0.868	0.266
		50%	1.501	2.560	1.279	1.366	2.818	0.608	1.326	1.857	1.620	1.117	1.277	0.965	1.498	3.759	1.172	1.132	1.515	0.829
		67%	2.459	3.293	2.567	1.791	4.757	0.859	1.817	2.509	2.702	1.963	1.462	1.595	1.918	3.349	2.736	1.398	1.884	1.640
		100%	4.342	4.226	5.883	3.419	8.144	1.834	3.130	4.647	4.894	3.283	2.719	2.472	3.055	6.478	4.957	2.112	2.388	2.932
Configuration #4	Wire restraints removed (fully unbraced two-story specimen)	25%	0.578	1.211	0.400	0.482	1.048	0.382	0.511	0.731	0.583	0.468	0.760	0.331	0.500	1.997	0.464	0.423	0.837	0.303
		50%	1.733	2.235	1.249	1.453	3.658	0.777	1.361	1.901	1.663	1.048	1.412	0.904	1.618	3.873	1.188	1.078	1.690	0.694
		67%	2.634	3.082	2.508	1.543	6.323	0.951	2.032	3.113	2.298	1.766	1.804	1.581	2.204	3.398	1.626	1.202	2.092	1.235
		100%	4.129	N/A	5.037	2.879	N/A	2.367	2.829	N/A	4.392	3.493	N/A	2.147	3.588	N/A	5.009	2.509	N/A	2.564
Configuration #5	Vertical riser disconnected, lateral and longitudinal braces reinstalled for main line at the first level	25%	0.347	N/A	0.318	0.443	N/A	0.258	0.666	N/A	0.625	0.708	N/A	0.329	0.751	N/A	0.743	0.617	N/A	0.274
		50%	0.718	N/A	0.991	1.311	N/A	0.659	1.141	N/A	2.178	1.000	N/A	0.930	1.304	N/A	1.502	1.072	N/A	0.560
		67%	1.146	N/A	1.624	2.489	N/A	0.842	1.845	N/A	3.505	1.417	N/A	1.278	2.066	N/A	1.868	1.316	N/A	1.010
		100%	1.500	N/A	3.604	3.538	N/A	1.239	2.739	N/A	5.104	2.228	N/A	2.322	2.991	N/A	2.714	2.845	N/A	2.199
Configuration #6	Lateral and longitudinal braces removed for main line at the first level (fully unbraced single-story specimen)	25%	0.543	N/A	0.621	0.970	N/A	0.407	0.690	N/A	0.703	0.402	N/A	0.542	0.829	N/A	0.585	0.418	N/A	0.409
		50%	1.784	N/A	1.325	2.747	N/A	0.660	1.209	N/A	1.483	0.874	N/A	1.094	1.521	N/A	1.080	0.827	N/A	0.826
		67%	2.106	N/A	1.768	2.910	N/A	1.254	1.869	N/A	2.089	1.500	N/A	2.198	1.957	N/A	1.970	0.951	N/A	1.034
		100%	2.644	N/A	2.448	3.899	N/A	2.254	3.062	N/A	4.839	1.882	N/A	2.607	4.275	N/A	2.869	1.503	N/A	1.177

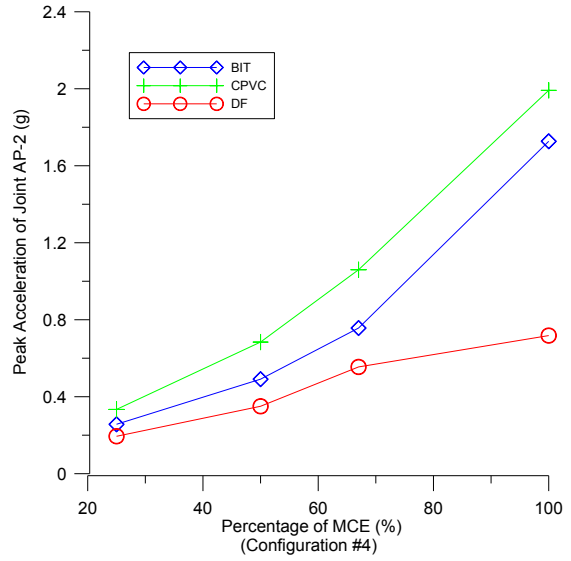
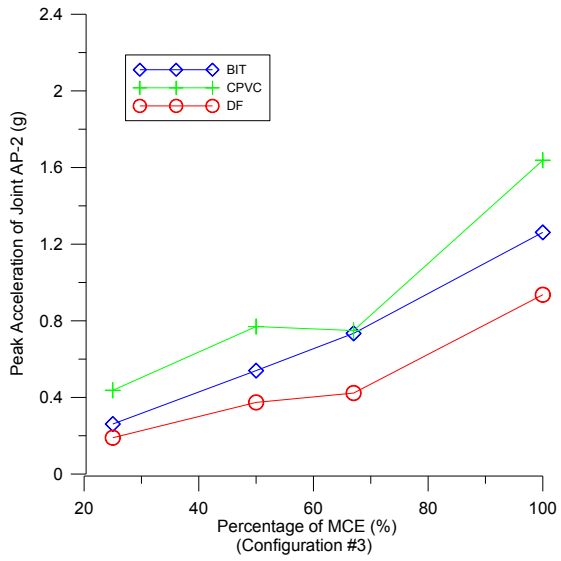
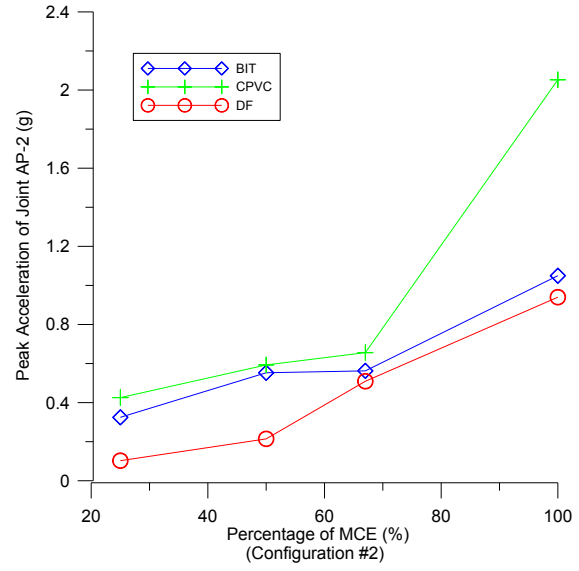
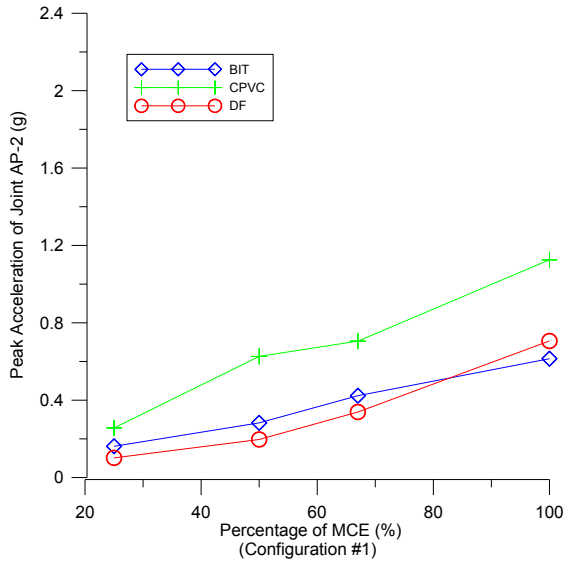


Figure 4-46 Comparison of peak acceleration response at AP-2 for three specimens across materials (BIT: Black Iron Threaded, CPVC: Thermoplastic, DF: Dyna-Flow Schedule 7)

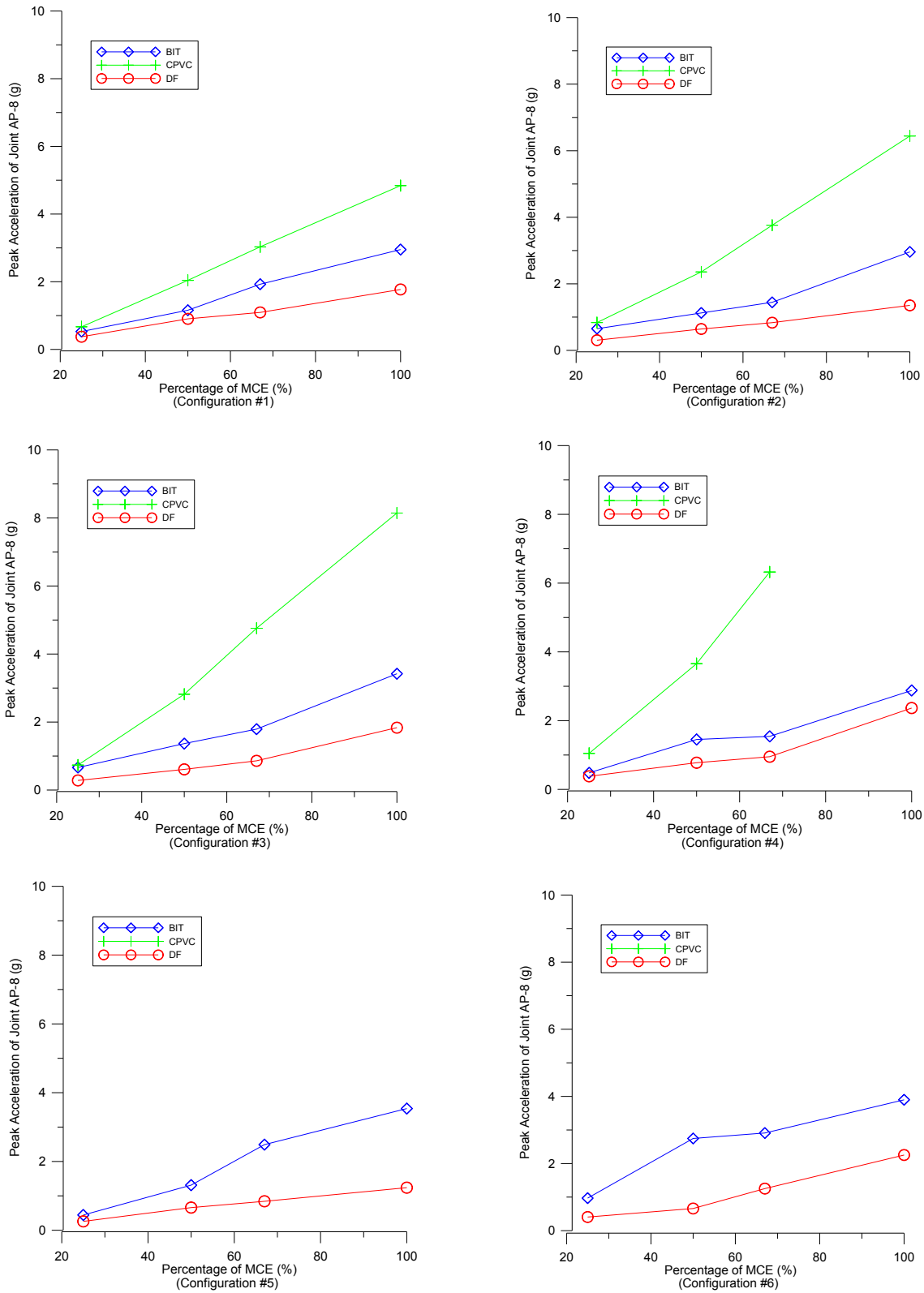
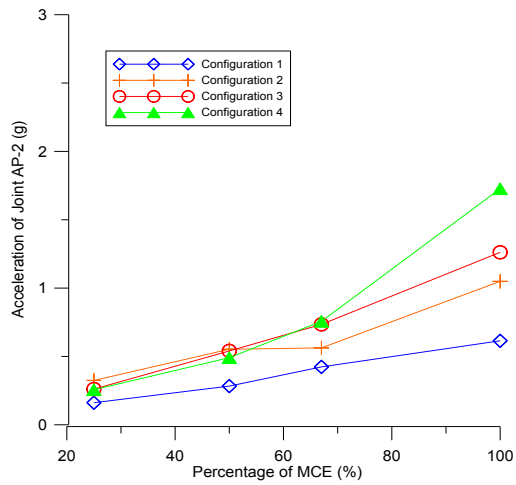
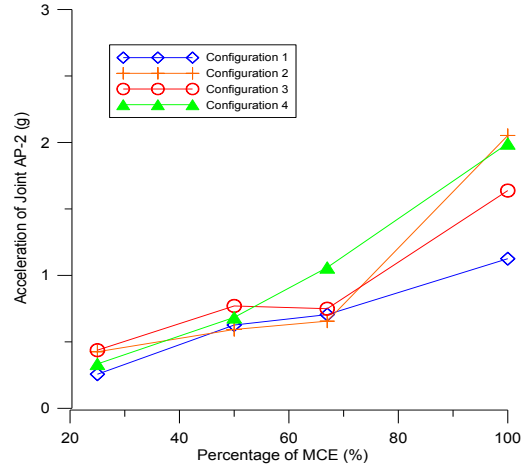


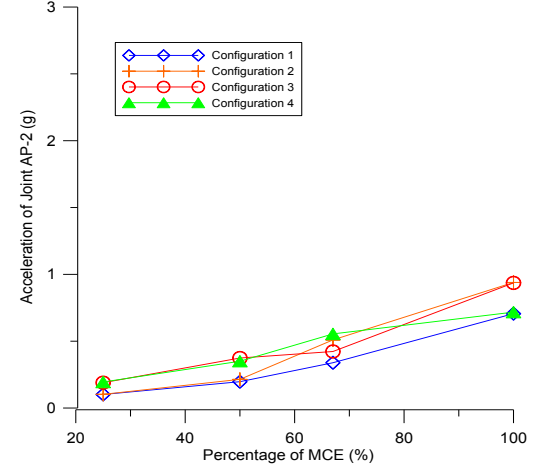
Figure 4-47 Comparison of peak acceleration response at AP-8 for three specimens across materials (BIT: Black Iron Threaded, CPVC: Thermoplastic, DF: Dyna-Flow Schedule 7)



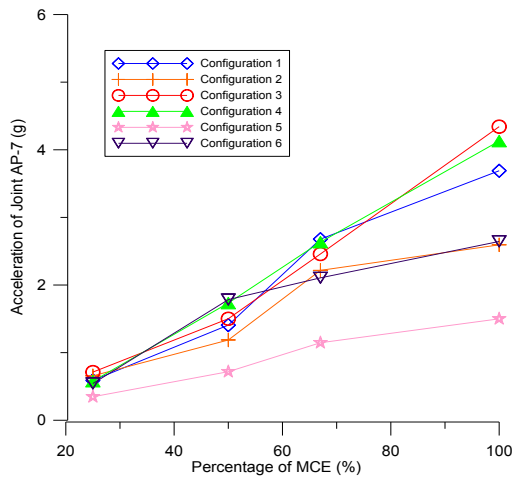
(a) Black iron with threaded joints at AP-2



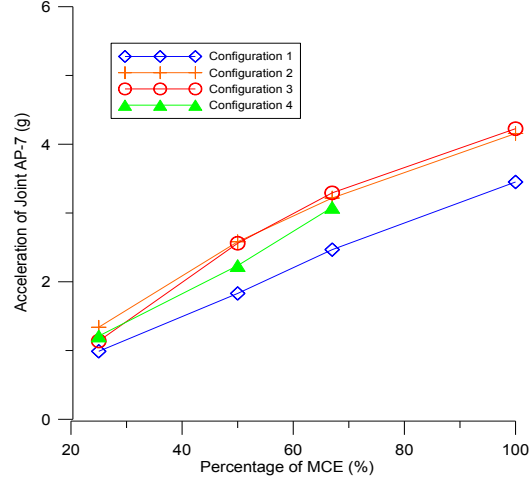
(b) CPVC with cement joint at AP-2



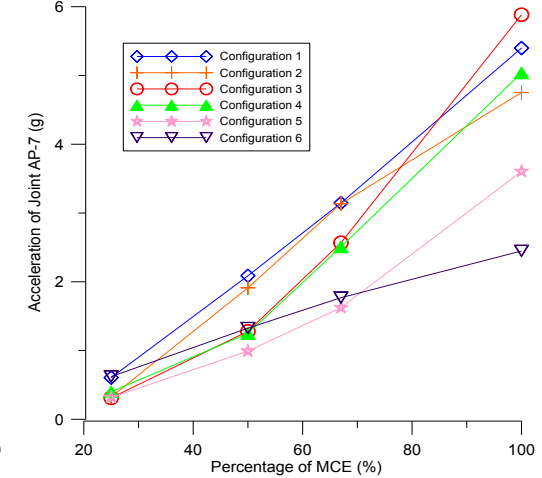
(c) DF with groove-fit connections at AP-2



(a) Black iron with threaded joints at AP-7



(b) CPVC with cement joint at AP-7



(c) DF with groove-fit connections at AP-7

Figure 4-48 Comparison of peak acceleration for three specimens across configurations

## Rotation

*Figure 4-49* shows the locations of the rotation measurement at the first level. The rotation was calculated for each joint based on Equation (3.2). A summary of the peak rotation capacities for all six tee joints at the first level is listed in *Table 4-12*. Again, no data are shown for the CPVC pipes with cement joints for Configuration #5 and Configuration #6 due to the early termination of the testing program.

*Figure 4-50* compares the peak rotations recorded at R29-30 location for each of the three test specimens. In each of the three figures, there are two vertical axes. The axis on the left shows the absolute magnitude of peak rotations measured during the testing, and the right axis illustrates the ratio of peak rotations over the median rotation capacities for the corresponding piping materials that were calculated for the piping with a nominal diameter of 2 inch, as described in Chapter 3. As experiments on the Dyna-Flow high-strength light wall sprinkler pipes were not conducted for the quasi-static tee joint component tests, the right axis for the test specimen made of Dyna-Flow pipes is not included.

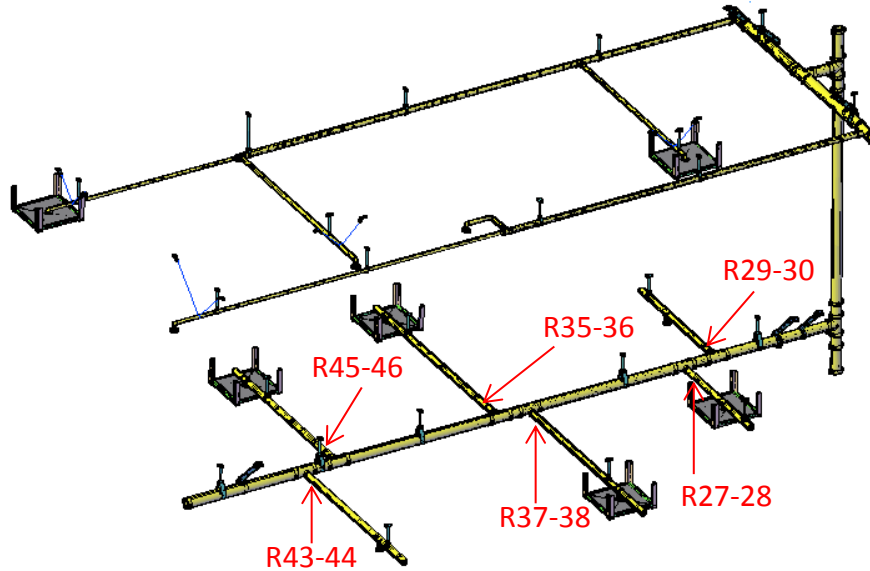


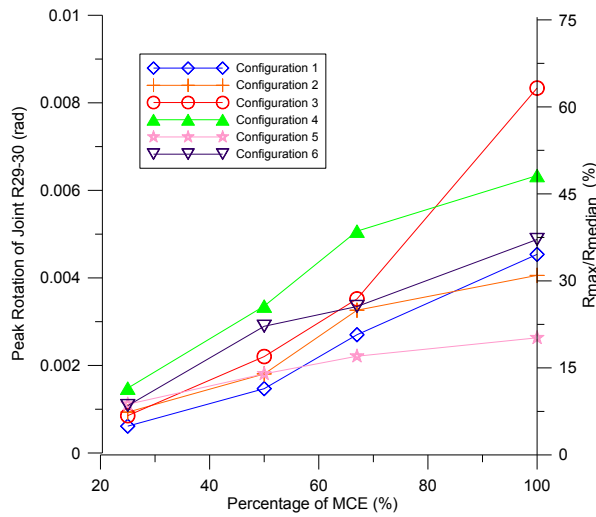
Figure 4-49 Locations of measurement for rotation

The specimens made of CPVC pipes and Dyna-Flow pipes experienced much larger joint rotational responses compared to the specimens made of black iron pipes. Specifically, for some particular locations such as R29-30, it can be observed that for all four configurations, the Dyna-Flow pipes with groove-fit connections exhibited the largest joint rotation. Similarly, the test specimens made of black iron pipes with threaded connections had the smallest joint rotation responses at the tips of branch lines, as shown in *Figure 4-51*.

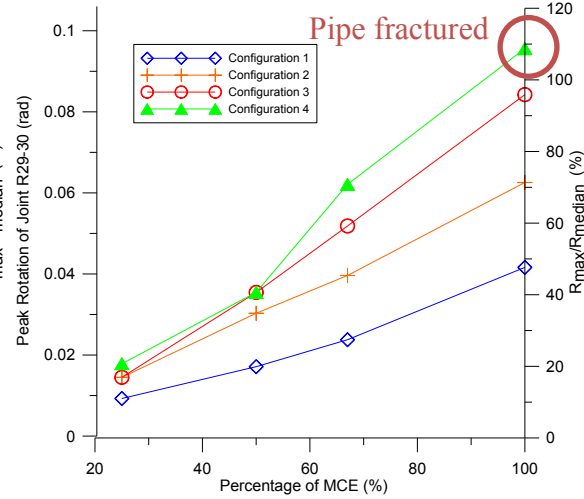
Table 4-12 Summary of peak rotations (BIT: Black Iron Threaded, CPVC: Thermoplastic, DF: Dyna-Flow Schedule 7)

Configuration	Bracing System	Percentage of Loading Protocol	BIT R27-28	CPVC R27-28	DF R27-28	BIT R29-30	CPVC R29-30	DF R29-30	BIT R35-36	CPVC R35-36	DF R35-36	BIT R37-38	CPVC R37-38	DF R37-38	BIT R43-44	CPVC R43-44	DF R43-44	BIT R45-46	CPVC R45-46	DF R45-46
			(rad)	(rad)	(rad)	(rad)	(rad)	(rad)	(rad)	(rad)	(rad)	(rad)	(rad)	(rad)	(rad)	(rad)	(rad)	(rad)	(rad)	(rad)
Configuration #1	Fully braced specimen (bracing systems installed according to NFPA 13)	25%	0.000437	0.000682	0.002108	0.000614	0.009268	0.036696	0.000467	0.001059	0.001277	0.000698	0.006378	0.053191	0.000593	0.008506	0.030775	0.000449	0.000942	0.003797
		50%	0.000681	0.001251	0.004150	0.001470	0.017117	0.066764	0.000817	0.001737	0.001960	0.000939	0.012031	error	0.001014	0.016049	0.060749	0.000774	0.002083	0.004598
		67%	0.000922	0.001938	0.005566	0.002701	0.023788	0.083211	0.001489	0.002182	error	0.001600	0.014430	error	0.001109	0.020562	0.069938	0.001171	0.005526	0.008595
		100%	0.001704	0.004684	0.010329	0.004539	0.041621	0.094163	0.002610	0.003361	0.007836	0.003344	0.018982	error	0.002635	0.029898	0.075304	0.001947	0.016754	0.056436
Configuration #2	Lateral and longitudinal braces removed from cross main line at the second level	25%	0.000474	0.000936	0.003258	0.000934	0.014493	0.019085	0.000625	0.001843	0.003941	0.000649	0.007804	0.032975	0.000507	0.004839	0.019241	0.000527	0.003860	0.037390
		50%	0.000788	0.001716	0.009902	0.001807	0.030298	0.075234	0.001065	0.002750	0.007804	0.001001	0.013103	0.065601	0.000790	0.008836	0.054813	0.001010	0.005002	0.056986
		67%	0.001098	0.003533	0.012340	0.003262	0.039628	0.105193	0.001540	0.003372	0.009440	0.001619	0.015334	0.084411	0.001078	0.010598	0.064538	0.001170	0.011063	0.060587
		100%	0.001946	0.006056	0.019992	0.004058	0.062577	0.113451	0.003486	0.005748	0.020608	0.002806	0.020630	0.097957	0.002118	0.013476	0.075072	0.001901	0.019432	0.063461
Configuration #3	Lateral and longitudinal braces removed from main line at the first level	25%	0.000522	0.002339	0.003567	0.000853	0.014496	0.014458	0.000524	0.002556	0.007165	0.000590	0.006955	0.022603	0.000400	0.004162	0.009424	0.000504	0.002827	0.024059
		50%	0.000957	0.004775	0.014093	0.002204	0.035437	0.061557	0.001084	0.005000	0.011783	0.001146	0.012610	0.050968	0.001017	0.007976	0.020383	0.000892	0.008437	0.044305
		67%	0.002002	0.008839	0.023168	0.003521	0.051839	0.084506	0.001421	0.006140	0.013553	0.001756	0.015922	0.065488	0.001221	0.009303	0.036027	0.001199	0.014197	0.051208
		100%	0.002749	0.016991	0.027192	0.008337	0.084240	0.107115	0.002886	0.009746	0.009424	0.004228	0.030973	0.074503	0.001627	0.012637	0.055942	0.002288	0.022106	0.062955
Configuration #4	Wire restraints removed (fully unbraced two-story specimen)	25%	0.000474	0.003195	0.003035	0.001482	0.017852	0.004086	0.000427	0.002525	0.008512	0.000494	0.006477	0.020689	0.000307	0.004462	0.002553	0.000496	0.003145	0.002374
		50%	0.001118	0.006327	0.010248	0.003357	0.035455	0.047301	0.001080	0.002893	0.013398	0.001118	0.013242	0.059261	0.000991	0.008351	0.012050	0.000859	0.008540	0.027058
		67%	0.001514	0.012008	0.017941	0.005068	0.062101	0.071891	0.001391	0.004126	0.013927	0.001672	0.019187	0.070964	0.001107	0.010396	0.021453	0.001078	0.014574	0.042018
		100%	0.002094	0.016219	0.028107	0.006339	0.095598	0.090627	0.002184	0.004673	0.024571	0.004362	0.019951	0.075761	0.002535	0.014856	0.042572	0.003173	0.017278	0.057794
Configuration #5	Vertical riser disconnected, lateral and longitudinal braces reinstalled for main line at the first level	25%	0.000391	N/A	0.000178	0.001113	N/A	0.022430	0.000793	N/A	0.009170	0.000724	N/A	0.031598	0.000684	N/A	0.008582	0.000756	N/A	0.004129
		50%	0.000606	N/A	0.001220	0.001808	N/A	0.058415	0.001563	N/A	0.014988	0.001119	N/A	0.052262	0.001209	N/A	0.016846	0.001150	N/A	0.012938
		67%	0.001137	N/A	0.002891	0.002211	N/A	0.068207	0.002035	N/A	0.021110	0.001389	N/A	0.063040	0.001586	N/A	0.028764	0.001372	N/A	0.020771
		100%	0.002470	N/A	error	0.002631	N/A	0.081726	0.002695	N/A	0.029128	0.002745	N/A	0.074953	0.003133	N/A	0.039800	0.002686	N/A	0.029020
Configuration #6	Lateral and longitudinal braces removed for main line at the first level (fully unbraced single-story specimen)	25%	0.001543	N/A	0.031734	0.001082	N/A	0.038829	0.000784	N/A	0.023350	0.000324	N/A	0.034699	0.000306	N/A	0.000531	0.000350	N/A	0.005844
		50%	0.002777	N/A	0.046095	0.002895	N/A	0.057425	0.002840	N/A	0.039168	0.000681	N/A	0.061090	0.000516	N/A	0.012379	0.000801	N/A	0.021086
		67%	0.004777	N/A	0.049192	0.003347	N/A	0.062872	0.003800	N/A	0.049992	0.001527	N/A	0.070310	0.000679	N/A	0.015505	0.000935	N/A	0.031193
		100%	0.007421	N/A	0.077448	0.004878	N/A	0.068034	0.007057	N/A	0.063010	0.002239	N/A	0.071059	0.001163	N/A	0.025654	0.002442	N/A	0.035175

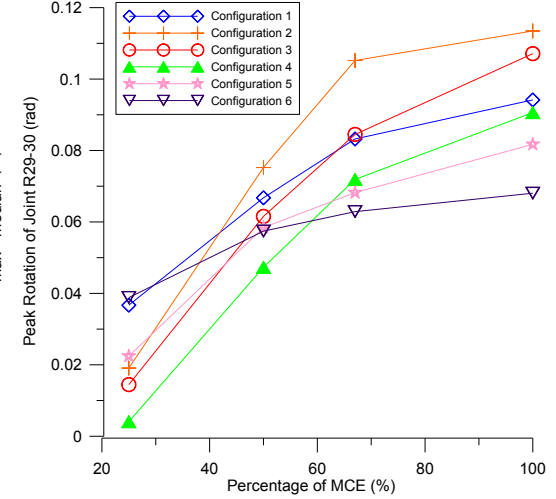




(a) Black iron with threaded joints at R29-30



(b) CPVC with cement joint at R29-30



(c) DF with groove-fit connections at R29-30

Figure 4-50 Comparison of peak rotations for three specimens at R29-30 across configurations (BIT: Black Iron Threaded, CPVC: Thermoplastic, DF: Dyna-Flow Schedule 7)

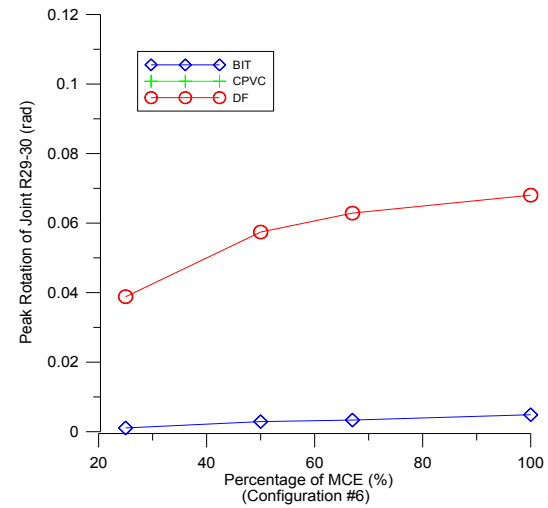
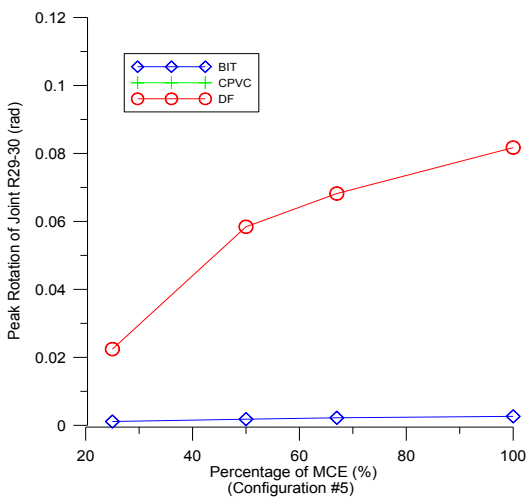
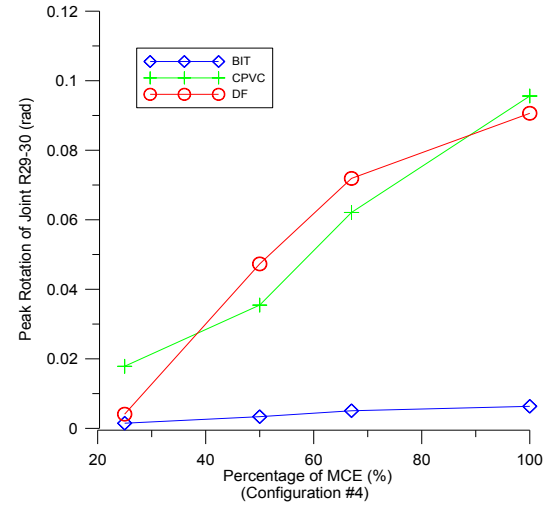
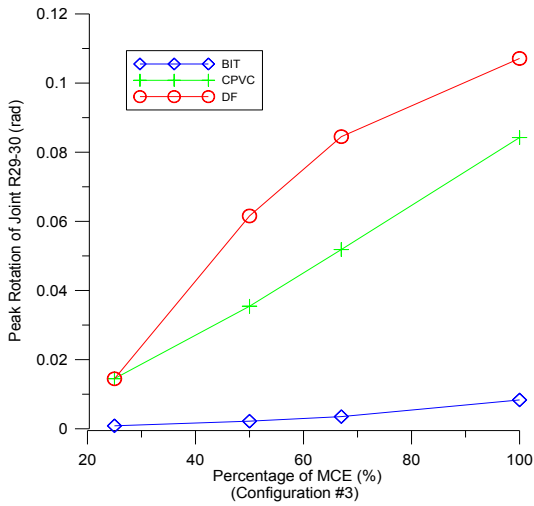
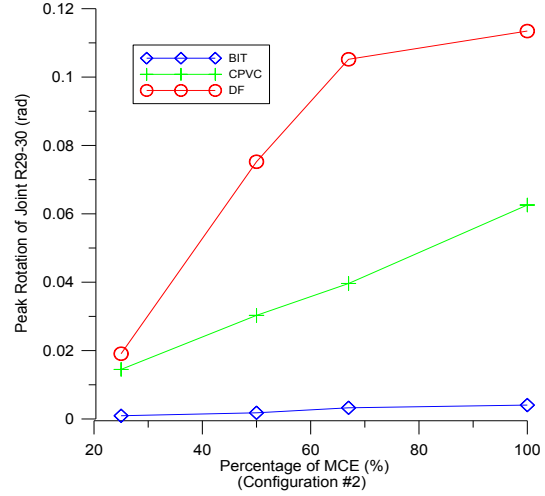
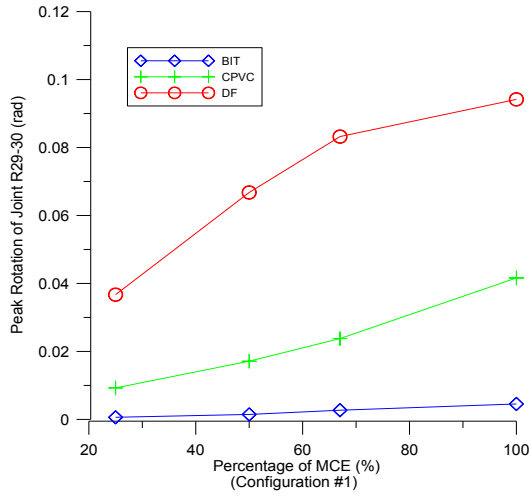
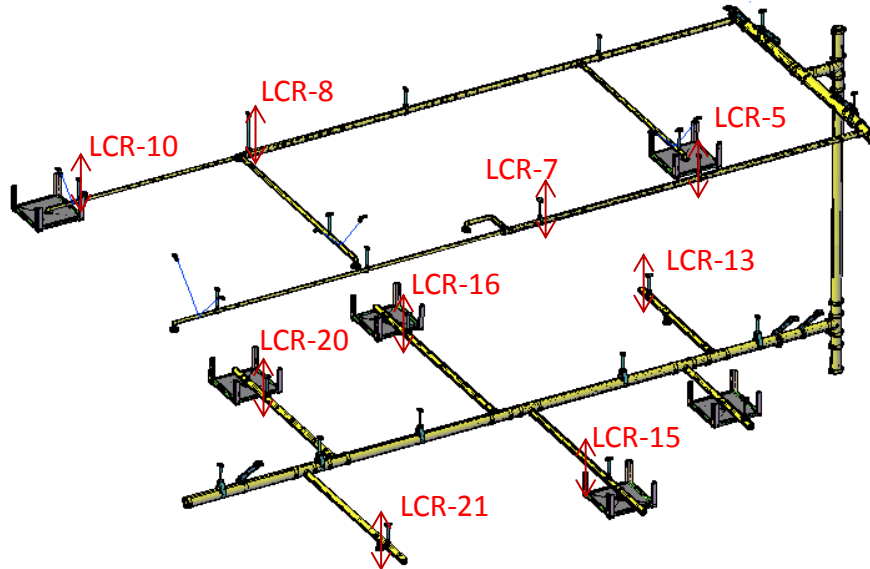


Figure 4-51 Comparison of peak rotation response at R29-30 for three specimens across materials (BIT: Black Iron Threaded, CPVC: Thermoplastic, DF: Dyna-Flow Schedule 7)

## Force

The peak forces measured in a number of vertical hanger rods are presented in *Table 4-13*. *Figure 4-52* shows the location of the miniature load cells installed on the selected vertical hanger rods.



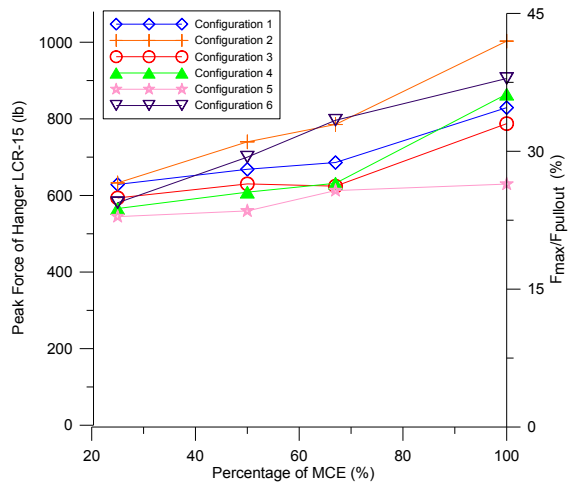
*Figure 4-52* Locations of miniature load cells on vertical hanger rods

Similar to *Figure 4-50*, each plot in *Figure 4-53* also has double vertical axes. The axis on the left shows the absolute magnitude of peak axial forces in the vertical hanger rods, while the right axis shows the ratio of the peak axial force to the rated pullout strength of the SAMMY screws. It is observed that all the failure of vertical hangers occurred even if the peak axial forces measured from the miniature loads cells were still within the pullout strength limit of the SAMMY screws, indicating that shear-off effect played a critical role in the failure of vertical hangers.

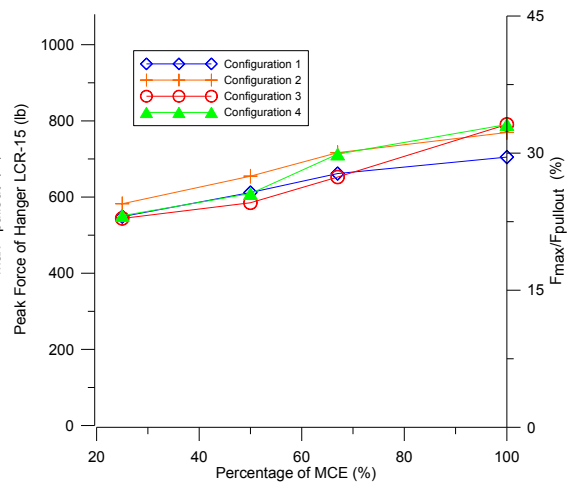
*Figure 4-53* compares the peak axial forces observed at the LCR-15 location for the various piping system configurations, and *Figure 4-54* shows the results at the LCR-5 location for the three test specimens. The results do not show consistent trend neither in terms of pipe materials or setup configurations. For some particular locations such as LCR-5 and LCR-16, however, it can be observed that the black iron pipes with threaded connections experienced the largest axial forces in the vertical hanger rods, and the test specimens made of CPVC pipes with cement joints had the smallest axial forces partially as a result of the light weight of the materials.

Table 4-13 Summary of peak axial forces (BIT: Black Iron Threaded, CPVC: Thermoplastic, DF: Dyna-Flow Schedule 7)

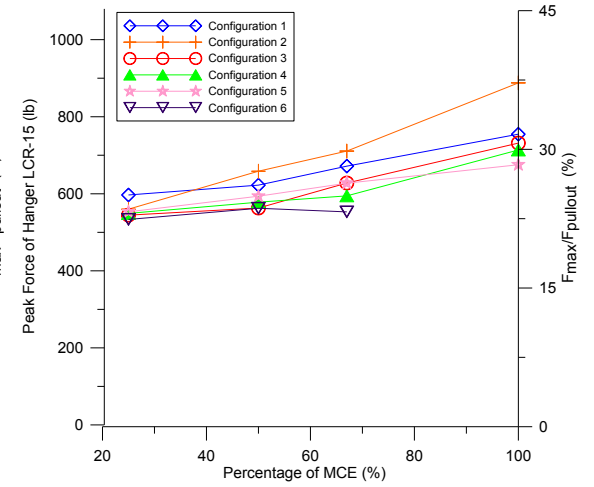
Configuration	Bracing System	Percentage of Loading Protocol	BIT LCR-5	CPVC LCR-5	DF LCR-5	BIT LCR-7	CPVC LCR-7	DF LCR-7	BIT LCR-8	CPVC LCR-8	DF LCR-8	BIT LCR-10	CPVC LCR-10	DF LCR-10	BIT LCR-13	CPVC LCR-13	DF LCR-13	BIT LCR-15	CPVC LCR-15	DF LCR-15	BIT LCR-16	CPVC LCR-16	DF LCR-16	BIT LCR-20	CPVC LCR-20	DF LCR-20	BIT LCR-21	CPVC LCR-21	DF LCR-21
			(lbs)	(lbs)	(lbs)	(lbs)	(lbs)	(lbs)	(lbs)	(lbs)	(lbs)	(lbs)	(lbs)	(lbs)	(lbs)	(lbs)	(lbs)	(lbs)	(lbs)	(lbs)	(lbs)	(lbs)	(lbs)	(lbs)	(lbs)	(lbs)	(lbs)	(lbs)	(lbs)
Configuration #1	Fully braced specimen (bracing systems installed according to NFPA 13)	25%	55.60	19.60	38.52	45.13	18.45	33.36	42.46	18.25	39.57	21.58	6.25	17.75	61.31	21.38	30.73	628.66	548.67	596.84	68.40	17.70	33.13	52.58	15.92	28.98	39.84	53.08	29.38
		50%	76.36	23.09	54.14	52.86	21.30	79.78	44.64	21.78	55.46	28.94	7.66	23.15	87.57	42.59	47.52	668.28	611.79	622.52	93.71	26.75	95.32	64.93	27.76	40.66	44.77	93.43	75.06
		67%	102.24	27.97	61.53	56.78	25.66	73.03	45.92	22.66	81.16	29.08	7.79	24.61	142.37	67.32	78.26	685.90	661.68	671.82	99.69	34.16	59.29	79.43	58.23	46.47	error	102.30	91.73
		100%	127.60	36.33	91.09	78.57	28.24	91.97	53.77	26.45	92.96	28.28	10.99	57.87	176.61	153.40	174.04	829.20	704.88	754.67	142.90	47.65	81.58	97.16	113.05	114.63	79.65	103.24	137.31
Configuration #2	Lateral and longitudinal braces removed from cross main line at the second level	25%	52.31	21.43	37.06	48.24	19.81	33.65	45.11	18.60	32.43	13.52	6.89	18.49	50.90	27.04	28.89	632.77	582.39	559.96	68.53	18.90	30.89	43.45	40.43	37.32	39.19	22.02	24.51
		50%	61.21	24.74	48.09	81.46	28.03	68.41	61.70	22.33	50.51	20.06	10.68	22.83	104.39	77.06	49.22	739.98	654.88	658.56	124.41	32.87	41.34	57.97	59.35	85.63	50.41	47.84	82.75
		67%	89.52	30.30	58.02	108.40	29.73	83.49	66.21	24.60	61.52	28.41	18.43	29.08	139.45	152.26	70.21	785.30	716.59	710.85	149.41	40.04	65.82	81.60	86.91	150.89	51.99	61.19	100.90
		100%	104.68	38.21	90.84	141.37	37.19	90.29	76.46	31.62	75.62	45.08	26.69	55.42	208.45	244.52	186.46	1003.01	769.54	887.75	196.15	53.96	95.32	116.66	152.03	error	90.62	92.17	120.76
Configuration #3	Lateral and longitudinal braces removed from main line at the first level	25%	54.23	21.54	38.19	48.12	21.21	34.86	51.50	18.72	34.46	23.01	6.92	19.16	46.35	27.40	30.01	593.55	543.85	544.54	66.20	21.65	34.03	47.20	27.31	35.38	38.24	24.67	23.16
		50%	63.83	25.83	51.13	65.80	25.28	69.37	72.95	22.55	44.74	26.29	11.82	22.15	130.99	78.42	38.66	630.25	585.01	562.98	107.77	36.43	48.68	68.12	82.47	59.25	58.61	48.07	28.65
		67%	83.21	31.45	56.52	126.95	29.52	71.67	77.98	25.51	53.39	30.56	18.08	23.37	198.98	167.85	60.88	624.23	652.57	627.88	136.37	48.28	62.11	89.94	84.97	82.03	67.32	61.18	48.39
		100%	118.90	35.23	93.17	147.24	34.46	88.39	93.23	30.61	85.21	55.11	31.06	62.71	254.76	261.80	183.62	787.54	790.65	731.60	161.14	59.97	92.26	154.24	113.57	error	122.71	95.98	97.27
Configuration #4	Wire restrains removed (fully unbraced two-story specimen)	25%	49.71	20.79	36.10	45.88	19.37	32.85	45.28	19.22	42.86	18.07	6.50	25.00	44.62	24.96	29.82	565.87	550.91	549.04	65.98	21.31	32.19	44.17	40.62	34.23	39.96	60.93	23.56
		50%	64.70	25.39	47.16	71.69	24.81	59.54	64.90	22.35	52.15	26.46	10.28	27.70	113.93	62.49	35.69	608.64	609.03	578.10	97.67	34.73	42.72	77.98	76.95	48.73	58.51	139.03	28.35
		67%	95.53	29.78	56.89	111.50	28.56	68.78	66.51	27.17	62.32	28.79	16.38	34.37	194.51	164.30	64.19	631.87	712.78	594.57	118.18	43.21	55.24	91.34	76.91	65.43	72.30	165.24	35.79
		100%	114.19	35.18	94.04	161.76	33.87	76.07	80.10	33.03	73.39	43.18	N/A	41.88	229.75	235.28	195.39	864.60	790.51	713.63	148.54	74.35	84.81	229.98	91.23	error	132.15	N/A	85.37
Configuration #5	Vertical riser disconnected, lateral and longitudinal braces reinstalled for main line at the first level	25%	N/A	N/A	N/A	N/A	N/A	N/A	N/A	N/A	N/A	N/A	N/A	N/A	46.03	N/A	28.73	544.75	N/A	553.13	61.27	N/A	34.17	45.53	N/A	31.67	36.94	N/A	24.59
		50%	N/A	N/A	N/A	N/A	N/A	N/A	N/A	N/A	N/A	N/A	N/A	N/A	53.38	N/A	44.60	559.65	N/A	593.72	81.66	N/A	49.91	68.70	N/A	61.67	51.06	N/A	27.18
		67%	N/A	N/A	N/A	N/A	N/A	N/A	N/A	N/A	N/A	N/A	N/A	N/A	66.87	N/A	48.99	612.68	N/A	627.35	103.47	N/A	58.23	95.21	N/A	57.12	68.39	N/A	36.43
		100%	N/A	N/A	N/A	N/A	N/A	N/A	N/A	N/A	N/A	N/A	N/A	N/A	113.05	N/A	154.63	629.56	N/A	675.44	147.08	N/A	79.18	160.30	N/A	65.95	100.29	N/A	80.83
Configuration #6	Lateral and longitudinal braces removed for main line at the first level (fully unbraced single-story specimen)	25%	N/A	N/A	N/A	N/A	N/A	N/A	N/A	N/A	N/A	N/A	N/A	N/A	55.50	N/A	24.19	580.84	N/A	533.40	72.97	N/A	31.35	62.03	N/A	27.63	41.94	N/A	20.90
		50%	N/A	N/A	N/A	N/A	N/A	N/A	N/A	N/A	N/A	N/A	N/A	N/A	130.58	N/A	36.06	700.06	N/A	562.28	107.13	N/A	36.22	91.50	N/A	34.02	71.24	N/A	27.51
		67%	N/A	N/A	N/A	N/A	N/A	N/A	N/A	N/A	N/A	N/A	N/A	N/A	173.88	N/A	54.94	796.34	N/A	552.88	142.25	N/A	61.38	139.24	N/A	31.45	136.63	N/A	37.92
		100%	N/A	N/A	N/A	N/A	N/A	N/A	N/A	N/A	N/A	N/A	N/A	N/A	291.62	N/A	61.44	905.33	N/A	error	221.28	N/A	63.72	312.48	N/A	40.91	345.98	N/A	48.87



(a) Black iron with threaded joints at LCR-15



(b) CPVC with cement joint at LCR-15



(c) DF with groove-fit connections at LCR-15

Figure 4-53 Comparison of peak axial forces for three specimens at LCR-15 across configurations (BIT: Black Iron Threaded, CPVC: Thermoplastic, DF: Dyna-Flow Schedule 7)

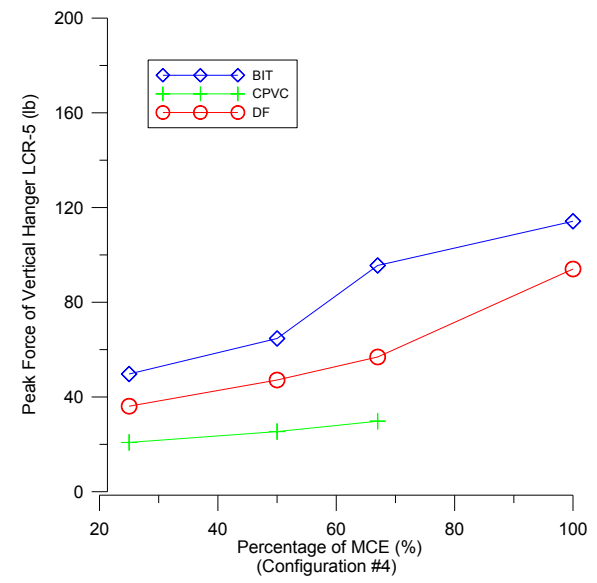
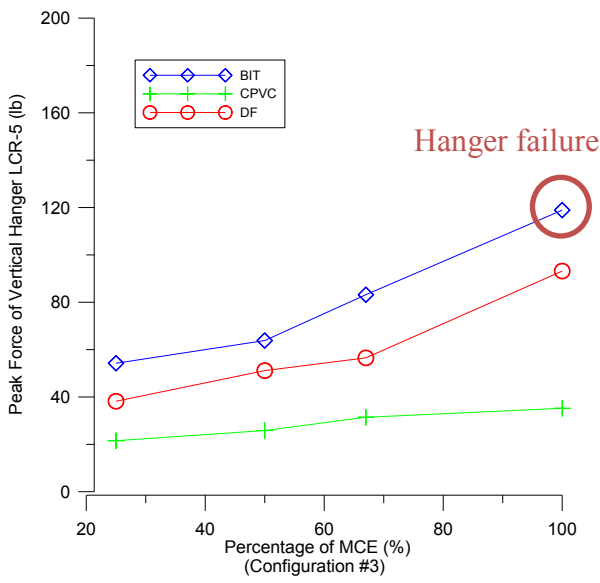
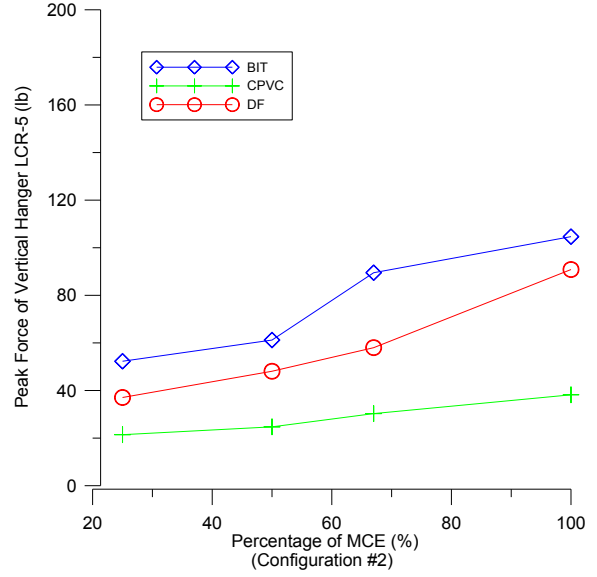
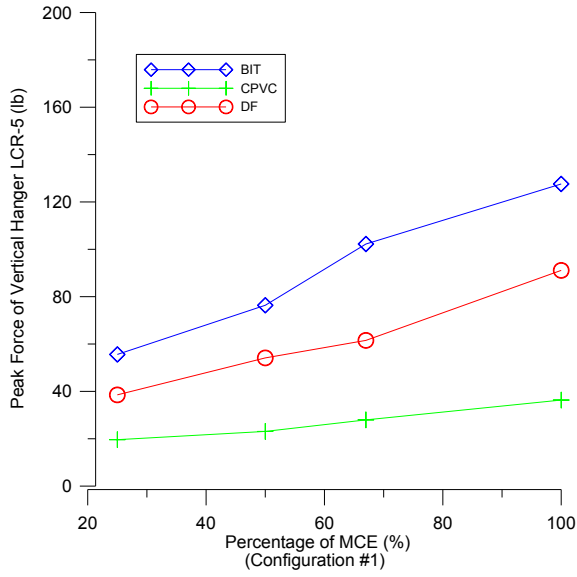


Figure 4-54 Comparison of peak axial forces for three specimens at LCR-5 across materials

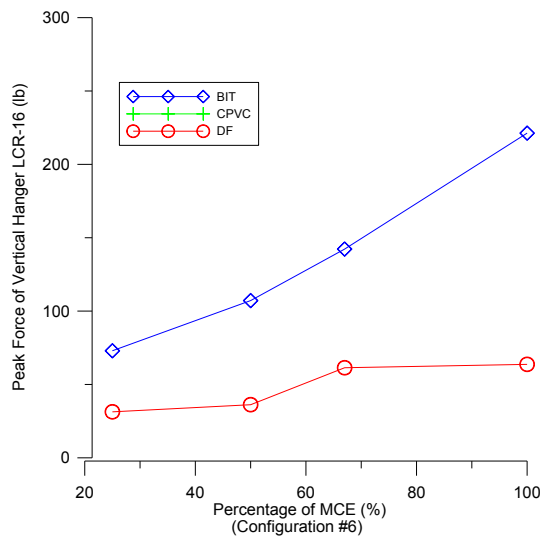
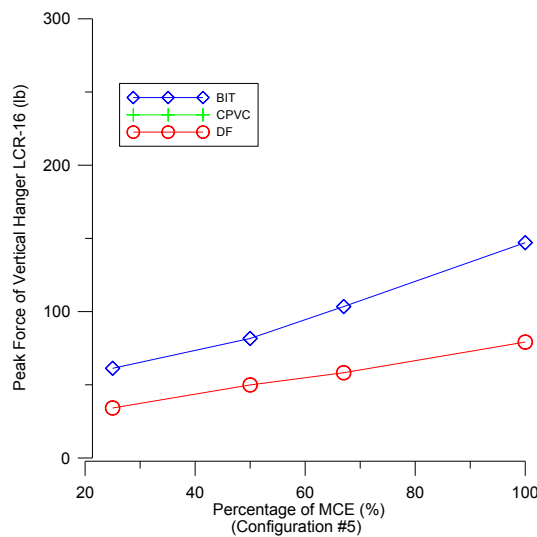
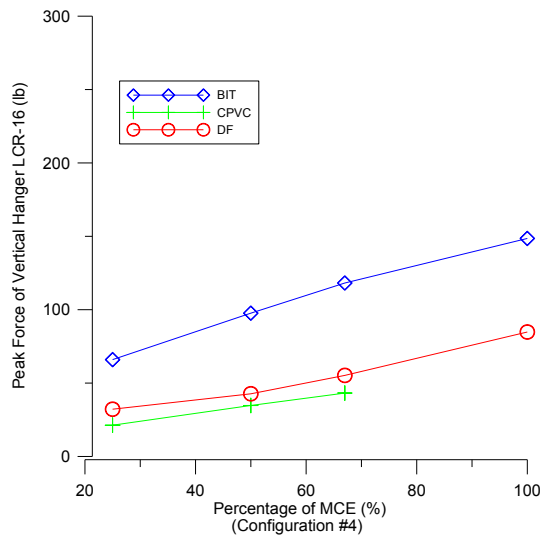
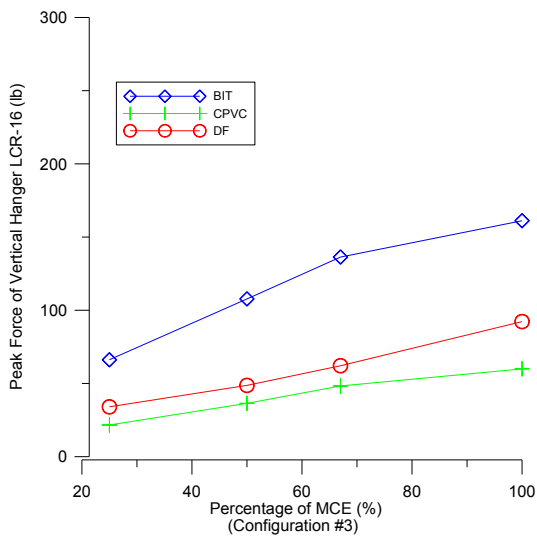
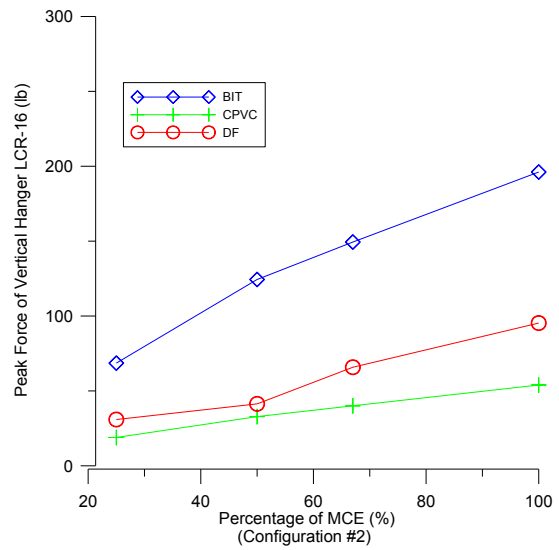
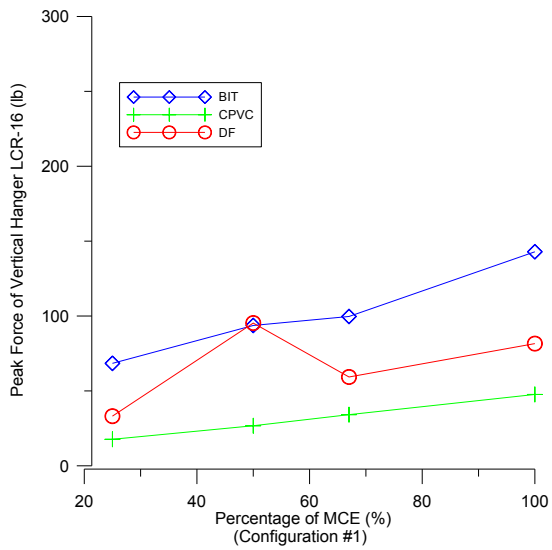


Figure 4-55 Comparison of peak axial forces for three specimens at LCR-16 across materials



#### 4.10 Summary

The main objective of this chapter was to evaluate the seismic performance of the full-scale fire suppression sprinkler piping systems under earthquake loading. A total of three specimens were tested with various bracing configurations. For each bracing configuration, the specimens were subjected to dynamic loading with increasing input intensities. Three different materials and joint types were considered for the branch lines: 1) black iron with threaded joints, 2) thermoplastic (CPVC) with cement joints and 3) Schedule 7 steel (Dyna-Flow high-strength light wall sprinkler pipes) with groove-fit connections.

The observations from this second phase of the experimental program are summarized as follows:

- All three fully braced specimens performed well and suffered no damage under the Maximum Considered Earthquake (MCE) level of loading, thereby validating the current code-based requirements for bracing system design. However, the unbraced systems, which are typically installed in low to moderate seismic regions or are present in older buildings, experienced extensive damage among the vertical hangers, ceiling tiles, sprinkler heads, and pipe joints.
- For a number of cases, although the fire suppression sprinkler piping system survived the dynamic shaking without any significant damage to the supporting system (vertical hangers, wire restraints and bracing), unexpected activation of sprinkler heads was triggered due to the pounding with ceiling tiles, which led to the loss of water pressure and failure of the entire system. This indicates that the differential displacement of suspended ceiling system and the

fire suppression sprinkler piping system remains a critical threat to the normal functionality of sprinkler piping system.

- Traditionally, a specific nominal annual space is cut to provide extra clearance for the riser that penetrates concrete and masonry floors. Moreover, according to the NFPA 13 (NFPA, 2010), flexible couplings are required on the riser above and below the floor in multistory buildings. Substantial margin is provided for the riser to accommodate the inter-story drifts. This was validated in the tests as no damage to the riser was observed during the entire testing program even though the maximum inter-story drift reached 3% of story height.
- Based on the observations obtained from Chapter 3, CPVC pipes with cement joints and steel pipes with groove-fit connections have significantly larger rotational capacities compared to the black iron pipes with threaded joints. However, it does not necessarily ensure that fire protection systems constructed with CPVC pipes with cement joints or steel pipes with groove-fit connections would be the best choice as far as seismic performance is concerned. The test results showed that specimens made of CPVC pipes and Dyna-Flow pipes also have much larger rotational responses at the pipe joints for similar levels of input intensities.

## Chapter 5

# PARAMETERIZATION AND NUMERICAL MODELING OF FIRE SUPPRESSION SPRINKLER PIPING SYSTEMS

### 5.1 Introduction

In this chapter, a number of rotational spring models were developed based on the experimental data obtained from the quasi-static tests described in *Chapter 3* to simulate the nonlinear moment-rotation hysteretic behavior of piping tee joints made of various materials and joint arrangements. The calibrated nonlinear rotational spring models were then used for the numerical modeling of full-scale fire sprinkler piping systems in the general-purpose analysis software SAP2000 (CSI, 2012) and OpenSees (McKenna *et al.*, 1999), respectively.

Due to the limited available material model options in SAP2000, the Multi-linear Pivot material model was considered to simulate piping tee joints across piping materials and joint configurations, while both Pinching4 and Hysteretic Material models were used to model different joint configurations in OpenSees. For validation, numerical simulations based on the second series of experiments conducted on the UB-NCS were performed and nonlinear time-history dynamic analyses were carried out to predict the dynamic test results. Close agreements were observed in terms of displacement, acceleration, and moment–rotation at piping joints between the predictions of numerical modeling and the experimental results.

## 5.2 Development of Analytical Models for Piping Tee Joints

### 5.2.1 Evaluation of experimental hysteretic behavior of piping tee joints

Based on the hysteresis loops from the tee joint component tests of black iron pipes with threaded joints presented in *Chapter 3*, the initial stiffness remained fairly constant within small amplitude of displacement-controlled loading. The initial stiffness could be interpreted as the bending stiffness that is determined by the elastic properties of materials and the cross sections of piping thread roots. When the piping tee joint was subjected to a larger displacement input, the initial stiffness started to decrease as the bending moment imposed to the thread roots reached the yielding limit of the cross section. Once the actuator retreated and triggers the unloading of the specimen, the hysteresis loop unloaded in a rate that was close to the initial stiffness, and before reloading, the hysteresis loop returned to the origin after the moment strength reached zero, as shown in *Figure 5-1*. This phenomenon, as well as the gradual strength and stiffness degradations, could be explained by the fact that the Teflon tapes were compressed and engaged threads deformed due to the yielding during the previous loading cycles. As a result, gaps were generated between threads, and delayed the re-engagement and contact of threads between the pipes and the tee joint.

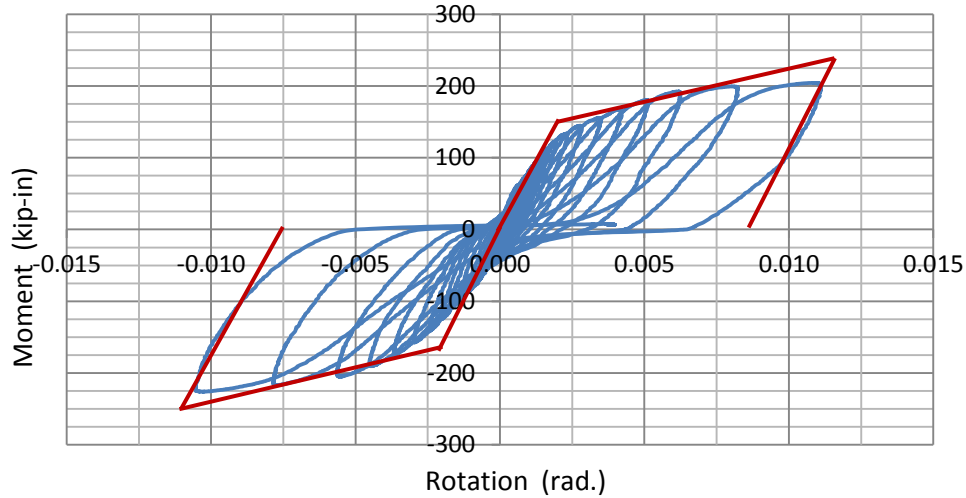


Figure 5-1 Moment-rotation cyclic response of 4-inch black iron pipes with threaded joints

Similar to the piping tee joints made of black iron pipes with threaded connections, the hysteresis loop of piping tee joints made of CPVC pipes with cement joints was characterized by multi-linear backbone curves and the initial stiffness remains constant within small amplitude of loading (Figure 5-2). However, it could be observed that CPVC plastic was relatively brittle and the plasticity the material had exhibited was far less than the black iron pipes with threaded joints.

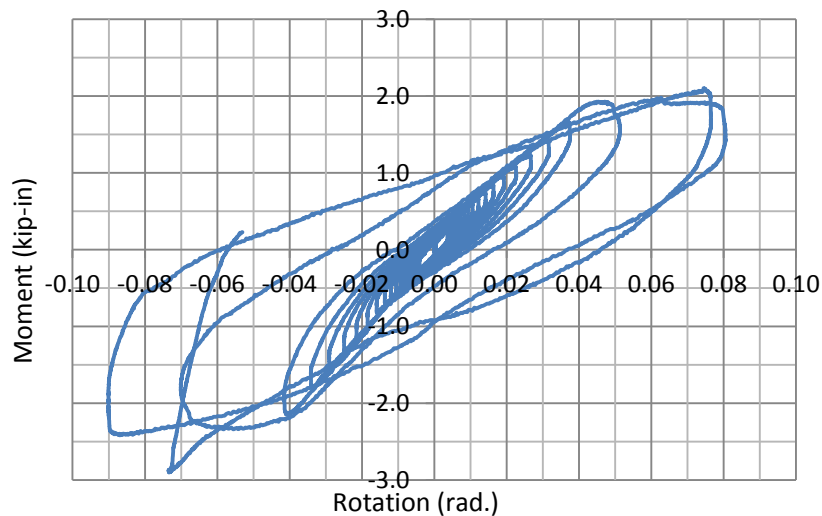
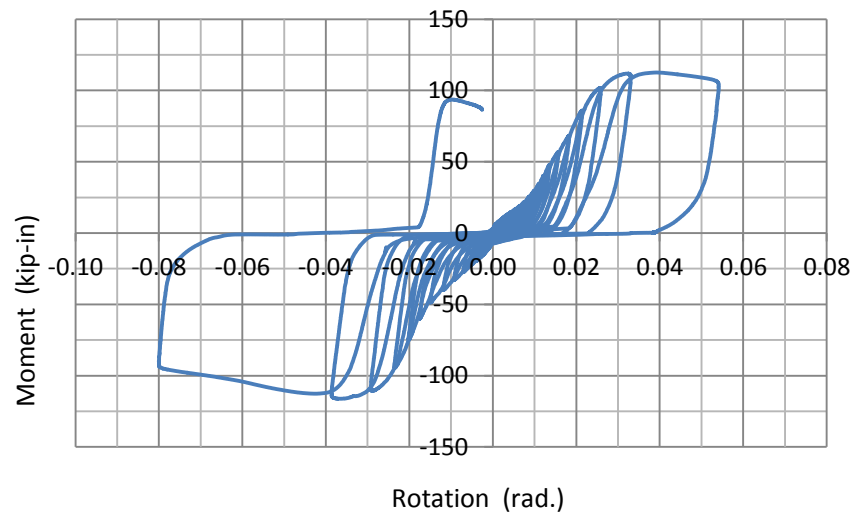


Figure 5-2 Moment-rotation cyclic response of 2-inch CPVC pipes with cement joints

For the steel pipes with groove-fit connections, the hysteretic response was characterized by triangularly pinched effects, as shown in *Figure 5-3*. When large displacement-controlled loading was applied to the piping tee joint, the stresses in the rubber gasket imposed by the flange coupling would increase, and meanwhile pipe ends tended to slip away from the rubber gasket due to the bending. As a result, it leads to the typical triangularly pinched hysteresis loops.



*Figure 5-3 Moment-rotation cyclic response of 4-inch Schedule-10 steel pipes with groove-fit connections*

### 5.2.2 Multi-linear Pivot model

The general-purpose analysis software SAP2000 (CSI, 2012) was first selected for the numerical modeling due to its extensive popularity for industrial and academic use in structural and earthquake engineering. Since there are limited options of material models available in SAP2000, the Multi-linear Pivot model is used based on *Section 5.2.1* to simulate the moment-rotation hysteretic behavior for all the piping joints that have been tested in the first phase of experiments (*Chapter 3*). The Multi-linear Pivot model is more suited for the simulation of various piping

joints than the Multi-linear Takeda model as it has more parameters to control the degrading properties and the shape of the hysteresis loop.

For the Multi-linear Pivot model, there are a total of five scalar parameters,  $\alpha_1$ ,  $\alpha_2$ ,  $\beta_1$ ,  $\beta_2$ , and  $\eta$  (Figure 5-4) available for the calibration of the hysteretic behavior. Descriptions for the parameters are listed in Table 5-1.

Table 5-1 Descriptions of parameters for Multi-linear Pivot model

Parameter	Description
$\alpha_1$	To locate the pivot point for unloading to zero from positive force
$\alpha_2$	To locate the pivot point for unloading to zero from negative force
$\beta_1$	To locate the pivot point for reverse loading from zero toward positive force
$\beta_2$	To locate the pivot point for reverse loading from zero toward negative force
$\eta$	To determine the amount of degradation of the elastic slopes after plastic deformation

The detailed description of the Multi-linear Pivot model can be found in Dowell et al. (1998).

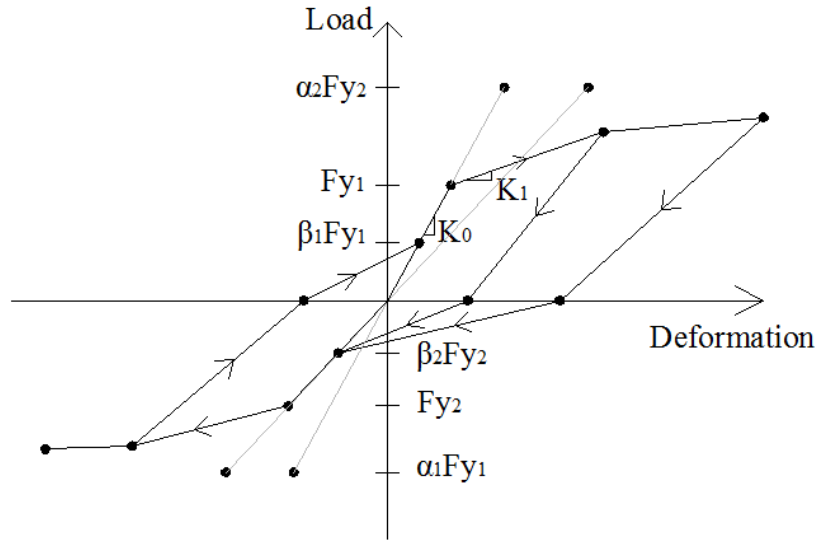


Figure 5-4 Multi-linear Pivot model (from CSI, 2012)

Furthermore, two assumptions were made to simplify the numerical modeling: (1) the load-deformation response for both positive and negative region was assumed to be symmetric; and (2) a bilinear relationship was assigned to the backbone curve of the Pivot model. As a result, the total number of parameters required to define the Pivot model was reduced to: yielding moment  $F_y$ , initial stiffness  $K_0$ , decreased stiffness  $K_1$ ,  $\alpha$ ,  $\beta$ , and  $\eta$ .

A bilinear Pivot model defined by the forementioned six parameters was developed in the numerical computing software MATLAB (MathWorks, Inc., 2012). With the input of rotation histories retained from the quasi-static tests, moment time histories were generated in MATLAB following the bilinear Pivot model behavior.



The calibration of the Pivot model was based on the moment-rotation relationship recorded for all pipe diameters during the piping tee joint component tests. Because of the malfunction of some of the potentiometers, moment-rotation relationship was not available for every specimen. However, there were at least three sets of data for each tee joint configuration. The optimized combination of the six parameters was derived according to the following two criteria:

1) The total cumulative dissipated energy difference ( $\Delta E$ )

The cumulative dissipated energy difference between the numerical and experimental results was calculated for each of the three data sets before the application of the Square Root of the Sum of the Square (SRSS). The total cumulative dissipated energy difference ( $\Delta E$ ) for one particular combination of parameters was then obtained, and iterations were carried out in MATLAB for different combinations of parameters. The optimized combination of parameters was achieved when the  $\Delta E$  was minimized;

2) The moment-rotation curves and the moment time history

If multiple options of parameter combination resulted in the same  $\Delta E$ , additional consideration was taken for the moment-rotation curves and the moment time history.

The detailed procedure for the optimization is presented in *Figure 5-5*. Based on this methodology, the optimized parameters for the Multi-linear Pivot model were obtained through iterations and are listed in Appendix C. Comparisons of analytical and experimental results for 4-inch steel pipes with grooved-fit connections, 2-inch black iron pipes with threaded joints, and 3/4-inch CPVC pipes with cement joints are shown in *Figure 5-6*, *Figure 5-7* and *Figure 5-8*, respectively.

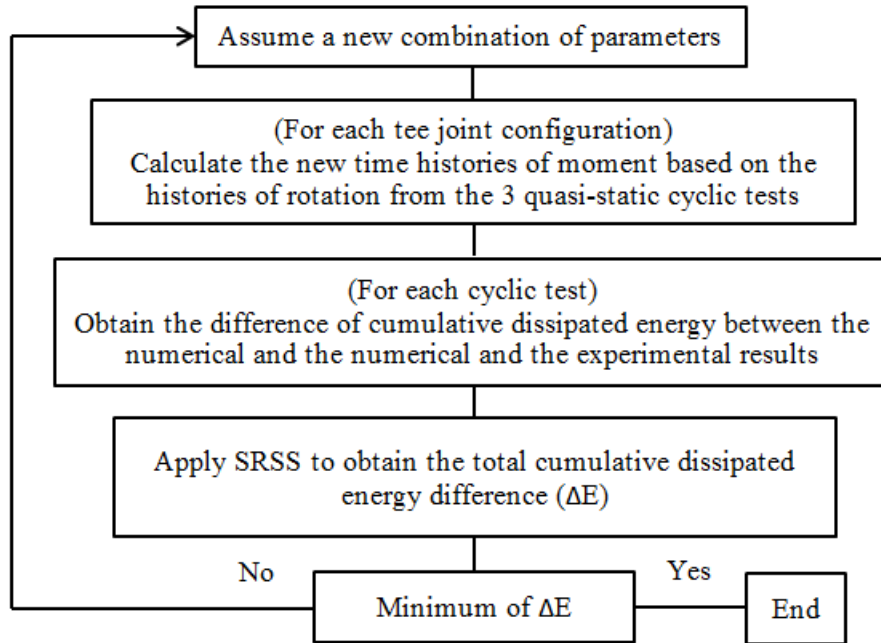
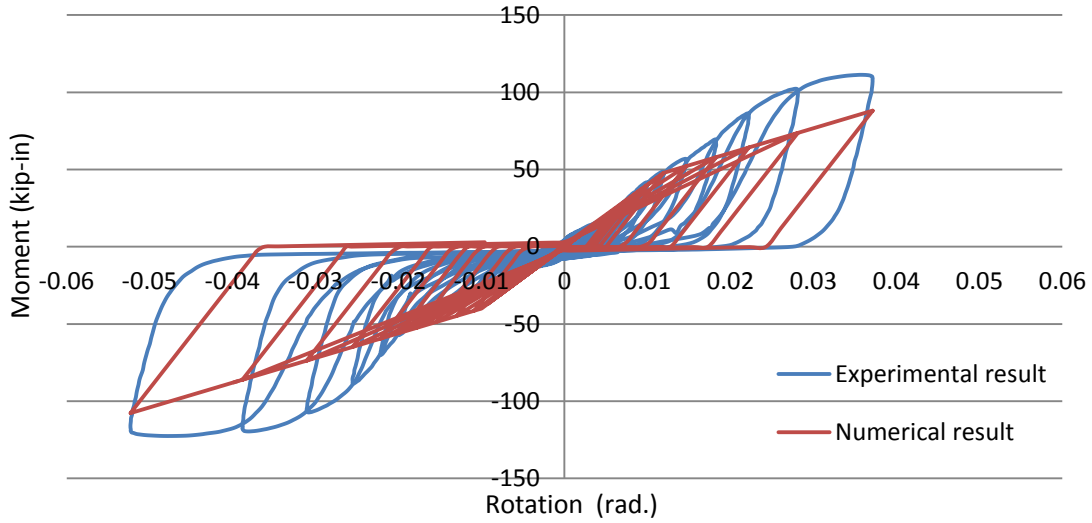
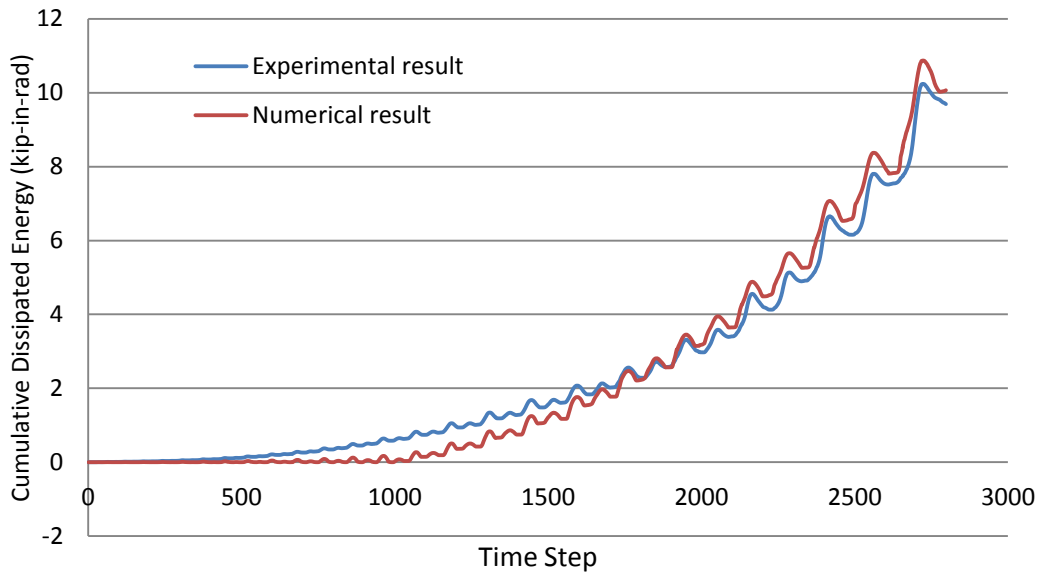


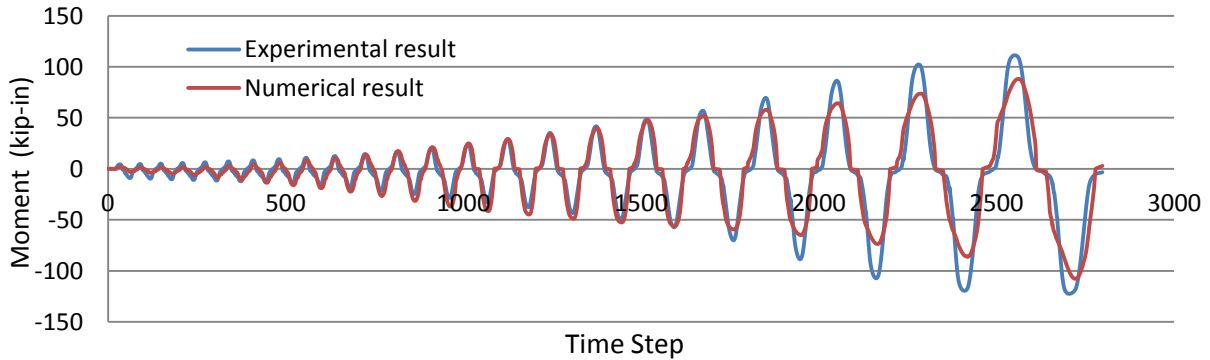
Figure 5-5 Procedure of optimization of parameter set for numerical models



(a) Moment-rotation cyclic responses

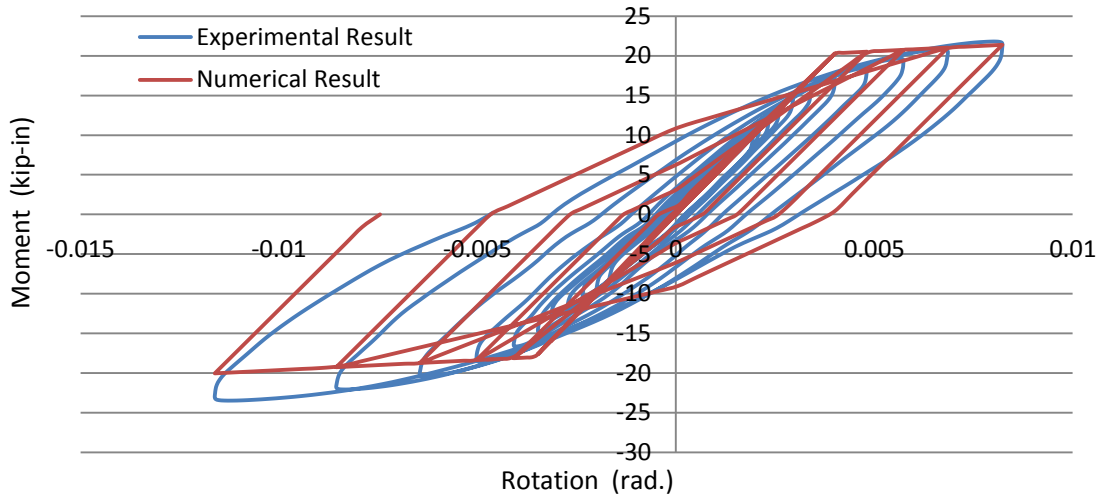


(b) Cumulative dissipated energies

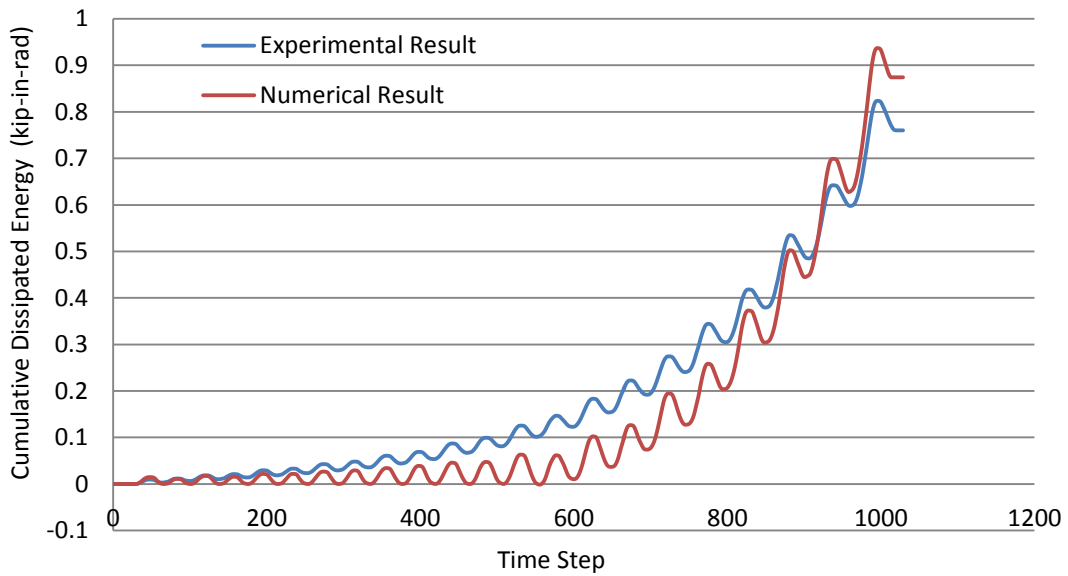


(c) Moment histories

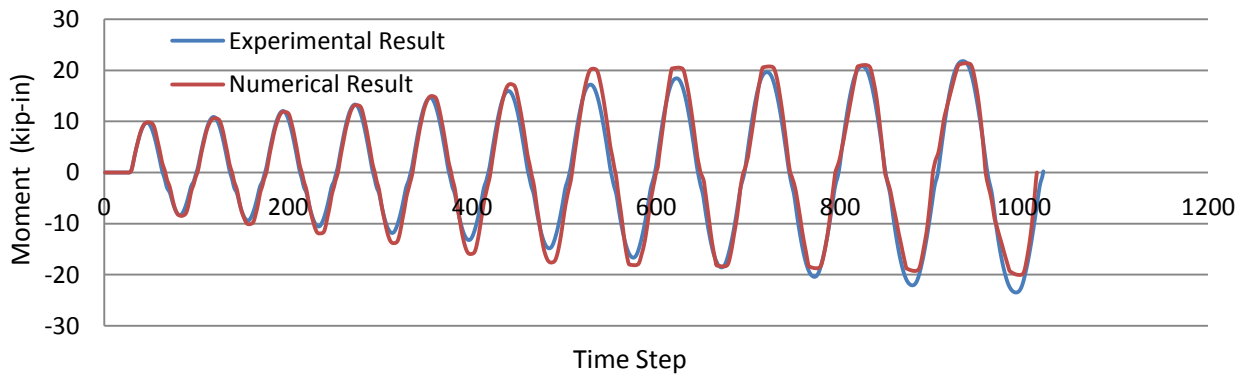
Figure 5-6 Comparisons of numerical and experimental results for 4-inch steel pipe with grooved-fit connections



(a) Moment-rotation cyclic responses

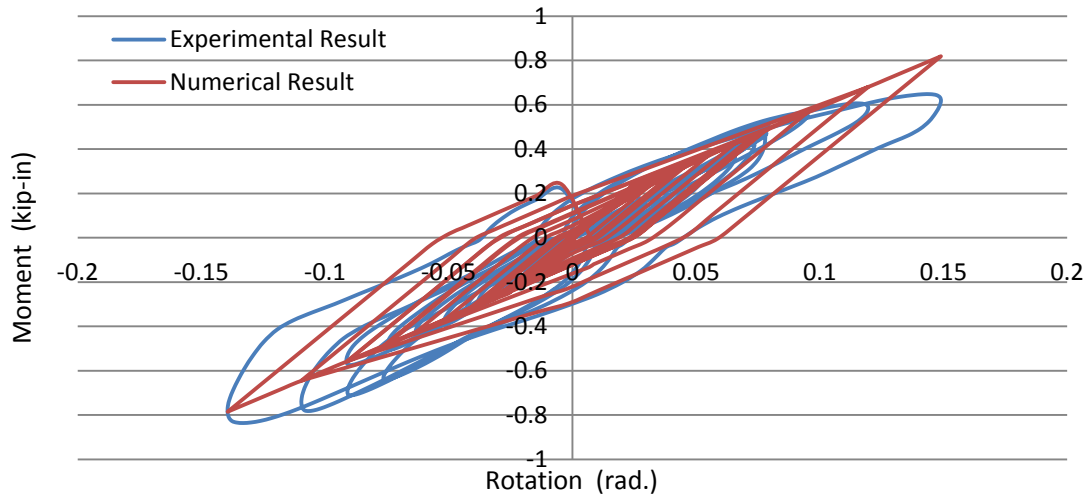


(b) Cumulative dissipated energies

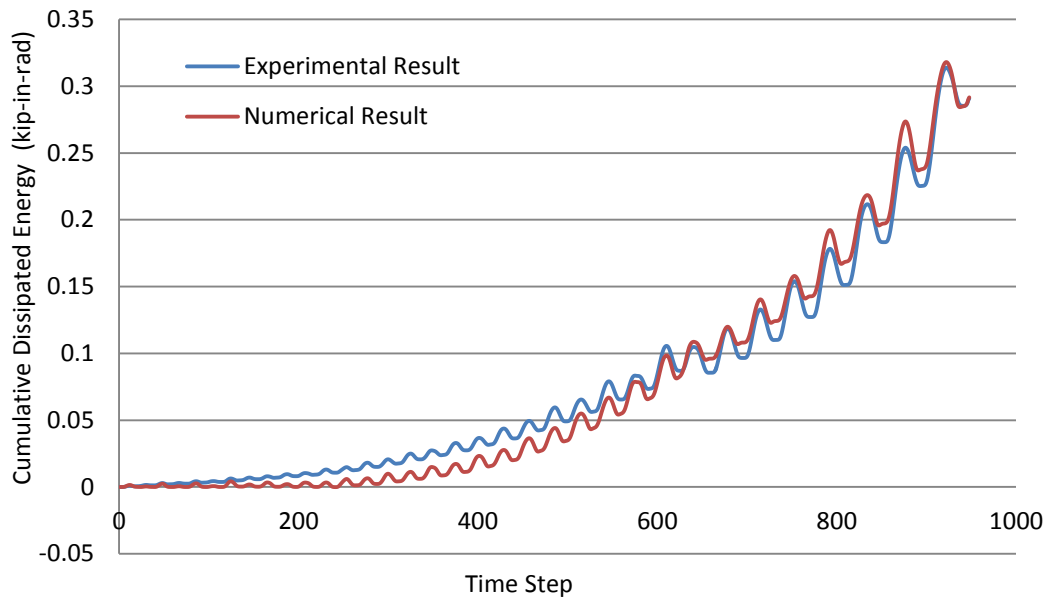


(c) Moment histories

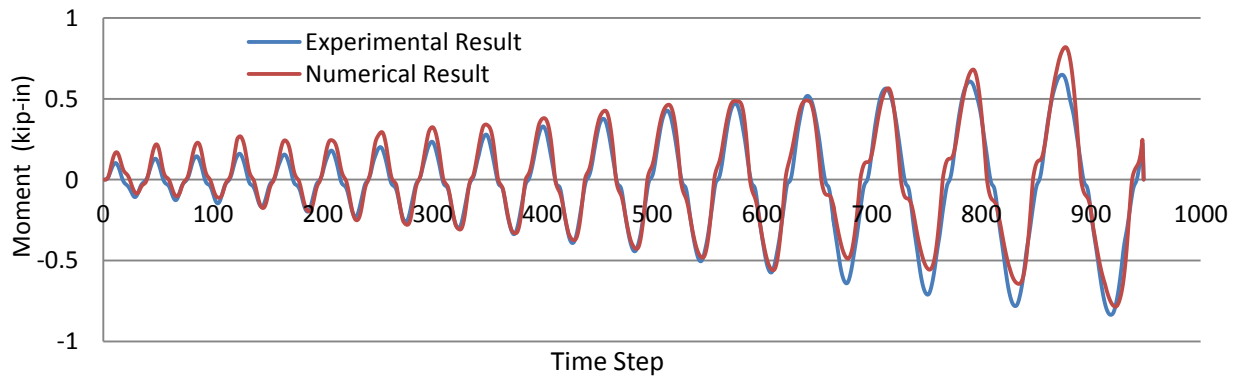
Figure 5-7 Comparisons of numerical and experimental results for 2-inch black iron pipe with threaded joints



(a) Moment-rotation cyclic responses



(b) Cumulative dissipated energies



(c) Moment histories

Figure 5-8 Comparisons of numerical and experimental results for 3/4-inch CPVC pipe with cement joints

The bilinear Pivot model provided by the SAP2000 was able to simulate reasonably well the hysteresis behavior of both of the black iron pipe with threaded joints and the CPVC pipe with cement joints. On the other hand, although the hysteresis loops generated for the steel pipe with grooved-fit connections by the bilinear Pivot model delivered close match in terms of cumulative dissipated energy and history of moment magnitude, the Pivot model lacked the capability of characterizing the triangular pinching effects due to the simplicity of the model. Therefore, these results are not presented here.

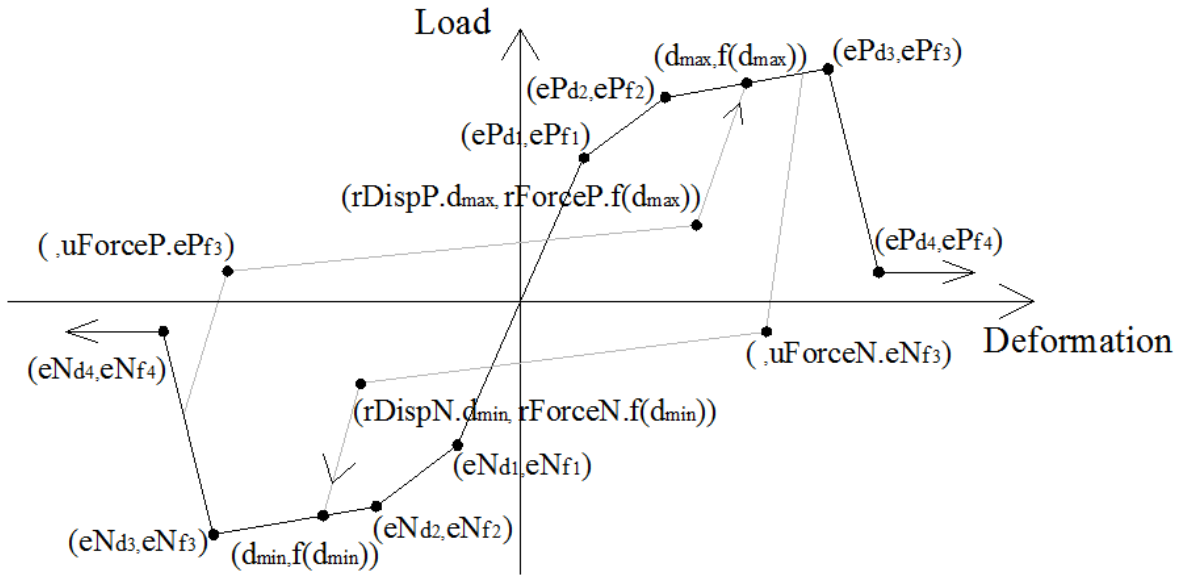
### 5.2.3 Pinching4 Material model

OpenSees (McKenna *et al.*, 1999) is an open-source software framework designed for simulation applications in earthquake engineering with the use of finite element methods. It is selected in this study for the numerical modeling of piping joints mainly due to two reasons:

- 1) OpenSees has a robust pool of over fifty material models available to simulate unique hysteretic behavior observed from piping tee joints of various materials and joint arrangements;
- 2) OpenSees has strong power and capability of conducting response-history nonlinear dynamic analysis which will greatly reduce the required computational time, and this becomes a significant advantage for Incremental Dynamic Analyses (IDA) described in the following chapter.

For the case of simulating piping tee joint constructed with steel pipes with groove-fit connections, the Pinching4 Material model developed by Nilinjan Mitra and *et al.* (2003) from

the University of Washington was adopted because of its capability of capturing the triangularly pinched effects. *Figure 5-9* shows the Pinching4 Material hysteretic model and portion of the parameter notation. This material model requires the definition of up to 39 parameters for the hysteretic behavior, while nineteen of the parameters are used to define the shape of the backbone curve, and the rest of the parameters describe pinching effect and stiffness degradation for both unloading and reloading. The detailed descriptions of the 39 parameters are listed in *Table 5-2*. The number of parameters can be reduced to 28 by assuming the load-deformation response is symmetric in both positive and negative direction.



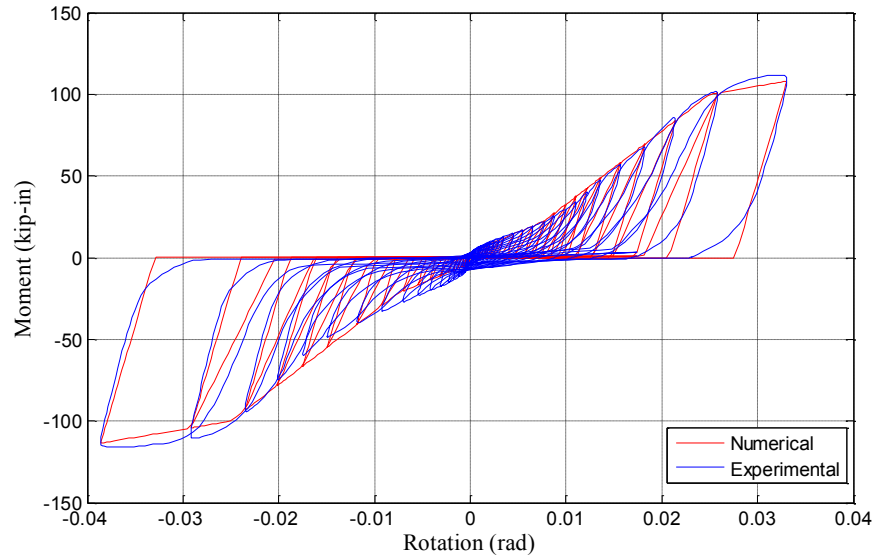
*Figure 5-9 Pinching4 Material model (from OpenSeesWiki, 2012)*

Table 5-2 Descriptions of parameters for Pinching4 Material model (from OpenSeesWiki, 2012)

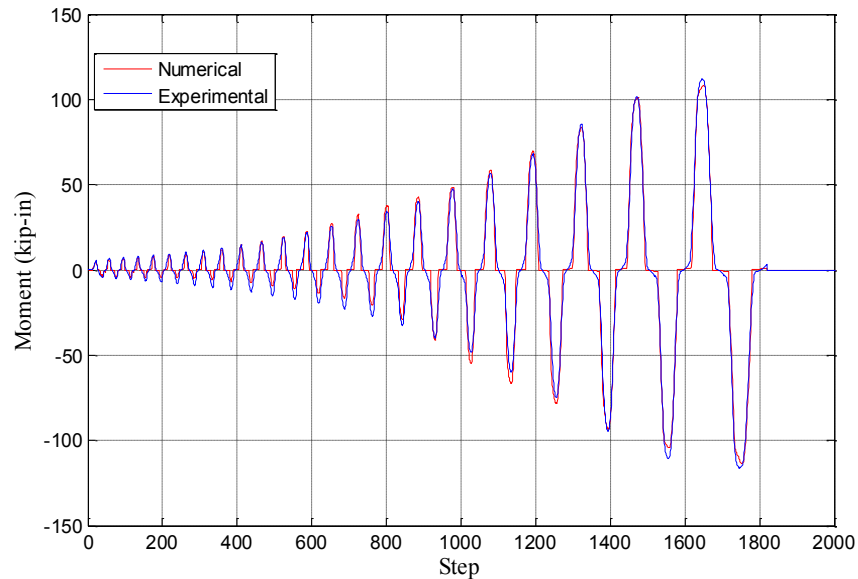
Parameter	Description
$eP_{f1}, eP_{f2}, eP_{f3}, eP_{f4}$	Floating point values defining force points on the positive response envelope
$eP_{d1}, eP_{d2}, eP_{d3}, eP_{d4}$	Floating point values defining deformation points on the positive response envelope
$eN_{f1}, eN_{f2}, eN_{f3}, eN_{f4}$	Floating point values defining force points on the negative response envelope
$eN_{d1}, eN_{d2}, eN_{d3}, eN_{d4}$	Floating point values defining deformation points on the negative response envelope
rDispP	Floating point value defining the ratio of the deformation at which reloading, occurs to the maximum historic deformation demand
rForceP	Floating point value defining the ratio of the force at which reloading begins to force corresponding to the maximum historic deformation demand
uForceP	Floating point value defining the ratio of strength developed upon unloading from negative load to the maximum strength developed under monotonic loading
rDispN	Floating point value defining the ratio of the deformation at which reloading, occurs to the minimum historic deformation demand
uForceN	Floating point value defining the ratio of strength developed upon unloading from negative load to the minimum strength developed under monotonic loading
$gK_1, gK_2, gK_3, gK_4, gK_{Lim}$	Floating point values controlling cyclic degradation model for unloading stiffness degradation
$gD_1, gD_2, gD_3, gD_4, gD_{Lim}$	Floating point values controlling cyclic degradation model for reloading stiffness degradation
$gF_1, gF_2, gF_3, gF_4, gF_{Lim}$	Floating point values controlling cyclic degradation model for strength degradation
gE	Floating point value used to define maximum energy dissipation under cyclic loading. Total energy dissipation capacity is defined as this factor multiplied by the energy dissipated under monotonic loading.
dmgType	String to indicate type of damage (option: "cycle", "energy")



The calibration of the Pinching4 Material model for various tee joint configurations followed the same procedures described in the previous section. Search of the optimized combination of parameters were performed through the iterations conducted in the MATLAB until the minimum of  $\Delta E$  was obtained, and the optimized parameters for the Pinching4 model are presented in *Appendix C*. In *Figure 5-10* the hysteresis loops and moment time histories for both experimental data and the numerical model are presented and compared.



(a) Comparison of hysteresis loops



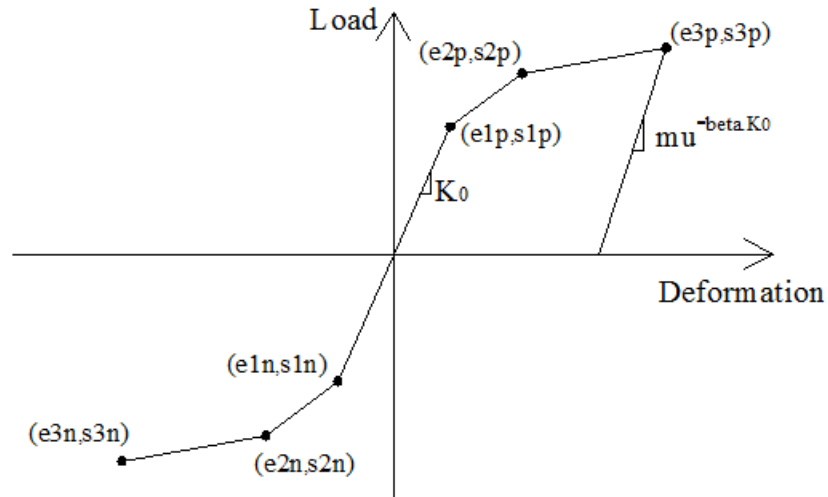
(b) Comparison of moment time histories

Figure 5-10 Comparisons of experimental data and numerical model

### 5.2.4 Hysteretic Material model

The Hysteretic Material model features a tri-linear backbone curves associated with extra parameters to control damage due to ductility and energy, as well as the degraded unloading stiffness based on the ductility (OpenSeesWiki, 2012). The number of the total parameters it

requires to define the model is seventeen, and this number can be reduced to eleven by assuming that the hysteretic behavior is symmetric in both positive and negative direction. *Figure 5-11* shows the Hysteretic Material model, and descriptions for the parameters are listed in *Table 5-3*.

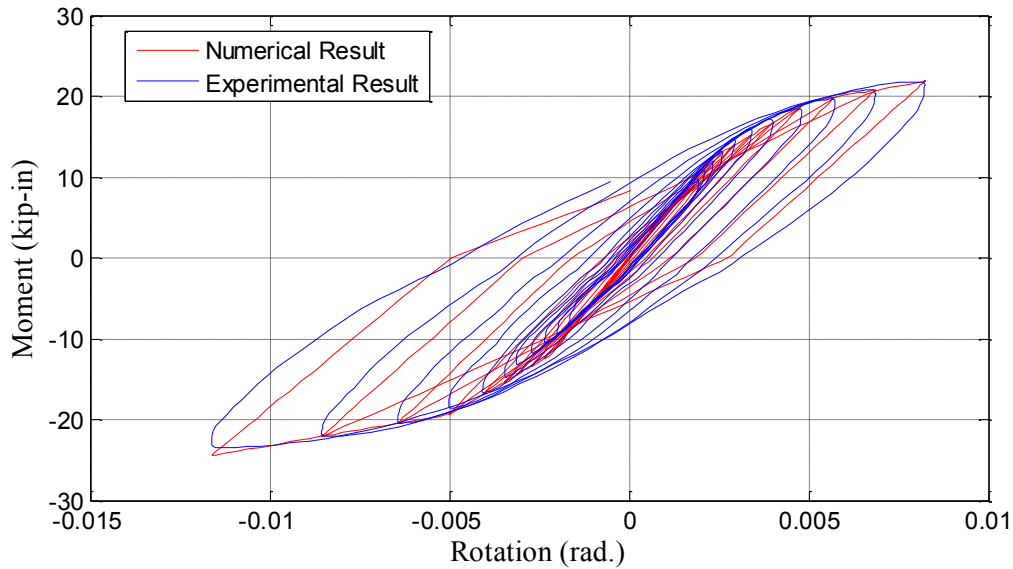


*Figure 5-11 Hysteretic Material model (from OpenSeesWiki, 2012)*

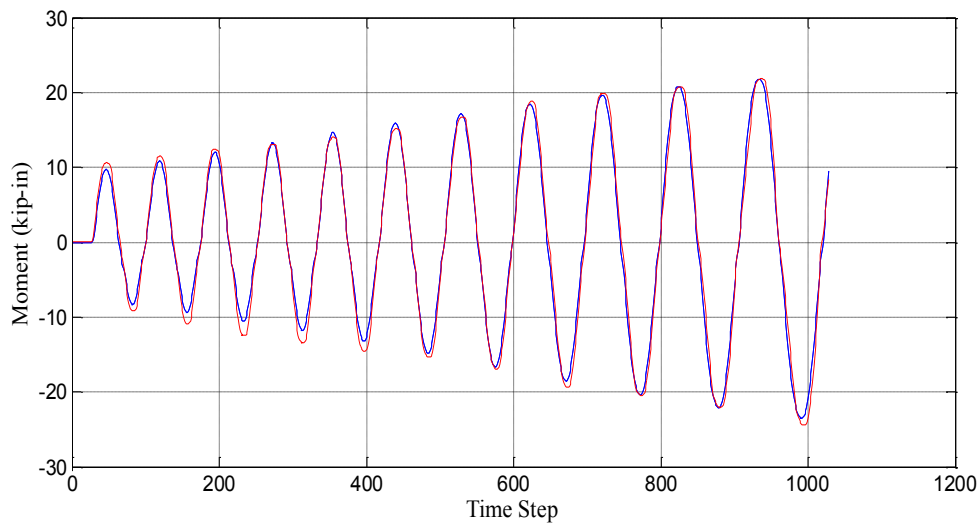
Table 5-3 Descriptions of parameters for Hysteretic Material model (from OpenSeesWiki, 2012)

Parameter	Description
s1p, e1p	Force and deformation at first point of the envelope in the positive direction
s2p, e2p	Force and deformation at second point of the envelope in the positive direction
s3p, e3p	Force and deformation at third point of the envelope in the positive direction (optional)
s1n, e1n	Force and deformation at first point of the envelope in the negative direction
s2n, e2n	Force and deformation at second point of the envelope in the negative direction
s3n, e3n	Force and deformation at third point of the envelope in the negative direction (optional)
pinchx	Pinching factor for deformation during reloading
pinchy	Pinching factor for force during reloading
damage1	Damage due to ductility
damage2	Damage due to energy
beta	Power used to determine the degraded unloading stiffness based on ductility, $\mu^{-\text{beta}}$ (optional, default = 0.0)

Comparisons of numerical and experimental results for the 2-inch black iron pipe with threaded joints, and 2-inch CPVC pipes with cement joints are respectively shown in *Figure 5-12* and *Figure 5-13*. The optimized parameters for the Pinching4 model are presented in *Appendix C*.

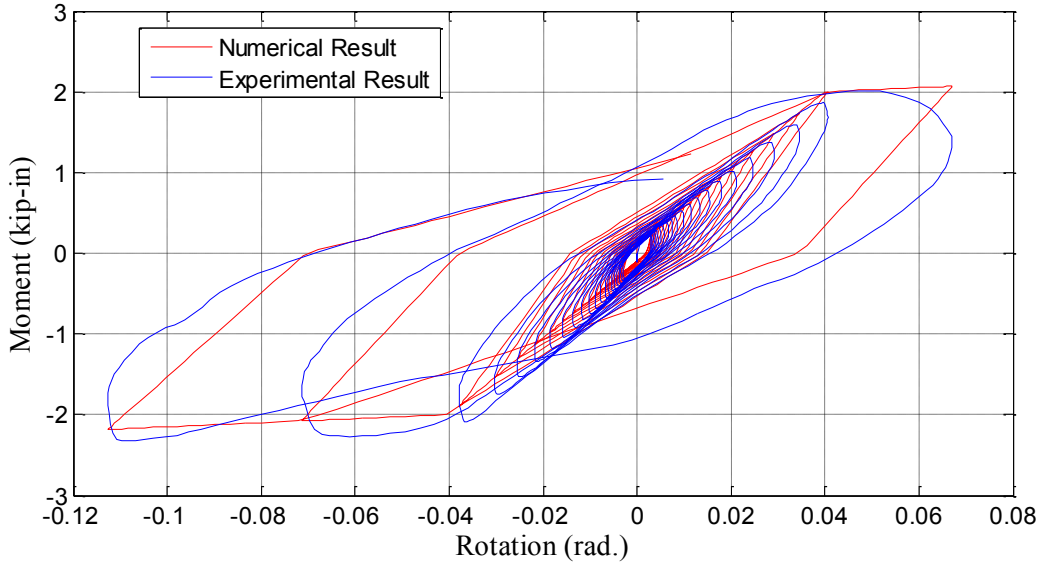


(a) Comparison of hysteresis loops

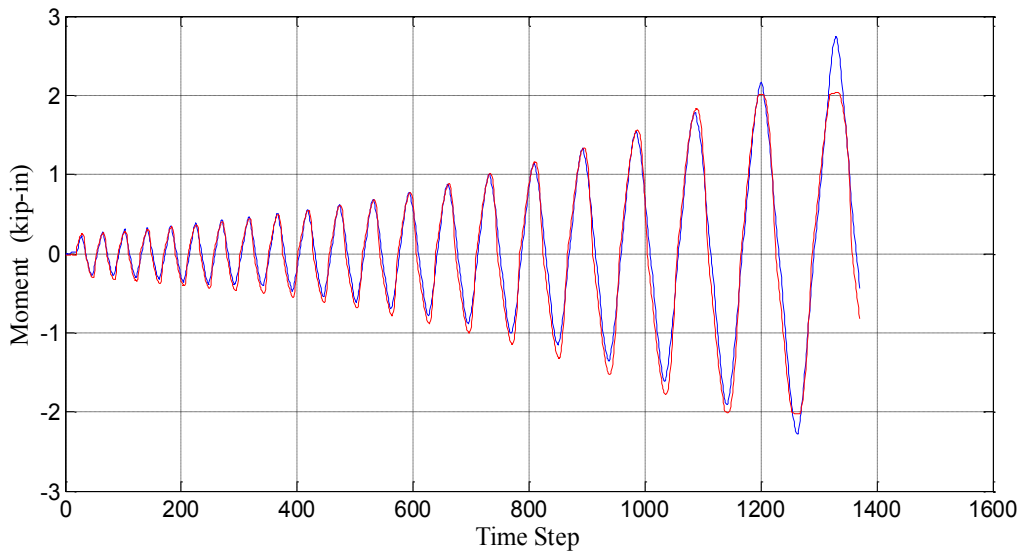


(b) Comparison of moment histories

Figure 5-12 Comparisons of experimental data and numerical model for 2-inch black iron pipe with threaded joints



(a) Comparison of hysteresis loops



(b) Comparison of moment histories

Figure 5-13 Comparisons of experimental data and numerical model for 2-inch CPVC pipe with cement joints

The Pinching4 Material model in OpenSees provides extremely accurate estimates of rotational hysteretic responses of steel pipes with grooved-fit connections compared to the Bilinear Pivot model available in SAP2000. The former numerical model was able to reproduce the triangular pinching effects, which was one of the unique behavioral characteristics observed for the

grooved-fit connections. On the other hand, the Hysteretic Material model successfully provide the same level of accuracy as the Bilinear Pivot model in simulating the black iron pipes with threaded joints and CPVC pipes with cement joints.

### **5.3 Numerical Modeling of Fire Sprinkler Piping Systems**

In this section, numerical models were developed in SAP2000 to simulate the two-story full-scale fire sprinkler piping systems for both Test Specimen 1 (Black iron pipes with threaded joints for branch lines) and Test Specimen 2 (CPVC pipes with cement joints for branch lines) used for the dynamic subsystem testing described in *Chapter 4*. Dynamic responses such as displacement, acceleration and joint rotation at critical locations, were compared for validation of the numerical models. The same process was conducted also in OpenSees.

#### **5.3.1 Implementation and validation of piping tee joint model in SAP2000**

##### **Construction of numerical models**

All pipes used in the two-story fire protection systems, including main lines, cross mains, branch lines, and vertical risers, were created in SAP2000 with the use of frame elements. The frame section properties were calculated automatically and assigned to each member with the input of pipe outside diameters and wall thickness. Extra mass was determined for each member and distributed along all the piping to take into account the water inside the pipes. The piping tee joints were simulated by the piping section with the corresponding pipe dimension, and the moment of inertia for both rotational degrees of freedom (DOFs) was multiplied by a frame property amplification factor of 1.5 to assume that the piping tee joints acted more like rigid

bodies as they had larger stiffness than the pipes that they were connected to. The threaded joints for the black iron pipes and cement joints for the CPVC pipes, as well as the grooved-fit connections for the steel pipes, were modeled with the bilinear Pivot models with the zero-length link element in SAP2000. The nonlinear properties for the piping joint connections in the rotational DOFs were specified by the bilinear Pivot model with the corresponding optimized parameters, while the zero-length link elements were fixed in the translational DOFs. The simulation of piping connections is illustrated in *Figure 5-14*. All vertical hangers were simulated as steel members with a diameter of 3/8 inch, and a modulus of elasticity of 29,000 ksi, Poisson's ratio of 0.3, and minimum yield stress of 36 ksi were assigned to the steel members. Furthermore, the vertical hangers were assumed to have a pin connection to the pipes and a fixed boundary condition at the top with the floors to which they were attached. Both longitudinal and lateral braces were modeled using frame elements with elastic section properties of the schedule 40 1-in steel pipes, and the seismic braces were assumed to have fixed boundary at both ends. As the wire restraints only had resistance in tension, cable sections provided by SAP2000 were adopted to simulate the Gauge #12 splay wires which were assumed to have pin connections for both ends. A modulus of 29,000 ksi, and minimum tensile stress of 58 ksi were assigned to the cable sections. A three-dimensional view of the numerical model created in SAP2000 for the fire sprinkler piping systems is shown in *Figure 5-15*.



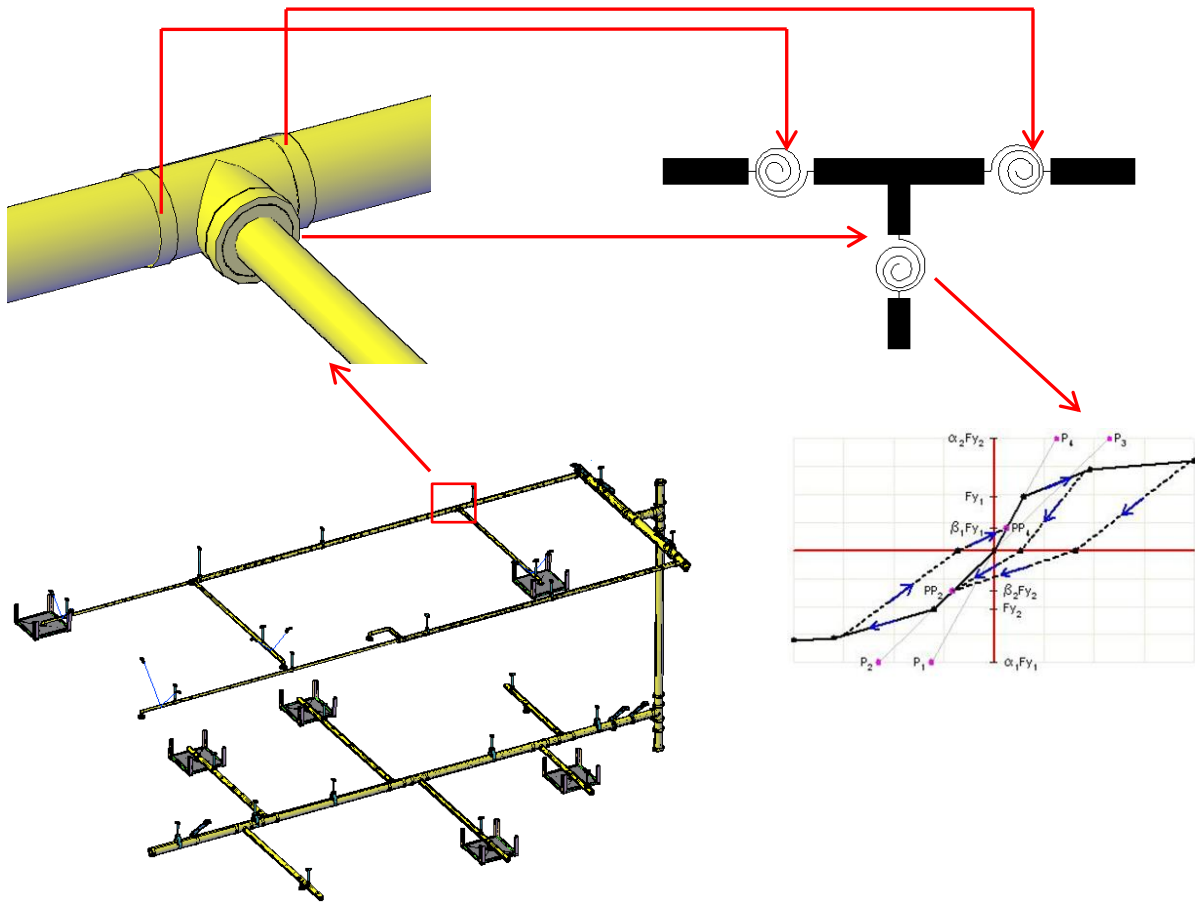


Figure 5-14 Illustration of simulation for tee joint in SAP2000

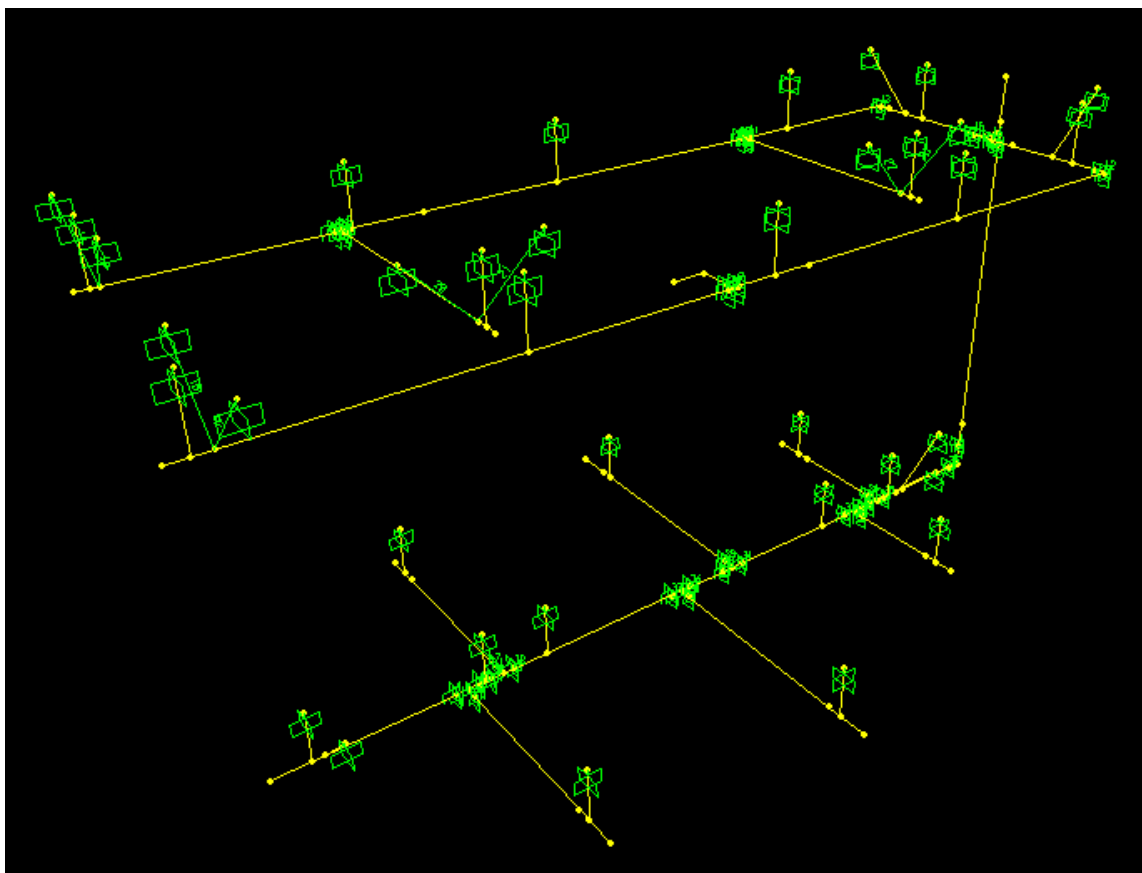


Figure 5-15 Numerical model of fire sprinkler piping system in SAP2000

Rayleigh damping was adopted for the numerical modeling and the damping ratio was determined based on the half-power bandwidth and then assigned to the first and third mode of the model. Rayleigh damping for both models are listed in *Table 5-4*. The “P-Delta plus Large Displacements” option of SAP2000 was selected in order to take into account the geometric nonlinearity. After the dead load was applied to the model, nonlinear response-history analysis was carried out. The same displacement-controlled protocol used for the dynamic testing described in *Chapter 4* was implemented on the building-attached components of the vertical hangers, seismic braces, and wire restraints as the input at a given floor.

Table 5-4 Rayleigh damping for numerical models

Rayleigh Damping	Test Specimen 1 (BIT)	Test Specimen 2 (CPVC)
	0.087	0.127

### Comparison of experimental and analytical results

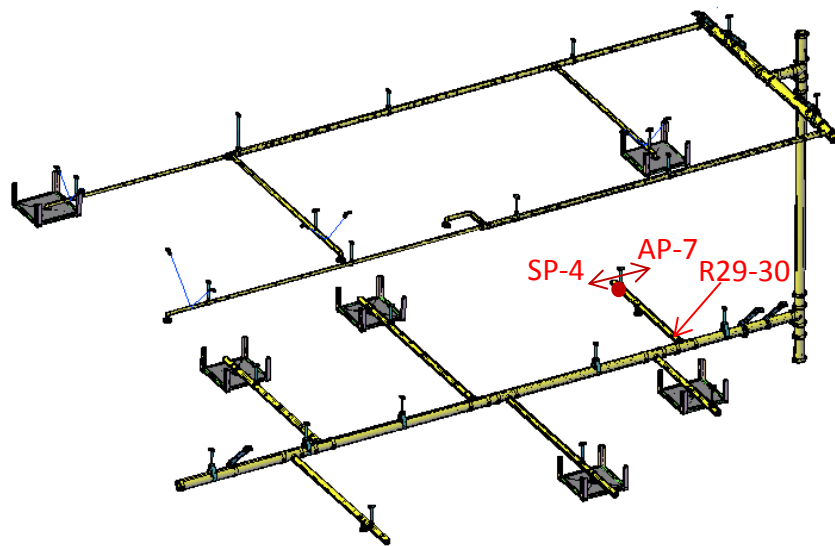
Before the nonlinear response-history dynamic analysis, modal analysis of the fire protection system was conducted in SAP2000. The natural periods of the fully braced fire sprinkler piping system predicted by the numerical model were compared with the results of the dynamic tests (Chapter 4), as shown in Table 5-5. Good agreements are observed.

Table 5-5 Comparison of natural periods obtained from dynamic tests and numerical model

Mode No.	Test Specimen 1 (BIT)			Test Specimen 2 (CPVC)		
	Period measured from dynamic tests (sec)	Period predicted by numerical model (sec)	Error	Period measured from dynamic tests (sec)	Period predicted by numerical model (sec)	Error
1	0.58	0.60	3.4%	2.20	2.32	5.5%
2	0.53	0.56	5.7%	2.05	2.19	6.8%

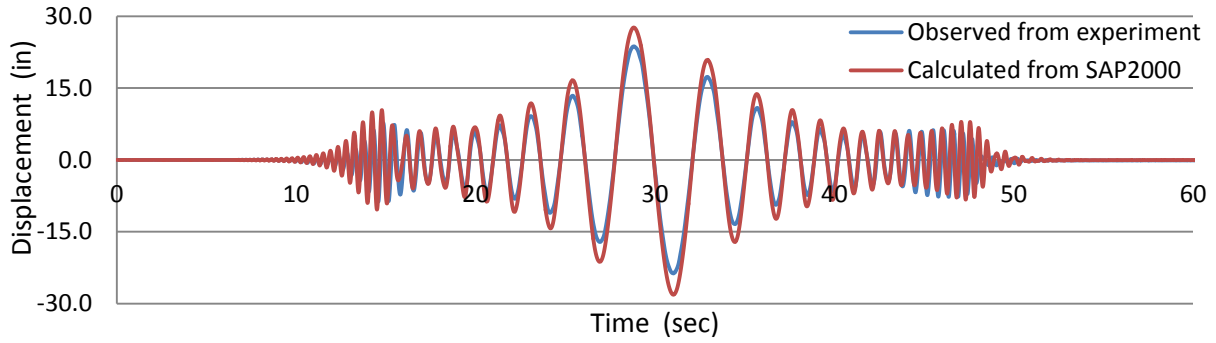
Once the nonlinear response-history dynamic analysis was completed, responses were extracted from SAP2000 and compared with the experimental data. Results exported from the analysis included displacement of branch lines relative to the reaction wall, acceleration at the tip of piping, and the tee joint rotation at critical locations. As an example, the fore-mentioned responses for one of the branch lines at the first floor (Figure 5-16) were used for comparison with the experimental results. There were three main reasons for the selection of this particular

branch line for comparison: (1) The branch lines on the first level experienced larger vibrations since extra mass was attached to the tips of the pipes and the branch lines were perpendicular to the direction of loading; (2) Since the numerical model lacked simulations of any artificial ceiling boxes, data recorded for those branch lines restrained with ceiling boxes was impossible to match with the results extracted for the same locations from the analytical model; (3) Because this branch line was the only one that experienced significant fracture at the tee joint due to excessive rotation during the dynamic testing for the second specimen (branch lines made of CPVC with cement joints), it would be persuasive if the analytical model was able to predict the joint failure with a close rotational response.

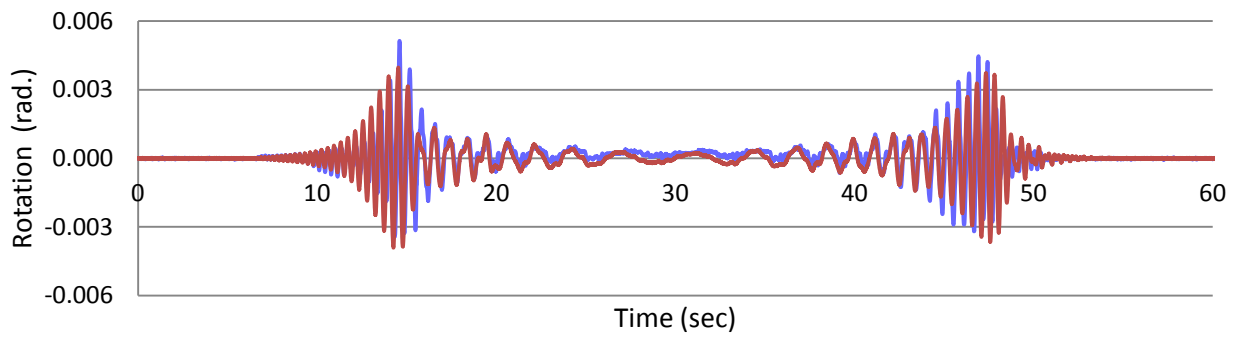


*Figure 5-16 Locations of responses for numerical model validation*

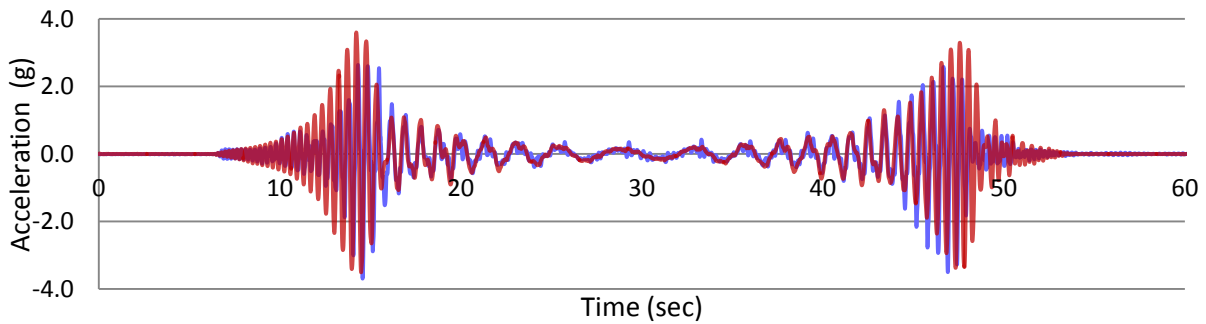
*Figure 5-17* compares the results observed from experiments and those predicted by the nonlinear response analysis in SAP2000 for the Configuration 1-1 (*Chapter 4*) conducted on the fully braced Specimen 1 (branch lines made of black iron with threaded joints). Again, good agreements are observed between the numerical and experimental results.



(a) Comparison of experimental results and numerical predictions for pipe displacement



(b) Comparison of experimental results and numerical predictions for joint rotation



(c) Comparison of experimental results and numerical predictions for pipe acceleration

Figure 5-17 Comparison of experimental results and numerical predictions (fully braced Specimen 1)

Particularly, the tee-joint (R29-30) hysteresis loops obtained from the experiment and the numerical model for the fore-mentioned branch line are compared in *Figure 5-18*. The numerical results achieve a good correlation with the test responses.

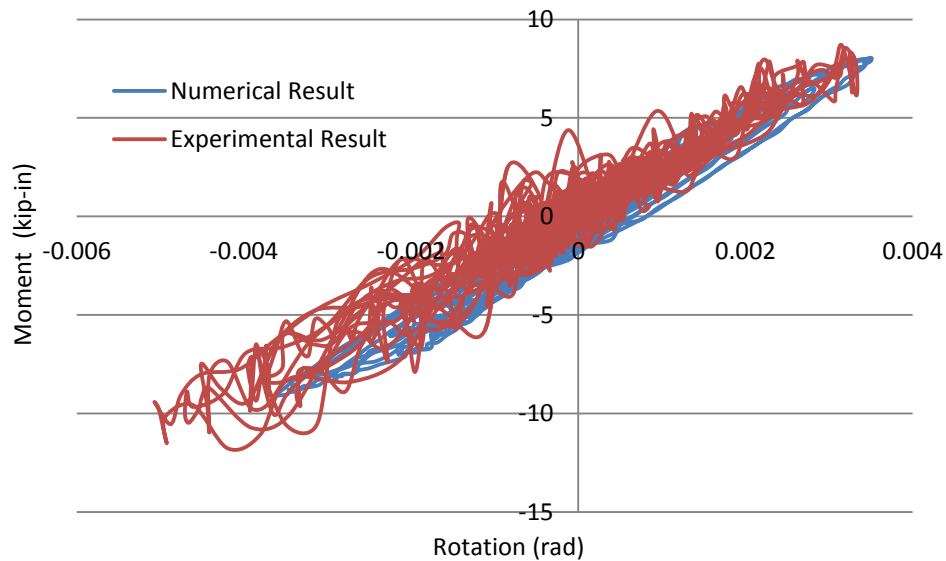
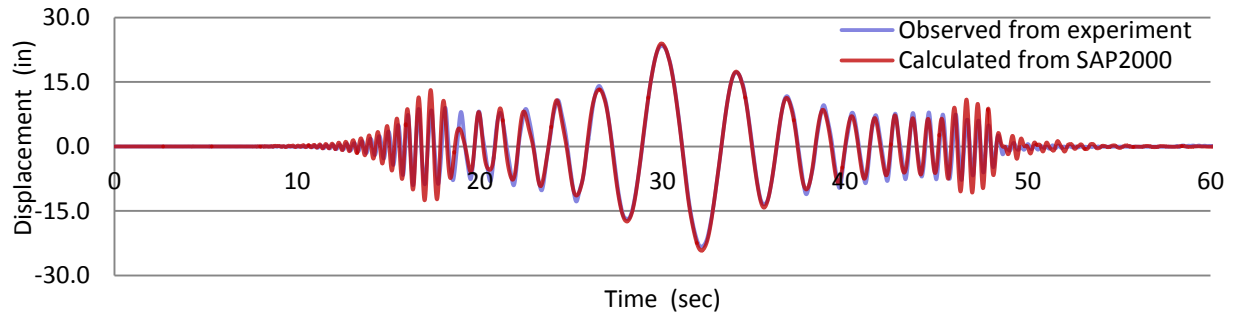
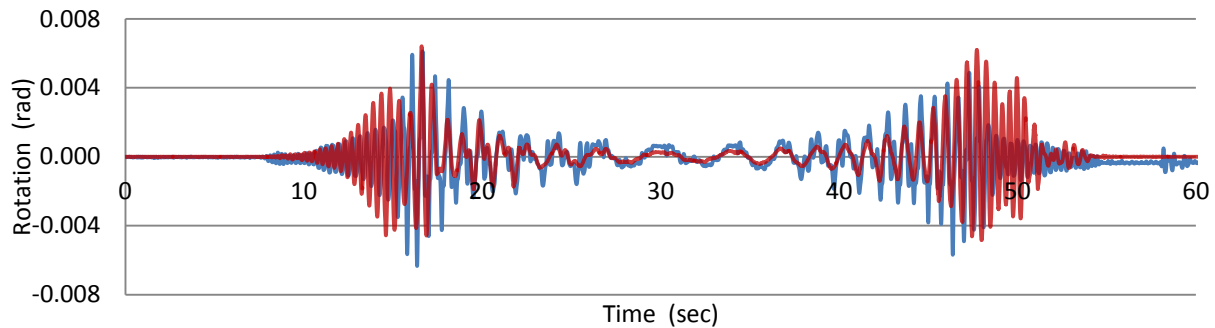


*Figure 5-18 Comparison of hysteresis loops obtained from experiment and numerical model for tee joint R29-30 (fully braced Specimen 1)*

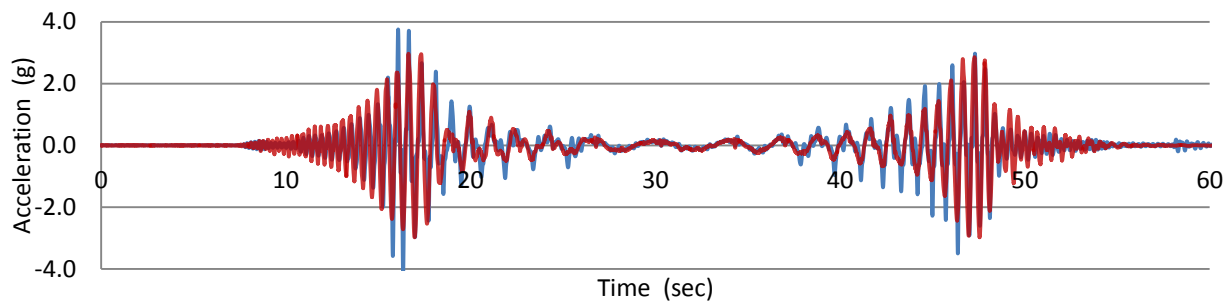
In *Figure 5-19*, experimental results are compared with the predictions from the numerical model for the Configuration 1-4 (*Chapter 4*) of the unbraced Specimen 1. For both cases, the numerical predictions achieve a good correlation with the experimental results in terms of piping displacements, piping accelerations, and tee joint rotations.



(a) Comparison of experimental results and numerical predictions for pipe displacement



(b) Comparison of experimental results and numerical predictions for joint rotation

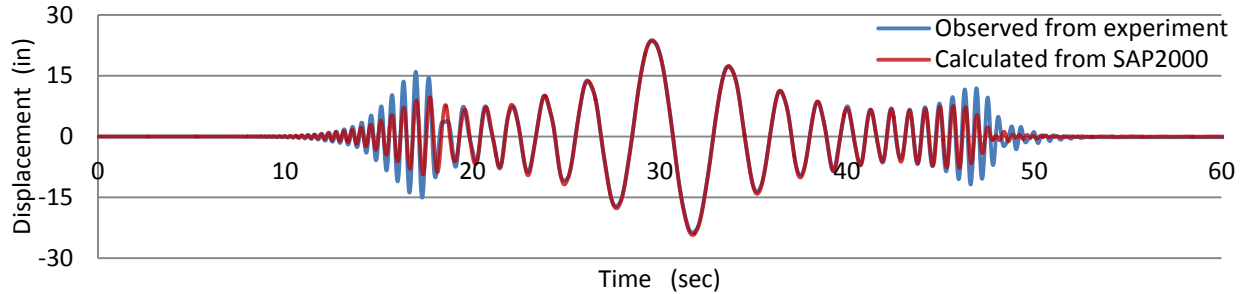


(c) Comparison of experimental results and numerical predictions for pipe acceleration

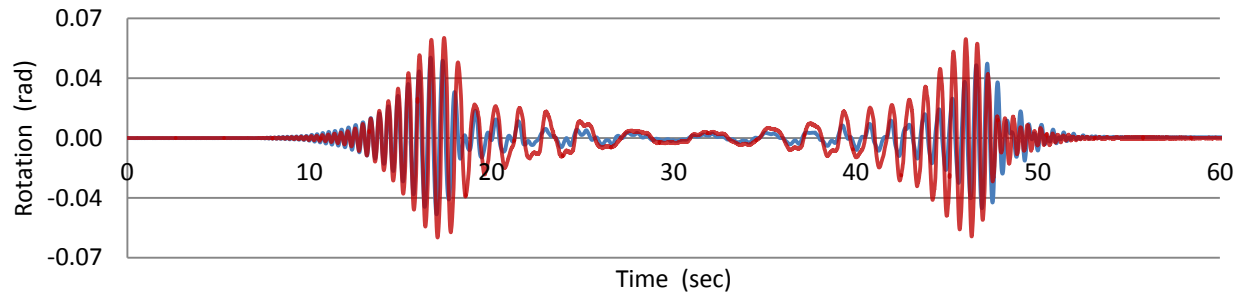
Figure 5-19 Comparison of experimental results and numerical predictions (unbraced Specimen 1)

Comparisons of data from the experiments and the dynamic responses from the numerical models are carried out for the fully braced Specimen 2 (branch lines made of CPVC pipes with cement joints) and unbraced Specimen 2, as shown in *Figure 5-20* and *Figure 5-21* respectively.

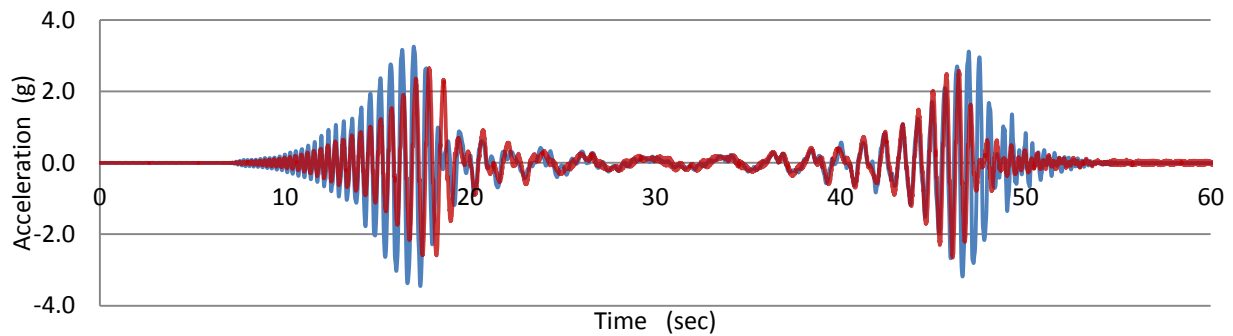
Again, responses calculated from both the fully braced model and unbraced model have provided good estimates of dynamic responses obtained from experimental study.



(a) Comparison of experimental results and numerical predictions for pipe displacement



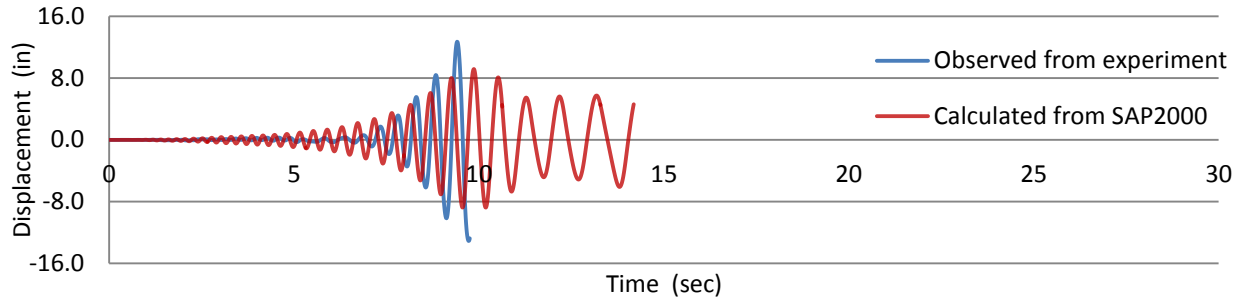
(b) Comparison of experimental results and numerical predictions for joint rotation



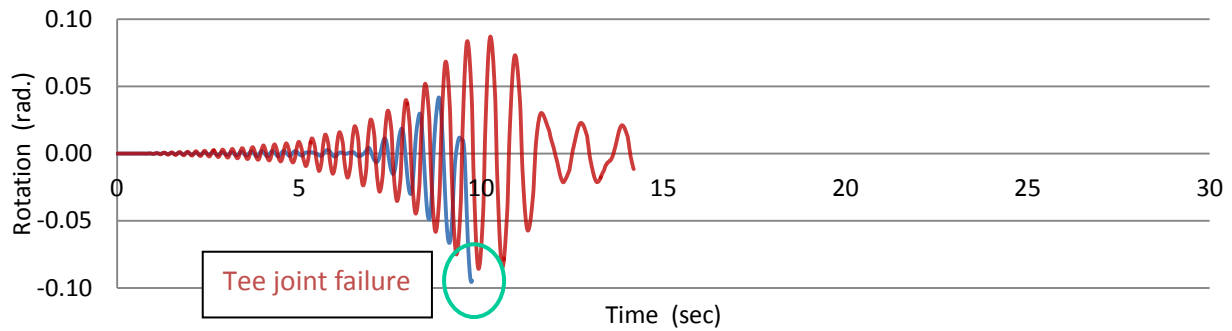
(c) Comparison of experimental results and numerical predictions for pipe acceleration

Figure 5-20 Comparison of experimental results and numerical predictions (fully braced Specimen 2)

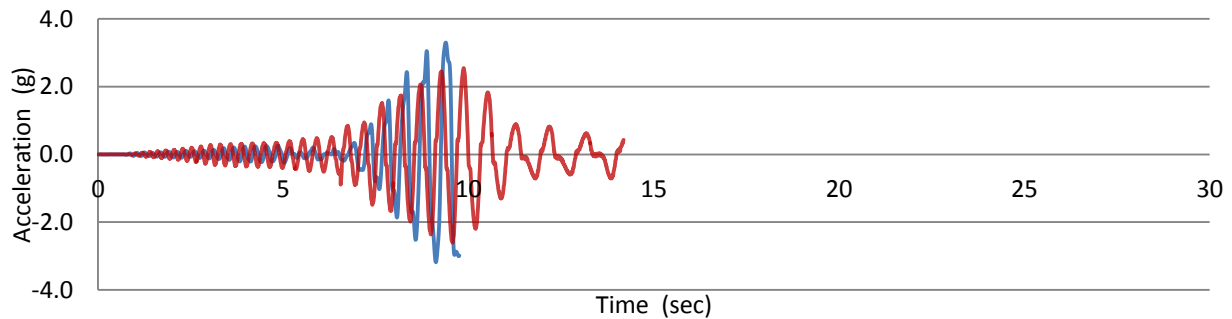




(a) Comparison of experimental results and numerical predictions for pipe displacement



(b) Comparison of experimental results and numerical predictions for joint rotation



(c) Comparison of experimental results and numerical predictions for pipe acceleration

Figure 5-21 Comparison of experimental results and numerical predictions (unbraced Specimen 2)

The unbraced Specimen 2 has experienced the only occurrence of pipe fracture and severe water leakage during the entire dynamic tests presented in *Chapter 4*. As shown in *Figure 5-21*, the numerical model constructed in SAP2000 for the unbraced Specimen 2 was able to predict close

amplitude of joint rotation that corresponds to the rotation resulting in joint failure during the dynamic tests (Table 5-6).

Table 5-6 Comparison of experimental result and numerical prediction for joint leakage

Maximum Joint Rotation	Experimental Result (rad.)	Numerical Prediction (rad.)	Error
	0.092	0.085	7.6%

As shown in Figure 5-22, the maximum joint rotation predicted by the numerical model was compared with the probability of leakage predicted by the fragility curve constructed for the 2-in. CPVC pipe with cement joints in Chapter 3, and it was observed that the probability of leakage was over 40%. As a result, it could be concluded that leakage was likely to occur and the numerical model was able to predict leakage due to excessive joint rotation.

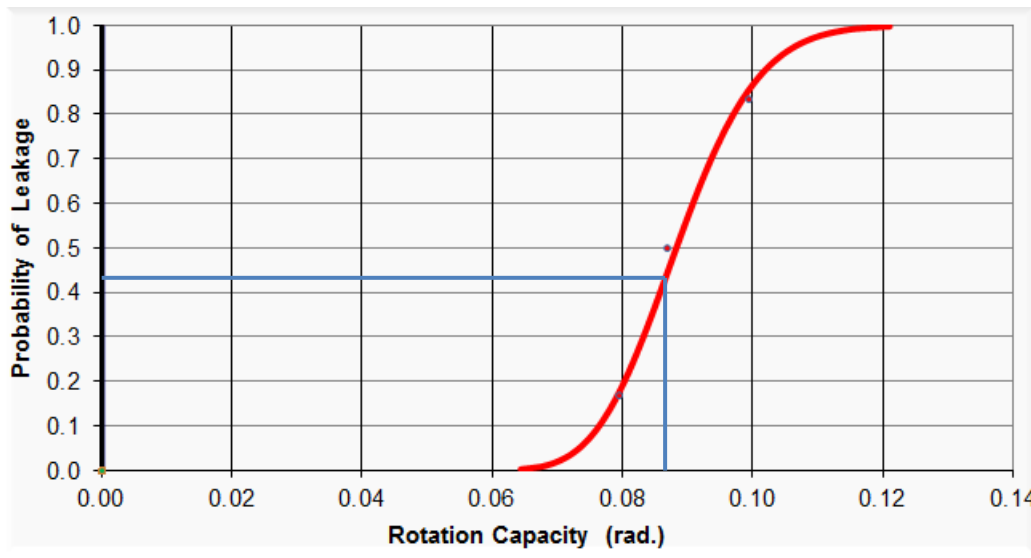


Figure 5-22 Comparison of the maximum joint rotation predicted by numerical model with probability of leakage predicted by the fragility curve for the 2-inch CPVC pipe with cement joints

### 5.3.2 Validation of piping tee joint model in OpenSees

The modeling of fire sprinkler piping systems in OpenSees followed the similar procedures presented in *Section 5.3.1*. All the pipe runs used in the two-story fire protection systems, including main lines, cross mains, branch lines, and vertical risers, were assumed to remain elastic and modeled by elastic beam-column elements, and the frame section properties corresponding to each member were imported manually. Water inside the pipes was taken into account by assigning extra mass along the piping. The grooved-fit connections in the vertical riser, longitudinal main lines on the first level and the cross mains on the second level were modeled with the “ZeroLength” element, while the rest of the piping connections for the branch lines were modeled using the Hysteretic Material model for both the black iron pipes with threaded joints and the CPVC pipes with cements joints. The wire restraints were simulated by the pinned Truss elements associated with the tension-only “Elastic-Perfectly Plastic Gap” Material. A modulus of elasticity of 29,000 ksi, and minimum tensile stress of 58 ksi were assigned to the Truss elements. A three-dimensional view of the numerical model created in OpenSees for the fire sprinkler piping systems is shown in *Figure 5-23*.

The same displacement-control protocol used for the second phase of experimental studies was applied to the building-attached components of all vertical hangers, seismic braces and wire restraints. Nonlinear response-history dynamic analysis was conducted in OpenSees.

*Figure 5-25* shows the comparison of dynamic responses at 100% of MCE level for the locations shown in *Figure 5-24* between numerical models created in SAP2000 and OpenSees. Dynamic

responses obtained from the OpenSees model have achieved a good match with the results calculated by the SAP2000 model.

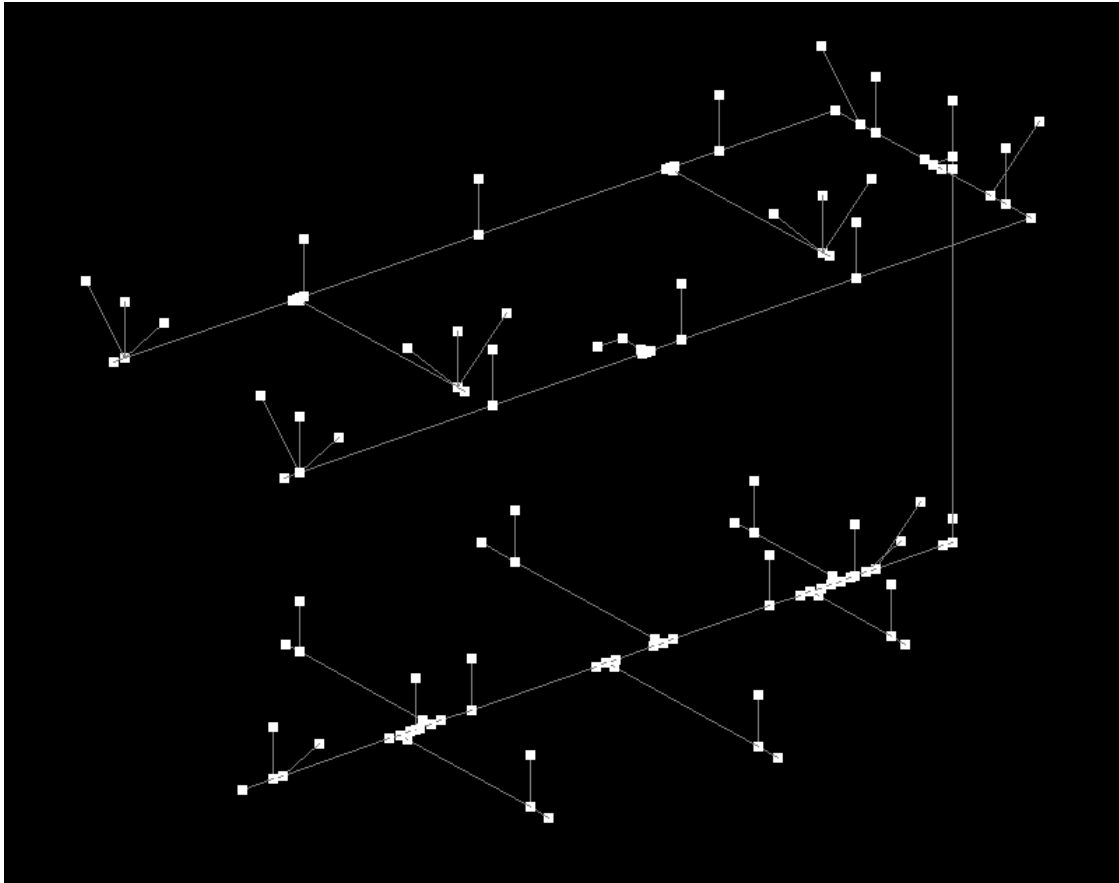


Figure 5-23 Numerical model of fire sprinkler piping system in OpenSees

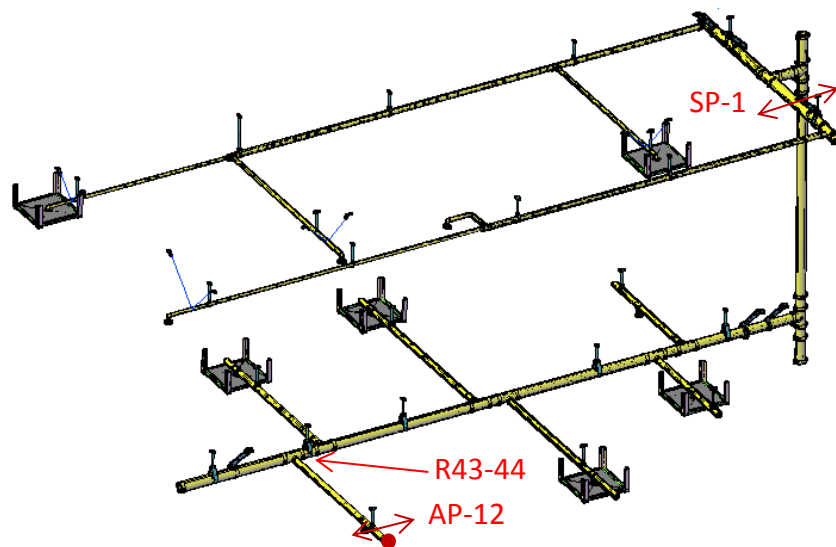
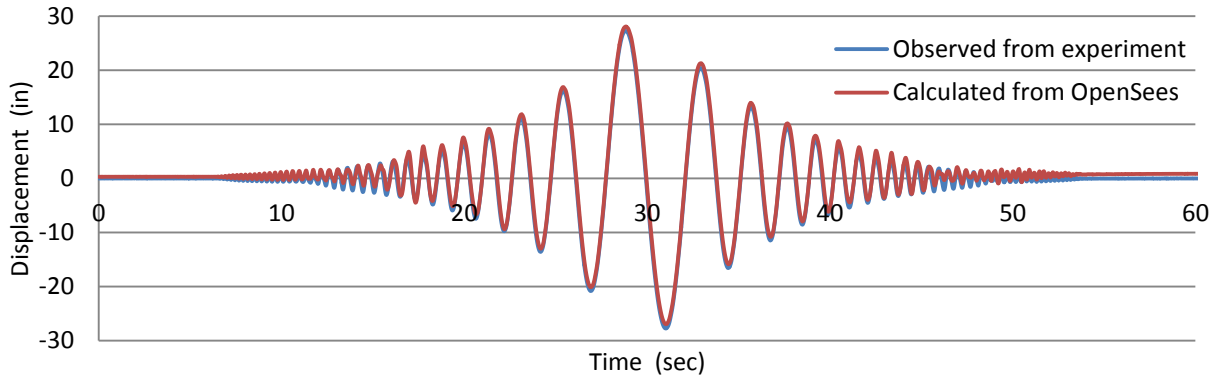
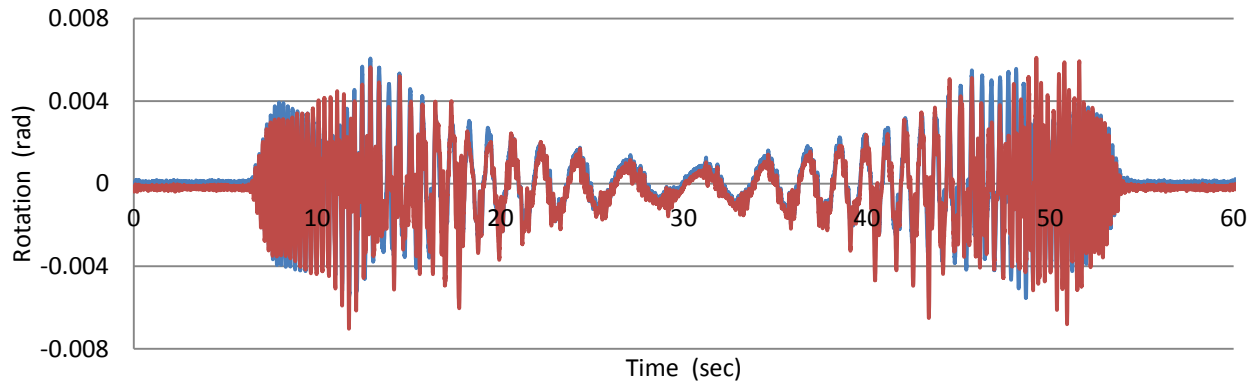


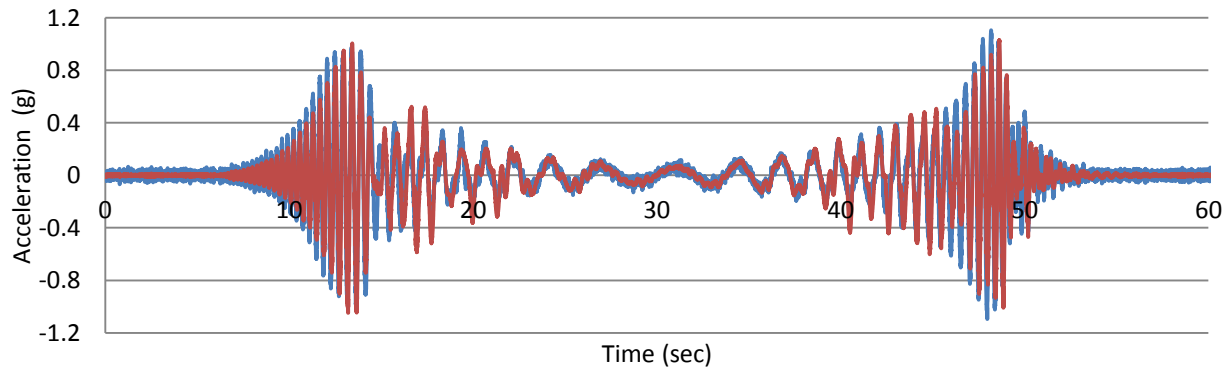
Figure 5-24 Locations of responses for numerical model validation



(a) Comparison of experimental results and numerical predictions for pipe displacement



(b) Comparison of experimental results and numerical predictions for joint rotation



(c) Comparison of experimental results and numerical predictions for pipe acceleration

Figure 5-25 Comparison of experimental results and numerical predictions (fully braced Specimen 1)

## **5.4 Summary and Discussions**

### **5.4.1 Summary**

The Multi-linear Pivot model in the general-purpose dynamic response analysis program SAP2000, as well as the Pinching4 and Hysteretic Material models in a second general purpose analysis software OpenSees, were selected to simulate the rotational hysteretic behavior of various piping tee joint configurations. The cyclic moment-rotation data from the quasi-static tests were used to calibrate the material models. For each tee joint configuration, the optimized combination of parameters was obtained when the Square Root of Sum of Square (SRSS) of the total cumulative energy difference between the experimental results and the numerical predictions for all three sets of data was minimized. Furthermore, these three material models with the optimized combination of parameters were assigned to the rotational spring elements in the corresponding software, and then incorporated in the complete numerical modeling of the two-story full-scale fire sprinkler piping systems used for the second series of the experimental study.

Both numerical models created in the SAP2000 and the OpenSees were capable of providing good estimates of dynamic responses in terms of piping displacements, piping accelerations, and tee joint rotations at critical locations, as well as severe water leakage prediction.

### **5.4.2 Discussions**

OpenSees has the great advantage over other general-purpose analysis software in terms of numerically simulating fire sprinkler systems, as OpenSees provides more choice of material

models with the capability of simulating different tee joint configurations. Although the results predicted by both numerical models created in SAP2000 and OpenSees show close agreements with the data recorded from the dynamic testing, it is an oversimplification to attempt to use the multi-linear Pivot model to simulate all tee joint configurations in SAP2000, for two main reasons:

- 1) Steel pipes with grooved-fit connections, for example, exhibit unique hysteretic behavior that is characterized by the triangular pinching effects. The Pivot model, which features manifest multi-linear backbone curve, is not suitable for simulation of hysteresis loops in that category.
- 2) For the particular two-story full-scale fire sprinkler piping systems considered, most of the grooved-fit connections were concentrated in the longitudinal main lines that coincide in the same direction of shaking. As a result, piping vibration in the grooved-fit connections was diminished, and the influence that the hysteretic behavior of grooved-fit connections has on the dynamic responses of the entire piping systems was limited.



## Chapter 6

# INCREMENTAL DYNAMIC ANALYSES OF FIRE SPRINKLER PIPING SYSTEMS

### 6.1 Introduction

This chapter describes how a number of full-scale fire sprinkler piping systems with different piping materials and various bracing systems were incorporated into a well-studied hypothetical acute care facility located in Southern California (MCEER WC70 demonstration hospital) (Yang *et al.*, 2002). This building model was adopted for a demonstration on the use of numerical modeling to conduct seismic fragility analyses of fire protection systems, with floor acceleration as the demand parameter. The four-story fire protection system had an identical layout at each floor, and the piping layout was the same as the first level of the full-scale test specimens constructed for the dynamic testing described in Chapter 4. A total of three building configurations (elastic building model, inelastic building model without strength degradation, and inelastic building model with strength degradation) were introduced and used for this numerical study.

Two general-purpose nonlinear dynamic analysis softwares, RUAUMOKO (Carr, 2005) and OpenSees (McKenna *et al.*, 1999), were utilized for conducting the Incremental Dynamic Analyses (IDA) as specified in FEMA P695 (2009). In order to investigate the effects of various piping materials and bracing systems on the first leakage seismic fragility curves, a total of 1,000 and over 820 nonlinear response-history dynamic analyses were performed in OpenSees and RUAUMOKO, respectively. Results obtained from the IDAs were used in the construction of

first-leakage seismic fragility curves for fire sprinkler piping systems. The performance objectives related to the first leakage were obtained from the results of the cyclic tests on tee-joints conducted in Chapter 3. Seismic fragility assessments obtained from analyses of all three building models are presented and compared at the end of the chapter.

## 6.2 Process of Incremental Dynamic Analyses (IDA)

The IDA applied for the first-leakage fragility assessment followed the process outlined in the flow chart illustrated in *Figure 6-1*.

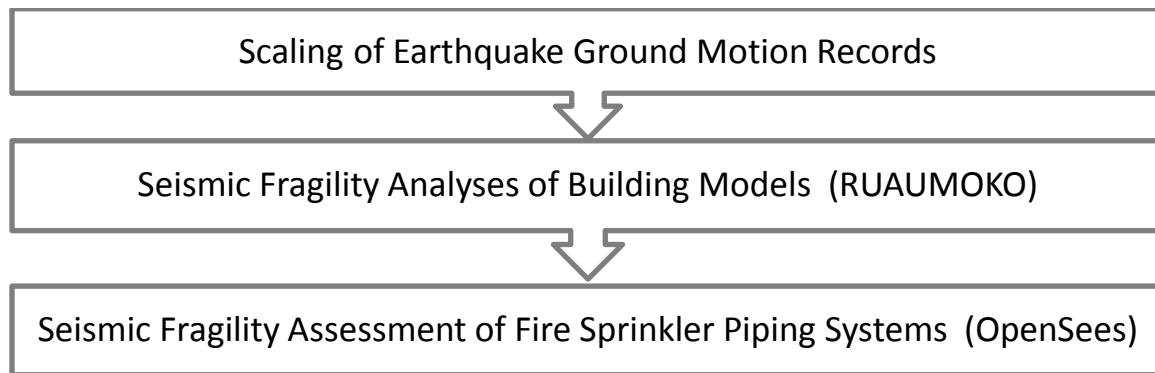


*Figure 6-1 Process of IDA on fire sprinkler piping systems*

The procedure is briefly described below and will be discussed in more detail in the following sections:

### 1) Scaling of an ensemble of ground motions (Section 6.4)

Ten earthquake records were selected from the FEMA P-695 (FEMA, 2009) Far-Field ground motion set for the IDA, and scaled up collectively in terms of the median spectral acceleration at

the fundamental period of the structure until the building model reached the performance objective of collapse prevention, which was associated with 3% of peak inter-story drift.

## 2) Seismic fragility analyses of building models (Section 6.5)

A total of three building configurations (elastic building model, inelastic building model without strength degradation, and inelastic building model with strength degradation) were used in the fragility assessment. For each building model, the IDA curve giving the relationship between the maximum inter-story drift ratio and the median spectral acceleration at the fundamental period of the structure was constructed for each of the ten earthquake records. Furthermore, the response history of total displacement relative to the ground for each floor were recorded and utilized as input for the seismic fragility analyses of fire sprinkler piping systems described in Section 6.6, and the peak floor acceleration for each floor was retained for developing fragility curves.

## 3) Seismic fragility analyses for fire sprinkler piping systems (Section 6.6)

The incremental dynamic analyses for the fire sprinkler piping systems were modified since the traditional ground motion records were replaced by the response histories of building floor displacement as the input for the IDA. For each historical floor displacement record, a nonlinear response-history dynamic analysis of fire sprinkler piping system under study was performed. This process was repeated with increasing intensities of floor displacement input, and the maximum pipe joint rotation was documented. This IDA process was conducted five times for

the combinations of various fire protection systems and building models, with the details of the combinations considered described in Section 6.6.

### **6.3 MCEER WC70 Building Model**

#### **6.3.1 Prototype of building model**

A hypothetical acute care facility assumed to be located in Southern California, known as WC70, was developed for earthquake engineering studies at UB by the Multidisciplinary Center for Earthquake Engineering Research (MCEER). The four-story steel framed building model was assumed to be constructed in the early 1970s and was designed to comply with the seismic requirements of the 1970 edition of Uniform Building Code (UBC).

As shown in *Figure 6-2* and *Figure 6-3*, the building model is symmetric and rectangular in plan, has ten bays with a total length of 275 feet in the east-west direction, three bays with a total dimension of 56.5 feet in the north-south direction, and 51 feet high. The seismic-force-resisting system of this prototype building is composed of four moment-resisting frames symmetrically located at grid lines B, F, J and N in the north-south direction. Lateral resistance in the east-west direction consists of two exterior moment-resisting frames. These seismic frames are constructed with ASTM A572 and A588 Grade 50 steel. ASTM A36 steel is used for all remaining structural members.

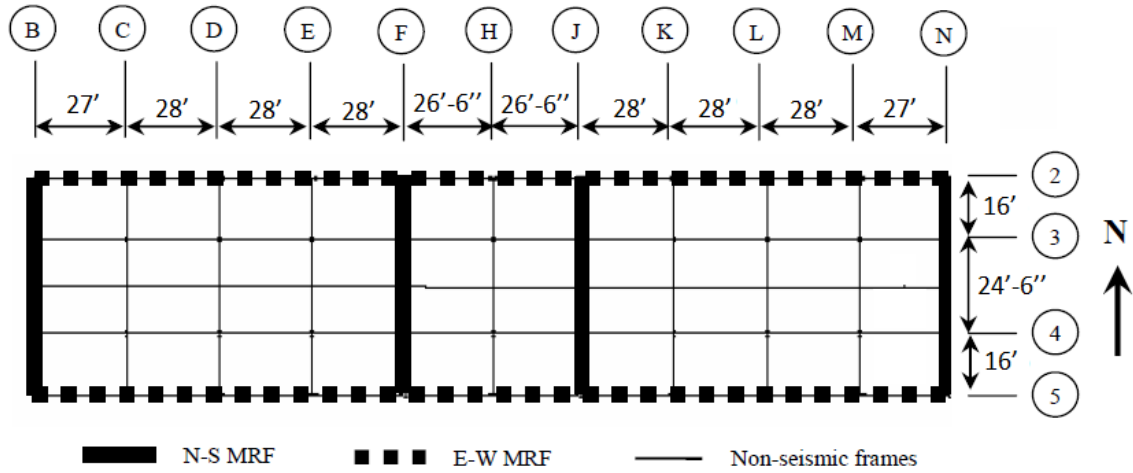


Figure 6-2 Plan view of WC70

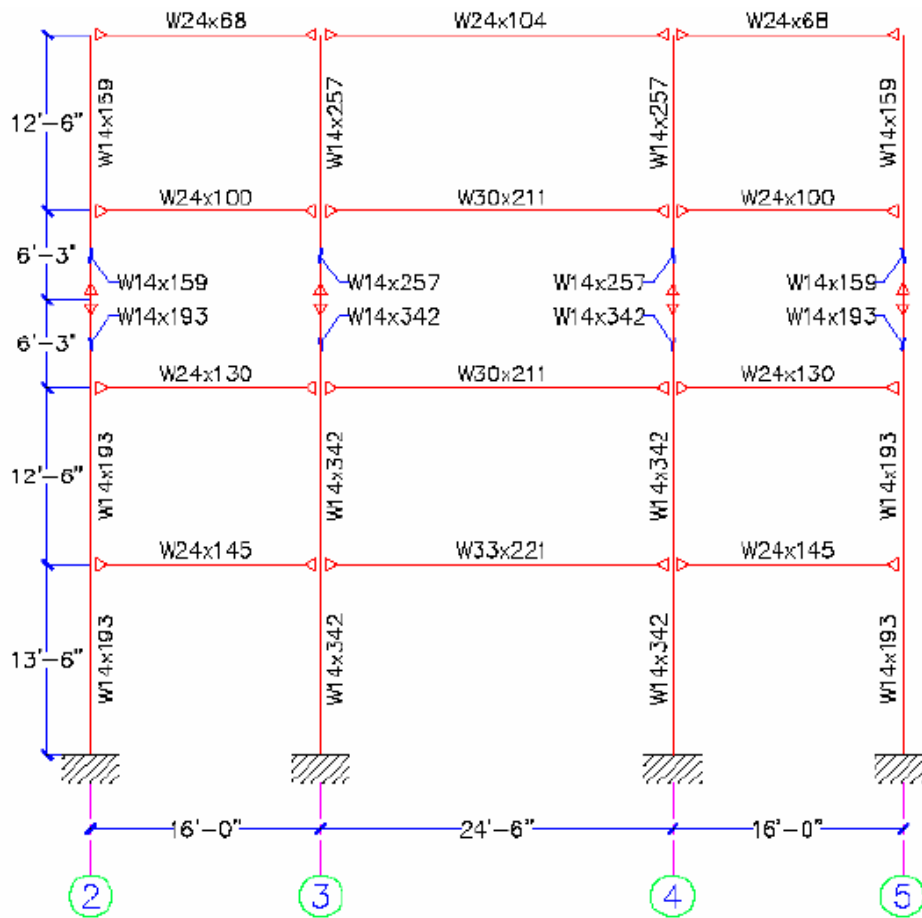


Figure 6-3 Elevation view of WC70 (N-S frame, Line B)

To make full use of symmetry of the structure, a two-dimensional model, which represents half of the building frames in the N-S direction, was developed by Wanitkorkul and Filiatrault (2005) in the RUAUMOKO software in order to simplify the modeling and the analysis. *Figure 6-4* illustrates the two-dimensional model developed in RUAUMOKO along with the corresponding frame member section numbers, summarized in *Table 6-1*. A number of assumptions were made for the model structure as follow:

- 1) The floor diaphragms were assumed to be rigid in-plane, and flexible out-of-plane;
- 2) The contribution to the stiffness from all the concrete slabs was neglected;
- 3) The contribution to the lateral stiffness and resistance from the gravity frames was neglected;
- 4) The shear deformations were neglected in the panel zones; and
- 5) No rigid-end offsets were considered at the beam and column ends.

For this RUAUMOKO model, the Frame element was adopted to represent all beams and columns. A gravity column was modeled with spring elements with a high axial stiffness and pin connection at each end, and the gravity column was assigned all gravity loads from the non-seismic frames to take into account the second order P- $\Delta$  effects. Furthermore, the gravity column was constrained to have the same lateral floor displacements as the seismic frames.

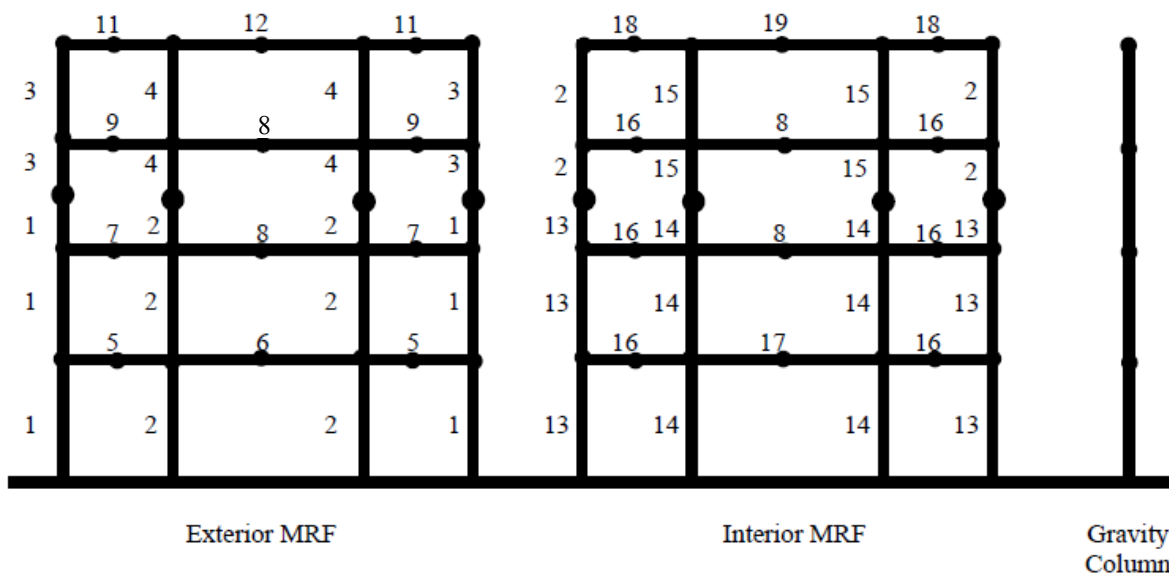


Figure 6-4 2-D model of WC70 with section numbers

Table 6-1 Member properties of the building model

Section No.	Designation	Section No.	Designation
1	W 14x193	10	W 24x68
2	W 14x342	11	W 24x104
3	W 14x159	12	W 14x398
4	W 14x257	13	W 14x455
5	W 24x146	14	W 14x370
6	W 33x221	15	W 24x162
7	W 24x131	16	W 33x241
8	W 30x211	17	W 24x94
9	W 24x103	18	W 30x173

Loads acting on the structure included dead load, live load and earthquake load, which were determined according to the member sections used for construction and the building code requirements. For seismic analysis, the seismic weight for each floor was the sum of dead load and 65% of the live load, as listed in *Table 6-2*.

Table 6-2 Floor seismic weights

Floor	Seismic Weight (kN)		
	Exterior MRF	Interior MRF	Gravity Column
Roof	546	1012	3415
4	622	1083	3562
3	635	1095	3562
2	659	1128	3562

Rayleigh damping with a 2% damping ratio in the first and third mode was adopted as the damping model. The modal properties and the mode shapes of the building are shown in *Table 6-3* and *Figure 6-5*, respectively.

Table 6-3 Modal properties of building model

Mode No.	Period (sec)	Cumulative Mass (%)
1	0.76	85
2	0.26	96
3	0.15	99
4	0.10	100



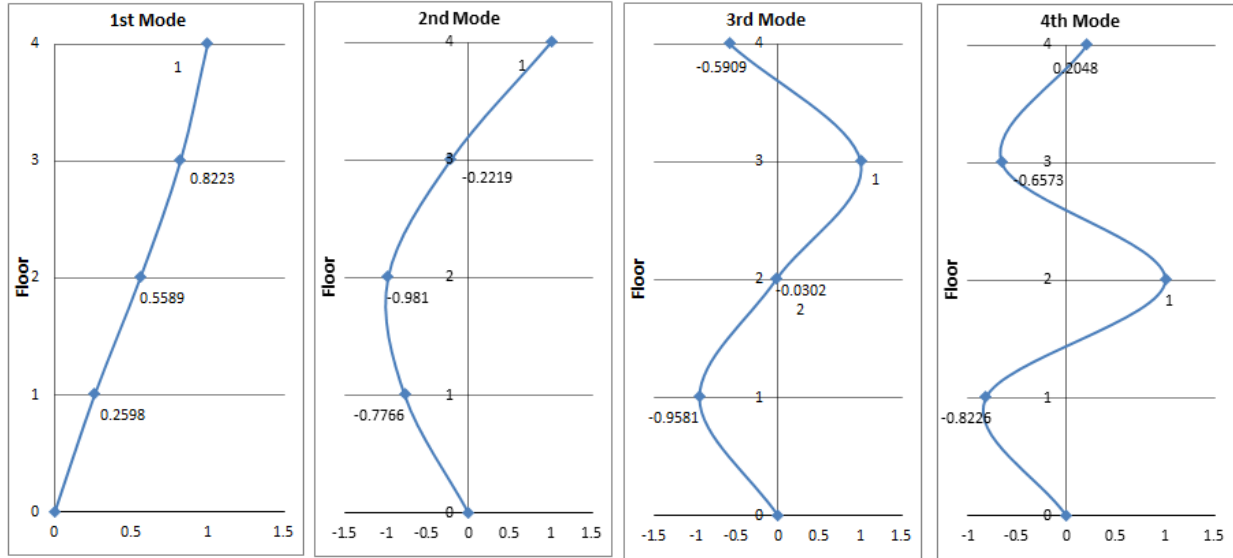


Figure 6-5 Elastic modes of vibration of the building

### 6.3.2 Building model configurations

#### Descriptions of building models

A total of three model configurations (elastic building model, inelastic building model without strength degradation, and inelastic building model with strength degradation) were utilized in the IDA. The prototype building model was adopted as the elastic building model without any change, while the inelastic building models were modified based on the inelastic properties of the member sections.

The inelastic building models were developed by assigning a bilinear moment-curvature hysteresis law with a 2% hardening ratio to all frame members. Furthermore, two assumptions were made for the inelastic building models:

- 1) The inelastic response was assumed to be concentrated in plastic hinges formed at both ends of the frame members; and
- 2) The plastic hinge length was assumed to be 90% of the total depth of a frame section.

In order to simulate the brittle behaviors and local failure mechanisms of pre-Northridge earthquake welded beam-to-column connections, a flexural strength degradation model (*Figure 6-6*) was developed by Filiatrault *et al.* (2001) and was introduced at both ends of all the beam elements for the inelastic building model with degradation. The strength degradation initiates when the curvature ductility reaches 4.3, corresponding to a plastic rotation of approximately 0.01 radians in all beam sections. The member strength drops to 1% of the initial value when the curvature ductility goes over 10.5. Furthermore, the strength degradation model was assumed to be independent in both positive and negative bending, and the occurrence of weld fractures would not result in loss in shear capacity of the beam-to-column connections.

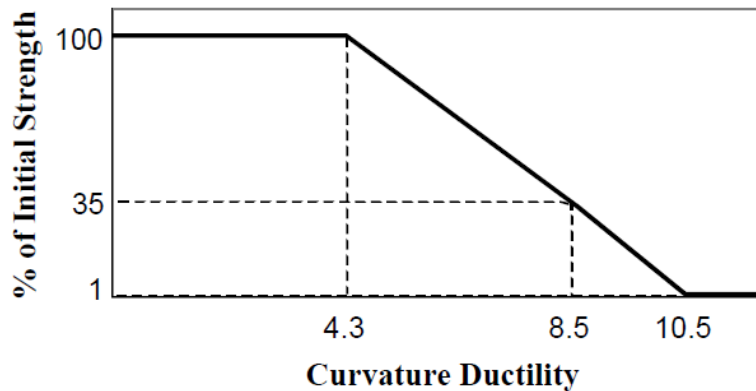


*Figure 6-6 Flexural strength degradation model (Filiatrault et al., 2001)*

## Static pushover analysis of building models

An inverse triangular distribution of lateral force along the story height was applied to the three building model configurations and static pushover analyses were conducted. *Figure 6-7* shows the plots of the base shear ratio (base shear  $V_B$  divided by the seismic weight of the building  $W_{\text{Building}}$ ) to the building drift ratio (roof displacement  $\Delta_R$  divided by the total height of the building model  $H_{\text{Building}}$ ).

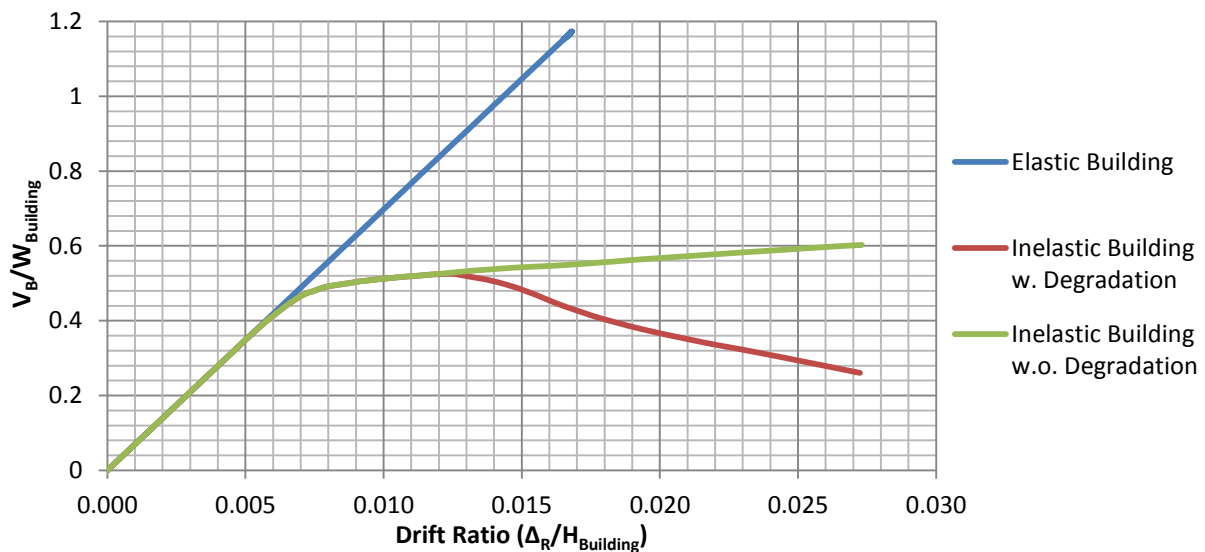


*Figure 6-7 Static pushover curves*

As shown in *Figure 6-7*, all three building models possess identical responses in the elastic range. Beyond the elastic response, the base-shear force obtained from the inelastic building model without strength degradation remains increasing due to the bilinear moment-curvature hysteresis law and the hardening of member properties, while the base-shear force of the second inelastic building model firstly enters the same yield plateau and starts to decrease as a result of the initiation of the strength degradation.

## 6.4 Earthquake Ground Motions

Ten out of the forty-four scaled historical ground motion records from the FEMA P-695 Far-Field ground motion set were used in the nonlinear dynamic response analyses as the input for the building models. The record set does not take into account the vertical component of the earthquake, as the vertical direction of the ground motion is usually not considered of primary importance for building collapse evaluation.

The original earthquake records of the forty-four ground motions were scaled according to the methodology described in FEMA P-695 (FEMA, 2009): each individual record was normalized according to its peak ground velocities (PGV) in order to remove record-to-record variability due to differences in magnitude of event, in distance to source, in source type and in soil conditions, while maintaining the inherent variability and the overall ground motion intensity of the record set.

*Figure 6-8* shows the acceleration time histories for the ten earthquake ground motions used for the IDA. The main characteristics of the unscaled horizontal ground motion ensemble considered in the numerical study, as well as the amplitude of scalar applied to each record, are summarized in *Table 6-4*.

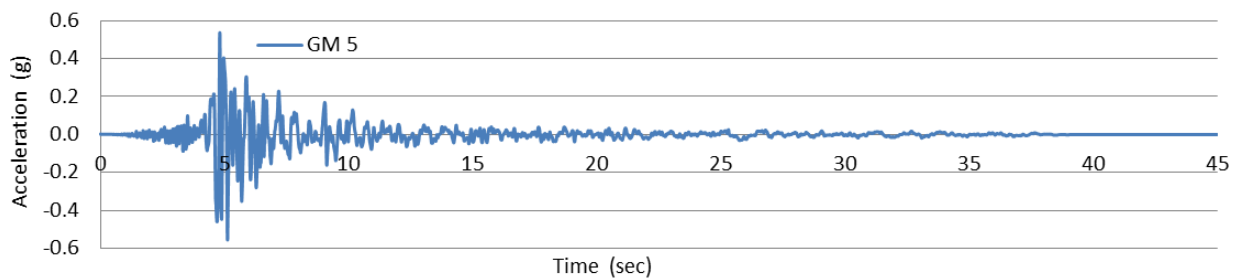
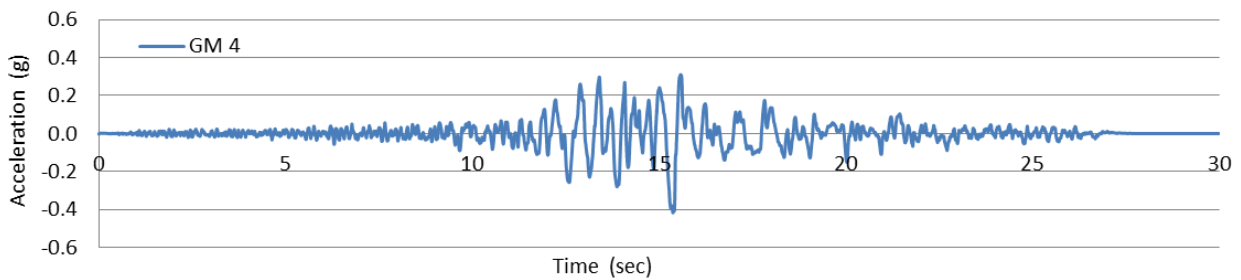
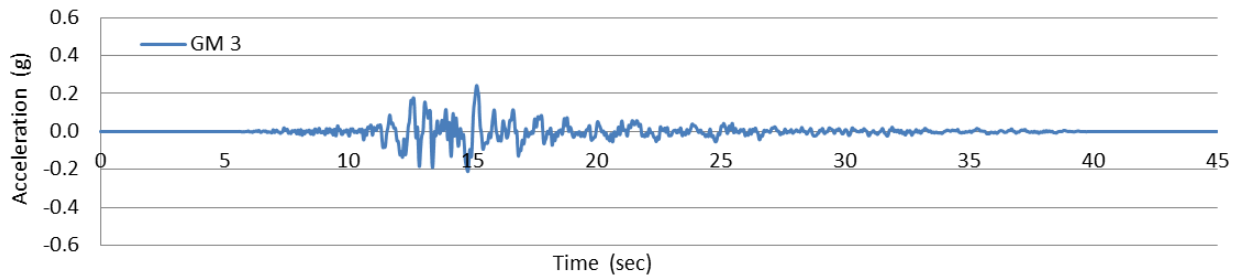
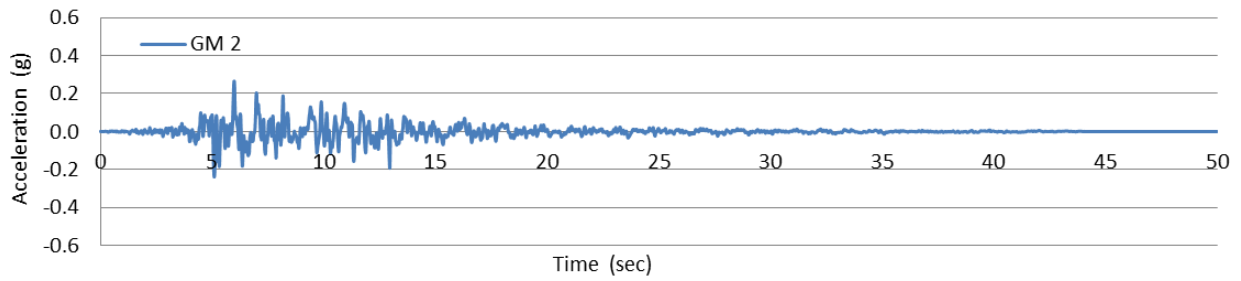
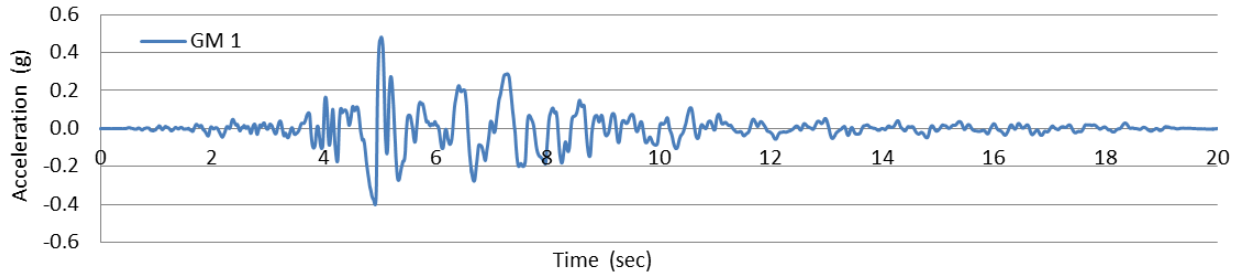


Figure 6-8 Time histories of ten Far-Field earthquake ground motions (GM indicates ground motion record)

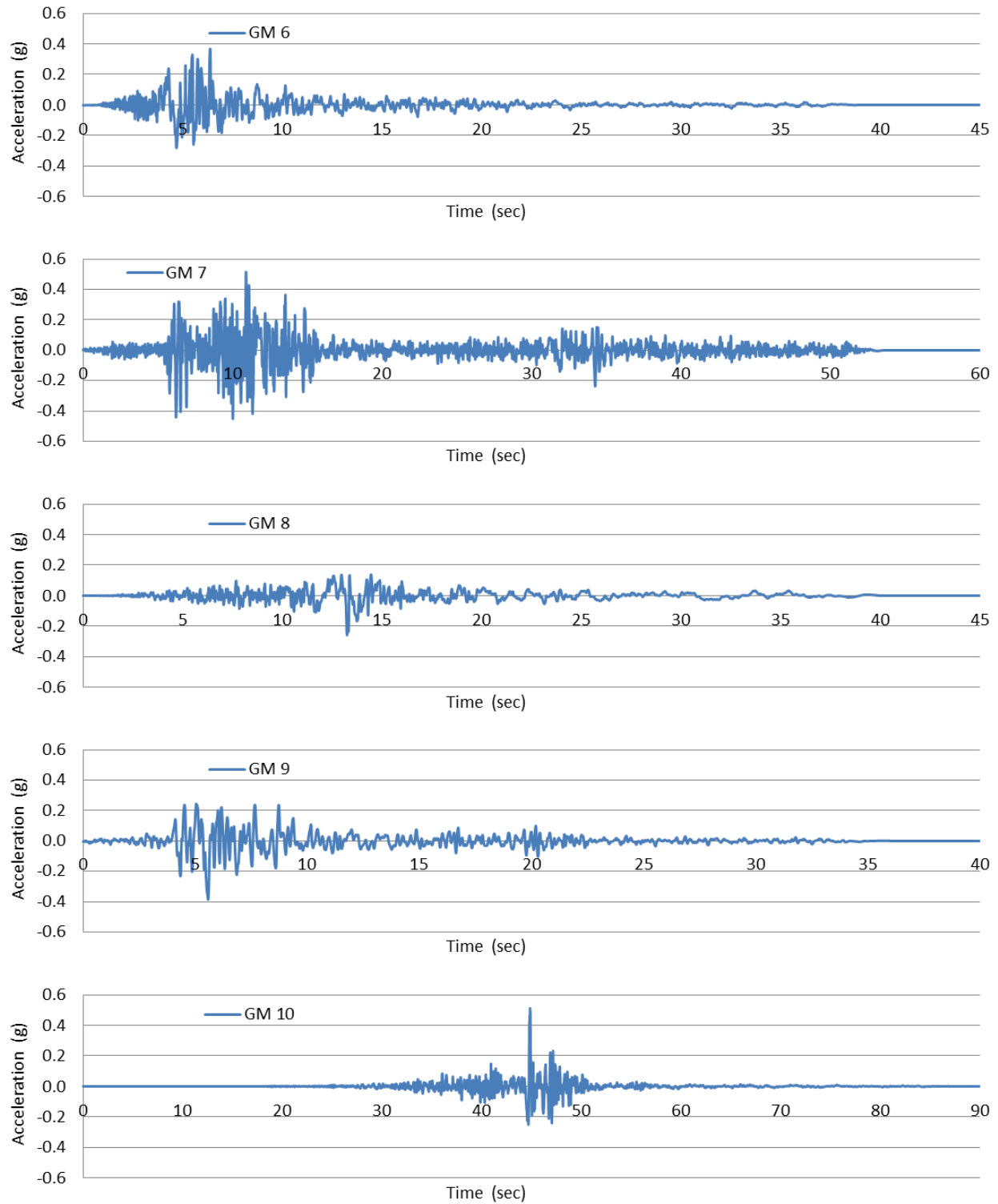


Figure 6-8 Time histories of ten Far-Field earthquake ground motions (GM indicates ground motion record)  
(Cont'd)

Table 6-4 Characteristics of reduced and unscaled ground motion ensemble

EQ Index	EQ ID	Earthquake	Year	Station	Magnitude	PGA (g)	Scalar
4	120122	Northridge	1994	Canyon Country – W Lost Cany	6.7	0.48	0.83
7	120521	Hector Mine	1999	Hector	7.1	0.27	1.09
15	120721	Kobe, Japan	1995	Shin-Osaka	6.9	0.24	1.10
24	120922	Landers	1992	Coolwater	7.3	0.42	1.15
27	121021	Loma Prieta	1989	Gilroy Array #3	6.9	0.56	0.88
28	121022	Loma Prieta	1989	Gilroy Array #3	6.9	0.37	0.88
29	121111	Manjil, Iran	1990	Abbar	7.4	0.51	0.79
32	121212	Superstition Hill	1987	El Centro, Imp. Co Cent	6.5	0.26	0.87
35	121321	Cape Mendocino	1992	Rio Dell Overpass – FF	7	0.39	0.82
40	121422	Chi-Chi, Taiwan	1999	TCU045	7.6	0.51	0.96

These ten historical ground motion records were selected by Nicknam *et al.* (2012) and were chosen in such a way that the geometric mean, median, and arithmetic mean of the spectral acceleration at the fundamental mode of vibration ( $\hat{S}_{a,T1}$ ) calculated from the ten ground motions matched reasonably well with those obtained from the forty-four ground motions, as can be seen from Table 6-5. Furthermore, all ten ground motion records are all from large-magnitude ( $M > 6.5$ ) events, which dominate the collapse risk and generally have longer durations of shaking that is critical for collapse evaluation of nonlinear degrading models (FEMA, 2009). Furthermore, large-magnitude earthquakes are more likely to result in large response of fire sprinkler piping systems and lead to damage and failure of the piping systems.

Table 6-5 Comparison of geometric mean, median and arithmetic mean of spectral accelerations

	Sa,T1 (10 ground motions)	Sa,T1 (44 ground motions)	Difference
Geometric Mean	0.494 g	0.479 g	3.0%
Median	0.512 g	0.488 g	4.7%
Arithmetic Mean	0.543 g	0.517 g	4.8%

Figure 6-9 presents the 5%-damped pseudo-acceleration response spectra for the ten individual ground motions along with the median acceleration response spectrum.

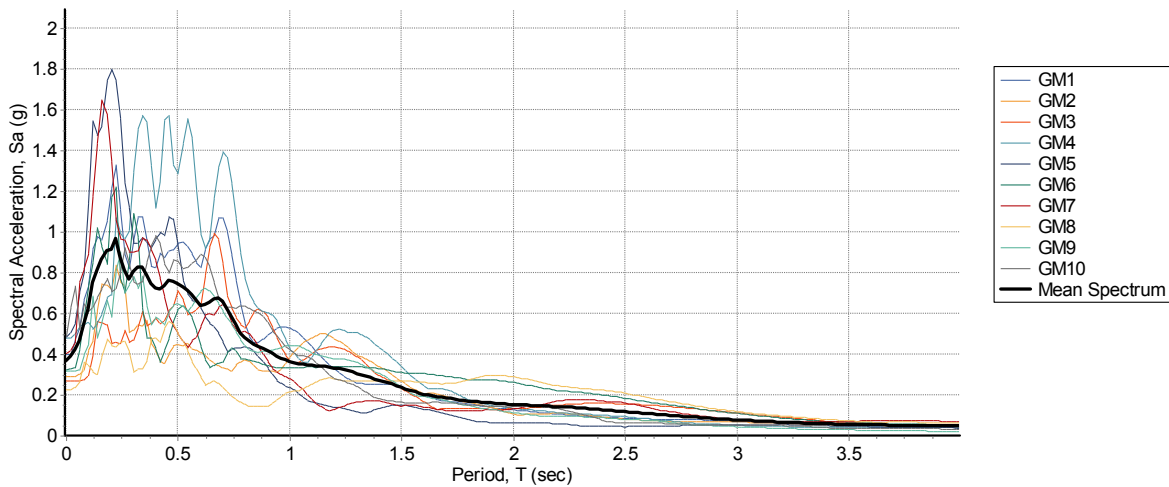


Figure 6-9 Acceleration response spectra of scaled ground motions (GM indicates ground motion record)

## 6.5 Seismic Fragility Analyses for Inelastic Building Models

### 6.5.1 Definition of failure (collapse of building model)

For the inelastic building model without strength degradation, a bilinear moment-curvature hysteresis law with a 2% hardening ratio was assigned to all structural elements. With this mechanical behavior, member forces continue to increase with the imposed deformation. Failure



(collapse of building model) is defined for the inelastic building model without strength degradation when the peak inter-story drift reaches 5%, which is traditionally associated with building performance objective of collapse prevention. For the inelastic building model with strength degradation, the time-history analysis performed in RUAUMOKO will terminate automatically if convergence cannot be reached, and the failure (collapse) mechanism of building the model occur once the curvature ductility ratio of any structural member reaches 10.5 and the structural member only retains 1% of its initial strength. For the elastic building model, failure (collapse) is also defined when the peak inter-story drift reaches 5%.

### **6.5.2 Fragility analyses**

After the procedure of normalization described in Section 6.2, the ensemble of ten ground motions was collectively scaled up to a specific intensity level based on the median spectral acceleration at the fundamental period of the structure. The building models were then individually subjected to each of the ten scaled Far-Field earthquake ground motions and nonlinear time-history dynamic analyses were performed. For each analysis, the peak inter-story drift and the median spectral acceleration were retained for construction of IDA curves and fragility curves, and the absolute displacement time history for all four floors were recorded as input for the IDA analysis on the four-story fire sprinkler piping systems described in Section 6.6. The procedure was repeated with increasing intensities of the earthquakes until collapse of the building models occurred. The process of fragility analyses is outlined in *Figure 6-10*.

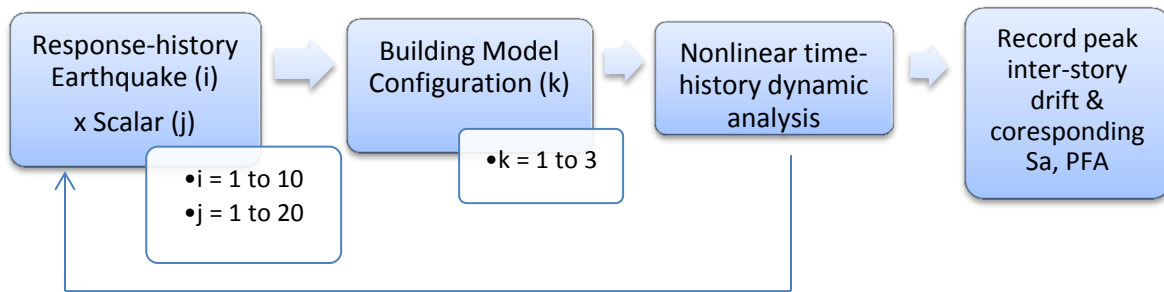


Figure 6-10 Fragility analyses for building models ( $S_a$  indicates spectral acceleration, and PFA indicates peak floor acceleration)

Results from the fragility analyses for all three building models are presented from *Figure 6-11* to *Figure 6-16*, respectively. And the comparison of the three collapse fragility curves is summarized in *Figure 6-17*. As the original building model remained elastic at all times, the IDA curves for the elastic building model are straight lines. *Table 6-6* summarizes the median spectral acceleration for the ten ground motions at the period of the structure for both inelastic building models.

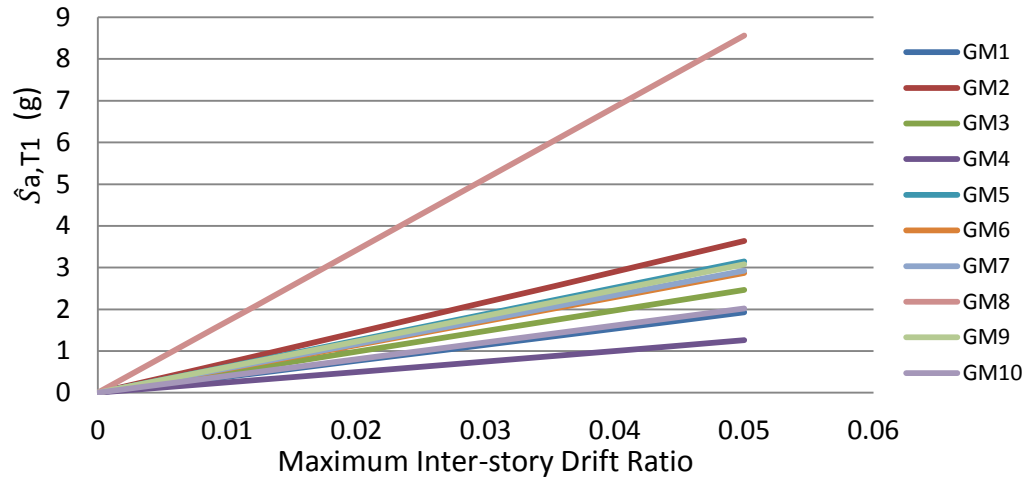


Figure 6-11 IDA curves for elastic building

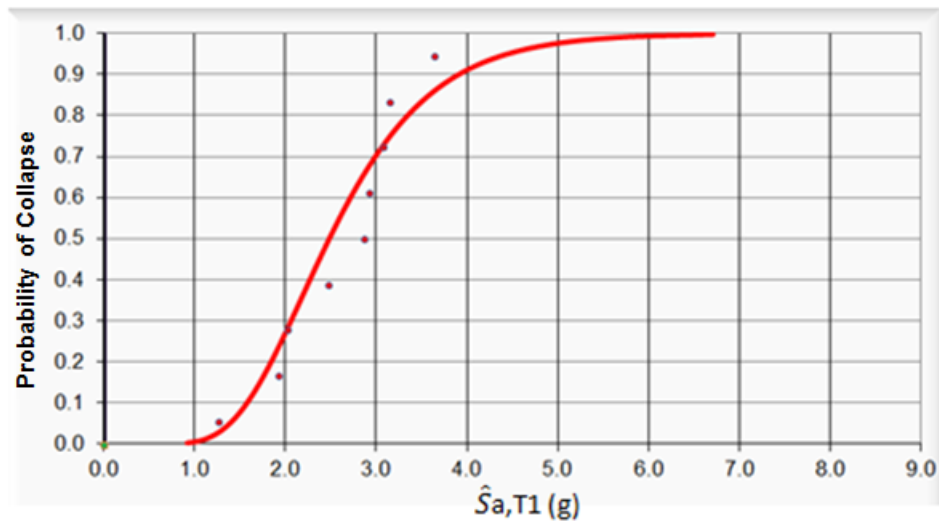


Figure 6-12 Collapse fragility curve for elastic building model

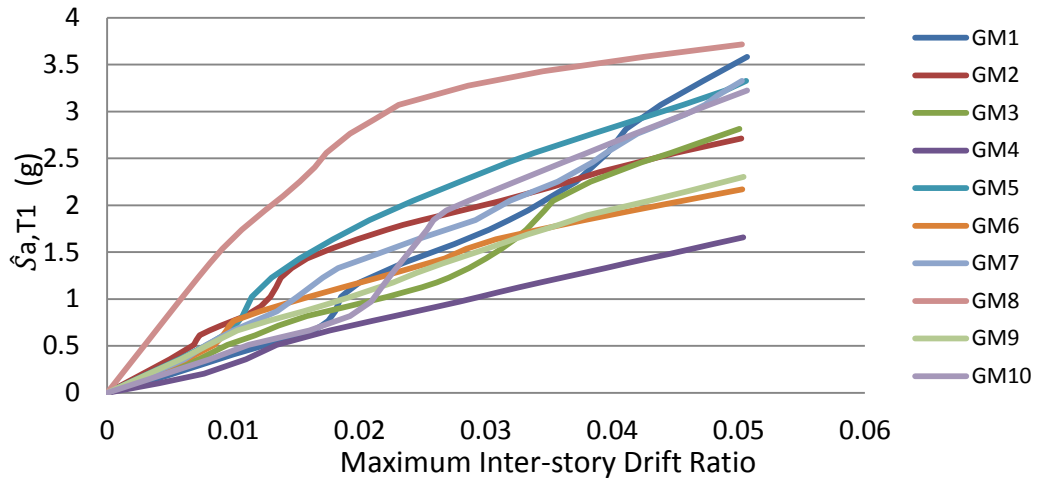


Figure 6-13 IDA curves for inelastic building without degradation

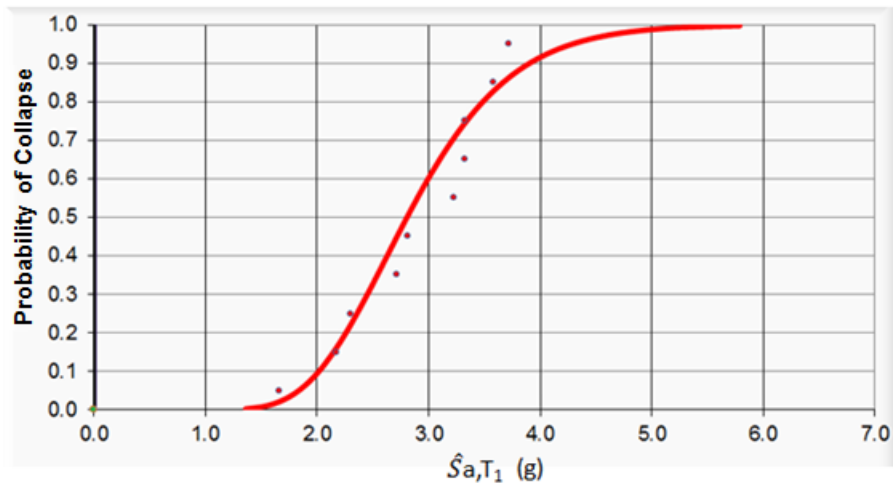


Figure 6-14 Collapse fragility curve for inelastic building model without degradation

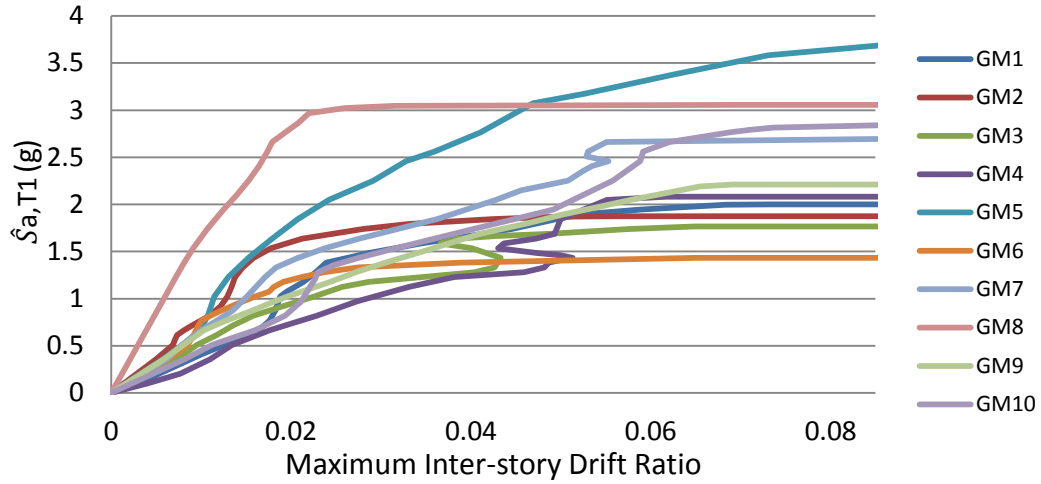


Figure 6-15 IDA curves for inelastic building with degradation

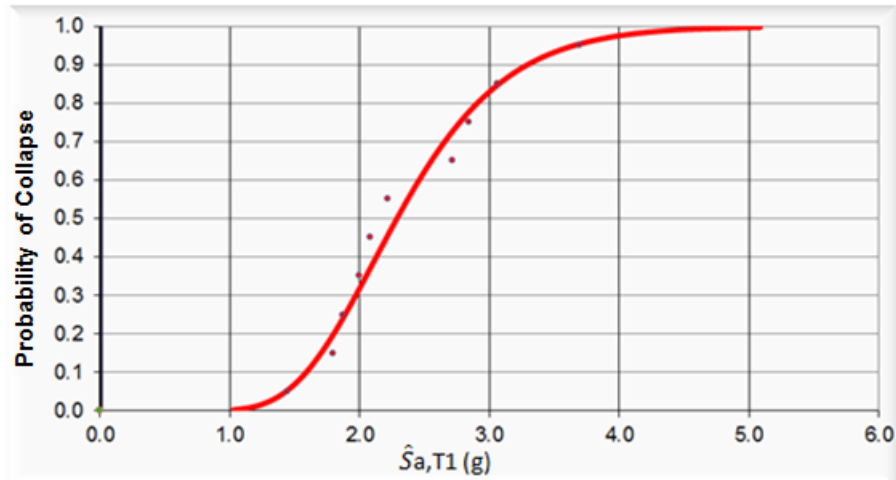


Figure 6-16 Collapse fragility curve for inelastic building model with degradation

Table 6-6 Median  $S_a$  for collapse of three building models

Building model	Median $S_{a,T1}$ (g)
Elastic	2.483
Inelastic without degradation	2.805
Inelastic with degradation	2.286

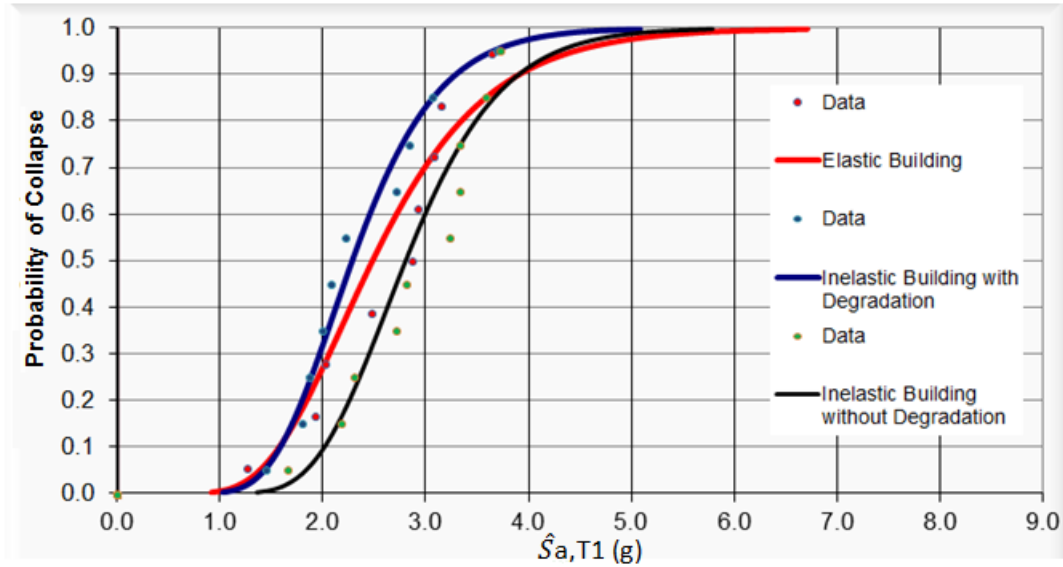


Figure 6-17 Comparison of collapse fragility curves for building models

## 6.6 Incremental Dynamic Analyses for Fire Sprinkler Piping Systems

A four-story fire sprinkler piping system model developed in OpenSees was adopted for the IDA in order to construct seismic fragility curves with peak floor acceleration (PFA) as the demand parameter.

The fire sprinkler piping system models used for IDA had identical layout for each floor, and the layout was the same as that from the first level of the fire sprinkler piping system assessed for the dynamic testing (see Chapter 4). The detailed layout and three-dimensional rendering of the fully braced systems are presented in *Figure 6-18* and *Figure 6-19*, respectively.

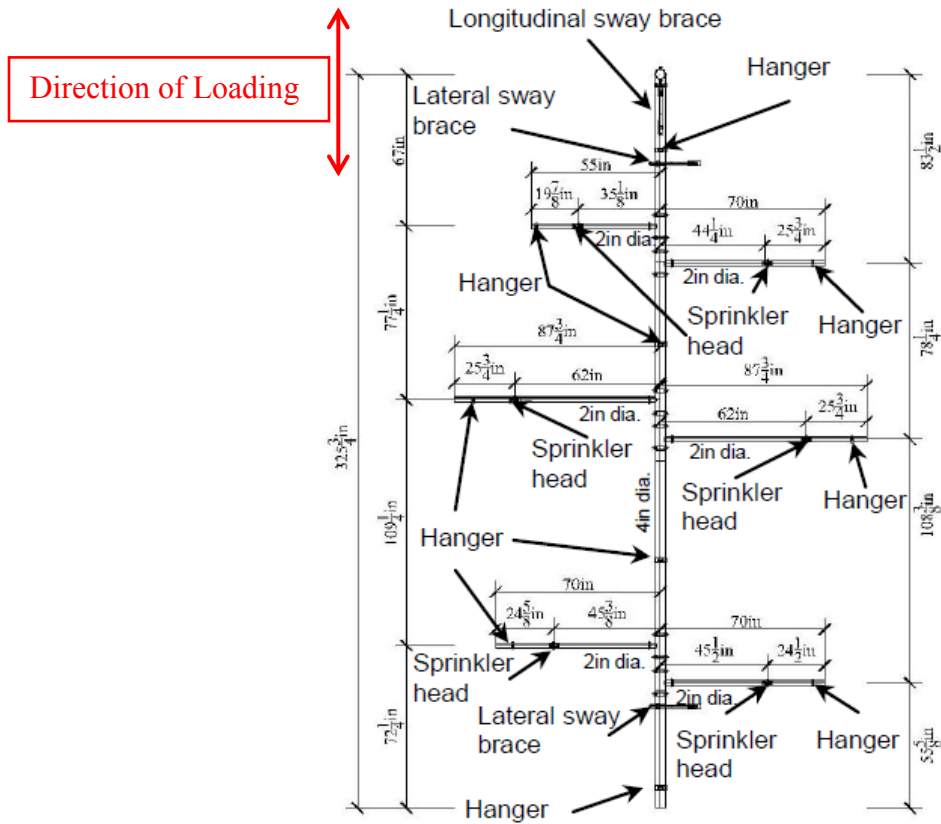


Figure 6-18 Layout of first level of test specimen

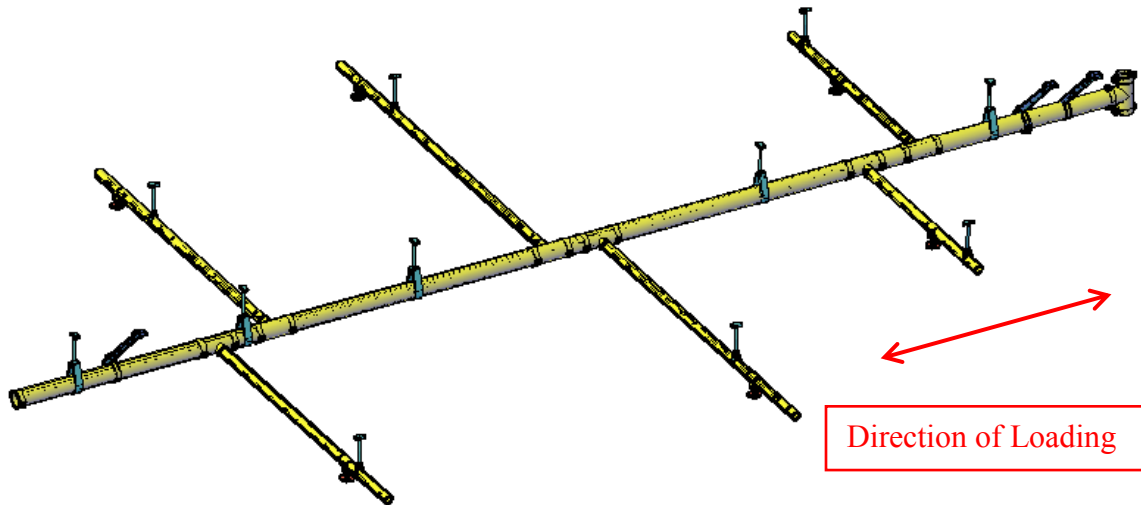


Figure 6-19 Three-dimensional rendering of layout

To take into account the effects of piping materials and bracing systems in the fragility assessment, a total of three configurations of fire sprinkler piping system were combined with various building model configurations in the numerical study presented in this section. The details of the combinations are summarized in *Table 6-7*.

*Table 6-7 Combinations of fire protection system configurations and building models*

Combination #	Building Model Configuration	Fire Sprinkler Piping System Configuration	
		Bracing Level	Piping Materials and Joint Types for Branch Lines
1	Elastic	Fully braced	Black iron with threaded connections
2	Inelastic without strength degradation	Fully braced	Black iron with threaded connections
3	Inelastic with strength degradation	Fully braced	Black iron with threaded connections
4		Fully braced	CPVC with cement joints
5		Unbraced	Black iron with threaded connections

According to NFPA 13 (NFPA, 2010), flexible couplings are required and installed on riser above and below the floor in multistory buildings and extra opening space is provided around the piping ground through the floor. Based on the observations from the dynamic testing, both requirements will isolate the dynamic response of each level of the fire sprinkler piping system from that of the adjacent levels. As a result, only a single-story fire sprinkler piping system with the layout shown in *Figure 6-18* was considered and used repeatedly for all IDA in order to shorten the computational overhead required in OpenSees.

The absolute displacement time histories from each floor obtained from the fragility analyses of the building models presented in Section 6.3 were utilized as the input for the seismic fragility



analyses of the single-story fire sprinkler piping systems. Each of the displacement floor response histories was applied to the building-attached components of the vertical hangers and the bracings. The direction of loading was assumed parallel to the main line and perpendicular to the six branch lines, as illustrated in *Figure 6-19*. The nonlinear dynamic response analysis was performed and the maximum rotations that occurred at the six tee joints connecting the branch lines to the main line were retained. The relationship between the maximum measured joint rotation at the tee joints and the peak floor acceleration (PFA) was first plotted; an example of this relationship is shown in *Figure 6-20* for the fire protection system located in first floor of the building model for Combination 2.

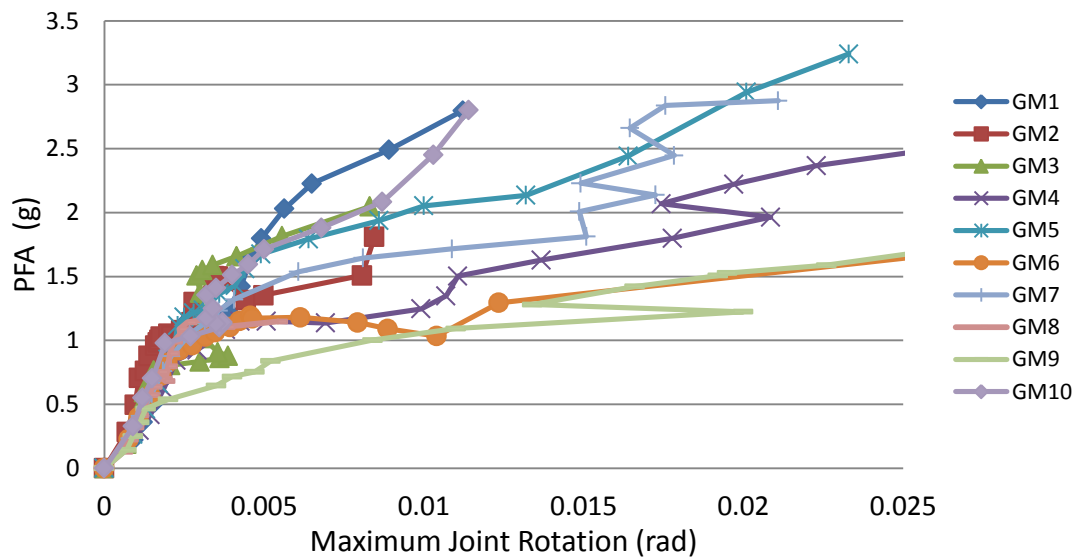


*Figure 6-20 Illustration of IDA curves for fire sprinkler piping system*

A number was pseudo-randomly generated following a log-normal distribution with the median first-leakage joint rotational capacity and the corresponding standard deviation for both types of piping materials and joint arrangements (black iron with threaded connections and CPVC with

cement joints), which were calculated from the tee joint component testing presented in Chapter 3. For each earthquake ground motion, this process was repeated and this pseudo-randomly generated number was then considered as the new rotational capacity for all the 2-inch tee joints, and the new rotational capacity was compared with the maximum joint rotation recorded from each of the nonlinear time-history dynamic analyses. This approach was taken to simulate the uncertainty in the properties of the tee joints installed in the sprinkler piping systems at a given floor. If the maximum joint rotation was larger than the rotational capacity, it was considered that the system had leaked, and the corresponding PFA was taken as a datum point. The fragility curve giving the relationship between the probability of exceeding the first-leakage joint rotational capacity and PFA was then constructed and a log-normal cumulative probability distribution was fitted to the data. The first-leakage fragility curves for all four stories (Combination #1) are presented in *Figure 6-21* as an illustration.

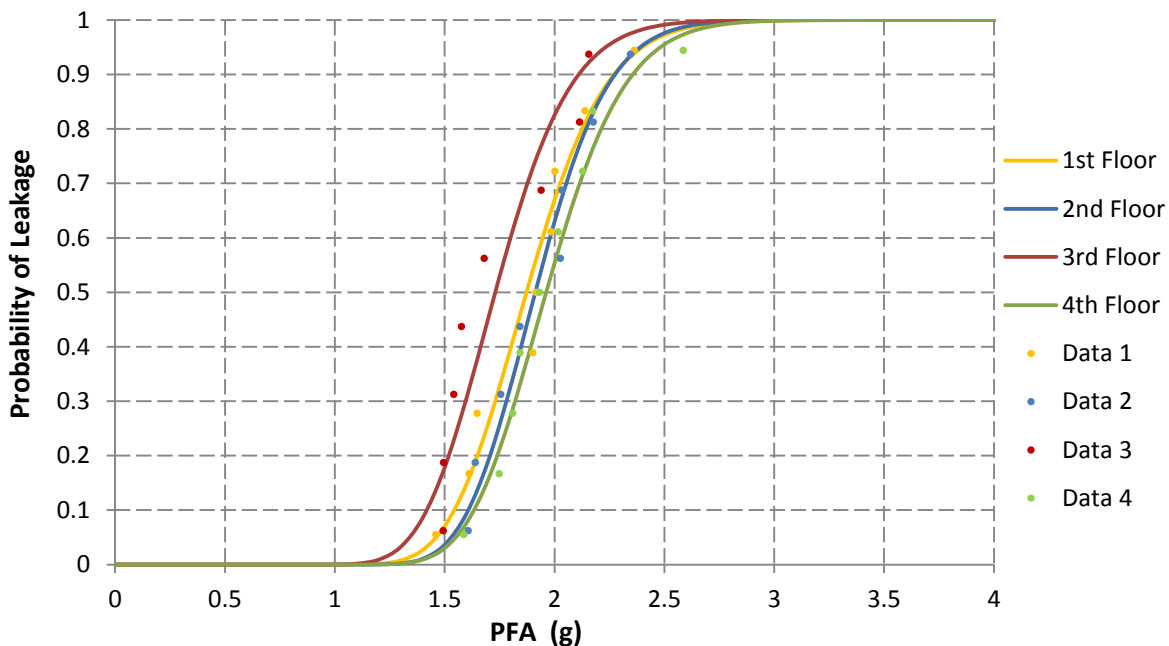


*Figure 6-21 First-leakage fragility curves of fire sprinkler piping system (Combination #1)*

## 6.7 IDA Results and Discussions

*Table 6-8* summarizes the median PFA and dispersion for the first leakage of the fire sprinkler piping system located at each floor of the building models for all five combinations. It can be observed from *Table 6-8* that the fragility of fire sprinkler piping systems appears to be insensitive to the floor on which they are located when it is considered in terms of PFA. However, as higher PFA is usually expected in upper levels of a multi-story building, fire sprinkler piping systems would be damaged during an earthquake shaking with a lower peak ground acceleration (PGA).

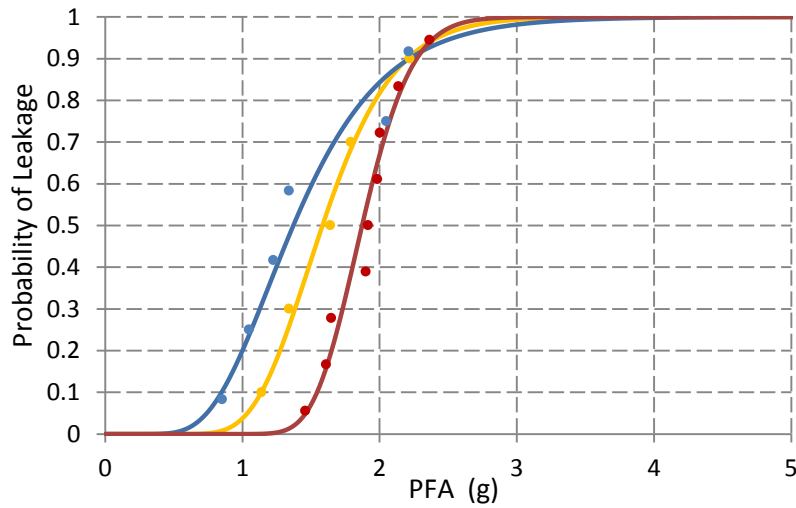
Table 6-8 Summary of median PFA and dispersion for first leakage of the fire sprinkler piping systems for all combinations considered

Combination #	1 <sup>st</sup> Floor		2 <sup>nd</sup> Floor		3 <sup>rd</sup> Floor		4 <sup>th</sup> Floor	
	Median PFA (g)	Dispersion	Median PFA (g)	Dispersion	Median PFA (g)	Dispersion	Median PFA (g)	Dispersion
1	1.87	0.15	1.91	0.14	1.73	0.15	1.96	0.14
2	1.58	0.26	1.23	0.28	1.27	0.25	1.45	0.11
3	1.37	0.37	1.08	0.30	1.12	0.23	1.35	0.20
4	1.23	0.33	1.04	0.26	1.05	0.23	1.28	0.18
5	1.10	0.32	1.02	0.25	1.04	0.18	1.28	0.12

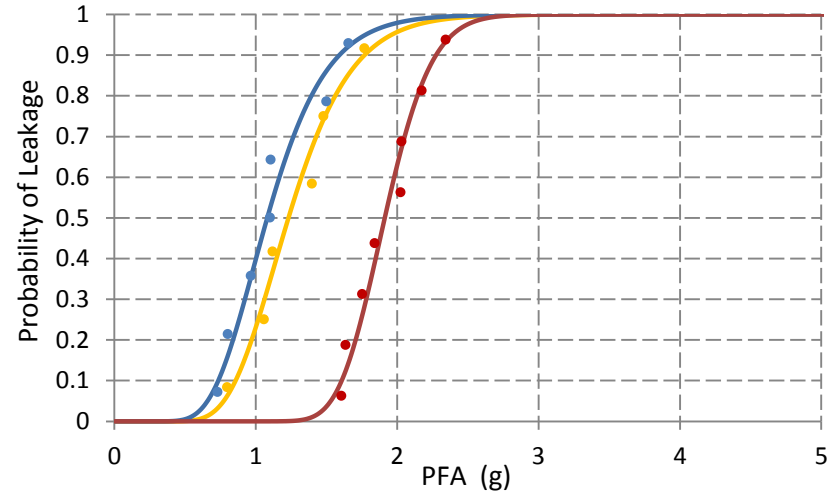
*Figure 6-22* compares the first-leakage fragility curves of fully braced fire protection systems (black iron piping with threaded connections for branch lines) at each floor for a total of three building model configurations (Combination 1: elastic building model, Combination 2: inelastic building model without strength degradation, and Combination 3: inelastic building model with strength degradation).

Fire sprinkler piping systems installed in the inelastic building model with degradation have the highest vulnerability to leak, while the fire protection systems located in the elastic building model are the least vulnerable to leakage. This general trend seems counterintuitive, since the elastic building, when subjected to the same level of earthquake shaking, experiences higher floor acceleration response compared to the inelastic building. The high floor acceleration in return will cause larger rotations of the piping joints. To explain this result, Fourier Transform was applied to two response histories of floor acceleration, which were both recorded from the first floor of the building models subjected to the same earthquake Ground Motion #1 under the same intensity. The first floor acceleration history was taken from the elastic building model, and the other one was from the inelastic building model with degradation. The frequency content for both floor accelerations obtained from the Fourier Transform is shown in *Figure 6-23*. The vertical red line indicates the fundamental period of the fire sprinkler piping system. It can be seen that the modal frequency of the fire protection systems have little overlap with the frequency content of the elastic building model, which will cause less system response and rotation at the piping joints. In contrast, the inelastic building model experiences quasi-resonance with the fire protection systems, which will result in larger joint rotations and lead to higher

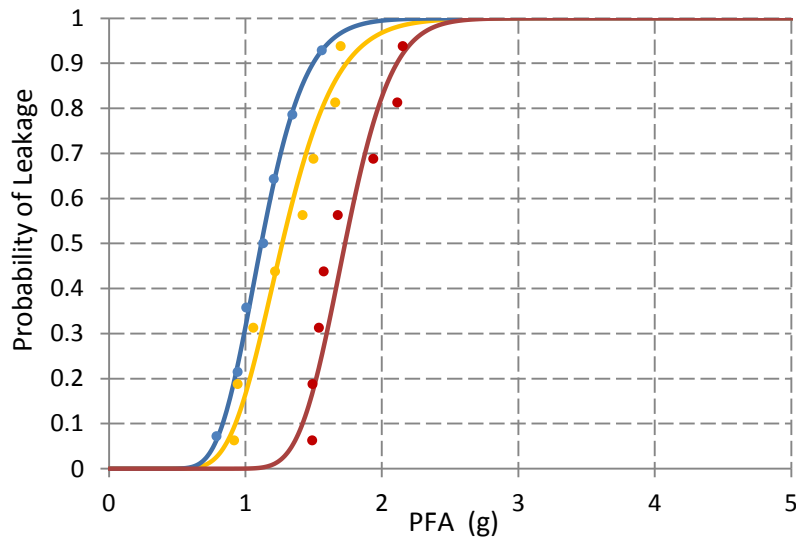
vulnerability of the entire system. Similar observations can also be made from other time histories of floor accelerations recorded from the elastic and the inelastic building models.



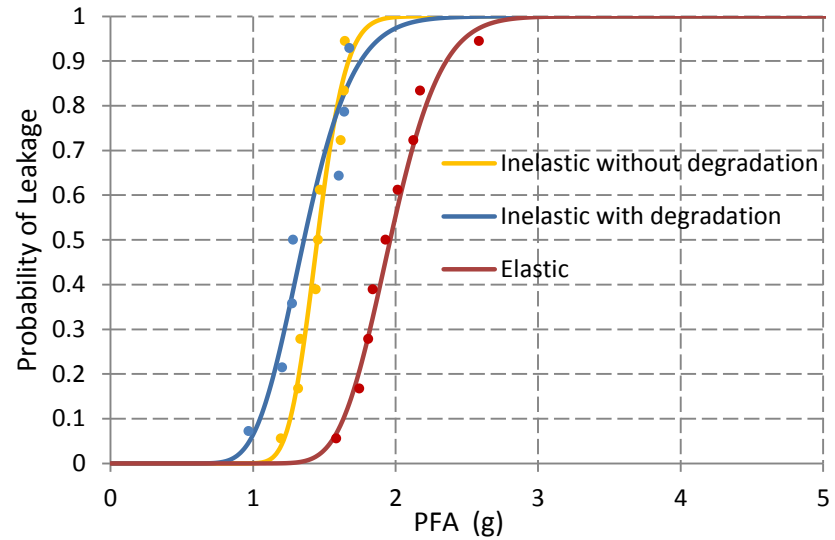
(a) First-leakage fragility curves for the first floor



(b) First-leakage fragility curves for the second floor

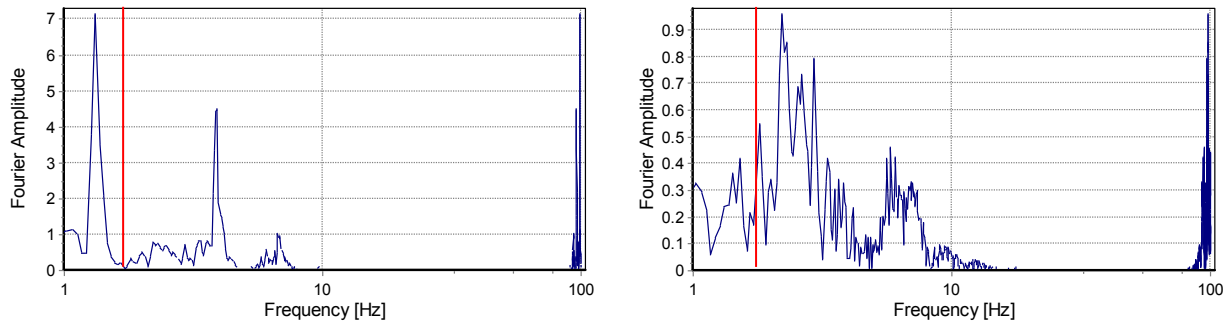


(c) First-leakage fragility curves for the third floor



(d) First-leakage fragility curves for the fourth floor

Figure 6-22 Comparison of first-leakage fragility curves for fully braced fire sprinkler piping systems made of black iron piping with threaded connections



(a) Frequency content of acceleration history (elastic) (b) Frequency content of acceleration history (inelastic)

Figure 6-23 Comparison of frequency content

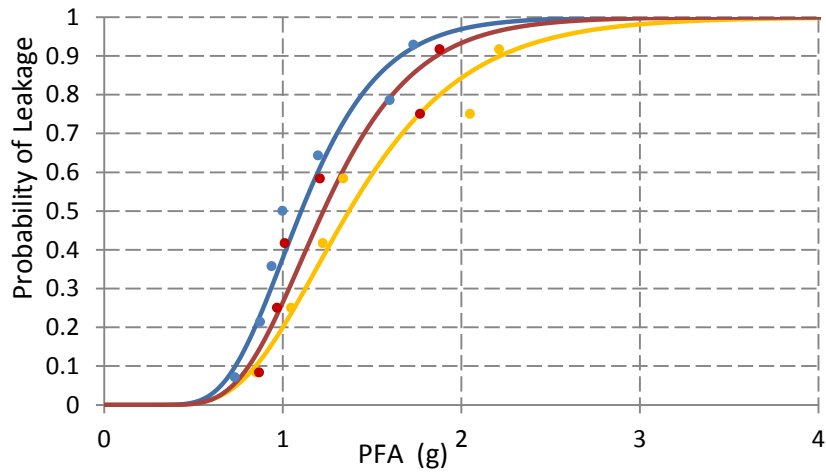
Figure 6-24 compares the first-leakage fragility curves for three types of fire sprinkler piping systems (Combination 3: fully braced fire protection systems with black iron piping for branch lines, Combination 4: fully braced fire protection systems with CPVC plastic piping for branch lines, and Combination 5: unbraced fire protection systems with black iron piping for branch lines), which were installed in the inelastic building model with strength degradation.

The unbraced fire sprinkler piping system with black iron piping for branch lines is the most vulnerable to leakage, while the fully braced counterpart possesses the least vulnerability. The fully braced fire protection system with CPVC piping for branch lines lies in between. However, the difference of median PFA for all three combinations is relatively small. Validations are made again for the observations made during the dynamic tests presented in *Chapter 4* as follows:

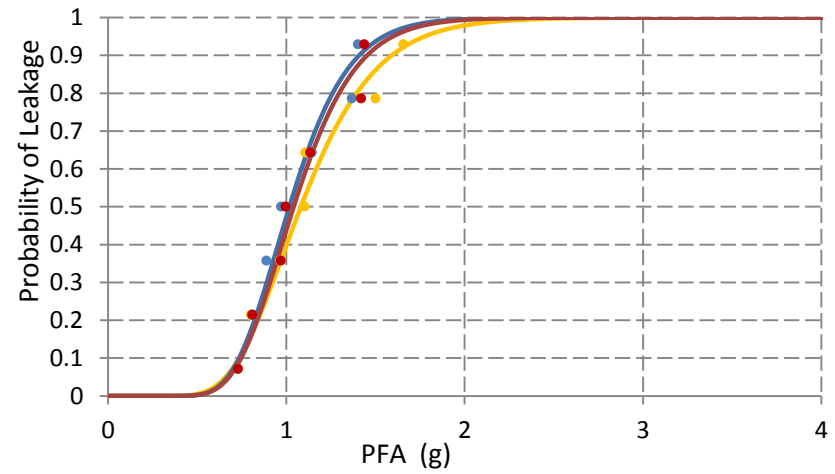
- even though CPVC pipes with cement joints have significantly larger rotational capacities, fire protection systems constructed with CPVC pipes may not outperform systems made of black iron pipes with threaded connections, since specimens made of CPVC pipes also have much larger rotational responses at the pipe joints with the same level of input intensities;



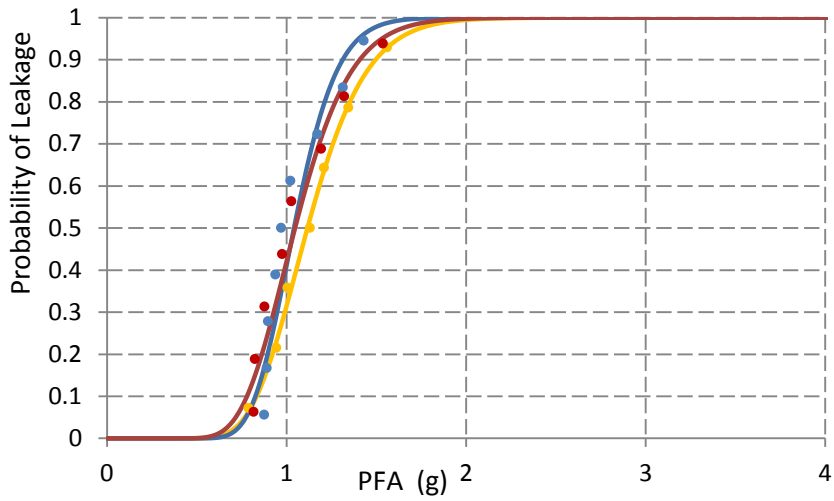
- the effect of bracing systems for protection the fire sprinkler piping systems is consistent between the observations made during the dynamic tests and the fragility curves, both of which show that fully braced fire protection systems are less vulnerable compared with the unbraced systems when subjected to the same level of seismic loading.



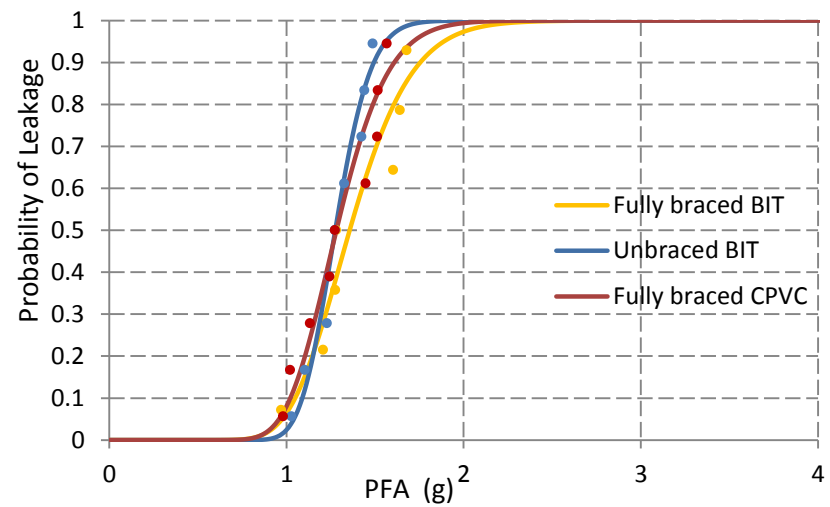
(a) First-leakage fragility curves for the first floor



(b) First-leakage fragility curves for the second floor



(c) First-leakage fragility curves for the third floor



(d) First-leakage fragility curves for the fourth floor

Figure 6-24 Comparison of first-leakage fragility curves for fire sprinkler piping systems in terms of piping materials and bracing systems (BIT indicates black iron piping with threaded connections for branch lines, and CPVC indicates CPVC piping with cement joints for branch lines)

## 6.8 Summary

The MCEER WC70 hospital was adopted in order to demonstrate the use of numerical modeling to conduct seismic fragility analyses of fire sprinkler piping systems. A total of three configurations (elastic building model, inelastic building model without strength degradation, and inelastic building model with strength degradation) were developed based on the prototype building and used for this fragility analyses. A four-story fire protection system with an identical layout at each floor was assumed to be installed in each of the three building models. Various piping materials and joint types (black iron with threaded joints, and CPVC with cement joints), as well as levels of bracing systems (fully braced and unbraced) were included in the numerical study.

Although the fire sprinkler piping systems considered in this Incremental Dynamic Analyses were relatively simple, the methodology for obtaining the first-leakage fragility curves of fire protection systems based on peak floor acceleration as demand parameter, however, can be generalized to real buildings with real sprinkler piping systems. The generalized procedures for constructing first-leakage fragility curves for fire protection systems are presented in *Figure 6-25*.

It has to be pointed out that real fire sprinkler piping systems consist of a large number of piping joints, each of which would be simulated by rotational spring element and rotational properties for the joint would be determined and assigned in a similar way that was presented in *Chapter 5*. As a result, the computer overhead required to conduct the complete IDA and to obtain the first-leakage fragility curves of fire protection systems is extremely high.

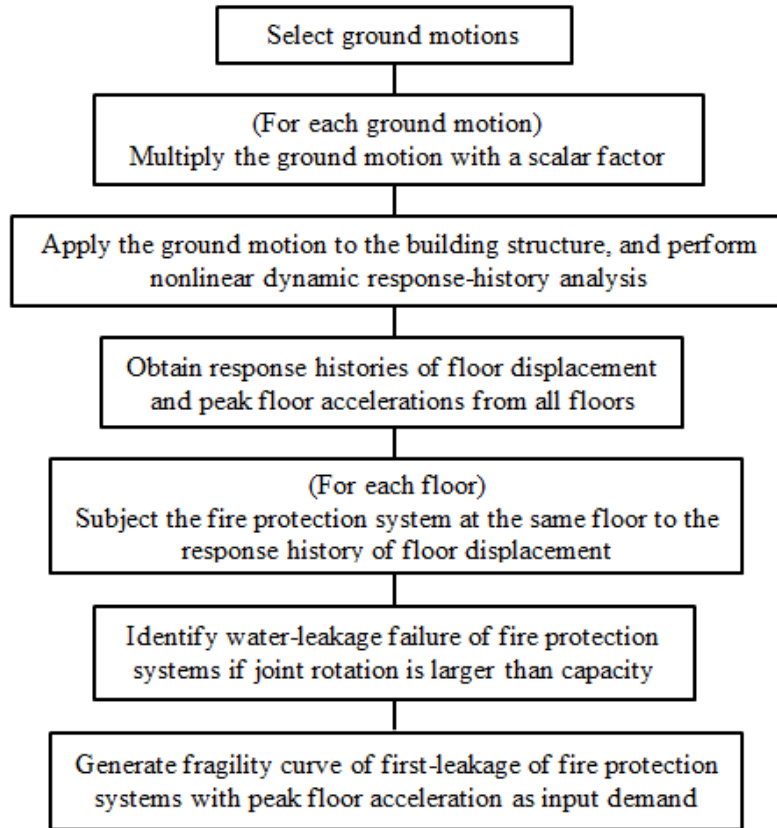


Figure 6-25 Procedures of conducting fragility analyses for fire sprinkler piping systems

## Chapter 7

# SUMMARY, CONCLUSIONS AND RECOMMENDATIONS FOR FUTURE RESEARCH

### 7.1 Summary

A fire sprinkler piping subsystem not only accounts for a significant portion of typical investment in building construction, but also represents one of the key components that ensures the functionality and safety of a building. However, recent earthquakes have sometimes demonstrated the vulnerability of the fire extinguishing sprinkler piping subsystem, which has led to a wide range of damage resulting in substantial property loss, loss of building functionality, and potential fire spread and loss of life. Limited research has been conducted on sprinkler piping subsystems under seismic loading and information obtained from previous studies is not sufficient to fully describe their dynamic response and failure mechanism. In order to better understand the seismic behavior of fire suppression systems and their interaction with other structural members and nonstructural subsystems, experimental and numerical studies were conducted as part of The George E. Brown, Jr., Network for Earthquake Engineering Simulation - Nonstructural Grand Challenge Project (NEES - NGC).

In this dissertation, two test series were carried out in the Structural Engineering and Earthquake Simulation Laboratory (SEESL) at the State University of New York in Buffalo. In the first series, a total of 48 tee joint components for sprinkler piping systems with nominal diameters from  $\frac{3}{4}$ " to 6" and made of various materials and joint types (black iron with threaded joints,

chlorinated polyvinyl chloride (CPVC) with cement joints, and steel with groove-fit connections) were tested under reverse cyclic loading to determine their rotational capacities at which leakage and/or fracture occurred. The failure mechanisms observed in the piping joints were identified and the ATC-58 framework was applied to develop a seismic fragility database for pressurized fire sprinkler joints.

Subsequently, two-story, full-scale (11 ft. × 29 ft.) fire extinguishing sprinkler piping subsystems were tested on the University at Buffalo Nonstructural Component Simulator (UB-NCS). A total of three specimens with different materials and joint arrangements were tested with various bracing systems under dynamic loading.

A number of hysteresis models were introduced to simulate the nonlinear moment-rotation behavior of tee joint components made of various materials and joint types. The proposed hysteresis models were capable of capturing the strength degradation, change of stiffness during unloading, as well as energy dissipation. As a result, nonlinear rotational springs using the calibrated analytical models were selected to model full-scale fire sprinkler piping systems. To validate the numerical model, simulations based on the UB-NCS seismic tests were conducted.

Finally, a hypothetical acute care facility equipped with full-scale fire sprinkler systems was selected as an example of the use of the numerical model to develop seismic fragility curves for sprinkler piping systems with floor accelerations as the demand parameter.

## 7.2 Conclusions

### 7.2.1 Conclusions from the experimental studies

The main conclusions drawn from the quasi-static component tests are listed as follows:

- All joint types exhibited significant rotational capacities at first leakage ranging from 0.005 rad. to 0.405 rad.
- Among the four joint types tested, the CPVC pipes with cement joints had the largest rotational capacities at first leakage but also had the smallest moment capacities (one tenth of the other joint types). CPVC piping, especially if unbraced, may experience large joint rotation demands due to its lower strength and stiffness.
- The monotonic rotational capacities at first leakage for both, black iron threaded and CPVC cement joints were significantly larger than their corresponding cyclic rotational capacities. This result indicates that these types of joints are susceptible to cumulative damage during small earthquakes, which could reduce their rotational capacities during larger events. On the other hand, monotonic and cyclic rotational capacities at first leakage were similar for the steel pipes with groove-fit connections.
- The rotational capacities at first leakage decreased with an increase of pipe diameter for black iron pipes with threaded joints and CPVC pipes with cement joints. This result can be explained by the fact that the average axial slip across a joint at first leakage of a given type is essentially a constant for all pipe diameters. This result indicates that pipes with black iron threaded and CPVC cement joints behave essentially as flexural beams in which first leakage occurs when a “critical extreme fiber strain” is reached, allowing for the prediction of rotation at leakage for any pipe diameter.

- The observed behavior of steel pipes with groove-fit joints was different depending on their wall thickness. For the thicker schedule 40 steel pipes (0.24 in. wall thickness), first leakage coincided with failure of the coupling flanges causing the rotational capacities to reduce with an increase of pipe diameter (2 in. to 4 in. pipes). For the thinner schedule 10 steel pipes (0.13 in. wall thickness), significant inelastic deformations occurred in the pipe sections before failure of the couplings. For this group, the rotational capacities increased with pipe diameter.

The main observations obtained from the dynamic tests are summarized as follows:

- All three fully braced specimens performed well and suffered no damage under the Maximum Considered Earthquake (MCE) level of loading, thereby validating the current code-based requirements for bracing system design. However, the unbraced systems, which are typically installed in low to moderate seismic regions or are present in older buildings, experienced extensive damage among the vertical hangers, ceiling tiles, sprinkler heads, and pipe joints.
- For a number of cases, although the fire suppression sprinkler piping system survived the dynamic shaking without any significant damage to the supporting system (vertical hangers, wire restraints and bracing), unexpected activation of sprinkler heads was triggered due to the pounding with ceiling tiles, which led to the loss of water pressure and failure of the entire system. This indicates that the differential displacement of suspended ceiling system and the fire suppression sprinkler piping system remains a critical threat to the normal functionality of sprinkler piping system.



- Traditionally, a specific nominal annual space is cut to provide extra clearance for the riser that penetrates concrete and masonry floors. Moreover, according to the NFPA 13 (NFPA, 2010), flexible couplings are required on the riser above and below the floor in multistory buildings. Substantial margin is provided for the riser to accommodate the inter-story drifts. This was validated in the tests as no damage to the riser was observed during the entire testing program even though the maximum inter-story drift reached 3% of story height.
- Based on the observations obtained from *Chapter 3*, CPVC pipes with cement joints and steel pipes with groove-fit connections have significantly larger rotational capacities compared to the black iron pipes with threaded joints. However, it does not necessarily ensure that fire protection systems constructed with CPVC pipes with cement joints or steel pipes with groove-fit connections would be the best choice as far as seismic performance is concerned. The test results showed that specimens made of CPVC pipes and Dyna-Flow pipes also have much larger rotational responses at the pipe joints for similar levels of input intensities.

### 7.2.2 Conclusions from the numerical study

- The proposal of using Multi-linear Pivot model in SAP2000, as well as Pinching4 and Hysteretic Material model in OpenSees to simulate the moment-rotation hysteretic responses for various tee joint configurations was successful, as the numerical models were capable to provide close agreements with the experimental results.
- OpenSees has the great advantage over other general-purpose analysis software in terms of numerically simulating fire sprinkler systems, because OpenSees provides robust

choice of material models with the capability of simulating different tee joint configurations.

- With the enhanced understanding of both tee joint components and full-scale fire sprinkler piping systems, it was possible to perform nonlinear response-history dynamic analysis on fire sprinkler piping systems with any building-specific layout, and construct the first-leakage fragility curves with floor accelerations as the demand parameter although the computational overhead would remain an issue.

### **7.3 Recommendations for Future Work**

Although the research work discussed in this dissertation has significantly enhance the understanding of the dynamic characteristics of fire sprinkler piping subsystems under seismic loading, more research is required. The recommendations for future research are:

- To include piping elbow joints for quasi-static tests and development of a seismic fragility for elbow joints with various sizes. Unlike the piping tee joints, elbow joints are subjected to both torque and moment simultaneously in most cases. The combination of torque and moment may considerably reduce the rotational capacities of piping connections.
- To cover more piping size. In this study, only some available pipe sizes for the three most common piping materials were considered. The information missing for the rest of configurations needs to be completed. This can be achieved in two ways: 1) Both experimental and analytical research has to be repeated for other sizes of pipe fittings; 2)

The analytical methodology needs to be developed so that interpolation can be applied to obtain the moment-rotation relation for other pipe sizes.

- To include vertical acceleration in the dynamic tests of full-scale fire sprinkler piping systems. Vertical acceleration is a crucial component that induces damage to nonstructural components and leads to severe interactions among nonstructural subsystems. One of the reasons that little damage has been observed during the second series of experimental study may be attributed to the lack of vertical acceleration inloading input.
- To include other nonstructural subsystems in the dynamic tests. The dynamic tests conducted at the subsystem level only consider the interactions between the fire sprinkler piping systems and the artificial ceiling boxes. In reality, the fire sprinkler piping systems are surrounded by a wide range of nonstructural components, such as ducts for heating, ventilation and air conditioning (HVAC), partition walls, and suspended ceiling subsystems.
- To use generic fire protection system layouts instead of building-specific piping system for IDAs.

## REFERENCES

- Antaki, G., and Guzy, D. (1998). "Seismic testing of grooved and threaded fire protection joints and correlation with NFPA seismic design provisions." *Proceedings: ASME Proceedings, Pressure Vessels and Piping Division, PVP-Vol. 364, Seismic Engineering*, 69-75.
- American Society of Civil Engineers (ASCE). (2010). "Minimum Design Loads for Buildings and Other Structures." *ASCE 7-10*, American Society of Civil Engineers.
- Ayres, J. M., and Ezer (1996). "Northridge Earthquake Hospital Water Damage Study." Office of Statewide Health Planning and Development, Sacramento, CA.
- Bachman, R. (1998). "Building Code Seismic Design Provisions for Nonstructural Components." *Proceedings: ATC 29-1: Seminar on Seismic Design, Retrofit, and performance of Nonstructural Components*, Applied Technology Council San Francisco, CA, 7-14.
- California. Office of Statewide Health Planning and Development., Ayres & Ezer Associates Inc., and Hillman Biddison & Loevenguth. (1996). "Northridge earthquake hospital water damage study." Office of Statewide Health Planning & Development, Division of Facilities Development, [Sacramento, Calif.
- Carr, A. J. (2005). Computer Program RUAUMOKO, Canterbury: Department of Civil Engineering, University of Canterbury.
- Chock, G. (2006). "Preliminary Observations on the Hawai'i Earthquakes of October 15, 2006." EERI Special Earthquake Report.
- CIRCOR (2012). "Fitting Installation Manual." CIRCOR Instrumentation Technologies  
CORR (2002). "Engineering Guide." CORR Tech. Inc.
- Davies, R. D. (2010). "Seismic Evaluation, Parameterization, and Effect of Light-Frame Steel Studded Gypsum Partition Walls." M.S. Thesis, State University of New York at Buffalo.
- Dillingham, J. S., and Goel, R. K. (2002). "Dynamic Properties of Fire Sprinkler Systems." Report CP/SEAM-2002/04.
- EERI (2010). "The M 8.8 Chile Earthquake of February 27, 2010." EERI Special Earthquake Report, Earthquake Engineering Research Institute.
- EQE (2001). "Seattle (Nisqually), Washington Earthquake of February 28, 2001 ", EQE International, San Francisco, CA.
- FEMA (2000). "FEMA 366: HAZUS-MH Estimated Annualized Earthquake Losses for the United States." Federal Emergency Management Agency Washington, D.C.

FEMA (2003). "FEMA 450: NEHRP Recommended Provisions and Commentary for Seismic Regulations for New Buildings and Other Structures." Federal Emergency Management Agency Washington, D.C.

FEMA (2006). "FEMA 461: Interim protocols for determining seismic performance characteristics of structural and nonstructural components through laboratory testing." Federal Emergency Management Agency Washington, D.C.

FEMA (2011). "FEMA E-74: Reducing the Risks of Nonstructural Earthquake Damage—A Practical Guide." Federal Emergency Management Agency Washington, D.C.

Filiatrault, A., Christopoulos, C., and Stearns, C. (2001). "Guidelines, Specifications, and Seismic Performance Characterization of Nonstructural Building components and Equipment." Report PEER 2002/05, Pacific Earthquake Engineering Research Center, University of California, Berkeley.

Fleming, R. P. (1998). "Analysis of Fire Sprinkler System Performance in the Northridge Earthquake." Report No. NIST-GCR-98-736, U.S. Department of Commerce, Building and Fire Research Laboratory, National Institute of Standards and Technology, Gaithersburg, MD.

Frank McKenna, G. L. F., Filip C. Filippou, Silvia Mazzoni, Michael Scott, Boris Jeremic, Ahmed Elgamal, Zhaohui Yang, Jinchu Lu, Pedro Arduino, Peter Mckenzie, Gregory G. Deierlein, Kincho Law (1999). Computer Program The Open System for Earthquake Engineering Simulation (OpenSees), Berkeley: Pacific Earthquake Engineering Research Center, University of California -- Berkeley.

Gasparini, D., and Vanmarke, E. (1976). Computer Program SIMQKE, <http://nisee.berkeley.edu/elibrary/getpkg?id=SIMQKE1>.

Global, F. (2001). "Nisqually (Seattle, Wash., USA) Earthquake." *Understanding the Hazard*, Report P0042, FM Global.

Goodwin, E. R., Maragakis, E. M., and Itani, A. M. (2007). "Experimental Evaluation of the Seismic Performance of Hospital Piping Subassemblies." *Technical Report MCEER-07-0013*, Multidisciplinary Center for Earthquake Engineering Research.

Hoehler, M. S., Panagiotou, M., Restrepo, J. I., Silva, J. F., Floriani, L., Bourgund, U., and Gassner, H. (2009). "Performance of Suspended Pipes and Their Anchorages During Shake Table Testing of a Seven-Story Building." *Earthq Spectra*, Vol. 25(1), 71-91.

ICBO (1997). "Uniform Building Code." International Conference of Building Officials, Whittier, CA.

ICC-ES (2007). "AC156: Acceptance criteria for seismic qualification by shake-table testing of nonstructural components and systems." International Code Council Evaluation Service.

International Code Council (ICC). (2004). "Acceptance Criteria for Seismic Certification by Shake-Table Testing of Nonstructural Components." *AC 156*, International Code Council.

IEEE (2006). "IEEE Recommended Practice for Seismic Design of Substations." Institute of Electrical and Electronic Engineers.

Inc., M. (2012a). Computer Program MATLAB, <http://www.mathworks.com/products/matlab/>.

Inc., O. (2012b). "Products Catalog." <http://www.omegadyne.com/ppt/prod.html?ref=LC202>.

Ju, B. S. (2011). "Seismic Fragility of Piping System." Ph.d. Dissertation, North Carolina State University.

Kircher, C. A. (2003). "It Makes Dollars and Sense to Improve Nonstructural System Performance." *Proceedings: ATC 29-2: Proceedings of Seminar on Seismic Design, Performance, and Retrofit of Nonstructural Components in Critical Facilities*, Applied Technology Council and the Multidisciplinary Center for Earthquake Engineering Research Newport Beach, CA, 109-120.

Lilliefors, H. (1967). "On the Kolmogorov-Smirnov Test for Normality with Mean and Variance Unknown." *Journal of the American Statistical Association*, 62, 399-402.

Lowes, L. N., and Mitra, N. (2004). "A Beam-Column Joint Model for Simulating the Earthquake Response of Reinforced Concrete Frames." *Technical Report PEER 2003/10*, Pacific Earthquake Engineering Research Center.

Malhotra, P. K., Senseny, P., Braga, A. C., and Allard, R. L. (2003). "Testing Sprinkler-Pipe Seismic-Brace Components." *Earthq Spectra*, Vol. 19(1), 87-109.

Martínez, G. E. S. (2007). "A Comparative Study of a Piping System Subjected to Earthquake Loads Using Finite Element Modeling and Analysis." *Proceedings: the 2007 Earthquake Engineering Symposium for Young Researchers*, Seattle, WA, 31-51.

McKevitt, W. E., Timler, P. A. M., and Lo, K. K. (1995). "Nonstructural Damage from the Northridge Earthquake." *Canadian Journal of Civil Engineering*, Vol. 22(2), 428-437.

Miranda, E., Mosqueda, G., Pekcan, G., and Retamales, R. (2010). "Brief Report on Earthquake Reconnaissance after the M 8.8 February 27th Maule, Chile Earthquake." Earthquake Engineering Research Institute.

NFPA (2010). "NFPA 13: Automatic Sprinkler Systems Handbook." National Fire Protection Association Quincy, MA.

Nicknam, A., and Filiatrault, A. (2012). "Seismic Design and Testing of Propped Rocking Wall Systems." *15th World Conference of Earthquake Engineering*, Lisbon.

NRC (1973). "The Great Alaska Earthquake of 1964." National Research Council, National Academy of Sciences, Washington, D.C.

OSHPD (1995). "The Northridge Earthquake : A Report to the Hospital Building Safety Board on the Performance of Hospitals." Office of Statewide Health Planning and Development, Facilities Development Division, Sacramento, CA.

Porter, K., Kennedy, R., and Bachman, R. (2007). "Creating Fragility Functions for Performance-Based Earthquake Engineering." *Earthq Spectra*, Vol. 23(2), 471-489.

R. K. Dowell, F. S. S., and E. L. Wilson (1998). "Pivot Hysteretic Model for Reinforced Concrete Members." *ACI Structural Journal*, Vol. 95, pp. 607-617.

Retamales, R., Mosqueda, G., Filiatrault, A., and Reinhorn, A. M. (2008). "New Experimental Capabilities and Loading Protocols for Seismic Qualification and Fragility Assessment of Nonstructural Components." *Technical Report MCEER-08-0026*, MCEER, State University of New York at Buffalo, NY.

Retamales, R., Mosqueda, G., Filiatrault, A., and Reinhorn, A. M. (2011). "Testing Protocol for Experimental Seismic Qualification of Distributed Nonstructural Systems." *Earthq Spectra*, Vol. 27(3), 835-856.

Simulia (2007). Computer Program ABAQUS,  
<http://www.3ds.com/products/simulia/portfolio/abaqus/latest-release/>.

SMACNA (1991). "Seismic Restraint Manual Guidelines for Mechanical Systems." Sheet Metal and Air Conditioning Contractors National Association, Inc. , Chantilly, VA.

Stevenson, J. D. (1998). "A Suggested Design Procedure for Piping Systems Defined as Hazardous or Essential by U.S. Building Codes." *Proceedings: ATC 29-1: Seminar on Seismic Design, Retrofit, and Performance of Nonstructural Components*, Applied Technology Council San Francisco, CA, 79-92.

Victaulic (2008). "Filed Installation Handbook." Victaulic Company.

Whittaker, A. S., and Soong, T. T. (2003). "An Overview of Nonstructural Components Research at Three U.S. Earthquake Engineering Research Center." *Proceedings: ATC 29-2: Seminar on Seismic Design, Performance, and Retrofit of Nonstructural Components in Critical Facilities*, Applied Technology Council and the Multidisciplinary Center for Earthquake Engineering Research Newport Beach, CA, 271-280.

Wittenberghe, J. V., Baets, P. D., and Waele, W. D. (2010). "Nonlinear Contact Analysis of Different API Line Pipe Coupling Modifications." *Journal of Pressure Vessel Technology*, Vol. 132, 1-7.

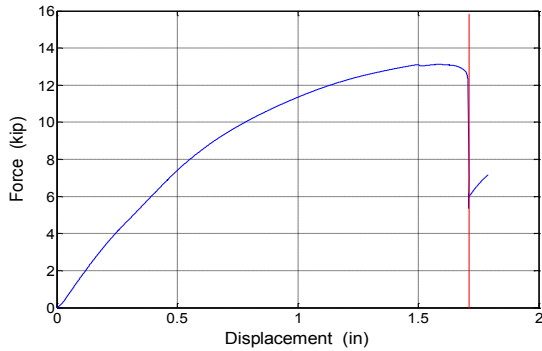
Yang, T. Y., and Whittaker, A. (2002). Computer Program "MCEER Demonstration Hospitals", Department of Civil, Structural and Environmental Engineering, University at Buffalo. (available online at <http://civil.eng.buffalo.edu/hospital/>).



## **APPENDIX A: RESULTS OF QUASI-STATIC TESTS**

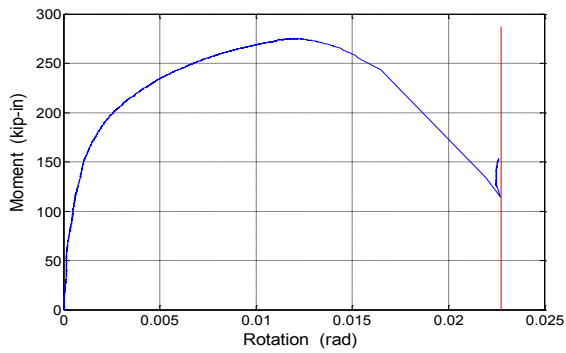
The complete results for the 48 tee joint component tests from the first phase of experimental study are presented in this section. For each tee joint configuration, one monotonic and three cyclic tests were conducted, and the result report consists of force-displacement response for the tee joint, as well as the moment-rotation responses for both side of the tee joint. For some cases, the moment-rotation response was not available due to the malfunction of potentiometers.

**MONOTONIC TEST FOR 6" BLACK IRON PIPES WITH THREADED JOINTS**

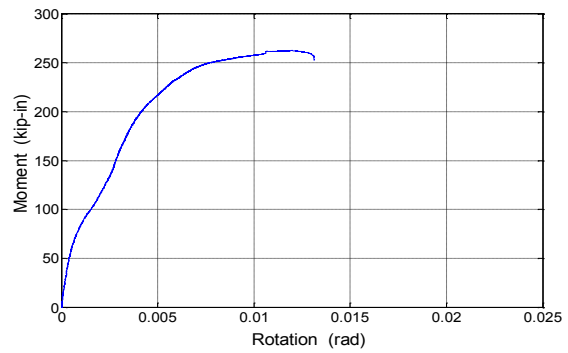


*\* The vertical red lines on these plots indicate the occurrence of the first leakage*

Force-displacement monotonic response at the tee joint



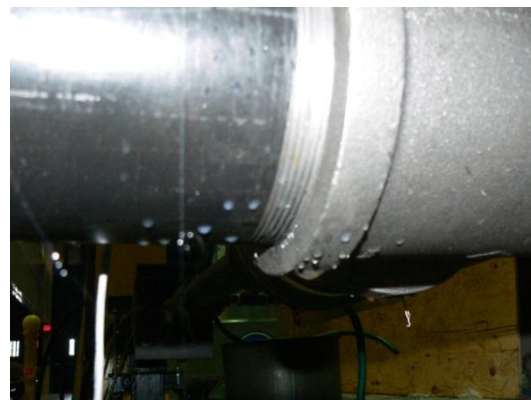
Moment-rotation monotonic response at the right end of the tee joint



Moment-rotation monotonic response at the left end of the tee joint

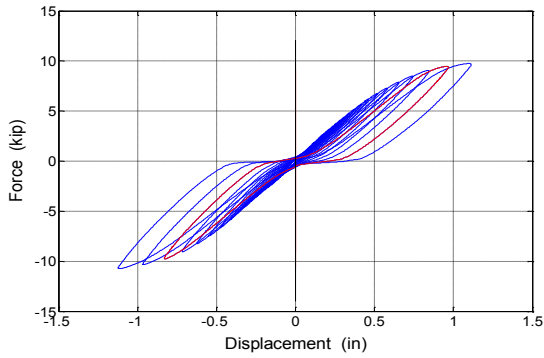


Pipe threads slip from tee threads



Water leakage from piping tee joint

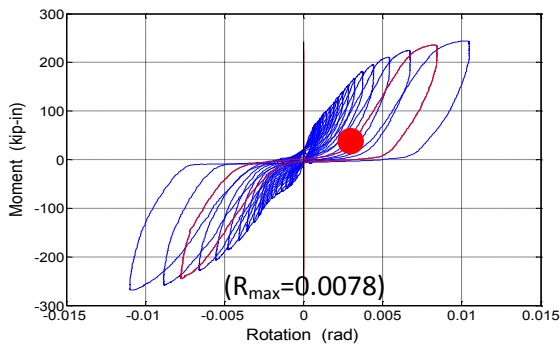
**CYCLIC TEST #1 FOR 6" BLACK IRON PIPES WITH THREADED JOINTS**



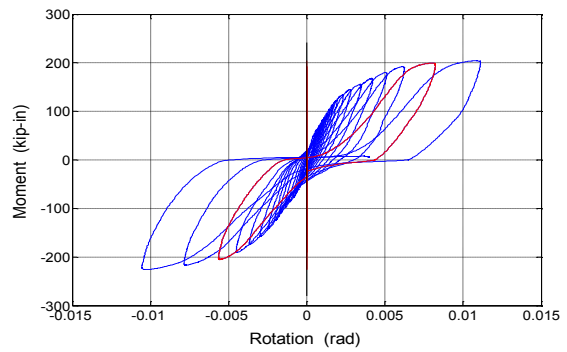
\* The red loops indicate the cycle during which the first leakage occurred.

\* The red solid dot indicates the occurrence of first leakage

Force-displacement cyclic response at the tee joint



Moment-rotation cyclic response at the right end of the tee joint



Moment-rotation cyclic response at the left end of the tee joint

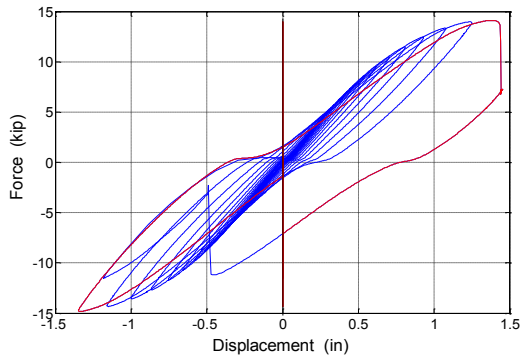


Pipe threads erode due to slippage



Pipe threads damage

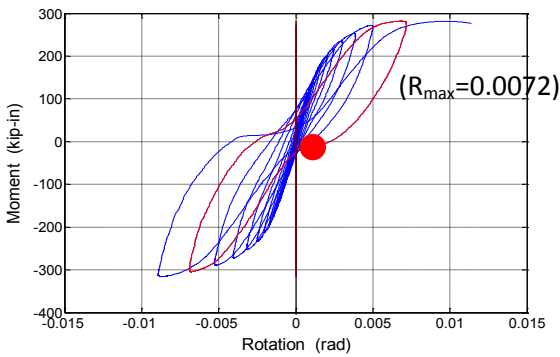
**CYCLIC TEST #2 FOR 6" BLACK IRON PIPES WITH THREADED JOINTS**



*\* The red loops indicate the cycle during which the first leakage occurred.*

*\* The red solid dot indicates the occurrence of first leakage*

Force-displacement cyclic response at the tee joint



Moment-rotation cyclic response at the left end of the tee joint

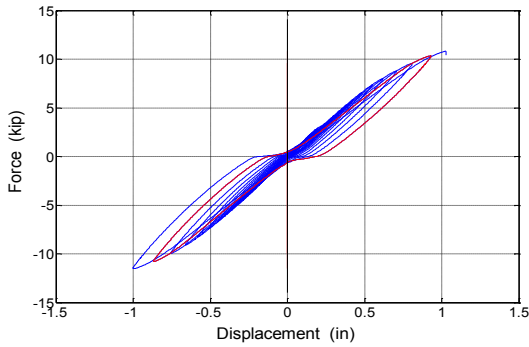


Pipe threads damage



Gap generated between pipe and tee joint due to imposed bending

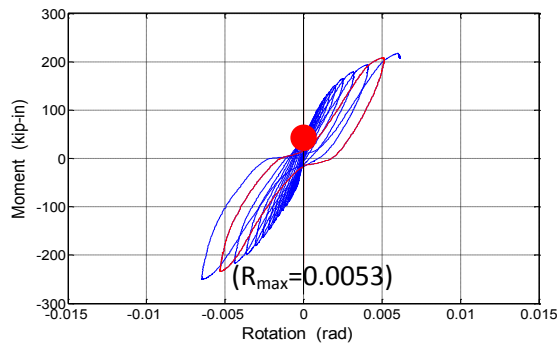
**CYCLIC TEST #3 FOR 6" BLACK IRON PIPES WITH THREADED JOINTS**



\* The red loops indicate the cycle during which the first leakage occurred.

\* The red solid dot indicates the occurrence of first leakage

Force-displacement cyclic response at the tee joint



Moment-rotation cyclic response at the left end of the tee joint

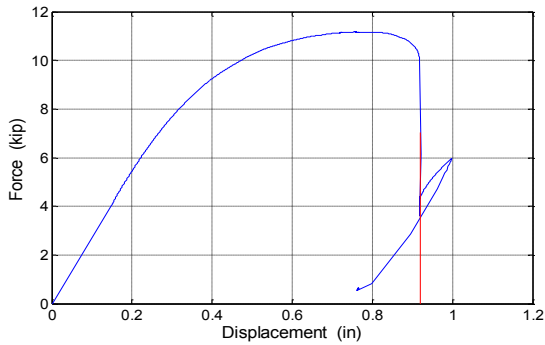


Gap generated between pipe and tee joint due to imposed bending



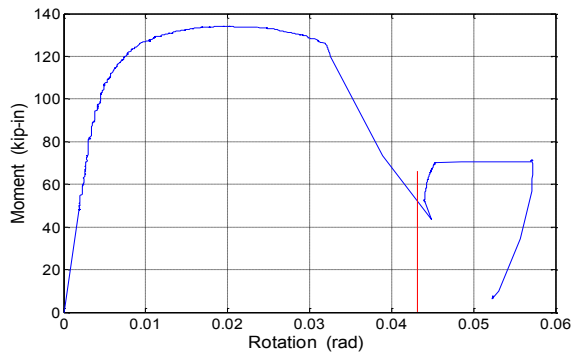
Thread sealant (Teflon tape) degraded

**MONOTONIC TEST FOR 4" BLACK IRON PIPES WITH THREADED JOINTS**



*\* The vertical red lines on these plots indicate the occurrence of the first leakage*

Force-displacement monotonic response at the tee joint



Moment-rotation monotonic response at the right end of the tee joint

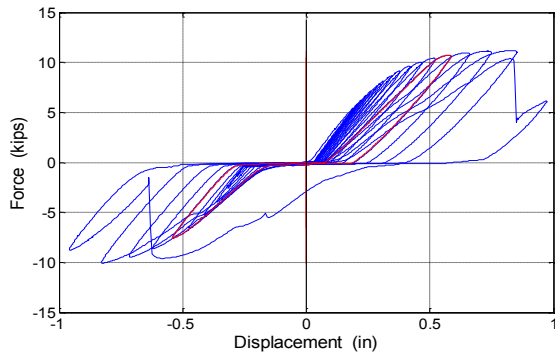


Gap generated between pipe and tee joint due to imposed bending



Pipe end bent due to imposed rotation

**CYCLIC TEST #1 FOR 4" BLACK IRON PIPES WITH THREADED JOINTS**



*\* The red loops indicate the cycle during which the first leakage occurred.*

*\* The red solid dot indicates the occurrence of first leakage*

Force-displacement cyclic response at the tee joint

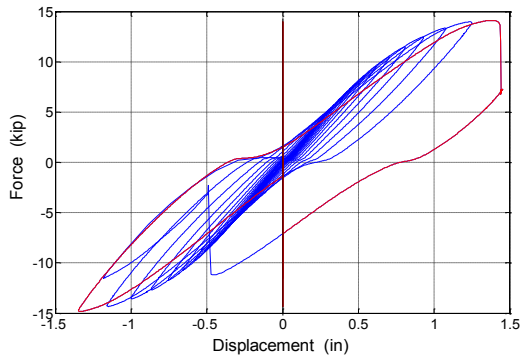


Thread sealant (Teflon tape) degraded



Pipe threads damage

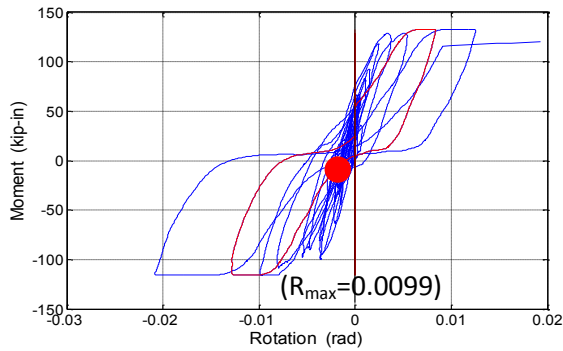
**CYCLIC TEST #2 FOR 4" BLACK IRON PIPES WITH THREADED JOINTS**



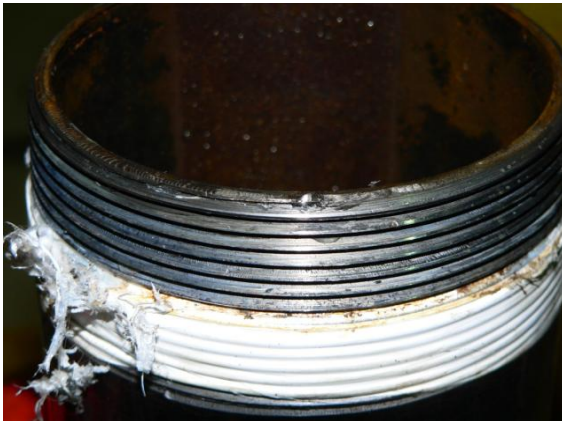
*\* The red loops indicate the cycle during which the first leakage occurred.*

*\* The red solid dot indicates the occurrence of first leakage*

Force-displacement cyclic response at the tee joint



Moment-rotation cyclic response at the left end of the tee joint



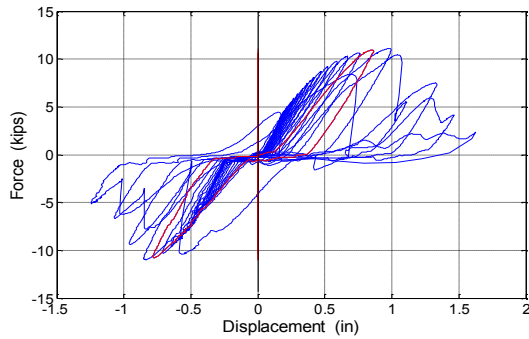
Thread sealant (Teflon tape) degraded



Gap generated between pipe and tee joint due to imposed bending



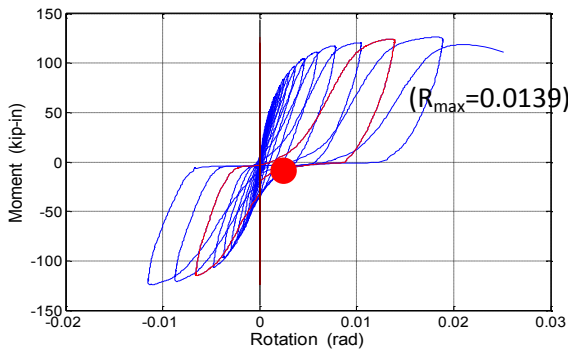
**CYCLIC TEST #3 FOR 4" BLACK IRON PIPES WITH THREADED JOINTS**



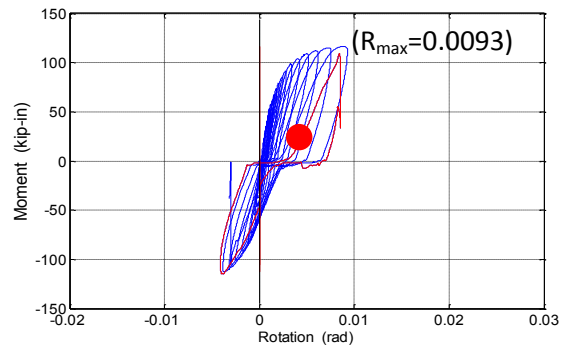
\* The red loops indicate the cycle during which the first leakage occurred.

\* The red solid dot indicates the occurrence of first leakage

Force-displacement cyclic response at the tee joint



Moment-rotation cyclic response at the right end of the tee joint



Moment-rotation cyclic response at the left end of the tee joint

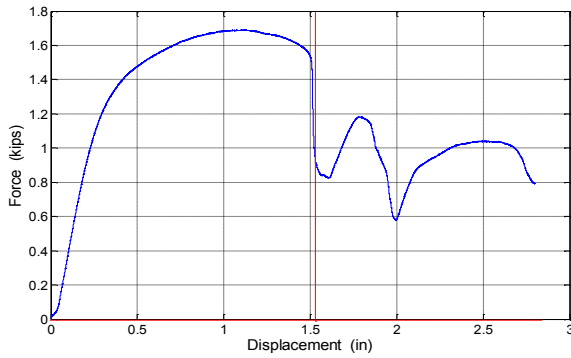


Pipe threads erode due to slippage



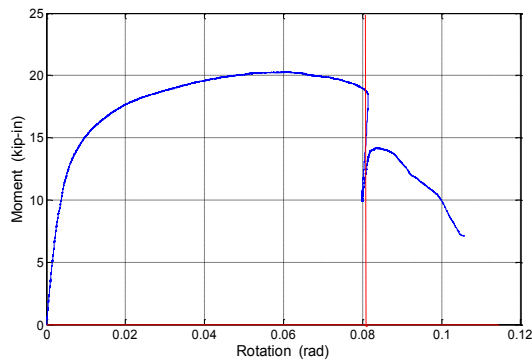
Thread sealant (Teflon tape) degraded

**MONOTONIC TEST FOR 2" BLACK IRON PIPES WITH THREADED JOINTS**

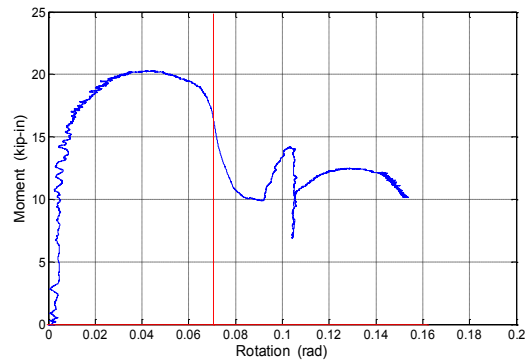


*\* The vertical red lines on these plots indicate the occurrence of the first leakage*

Force-displacement monotonic response at the tee joint



Moment-rotation monotonic response at the right end of the tee joint



Moment-rotation monotonic response at the left end of the tee joint

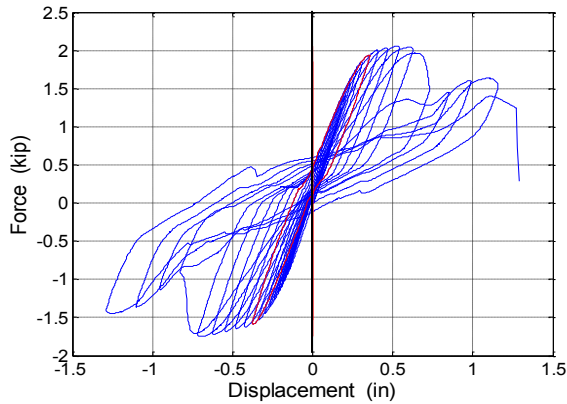


Pipe end bends due to imposed rotation



Pipe threads slip from tee threads

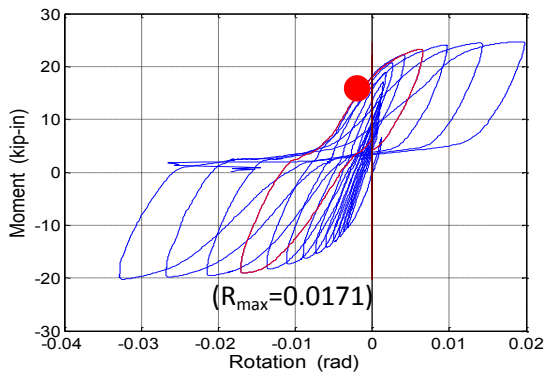
**CYCLIC TEST #1 FOR 2" BLACK IRON PIPES WITH THREADED JOINTS**



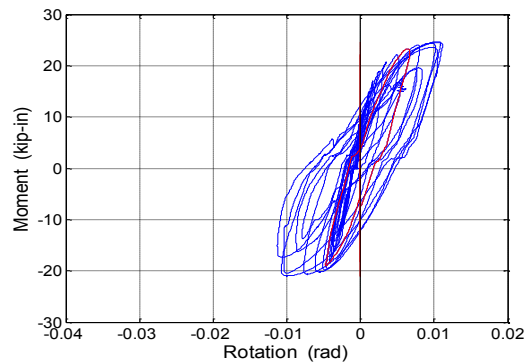
Force-displacement cyclic response at the tee joint

\* The red loops indicate the cycle during which the first leakage occurred.

\* The red solid dot indicates the occurrence of first leakage



Moment-rotation cyclic response at the right end of the tee joint



Moment-rotation cyclic response at the left end of the tee joint

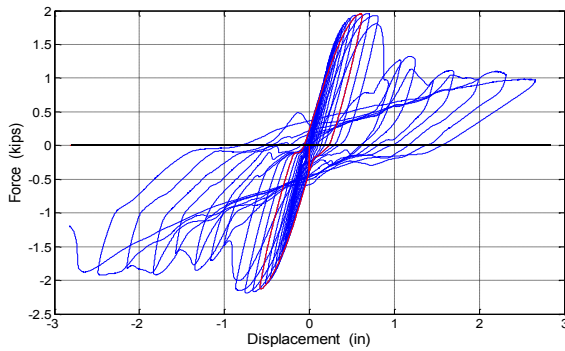


Pipe threads erode due to slippage



Pipe threads damage

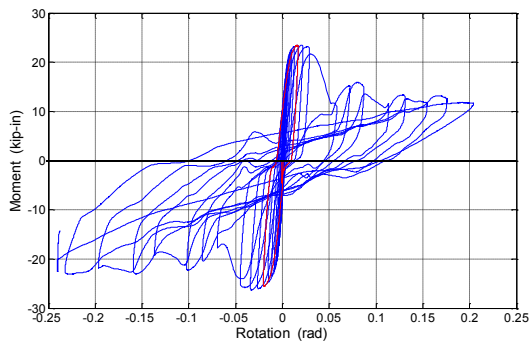
**CYCLIC TEST #2 FOR 2" BLACK IRON PIPES WITH THREADED JOINTS**



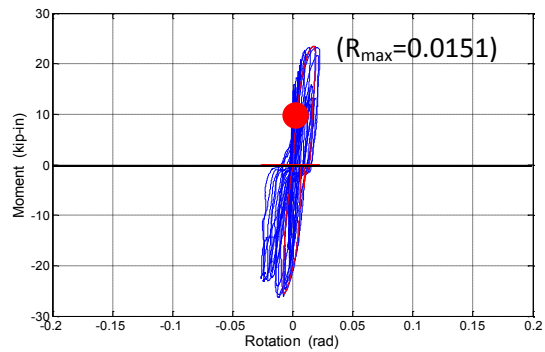
\* The red loops indicate the cycle during which the first leakage occurred.

\* The red solid dot indicates the occurrence of first leakage

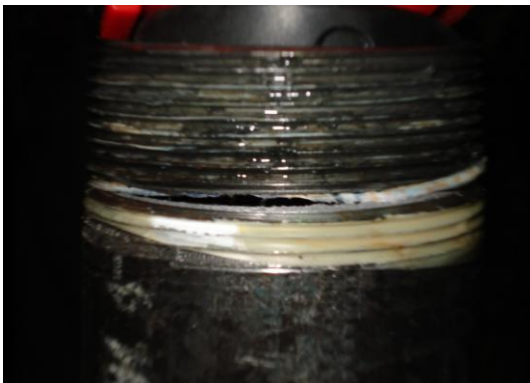
Force-displacement cyclic response at the tee joint



Moment-rotation cyclic response at the left end of the tee joint



Moment-rotation cyclic response at the right end of the tee joint

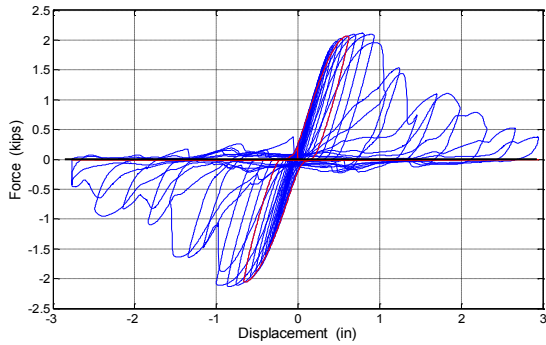


Pipe threads erode due to slippage



Thread sealant (Teflon tape) degraded

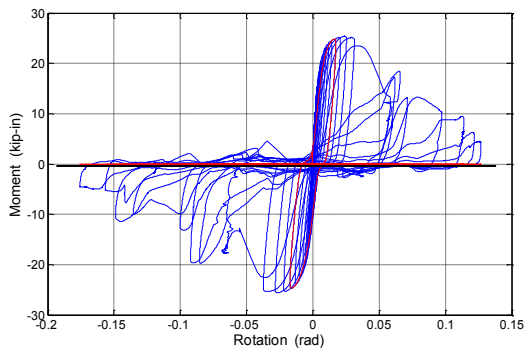
**CYCLIC TEST #3 FOR 2" BLACK IRON PIPES WITH THREADED JOINTS**



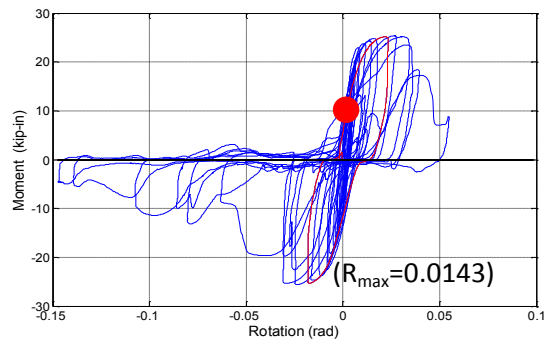
\* The red loops indicate the cycle during which the first leakage occurred.

\* The red solid dot indicates the occurrence of first leakage

Force-displacement cyclic response at the tee joint



Moment-rotation cyclic response at the left end of the tee joint



Moment-rotation cyclic response at the right end of the tee joint

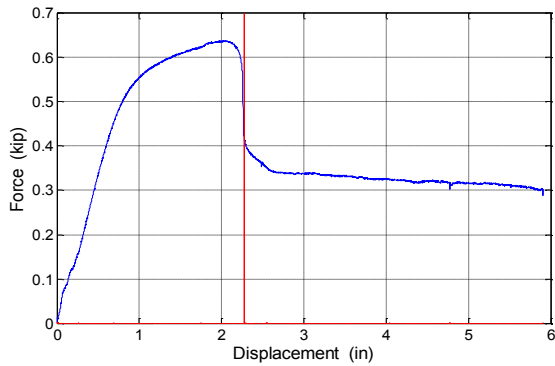


Pipe threads erode due to slippage



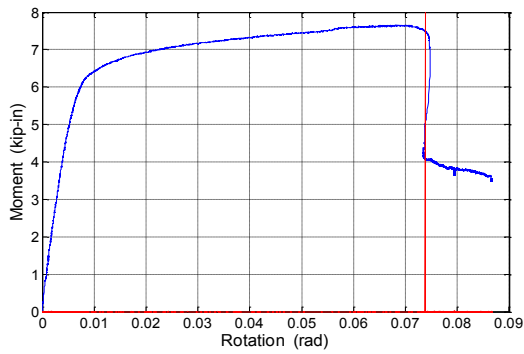
Thread sealant (Teflon tape) degraded

**MONOTONIC TEST FOR 1" BLACK IRON PIPES WITH THREADED JOINTS**

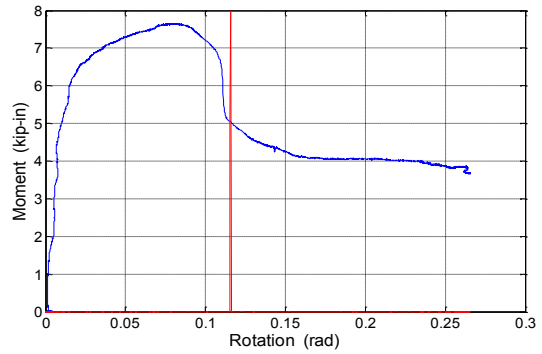


*\* The vertical red lines on these plots indicate the occurrence of the first leakage*

Force-displacement monotonic response at the tee joint



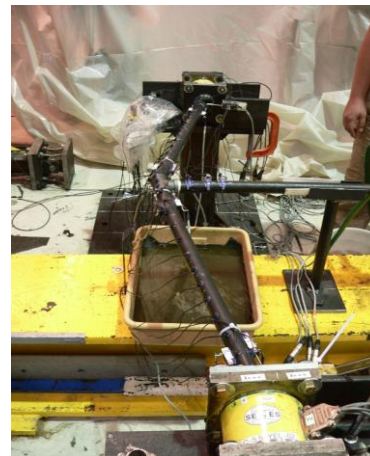
Moment-rotation monotonic response at the right end of the tee joint



Moment-rotation monotonic response at the left end of the tee joint

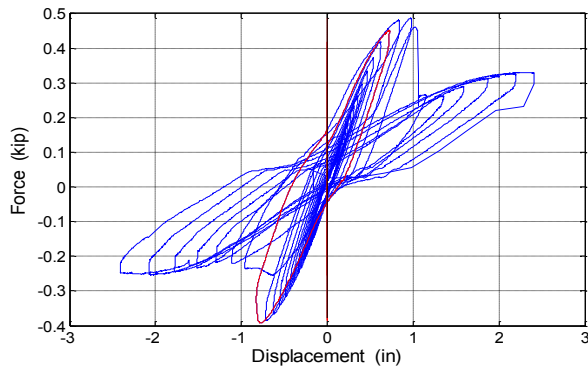


Pipe fractured at the edge of tee



Pipe end bends due to imposed rotation

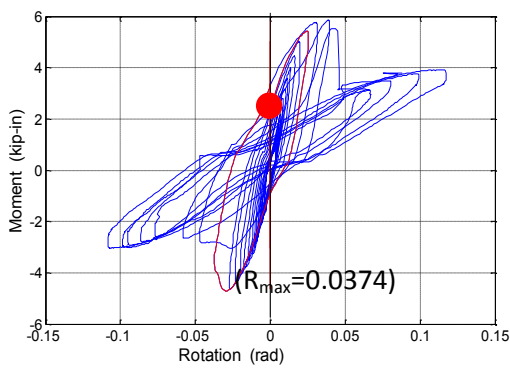
**CYCLIC TEST #1 FOR 1" BLACK IRON PIPES WITH THREADED JOINTS**



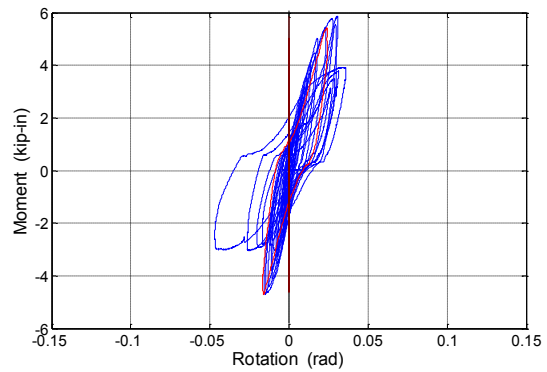
*\* The red loops indicate the cycle during which the first leakage occurred.*

*\* The red solid dot indicates the occurrence of first leakage*

Force-displacement cyclic response at the tee joint



Moment-rotation cyclic response at the right end of the tee joint



Moment-rotation cyclic response at the left end of the tee joint

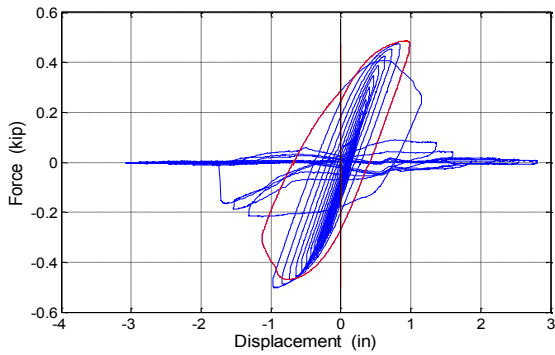


Pipe fractured at the edge of tee



Thread sealant (Teflon tape) degraded

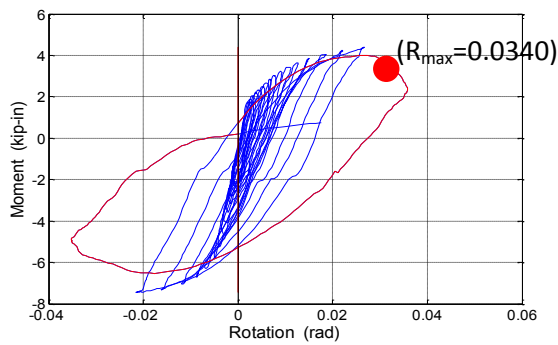
**CYCLIC TEST #2 FOR 1" BLACK IRON PIPES WITH THREADED JOINTS**



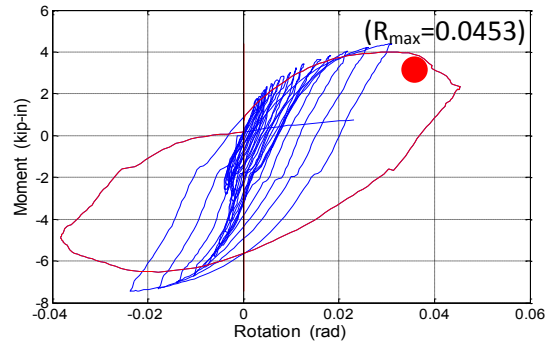
\* The red loops indicate the cycle during which the first leakage occurred.

\* The red solid dot indicates the occurrence of first leakage

Force-displacement cyclic response at the tee joint



Moment-rotation cyclic response at the left end of the tee joint



Moment-rotation cyclic response at the right end of the tee joint

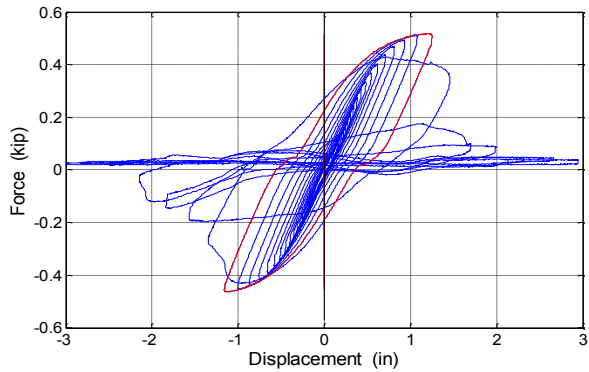


Pipe fractured at the edge of tee



Thread sealant (Teflon tape) degraded



**CYCLIC TEST #3 FOR 1" BLACK IRON PIPES WITH THREADED JOINTS**

*\* The red loops indicate the cycle during which the first leakage occurred.*

*\* The red solid dot indicates the occurrence of first leakage*

Force-displacement cyclic response at the tee joint

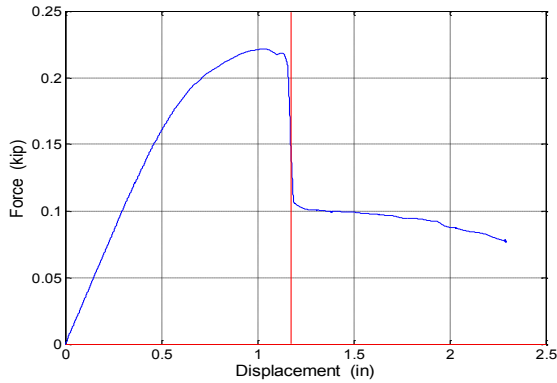


Pipe fractured at the edge of tee



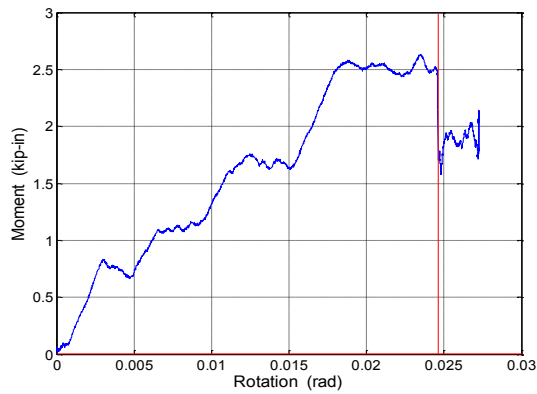
Thread sealant (Teflon tape) degraded

**MONOTONIC TEST FOR 3/4" BLACK IRON PIPES WITH THREADED JOINTS**

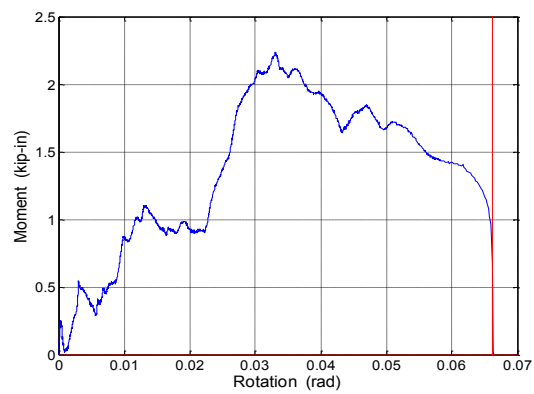


*\* The vertical red lines on these plots indicate the occurrence of the first leakage*

Force-displacement monotonic response at the tee joint



Moment-rotation monotonic response at the right end of the tee joint



Moment-rotation monotonic response at the left end of the tee joint

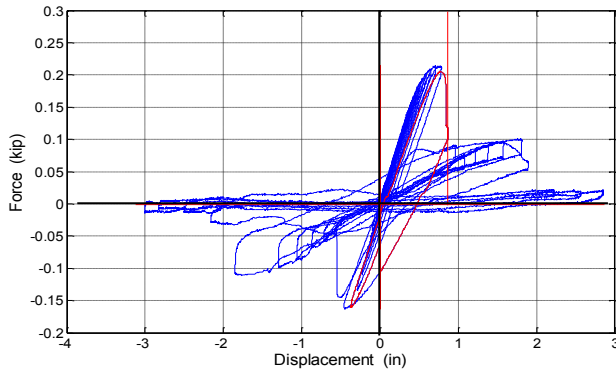


Thread sealant (Teflon tape) degraded



Pipe fractured at the edge of tee

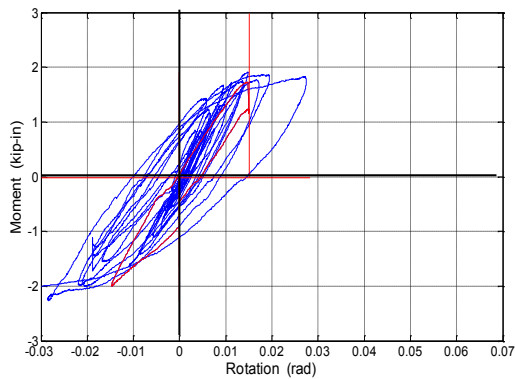
**CYCLIC TEST #1 FOR 3/4" BLACK IRON PIPES WITH THREADED JOINTS**



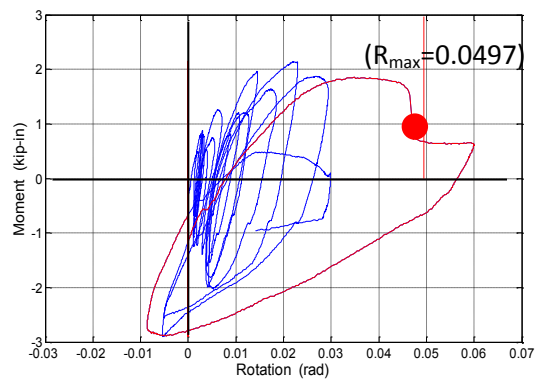
\* The red loops indicate the cycle during which the first leakage occurred.

\* The red solid dot indicates the occurrence of first leakage

Force-displacement cyclic response at the tee joint



Moment-rotation cyclic response at the right end of the tee joint



Moment-rotation cyclic response at the left end of the tee joint

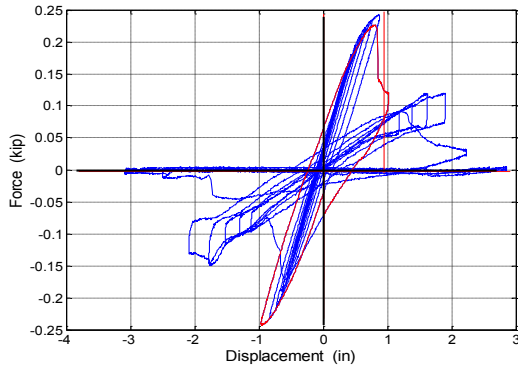


Pipe threads erode due to imposed rotation



Pipe fractured at the edge of tee

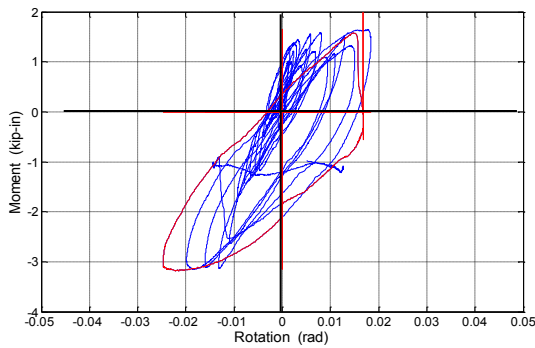
**CYCLIC TEST #2 FOR 3/4" BLACK IRON PIPES WITH THREADED JOINTS**



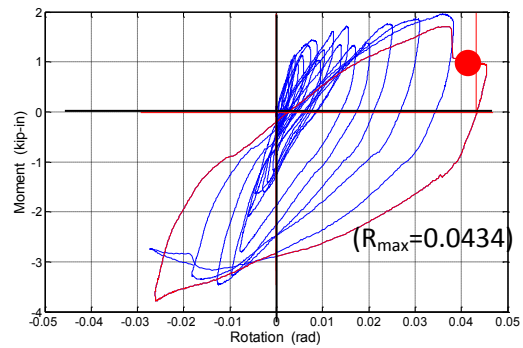
Force-displacement cyclic response at the tee joint

\* The red loops indicate the cycle during which the first leakage occurred.

\* The red solid dot indicates the occurrence of first leakage



Moment-rotation cyclic response at the left end of the tee joint



Moment-rotation cyclic response at the right end of the tee joint

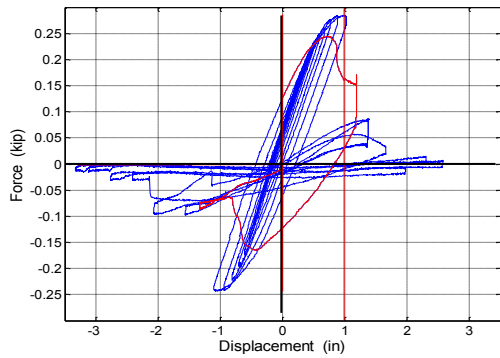


Pipe threads erode due to imposed rotation



Pipe fractured at the edge of tee

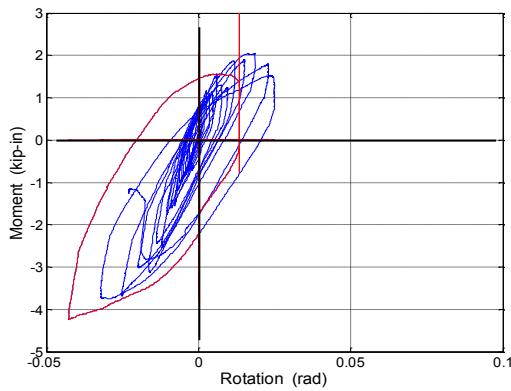
**CYCLIC TEST #3 FOR 3/4" BLACK IRON PIPES WITH THREADED JOINTS**



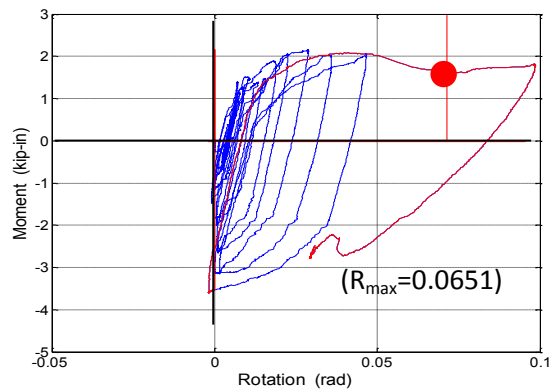
\* The red loops indicate the cycle during which the first leakage occurred.

\* The red solid dot indicates the occurrence of first leakage

Force-displacement cyclic response at the tee joint



Moment-rotation cyclic response at the left end of the tee joint



Moment-rotation cyclic response at the right end of the tee joint

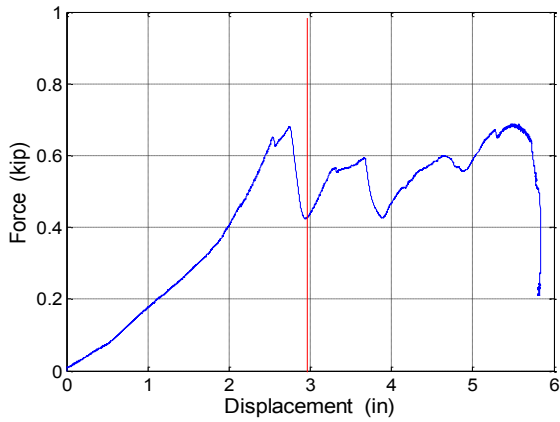


Pipe threads erode due to imposed rotation



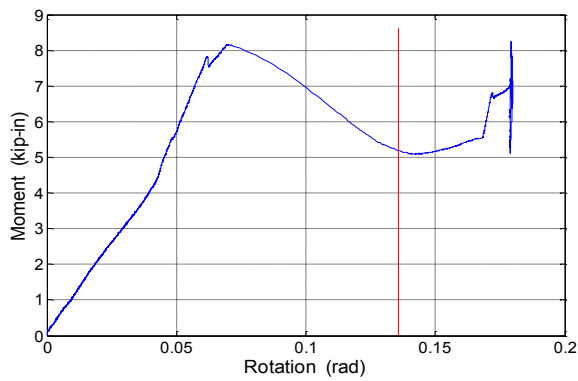
Pipe fractured at the edge of tee

**MONOTONIC TEST FOR 2" CPVC PIPES WITH CEMENT JOINTS**

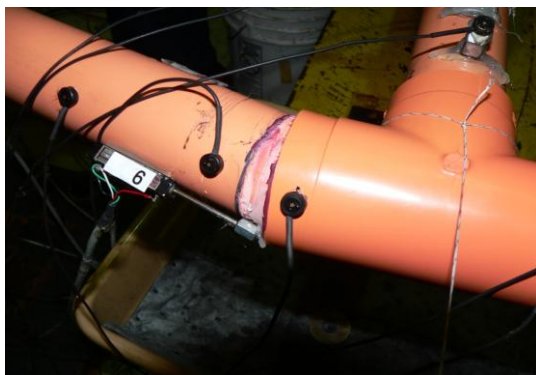


*\* The vertical red lines on these plots indicate the occurrence of the first leakage*

Force-displacement monotonic response at the tee joint



Moment-rotation monotonic response at the right end of the tee joint

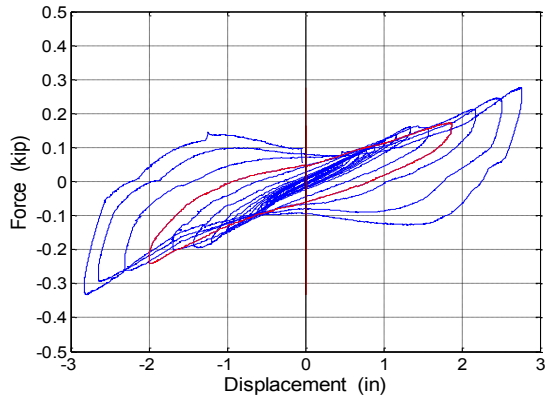


Cement Glue slipped



Cement Glue slipped

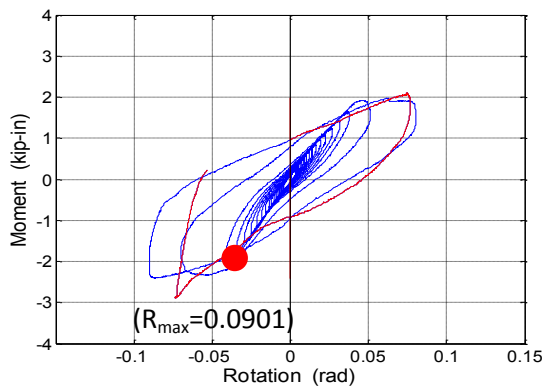
**CYCLIC TEST #1 FOR 2" CPVC PIPES WITH CEMENT JOINTS**



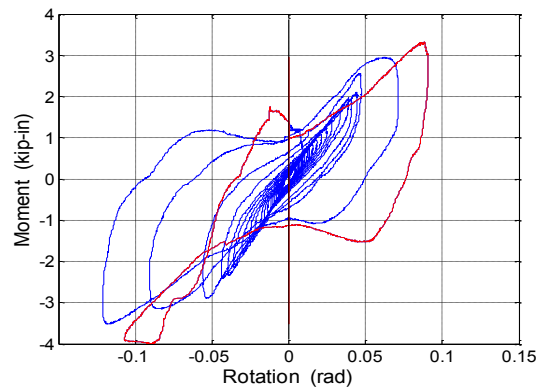
*\* The red loops indicate the cycle during which the first leakage occurred.*

*\* The red solid dot indicates the occurrence of first leakage*

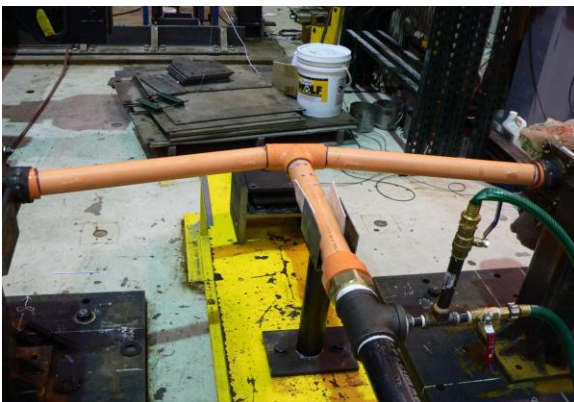
Force-displacement cyclic response at the tee joint



Moment-rotation cyclic response at the right end of the tee joint



Moment-rotation cyclic response at the left end of the tee joint

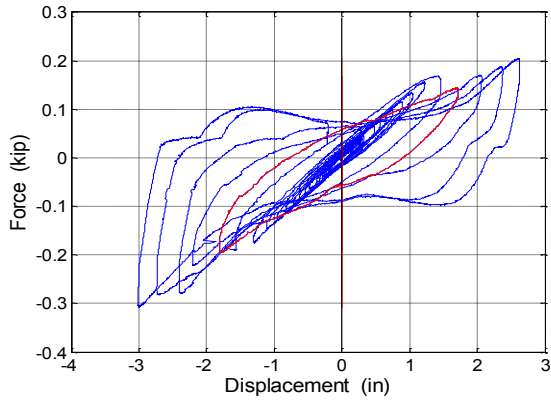


Pipe end bent due to imposed rotation



Cement Glue slipped

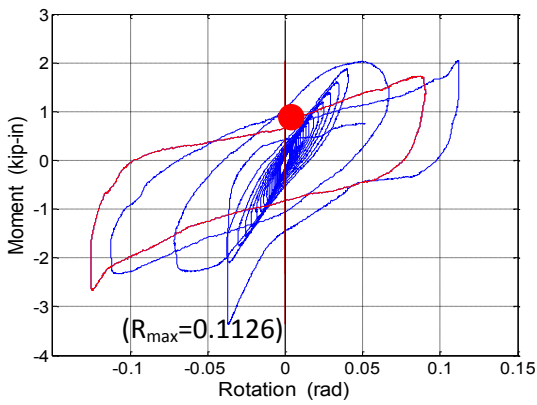
**CYCLIC TEST #2 FOR 2" CPVC PIPES WITH CEMENT JOINTS**



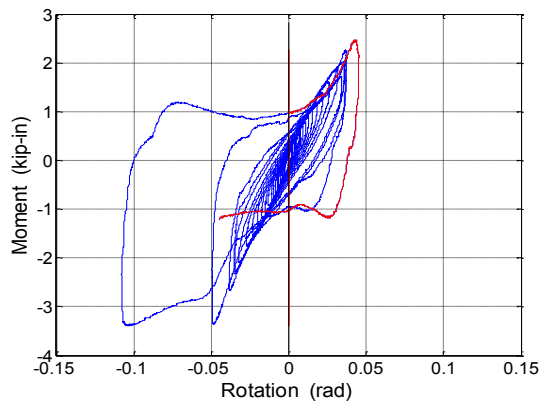
\* The red loops indicate the cycle during which the first leakage occurred.

\* The red solid dot indicates the occurrence of first leakage

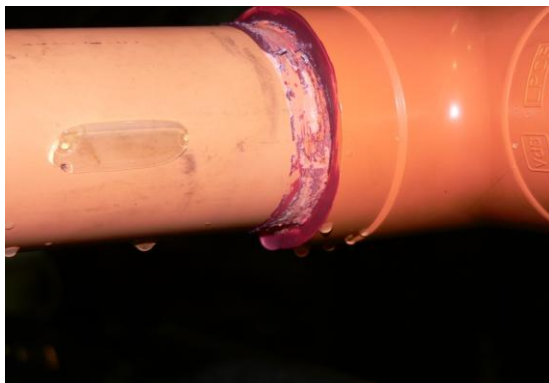
Force-displacement cyclic response at the tee joint



Moment-rotation cyclic response at the left end of the tee joint



Moment-rotation cyclic response at the right end of the tee joint



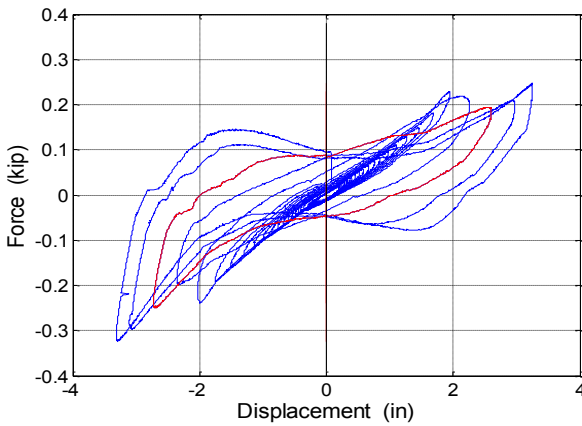
Cement glue slipped



Pipe pulled out from tee joint



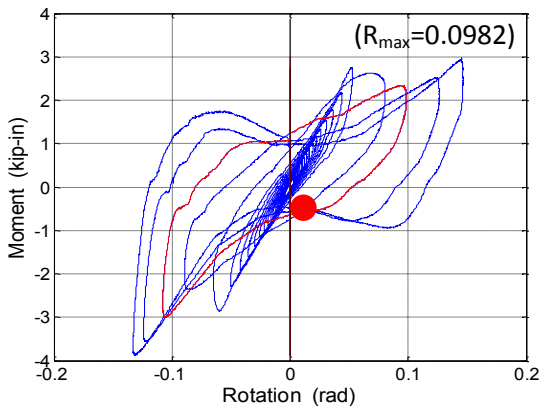
**CYCLIC TEST #3 FOR 2" CPVC PIPES WITH CEMENT JOINTS**



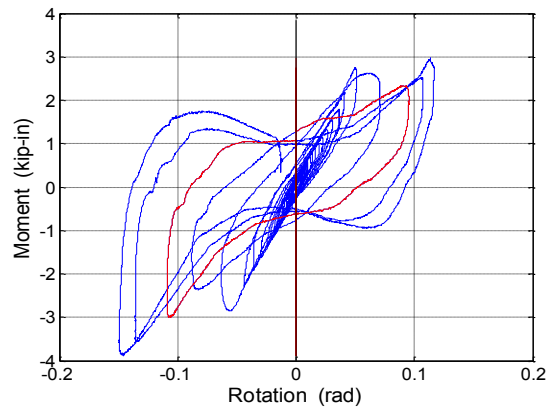
Force-displacement cyclic response at the tee joint

\* The red loops indicate the cycle during which the first leakage occurred.

\* The red solid dot indicates the occurrence of first leakage



Moment-rotation cyclic response at the left end of the tee joint



Moment-rotation cyclic response at the right end of the tee joint

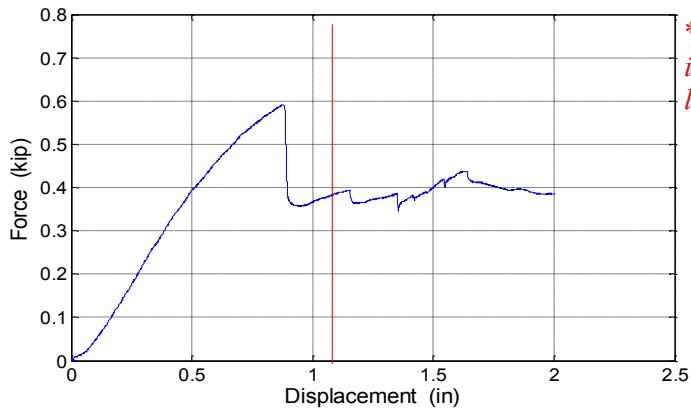


Pipe pulled out from tee joint



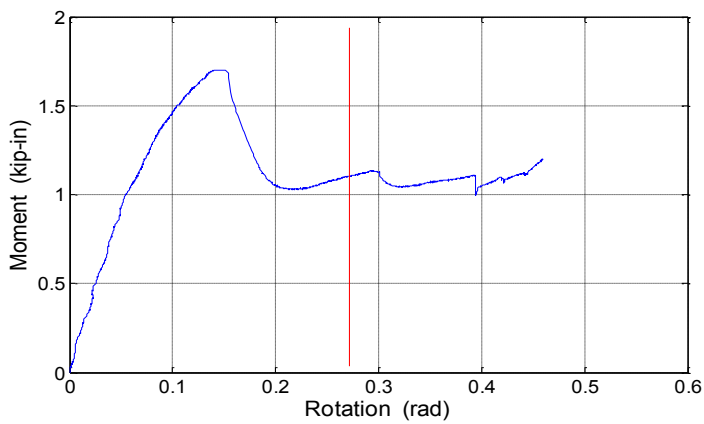
Pipe peeled off the inner surface of tee joint

**MONOTONIC TEST FOR 1" CPVC PIPES WITH CEMENT JOINTS**

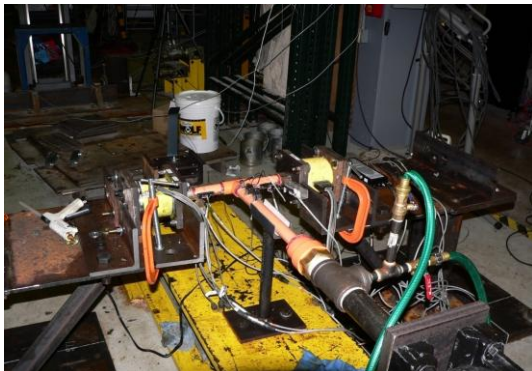


*\* The vertical red lines on these plots indicate the occurrence of the first leakage*

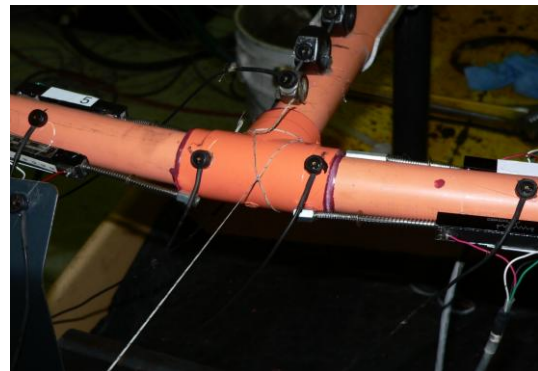
Force-displacement monotonic response at the tee joint



Moment-rotation monotonic response at the right end of the tee joint

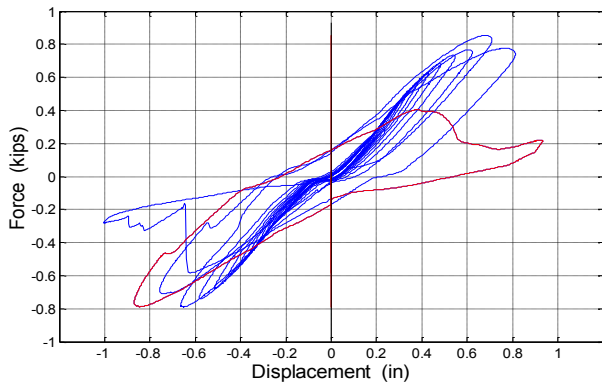


Pipe end bent due to imposed rotation



Cement glue slipped

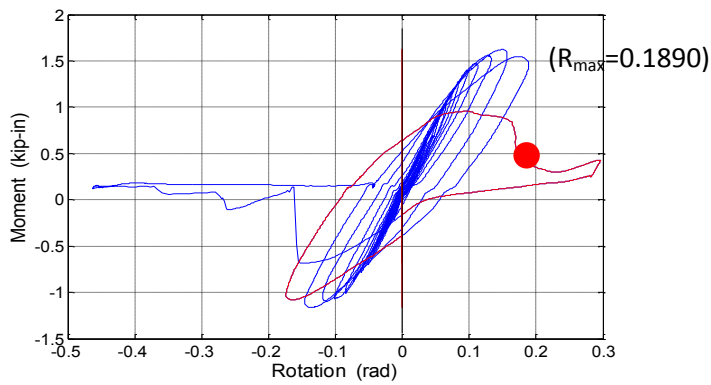
**CYCLIC TEST #1 FOR 1" CPVC PIPES WITH CEMENT JOINTS**



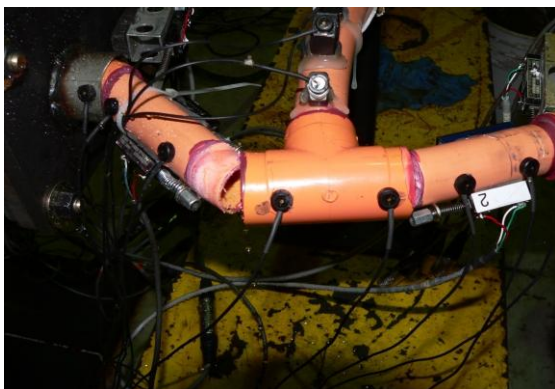
*\* The red loops indicate the cycle during which the first leakage occurred.*

*\* The red solid dot indicates the occurrence of first leakage*

Force-displacement cyclic response at the tee joint



Moment-rotation cyclic response at the left end of the tee joint

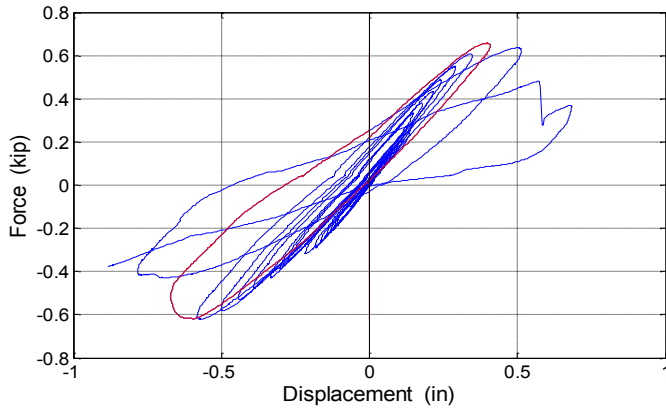


Pipe pulled out from tee joint



Pipe peeled off the inner surface of tee joint

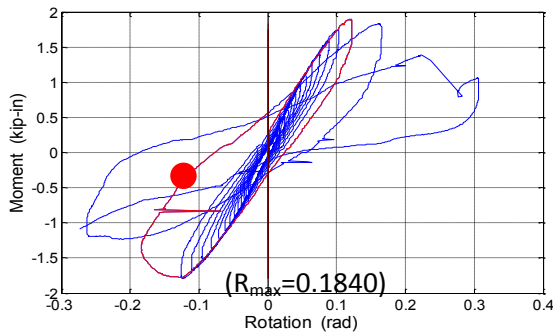
**CYCLIC TEST #2 FOR 1" CPVC PIPES WITH CEMENT JOINTS**



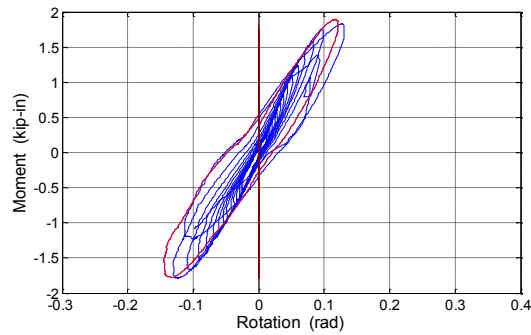
\* The red loops indicate the cycle during which the first leakage occurred.

\* The red solid dot indicates the occurrence of first leakage

Force-displacement cyclic response at the tee joint



Moment-rotation cyclic response at the right end of the tee joint



Moment-rotation cyclic response at the left end of the tee joint

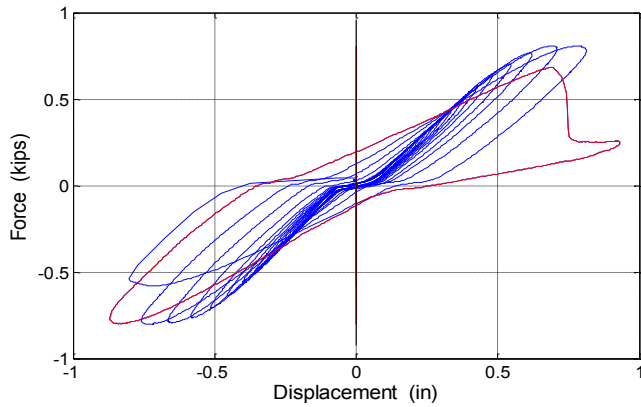


Pipe pulled out from tee joint



Pipe end bent due to imposed rotation

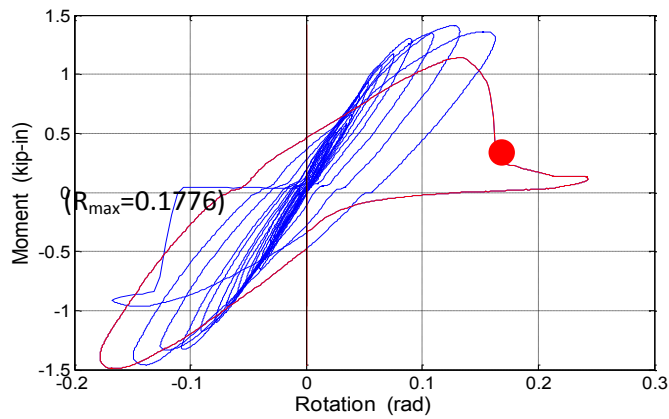
**CYCLIC TEST #3 FOR 1" CPVC PIPES WITH CEMENT JOINTS**



\* The red loops indicate the cycle during which the first leakage occurred.

\* The red solid dot indicates the occurrence of first leakage

Force-displacement cyclic response at the tee joint



Moment-rotation cyclic response at the left end of the tee joint

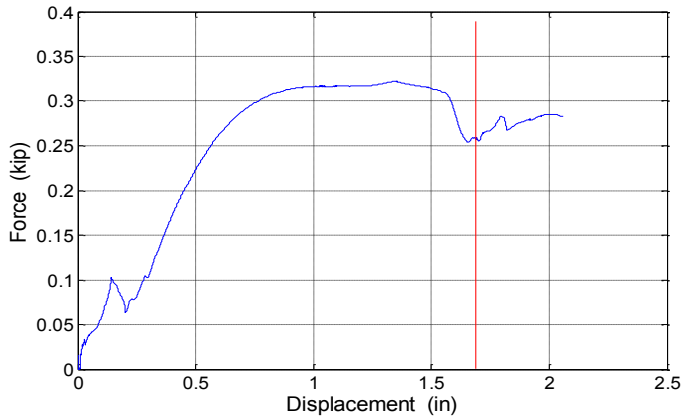


Pipe pulled out from tee joint



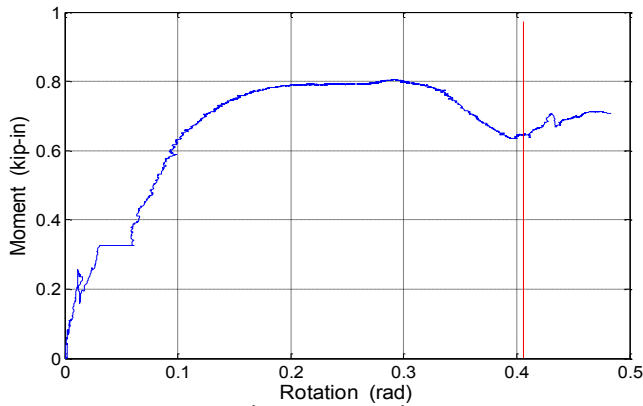
Pipe peeled off the inner surface of tee joint

**MONOTONIC TEST FOR 3/4" CPVC PIPES WITH CEMENT JOINTS**

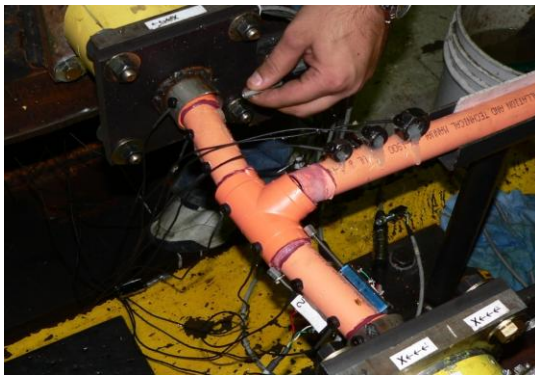


*\* The vertical red lines on these plots indicate the occurrence of the first leakage*

Force-displacement monotonic response at the tee joint

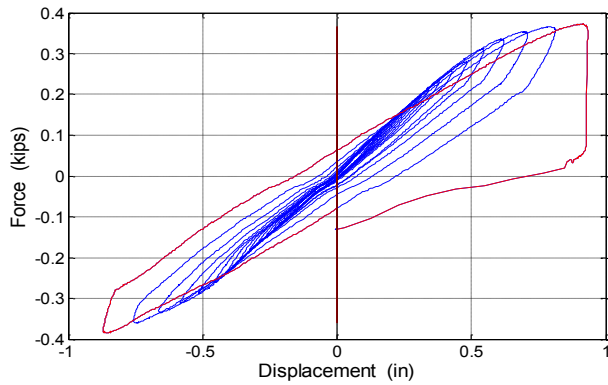


Moment-rotation monotonic response at the right end of the tee joint



Pipe pulled out from tee joint

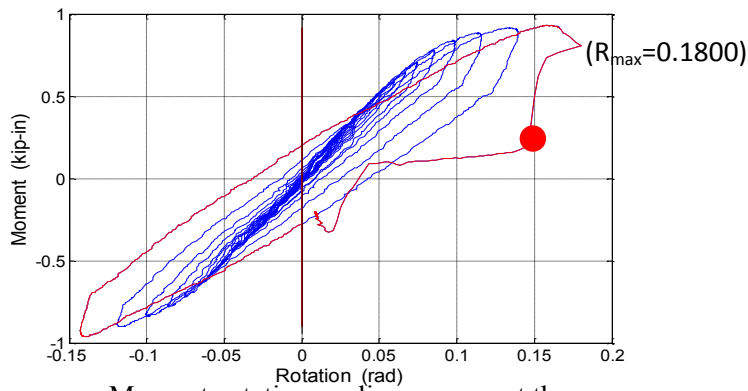
**CYCLIC TEST #1 FOR 3/4" CPVC PIPES WITH CEMENT JOINTS**



\* The red loops indicate the cycle during which the first leakage occurred.

\* The red solid dot indicates the occurrence of first leakage

Force-displacement cyclic response at the tee joint



Moment-rotation cyclic response at the left end of the tee joint

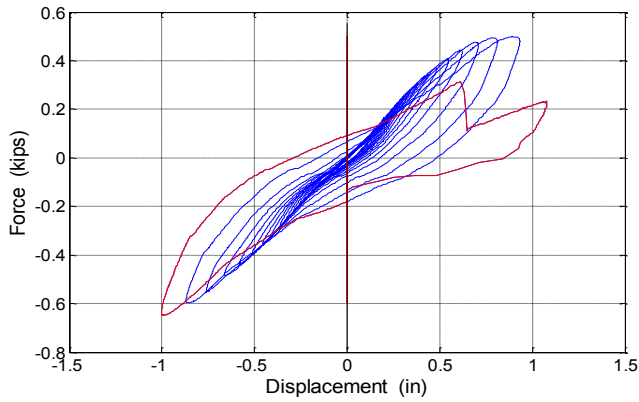


Pipe fractured at the edge of tee



Pipe fractured at the edge of tee

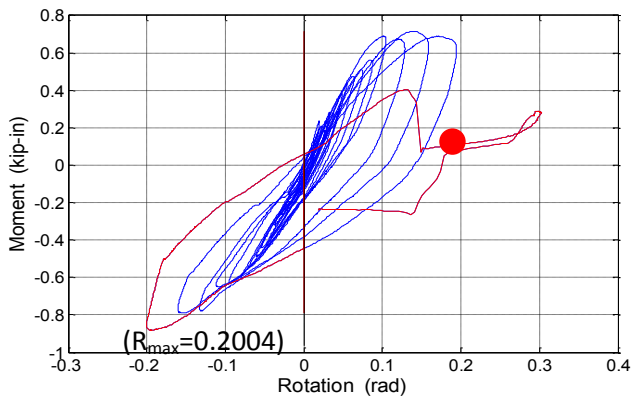
**CYCLIC TEST #2 FOR 3/4" CPVC PIPES WITH CEMENT JOINTS**



\* The red loops indicate the cycle during which the first leakage occurred.

\* The red solid dot indicates the occurrence of first leakage

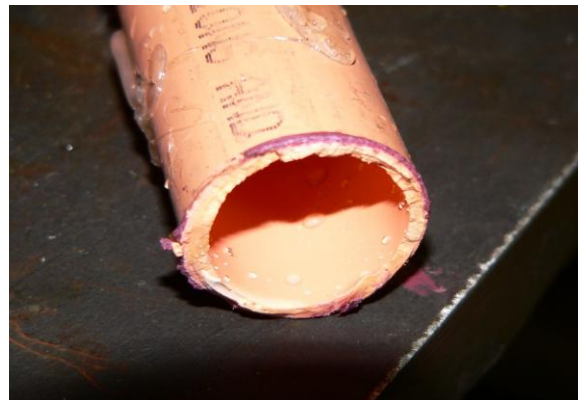
Force-displacement cyclic response at the tee joint



Moment-rotation cyclic response at the right end of the tee joint



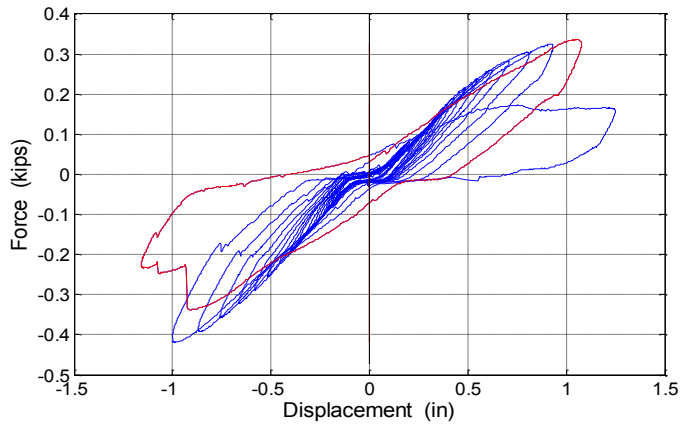
Pipe fractured at the edge of tee



Pipe fractured at the edge of tee



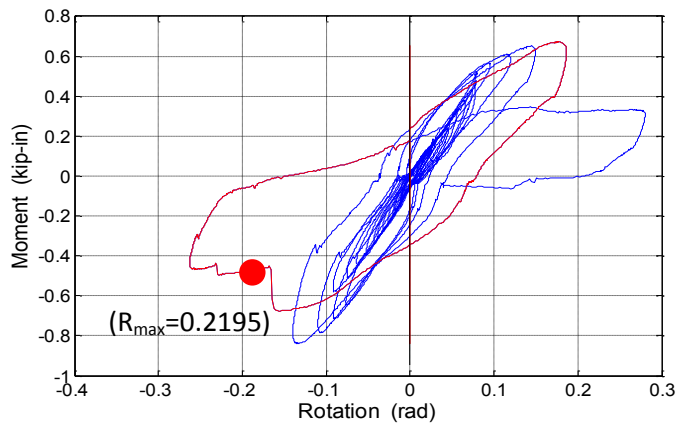
**CYCLIC TEST #3 FOR 3/4" CPVC PIPES WITH CEMENT JOINTS**



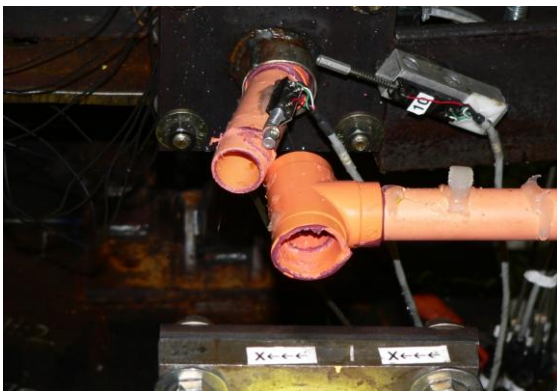
\* The red loops indicate the cycle during which the first leakage occurred.

\* The red solid dot indicates the occurrence of first leakage

Force-displacement cyclic response at the tee joint



Moment-rotation cyclic response at the left end of the tee joint

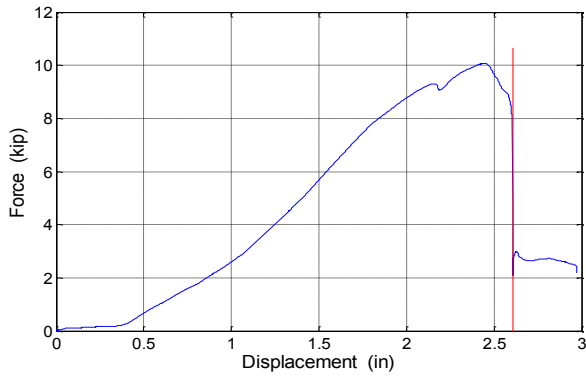


Pipe pulled out from tee joint



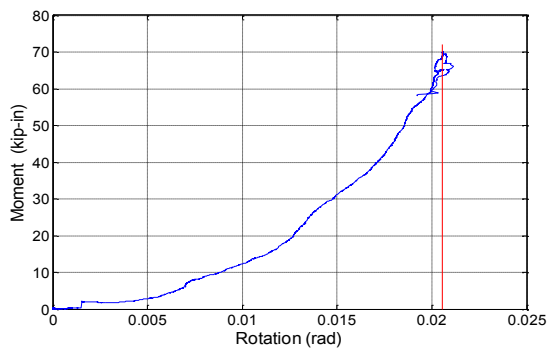
Pipe end bent due to imposed rotation

**MONOTONIC TEST FOR SCHEDULE-40 4" CPVC PIPES WITH CEMENT JOINTS**

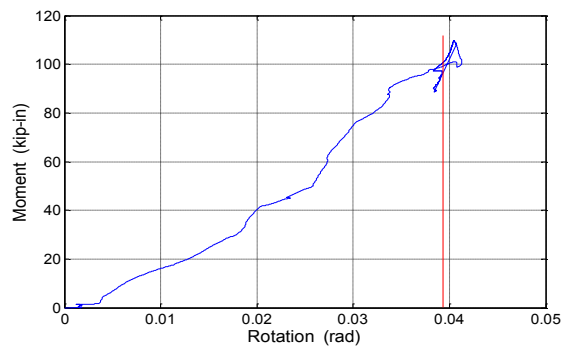


*\* The vertical red lines on these plots indicate the occurrence of the first leakage*

Force-displacement monotonic response at the tee joint



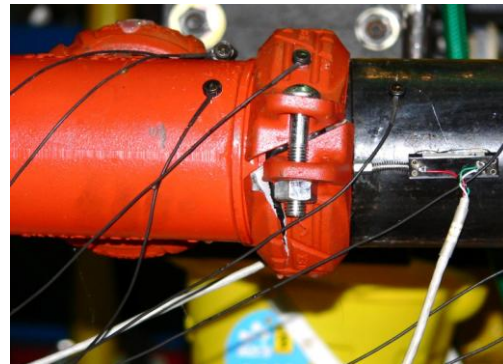
Moment-rotation monotonic response at the right end of the tee joint



Moment-rotation monotonic response at the left end of the tee joint

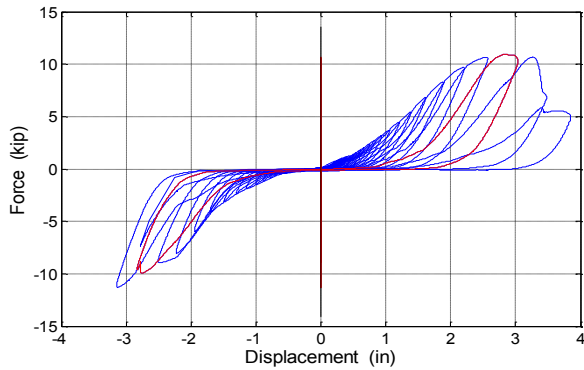


Pipe end bent due to imposed rotation



Coupling flange fractured

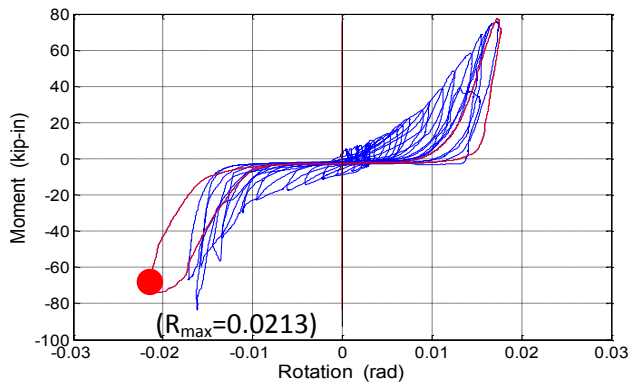
**CYCLIC TEST #1 FOR SCHEDULE-40 4" CPVC PIPES WITH CEMENT JOINTS**



*\* The red loops indicate the cycle during which the first leakage occurred.*

*\* The red solid dot indicates the occurrence of first leakage*

Force-displacement cyclic response at the tee joint



Moment-rotation cyclic response at the right end of the tee joint

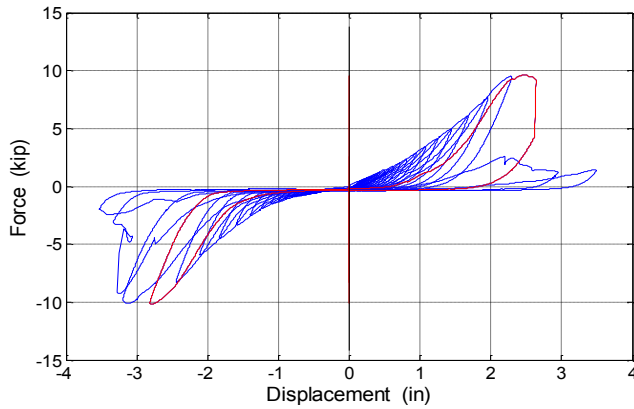


Coupling flange fractured



Groove of pipe wore away

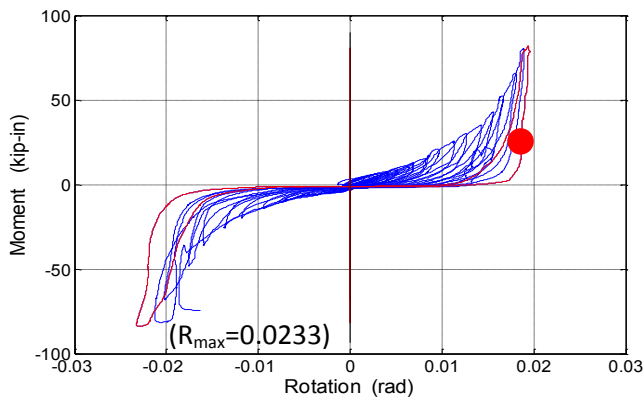
**CYCLIC TEST #2 FOR SCHEDULE-40 4" CPVC PIPES WITH CEMENT JOINTS**



\* The red loops indicate the cycle during which the first leakage occurred.

\* The red solid dot indicates the occurrence of first leakage

Force-displacement cyclic response at the tee joint



Moment-rotation cyclic response at the left end of the tee joint

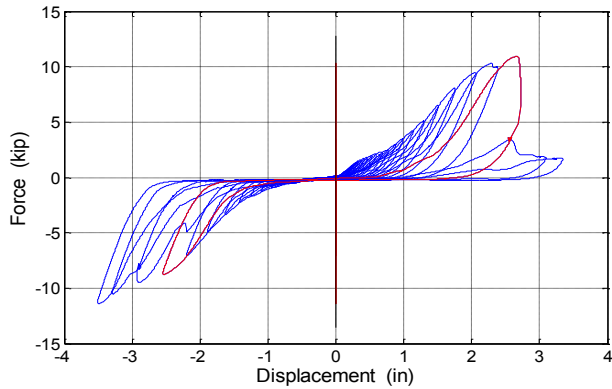


Coupling flange fractured



Coupling flange fractured

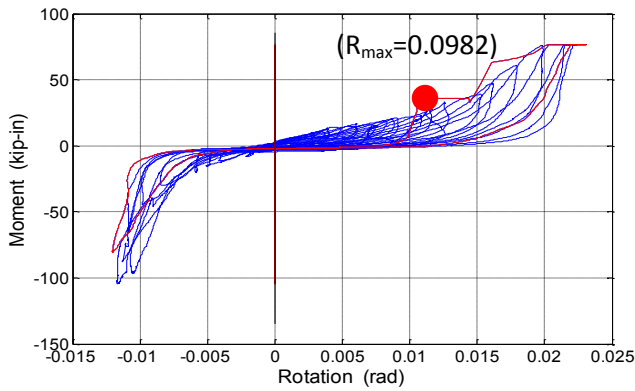
**CYCLIC TEST #3 FOR SCHEDULE-40 4" CPVC PIPES WITH CEMENT JOINTS**



\* The red loops indicate the cycle during which the first leakage occurred.

\* The red solid dot indicates the occurrence of first leakage

Force-displacement cyclic response at the tee joint



Moment-rotation cyclic response at the left end of the tee joint

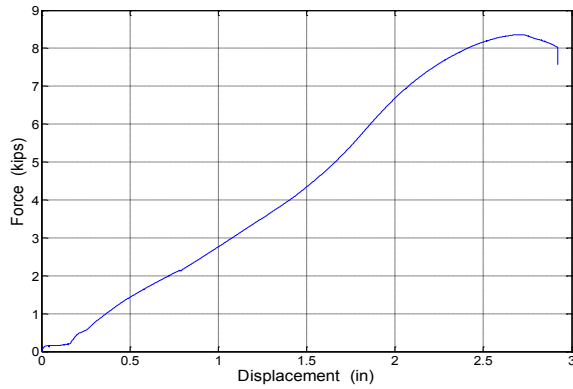


Coupling flange fractured

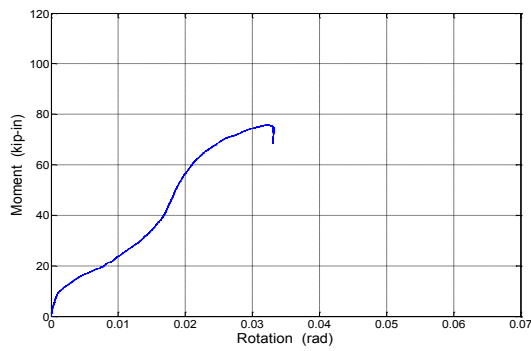


Groove of pipe wore away

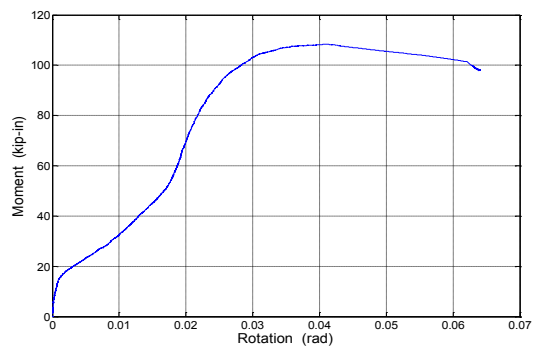
**MONOTONIC TEST FOR SCHEDULE-10 4" CPVC PIPES WITH CEMENT JOINTS**



Force-displacement monotonic response at the tee joint



Moment-rotation monotonic response at the right end of the tee joint



Moment-rotation monotonic response at the left end of the tee joint

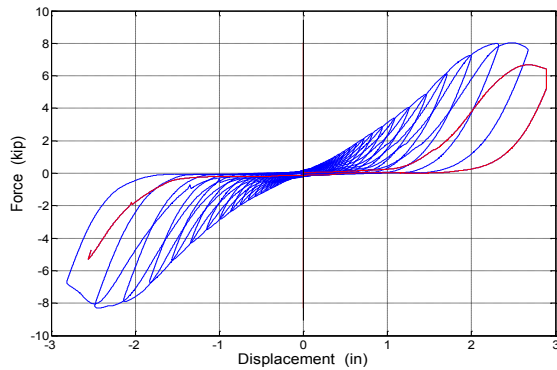


Pipe end bent due to imposed rotation



Groove of pipe wore away

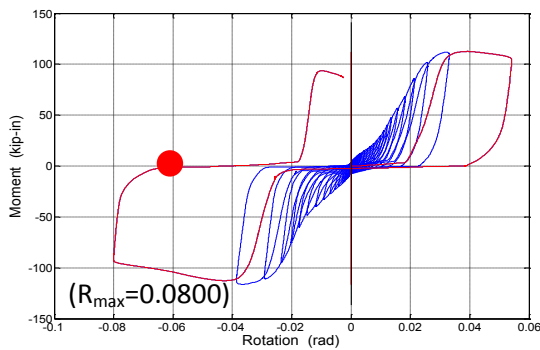
**CYCLIC TEST #1 FOR SCHEDULE-10 4" CPVC PIPES WITH CEMENT JOINTS**



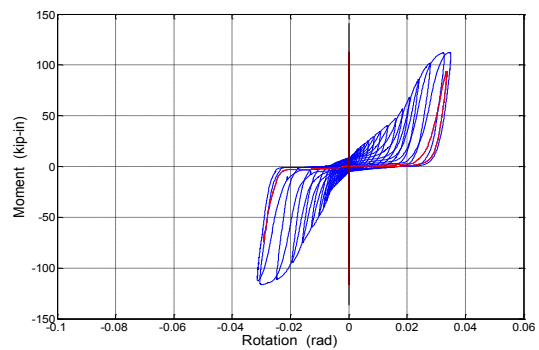
\* The red loops indicate the cycle during which the first leakage occurred.

\* The red solid dot indicates the occurrence of first leakage

Force-displacement cyclic response at the tee joint



Moment-rotation cyclic response at the right end of the tee joint



Moment-rotation cyclic response at the left end of the tee joint

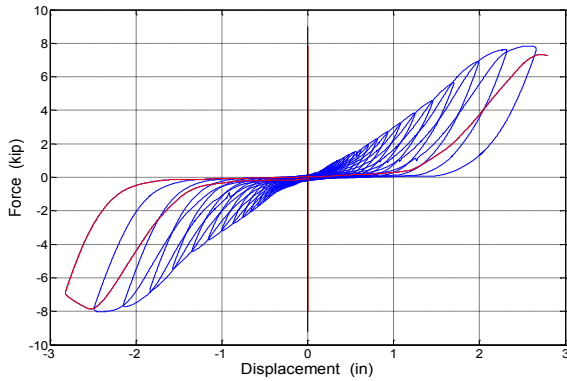


Coupling flange fractured



Groove of pipe wore away

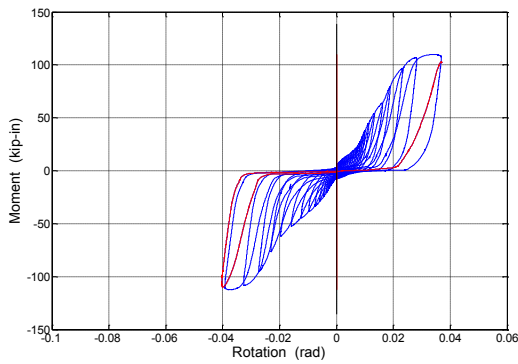
**CYCLIC TEST #2 FOR SCHEDULE-10 4" CPVC PIPES WITH CEMENT JOINTS**



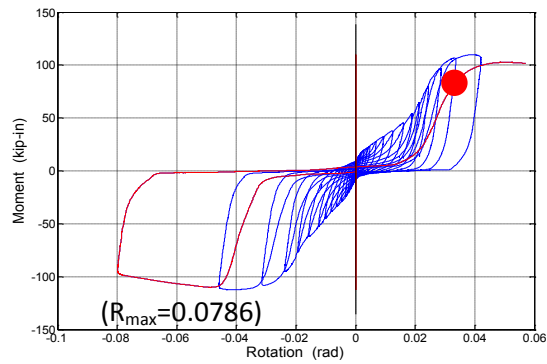
\* The red loops indicate the cycle during which the first leakage occurred.

\* The red solid dot indicates the occurrence of first leakage

Force-displacement cyclic response at the tee joint



Moment-rotation cyclic response at the right end of the tee joint



Moment-rotation cyclic response at the left end of the tee joint



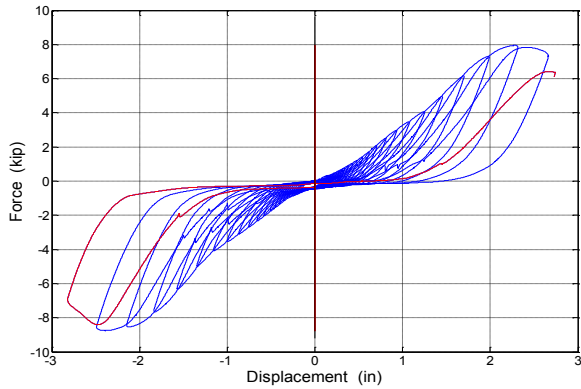
Groove of pipe wore away



Cross section of pipe yielded and deformed



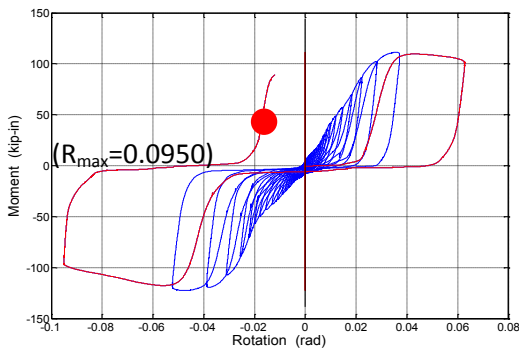
**CYCLIC TEST #3 FOR SCHEDULE-10 4" CPVC PIPES WITH CEMENT JOINTS**



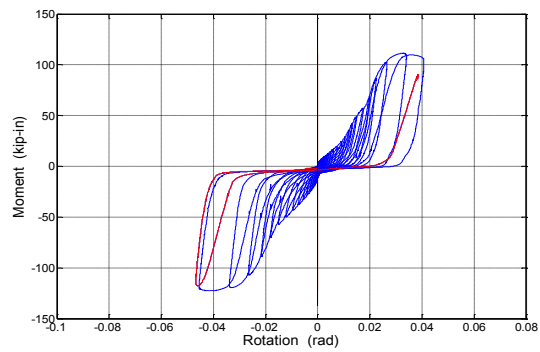
\* The red loops indicate the cycle during which the first leakage occurred.

\* The red solid dot indicates the occurrence of first leakage

Force-displacement cyclic response at the tee joint



Moment-rotation cyclic response at the right end of the tee joint



Moment-rotation cyclic response at the left end of the tee joint

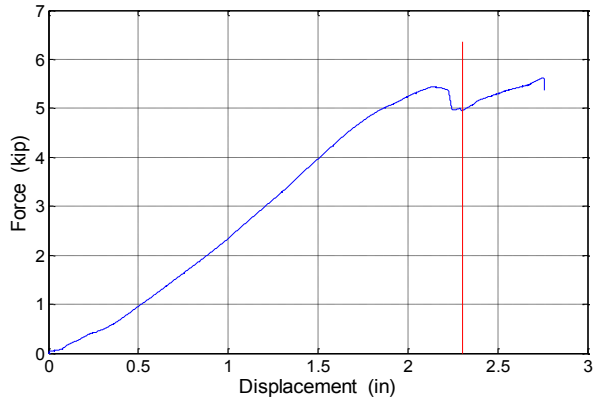


Cross section of pipe yielded and deformed



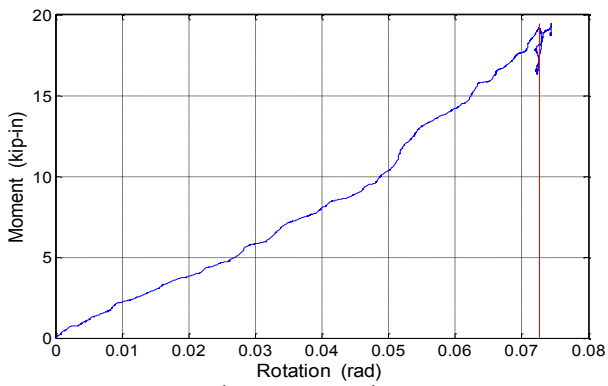
Groove of pipe wore away

**MONOTONIC TEST FOR SCHEDULE-40 2" CPVC PIPES WITH CEMENT JOINTS**



*\* The vertical red lines on these plots indicate the occurrence of the first leakage*

Force-displacement monotonic response at the tee joint



Moment-rotation monotonic response at the right end of the tee joint

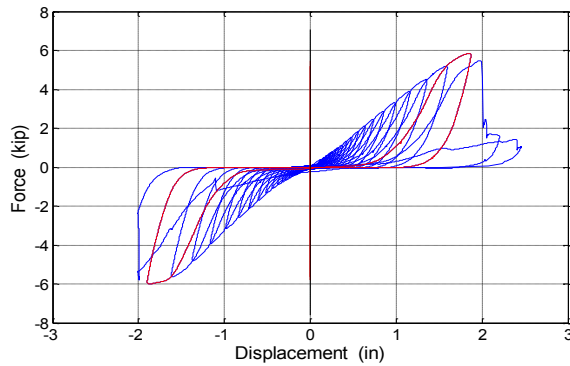


Flange coupling fractured



Groove of pipe wore away

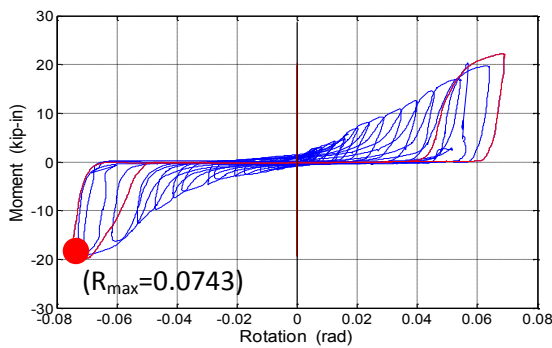
**CYCLIC TEST #1 FOR SCHEDULE-40 2" CPVC PIPES WITH CEMENT JOINTS**



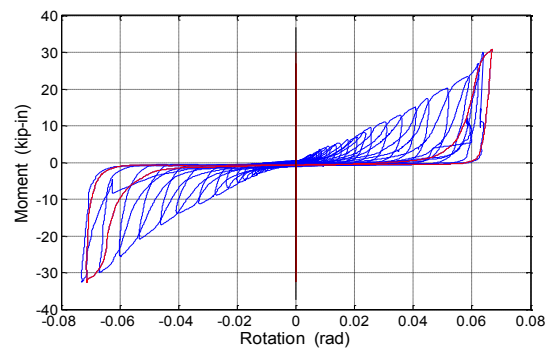
*\* The red loops indicate the cycle during which the first leakage occurred.*

*\* The red solid dot indicates the occurrence of first leakage*

Force-displacement cyclic response at the tee joint



Moment-rotation cyclic response at the right end of the tee joint



Moment-rotation cyclic response at the left end of the tee joint

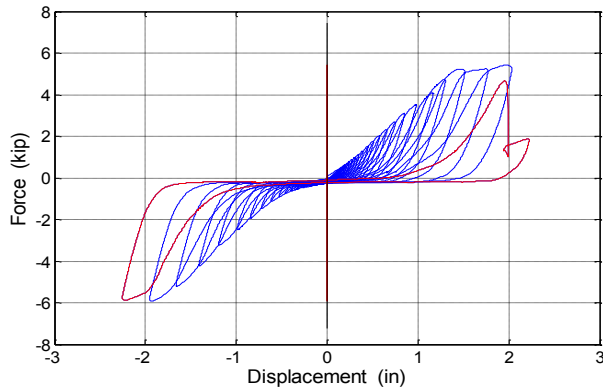


Coupling flange fractured



Groove of tee joint wore away

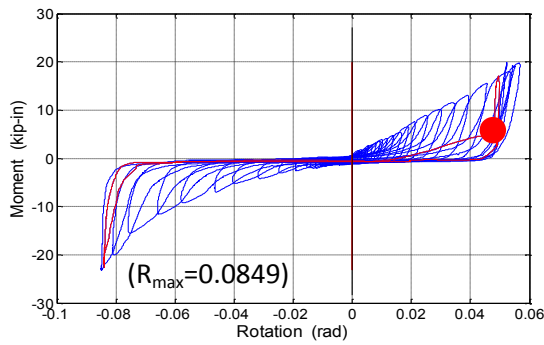
**CYCLIC TEST #2 FOR SCHEDULE-40 2" CPVC PIPES WITH CEMENT JOINTS**



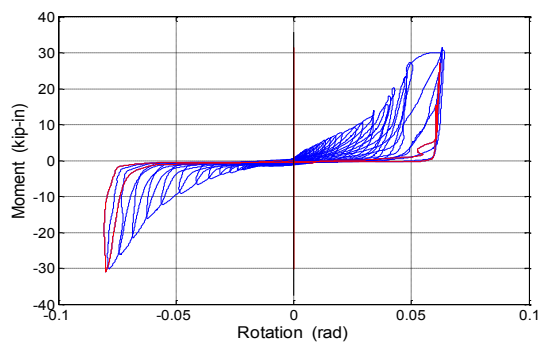
\* The red loops indicate the cycle during which the first leakage occurred.

\* The red solid dot indicates the occurrence of first leakage

Force-displacement cyclic response at the tee joint



Moment-rotation cyclic response at the right end of the tee joint



Moment-rotation cyclic response at the left end of the tee joint

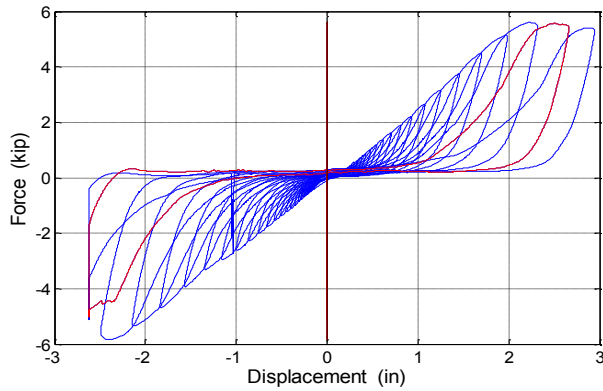


Groove of pipe wore away



Groove of tee joint wore away

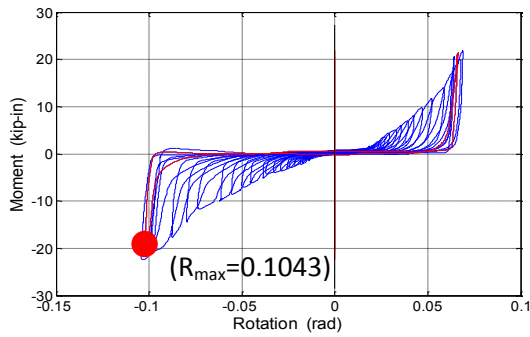
**CYCLIC TEST #3 FOR SCHEDULE-40 2" CPVC PIPES WITH CEMENT JOINTS**



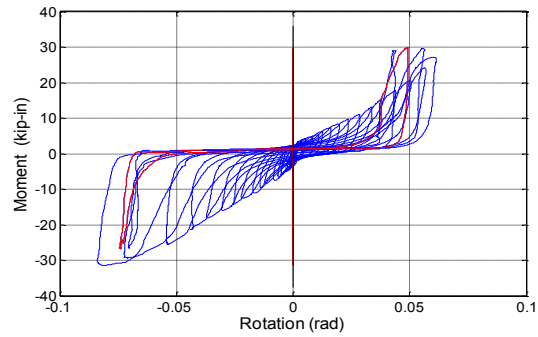
\* The red loops indicate the cycle during which the first leakage occurred.

\* The red solid dot indicates the occurrence of first leakage

Force-displacement cyclic response at the tee joint



Moment-rotation cyclic response at the right end of the tee joint



Moment-rotation cyclic response at the left end of the tee joint

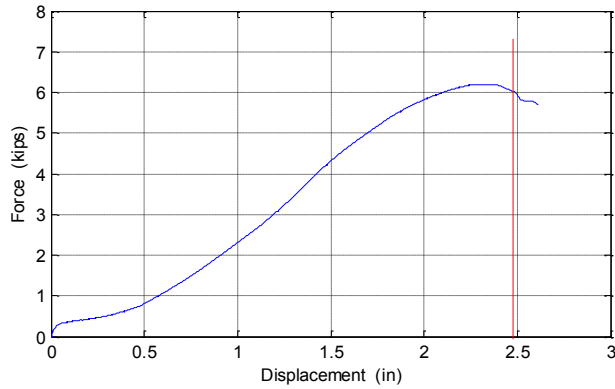


Flange coupling fractured



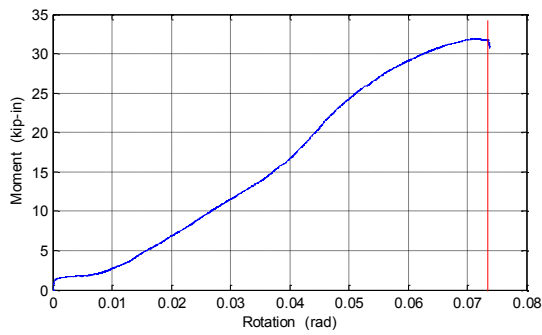
Groove of pipe wore away

**MONOTONIC TEST FOR SCHEDULE-10 2" CPVC PIPES WITH CEMENT JOINTS**

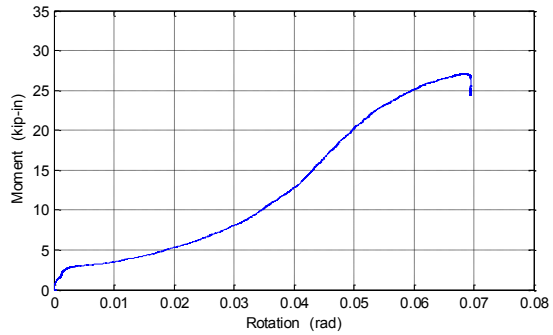


*\* The vertical red lines on these plots indicate the occurrence of the first leakage*

Force-displacement monotonic response at the tee joint



Moment-rotation monotonic response at the right end of the tee joint



Moment-rotation monotonic response at the left end of the tee joint

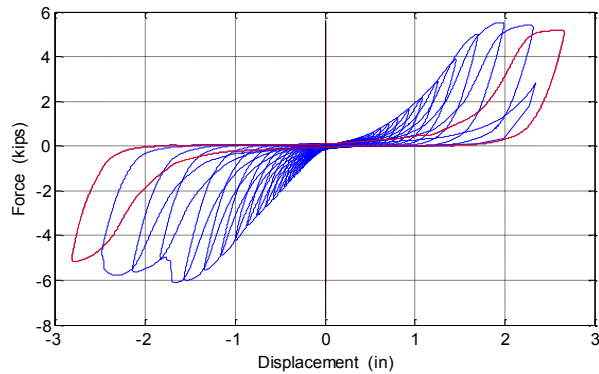


Cross section of pipe yielded and deformed



Groove of pipe wore away

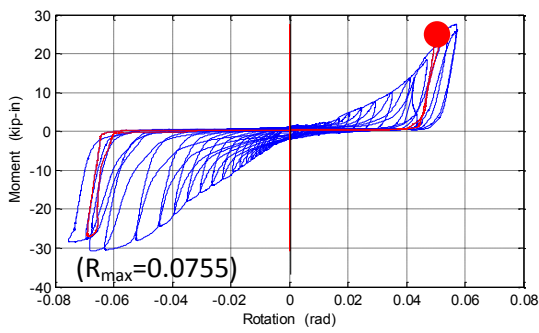
**CYCLIC TEST #1 FOR SCHEDULE-10 2" CPVC PIPES WITH CEMENT JOINTS**



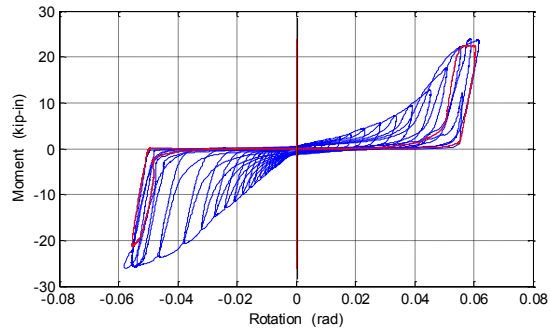
\* The red loops indicate the cycle during which the first leakage occurred.

\* The red solid dot indicates the occurrence of first leakage

Force-displacement cyclic response at the tee joint



Moment-rotation cyclic response at the right end of the tee joint



Moment-rotation cyclic response at the left end of the tee joint

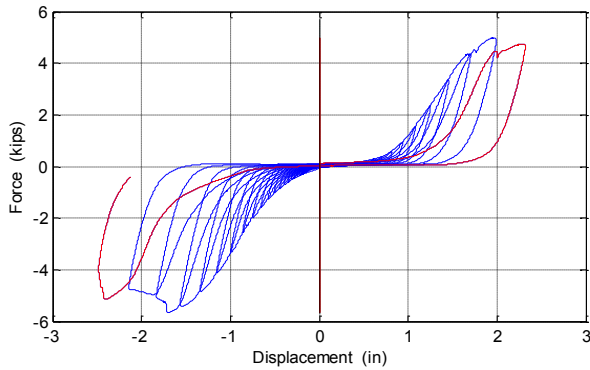


Coupling flange fractured



Groove of pipe wore away

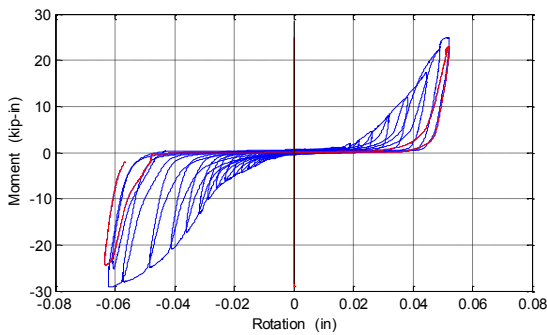
**CYCLIC TEST #2 FOR SCHEDULE-10 2" CPVC PIPES WITH CEMENT JOINTS**



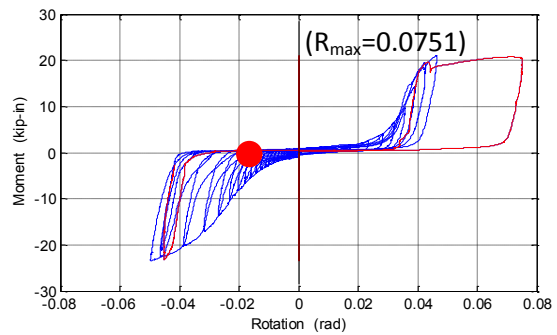
\* The red loops indicate the cycle during which the first leakage occurred.

\* The red solid dot indicates the occurrence of first leakage

Force-displacement cyclic response at the tee joint



Moment-rotation cyclic response at the right end of the tee joint



Moment-rotation cyclic response at the left end of the tee joint



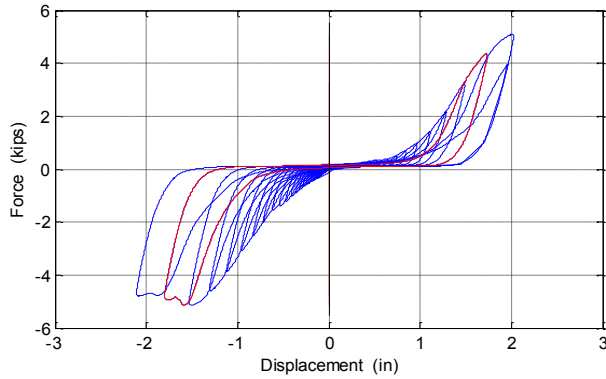
Gap generated between flange couplings



Pipe end bent due to imposed rotation



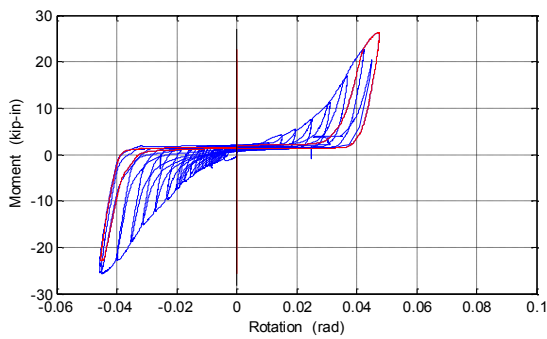
**CYCLIC TEST #3 FOR SCHEDULE-10 2" CPVC PIPES WITH CEMENT JOINTS**



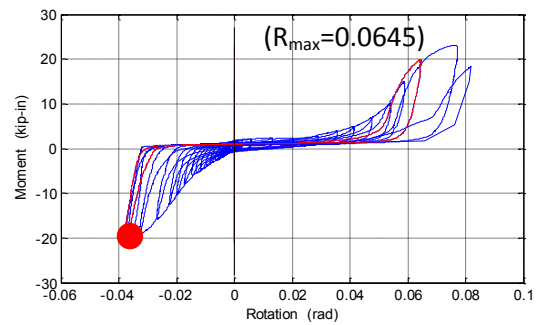
\* The red loops indicate the cycle during which the first leakage occurred.

\* The red solid dot indicates the occurrence of first leakage

Force-displacement cyclic response at the tee joint



Moment-rotation cyclic response at the right end of the tee joint



Moment-rotation cyclic response at the left end of the tee joint



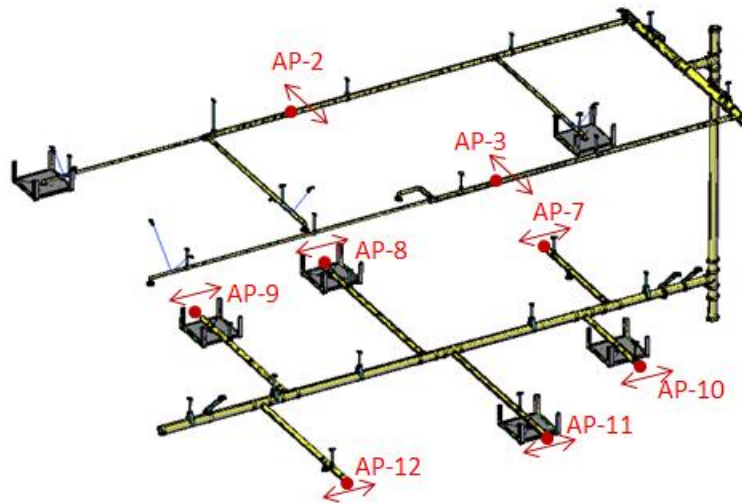
Flange coupling fractured



Groove of pipe wore away

## APPENDIX B: RESULTS OF DYNAMIC TESTS

### Summary of Peak Accelerations for Dynamic Tests



Locations of selected accelerometers

Summary of peak accelerations

Configuration	Bracing System	Percentage of Loading Protocol	BIT AP-7	CPVC AP-7	DF AP-7	BIT AP-8	CPVC AP-8	DF AP-8	BIT AP-9	CPVC AP-9	DF AP-9	BIT AP-10	CPVC AP-10	DF AP-10	BIT AP-11	CPVC AP-11	DF AP-11	BIT AP-12	CPVC AP-12	DF AP-12
			(g)	(g)	(g)	(g)	(g)	(g)	(g)	(g)	(g)	(g)	(g)	(g)	(g)	(g)	(g)	(g)	(g)	(g)
Configuration #1	Fully braced specimen (bracing systems installed according to NFPA 13)	25%	0.590	0.989	0.606	0.528	0.669	0.375	0.682	0.778	0.444	0.137	0.751	0.440	0.552	1.201	0.347	0.554	0.954	0.387
		50%	1.407	1.830	2.087	1.158	2.041	0.904	1.029	1.542	1.507	0.152	1.373	0.908	1.225	2.519	0.826	0.882	1.852	1.400
		67%	2.678	2.467	3.146	1.927	3.031	1.094	1.487	2.129	2.454	1.678	1.469	1.194	1.329	3.216	1.005	1.142	2.115	1.792
		100%	3.690	3.451	5.398	2.952	4.841	1.772	2.665	3.048	3.824	3.100	1.797	2.032	3.223	5.032	3.392	2.501	2.764	3.219
Configuration #2	Lateral and longitudinal braces removed from cross main line at the second level	25%	0.657	1.339	0.326	0.651	0.837	0.307	0.435	0.638	0.610	0.650	0.890	0.465	0.508	2.237	0.564	0.508	0.970	0.318
		50%	1.187	2.582	1.912	1.126	2.358	0.643	0.917	1.966	1.477	1.028	1.246	1.005	1.240	3.477	1.253	0.773	1.673	1.354
		67%	2.217	3.218	3.135	1.446	3.762	0.833	1.384	2.263	2.204	1.548	1.396	1.368	1.670	3.558	2.893	1.047	2.020	1.947
		100%	2.594	4.156	4.752	2.960	6.442	1.353	2.692	3.632	4.917	2.852	1.835	2.447	3.129	3.848	4.354	1.912	2.454	2.989
Configuration #3	Lateral and longitudinal braces removed from main line at the first level	25%	0.712	1.138	0.312	0.663	0.735	0.284	0.562	0.828	0.483	0.587	0.828	0.373	0.508	1.997	0.488	0.575	0.868	0.266
		50%	1.501	2.560	1.279	1.366	2.818	0.608	1.326	1.857	1.620	1.117	1.277	0.965	1.498	3.759	1.172	1.132	1.515	0.829
		67%	2.459	3.293	2.567	1.791	4.757	0.859	1.817	2.509	2.702	1.963	1.462	1.595	1.918	3.349	2.736	1.398	1.884	1.640
		100%	4.342	4.226	5.883	3.419	8.144	1.834	3.130	4.647	4.894	3.283	2.719	2.472	3.055	6.478	4.957	2.112	2.388	2.932
Configuration #4	Wire restraints removed (fully unbraced two-story specimen)	25%	0.578	1.211	0.400	0.482	1.048	0.382	0.511	0.731	0.583	0.468	0.760	0.331	0.500	1.997	0.464	0.423	0.837	0.303
		50%	1.733	2.235	1.249	1.453	3.658	0.777	1.361	1.901	1.663	1.048	1.412	0.904	1.618	3.873	1.188	1.078	1.690	0.694
		67%	2.634	3.082	2.508	1.543	6.323	0.951	2.032	3.113	2.298	1.766	1.804	1.581	2.204	3.398	1.626	1.202	2.092	1.235
		100%	4.129	N/A	5.037	2.879	N/A	2.367	2.829	N/A	4.392	3.493	N/A	2.147	3.588	N/A	5.009	2.509	N/A	2.564
Configuration #5	Vertical riser disconnected, lateral and longitudinal braces reinstalled for main line at the first level	25%	0.347	N/A	0.318	0.443	N/A	0.258	0.666	N/A	0.625	0.708	N/A	0.329	0.751	N/A	0.743	0.617	N/A	0.274
		50%	0.718	N/A	0.991	1.311	N/A	0.659	1.141	N/A	2.178	1.000	N/A	0.930	1.304	N/A	1.502	1.072	N/A	0.560
		67%	1.146	N/A	1.624	2.489	N/A	0.842	1.845	N/A	3.505	1.417	N/A	1.278	2.066	N/A	1.868	1.316	N/A	1.010
		100%	1.500	N/A	3.604	3.538	N/A	1.239	2.739	N/A	5.104	2.228	N/A	2.322	2.991	N/A	2.714	2.845	N/A	2.199
Configuration #6	Lateral and longitudinal braces removed for main line at the first level (fully unbraced single-story specimen)	25%	0.543	N/A	0.621	0.970	N/A	0.407	0.690	N/A	0.703	0.402	N/A	0.542	0.829	N/A	0.585	0.418	N/A	0.409
		50%	1.784	N/A	1.325	2.747	N/A	0.660	1.209	N/A	1.483	0.874	N/A	1.094	1.521	N/A	1.080	0.827	N/A	0.826
		67%	2.106	N/A	1.768	2.910	N/A	1.254	1.869	N/A	2.089	1.500	N/A	2.198	1.957	N/A	1.970	0.951	N/A	1.034
		100%	2.644	N/A	2.448	3.899	N/A	2.254	3.062	N/A	4.839	1.882	N/A	2.607	4.275	N/A	2.869	1.503	N/A	1.177

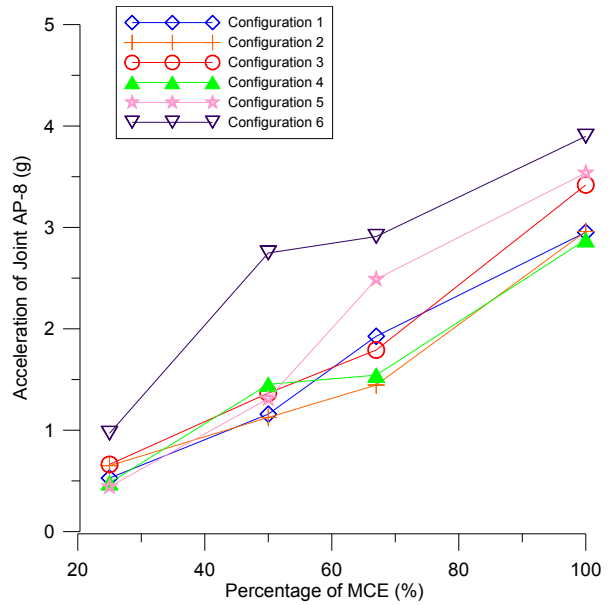
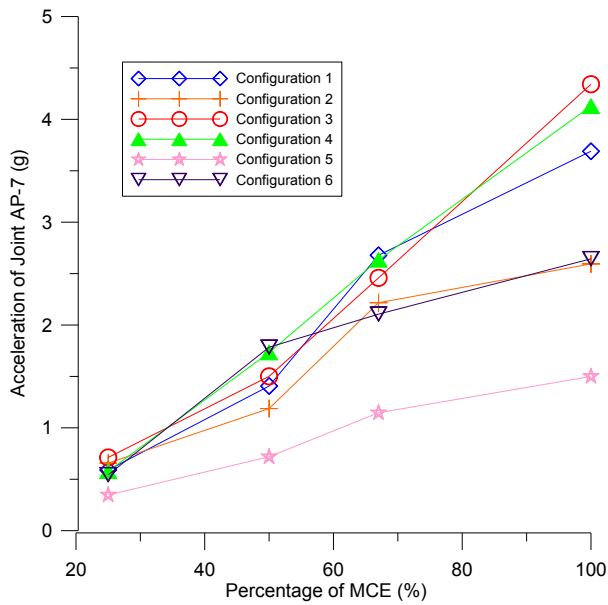
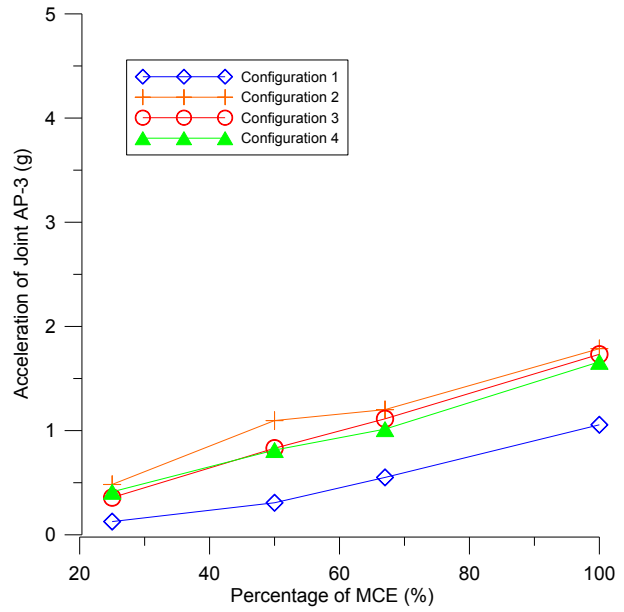
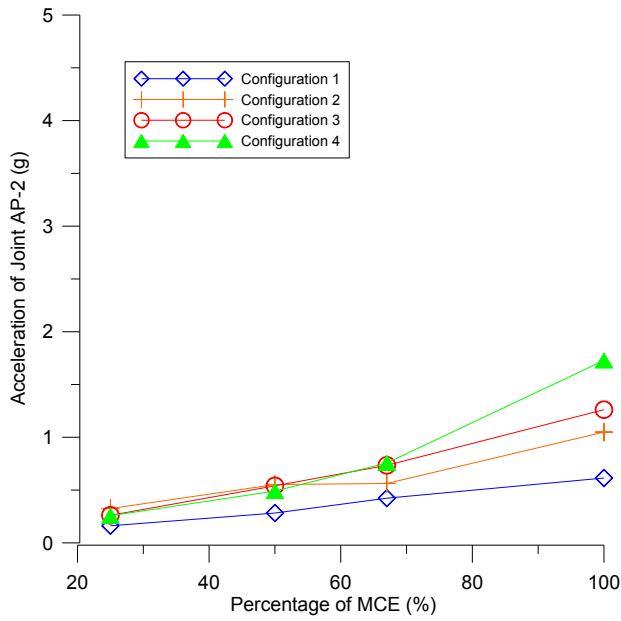
Note:

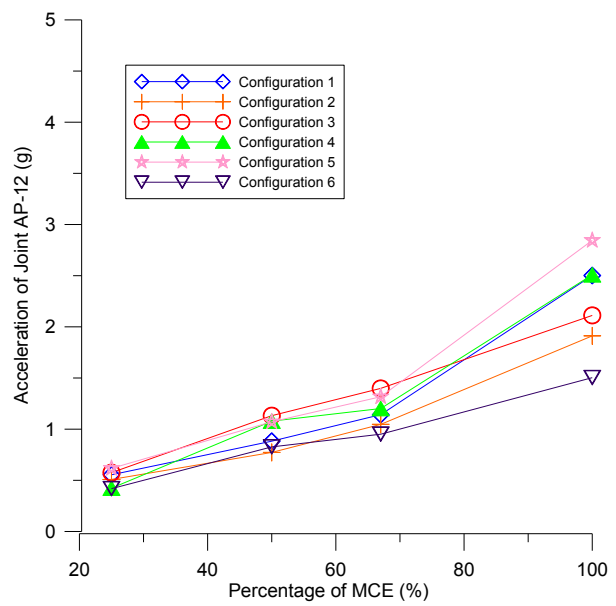
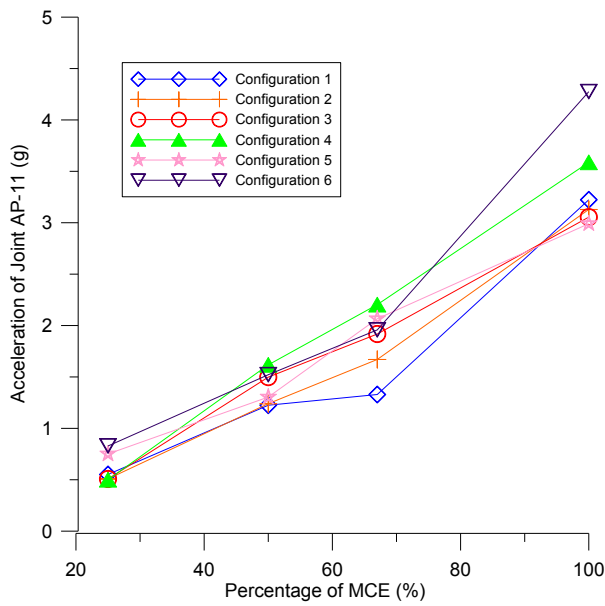
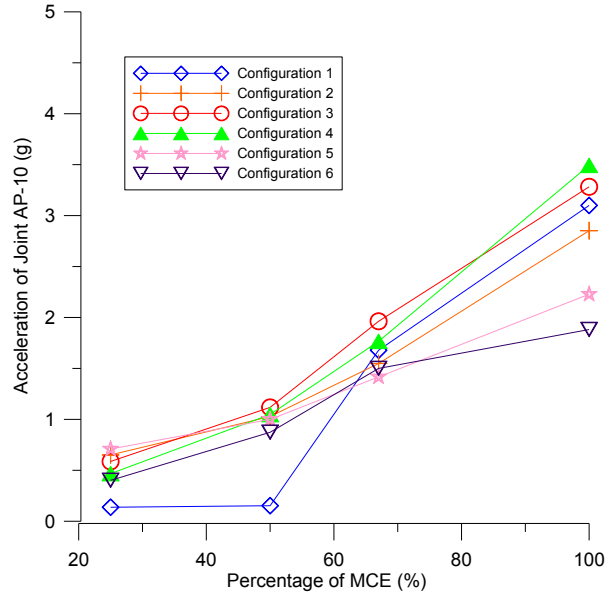
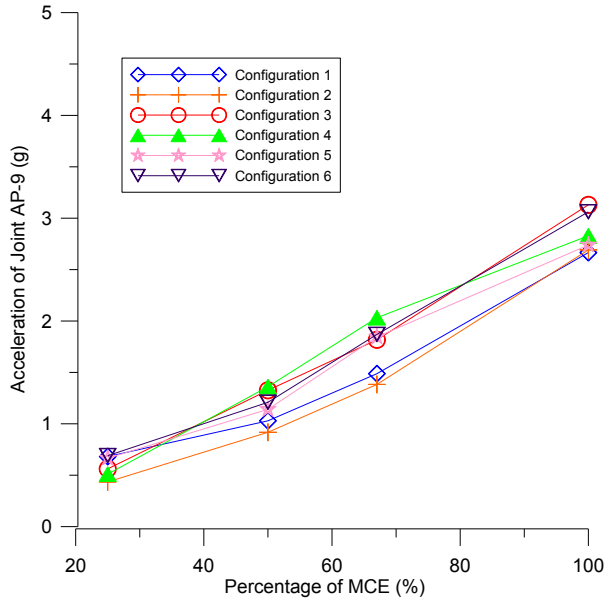
BIT indicates black iron pipes with threaded joints;

CPVC indicates CPVC pipes with cement joints;

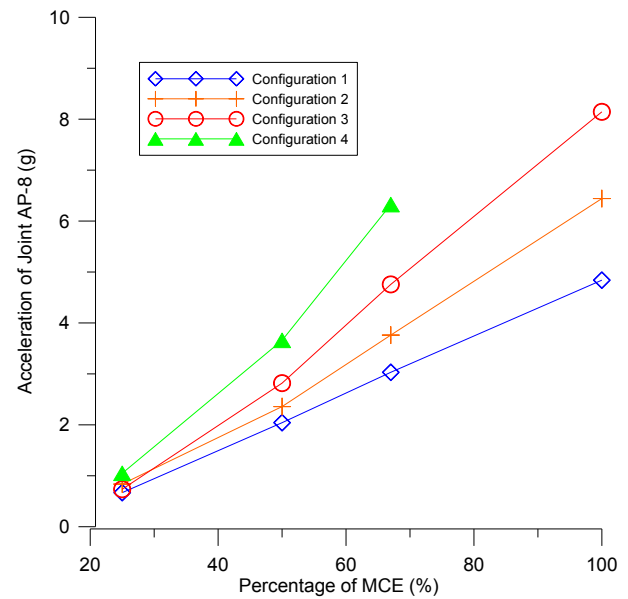
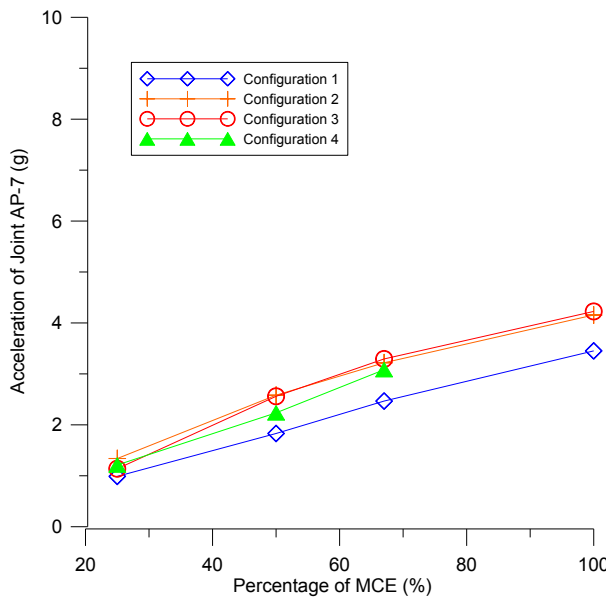
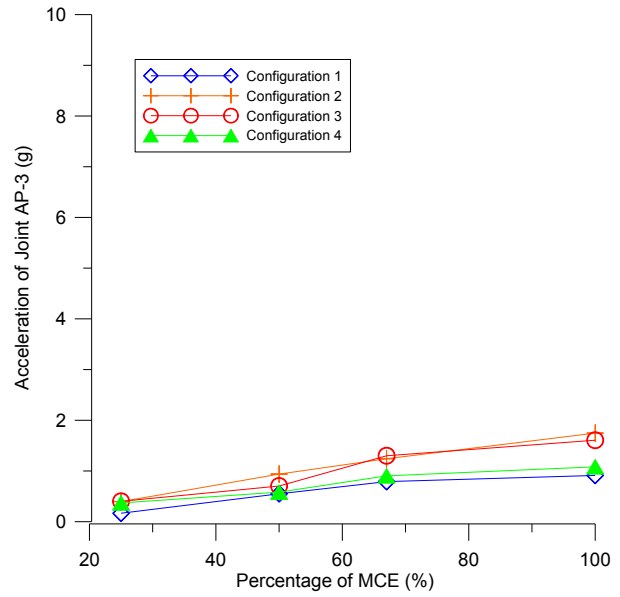
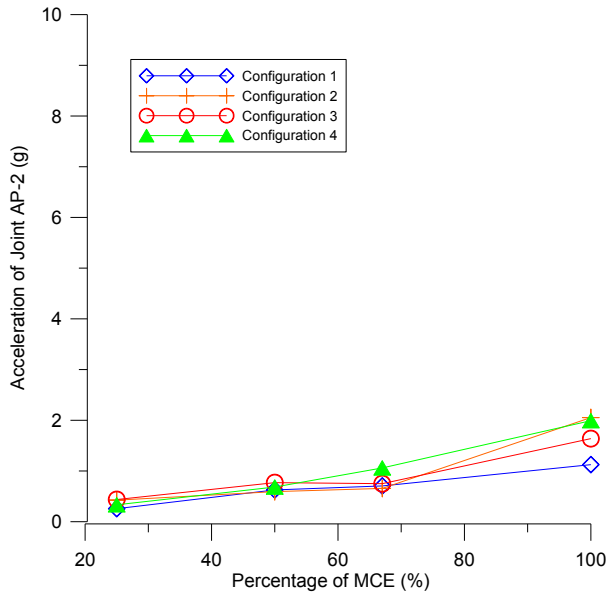
DF indicates Dyna-Flow steel pipes with groove-fit connections.

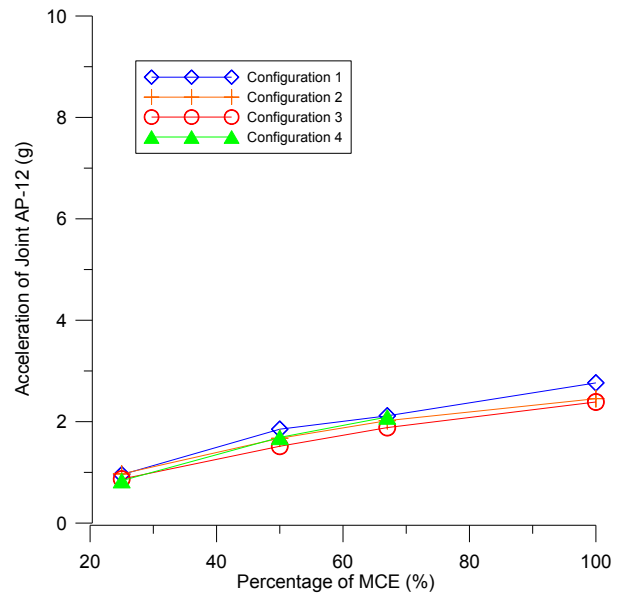
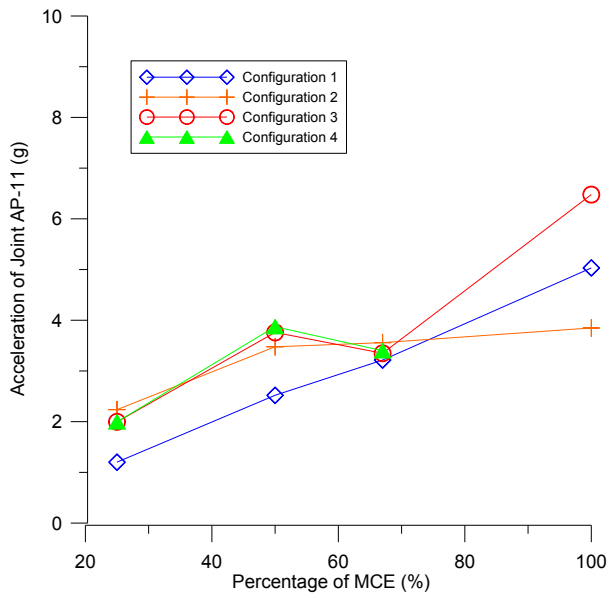
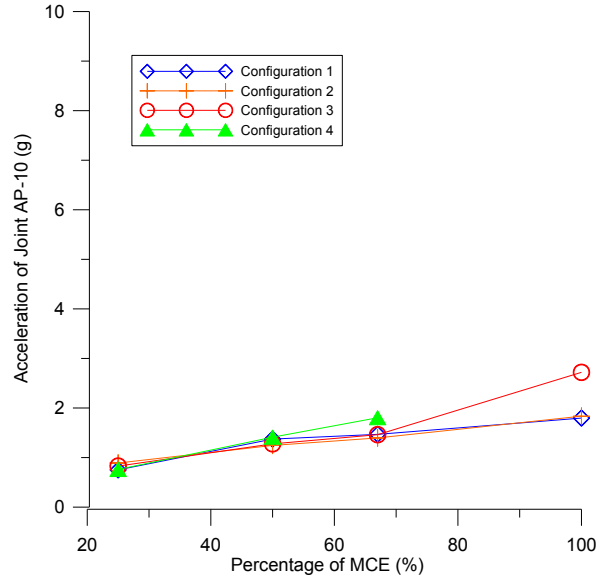
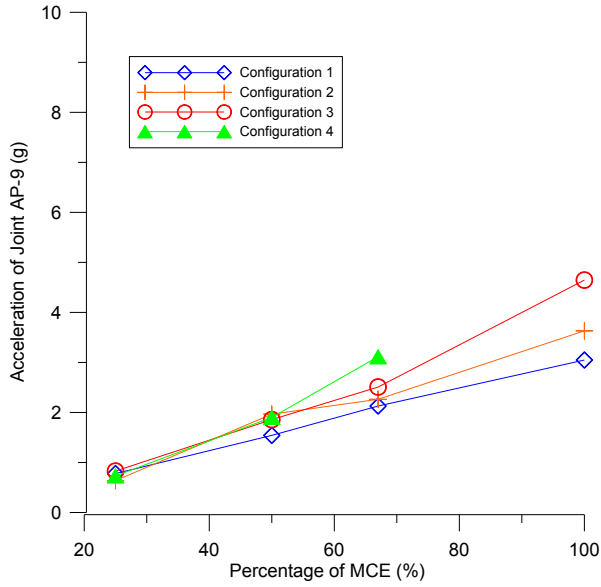
Peak accelerations at critical locations for Specimen #1 (black iron pipes with threaded joints)



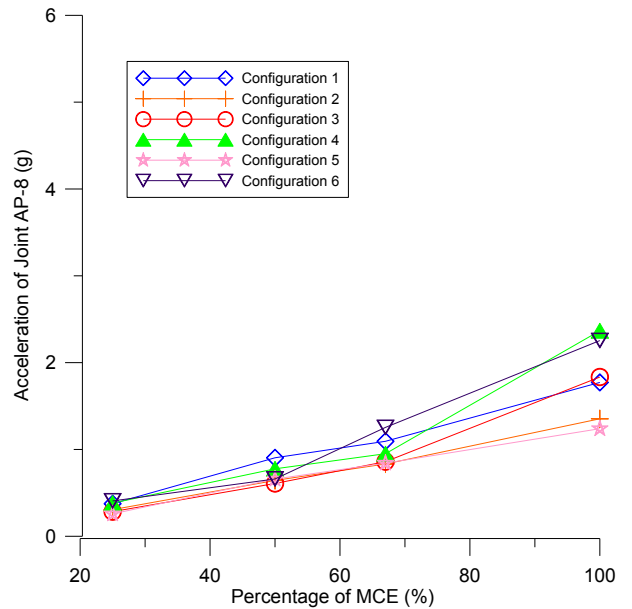
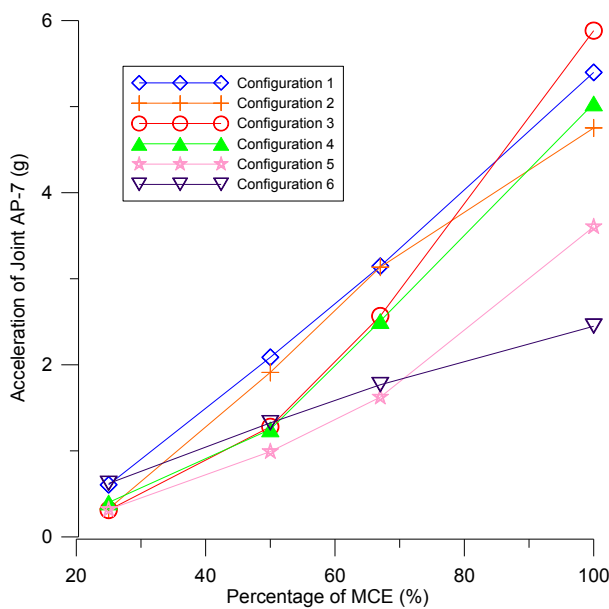
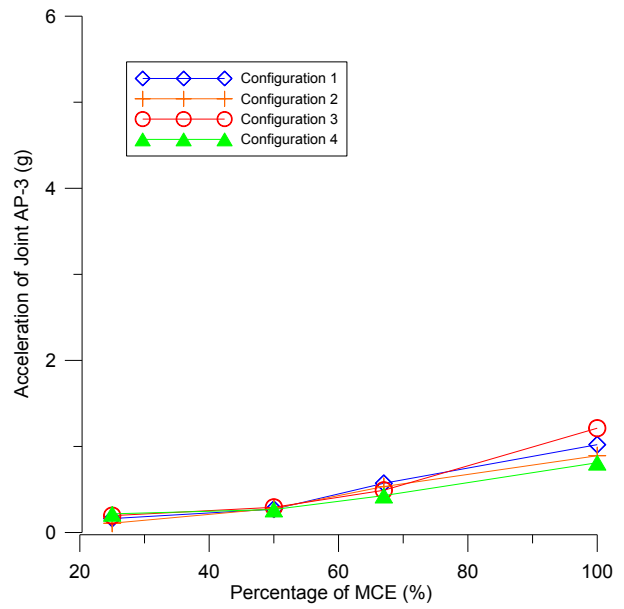
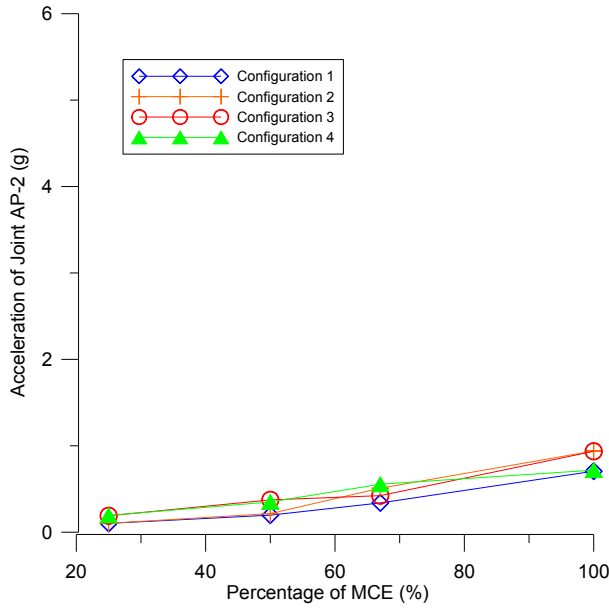


Peak accelerations at critical locations for Specimen #2 (CPVC pipes with cement joints)

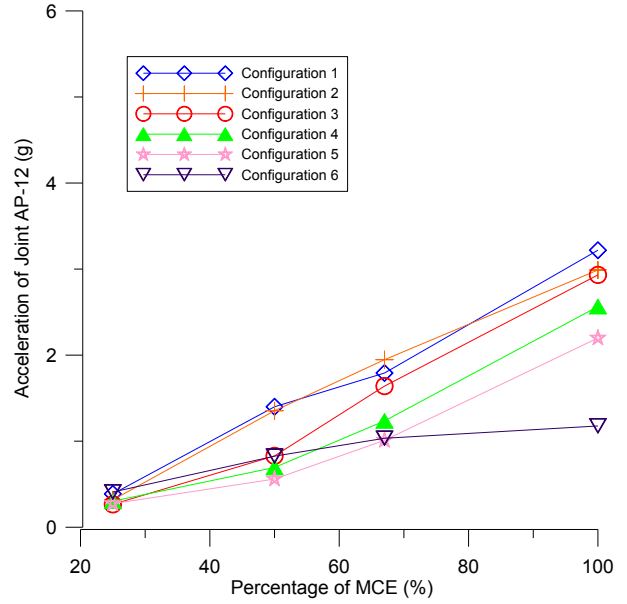
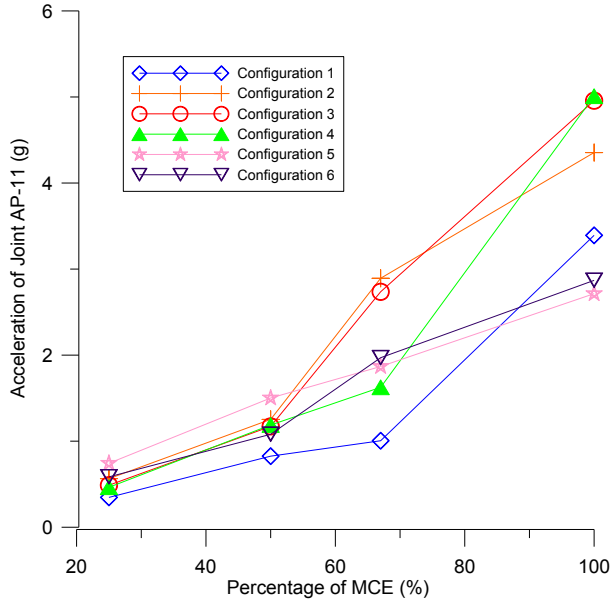
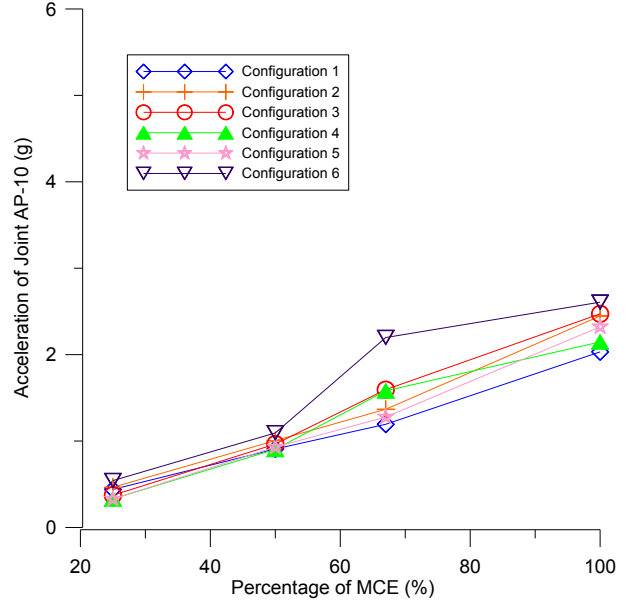
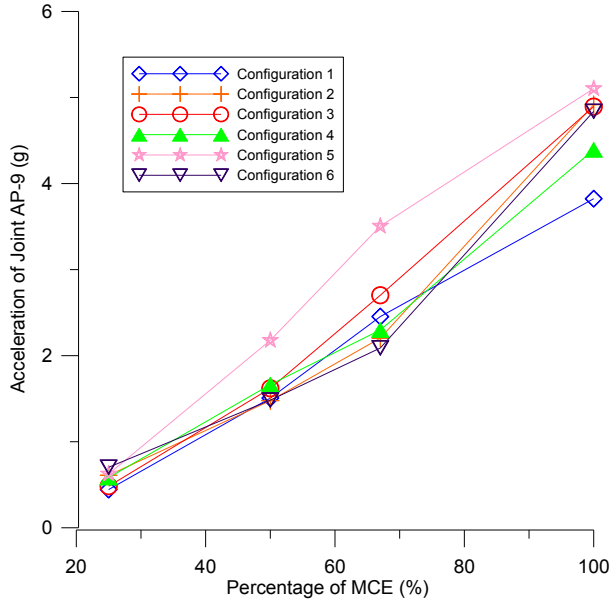




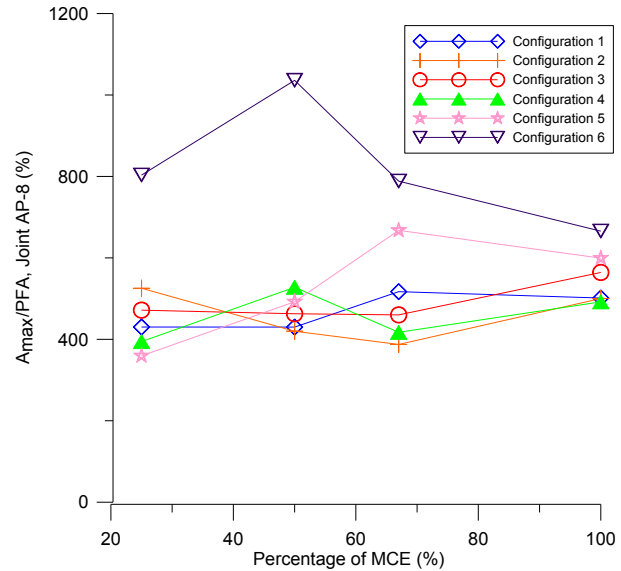
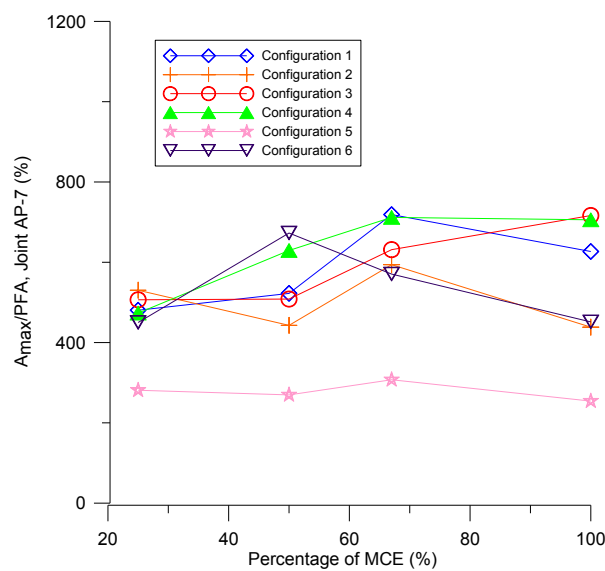
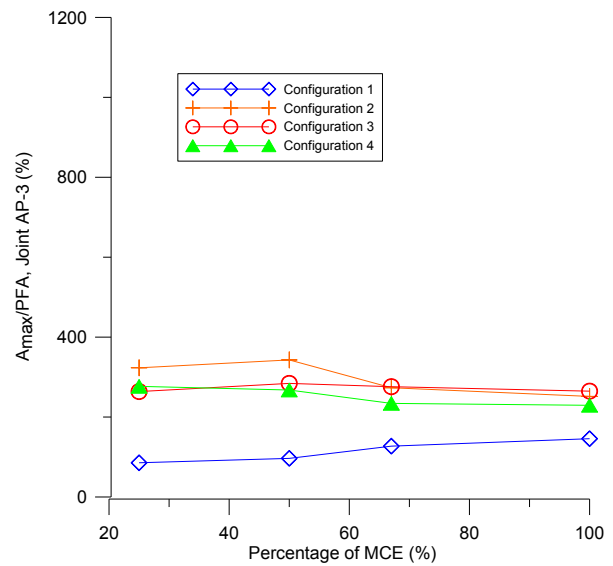
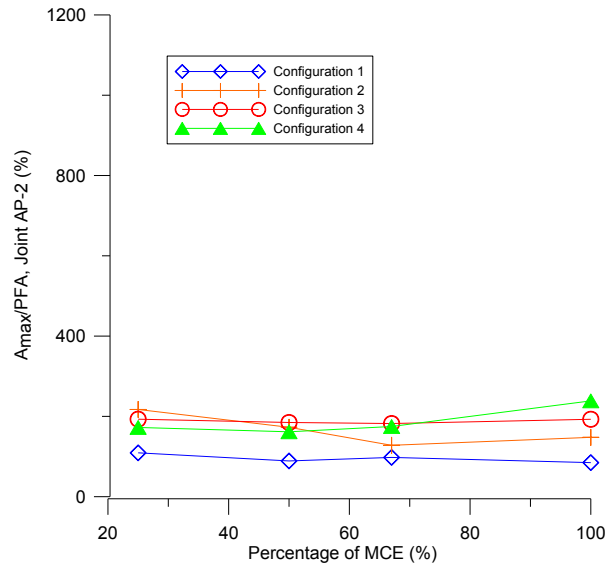
Peak accelerations at critical locations for Specimen #3 (Dyna-Flow steel pipes with groove-fit connections)

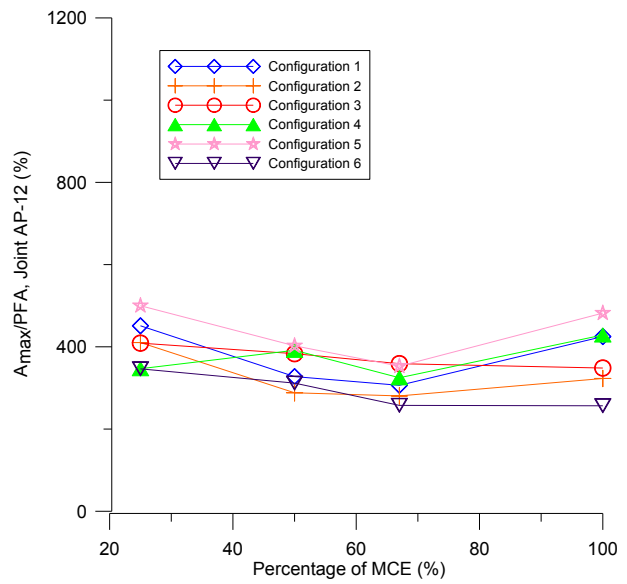
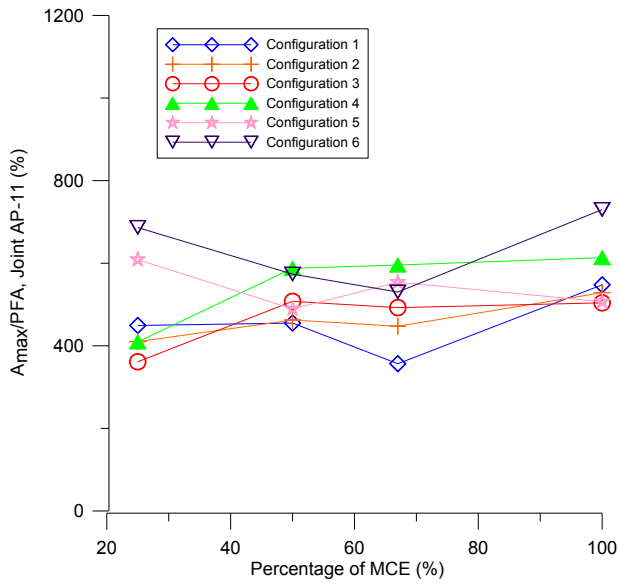
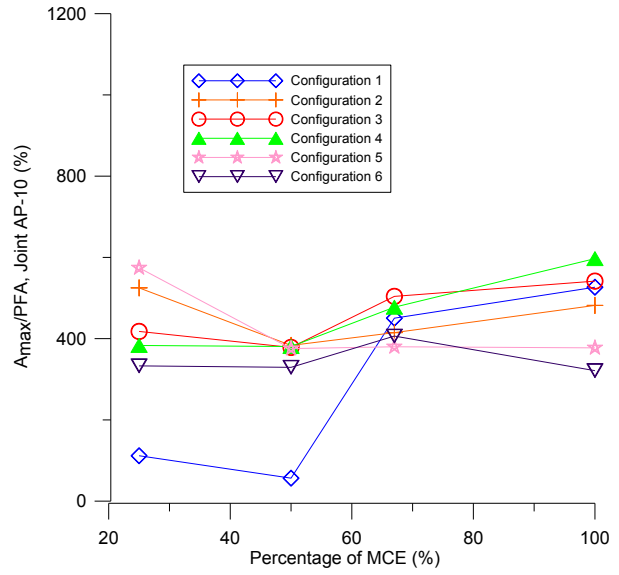
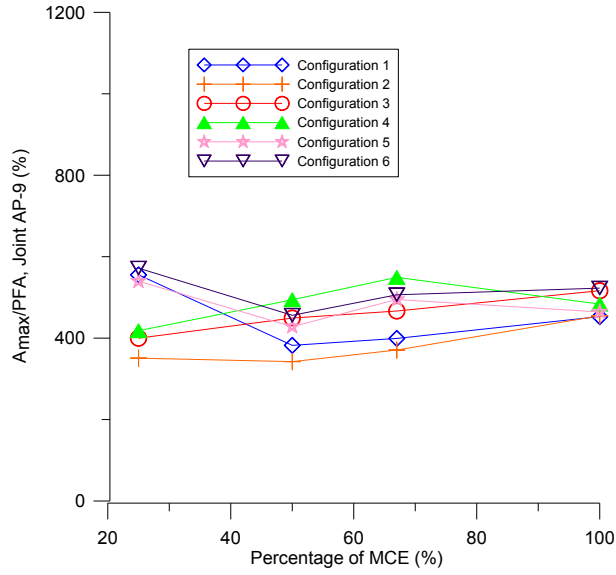




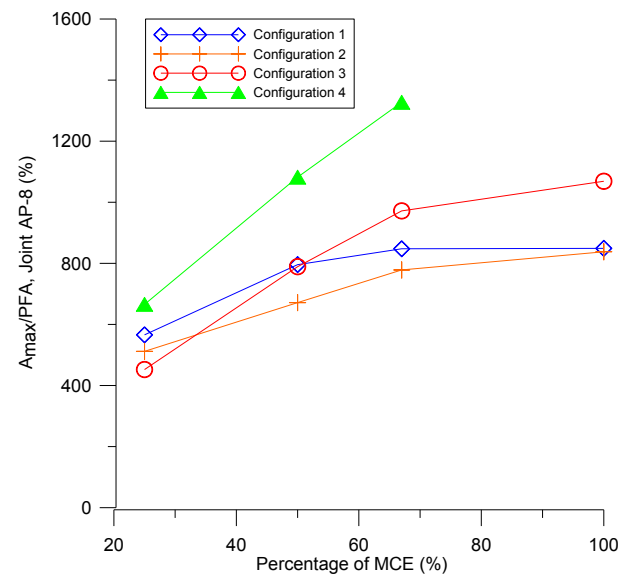
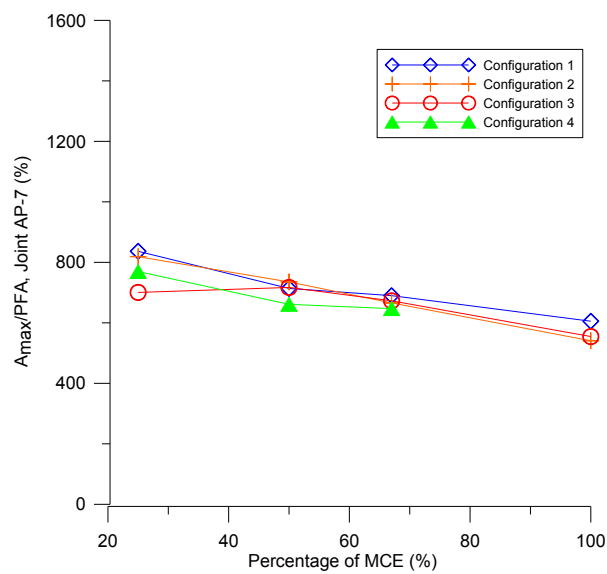
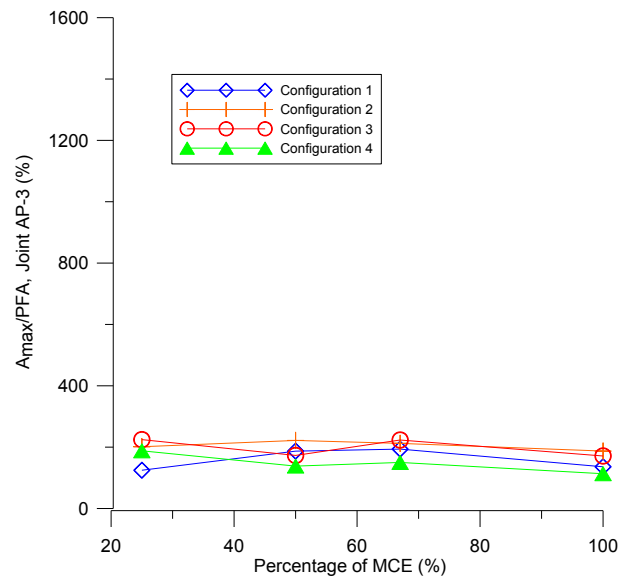
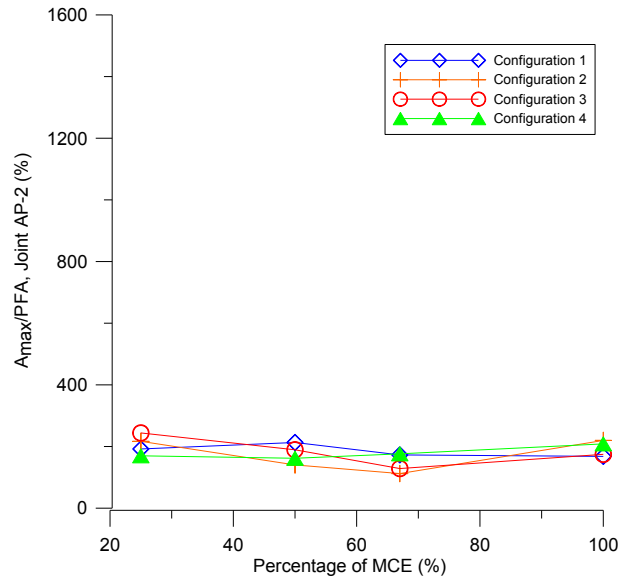


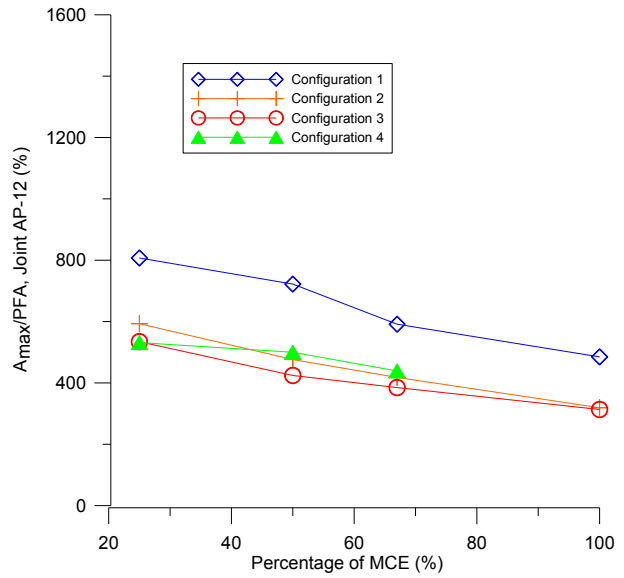
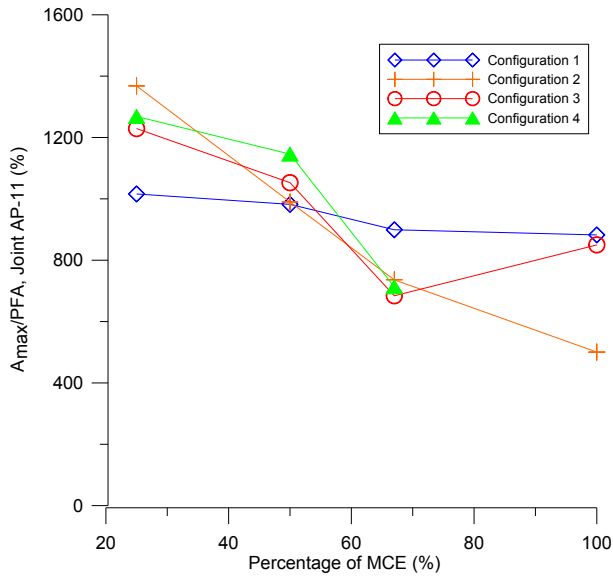
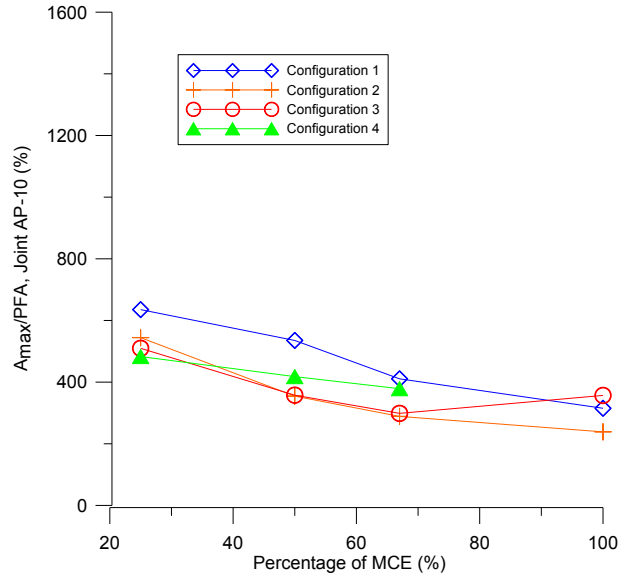
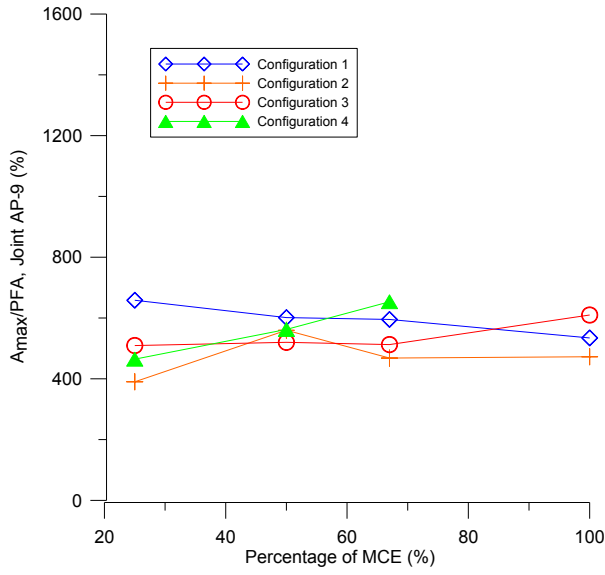
Amplification factors of accelerations for Specimen #1 (black iron pipes with threaded joints) compared to peak floor acceleration (PFA)



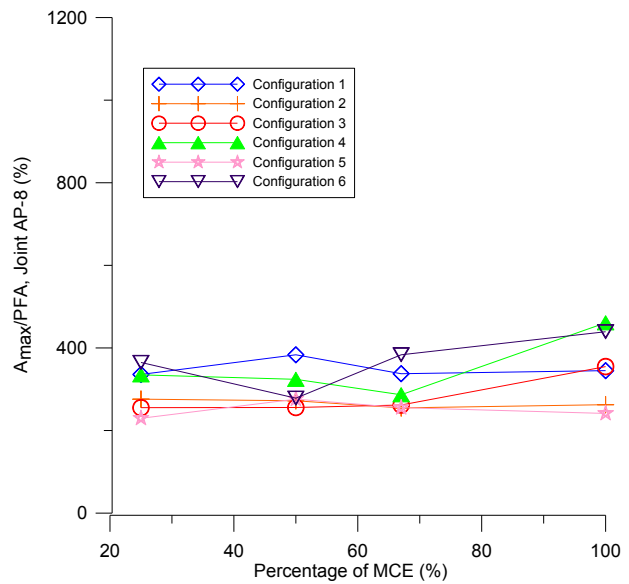
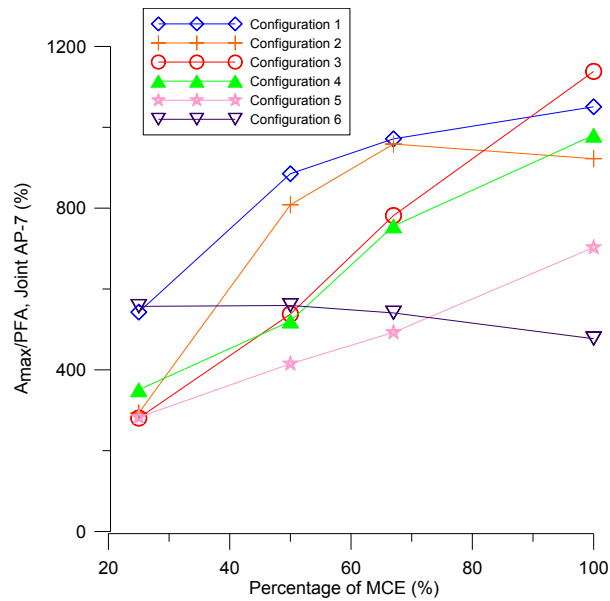
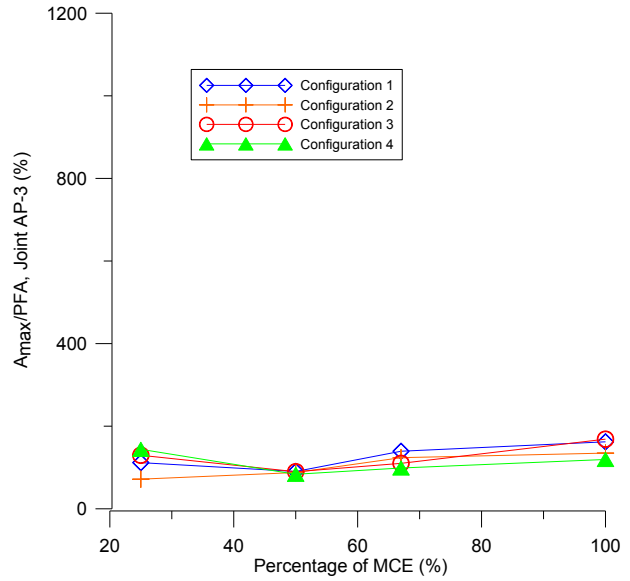
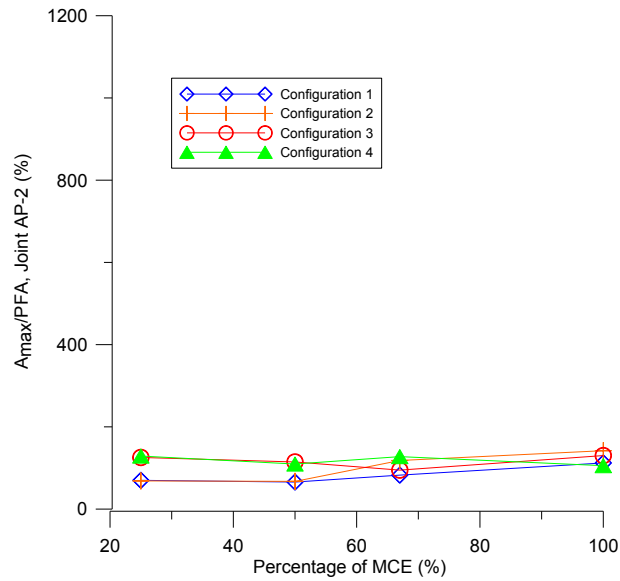


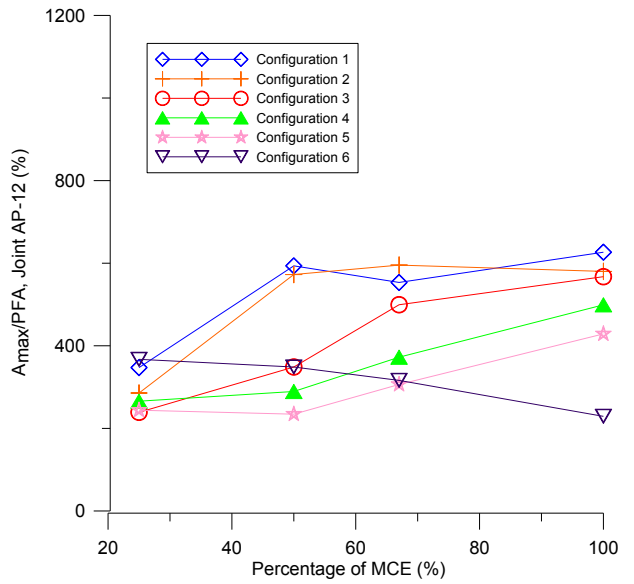
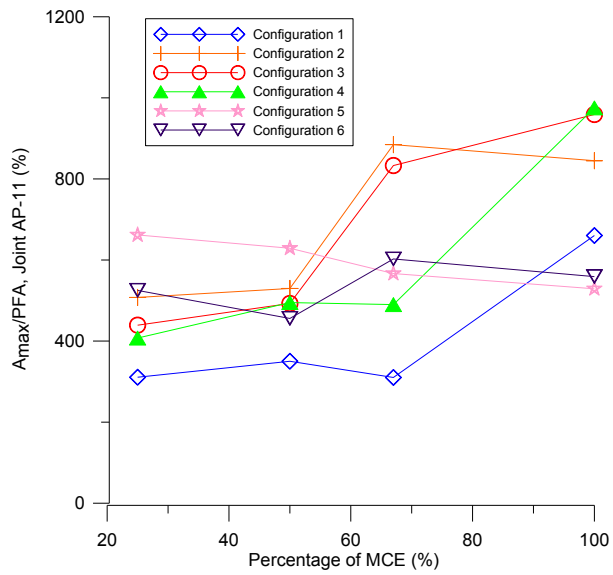
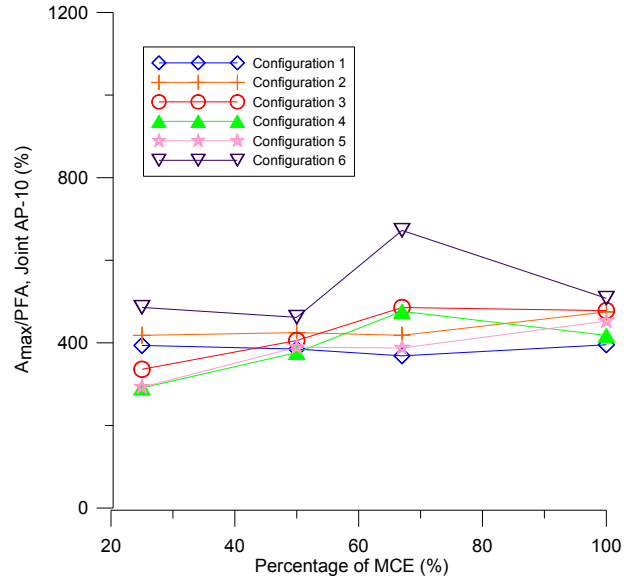
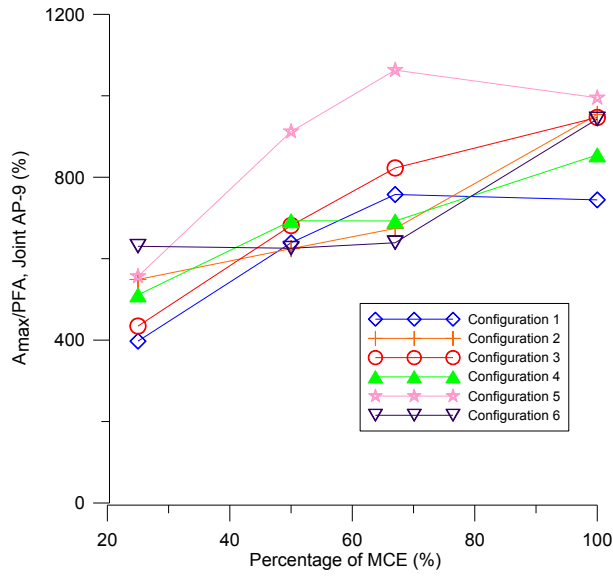
Amplification factors of accelerations for Specimen #2 (CPVC pipes with cement joints) compared to PFA



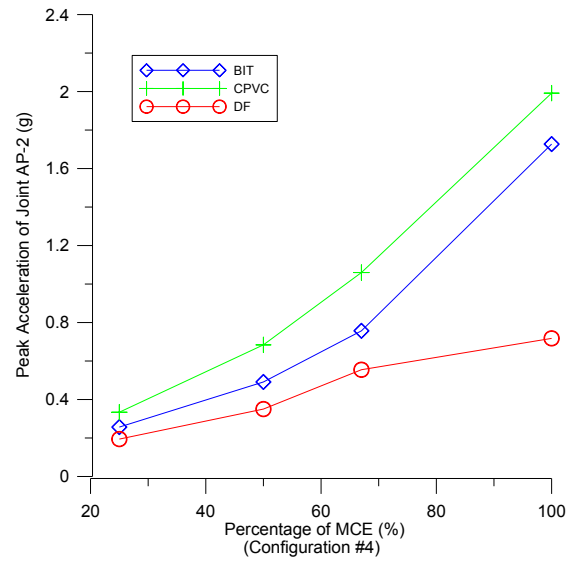
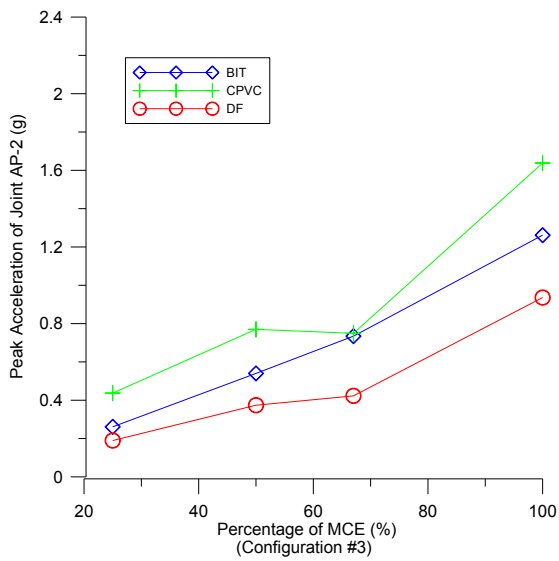
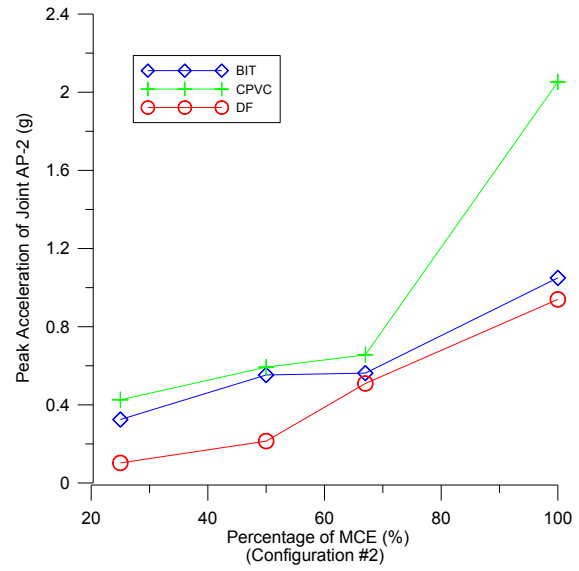
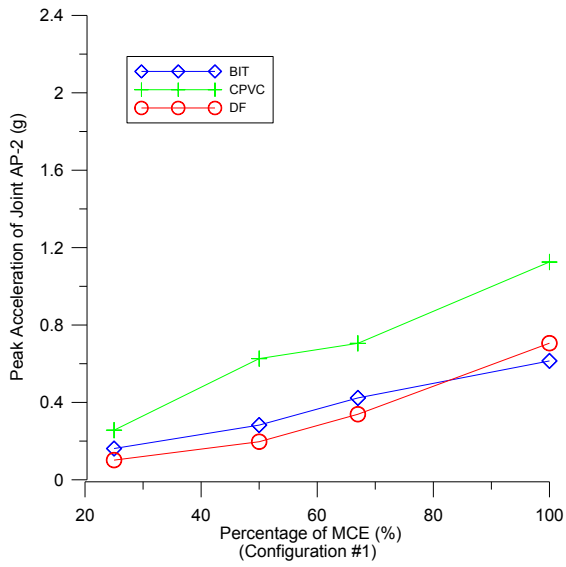


Amplification factors of accelerations for Specimen #3 (Dyna-Flow steel pipes with groove-fit connections) compared to PFA



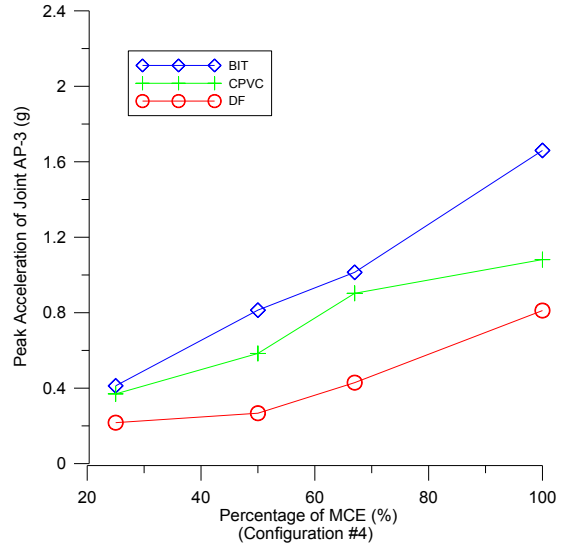
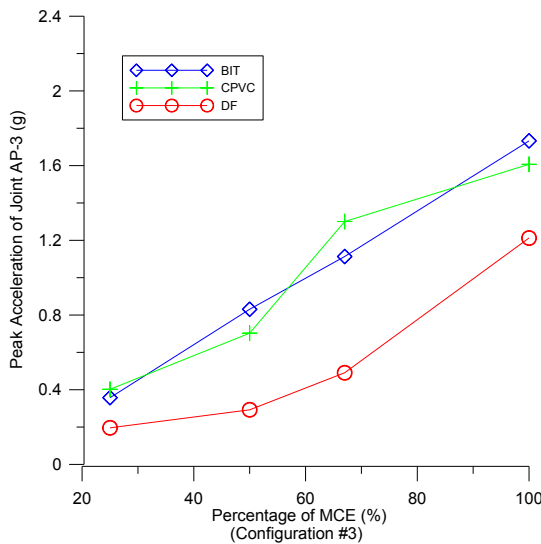
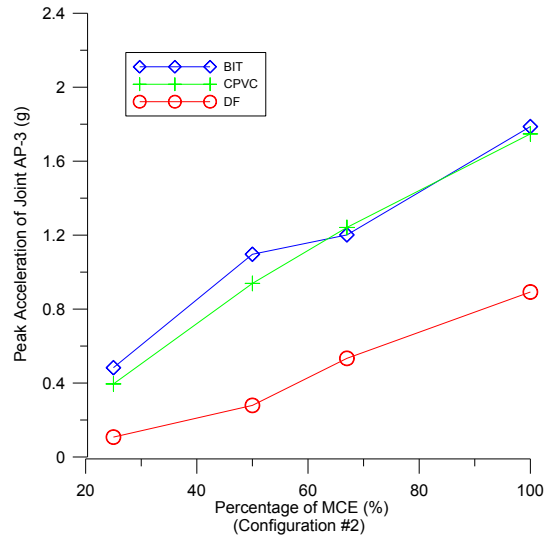
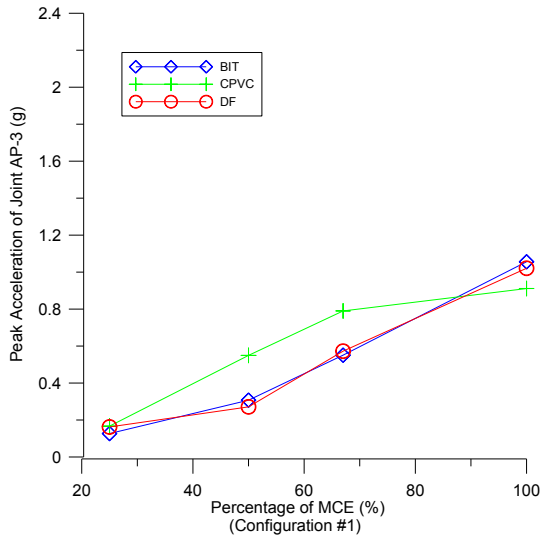


Comparison of peak accelerations for AP-2 across materials

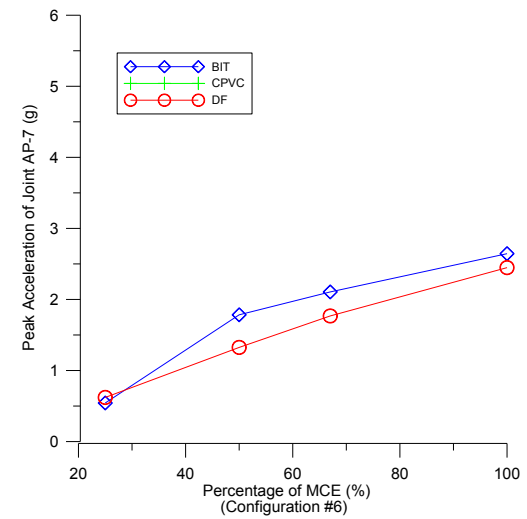
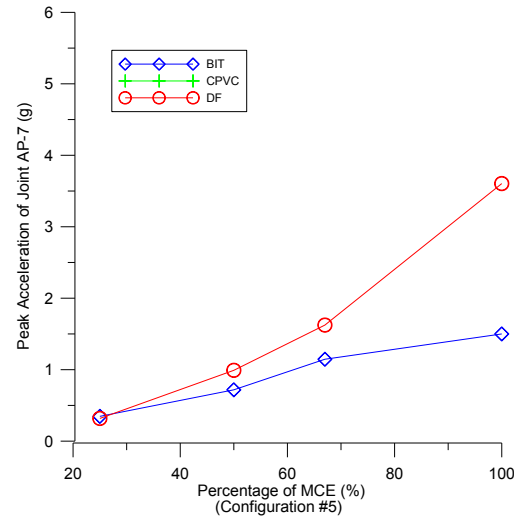
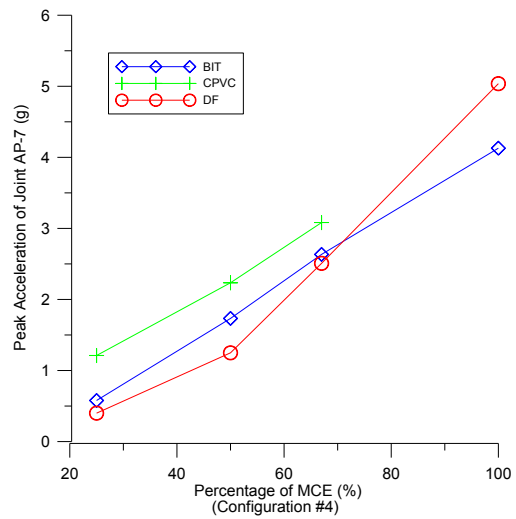
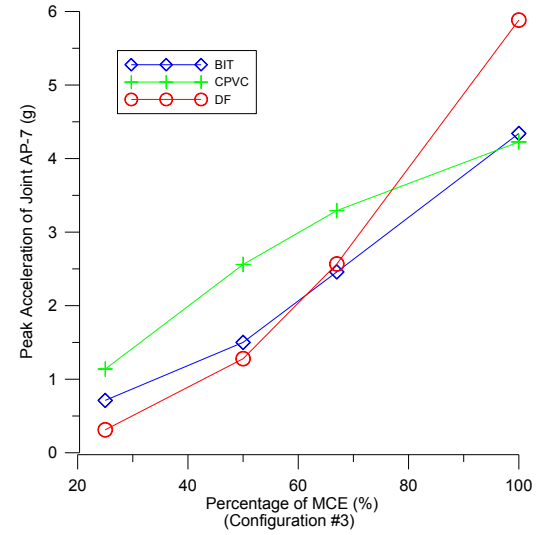
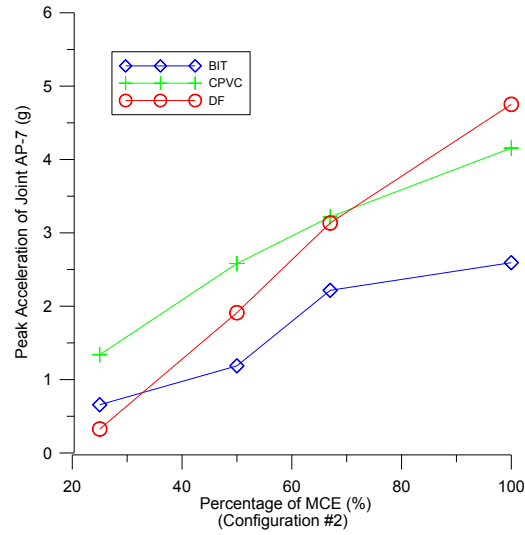
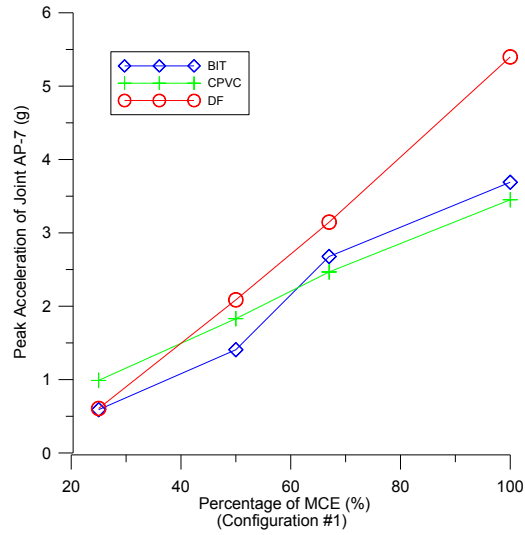




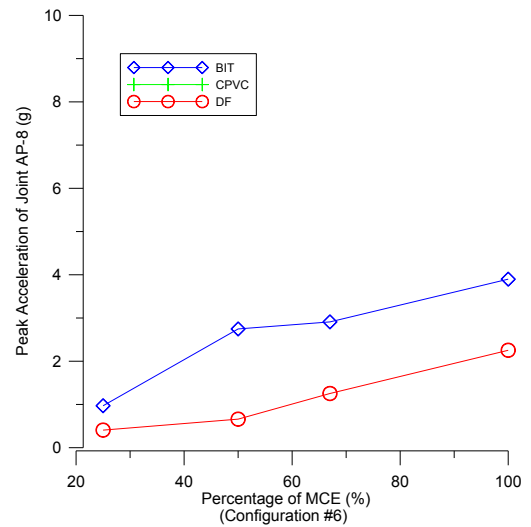
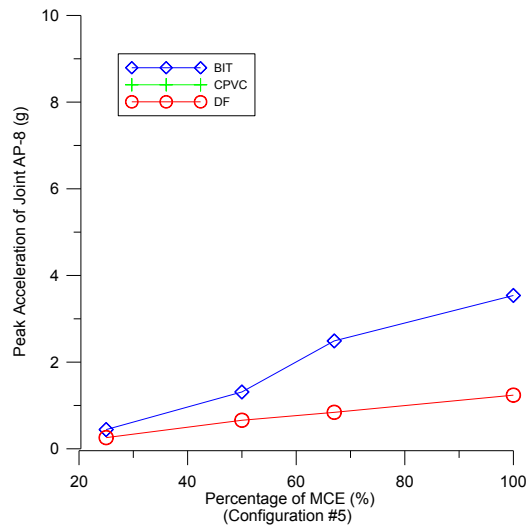
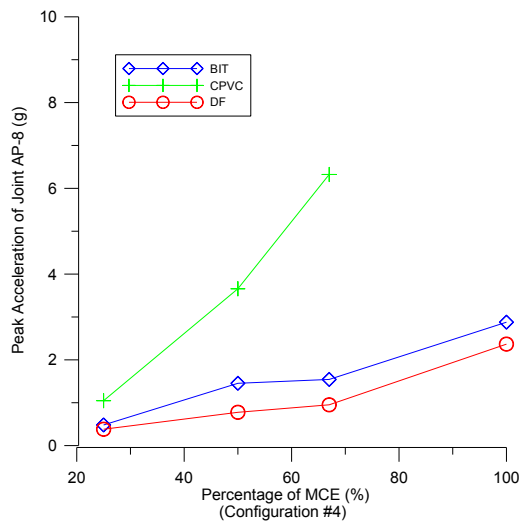
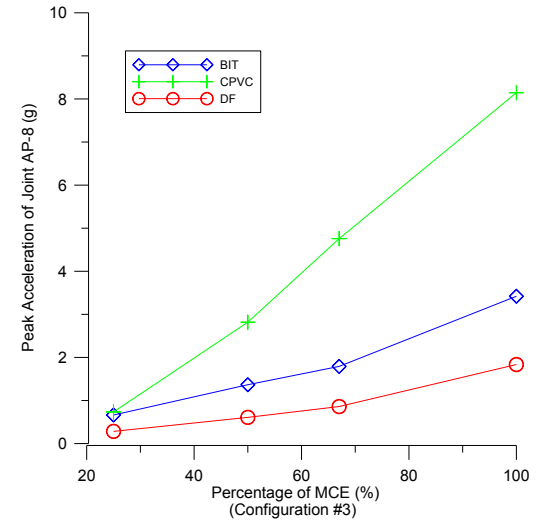
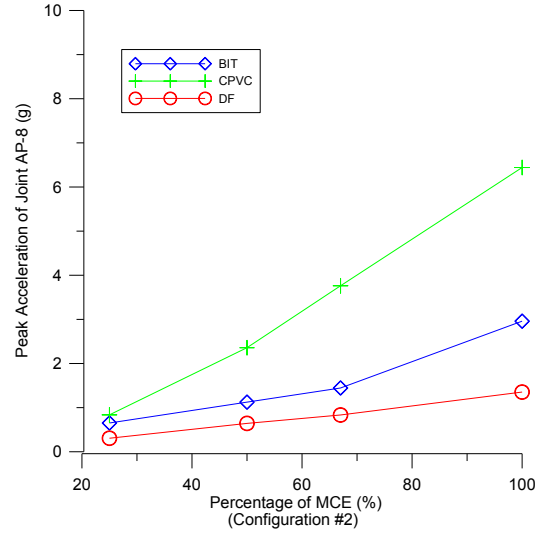
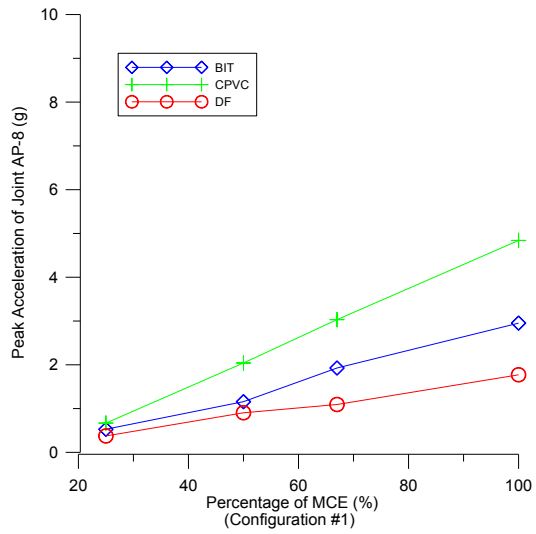
Comparison of peak accelerations for AP-3 across materials



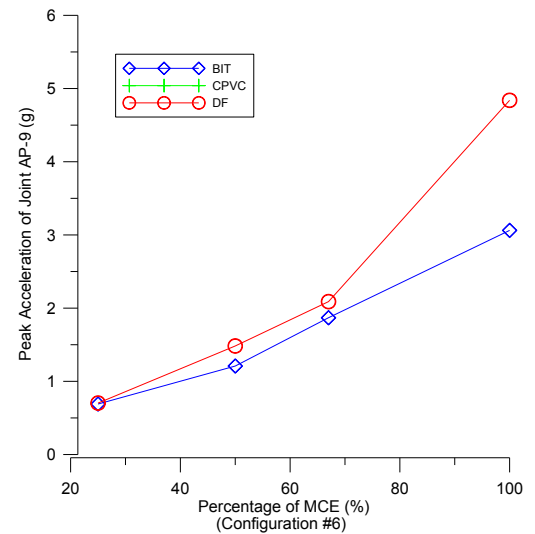
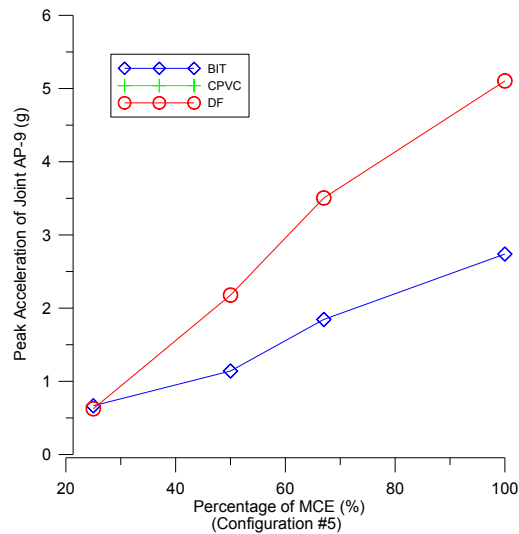
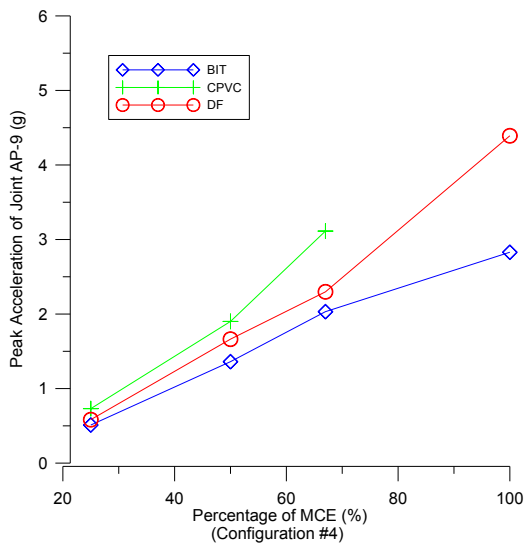
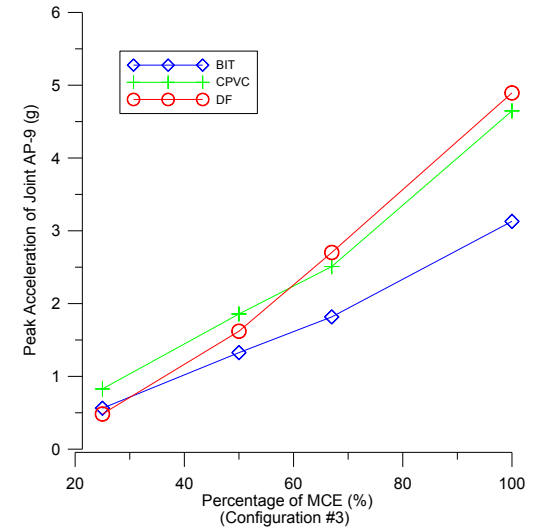
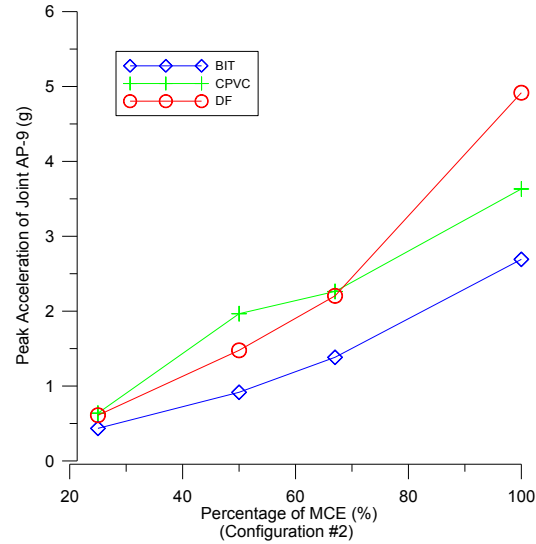
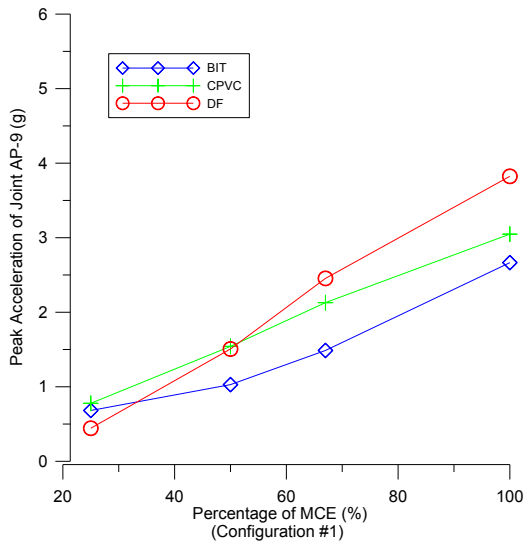
Comparison of peak accelerations for AP-7 across materials



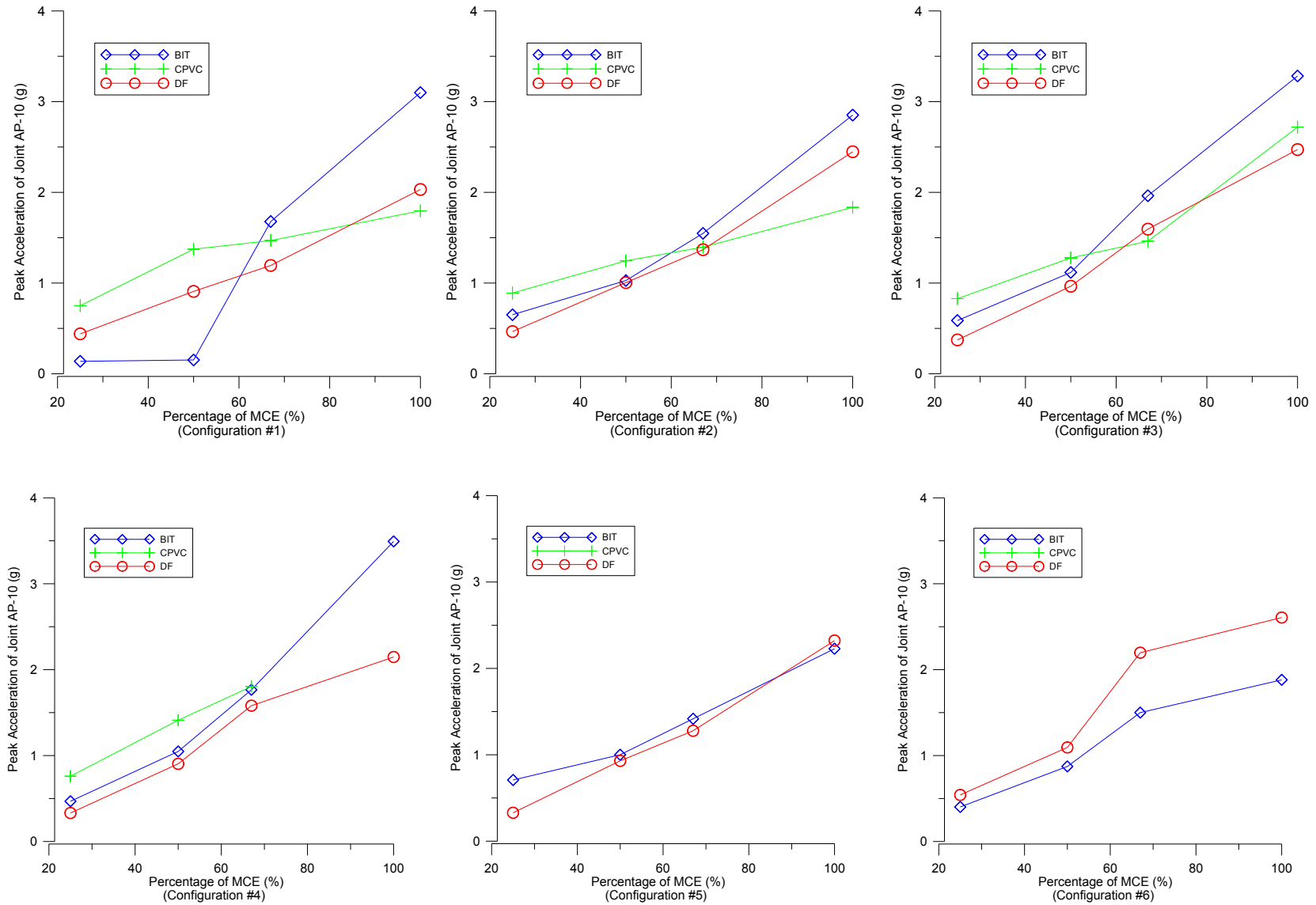
Comparison of peak accelerations for AP-8 across materials



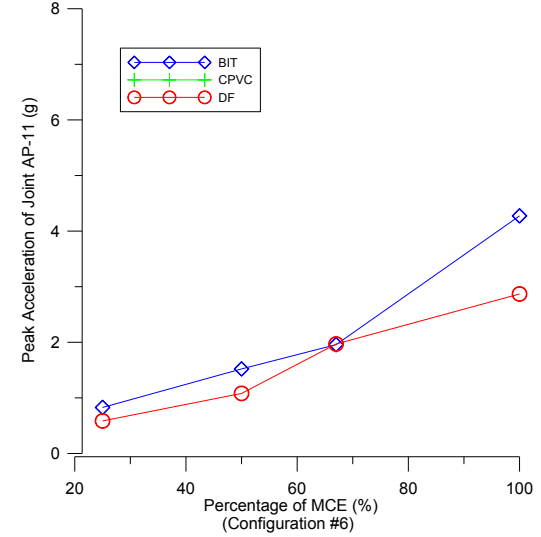
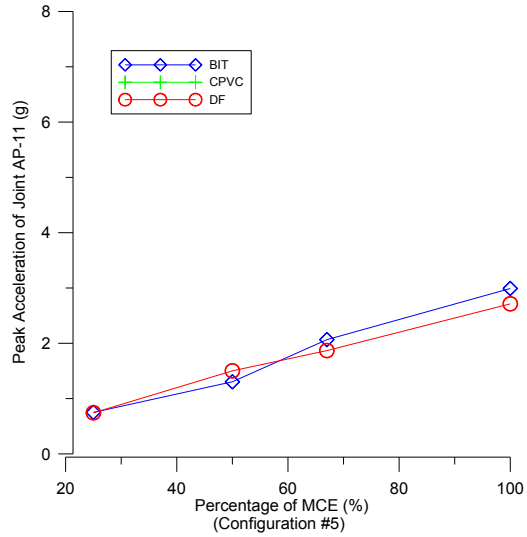
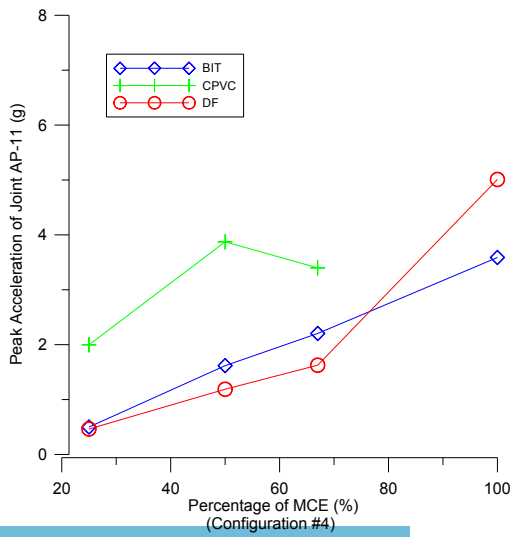
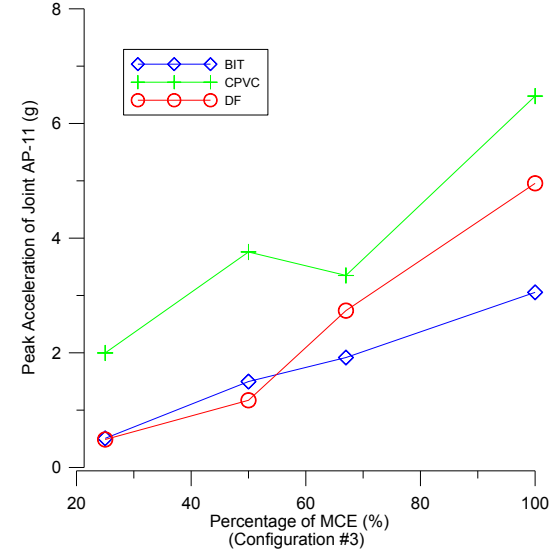
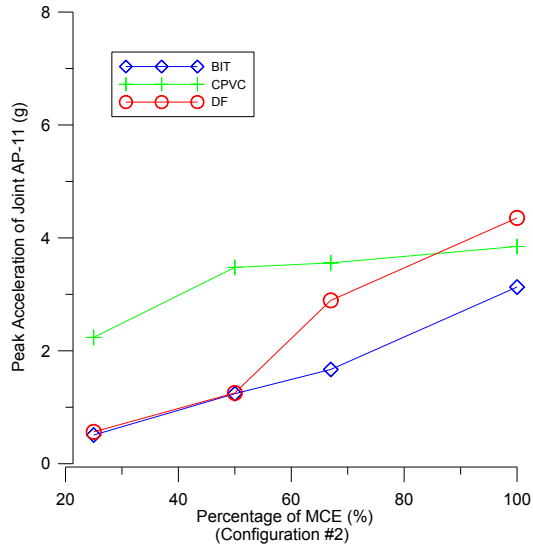
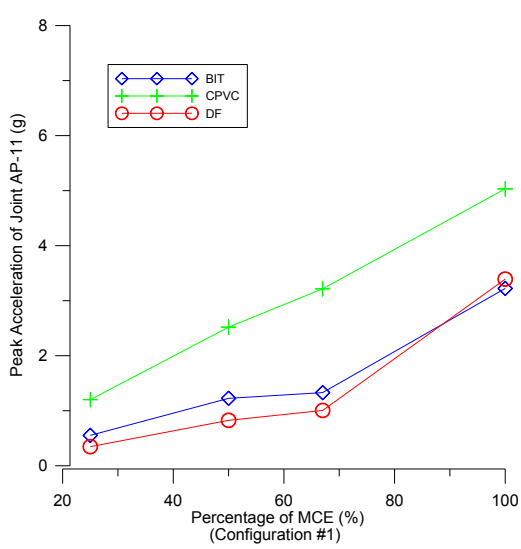
Comparison of peak accelerations for AP-9 across materials



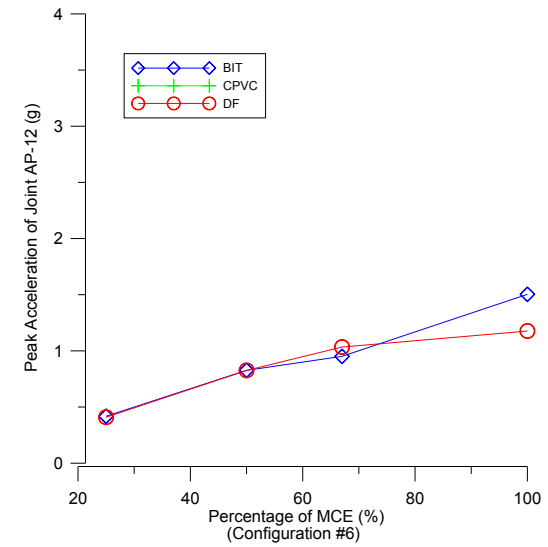
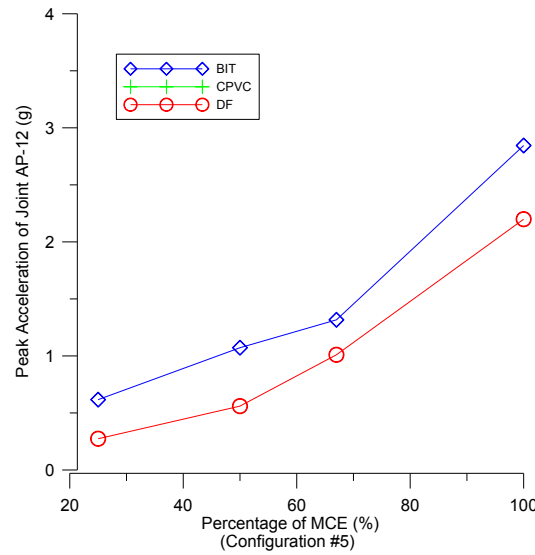
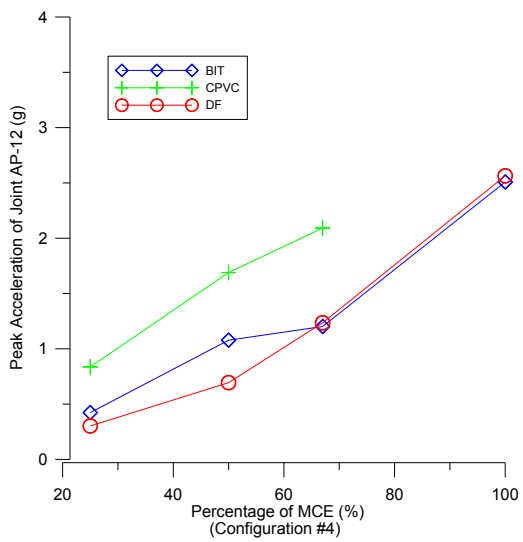
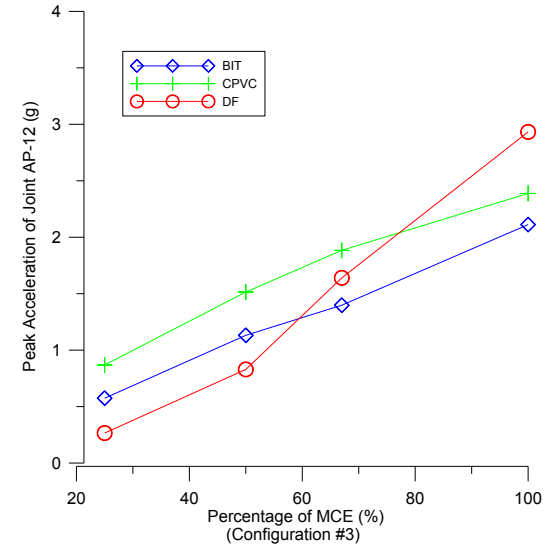
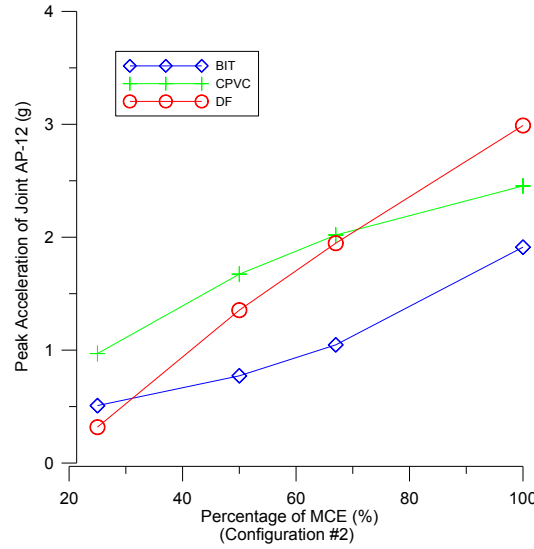
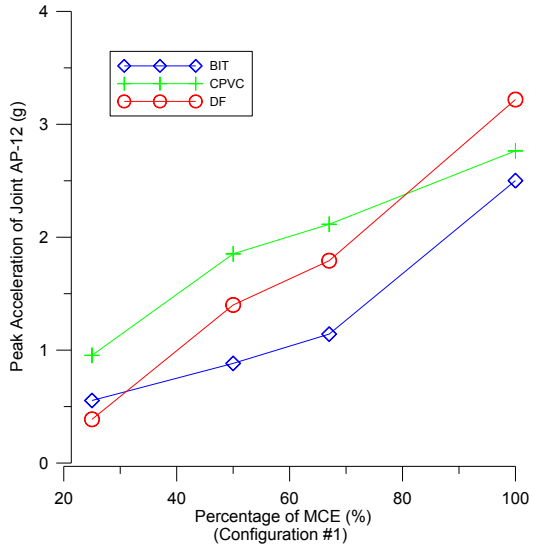
Comparison of peak accelerations for AP-10 across materials



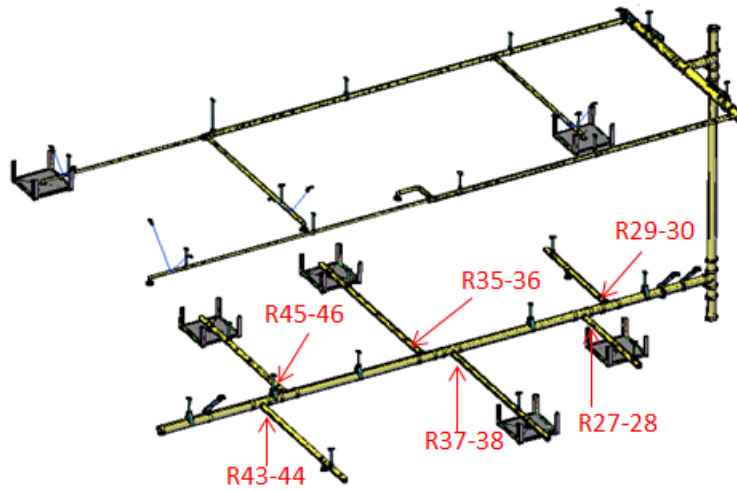
Comparison of peak accelerations for AP-11 across materials



Comparison of peak accelerations for AP-12 across materials



Summary of Peak Rotations for Dynamic Tests



Locations of selected joint rotations



Summary of peak rotations

Configuration	Bracing System	Percentage of Loading Protocol	BIT R27-28	CPVC R27-28	DF R27-28	BIT R29-30	CPVC R29-30	DF R29-30	BIT R35-36	CPVC R35-36	DF R35-36	BIT R37-38	CPVC R37-38	DF R37-38	BIT R43-44	CPVC R43-44	DF R43-44	BIT R45-46	CPVC R45-46	DF R45-46
			(rad)	(rad)	(rad)	(rad)	(rad)	(rad)	(rad)	(rad)	(rad)	(rad)	(rad)	(rad)	(rad)	(rad)	(rad)	(rad)	(rad)	(rad)
Configuration #1	Fully braced specimen (bracing systems installed according to NFPA 13)	25%	0.000437	0.000682	0.002108	0.000614	0.009268	0.036696	0.000467	0.001059	0.001277	0.000698	0.006378	0.053191	0.000593	0.008506	0.030775	0.000449	0.000942	0.003797
		50%	0.000681	0.001251	0.004150	0.001470	0.017117	0.066764	0.000817	0.001737	0.001960	0.000939	0.012031	error	0.001014	0.016049	0.060749	0.000774	0.002083	0.004598
		67%	0.000922	0.001938	0.005566	0.002701	0.023788	0.083211	0.001489	0.002182	error	0.001600	0.014430	error	0.001109	0.020562	0.069938	0.001171	0.005526	0.008595
		100%	0.001704	0.004684	0.010329	0.004539	0.041621	0.094163	0.002610	0.003361	0.007836	0.003344	0.018982	error	0.002635	0.029898	0.075304	0.001947	0.016754	0.056436
Configuration #2	Lateral and longitudinal braces removed from cross main line at the second level	25%	0.000474	0.000936	0.003258	0.000934	0.014493	0.019085	0.000625	0.001843	0.003941	0.000649	0.007804	0.032975	0.000507	0.004839	0.019241	0.000527	0.003860	0.037390
		50%	0.000788	0.001716	0.009902	0.001807	0.030298	0.075234	0.001065	0.002750	0.007804	0.001001	0.013103	0.065601	0.000790	0.008836	0.054813	0.001010	0.005002	0.056986
		67%	0.001098	0.003533	0.012340	0.003262	0.039628	0.105193	0.001540	0.003372	0.009440	0.001619	0.015334	0.084411	0.001078	0.010598	0.064538	0.001170	0.011063	0.060587
		100%	0.001946	0.006056	0.019992	0.004058	0.062577	0.113451	0.003486	0.005748	0.020608	0.002806	0.020630	0.097957	0.002118	0.013476	0.075072	0.001901	0.019432	0.063461
Configuration #3	Lateral and longitudinal braces removed from main line at the first level	25%	0.000522	0.002339	0.003567	0.000853	0.014496	0.014458	0.000524	0.002556	0.007165	0.000590	0.006955	0.022603	0.000400	0.004162	0.009424	0.000504	0.002827	0.024059
		50%	0.000957	0.004775	0.014093	0.002204	0.035437	0.061557	0.001084	0.005000	0.011783	0.001146	0.012610	0.050968	0.001017	0.007976	0.020383	0.000892	0.008437	0.044305
		67%	0.002002	0.008839	0.023168	0.003521	0.051839	0.084506	0.001421	0.006140	0.013553	0.001756	0.015922	0.065488	0.001221	0.009303	0.036027	0.001199	0.014197	0.051208
		100%	0.002749	0.016991	0.027192	0.008337	0.084240	0.107115	0.002886	0.009746	0.009424	0.004228	0.030973	0.074503	0.001627	0.012637	0.055942	0.002288	0.022106	0.062955
Configuration #4	Wire restrains removed (fully unbraced two-story specimen)	25%	0.000474	0.003195	0.003035	0.001482	0.017852	0.004086	0.000427	0.002525	0.008512	0.000494	0.006477	0.020689	0.000307	0.004462	0.002553	0.000496	0.003145	0.002374
		50%	0.001118	0.006327	0.010248	0.003357	0.035455	0.047301	0.001080	0.002893	0.013398	0.001118	0.013242	0.059261	0.000991	0.008351	0.012050	0.000859	0.008540	0.027058
		67%	0.001514	0.012008	0.017941	0.005068	0.062101	0.071891	0.001391	0.004126	0.013927	0.001672	0.019187	0.070964	0.001107	0.010396	0.021453	0.001078	0.014574	0.042018
		100%	0.002094	0.016219	0.028107	0.006339	0.095598	0.090627	0.002184	0.004673	0.024571	0.004362	0.019951	0.075761	0.002535	0.014856	0.042572	0.003173	0.017278	0.057794
Configuration #5	Vertical riser disconnected, lateral and longitudinal braces reinstalled for main line at the first level	25%	0.000391	N/A	0.000178	0.001113	N/A	0.022430	0.000793	N/A	0.009170	0.000724	N/A	0.031598	0.000684	N/A	0.008582	0.000756	N/A	0.004129
		50%	0.000606	N/A	0.001220	0.001808	N/A	0.058415	0.001563	N/A	0.014988	0.001119	N/A	0.052262	0.001209	N/A	0.016846	0.001150	N/A	0.012938
		67%	0.001137	N/A	0.002891	0.002211	N/A	0.068207	0.002035	N/A	0.021110	0.001389	N/A	0.063040	0.001586	N/A	0.028764	0.001372	N/A	0.020771
		100%	0.002470	N/A	error	0.002631	N/A	0.081726	0.002695	N/A	0.029128	0.002745	N/A	0.074953	0.003133	N/A	0.039800	0.002686	N/A	0.029020
Configuration #6	Lateral and longitudinal braces removed for main line at the first level (fully unbraced single-story specimen)	25%	0.001543	N/A	0.031734	0.001082	N/A	0.038829	0.000784	N/A	0.023350	0.000324	N/A	0.034699	0.000306	N/A	0.000531	0.000350	N/A	0.005844
		50%	0.002777	N/A	0.046095	0.002895	N/A	0.057425	0.002840	N/A	0.039168	0.000681	N/A	0.061090	0.000516	N/A	0.012379	0.000801	N/A	0.021086
		67%	0.004777	N/A	0.049192	0.003347	N/A	0.062872	0.003800	N/A	0.049992	0.001527	N/A	0.070310	0.000679	N/A	0.015505	0.000935	N/A	0.031193
		100%	0.007421	N/A	0.077448	0.004878	N/A	0.068034	0.007057	N/A	0.063010	0.002239	N/A	0.071059	0.001163	N/A	0.025654	0.002442	N/A	0.035175

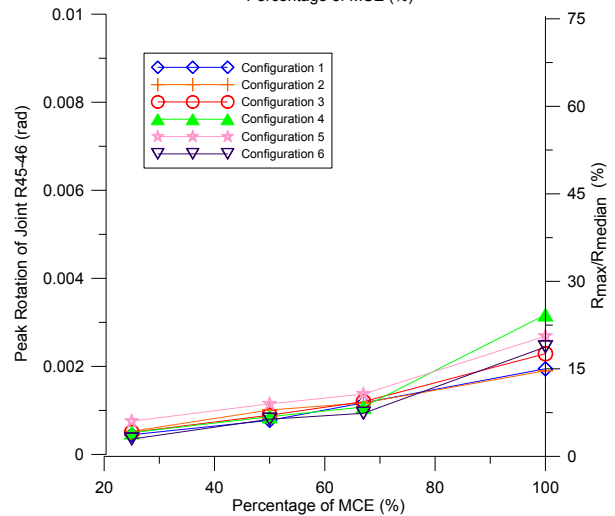
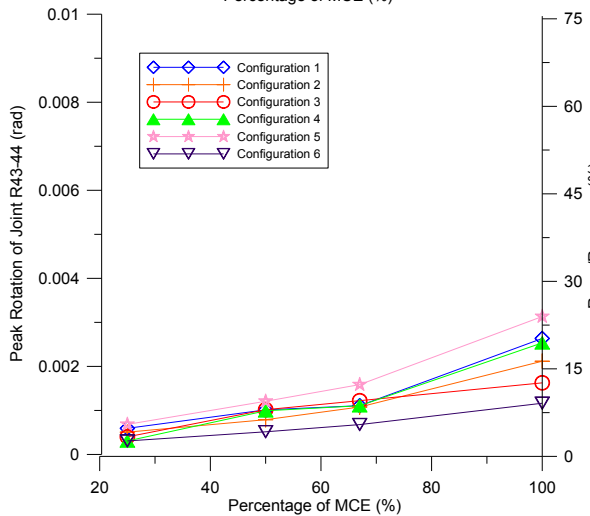
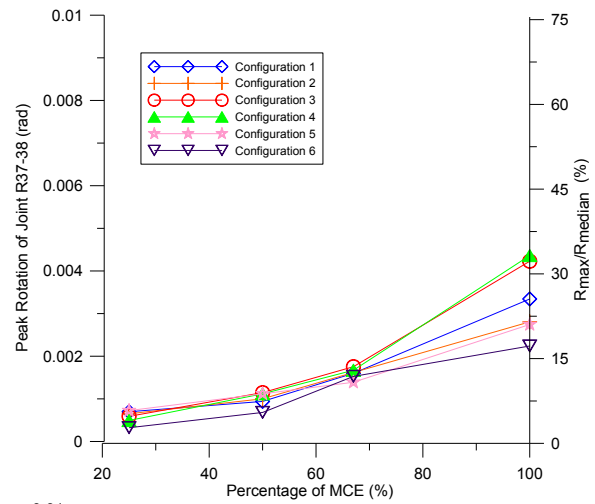
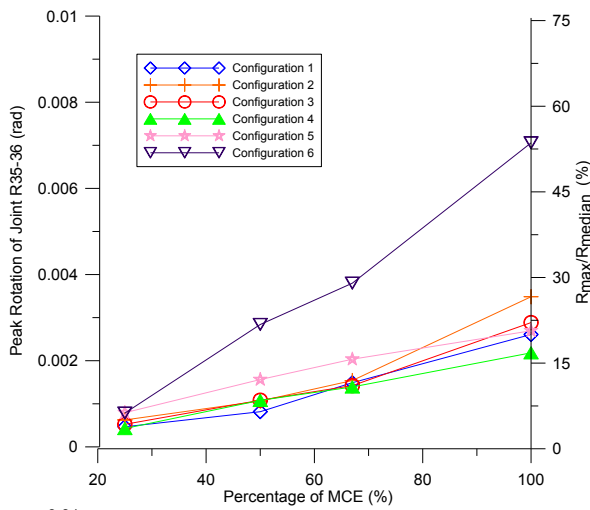
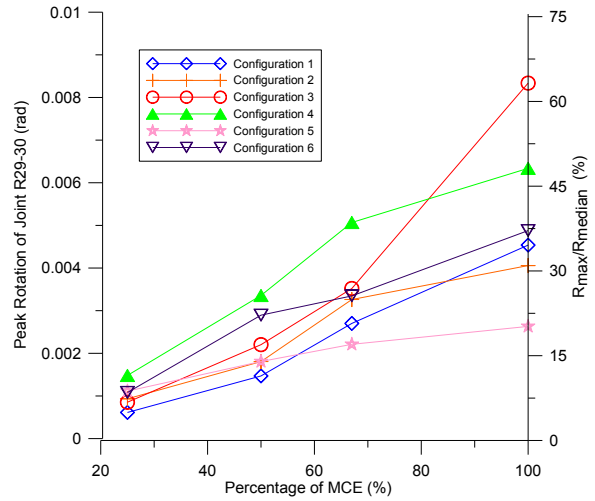
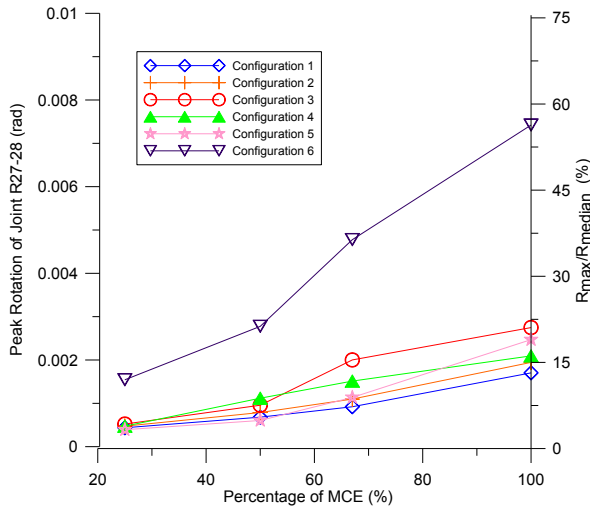
Note:

BIT indicates black iron pipes with threaded joints;

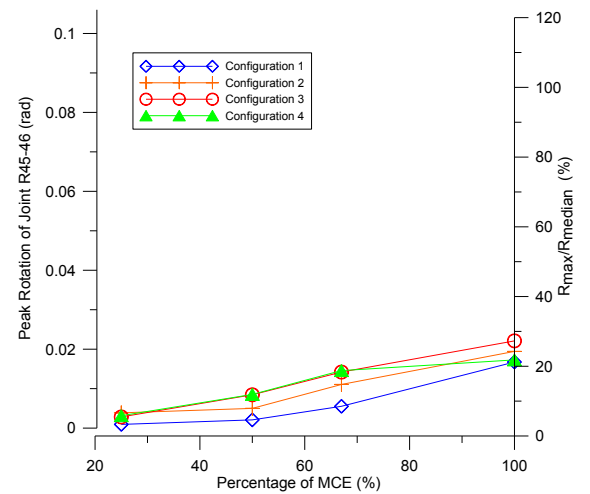
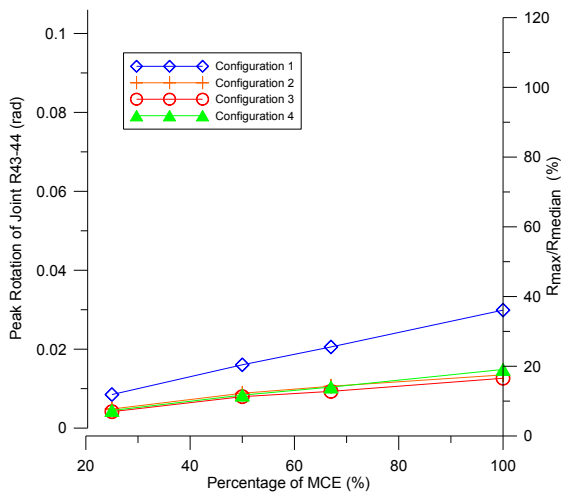
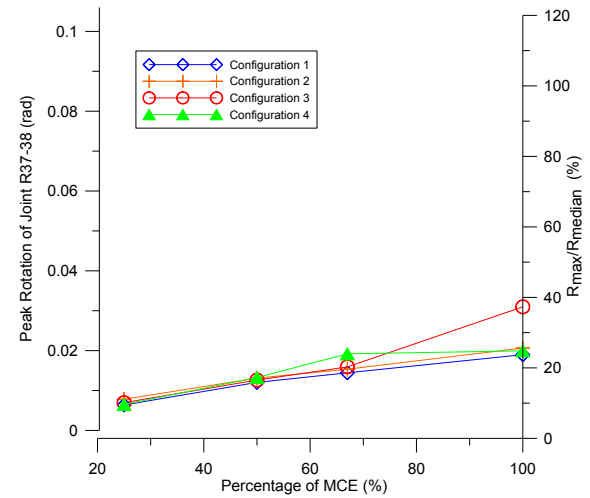
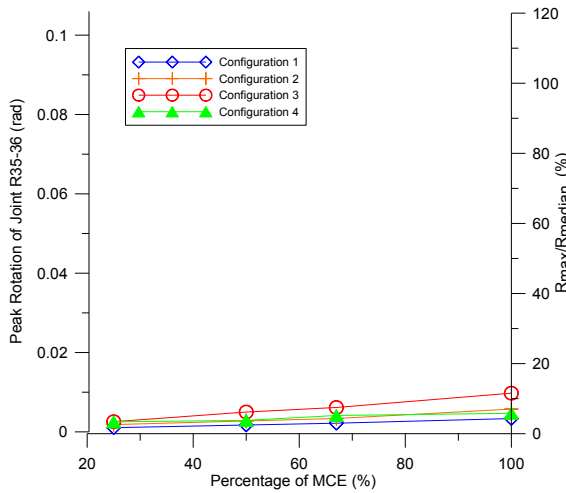
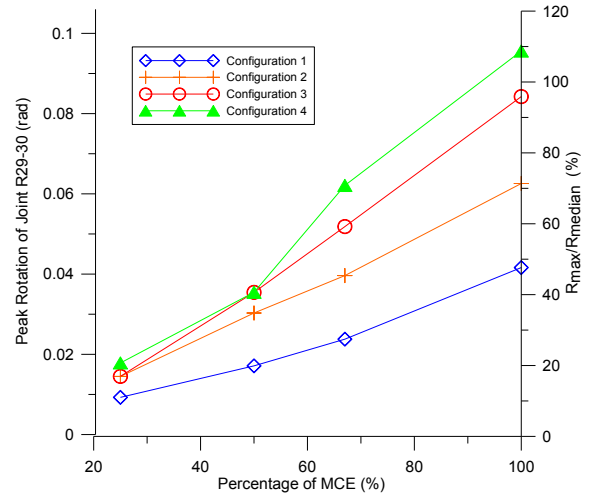
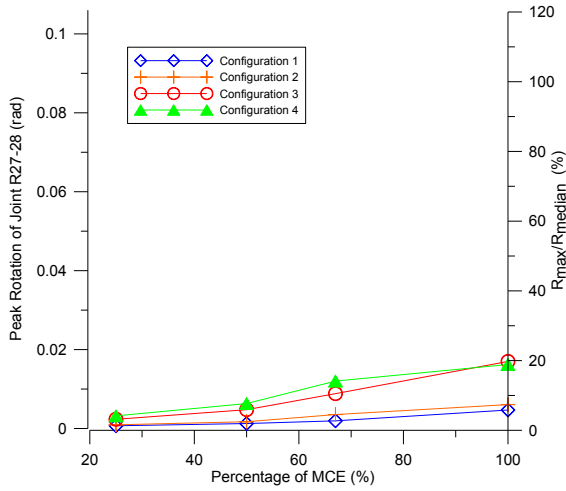
CPVC indicates CPVC pipes with cement joints;

DF indicates Dyna-Flow steel pipes with groove-fit connections.

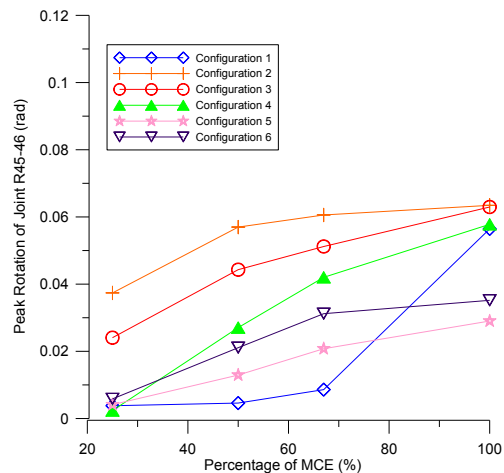
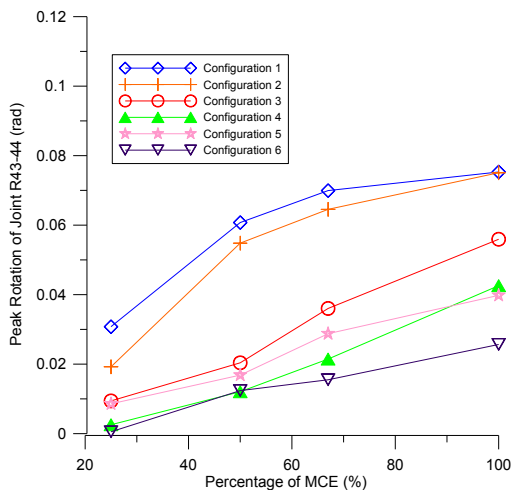
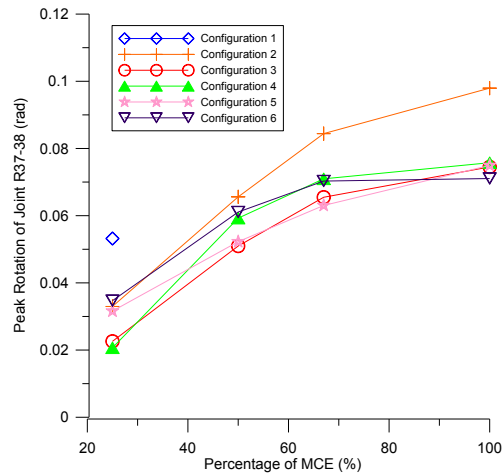
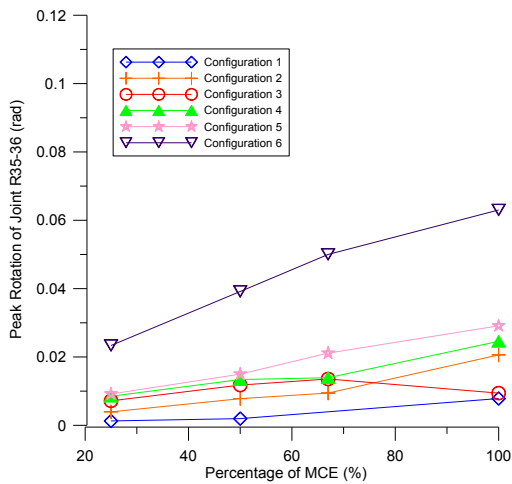
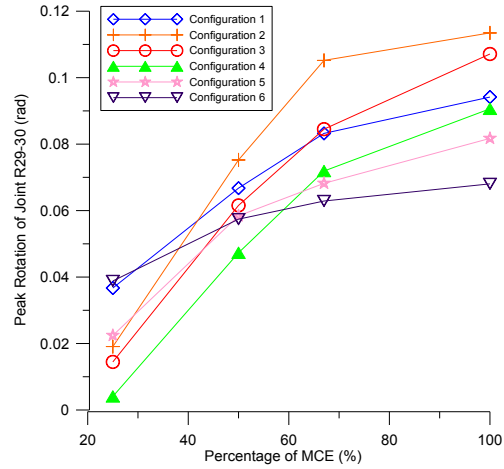
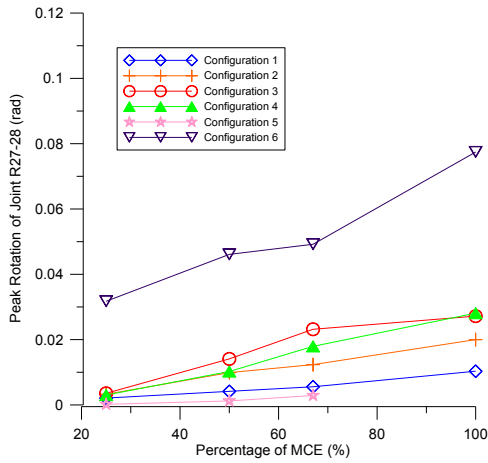
Peak rotations at critical locations for Specimen #1 (black iron pipes with threaded joints)



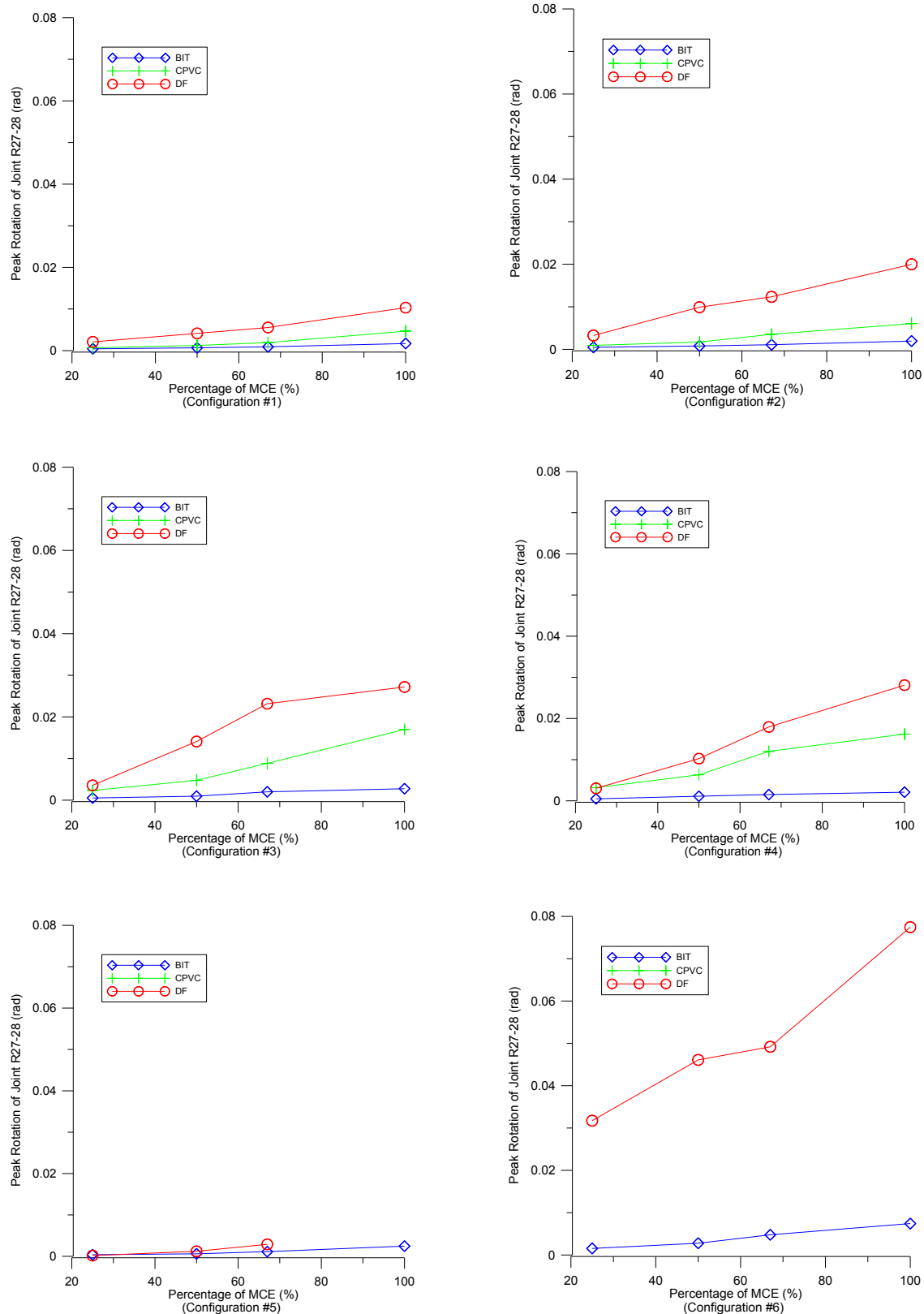
Peak rotations at critical locations for Specimen #2 (CPVC pipes with cement joints)



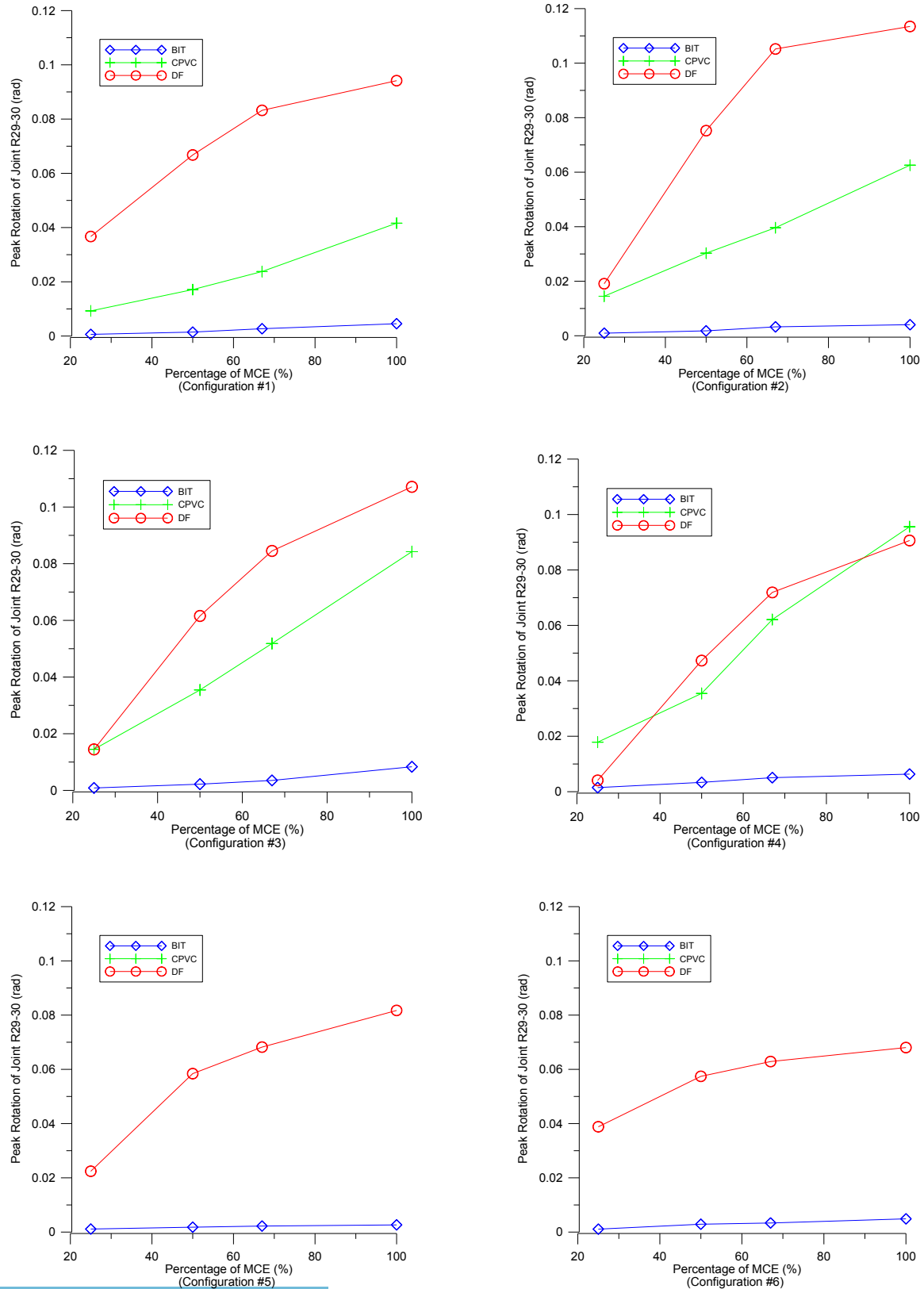
Peak rotations at critical locations for Specimen #3 (Dyna-flow steel pipes with groove-fit connections)



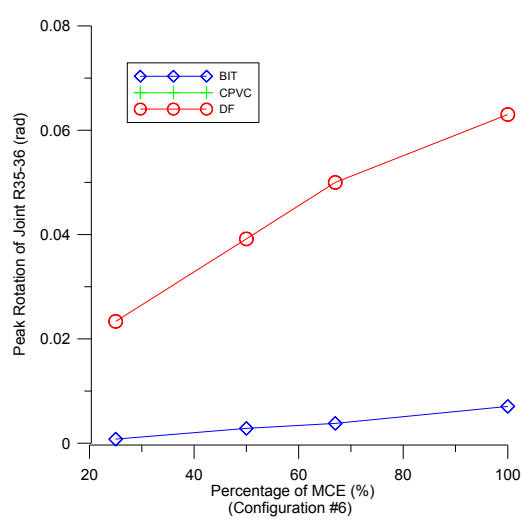
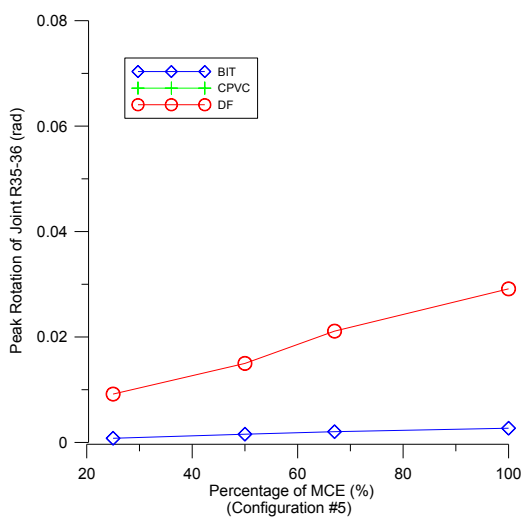
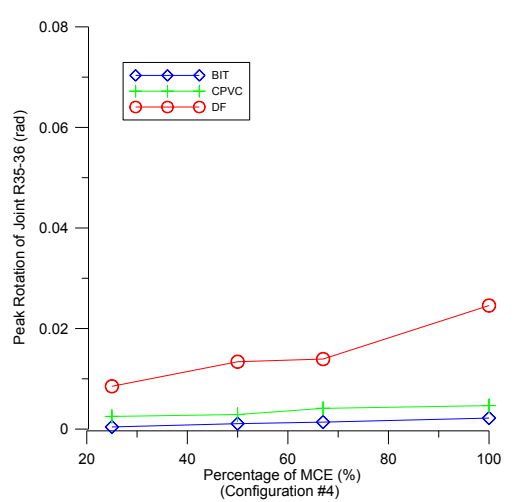
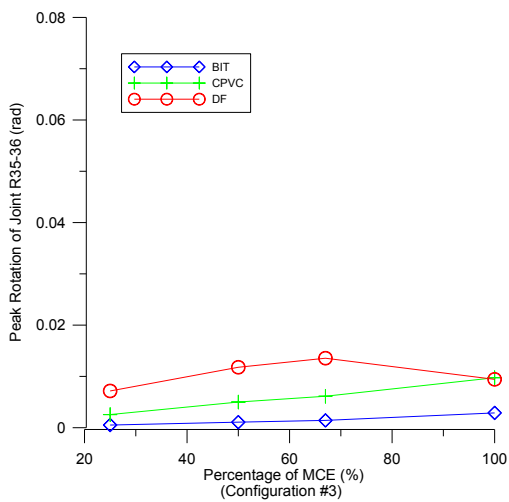
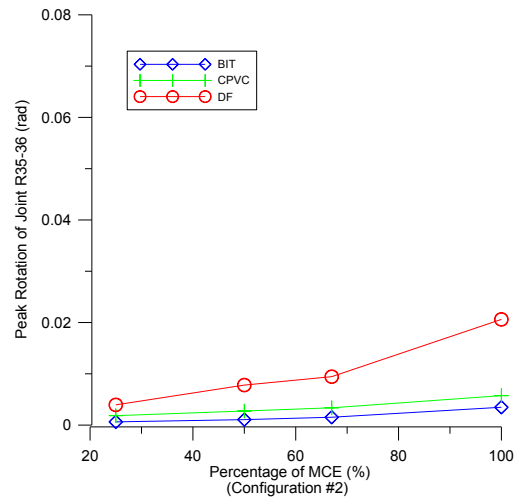
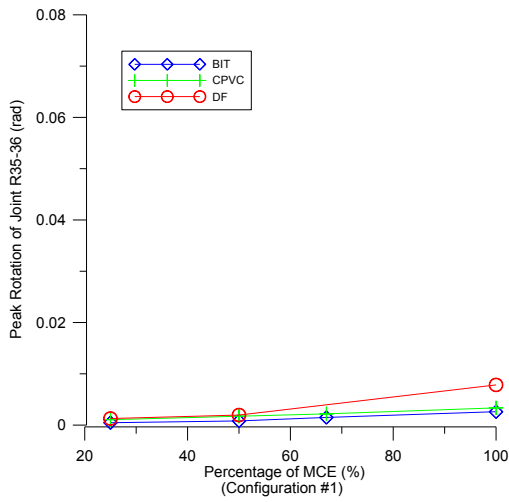
Comparison of peak rotation of Joint R27-28 across materials



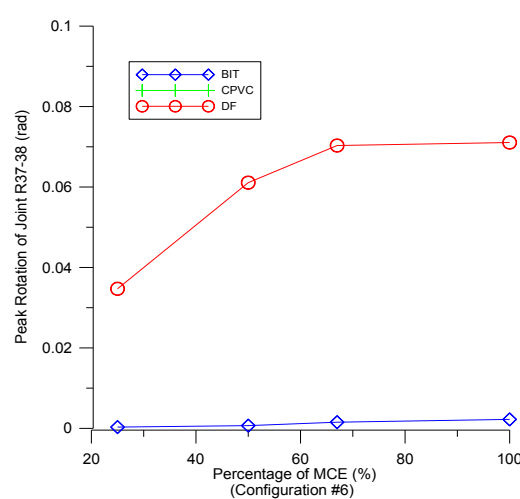
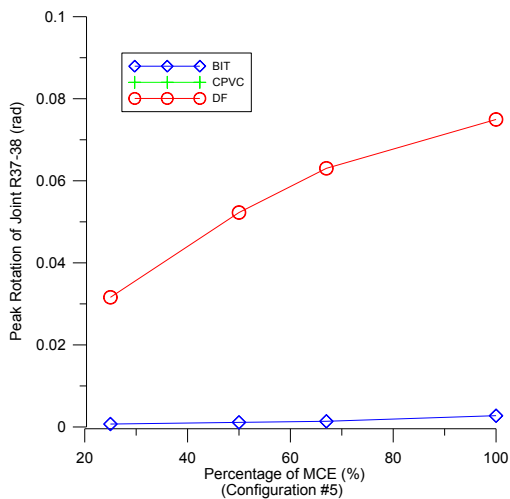
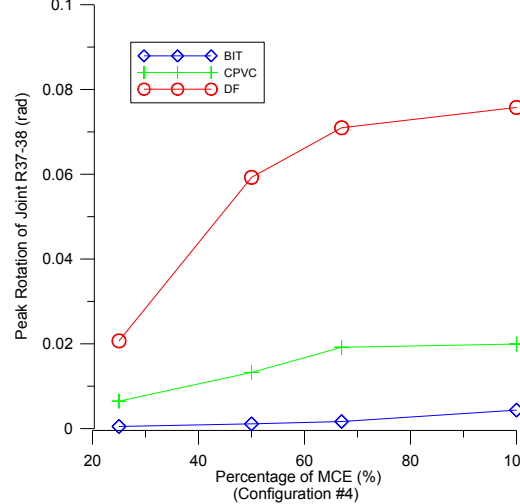
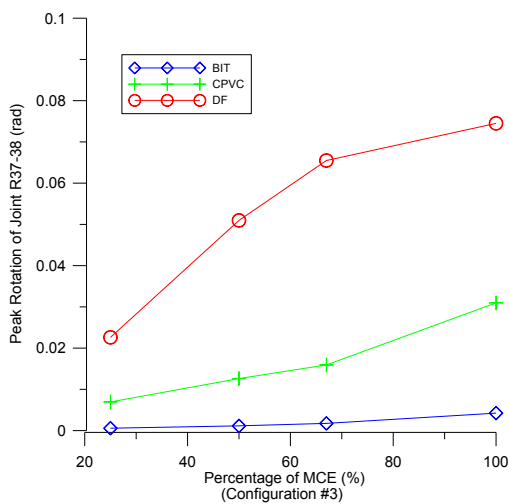
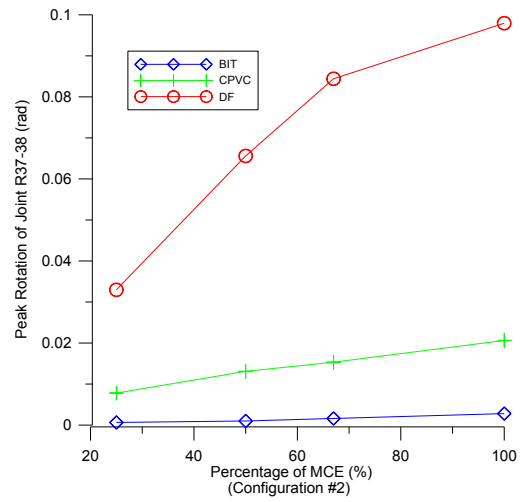
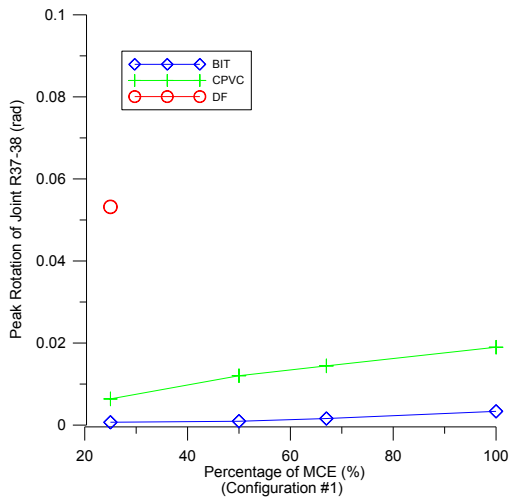
Comparison of peak rotation of Joint R29-30 across materials



Comparison of peak rotation of Joint R35-36 across materials

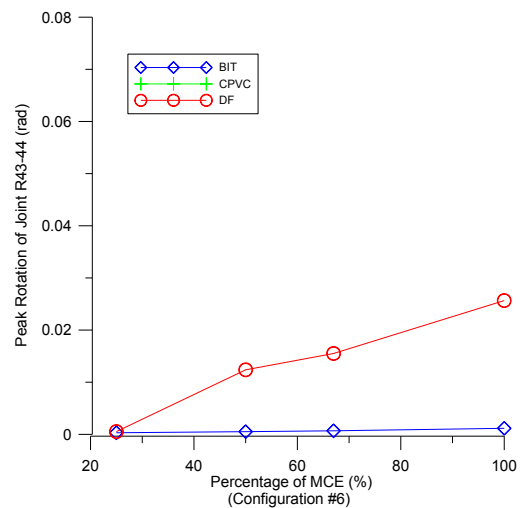
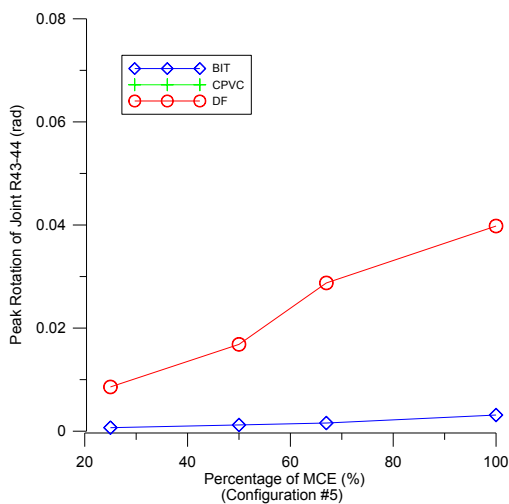
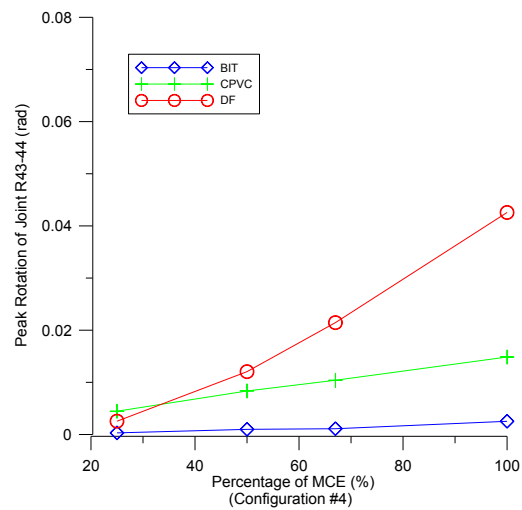
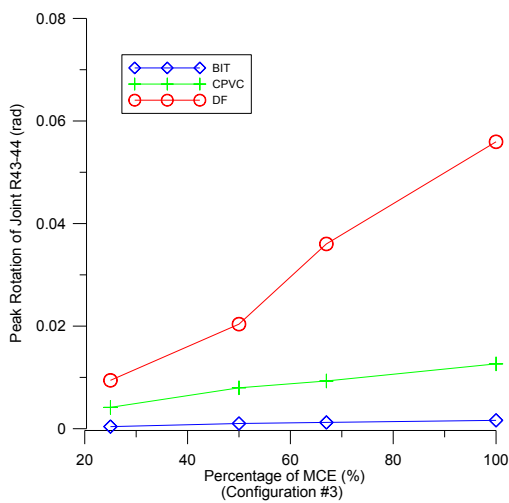
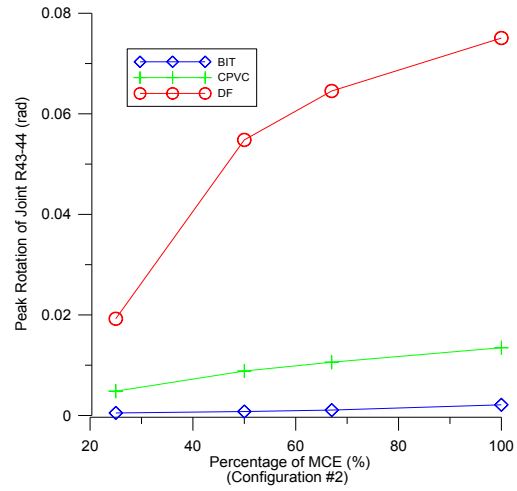
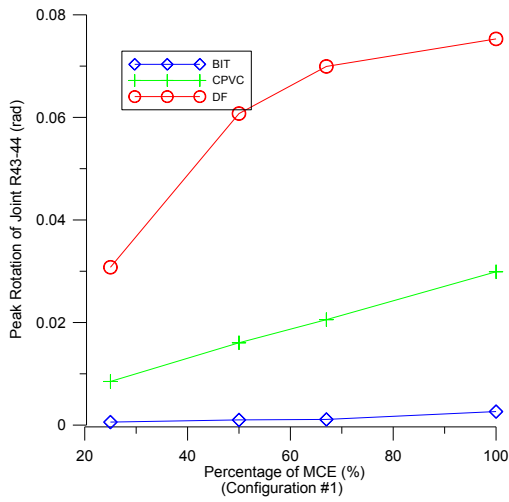


Comparison of peak rotation of Joint R37-38 across materials

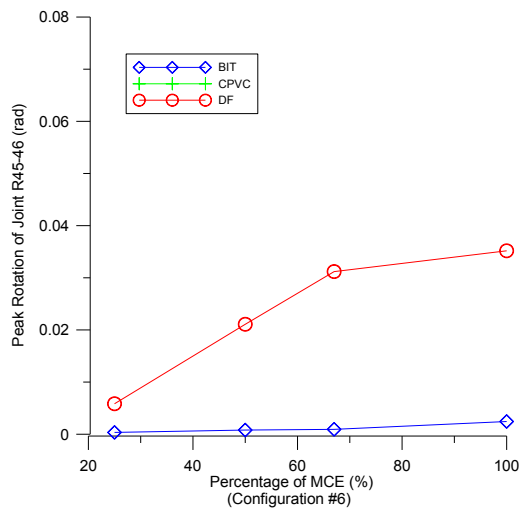
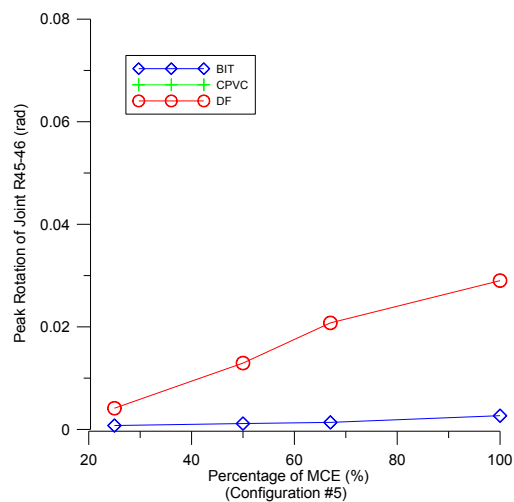
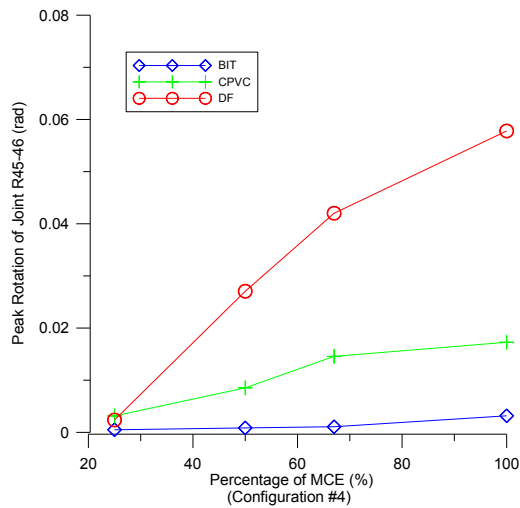
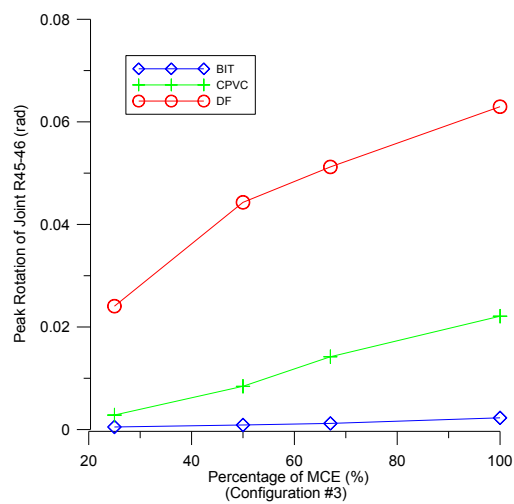
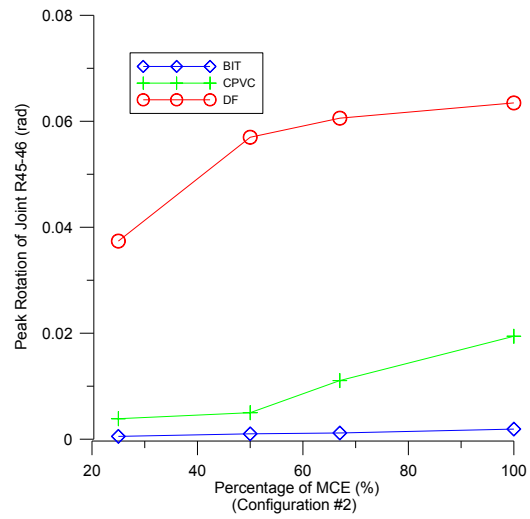
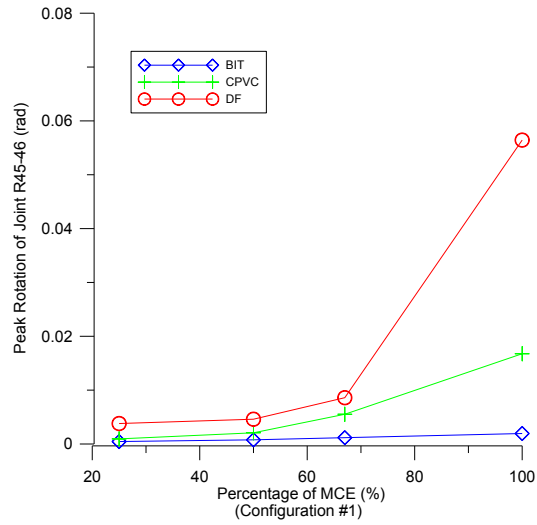




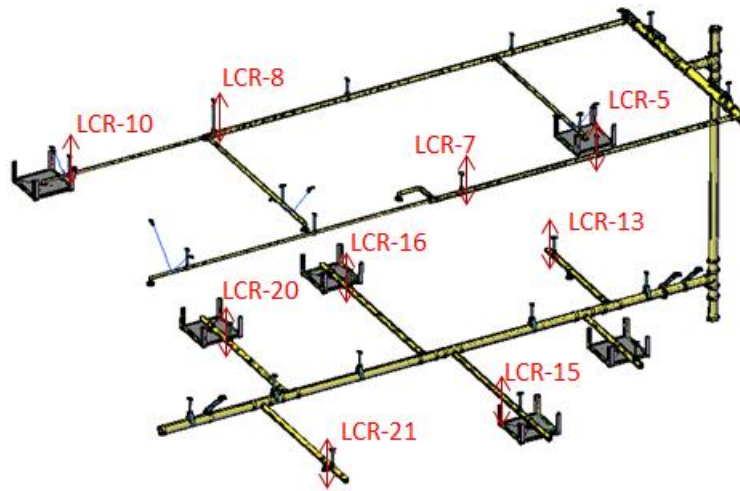
Comparison of peak rotation of Joint R43-44 across materials



Comparison of peak rotation of Joint R45-46 across materials



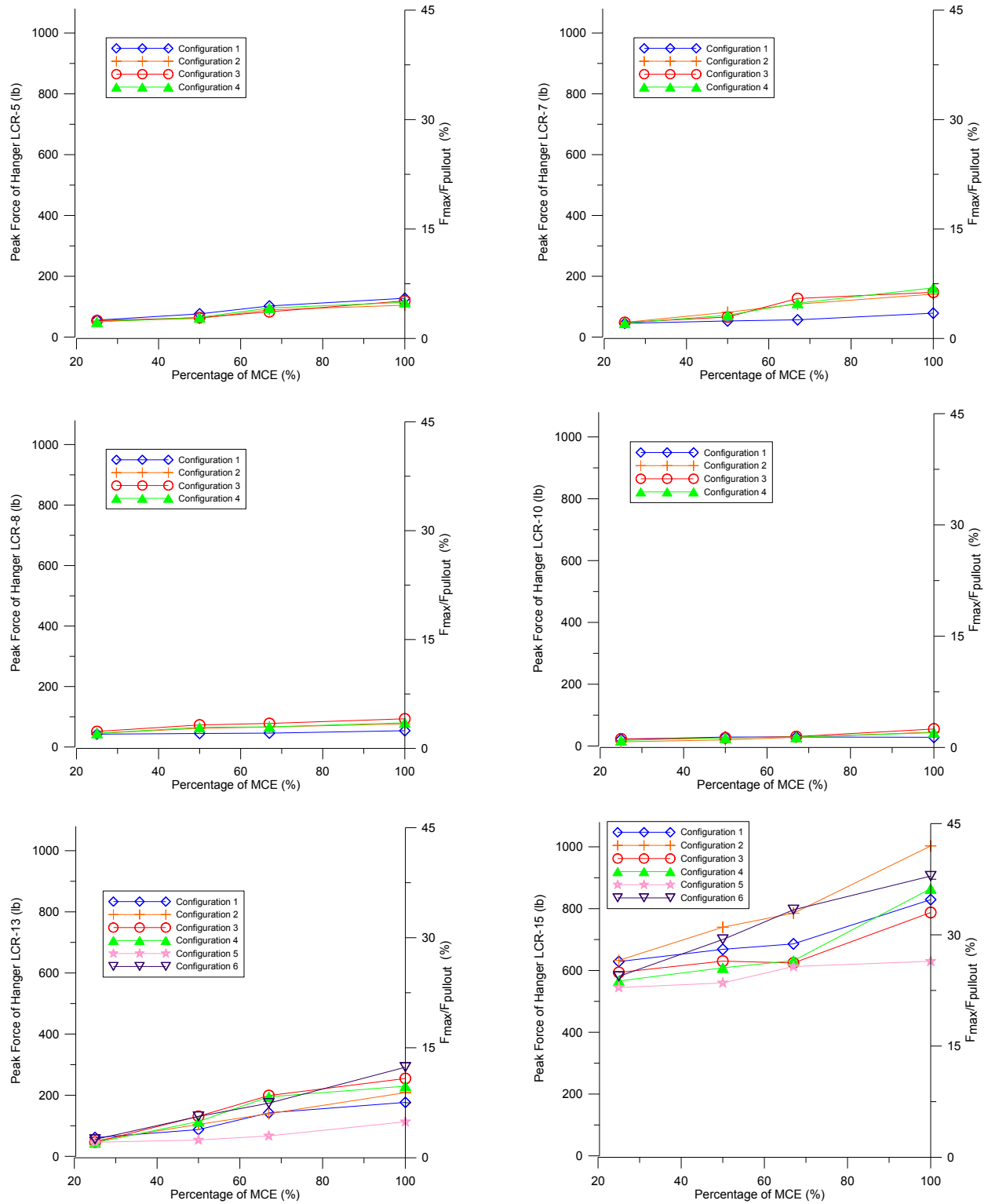
**Summary of Peak Forces for Dynamic Tests**

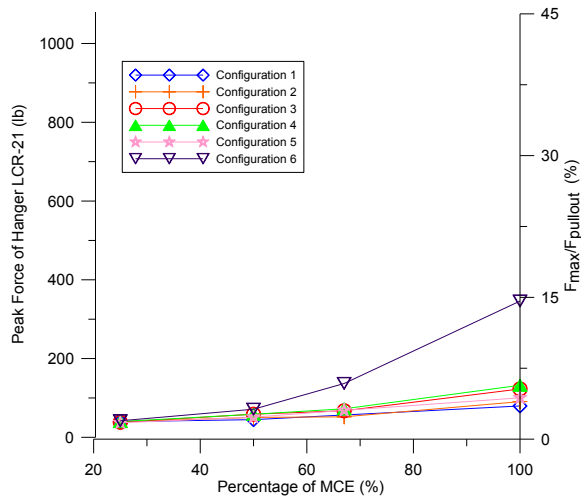
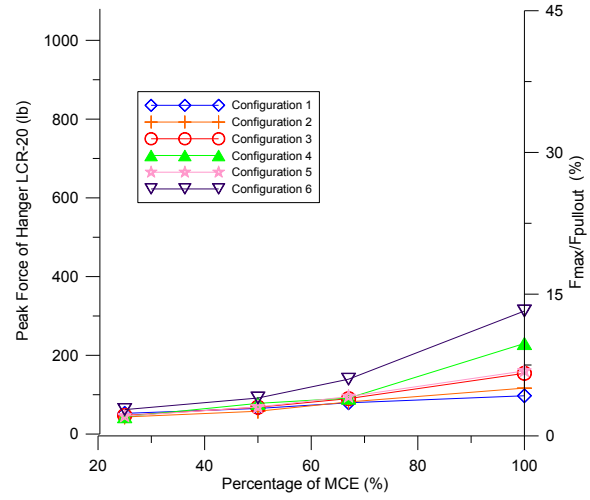
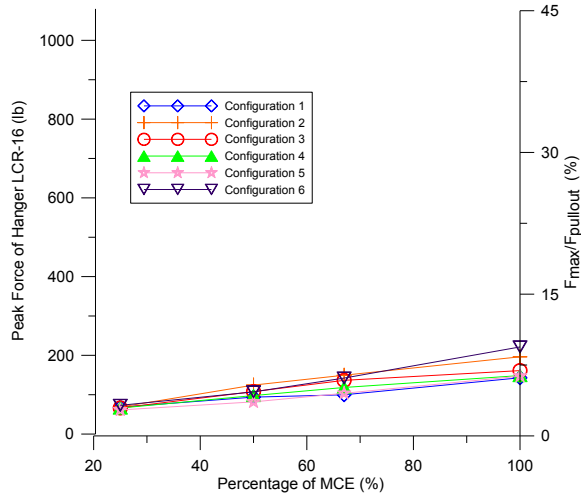


Locations of load cells for selected vertical hangers

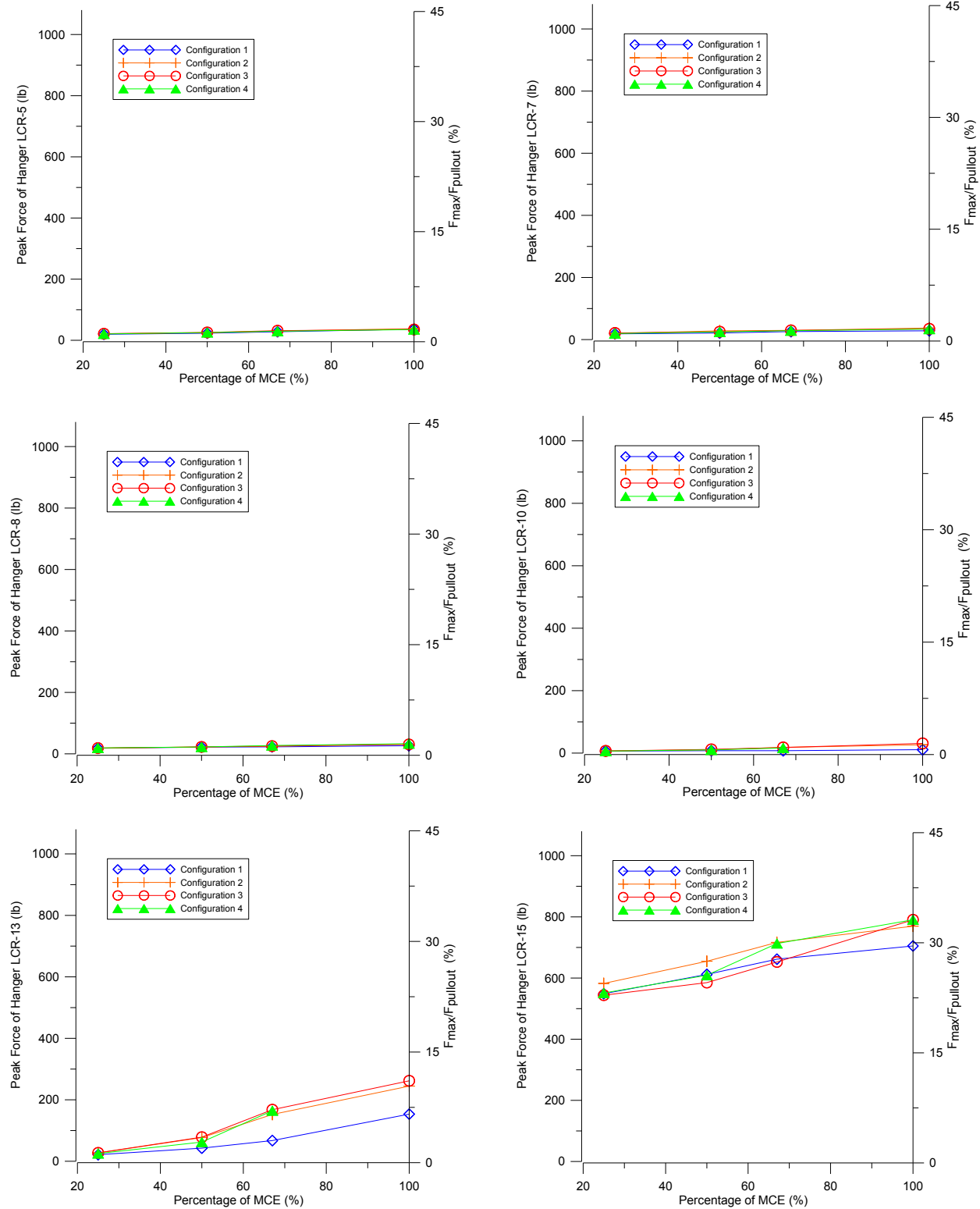


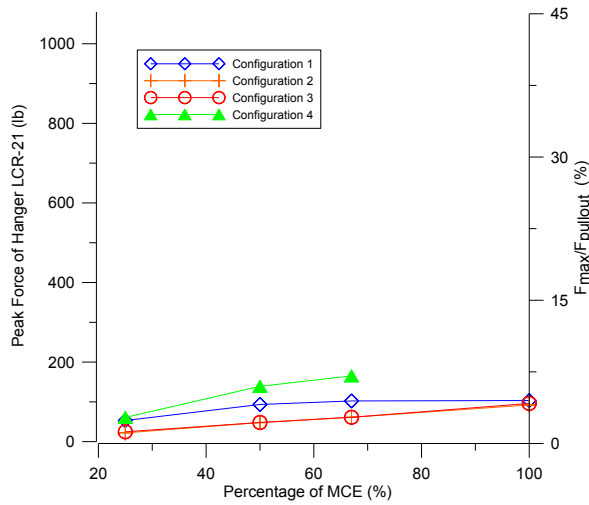
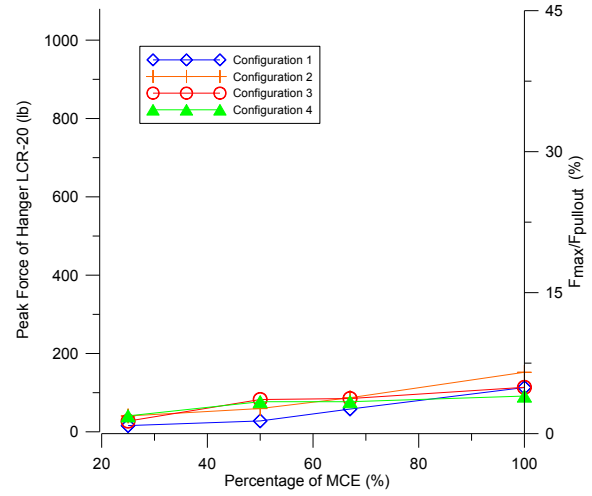
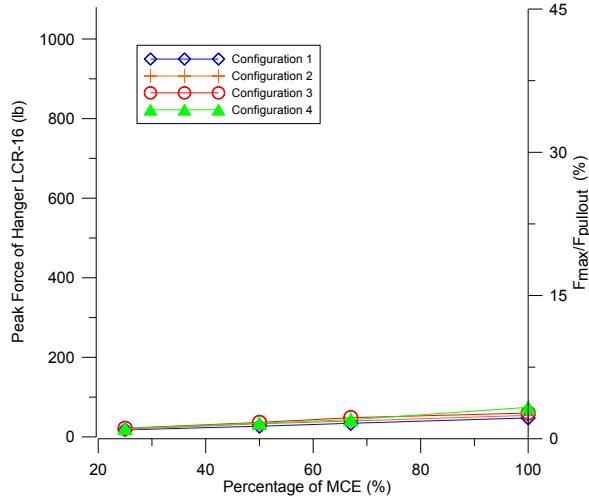
Peak forces at critical locations for Specimen #1 (black iron pipes with threaded joints)





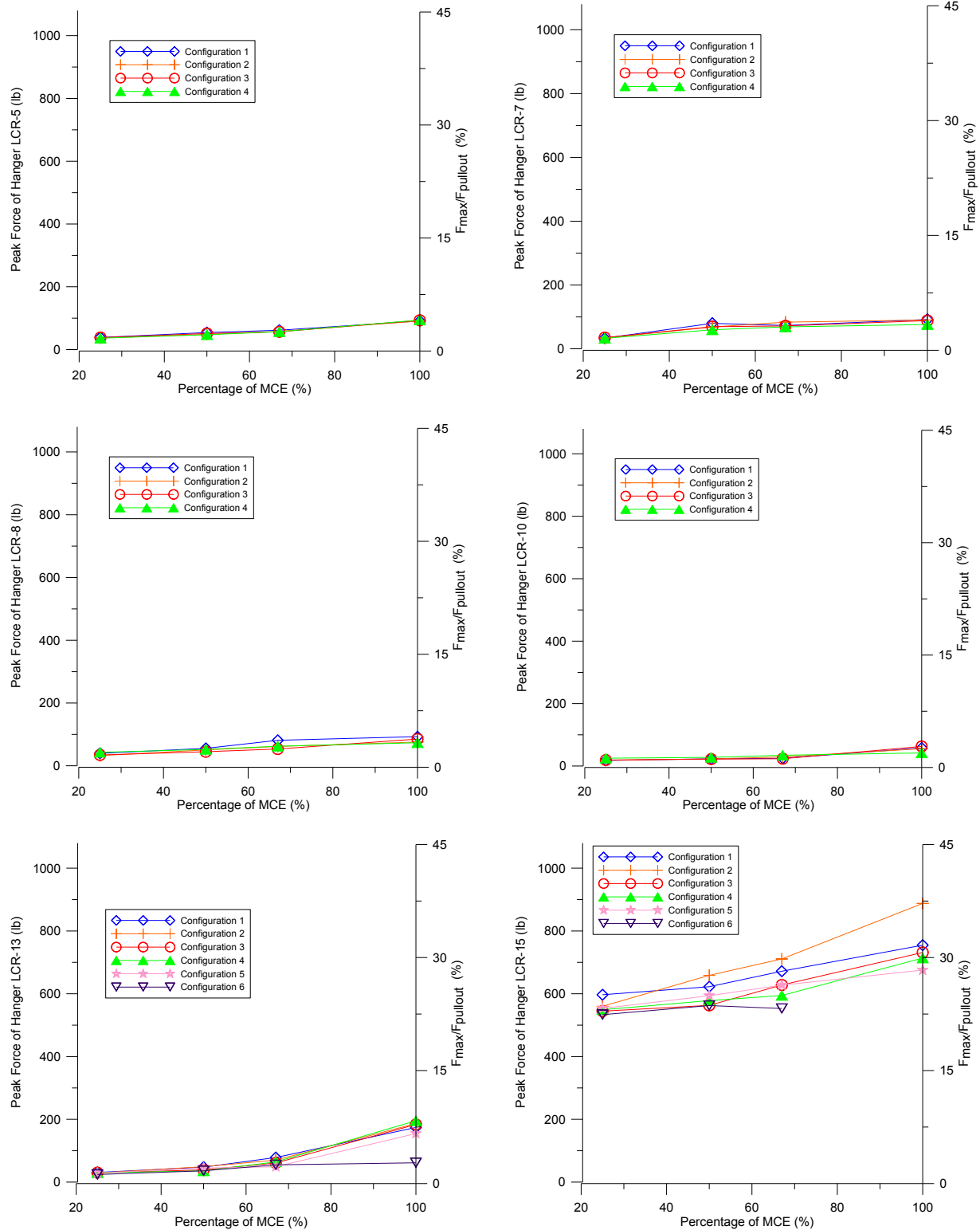
Peak forces at critical locations for Specimen #2 (CPVC pipes with cement joints)

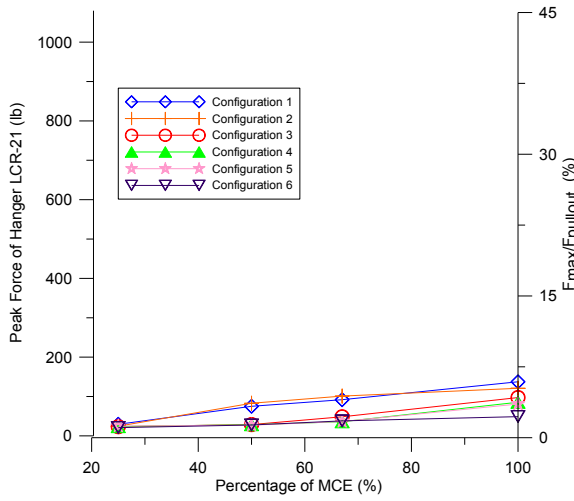
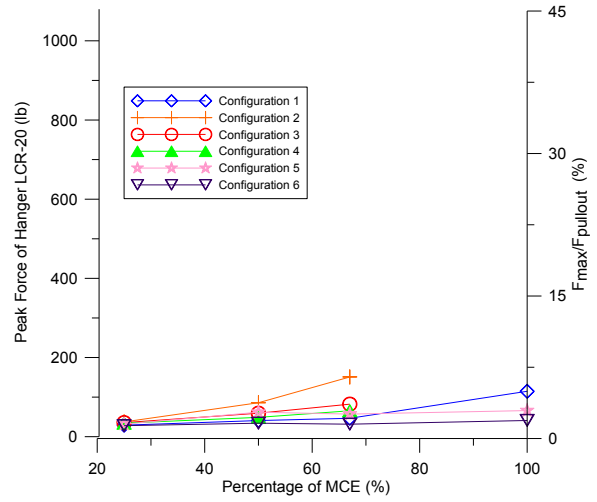
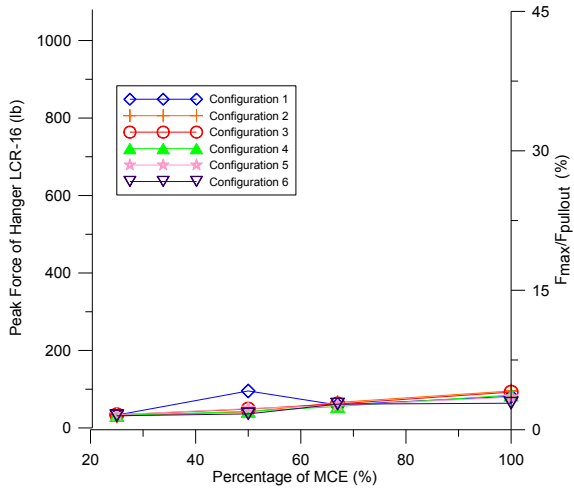




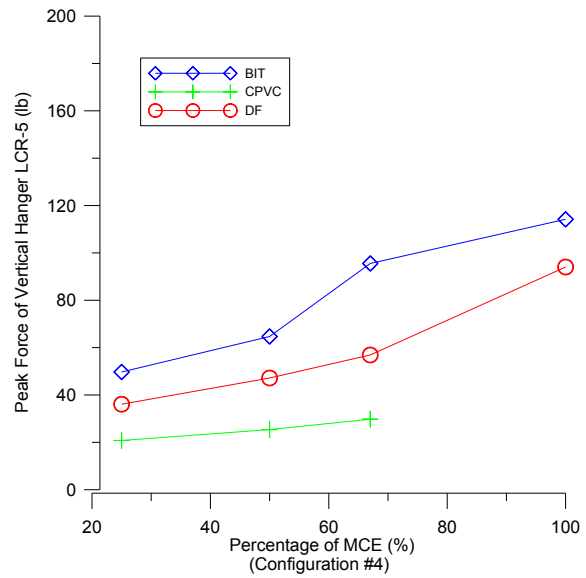
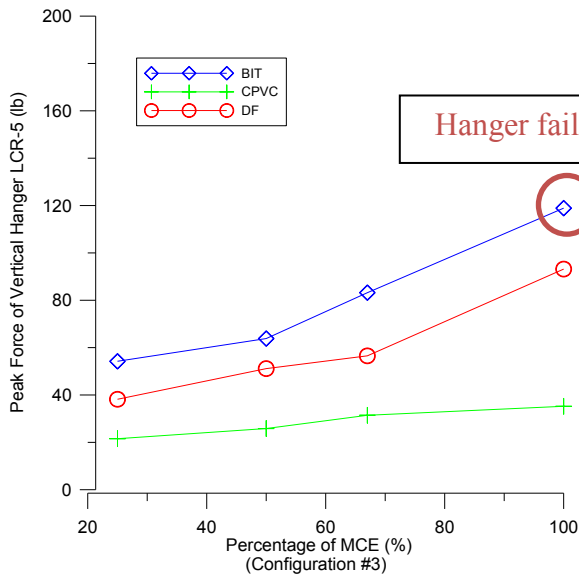
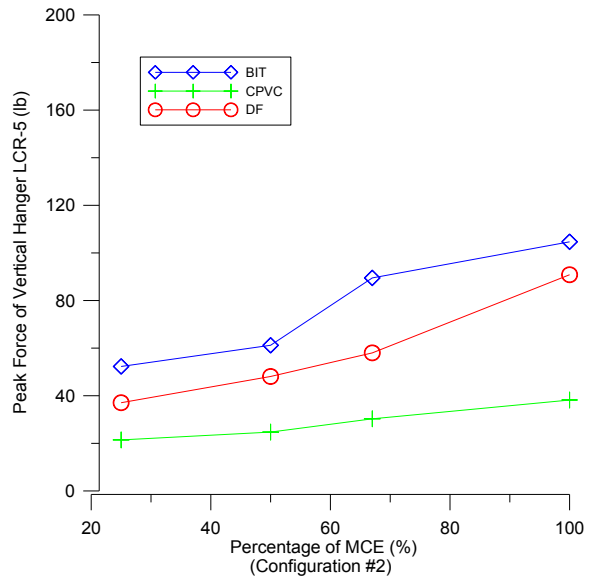
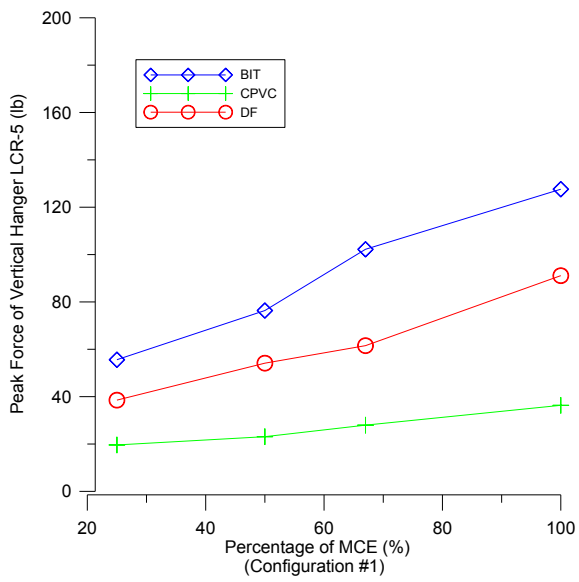


Peak forces at critical locations for Specimen #3 (Dyna-Flow steel pipes with groove-fit connections)

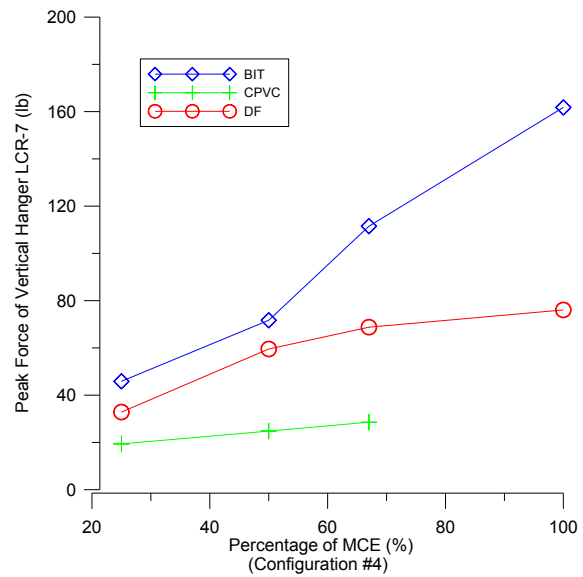
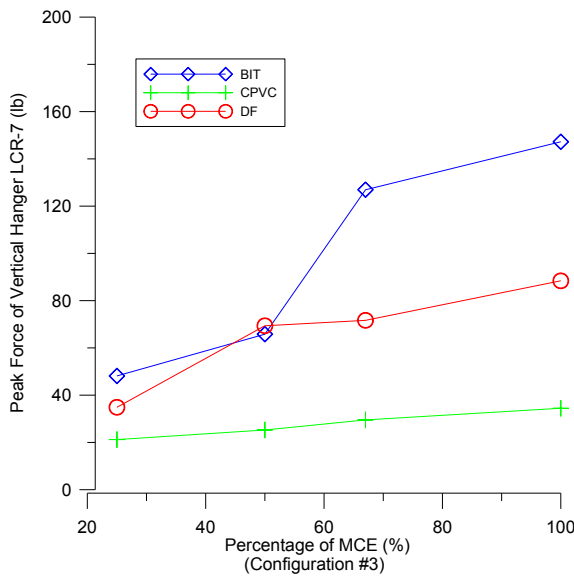
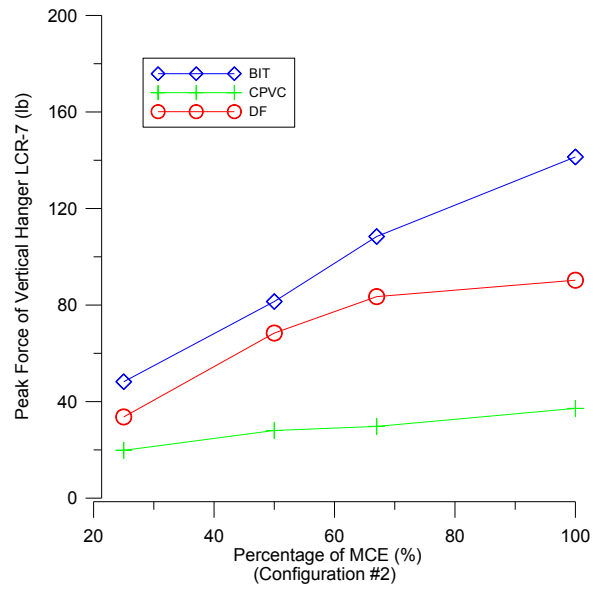
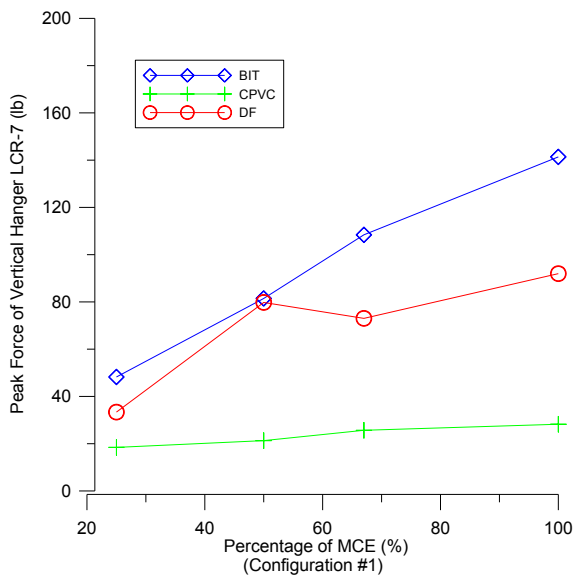




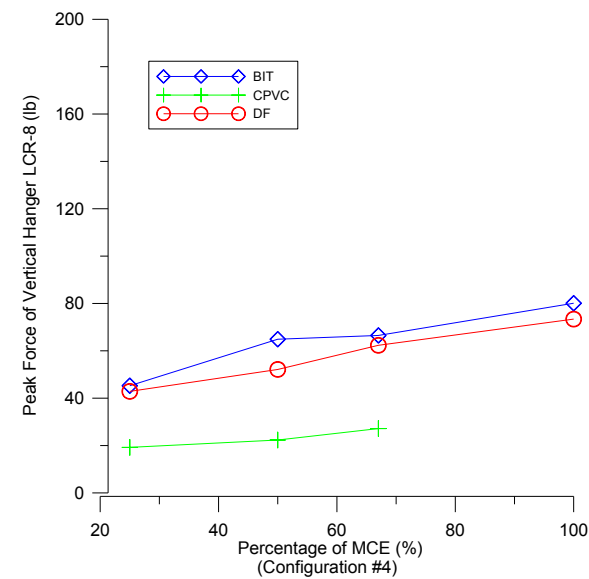
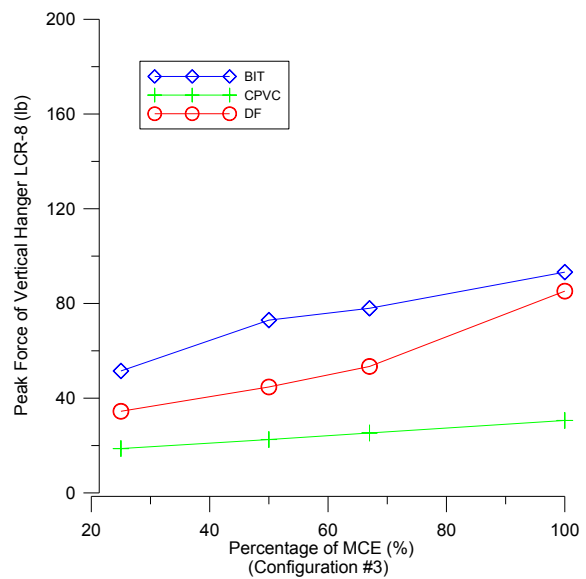
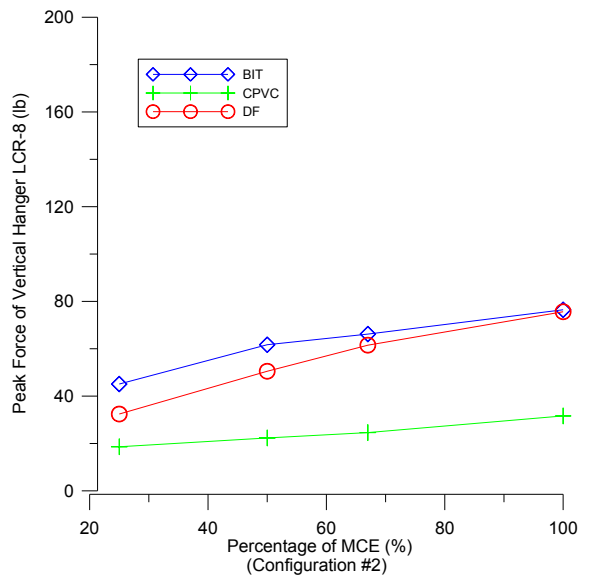
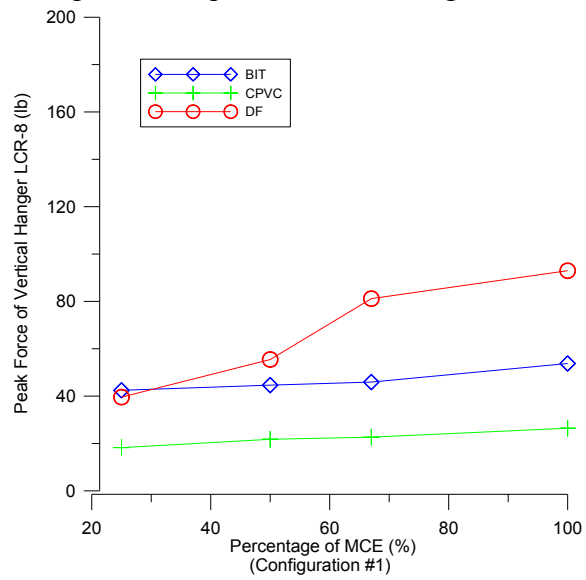
Comparison of peak force for hanger LCR-5 across materials



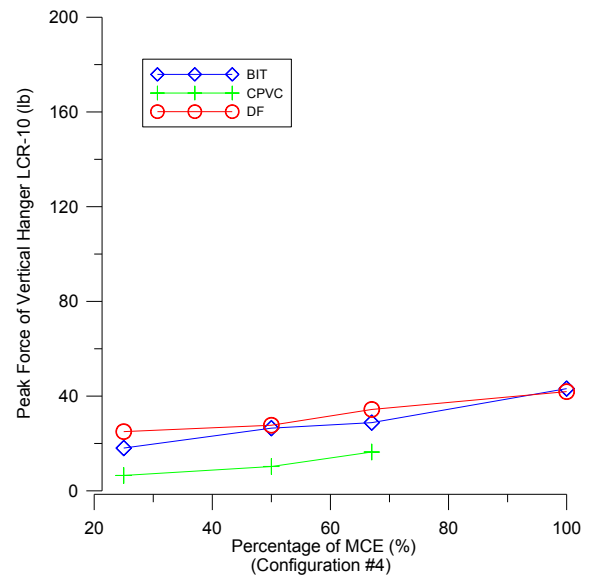
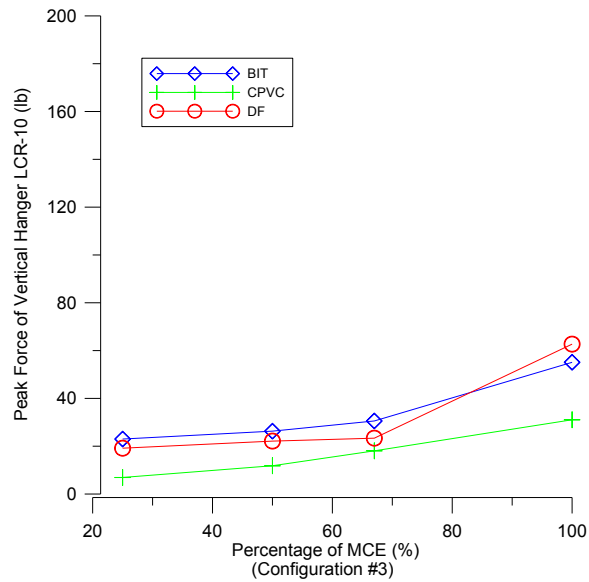
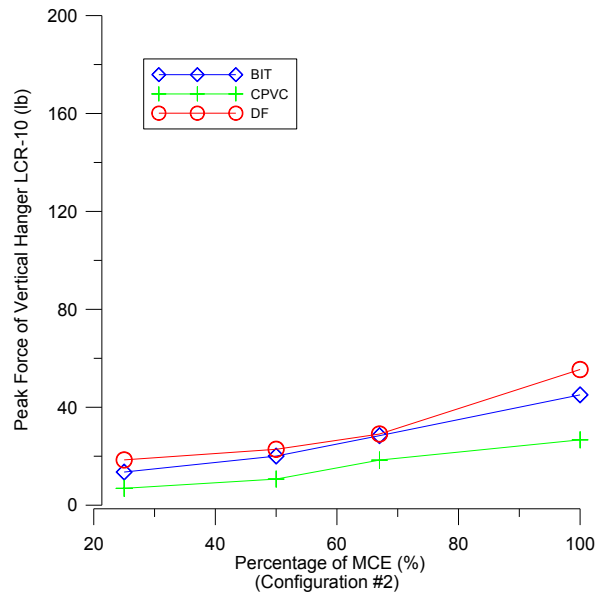
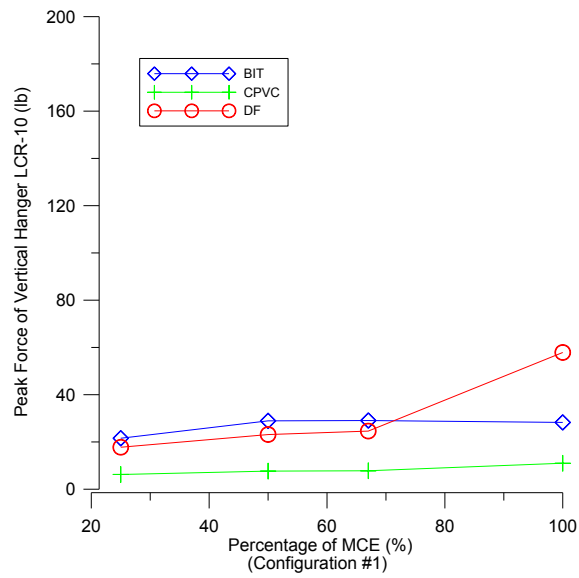
Comparison of peak force for hanger LCR-7 across materials



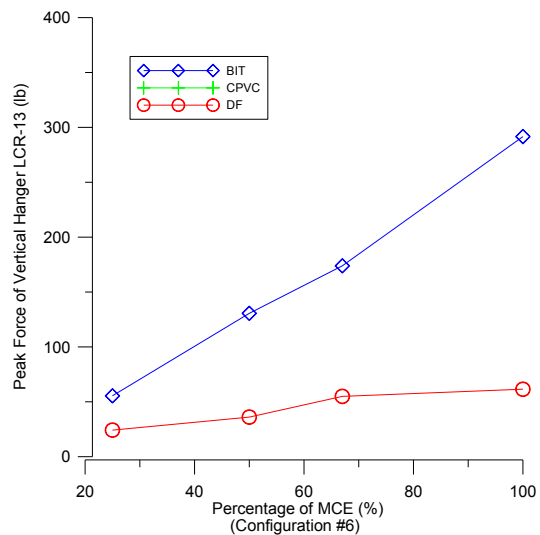
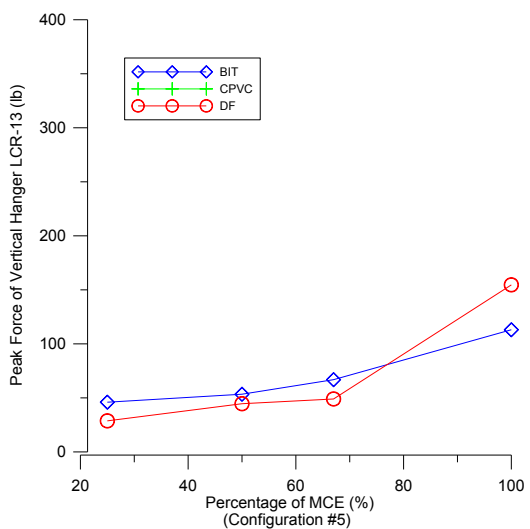
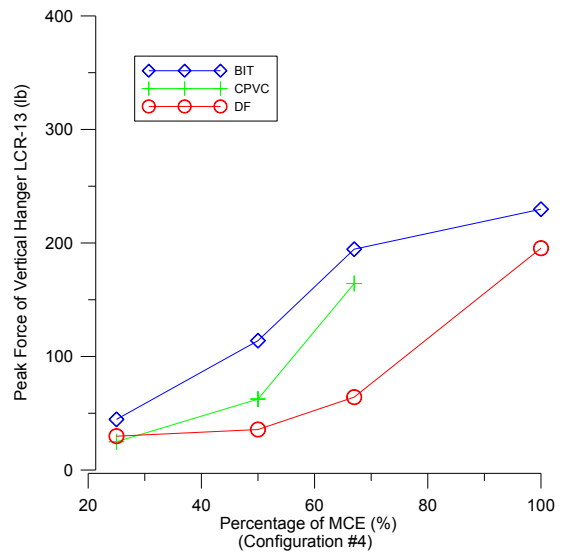
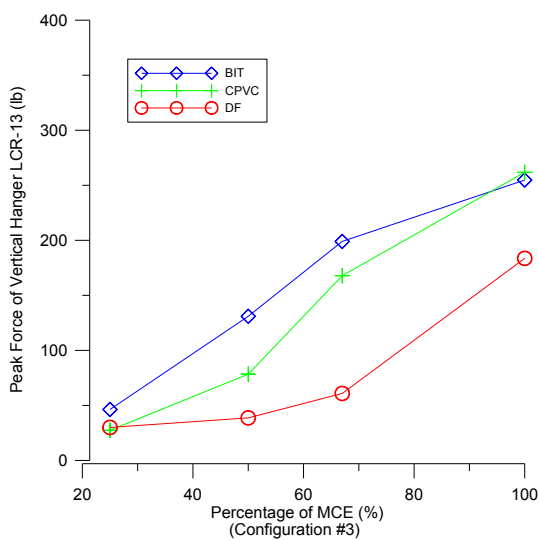
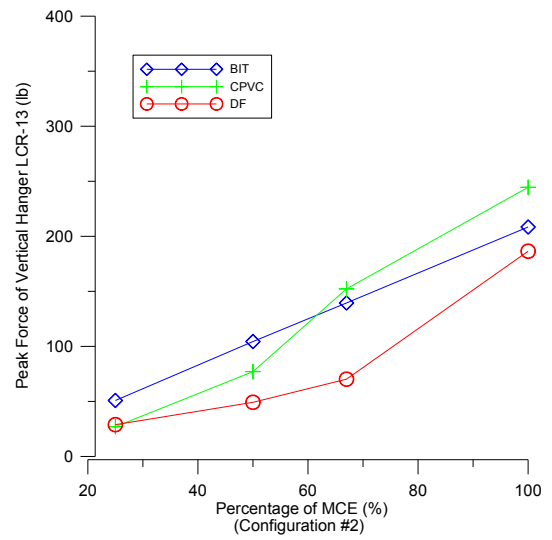
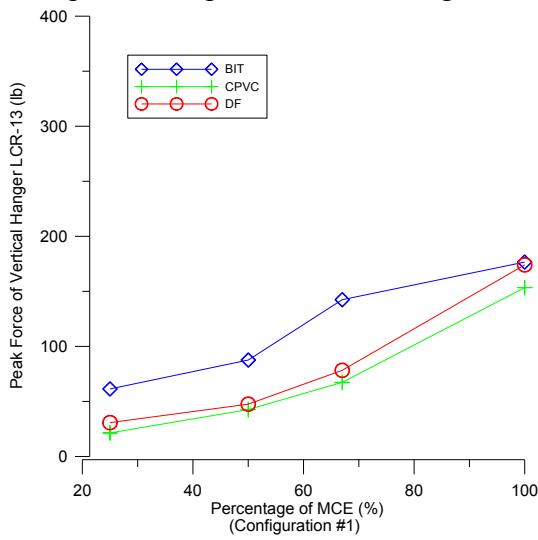
Comparison of peak force for hanger LCR-8 across materials



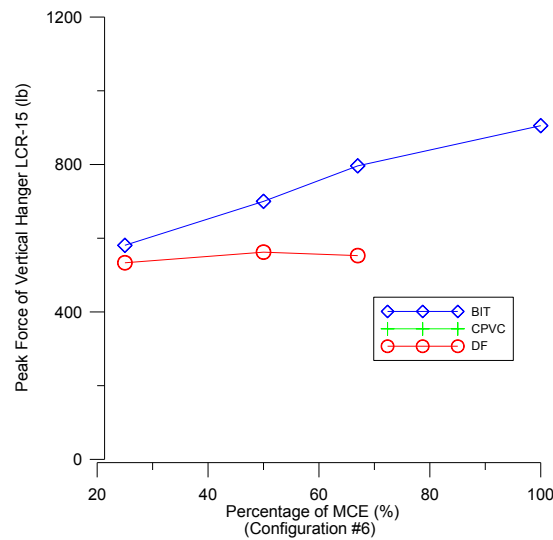
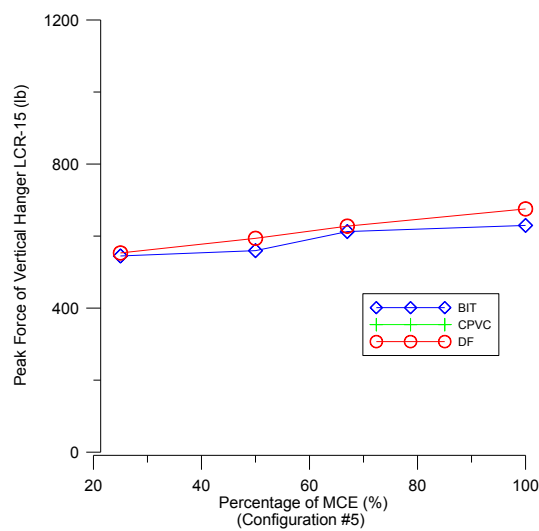
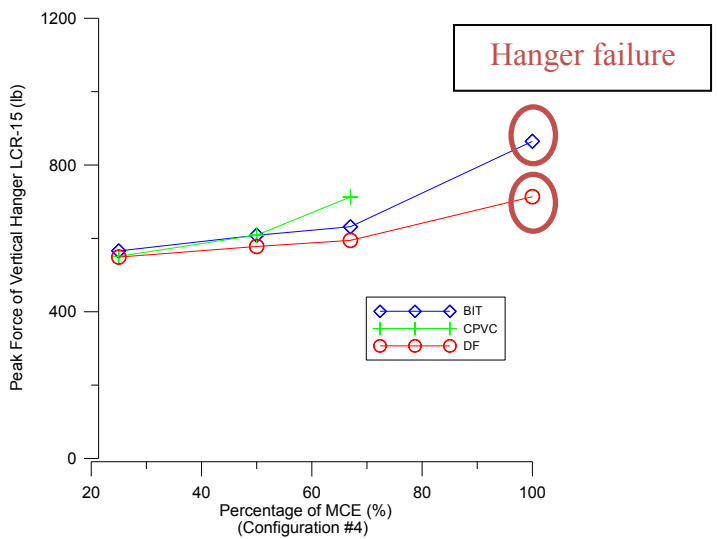
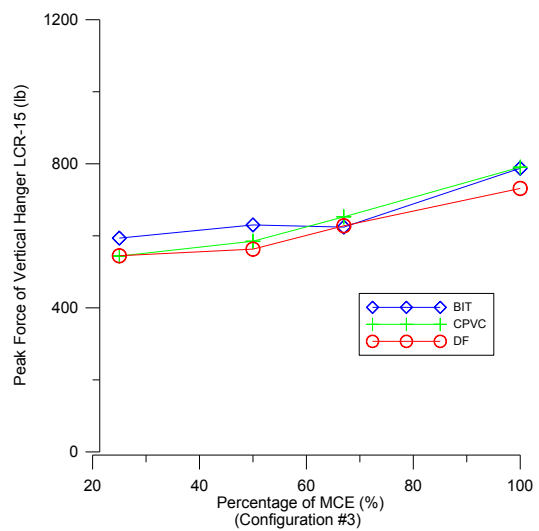
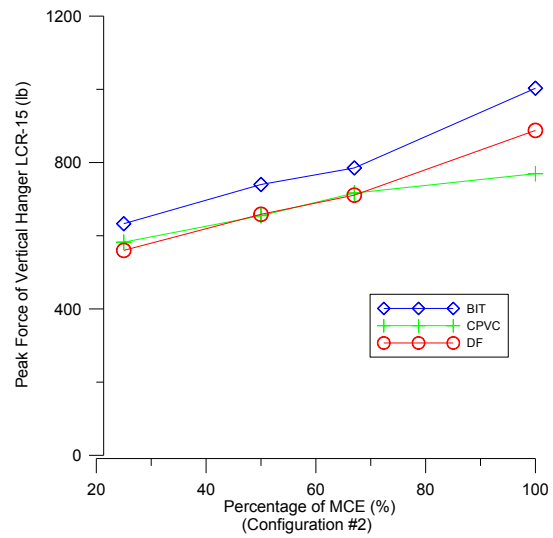
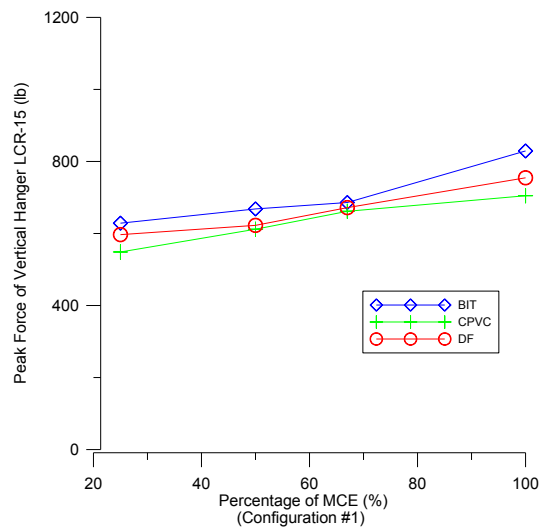
Comparison of peak force for hanger LCR-10 across materials



Comparison of peak force for hanger LCR-13 across materials

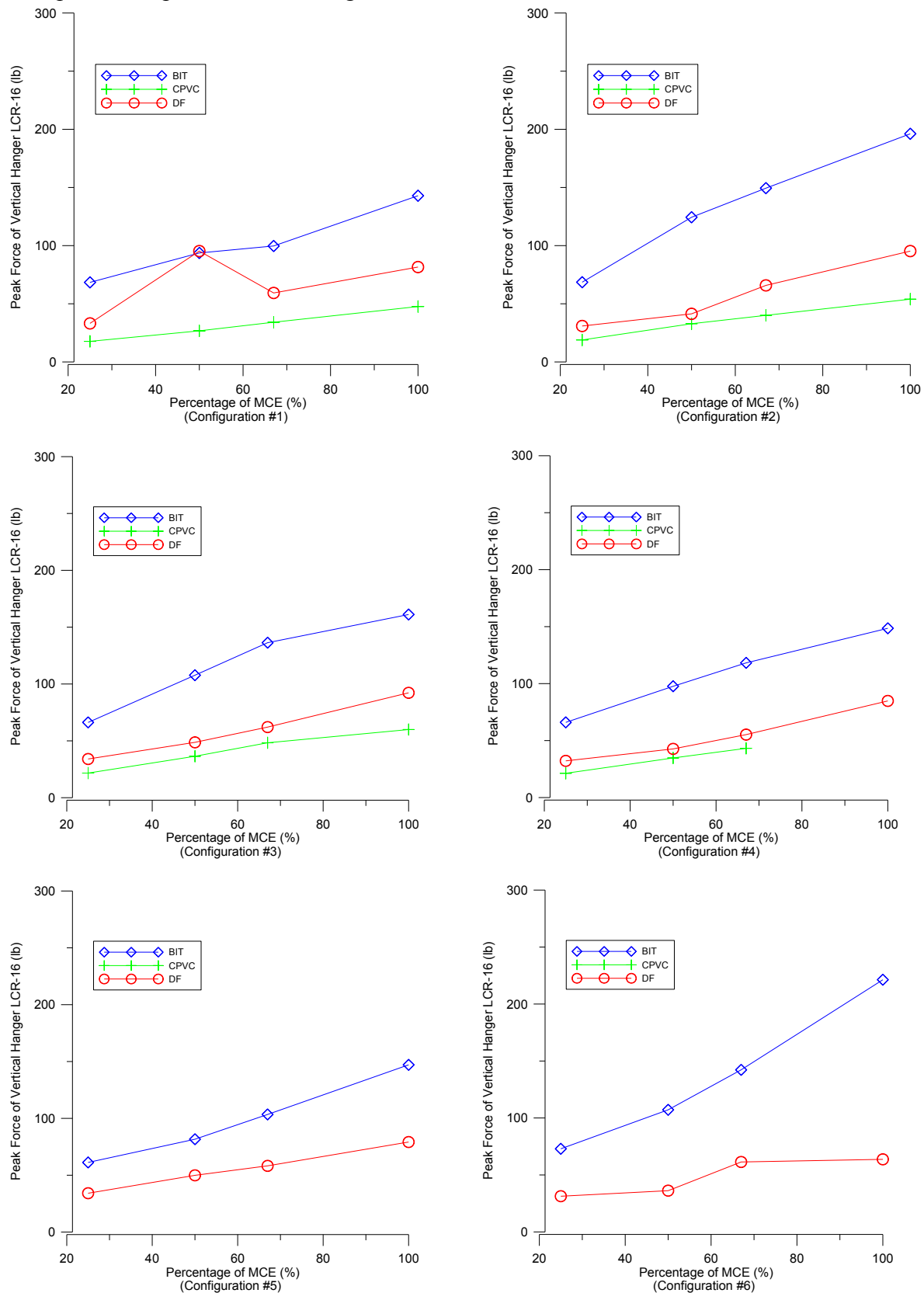


Comparison of peak force for hanger LCR-15 across materials

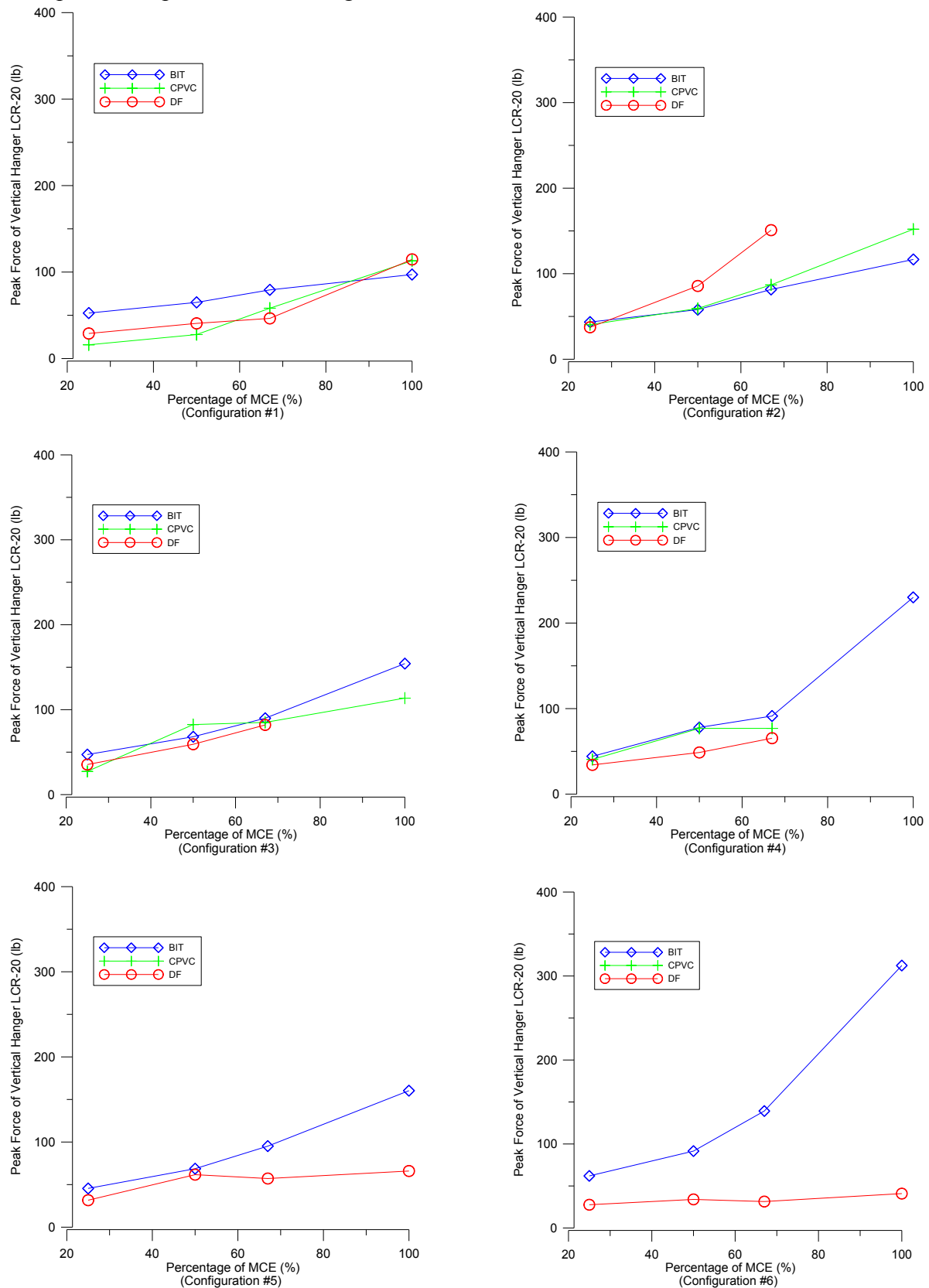




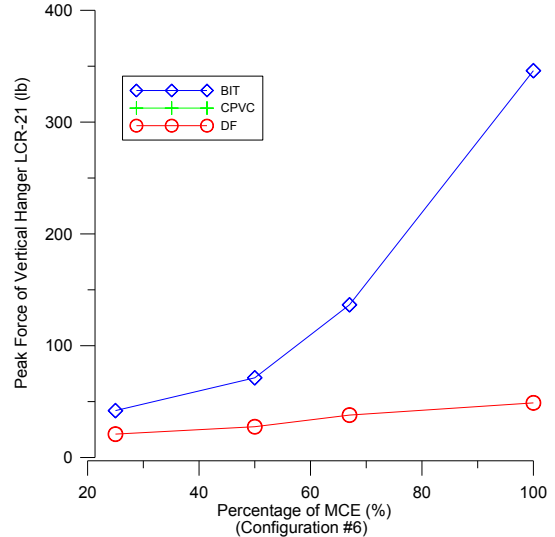
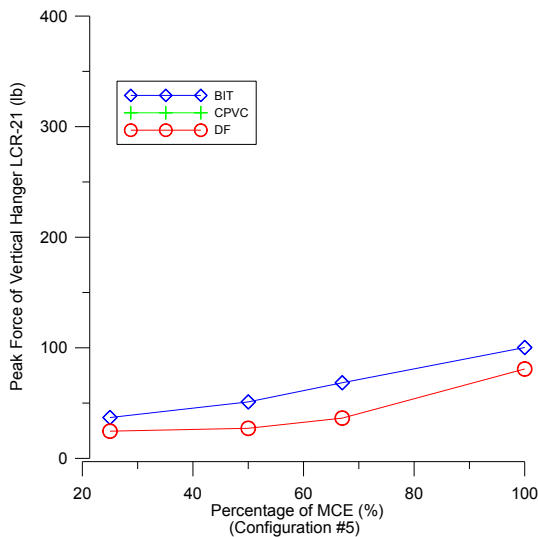
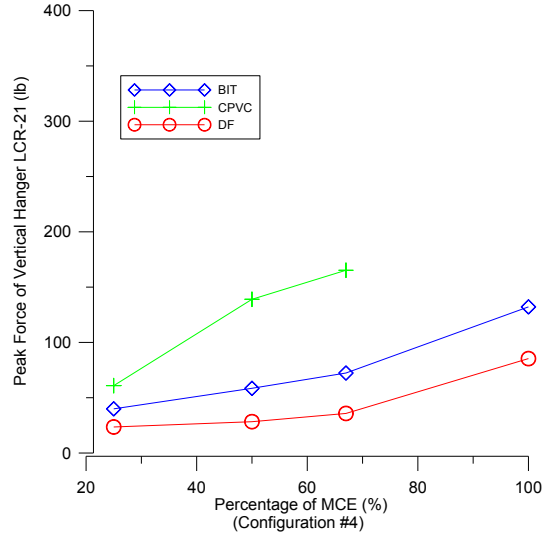
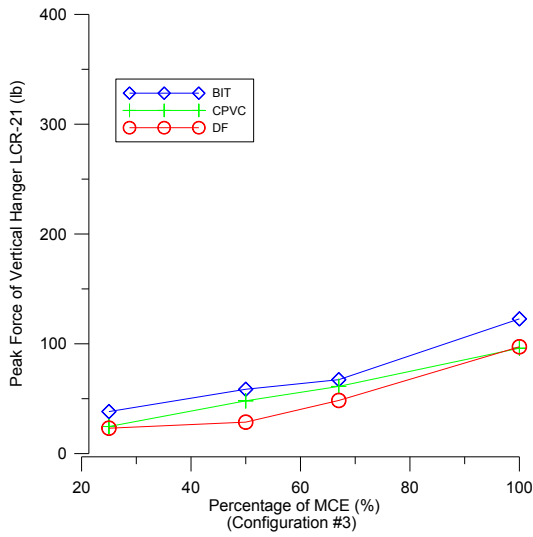
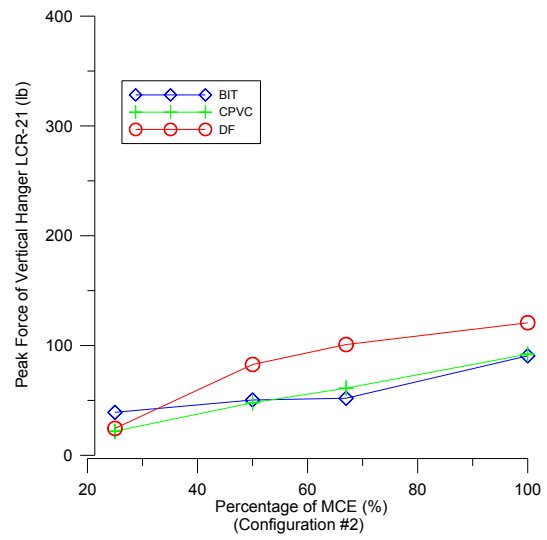
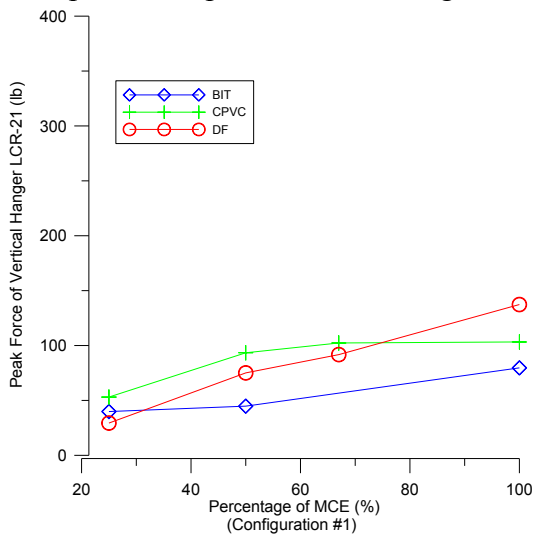
Comparison of peak force for hanger LCR-16 across materials



Comparison of peak force for hanger LCR-20 across materials



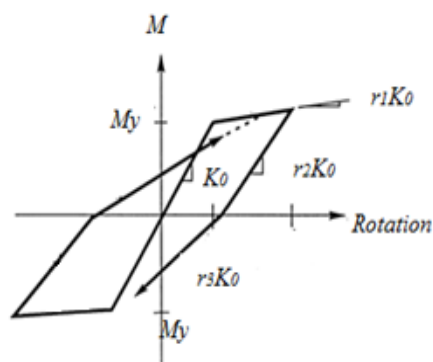
Comparison of peak force for hanger LCR-21 across materials



## APPENDIX C: OPTIMIZED PARAMETERS FOR NUMERICAL MODELS

The optimized parameters for the generic bilinear model are presented in the following table.

The optimizations for the Multi-linear Pivot model in SAP2000 and the Hysteretic material model in OpenSees were both developed based on the generic bilinear model.



Material and Joint Type	Nominal Pipe Size (in)	$M_y$ (kip-in)	$K_0$ (kip-in/rad)	$r_1$	$r_2$	$r_3$
Black Iron with Threaded Joints	6	162.76	77,877.0	0.200	1.220	0.006
	4	107.0	62,100.0	0.001	0.930	0.016
	2	18.0	5,070.0	0.050	0.98	0.460
	1	2.29	471.86	0.291	0.877	0.482
CPVC with Cement Joints	2	0.61	134.97	0.303	1.192	0.032
	1	0.54	12.35	1.092	2.574	0.004
	3/4	0.25	9.71	0.486	0.943	0.496
Schedule 10 Steel with Groove-Fit Connections	4	55.59	3,720.70	0.3804	4.036	0.001
	2	5.40	335.72	0.7459	2.2213	0.010

## Appendix C

Optimized parameters for the Hysteretic material model and the Pinching-4 material model in OpenSees

Material and Joint Type	s1p	e1p	s2p	e2p	s3p	e3p	s1n	e1n	s2n	e2n	s3n	e3n	pinchx
2" Sch. 40 black iron with threaded Connections	12.05	0.002199	19.35	0.005	21.77	0.00815	-12.05	-0.002199	-19.35	-0.005	-21.77	-0.00815	1.00
	pinchy	damage1	damage2	beta									
	1.00	0.00	0.00	0.24									
Material and Joint Type	s1p	e1p	s2p	e2p	s3p	e3p	s1n	e1n	s2n	e2n	s3n	e3n	pinchx
2" Sch. 40 CPVC with cement joints	0.1021	0.000133	2.04	0.04	2.11	0.08	-0.1021	-0.000133	-2.04	-0.04	-2.11	-0.08	0.00
	pinchy	damage1	damage2	beta									
	0.00	0.00	0.00	0.40									
Material and Joint Type	eP <sub>f1</sub>	eP <sub>f2</sub>	eP <sub>f3</sub>	eP <sub>f4</sub>	eP <sub>d1</sub>	eP <sub>d2</sub>	eP <sub>d3</sub>	eP <sub>d4</sub>	eN <sub>f1</sub>	eN <sub>f2</sub>	eN <sub>f3</sub>	eN <sub>f4</sub>	eN <sub>d1</sub>
4" Sch. 10 Steel with Groove-fit Connections	4.00	22.00	100.00	110.00	0.0002	0.0076	0.025	0.035	-4.00	-22.00	-100.00	-110.00	-0.0002
	eN <sub>d2</sub>	eN <sub>d3</sub>	eN <sub>d4</sub>	rDispP	rForceP	uForceP	rDispN	uForceN	gK <sub>1</sub>	gK <sub>2</sub>	gK <sub>3</sub>	gK <sub>4</sub>	gK <sub>Lim</sub>
	-0.0076	-0.025	-0.035	0.70	0.01	0.00	0.70	0.01	0.00	0.70	0.50	0.50	0.00
	gD <sub>1</sub>	gD <sub>2</sub>	gD <sub>3</sub>	gD <sub>4</sub>	gD <sub>Lim</sub>	gF <sub>1</sub>	gF <sub>2</sub>	gF <sub>3</sub>	gF <sub>4</sub>	gF <sub>Lim</sub>	gE	dmgType	
	0.05	0.05	0.05	0.05	0.00	0.05	0.05	0.05	0.05	0.05	0.00	10.00	cycle